P-Stereogenic ligands with the *tert*-butylmethylphosphine fragment. Coordination chemistry and catalysis of their organometallic complexes

Guillem Vázquez Bigas

Oligopeptides as highly versatile agents against copper-mediated oxidative stress and amyloid-β aggregation

Guillem Vázquez Bigas

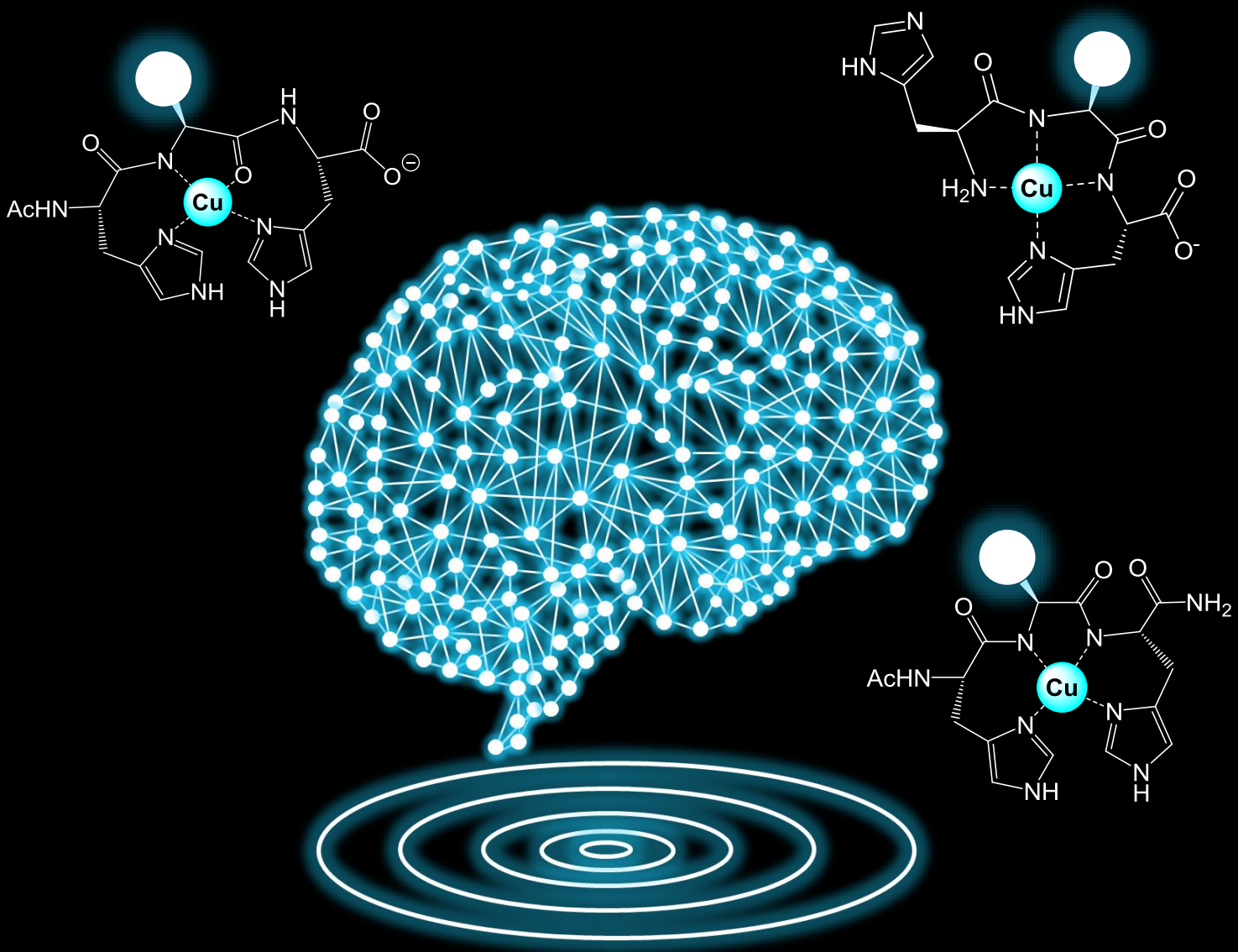

UNIVERSITAT DE BARCELONA

UNIVERSITAT DE BARCELONA

Facultat de Química

Departament de Química Inorgànica i Orgànica, Secció de Química Inorgànica

Programa de doctorat: Química Orgànica

Línia de recerca: Química biològica i química mèdica

Oligopeptides as highly versatile agents against copper-mediated oxidative stress and amyloid-β aggregation

Guillem Vázquez Bigas

2019

Grup de Química Bioinorgànica

Prof. Patrick Gamez Enamorado
Director i Tutor

Dra. Ana Belén Caballero Hernández
Codirectora

Patrick Gamez Enamorado, investigador ICREA Senior i professor associat del Departament de Química Inorgànica i Orgànica, Secció de Química Inorgànica, de la Universitat de Barcelona, i **Ana Belén Caballero Hernández**, professora associada del Departament de Química Inorgànica i Orgànica, Secció de Química Inorgànica, de la Universitat de Barcelona,

CERTIFIQUEN que el treball "**Oligopeptides as highly versatile agents against copper-mediated oxidative stress and amyloid-β aggregation**", que presenta Guillem Vázquez Bigas per optar al grau de Doctor, ha estat realitzat sota la seva direcció al Departament de Química Inorgànica i Orgànica, Secció de Química Inorgànica, de la Universitat de Barcelona.

Barcelona, febrer de 2019

Prof. Patrick Gamez Enamorado

Dra. Ana Belén Caballero Hernández

Patrick Gamez Enamorado, investigador ICREA Senior i professor associat del Departament de Química Inorgànica i Orgànica, Secció de Química Inorgànica, de la Universitat de Barcelona,

CERTIFICA que el treball "**Oligopeptides as highly versatile agents against copper-mediated oxidative stress and amyloid-β aggregation**", que presenta Guillem Vázquez Bigas per optar al grau de Doctor, ha estat realitzat sota la seva tutela al Departament de Química Inorgànica i Orgànica, Secció de Química Inorgànica, de la Universitat de Barcelona.

Barcelona, febrer de 2019

Prof. Patrick Gamez Enamorado

"That process," said I, "starts upon the supposition that when you have eliminated all which is impossible, then whatever remains, however improbable, must be the truth."

Sherlock Holmes

The Adventure of the Blanched Soldier, 1926 (Sir Arthur Conan Doyle)

Dedicat als meus avis: la "Domi", el Lluís i, en especial, la Celia.

Agraïments

És possible que no sigui la persona a qui li sigui més fàcil expressar els seus sentiments i afectes, cosa que no significa de cap manera que no senti d'una manera molt intensa. Escriure-ho, des de la perspectiva (però tenint molt present el sentiment que hi ha darrere), és força més senzill. Per tant, m'he pres aquesta secció d'agraïments com una oportunitat per manifestar el que penso i sento envers algunes persones que per a mi són o han sigut importants. No obstant, també és un recull (francament desordenat, però que d'aquesta manera forma un tot que per a mi té una càrrega emocional molt forta) de diversos records i vivències que em venen al cap quan penso en com han sigut aquests anys al Departament/Secció de Química Inorgànica.

Evidentment, en el temps que dura el desenvolupament d'una tesi doctoral es viuen molt moments difícils. No em dignaré a dedicar-hi gaire més que aquestes línies. Aquesta secció és només per fer un petit reconeixement a aquelles persones que, d'alguna manera, m'han marcat durant aquests anys.

Dit això, vull mostrar el meu agraïment més sincer:

Al Patrick que, quan no em coneixia ni sabia res de mi, va decidir donar-me la seva confiança, i que em va donar l'oportunitat no només de formar part del Grup de Química Bioinorgànica i de realitzar aquesta tesi doctoral, sinó també d'assistir a molts congressos, on he pogut conèixer molta gent i aprendre quina recerca es realitza a nivell espanyol i europeu; i a l'Ana, amb la seva energia il·limitada, que sempre està disposada a donar un cop de mà encara que tingui a vuit alumnes fent cua per demanar-li ajuda, i que sempre ha tingut algun consell quan m'he trobat encallat. Els dos han sigut més que uns directors de tesi.

A l'Ernesto, a qui vaig conèixer com a professor de Química Bàsica I, i que ha sigut el meu guia en la síntesi de pèptids; al Raimon, que ha aportat un enfoc diferent i la seva inestimable experiència amb la β-amiloide; i als doctors Arnau Hervera i José Antonio del Río, del grup de Neurobiotecnologia Molecular i Cel·lular, pels estudis de citotoxicitat de les nanopartícules d'or.

A la família Bioinorgànica: a la Rosa, la mamà Brissos, posseïdora d'una imaginació desbordant que viatja a una velocitat inassumible per a la resta dels mortals, però també la personificació de l'abnegació, una dona que no escatima energies a l'hora d'ajudar els altres, quan penso com vull ser com a persona em ve ella al cap; l'Andreu,

la reencarnació del *grumpy cat* a la superfície, una gran i brillant persona amagada a sota, va ser el meu mestre durant el Màster; a la Laia, que va fer un gran treball amb els pèptids ATCUN, i al Jordi (Molas), el meu company de primer de carrera, que van donar molt de caliu al grup; al Jordi (Grau), una aparició fugaç durant la setmana, però que sempre deixa petja amb el seu particular humor; la Marta, sempre encantadora, sempre positiva; a la Neus, amb qui comentava els llibres que anàvem llegint; a l'Amparo, la botànica del grup; a la Valentina, pura passió siciliana; i ala Francesca, que després d'una mala sort que semblava inacabable, va veure el seu esforç recompensat.

També als estudiants estrangers, tota una constel·lació de nacionalitats, com el James, l'Annie, la Valentina, l'Iza, el Jakub, la Taru, la Helen, l'Alyson, el Nils, el Tommy, el Víctor, la Susan, la Nora, el Josemarco, l'Alina, el Harry, l'Ailsa o el Marcos. Sempre és d'agrair estar en contacte amb diferents cultures i formes de pensar, però avui en dia més que mai. I que contents estan tots de ser a Barcelona!

Al Fran, el químic-submarinista-bomber-pilot d'avionetes-cinèfil-cinturó negre de taekwondo-manetes-geni del mal... podria allargar-me més que amb la tesi en si; a la Lídia, la *senyo*, futbolista, dona del temps, "madre de gatos"; a la Berta, que és, i sempre serà, del Poblenou, (o sigui, sublim); a la Bet la princesa del pèsol, una metàfora que la vida cal viure-la intensament i que dels problemes i les preocupacions ja ens n'encarregarem a la propera, si cal; al Ferran que les poques vegades que el veig o que fem Skype me n'adono de quant el trobo a faltar. Amb ben poca gent he connectat i compartit (amb tot el significat que puc donar a aquesta paraula, i qui em conegui una mica podrà entendre de què parlo) tant com amb vosaltres.

A la Raquel, sempre plena d'energia positiva, i al Diego, el català de Salamanca. Tant de bo s'haguessin pogut quedar els dos a Barcelona.

Als meus "nens", en especial a la Macarena, la Marta, i la Carol, que van treballar més estretament amb mi en la síntesi de pèptids, però també a l'Hélder, la Isabel, la Jennifer i l'Adam; jo els hi vaig ensenyar el que vaig poder i ells a mi em van ensenyar moltíssim. Que ràpid que creixen.

Als companys del Departament/Secció de Química Orgànica: a la Blanca, amb qui vaig passar divertidíssimes hores d'"anenia" col·lectiva; a la Roser, "la jefa", no sé per què alguns pensaven que era l'Ariza qui manava al lab; a la Sadurnina, que ens va fer a tots dels Castellers de Vilafranca; al Stuart, amb qui vaig comentar els partits de la NBA al més alt nivell professional; a l'Ari, que sempre s'aturava per a interessar-se en com

m'anava, tot i anar permanentment atabalada; i a la Cristinita, aquelles amargues tardes amb l'HPLC van ser molt més curtes mentre parlàvem de tot una mica (per exemple, de les seves maleïdes corbes de calibratge amb R^2 = 0,9999(9)). Tots ells em van fer sentir molt còmode en un departament nou per a mi i, a més, als inicis de la tesi (doble mèrit, per tant).

A l'Andrea, fins i tot el Clot sembla un lloc alegre amb ella; al Raúl, el "ceniciento sueco", un dels pares fundadors del Masterchef Inorgànica; a la Rosa, l'artista, el talent, l'admiro i l'odio a parts iguals per aquest motiu; a la Beltzane, la senyora Potato, pura energia concentrada, i de la mateixa escola que la Rosa; al Pau, el geni del bàsquet, l'ídol de les nenes (i d'uns quants nens) de pràctiques; a la Mariona, que sempre riu quan li dic la immensa xorrada que quantes cabres té al lavabo i em convida a casa seva a comprovar que cap, en comptes d'engegar-me a pastar; al David, capaç d'animar qui sigui i de convèncer-lo per sortir de festa; a l'Arnald, que juntament amb el Fran, em va introduir a les mítiques sessions de pel·lícules dolentes (gràcies, crec).

A la Marta, la Saskia, el Pato, l'Albert i l'Alberto, que van omplir de diversió i bogeria (fins i tot per als estàndards d'un departament de química inorgànica) aquelles vibrants nits de divendres.

A l'Ana, la Cristina i la Teresa, les "tres bessones", que diàriament ens treuen un somriure a tots i que, no sé com s'ho fan, però sempre aconsegueixen ser les més divertides als vídeos de les tesis.

Als meus germans no de sang: el Sergi, el Víctor, la Carol, el Cristian, la Laia, la Patri, la Nere, l'Adri i l'Iván. I als qui els aguanten a diari, per tant família també: la Neus, l'Aitor, el Henry, el Jona, l'Alejandra i l'Ana. Que els anys de jocs no acabin mai.

A la Laila i la Nica, que tot i que ja fa molt que vam sortir de l'institut i que van haver de marxar per guanyar-se la vida, encara troben temps per veure'ns de tant en tant. A la Irina i la seva fe incondicional en què jo valia per al món docent i investigador. A l'Ainoa, l'Andrea i l'Ari, que sé que farien qualsevol cosa per l'Ana, i que em van acceptar al seu grup des del primer moment; amb elles mai m'avorreixo.

També vull aprofitar per donar les gràcies a les meves professores de Química de l'escola i el batxillerat, que van decantar una balança on també hi havia la Física: a l'Anna, amb el seu tracte tan proper als alumnes i una habilitat com la de cap altre per despertar l'interès; i a la Carme, que va saber alimentar aquesta competitivitat que per

a mi sempre ha sigut inseparable dels estudis. Dues professores diferents de la resta. Si no fos per elles, aquesta tesi (que com a mínim té el valor de ser important per a mi) molt probablement no existiria.

A l'Ana, la meva companya de viatge, que vas aparèixer en un moment complicat i vas posar la meva vida cap per avall (cap amunt, més aviat); tu m'has fet millor i més feliç. Tinc molt, moltíssim que agrair-te. Això no ha fet més que començar.

Als meus pares Dante i Isabel i a la meva germana Hebe, que sempre m'han donat suport en tot allò que he fet i, potser el més important, m'han donat plena llibertat en les decisions que he pres, sense empènyer-me en cap direcció. Al Sergio, l'Olga, la Maite, la Laura, el Míguel, el Chus, el Martín i la Gloria; tot i que ens veiem poc sovint, els tinc constantment presents. Finalment, als meus avis Lluís i Celia, que em van criar com uns segons pares, i la Vicenta (la Domi), a qui no vaig arribar a conèixer del tot per culpa d'una malaltia semblant a la tractada en aquest treball, però a qui recordo amb molt d'afecte. No es pot demanar una família millor.

A tots vosaltres, que us vagi tot molt bé. Més que un desig, és una petició. Si us plau, que us vagi sempre tot molt bé. Perquè si jo soc com soc, és per (i vull pensar que gràcies a) tots vosaltres.

Un dia, una habitació.

Parts of this PhD thesis can be found in the following publication:

'Histidine-Rich Oligopeptides To Lessen Copper-Mediated Amyloid-β Toxicity'

Ana Belén Caballero, Laia Terol-Ordaz, Alba Espargaró, Guillem Vázquez, Ernesto Nicolás, Raimon Sabaté and Patrick Gamez.

Chem. Eur. J. **2016**, *22*, 7268-7280.

Index

Abstract

Alzheimer's disease (AD) is currently the most prevalent cause of dementia for people aged 60 and over, with more than 35 million patients worldwide. This number is expected to massively increase within the next years; therefore, there is an urgent necessity to find effective treatments and improved diagnostic techniques for this, to date, incurable pathology. Although the origin of the disease is still a matter of intense debate, the amyloid cascade hypothesis has reached general acceptance. According to this hypothesis, the aberrant aggregation of β-amyloid (Aβ), a 39-43 amino acid peptide, is believed to trigger the events leading to AD. Fibrillary aggregates of Aβ(1-40) and Aβ(1-42) represent the major components of the senile plaques found in AD brains. However, oligomeric aggregates rather than fibres are currently considered to be the most toxic species since they hinder the synaptic function, disrupt the integrity of membrane bilayers and generate reactive oxygen species (ROS).

An increasing body of evidence indicates that AD brains present unbalanced levels of some metal ions such as Cu(I/II), Zn(II) and Fe(II/III). Furthermore, high concentrations of copper and zinc have been detected in senile plaques. Aβ has indeed been found to bind such metal ions, modulating its aggregation through rapidly exchangeable coordination modes. Among them, copper has been reported to stabilise toxic oligomeric species and to catalyse the generation of ROS. Hence, preventing the copper-associated toxicity of Aβ may represent a promising approach to develop anti-AD agents. However, the role of metal ions at the origin and expansion of the pathology has not been extensively explored. Some 8-hydroxyquinolines, such as clioquinol and PBT2, have recently shown promising results in clinical trials. This class of compounds, which have been called metal-protein attenuating compounds (MPACs), are intended to redistribute mis-localised metal ions. MPACs exhibit moderate Cu(II)- and Zn(II)-binding affinities, are able to cross the blood-brain barrier (BBB) and can prevent the copper-catalysed production of ROS.

The imidazole rings of histidine residues are efficient Cu(II)-ligands and histidinic peptides hence represent valuable synthons for the discovery of new drugs aimed at reducing the copper-associated toxicity of Aβ. Peptides present high biocompatibility, low toxicity and water solubility; furthermore, they display a great versatility and their Cu(II)-chelating properties can be easily tuned. In our group, the Cu(II)-chelating properties of peptides with different sequences have been studied, and those with the sequence His-Xaa-His (Xaa = randomly-chosen amino acid) have led to interesting

results. In the present PhD thesis, short peptides (containing 3-4 L-amino acids) with the *N*-terminal His-Xaa-His sequence were rationally designed to be applied in *i)* the chelation and detection of copper ions, *ii)* their grafting onto gold nanocarriers to improve their pharmacological properties and *iii)* the detection of Aβ aggregates. Chapter 1 comprises a detailed introduction on the state-of-the-art in the field and the description of the objectives of the present work.

As described in Chapter 2, the peptides were either custom-made or prepared by Fmoc solid-phase peptide synthesis (SPPS). The chelating agents contained indole (tryptophan residue), coumarin (Coum), 4-*N,N*-dimethylamino-1,8-naphthalimide (4DMN) or fluorescein emissive probes for their application as fluorescent sensors. The non-natural probes were incorporated either by derivatisation of Fmoc-Lys-OH or by labelling the preformed peptide. Some of the peptides had their *N*-terminal amino function or both the *N*-terminal amino and *C*-terminal carboxylate groups protected as amides.

In Chapter 3, the evaluation of the Cu(II)-binding properties of the His-Xaa-His tripeptides is reported, which was evaluated by mass spectrometry (MS), UV-Vis spectroscopy, circular dichroism (CD), electron paramagnetic resonance (EPR) and nuclear magnetic resonance (NMR). Besides, the Cu(II)-binding affinities were determined by fluorescence spectroscopy. The *N*-terminal free peptides presented a 4N albumin-like ATCUN coordination donor set, and were able to remove Cu(II) ions bound to Aβ(1-16), and to inhibit the copper-induced stabilisation of oligomeric Aβ species and the generation of ROS. The *N*-terminal protected peptides acted as a different donor set, namely 3N1O, which involves the two imidazole rings; these peptides were less effective than the ATCUN ones regarding their inhibition of the Cu-induced production of ROS.

The fluorescent properties of a peptide containing the (potential) Förster resonance energy transfer (FRET) coumarin-fluorescein pair were investigated in the presence and absence of Cu(II) ions. Unfortunately, the emission of the coumarin probe was remarkably lower than that of fluorescein and the occurrence of a FRET process could not be confirmed. Nonetheless, the coumarin-fluorescein intensity ratio increased with the concentration of Cu(II), which might be exploited for the ratiometric detection of this metal ion.

In Chapter 4, the generation of Aβ(1-40) dityrosine cross-links in the presence of copper(II) and H_2O_2 is described. Aβ dityrosine cross-links are created through the formation of an ortho-ortho C-C bond between two Tyr10 residues. Dityrosine-bridged Aβ dimers have been found in AD brains, where they are believed to display an intense Cu-induced redox activity within prolonged periods of time. Besides, they have been proposed as initiators of Aβ aggregation. Dityrosine was prepared using horseradish peroxidase in the presence of H_2O_2; it was subsequently used as a reference compound to quantify, by fluorescence spectroscopy, the formation of dityrosine cross-links in Aβ(1-40). Hence, the aggregation of Aβ(1-40) under various oxidative conditions was analysed by fluorescence spectroscopy and transmission electron microscopy (TEM). Dityrosine-cross-linked Aβ(1-40) did not lead to the formation of fibres, while the addition of an ATCUN peptide restored the fibrillation process.

Chapter 5 describes the preparation of monodisperse suspensions of spherical gold nanoparticles (of size 5 and 15 nm) with the objective to use them as peptide-nanocarriers. These Au NPs were functionalised with HS-PEG_{2100}-COOH (PEG = poly(ethylene glycol)) to improve their stability and resistance against particle aggregation. The Cu(II)-chelating peptide Ac-His-Lys(Coum)-His-Lys-NH_2 was grafted onto the surface of the PEGylated gold nanoparticles through its Lys4 side chain, by means of an amide bond. The nanoparticles were characterised by TEM, UV-Vis spectroscopy, thermogravimetric analysis (TGA), dynamic light scattering (DLS), Z-potential measurements and agarose gel electrophoresis. The amount of peptide coupled was quantified by fluorescence spectroscopy. The peptide-functionalised Au NPs were able to (partially) extract Cu(II) ions bound to Aβ(1-16). Ac-His-Lys(Coum)-His-OH and nanoparticles of 15 nm, containing or not the peptide, were non-toxic to neuronal embryo cells of wildtype mice.

In Chapter 6, the design and preparation of fluorescent dyes to detect aggregated Aβ are reported. An analogue of thioflavin T (ThT, an amyloid-selective fluorescent dye) and its lysine derivative, which would allow its inclusion into peptides, were prepared by click chemistry. Unfortunately, spectroscopic changes did not take place upon interaction with fibrillary Aβ. The environment-sensitive properties of a naphthalimide derivative (4DMN), whose fluorescent emission is blue-shifted and enhanced as the polarity of the solvent decreases, were then exploited for the detection of different types of Aβ aggregates. The emission of Boc-Lys(4DMN)-OH and 4DMN-containing peptides displayed hypsochromism and intensity enhancements in the presence of Aβ

fibres, which allowed to monitor Aβ aggregation; the 4DMN peptides also detected Cu(II)- and Zn(II)-induced Aβ aggregates. The presence of the peptides did not alter Aβ aggregation as evidenced by ThT experiments; the 4DMN-containing peptides may thus be used as bimodal probes for the detection of different types of Aβ aggregates.

The promising results achieved during this doctoral research validate the proposed approach to use His-containing Cu(II)-chelating peptides to reduce the copper-induced production of ROS and the generation of oligomeric Aβ *in vitro*. Furthermore, the incorporation of functional fluorescent probes to these peptides allows to *i)* monitor the Cu(II)-binding process and *ii)* detect aggregated species of Aβ. Hence, such Cu(II)-chelating peptides may find applications in therapy, diagnosis, and theranosis of AD.

Acronyms and abbreviations

2-CTC	2-chlorotrityl chloride
4DAPA	4-*N,N*-dimethylaminophthalimidoalanine
4DMAP	4-*N,N*-dimethylaminophthalimide
6DMN	6-*N,N*-dimethylamino-2,3-naphthalimide
6DMNA	6-*N,N*-dimethylamino-2,3-naphthalimidoalanine
4DMN	4-*N,N*-dimethylamino-1,8-naphthalimide
4DMNA	4-*N,N*-dimethylamino-1,8-naphthalimidoalanine
AD	Alzheimer's disease
AFM	atomic force microscopy
ALADAN	6-(2-dimethylaminonaphthoyl) alanine
alloc	allyloxycarbonyl
APLP2	amyloid-like protein 2
apoE	apolipoprotein E
APP	amyloid precursor protein
ATCUN	amino terminal Cu(II)- and Ni(II)-binding motif
A. U.	arbitrary units
BBB	blood-brain barrier
Boc	*tert*-butoxycarbonyl
Bzl	benzyl
BzTz	1-(benzo[*d*]thiazol-2-yl)-1*H*-1,2,3-triazole-4-carboxylic acid
CD	circular dichroism
COSY	correlation spectroscopy

CSF	cerebrospinal fluid
CuAAC	Cu(I)-catalysed alkyne-azide cycloadditions
Coum	coumarin-3-ylcarbonyl
DANA	6-(2-dimethylaminonaphthoyl)alanine
DCC	*N,N'*-dicyclohexylcarbodiimide
DCM	dichloromethane
DIC	*N,N'*-dicyclopropylcarbodiimide
DIPEA	*N,N*-diisopropylethylamine
DKP	2,5-diketopiperazine
DLS	dynamic light scattering
DMF	*N,N*-dimethylformamide
DMSO	dimethylsulfoxide
DOPA	3,4-dihydroxyphenylalanine
DVLO	Derjaguin-Verwey-Landau-Overbeek
EDC	1-(3-dimethylaminopropyl)-3-ethylcarbodiimide
EPR	electron paramagnetic resonance **or** enhanced permeation and retention
ESI	electrospray ionisation
EXAFS	extended X-ray absorption fine structure
FDA	Food and Drug Administration
Fluo	5(6)-carboxyfluorescein
Fmoc	9-fluorenylmethoxycarbonyl
FRET	Förster resonance energy transfer

HIV	human immunodeficiency virus
HOAt	1-hydroxy-7-azabenzotriazole
HATU	*N*-[(dimethylamino)-1*H*-1,2,3-triazolo-[4,5-*b*]pyridin-1-ylmethylene]-*N*-methylmethanaminium hexafluorophosphate *N*-oxide
HBTU	*O*-(benzotriazol-1-yl)-*N,N,N′,N′*-tetramethyluronium hexafluorophosphate
HCTU	*O*-(6-chlorobenzotriazole-1-yl)-*N,N,N′,N′*-tetramethyluronium hexafluorophosphate
HD	Huntington's disease
HEPES	*N*-2-hydroxyethylpiperazine-*N*-2-ethanesulfonic acid
HFIP	1,1,1,3,3,3-hexafluoro-2-propanol
HMBC	heteronuclear multiple bond correlation
HOBt	1-hydroxybenzotriazole
HPLC	high-performance liquid chromatography
HRP	horseradish peroxidase
HSQC	heteronuclear single quantum coherence
IR	infrared
ITC	isothermal calorimetry
LRP1	low-density lipoprotein receptor-related protein 1
MCO	metal-catalysed oxidation
MEF	murine embryonic fibroblast
MPAC	metal-protein attenuating compounds
MS	mass spectrometry
NAdT	*N*-acetyldityrosine

NFT	neurofibrillary tangle
NIR	near infrared
NMR	nuclear magnetic resonance
NP	nanoparticle
Oxyma	ethyl 2-cyano-2-(hydroxyimino)acetate
PBS	phosphate buffered saline
PBT2	2-(dimethylamino)methyl-5,7-dichloro-8-hydroxyquinoline
PD	Parkinson's disease
PDI	polydispersity index
PEG	poly(ethylene glycol)
PET	positron emission tomography
PG	protecting group
PiB	Pittsburgh compound B
PRODAN	6-propionyl-2-(dimethylamino)naphthalene
PyAOP	(7-azabenzotriazol-1-yloxy)tripyrrolidinophosphonium hexafluorophosphate
PyBOP	(benzotriazol-1-yloxy)tripyrrolidinophosphonium hexafluorophosphate
RA AM	Rink amide aminomethyl
R_f	retention factor
RhoB	rhodamine B isothiocyanate
ROS	reactive oxygen species
rt	room temperature
SDS	sodium dodecyl sulphate

S_N1	unimolecular nucleophilic substitution
SOD	superoxide dismutase
SPECT	single-photon emission computed tomography
SPPS	solid phase peptide synthesis
spr	surface plasmon resonance
tBu	*tert*-butyl
TEM	transmission electron microscopy
TFA	trifluoroacetic acid
TGA	thermogravimetric analysis
THF	tetrahydrofuran
ThT	thioflavin T
TIPS	triisopropylsilane
TIRFM	total internal reflection fluorescence microscopy
TLC	thin-layer chromatography
TMS	tetramethylsilane
TNF	tumour necrosis factor
TSP	[D_4]-3-(trimethylsilyl)propanoic acid
t_R	retention time
Tris	tris(hydroxymethyl)aminomethane
UV	ultraviolet
Vis	visible
WHO	World Health Organization
XANES	X-ray absorption near-edge spectroscopy

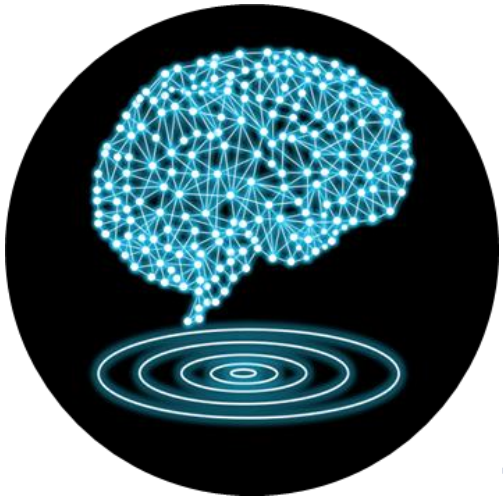

1. Introduction

1. Introduction

1.1 Alzheimer's disease: Figures and facts

Alzheimer's disease (AD), a lethal neurodegenerative pathology, is currently the most common cause of dementia in the adult population. The most important symptoms exhibited by patients are memory loss, cognitive decline, mood changes and difficulty in remembering new information. Such disturbances are related to the injury and death of neurons, which begin at the hippocampus, the area of the brain involved in memory and learning.[1,2] It must be differentiated from cognitive decline naturally associated with aging, which develops gradually and presents less severe symptoms.[3] AD primarily affects people aged over 65, and women present a higher risk of developing the disease (approximately two thirds of the AD patients worldwide are women). Moreover, no effective treatment is known yet.

According to the World Health Organization (WHO) and Alzheimer's Disease International (ADI), about 35.6 million people throughout the world suffered from dementia in 2010, an amount that is expected to increase to 74.7 million in 2030 and 131.5 million in 2050 as elderly population continues to grow; one new case of AD was diagnosed around the world every 3 seconds in 2015.[1,2,4] Much of this increase is expected to occur in low and middle income countries: 58% of the people suffering from dementia lived in such countries in 2015, a number which will rise to 63% in 2030 and to 68% in 2050.[4]

Figure 1.1 shows the estimated number of people living with dementia in each continent in 2015.[4] In Europe, the number of people suffering from dementia in 2015 was estimated to 10.5 million cases and is forecasted to rise to 14 million by 2030.[4]

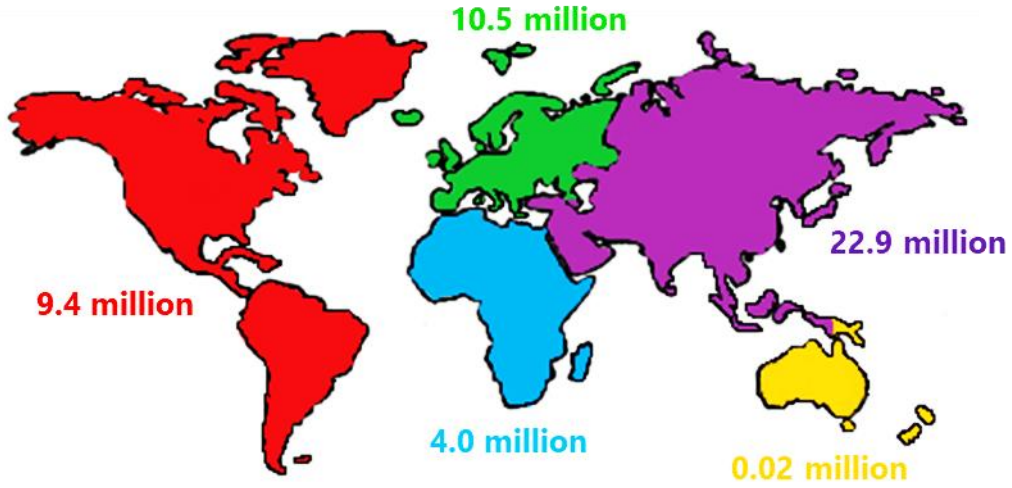

Figure 1.1: Estimated number of people living with dementia in each continent in 2015.[4]

Taking these figures into account, it is not surprising that dementia (and especially Alzheimer's disease) causes a massive socio-economic impact, hence putting the health-care system into increasing pressure. The cost of dementia in 2018 was estimated to be 1 trillion US dollars and is projected to increase to 2 trillion by 2030.[4] More specifically, AD costs the world over 600 billion US dollars per year, while the annual cost in Europe is projected to reach 250 billion euros in 2030.[1,2]

As far as diagnosis is concerned, the advent of the disease is thought to occur 20-30 years before the first detectable psychological symptoms appear.[3,5-8] Despite the existence of some biomarkers of the pathology, the diagnosis cannot be definitively confirmed until post-mortem autopsy by examining brain tissue.[3,5,6] Thus, it is necessary to develop new diagnostic techniques for the early stage of the disease, when therapeutic treatments are likely to be more efficient.

It is currently believed that the vast majority of AD cases are not genetically inherited and are usually called sporadic. Most of them are late-onset AD cases, presenting their onset over the age of 60 years old. Genetic cases, also termed familial, are heterogeneous in their origin and are estimated to represent 0.1-1% of total AD cases.[9-12] Most familial cases are early-onset AD, some people presenting advent of the disease as early as 30-40 years old. The presence of some alleles is considered a risk factor. However, it is remarkably difficult to determine the actual contribution of genetic factors, especially taking into account that sporadic and familial AD show indistinguishable symptoms.[9]

Since genetic factors are believed to account for a small number of AD cases, it has been hypothesised that certain environmental factors might be decisive in the occurrence of the disease. Nonetheless, prevention trials are so far scarce and many of them recruited elder volunteers, in which preventive strategies would probably come too late to show clear effects.[2] Accumulating evidence is however pointing towards some risk as well as protective factors.[1,2,13] For example, regular physical activity, education and a healthy diet (Mediterranean diet is usually remarked) have been underscored as decreasing the risk of suffering AD, whereas some pre-existing pathologies (such as cardiovascular diseases or type II diabetes), depression or obesity have been associated with increased risk of AD. In contrast, occupational exposures showed no relationship, either positive or negative, with AD, including exposures to low electromagnetic fields, solvents, pesticides or aluminium.[13]

In summary, AD represents a titanic challenge which requires the collaboration of highly skilled professionals of a very wide range of scientific fields. Transversal works have indeed produced the major advances in the understanding of the pathology in the last three decades. Hence, despite the daunting complexity of AD, the growing knowledge of how such a devastating disease originates from should be received with optimism by scientists and spur further fundamental research, as the elucidation of its mechanistic features has led to the rational development of, by far, the most promising anti-AD strategies.

1.2 AD's aetiology

The German psychiatrist Alois Alzheimer, after whom the disease is named, was the first to describe the symptoms and study post mortem brains of affected patients in 1906. In his observations, he described the two distinct hallmarks which are present in AD brain tissues: intracellular neurofibrillary tangles and extracellular senile plaques.

- Intracellular neurofibrillary tangles (NFTs). NFTs are mainly composed of an abnormally hyperphosphorylated form of the microtubule-associated protein tau, a 352-441 amino-acid residues protein involved in cell polarity, intracellular transport and neurite outgrowth.[9,14,15] This highly hydrophilic protein contains an acidic *N*-terminal domain and two basic domains. Besides, it presents many sites susceptible to

phosphorylation such as serine and threonine residues. Specifically, phosphorylation of Ser214 or Ser262 leads to the dissociation of the protein from the microtubules and its precipitation into NFTs in AD. The presence of NFTs has been correlated with the severity of dementia and neuronal loss.[14]

- Extracellular senile plaques. The major component of senile plaques, which are also found in Down syndrome individuals, are aggregated species of a peptide called amyloid-β or simply Aβ, usually in the form of fibrils.[12] This 39-43 amino acid peptide is ubiquitous in the body but aggregated forms are only found in the brain, and its role in the organism is unknown.[16,17] The most common forms of Aβ peptide are Aβ(1-40) and Aβ(1-42), the latter being the most prone to aggregate. Aβ encompasses a hydrophilic *N*-terminus domain (1-28), responsible of the interaction with certain metal ions such as Cu(II) and Zn(II), and a hydrophobic *C*-terminal domain (29-43), responsible of the intermolecular interactions that ultimately lead to the aggregation of the protein.[18]

Despite these observations and all the effort, time and resources invested in the study of AD during the last decades, its aetiology remains unclear due to the high complexity of the processes that are involved and their slow progression over decades. However, it is mostly accepted that aggregated Aβ has a causative role in the disease; it is the so-called **Amyloid cascade hypothesis**.[9,12,15,19] According to this concept, the neuropathological events that culminate in the clinical manifestation of AD are downstream to the aggregation processes of the Aβ peptide. The amyloid cascade hypothesis is mainly supported by the following two arguments:

***i)* Aβ species seem to induce NFT formation.** Lewis and Dickson reported that double-mutant mice expressing both tau protein and Aβ peptide showed higher NFT levels compared to those expressing only tau, but Aβ levels were similar to those for mice expressing only Aβ.[20] Similarly, Götz and co-workers found that mutant tau transgenic mice injected with Aβ fibrils contained 5-fold increased NFT levels in amygdala, while Jin and Selkoe obtained comparable results using Aβ dimers directly extracted from AD brains.[21,22] Conversely, Roberson and Mucke reported that reduction of endogenous tau did not alter Aβ levels in mice.[23] Therefore, Aβ species are thought to induce the formation of NFTs, although little is known about the mechanism of this interaction. It is hypothesised that it might involve disturbances in calcium homeostasis, inflammation and oxidative stress.[7]

***ii)* Mutations that enhance the production of Aβ peptide cause familial AD.** Several forms of familial AD have been associated with mutations of proteins implicated in either increased production or increased aggregation of Aβ peptide.[9,11,17] Mutations of the amyloid-precursor protein (**APP**), the protein from which Aβ peptide is cleaved, have been found in chromosome 21 of some families affected of hereditary AD, especially for early-onset variants.[24] The apolipoprotein E (**apoE**) allele ε4, located in chromosome 19, is implicated in late-onset and sporadic forms of AD, where enhanced Aβ deposition has been detected.[25] The apoE protein avidly binds Aβ and has been found surrounding amyloid plaques. Finally, mutations in presenilins, *viz.* proteins involved in the processing of Aβ from the APP, have been associated with 70% of early-onset autosomal dominant AD cases, including the most aggressive forms of early-onset AD.[26] In such cases, elevated Aβ(1-42) levels have been found.[10,17]

Accordingly, most researchers focused on Aβ peptide as the putative root of AD, since this peptide is believed to trigger the cascade of aberrant processes that cause this devastating disease. In line with this hypothesis, Aβ peptide is considered the main potential therapeutic target of this disease in the present PhD work.

1.3 The Aβ peptide

1.3.1 Production, structure and self-assembly of Aβ peptides

As aforementioned, Aβ peptides are fragments of the amyloid-precursor protein (APP). APP is a ubiquitous, highly-conserved, multi-domain transmembrane protein encompassing 751/770 amino acid residues, although neurons mostly express a 695-residue isoform.[10,17] This protein is present in the plasma membrane as well as in the membranes of the Golgi and endoplasmic reticulum. Despite its wide expression, the function of APP remains unknown. Suppression of APP expression did not lead to serious health problems in mice, probably due to the presence of other highly homologous proteins.

α-, β- and γ- secretases promote the cleavage of Aβ from APP and its release into the cerebrospinal fluid (CSF), which is the fluid surrounding the brain and the spinal cord.[9,10,17] The amyloidogenic processing of APP is carried out by β-secretase (also

called BACE1), which cleaves the peptide fragment at the *N*-terminal Aβ domain (Asp1), and γ-secretases, which cleave APP at the Aβ *C*-terminus (**Figure 1.2**). γ-secretases can cleave APP between Val40 and Ile41, thus generating Aβ(1-40), or between Ala42 and Thr43, hence producing Aβ(1-42). Aβ(1-40) is the most abundant fragment; it is produced 10-fold more than Aβ(1-42), which is more prone to aggregate and is thus considered more toxic.[10,12] In contrast, α-secretase cleaves APP between Lys16 and Leu17 and generates the non-aggregating fragment Aβ(1-16).

Figure 1.2: APP domain containing the different fragments of the Aβ peptide.

Aβ peptide is an intrinsically disordered peptide, that is, it lacks a well-defined 3D structure.[18,19,27] In aqueous solution, Aβ adopts a random coil conformation, although it presents a considerable degree of α-helicity in hydrophobic environments. Thus, the protein presents a high number of conformations, which co-exist in fast equilibria with very similar energies.

The aggregation of Aβ peptide into mature fibres, which are found in senile plaques, occurs in several steps and involves a number of intermediates, usually classified as soluble oligomers and protofibrils (**Figure 1.3**).[18,28] In classical peptide aggregation, prior monomer destabilisation must take place. However, this is not necessary for Aβ since it is an intrinsically disordered peptide.

In a first step, monomeric Aβ self-assembles into oligomeric species (dimers, trimers, tetramers...). Oligomers are defined as the species that remain in the supernatant following centrifugation at 100000 × *g*; they are structurally very diverse and present different degrees of order.[29] The formation of these oligomers is thermodynamically unfavourable due to the associated entropy decrease. Therefore, their generation represents the rate-limiting step in the aggregation process, which is thus illustrated by the presence of a lag time.[30] Oligomers appear to serve as seeds for the fibrillation process (nucleation phase), although it remains unclear if some oligomeric species might be off-pathway intermediates, hence not resulting in fibril formation.[31]

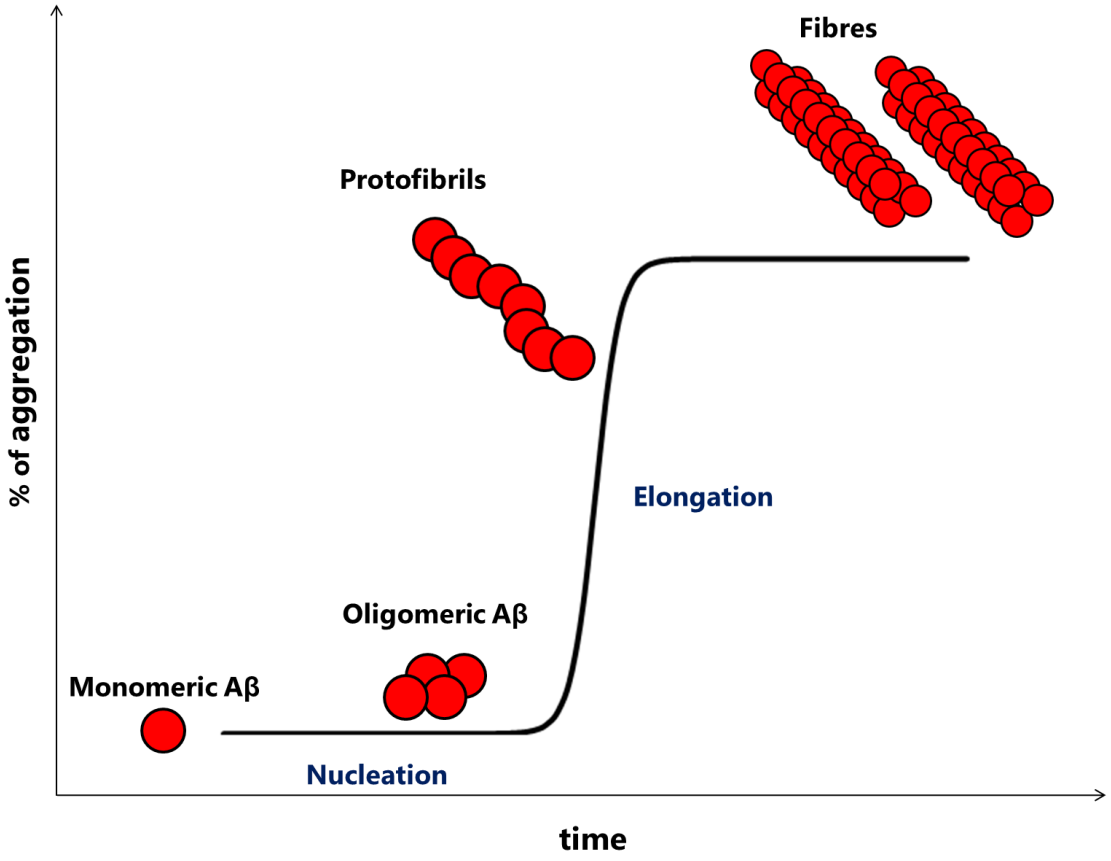

Figure 1.3: Aggregation steps of Aβ peptide.

Once a critical number of nuclei are formed, they template the addition of further monomeric or oligomeric Aβ resulting in an abrupt acceleration of the formation of fibres (elongation phase).[32] A typical sigmoidal curve characterises the aggregation progression. Intermediate species termed protofibrils are generated, which are progressively enriched with β-sheets. Such protofibrils are believed to suffer fragmentation, hence providing further seeds for the formation of fibres and the acceleration of the process.[33]

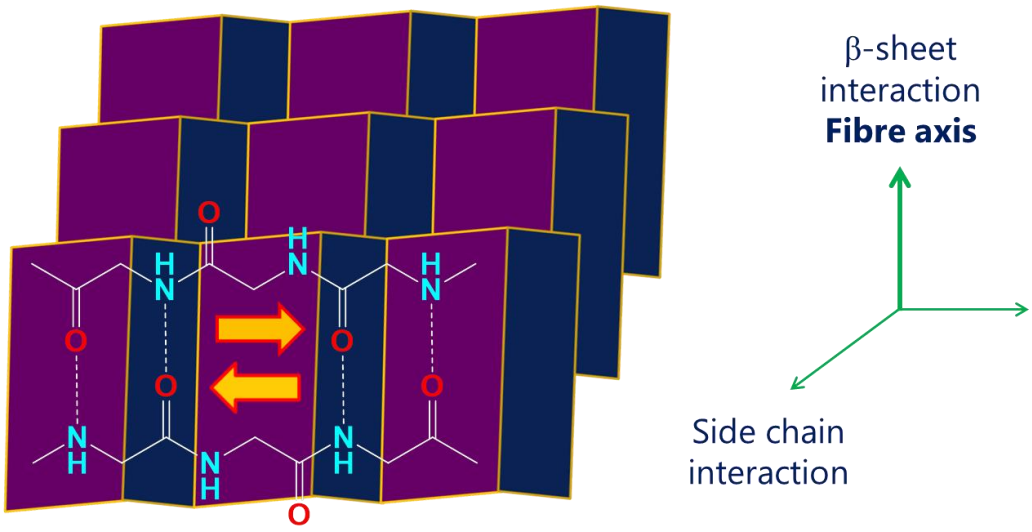

Figure 1.4: Frontal schematic view of the β-sheet structure of Aβ fibres.

Finally, highly ordered, mature fibres are produced, which accumulate into senile plaques. Such fibres are also called amyloids, which are fibrillary protein aggregates presenting cross-β-sheet structures, thus giving the name to the infamous peptide.[34] A high number of human diseases involve amyloids, such as spongiform encephalopathies, Parkinson's disease (PD) or Huntington's disease (HD), among many others. Alternatively, amorphous aggregates, which lack the presence of ordered fibres, can be generated, especially when a very rapid aggregation takes place.

In Aβ amyloids, the peptide chains lie parallel or antiparallel to each other and are perpendicular to the fibre axis (**Figure 1.4**). The interpeptidic hydrogen bonds between the NH and O=C groups of the amide backbones and the side-chain interactions are parallel to each other and perpendicular to the axis.

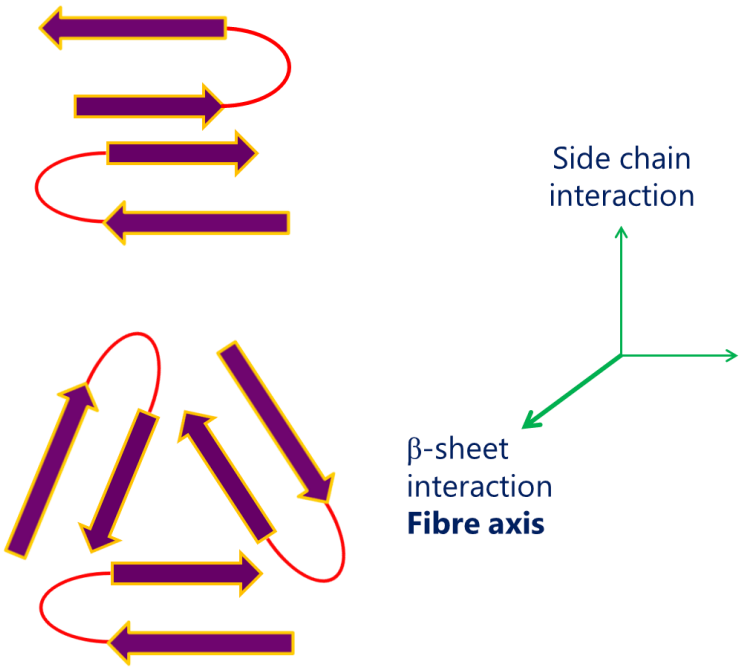

Figure 1.5: Cross-section schematic views of fibrillary Aβ polymorphs constituted by two or three molecules of Aβ peptide.

The fibres present different polymorphisms. Solid-state nuclear magnetic resonance (NMR) studies suggest that the Aβ peptide molecules constituting amyloid fibres exhibit a β-sheet conformation in the *C*-terminus, a turn in the middle and a rather flexible *N*-terminus, with probably some degree of β-sheet content. Besides, the fibres are generated by a varying number of Aβ piles, as illustrated in **Figure 1.5**.

1.3.2 Oligomeric Aβ are the most toxic species

It is stated that senile plaques containing 99% of total Aβ are a clear hallmark of AD; however, the presence of plaques has also been observed in healthy individuals.[10,35,36] For long, it was believed that such people would develop AD as they age, but subsequent studies determined that the levels of insoluble Aβ (and actually total Aβ levels) were poorly correlated to the severity of the disease.[7,35,37]

Actually, the oligomer-containing soluble fraction, especially that of Aβ(1-40), presented the best correlation. Soluble Aβ can diffuse freely and thus be more harmful than the plaques, which can produce rather local damage. Moreover, oligomers form channel-like structures that can penetrate cell membranes, giving rise to an influx of Ca^{2+} ions into the cytosol causing cell dysfunction.[12,38-40]

The study of oligomers' toxicity is therefore remarkably challenging due to their transient character. The purification of various species in equilibrium and with often poorly defined 3D structures is required; such purification can shift the equilibrium to certain oligomeric species or conformations while concealing others.[18] Furthermore, amyloid plaques are hypothesised to serve as pools of soluble oligomers.

Some authors have succeeded in studying isolated oligomeric species. Ono *et al.* found that the toxicity of oligomers increased with the oligomer order (that is, with the number of Aβ molecules constituting the assembly); thus, high-order oligomers are much more toxic than low-order ones.[31] Yet, the occurrence of such high-order oligomers has a negative exponential dependence with the oligomer order, and hence their contribution might be less significant. In turn, Chiti and collaborators used the *N*-terminal domain of *Escherichia coli* HypF-N peptide as a model for the study of the relationship between the structure of oligomeric peptides and their toxicity; they found that the flexibility and exposure of the hydrophobic domains were strongly related with the toxicity.[38] Finally, Selkoe and co-workers reported that injection of Aβ dimers extracted directly from AD brains into mice brains potently induced cognitive impairment.[41]

Indeed, Aβ oligomers are thought to induce neurotoxicity by disrupting membrane bilayers, compromising synaptic plasticity and producing oxidative stress.[10,15,19] Therefore, intense efforts are being invested in the development of therapeutic approaches targeting oligomeric species, such as immunotherapy. Current clinical medications and the foremost experimental anti-AD strategies are summarised in section **1.6.3**.

1.3.3 Accumulation of metal ions in aggregated Aβ

Despite the growing knowledge on the biochemistry of Aβ and its implications in AD, some questions regarding how Aβ peptide becomes toxic, ultimately leading to dementia, remain to be answered. APP is a highly conserved and ubiquitous protein, and Aβ peptide is produced by healthy humans and other mammals, as it is detected in plasma and CSF.[9,16,17] Why then aggregated Aβ is only found in certain areas of the brain? Why rat and mice Aβ does not undergo self-assembly? Why Aβ deposition occurs exclusively (except in early-onset AD) in elder age?

A possible explanation for such conundrums emerged upon the observation that high (millimolar) concentrations of some transition-metal ions, especially Cu(II), Zn(II) and Fe(II), are found in amyloid plaques.[16,18,27,42,43] Among these, Cu(II) and Zn(II) are bound to the fibrils.

Indeed, Aβ aggregation has only been observed in areas where prominent levels of loosely bound metal ions are found. Senile plaques and these metal ions are enriched in the synaptic cleft, where they are released in higher concentrations during neuronal excitation. Furthermore, metal homeostasis is much less efficiently regulated in elder age, thus exacerbating the possibility of Aβ-metal interaction.[42] Finally, the sequence of rat and mice Aβ presents three mutations compared to other mammals: R5G (glycine instead of arginine), Y10F (phenylalanine instead of tyrosine) and H13R (arginine instead of histidine).[44] Of these amino acid residues, histidine is crucial in metal binding, and tyrosine participates in metal-induced redox chemistry, as will be explained in section **1.5.4**. These combined findings suggest a pathological role of metal ions in the advent of Aβ toxicity.

The coordination of Cu(II) and Zn(II) to Aβ peptide is relatively weak and dynamic.[16,18,27,42] They are therefore considered a labile pool of metal ions, which has important consequences in the modulation of the aggregation and toxicity of Aβ, as will be discussed in the following sections. The pathophysiological properties of both zinc and copper ions will be first described, and then the specific interaction of copper with Aβ and its implications in AD will be addressed.

Despite the active role attributed to zinc ions in the aggregation of the peptide, this work is focused on the aberrant interaction of copper with Aβ for several reasons. First, copper is considered more toxic since it can undergo redox cycling with concomitant production of highly harmful reactive-oxygen species (**ROS**). Second, copper is thought to induce the formation of toxic oligomers under certain conditions. Finally, its paramagnetic behaviour can be used to study its binding properties by techniques such as fluorescence (fluorescence quenching), EPR and paramagnetic NMR spectroscopies.

1.4 The role of metals in AD

1.4.1 Biological roles of Zn and Cu

Zinc and copper (respectively the second and third most abundant transition metals in humans, only after iron) are essential metal ions that play vital roles in living organisms.[42,45] Copper is for instance found in tyrosinase (implicated in melanin production), cytochrome c oxidase (participates in electron transport in mitochondria) and in superoxide dismutase (SOD, involved in antioxidant defence *via* dismutation of the superoxide anion). Besides, Wilson's and Menkes diseases, two severe copper metabolism pathologies, are caused by copper accumulation or deficiency, respectively. Zinc is also present in SOD, in zinc fingers (crucial for the synthesis and stabilisation of DNA) and in lactate dehydrogenase (which catalyses the oxidation of lactate to pyruvate and *vice versa*). It also participates in the production of antibodies and the absorption of calcium.

However, the uncontrolled interaction of these metal ions with biomolecules can shatter the intricate organisation of biological systems, since metal-bound biomolecules can change their conformation and/or lose their function.[42] Moreover, copper is redox-active and can react with dioxygen and generate ROS, which may lead to oxidative stress and cause severe damage to proteins, nucleic acids and fatty acids. Thus, zinc and copper ions are tightly controlled and always bound to proteins and other naturally occurring ligands, which only release them upon highly regulated stimuli. Such regulation mechanisms, though, are energy-dependent and lose efficiency with aging.

High concentrations of exchangeable zinc (300 μM) and copper (15 μM) ions are found in the grey matter, which are released in synapses upon neuronal excitation. The proteins involved in the traffic of Zn(II) and Cu(II) are shown in **Figure 1.6**.

Zinc ions have been proposed as second messengers and neurotransmitters.[18,27,42] Glutamatergic neurons release glutamate together with zinc ions in the hippocampus, which plays a key role in memory. Slc30a proteins, also called ZnT, are responsible of the efflux of Zn^{2+} ions from the cytoplasm, while Slc39a proteins, called ZIPs, regulate the uptake of zinc ions into the cytoplasm.

The situation of copper is less clear, although the severity of diseases where brain copper is imbalanced is indicative of its importance. The transport of extracellular

copper to target tissues is mediated by high-affinity proteins such as albumin, transcuprein and ceruloplasmin.[27,42,43] Cellular uptake is regulated by Ctr1 (and probably by ZIPs as well), whereas its efflux is controlled by ATP7A and ATP7B. Inside cells, copper is trafficked and delivered to the target organelles by chaperones.

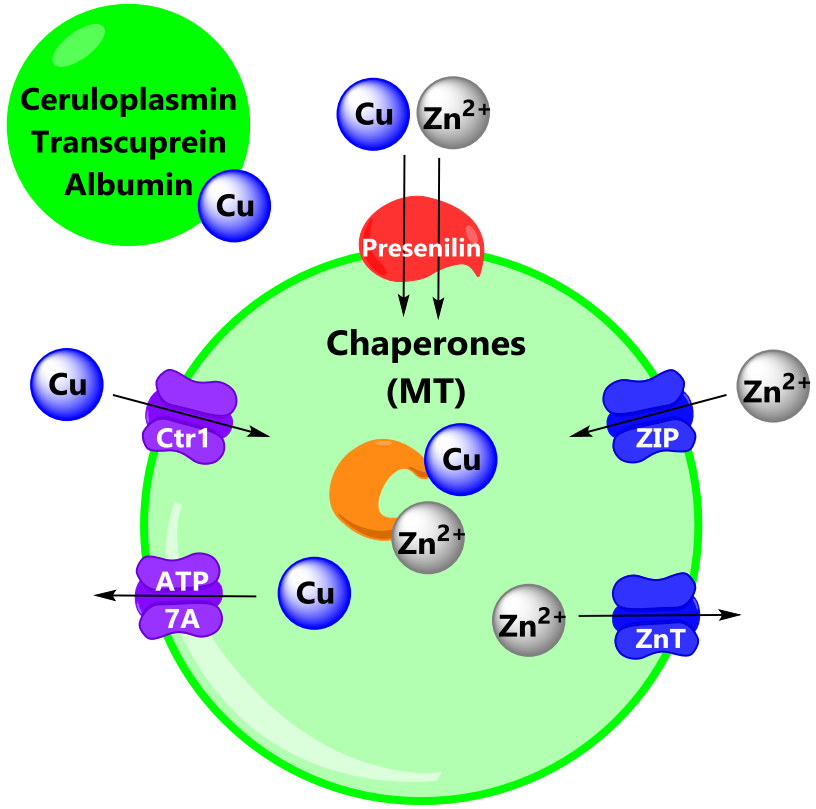

Figure 1.6: Proteins involved in the traffic of copper and zinc.

Recent reports indicate that presenilins are involved in the uptake of a high percentage of total copper and zinc. Indeed, Bush and coworkers found that presenilins were necessary for the fast uptake of copper and zinc in murine embryonic fibroblasts (MEFs).[46] They also observed a reduced antioxidant activity of SOD1 in MEFs and mouse brain tissue, indicating that presenilins also play a role in the intracellular distribution of copper and zinc. As a matter of fact, mutations in presenilins are responsible for familial (genetic) AD.

Even though the uptake and intracellular transport of copper is performed in the Cu(I) oxidation state, it is found as non-bound, exchangeable Cu(II) when released by neurons. Hence, a labile pool of copper ions is generated in synapses; such labile pool has to be cleared from the synaptic cleft since non-bound Cu(II) ions can lead to ROS formation and harmful interactions with biomolecules.[27]

1.4.2 Metal dyshomeostasis in AD

The total metal levels are altered in AD-affected tissues. Although regulatory systems become less efficient with normal aging, resulting in a certain dyshomeostasis, such imbalance is severe in patients suffering from this pathology. In AD, the concentrations of iron and zinc (this last one is controversial) are higher than those found in healthy brains, whereas copper levels are decreased.

Moreover, these metal ions are mis-compartmentalised.[43] Both copper and zinc ions accumulate in the synaptic cleft together with the Aβ peptide. Cortical intracellular copper is decreased within normal aging, but it is more pronouncedly reduced in AD. Conversely, zinc is elevated 2-3 fold in AD-affected neuropil.

The breakdown of zinc homeostasis may be caused by incorrect regulation of ZnT transporters, which play crucial roles in cognition.[42,47] One of the most studied transporters of this family is ZnT3, which loads zinc into the synaptic vesicles of neurons, and whose suppression leads to depletion of synaptic zinc.[48] Oestrogens have been found to regulate the levels of ZnT3 (and in consequence, of synaptic vesicle zinc): oestrogens reduced the expression of this Zn transporter in mice, whereas ovariectomy caused an elevation in ZnT3 levels.[49] This is important as postmenopausal women experience a drop on oestrogen production and present a higher risk of suffering AD. Furthermore, dysfunctional zinc buffering may lead to zinc release in cytoplasm, which activates neuronal death by oxidative stress.[50,51] The administration of oestrogens to postmenopausal women has been one of the leading anti-AD approaches, as will be discussed in section **1.6.3**.

Experiments with model mice have provided important insights regarding the biochemistry of AD. Tg2576 mice present the Swedish mutation of APP (*hAPP*$^{+}$), responsible of the production of human Aβ peptides; such mice are thus used to evaluate the cognitive decline caused by Aβ accumulation. In a relevant experiment, Koh and collaborators bred Tg2576 mice with ZnT3-knockout mice (*ZnT3*$^{-/-}$).[52] Whereas abundant plaque formation was found in the brains of control mice, the production of plaques was remarkably reduced in the *hAPP*$^{+}$*:ZnT3*$^{-/-}$ descendants, which exhibited both Aβ production and reduced synaptic zinc. This suggests that synaptic vesicle zinc is paramount in the formation of amyloid plaques. Importantly, differences in plaque generation between sexes disappeared. These results are of great interest since female mice and humans present more abundant senile plaques.[53] Accumulation of Zn ions in

synaptic senile plaques is hypothesised to further reduce the concentration of available functional zinc ions.

Although total copper levels are lower in AD brains, the origin of such copper imbalance is not likely to lie in an inappropriately low dietary intake. Despite previous reports on the beneficial effects of supplementary copper in cell cultures and AD animal models, the administration of copper in diet to patients with mild AD did not present preventive nor promoting effects in the pathology.[54] This may be explained by the fact that only a minute fraction of copper could cross the blood brain barrier.

On the contrary, different mouse models fed with low (10% of the amount considered toxic) doses of copper for 90 days showed decreased Aβ removal from brain tissue. Such loss in the elimination of Aβ was due to oxidative modifications of low-density lipoprotein receptor-related protein 1 (LRP1), which is responsible of Aβ clearance through the blood brain barrier. Under the studied conditions, copper accumulated in brain capillaries and, in mice with compromised blood brain barrier, in parenchyma.[55] Through the generation of peroxynitrite, copper ions induced the nitrotyrosination of LRP1. Nitrotyrosinated LRP1 suffered increased proteosomal degradation, which thus led to decreased Aβ clearance.

Further, the addition of low levels of copper to cholesterol-fed rabbits induced significant amyloid-plaque formation.[56] Cholesterol-rich diets have been identified as a potential risk factor for AD. Rabbits fed with both cholesterol and copper displayed retarded ability to learn difficult tasks. These experiments led to propose cholesterol-fed rabbits as potential models for AD since the animals presented at least 12 different biomarkers of AD.

Changes in local levels of metal ions directly affect the processing of some of the proteins involved in the pathology. One example is APP, which is believed to be involved in the regulation of copper homeostasis and neuroprotection through reduction of Cu(II) to Cu(I).[57] Whereas elevated concentrations of copper within cells promote the expression of APP, decreased intracellular copper promotes the cleavage of Aβ peptide from APP in lipid rafts (cholesterol-rich domains of the cellular membrane).[58] Zinc also regulates the processing of APP since the activity of proteins involved in its cleavage, such as presenilin 1 and γ-secretase, is dependent on the concentration of this metal ion.

Lipid rafts are involved in the homeostasis of copper and the traffic of metalloproteins and, under intracellular copper deficiency, they paradoxically become rich in this metal.[59] There, copper ions interact with Aβ peptide, potentially leading to the formation of hypermetallated aggregates of the protein. Copper can also catalyze the oxidation of cholesterol with a concomitant production of dihydrogen peroxide, as will be discussed in section **1.5.4**.

In summary, AD seems to be caused by both aberrant metal and protein homeostasis with intricate links between each other. Hence, mis-localised metal ions represent a promising target for potential anti-AD drugs, although researchers have mainly focused in Aβ peptide and secretases so far. The cause-consequence relationships between the metal dysfunction and the proteopathy (that is, which causes which) also remain to be elucidated.

1.4.3 Impact of Zn and Cu on the aggregation of Aβ

In AD, metal ions co-enrich with the proteins implicated in the disease, where the organism regulatory mechanisms fail to relocate them and restore metallostasis. While Aβ peptide co-enriches with copper and zinc in the synaptic cleft, intracellular tau protein co-enriches with iron inside neurons.[16]

According to the amyloid cascade hypothesis, metal ions promote the aggregation of monomeric Aβ peptide. Such metal-induced aggregation of Aβ peptide leads to the formation of distinct species, but the published data are often contradictory. Both the inhibition and promotion of amyloid generation have been reported for similar conditions, suggesting both protective and deleterious effects for both copper and zinc.[60-64] This underscores the extreme sensitivity of the aggregation process of Aβ. Indeed, the speciation of aggregated Aβ depends on many factors such as the metal ion, the peptide-to-metal ratio, the stirring, temperature, the pH, the presence of salts and so on. Besides, differences among peptide batches are often observed *in vitro* since some of them may contain preformed aggregates, which can affect the nature of the species formed and the aggregation rate (since they can work as aggregation nuclei).

A summary of the Zn(II)- and Cu(II)-induced aggregation of Aβ is displayed in **Figure 1.7**. The metal-to-peptide ratio has been recognised to be more useful than their concentration to study the influence of the metal on the final aggregates formed.

Although controversial, both Zn(II) and Cu(II) might promote the generation of amyloid fibrils at substoichiometric amounts of metal relative to the peptide. Such fibres are similar in shape and size to those produced in absence of metals. On the other hand, it seems more widely accepted that they inhibit amyloid formation at stoichiometric or overstoichiometric amounts. Stoichiometric quantities of zinc ions have been reported to induce aggregates with a high content of α-helicity.[65] In contrast, stoichiometric amounts of copper ions are thought to stabilise dimers or/and oligomers.[66-68] Hemmingsen and collaborators suggested that Aβ-Cu-Aβ dimeric species are not precursors of Aβ fibrils, although this assumption requires further experimental data.[69]

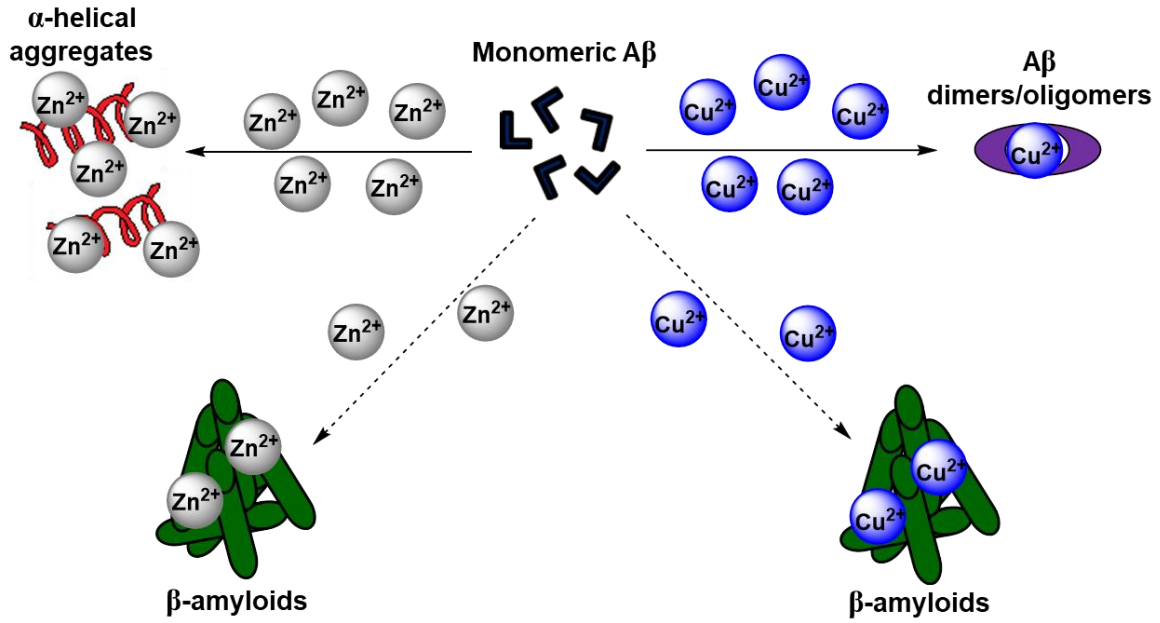

Figure 1.7: Aggregated Aβ species depending on the metal ion and metal/peptide ratio.

Little is known about how metal ions influence the aggregation of Aβ. In fact, the fibres generated in presence or absence of metal ions are very similar. The more pronounced effect is observed on the kinetics, especially on the nucleation step. Reduced rates have been reported for the elongation, whereas acceleration has been observed for the nucleation step.[18] However, it is still unclear how the interaction with metal ions affects nucleation. Metal-induced shifts in the conformation or the population of Aβ peptide have been proposed as plausible mechanisms. Additionally, a catalytic mechanism, in which the metal ions bring together two peptide molecules and are then released, has also been suggested since the acceleration of amyloid formation with substoichiometric amounts of metals has been reported.

Amorphous Aβ precipitates, whose structures are very different from those of the highly ordered amyloid fibres, can also be generated when the aggregation is particularly fast. Fast aggregation dynamics usually take place when (i) the pH is close to the isoelectric point of Aβ peptide (≈ 5.5), (ii) when the concentration of protein and/or metal ions is high, (iii) or for Aβ(1-42).[18]

As described in section **1.4.2**, zinc is believed to be the principal contributor to amyloid formation under physiological conditions, although copper is also thought to be able to induce the generation of amyloid plaques. In contrast, copper is thought to be the main responsible of the production of Aβ oligomeric species.

Copper is therefore considered to play a double contribution to Aβ toxicity, namely (i) stabilisation of toxic oligomers and (ii) ROS production through redox cycling. Actually, protective properties have been attributed to zinc, due to the partial displacement of copper by zinc ions.[16] For this reason, copper has emerged as a preferential target for researchers working in the metal hypothesis, including our group. In the following sections, the interaction of Aβ peptide with copper(I/II) will be discussed, with special emphasis on its putative implications in AD.

1.5 Interaction of copper with Aβ peptide

1.5.1 Impact of the flexibility of Aβ peptide on the properties of the Cu-Aβ complex

The *N*-terminal domain of Aβ is the binding region of copper. This domain is usually considered to contain the first 28 amino acids, *i.e.* Aβ(1-28).[70] Within this *N*-terminal fragment, the hydrophilic section comprising the first 16 amino acids is believed to play a role in the coordination of copper. Accordingly, the Aβ(1-16) and Aβ(1-28) fragments are often used as non-aggregating models of Aβ peptide for the study of the binding of copper.

The fact that Aβ is an intrinsically disordered protein has important implications in the coordination mode of copper, the binding affinity and the redox properties of the Cu-Aβ complex.[18,71] Even within fibrils, the *N*-terminal domain of Aβ is highly flexible, in contrast with the metal-binding domains of metalloenzymes. While metalloenzymes

present a rigid, well established binding site that is only suitable for a specific metal, the Aβ peptide can adapt its conformation to different metal ions.

This flexibility allows the presence of several binding sites for copper ions. Hence, different coordination species coexist in equilibrium with relatively low energy barriers. This means that subtle perturbations in the system can dramatically shift the equilibrium and alter the populations of the different species, which hampers the determination of the amino acid residues involved in the coordination of the metal ions. Considering this complexity, it is not surprising that the elucidation of the coordination mode of Cu(I/II)-Aβ complexes and the binding affinity of the different aggregated species are somehow controversial.

1.5.2 Coordination sphere in the Cu(II)-Aβ complex

Due to the absence of crystallographic structures, most studies regarding the coordination environment of Cu-Aβ species rely on spectroscopic techniques. Electron paramagnetic resonance (EPR), circular dichroism (CD), extended X-ray absorption fine structure (EXAFS) and X-ray absorption near-edge spectroscopy (XANES) have been widely exploited for the determination of the (amino acid) ligands involved in the chelation of Cu(I/II) ions.

In general, it has been considered that monomeric, oligomeric and amyloid forms of Aβ present the same Cu(II)-binding modes since no significant differences in the spectroscopic features have been observed upon aggregation. Nonetheless, a distinct coordination was suggested for covalently cross-linked dimers.[72,73]

Two main coordination modes coexist at physiological pH, and their population ratio is highly dependent on the pH (**Figure 1.8**). The main one, *i.e.* type I, involves the terminal amino group, the oxygen atom of the amide function of Asp1, and two out of the three histidine residues available in the peptide (His6, His13 and His14).[18,27]

The secondary coordination mode, namely type II, involves the terminal amino group of Asp1, the carboxylic and amino functions of Ala2 and one of the three histidine residues. Also, an additional Cu(II)-binding mode implicating all three histidine residues and the oxygen atom of Ala2 amide backbone has been suggested. In both coordination types, the side-chain carboxylic acids of aspartate/glutamate residues, as

well as water molecules, can bind to copper too, yielding complexes with square-planar or octahedral geometries.

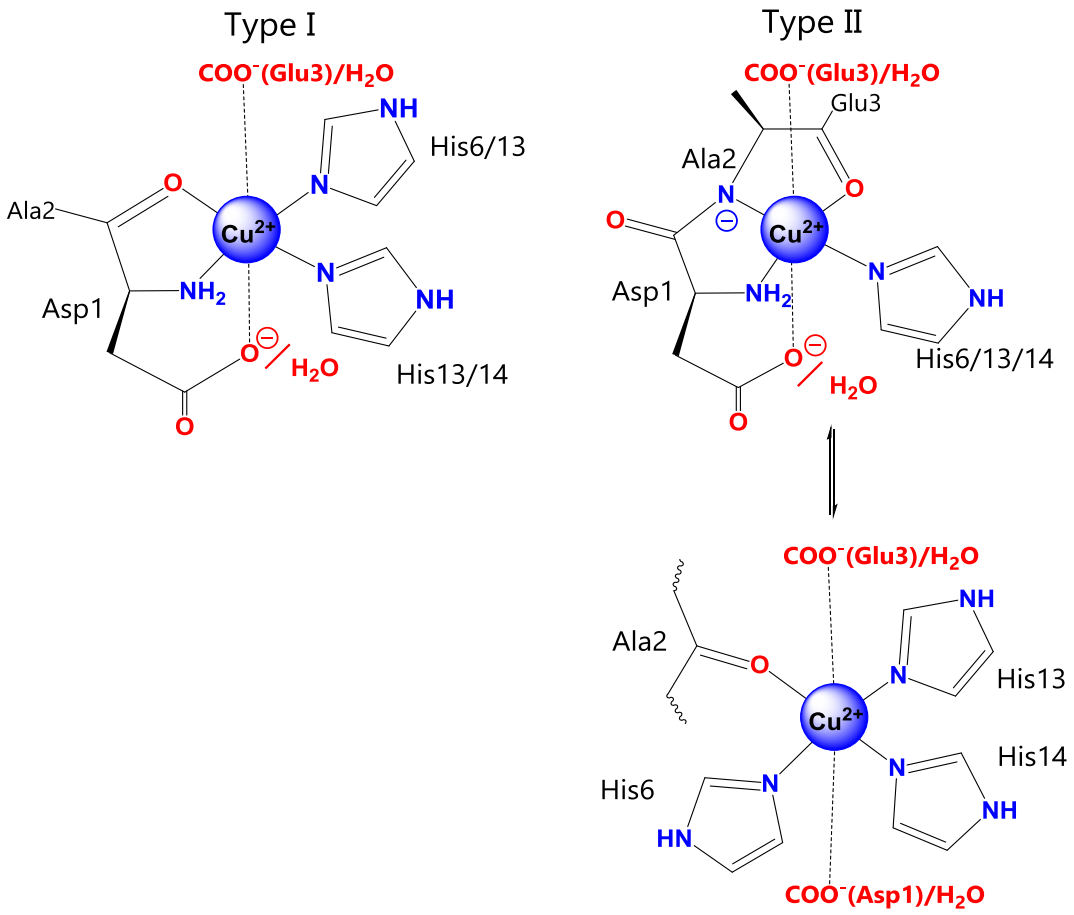

Figure 1.8: Binding sites for Cu(II) in Aβ peptide.

For Cu(I), a linear coordination involving two histidine residues, preferentially His13 and His14, has been suggested for monomeric Aβ (**Figure 1.9**).[74,75] However, studies with X-ray absorption and EPR spectroscopy carried out by Shearer and co-workers suggested a distinct tetrahedral coordination type for oligomeric forms of the peptide.[76] Such tetrahedral complex exhibits a high redox activity through Cu(II)/Cu(I) cycling, in marked contrast to linear Cu(I)-Aβ species.[77] This would explain the low reactivity of linear monomeric Aβ-Cu(I) complexes with dioxygen, since a high energy is required to re-accommodate the resulting Cu^{2+} ion.

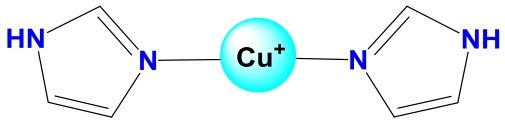

His6/**13** His13/**14**

Figure 1.9: Linear binding mode for Cu(I) in Aβ. The preferential histidine residues implicated are indicated in bold numbers.

1.5.3 Binding affinity of the Aβ peptide towards copper ions

The binding affinity of a protein towards a certain metal ion is an important parameter since it determines its selectivity in the presence of other metal-binding species, or when other competing metal ions are present. In this context, divergent results have been reported regarding the affinity of the Aβ protein towards the metal ions involved in AD.[78]

Affinity values for Cu(II) ions obtained by potentiometry and isothermal calorimetry (ITC) are usually two orders of magnitude higher than those obtained by Tyr10 fluorescence assays (10^9-10^{10} *versus* 10^7-10^8 M^{-1}, respectively). Such discrepancies have been attributed to concentration-dependent factors, since the concentrations used in the fluorescence experiments are much lower. Moreover, the nature of the Aβ fragment used has also been pointed out as a source of variability: the Aβ(1-16) fragment is used for the ITC/potentiometry experiments, whereas full-length Aβ peptide is used for the fluorescence analyses. Finally, there is also a contribution of the buffer, since more coordinating buffers like Tris (tris(hydroxymethyl)aminomethane) yield higher affinity constants that weaker ones, such as HEPES (*N*-2-hydroxyethylpiperazine-*N*'-2-ethanesulfonic acid).

However, Alies, Bal and Faller contributed to a consensus by conducting a set of Tyr10 fluorescence experiments using both Aβ(1-16) and full-length Aβ at concentrations varying within 2 orders of magnitude.[70] Applying a rigorous three-part analysis, they found an affinity constant value of about 10^{10} M^{-1}, independent of both the concentration and the peptide fragment used.

Then, the copper-binding affinity of Aβ would be much lower than most metalloproteins; for example, superoxide dismutase, SOD, has an affinity constant of

10^{17}-10^{18} M^{-1}. This allows a fast intra- and intermolecular exchange of copper ions, and Aβ species are thus considered labile pools of copper.

Studies with EPR, ITC and CD demonstrated that a second Cu(II) ion can be bound to the Aβ peptide.[79] However, the affinity of the second binding site was found to be 100 times weaker, which explains why it was not detected in most of the earlier studies. Physiologically, this site is unlikely to be occupied, since the levels of Aβ peptide are higher than those of copper ions and the binding affinity is rather weak.

In general, it has been considered that the binding affinity of Aβ for Cu(II) does not depend on its aggregation state. However, controversy was also brought to this topic as Atwood *et al.* found that Aβ(1-42) binds Cu(II) with attomolar affinity, almost seven orders of magnitude higher than that of Aβ(1-40), due to cooperativity effects upon aggregation.[80] They also attributed the apparently spontaneous aggregation of Aβ peptide to trace amounts of Cu and Zn contamination since aggregation was precluded by addition of high-affinity copper chelators. Contrarily, Sarell *et al.* used fluorescence quenching and circular dichroism experiments to demonstrate that both monomeric and fibrillary Aβ bind Cu(II) with picomolar affinities, with almost identical binding curves.[81]

Regarding Cu(I), in a competitive experiment using the Cu(I)-chelator bathocuproinedisulfonic acid, Feaga and co-workers found that the Aβ(1-16) fragment binds Cu(I) with an affinity within the femtomolar range, even for mutant species lacking one of the three histidine residues.[82] However, using the weak Cu(I)-chelator ferrozine as competitor, Hureau and Alies found that the binding affinity of both Aβ(1-16) and Aβ(1-42) for Cu(I) was in the order of 10^{7} M^{-1}, that is, 2-3 orders of magnitude lower than that obtained for Cu(II).[83] In that work, they attributed those differences with the values obtained by Feaga to an inappropriate pH buffering, which would facilitate the release of Cu(I) by the Cu(I)-competitor used in the experiment. Besides, they found a 3-fold higher Cu(I)-affinity for Aβ(1-42) than that for Aβ(1-16), which was attributed to the presence of aggregated Aβ(1-42) species that present a different binding geometry.[76]

1.5.4 Redox properties of Cu-Aβ species

Metalloenzymes usually have a well-defined binding site that coordinates a unique, specific metal ion. Moreover, this binding site is often wrapped in an adequately oriented pocket that is only accessible for the proper substrate. Such features confer a high specificity and efficiency to the catalytic metal. In contrast, the disordered and flexible nature of Aβ peptide renders an uncontrolled production of ROS, *e.g.* hydroxyl or superoxide radicals. Actually, only some of the conformations adopted by the Cu-Aβ complex are able to catalyse ROS production.[84]

Indeed, Aβ peptide has been found to be more toxic in the presence of copper.[62] Upon binding to Aβ, Cu(II) is more easily reduced to Cu(I) (the Cu(II)-Aβ complex presents a reduction potential of approximately + 550 mV, compared to +150 mV for free Cu^{2+}), and can be subsequently re-oxidised by dioxygen, the superoxide anion or dihydrogen peroxide (**Figure 1.10**).[85,86]

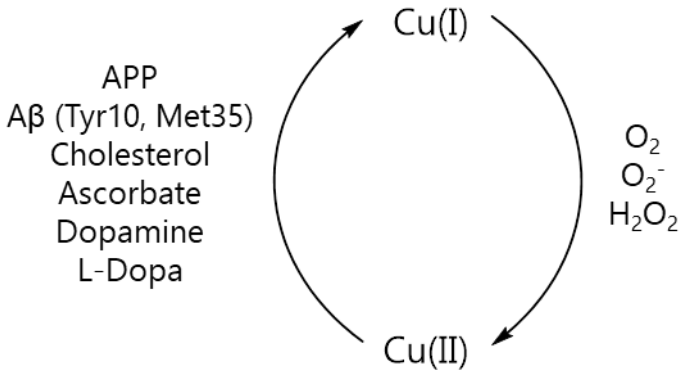

Figure 1.10: Species participating in the redox cycle of Cu(I/II).

Dioxygen is abundant in the brain since there is an intense glucose metabolism. Upon Cu(I) re-oxidation, there is a concomitant production of ROS, which may lead to oxidative stress (**Figure 1.11**). Indeed, these oxidising radicals damage DNA and cell membranes, and induce lipid peroxidation and protein oxidation, among other adverse effects. First, copper(I) reacts with dioxygen and generates the superoxide anion, which can subsequently react with another Cu(I) ion to produce dihydrogen peroxide. Dihydrogen peroxide is able to diffuse through biological membranes and perform oxidative damage in different cell compartments from where it was generated. An alternative mechanism for two-electron donors (such as ascorbic acid) where H_2O_2 is directly produced (that is, skipping superoxide formation) has been proposed.[87]

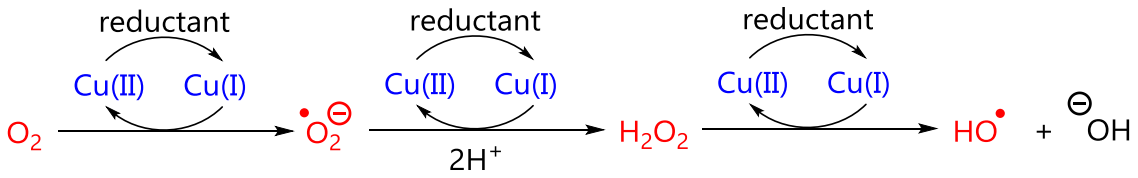

Figure 1.11: Copper-catalysed generation of ROS.

In a last step, H_2O_2 can be reduced to hydroxide and the highly reactive hydroxyl radical. As suggested by Zhou *et al.*, the hydroxyl radicals are generated by free Cu^{2+} ions rather than Aβ-complexed ions.[87]

Hydroxyl radicals are extremely aggressive and react almost immediately by subtracting a proton of a surrounding biomolecule. Hence, this biomolecule becomes a radical itself and can subtract another proton, and this process is repeated until the reaction is terminated by radical condensation.

In healthy brains, the production of ROS is strictly regulated, and antioxidant defence decreases the presence of such oxidising agents to levels that are tolerated by the organism. Superoxide dismutase, SOD, is one of the most prominent enzymes responsible for the scavenging of ROS (more specifically, scavenging of the superoxide anion).[88] Nonetheless, these regulatory mechanisms are energy-dependent, and lose efficiency upon normal aging; these are highly impaired in AD. Enhancement of SOD activity or administration of SOD-like drugs have thus been suggested as potential approaches to prevent AD symptoms.

Several species can trigger the reduction of the Aβ-complexed Cu(II) ions, ascorbate (vitamin C) being the most abundant. However, other substances such as cholesterol (abundant in lipid rafts, where it co-enriches with Aβ), APP or the Aβ peptide itself can also be oxidised by Cu(II).

As a matter of fact, Aβ peptide has been reported to exhibit antioxidant properties, paradoxically. Faller and Collin identified the amino acid residues of Aβ which were more affected by oxidation through this Cu-Aβ redox cycling and ROS production.[89] They found that phenylalanine residues suffered oxidation to hydroxyphenylalanine, while histidine was oxidised to 2-oxohistidine. In turn, Asp1 underwent oxidative cleavage as well as decarboxylation and deamination.

The methionine residue (Met35) is also susceptible to oxidation.[40] Met35 oxidised to sulfoxide (and further to sulfone) has been observed at a high extent in deposited Aβ

of human AD brains. This is relevant since the presence of Met35 sulfoxide has been reported to increase the fraction of soluble Aβ and to inhibit the formation of oligomeric, α-helical channel-like structures, which compromise the permeability of the cellular membrane.

The oxidation of Aβ peptide to yield covalently linked peptide dimers deserves particular consideration. The Tyr10 residue is known to be prone to oxidation, yielding covalent dityrosine cross-links, as depicted in **Figure 1.12**, which have important implications in the self-assembly of Aβ species and the stability of the aggregated species.[90]

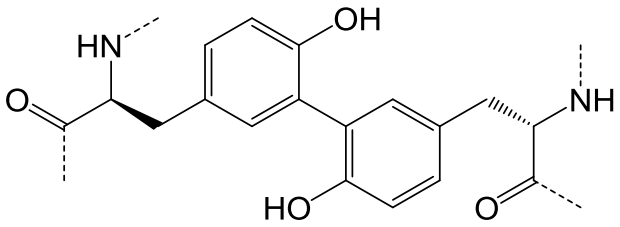

Figure 1.12: Dityrosine-cross-links.

Fibrillary Aβ containing dityrosine cross-links is highly resistant to acidolytic and proteolytic degradation. Moreover, soluble Aβ dimers obtained from AD-affected cortex resulted in impaired cognitive performance in adult rats, whilst an Aβ mutant with the tyrosine residue substituted by alanine was found to be devoid of neurotoxicity.[41,44] In addition, dityrosine cross-linked Aβ dimers have been proposed as aggregation nuclei for the formation of larger and potentially toxic Aβ species.[90,91] Therefore, preventing the generation of such cross-links might reduce Aβ–associated toxicity.

Alongside the oxidative modifications that are produced in the Cu(II)-Aβ complex itself, the copper-protein system presents sluggish redox cycling either in its monomeric or in its fibrillary form. Apparently, there is a high reorganisation cost to accommodate the initial square-pyramidal geometry of the Cu(II) complexes into the linear, bis-histidinic coordination of the Cu(I) species.[92] ROS production is thus considered to be specific for oligomers.[93] As a matter of fact, Shearer and co-workers found, by EPR and X-ray absorption spectroscopy, a Cu(I) tetrahedral coordination species in oligomeric Aβ(1-42) with a high propensity to react with dioxygen and undergo redox cycling.[76]

Recently, Karlin and collaborators reported totally different reactivities of Cu(I) complexes with His-Gly-His peptides depending on the binding of the imidazole rings,

i.e. the δ nitrogen atom or the ε nitrogen atom (**Figure 1.13**).[94] Whereas the δ complex was dimeric and had an almost linear coordination geometry, the ε one was a monomer and displayed a geometry deviated from linearity (N-Cu-N angle = 160°).

Interestingly, the linear δ species did not present reactivity with O_2 (producing H_2O_2), suggesting that the 180° His-Cu-His coordination is highly stable. This would explain why the Cu(I) complexes with monomeric Aβ peptide exhibit poor ROS production. In contrast, the distorted ε complex readily reacted with dioxygen to yield dihydrogen peroxide. Hence, the redox activity of Cu(I)-Aβ complexes could be triggered by modifying the inert linear coordination, for instance through the binding of a third ligand.

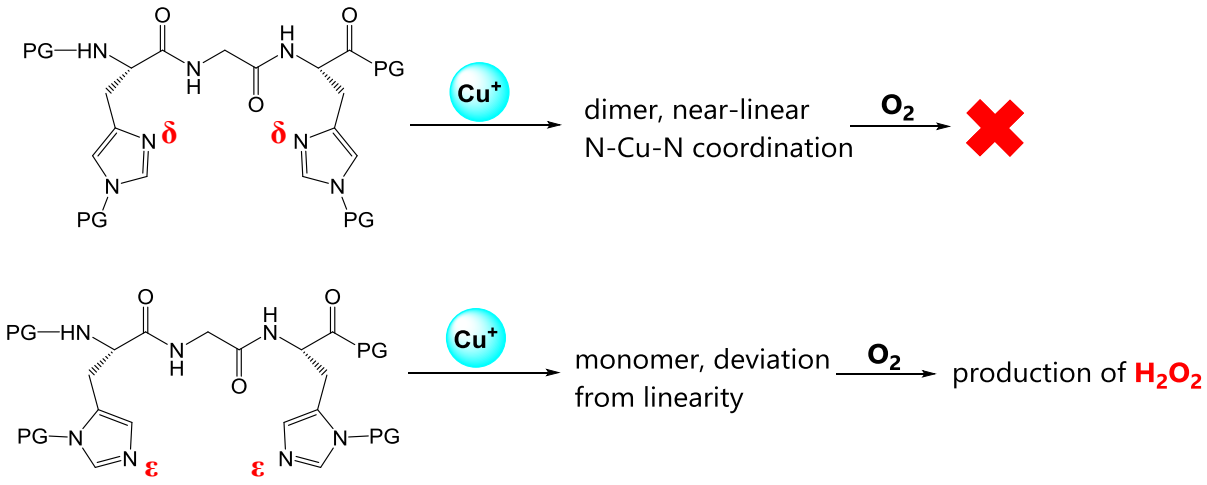

Figure 1.13: Different coordination and redox properties of the Cu^{I}(His-Gly-His) complexes depending on the δ/ε coordination of the imidazole rings. PG stands for protecting group.

Subsequently, Faller and Collin reported that the redox cycling might take place *via* a transient in-between species involving Asp1, His13 and His14 (**Figure 1.14**).[89] Such low-populated intermediate would be more structurally similar to the major coordination geometries of CuI/II species, facilitating the accommodation of copper in both oxidation states. Thus, the aspartate residue would be responsible of the activation of such reactivity.

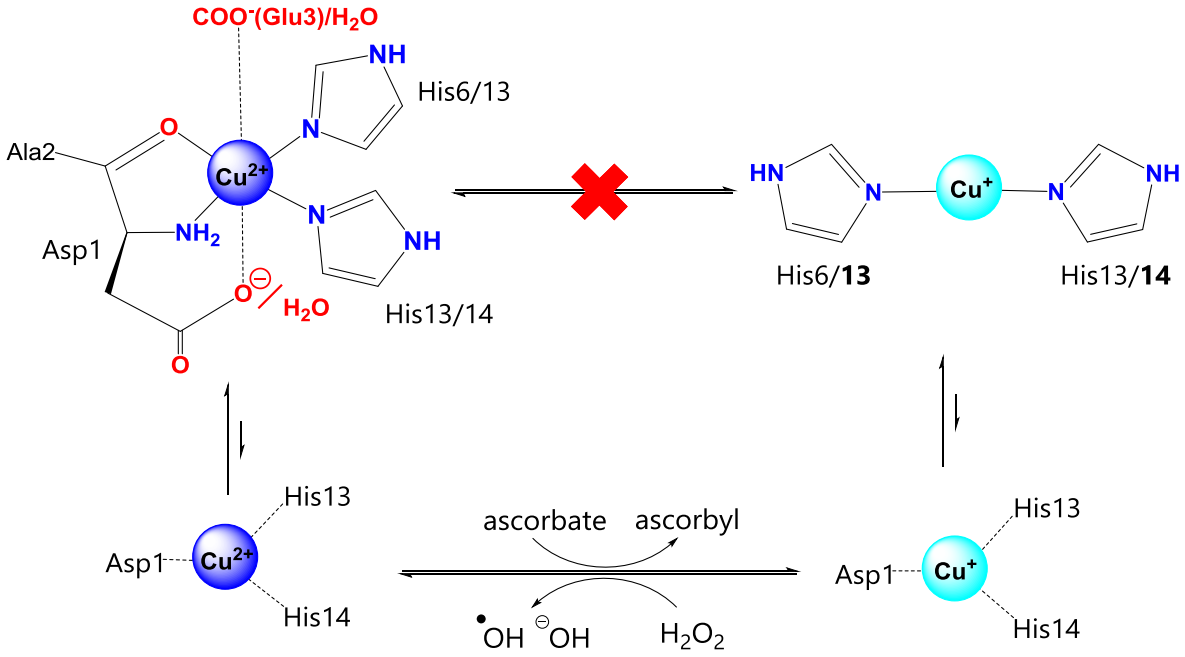

Figure 1.14: Proposed rearrangement of the Cu-bound Aβ centre upon one-electron reduction of Cu(II) to Cu(I).

1.6 Therapeutics and diagnostics for AD

1.6.1 The blood-brain barrier (BBB)

The effective treatment of AD, as well as the visualisation of the pathophysiological features of AD-brains, present a remarkable obstacle: the blood-brain barrier (**BBB**). Indeed, the supply of drugs and probes to the CNS is greatly hampered by the presence of this natural barrier, a tightly joined layer of endothelial cells, pericytes and the end feet of astrocytes, which selectively regulates the access of compounds to the brain (**Figure 1.15**).[95] As a matter of fact, less than 2% of the small molecules and none of the large molecules so far tested as potential drug candidates possess the ability to cross the BBB. A low molecular weight and a certain lipophilicity are indispensable to exhibit BBB permeability.

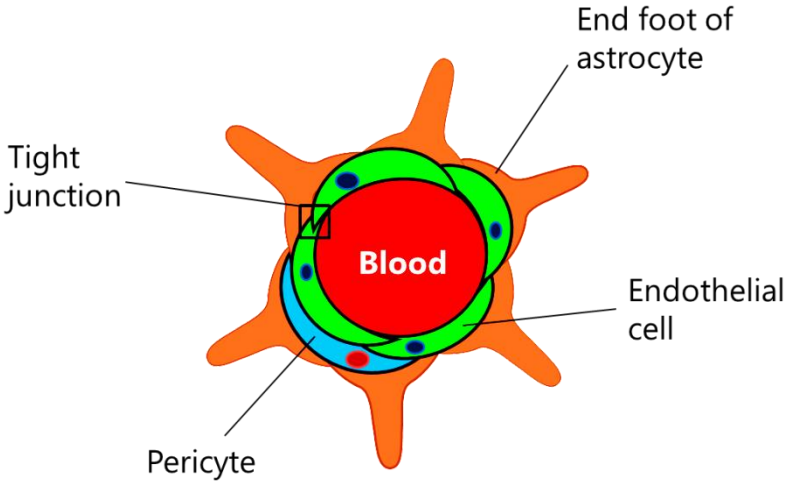

Figure 1.15: Brain capillary insulated by the BBB.

In order to solve this problem, trans-cranial and trans-nasal administration as well as direct injection into the spinal cord have been employed.[96] The delivery of extremely high doses of the drug, BBB disruption with vaccines or solvents and administration of inhibitors of efflux transporters are also used to achieve sufficiently high drug concentrations in the brain tissue. More recently, ultrasounds and magnetic nanoparticles have been added to the toolbox.

However, all these strategies are drastic and highly harmful to the brain. Besides, the BBB is not completely impermeable as the brain needs a supply of nutrients and biomolecules. Therefore, current research is being focused on the design of systems, called BBB shuttles, with the ability to cross the BBB and deliver therapeutic or diagnostic agents.[97]

BBB shuttles include 1) chemical delivery systems (mainly dihydropyridine and derivatives); 2) substrates for transporters present on the BBB (for example tyrosine and glucose); 3) molecular Trojan horses (ligands for receptors on the BBB); 4) peptides that efficiently cross cell membranes and 5) colloidal systems, such as liposomes. Many of these strategies yet need to be complemented with specific brain-targeting ligands since they can also accumulate in other organs.[97]

Nanoparticulate systems have also been found to be able to reach the brain.[98] More specifically, gold nanoparticles have been studied for therapeutic and diagnostic brain-targeted purposes.[99,100] Gold nanoparticles accumulate in the brain in a size-dependent manner, but in significantly lower concentrations than in liver, spleen or kidneys. In

order to increase the access into the brain, peptides that interact with receptors on the BBB have been used to enhance selectivity and hence accumulation in brain tissue; for example, peptides that interact with the transferrin receptors of endothelial cells have been employed.[101,102] Specific targeting is a field which has not been extensively studied so far and which may represent a key step forward for CNS therapeutics.

1.6.2 Detection and visualisation of Aβ aggregates

As discussed previously, AD is currently diagnosed by means of tests that subjectively evaluate the cognitive deficits displayed by potential AD patients. However, the accuracy and sensitivity of such tests are very low. The first detectable symptoms are believed to appear 20-30 years after the onset of the pathology, when potential therapies are, most likely, much less effective. As a matter of fact, the diagnosis can only be confirmed in a post-mortem autopsy.

For this reason, the real-time visualisation and monitoring of Aβ aggregation is one key aspect in anti-AD research. Aβ-imaging agents can assist in three different ways: *i)* improve diagnosis of Alzheimer's disease, probably allowing for a more efficient treatment; *ii)* evaluate the amyloid cascade hypothesis and achieve a deeper insight on the kinetics and the mechanism of formation of Aβ aggregates, and *iii)* test the efficacy of drugs aimed at decreasing the presence of aggregated Aβ peptide.[103]

In order to detect and monitor the formation of amyloid fibres, there are several fluorescent dyes available. Yet, their access into the brain is hampered by the blood-brain barrier since they are charged and relatively large. It is thus not surprising that the current search for new imaging agents involves the design of derivatives with improved internalisation properties or the development of radiolabelled molecular probes.[104]

New nuclear probes are designed for *in vivo* imaging by positron emission tomography (PET) or single-photon emission computed tomography (SPECT), and they are mainly based on ^{18}F or ^{11}C radiomarkers. Among these, the so-called Pittsburgh compound B ([^{11}C]PiB) is probably the most promising probe so far described (**Figure 1.16**). The metastable isotope ^{99m}Tc is also employed, which presents a longer half-life of 6 hours.

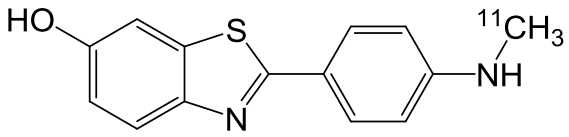

Figure 1.16: Pittsburgh compound B (PiB).

Despite the poor properties displayed by fluorescent probes *in vivo*, they are extensively used for *ex vivo* and *in vitro* staining due to their much more affordable prices, availability and ease of manipulation. The most commonly used dyes, namely Congo red and Thioflavin T, are briefly described below.

1.6.2.1 Congo red

Congo red (**Figure 1.17**) was first synthesised in 1884 by Paul Böttiger, who was seeking a pH indicator. However, it was not until 1922 that Hans Hermann Bennhold used it for the diagnosis of amyloidosis, and until 1927 when it was employed to stain brain tissue by Paul Divry.

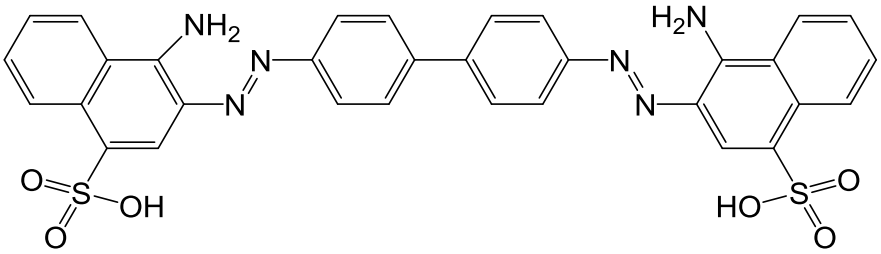

Figure 1.17: Representation of the structure of Congo red.

Congo red yields a green birefringence in the presence of amyloid deposits when irradiated with polarised light, providing evidence of the presence of the protein fibres. Like for ThT (see section **1.6.2.2**), its mechanism of action is not well understood. The dye is supposed to lie parallel to the long axis of the fibrils, confined among the peptide chains, thus splitting the light ray into two. Electrostatic as well as hydrophobic interactions are thought to account for the affinity towards the protein chains.

Despite its favourable features, Congo red presents some drawbacks. First, it is not totally amyloid-selective. Fink and co-workers demonstrated that it affords induced circular dichroism in the presence of proteins with secondary structures other than β-sheets, such as α, α + β, parallel β-helical and native conformations.[105] Second, Congo

red binds to protein molecules and yields supramolecular oligomers, altering the normal growth of the amyloids.

This apparently serious disadvantage for amyloid staining represents a promising approach for the treatment of several diseases.[106] Indeed, Congo red stabilises monomeric proteins at appropriate Congo red/protein ratios and prevents the formation of more toxic aggregates. Aggregation of Aβ peptide was shown to be blocked in rat neuron cultures, while the effects of Huntington's and prion diseases in model mice were lessened when treated with this dye.

Derivatives and compounds exhibiting structures resembling that of Congo red, such as Chrysamine G and X-34, have also been tested as *in vivo*, amyloid-selective dyes.[107] Unfortunately, they contain carboxylic acids which are deprotonated at physiological pH, hence yielding a poor access to the brain.

1.6.2.2 Thioflavin T

The fluorescent properties of the dye Thioflavin T (ThT), which binds selectively to amyloid fibrils, were first reported in 1959 by Culling and Vassar (**Figure 1.18**). When ThT is unbound, it (poorly) emits at 445 nm when excited at 385 nm. In the presence of amyloids, though, the excitation and emission wavelengths shift dramatically to 450 and 482 nm, respectively. In addition, the fluorescent intensity is greatly enhanced. Therefore, ThT is an invaluable tool for the study of fibrillation processes and the observation of amyloid deposits *in vitro* or in diseased organs.[108-110]

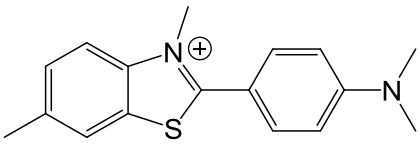

Figure 1.18: The β-sheet selective dye Thioflavine T (ThT).

In 2003-2004, Goto and collaborators reported the real-time observation of fibril formation for the Aβ peptide and β2-microglobulin, which is involved in dialysis-related amyloidosis.[111] In that work, they combined ThT with total internal reflection fluorescence microscopy (TIRFM) to visualise individual fibrils along the slide glass. Hence, they were able to measure Aβ fibrils and study the aggregation kinetics, which was found to be very cooperative and dependent on the presence of seed fragments.

Currently, ThT is the probe of choice for the vast majority of *in vitro* studies with amyloid proteins, and most particularly with Aβ.

1.6.3 Current anti-AD approaches

To date, no effective medication has been found that reverses or stops the progression of AD. As a matter of fact, medication has mainly been directed to the treatment of the symptoms and to relieve behavioural disturbances; it includes anxiolytics, antidepressants, serotonin reuptake inhibitors or anticonvulsants. Only a recent and modest success in the prevention or delay of the disease has been achieved.[112-115]

The current design of anti-AD agents is mainly based on: 1) the assessment of the neuropathology and the aberrant biochemical features in AD brains and 2) epidemiological and genetic studies of risk factors.[112,116] The former approach has been by far the most prolific strategy. The first important anti-AD medications being tested in clinical trials or having reached the clinic are listed in **Figure 1.19**.

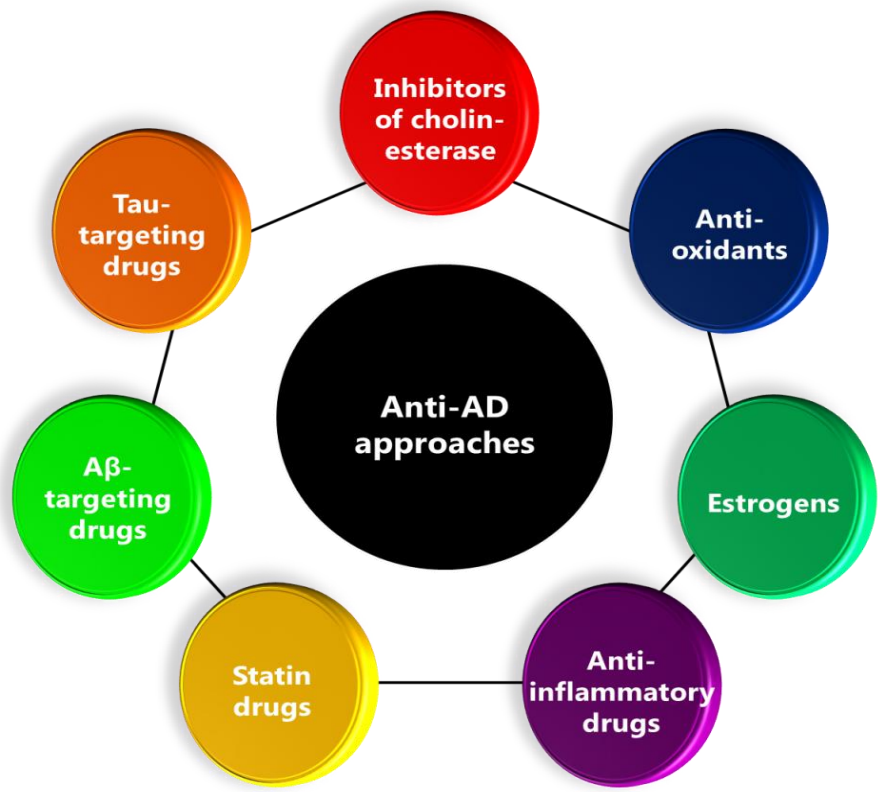

Figure 1.19: Main anti-AD approaches in clinical trials or already in the clinic.

Acetylcholine is a key neurotransmitter in learning and memory, and its levels are reduced in AD brains. However, supplementation of acetylcholine precursors has shown no significant results. Contrarily, inhibitors of cholinesterase (an acetylcholine-degrading enzyme) produced consistent but modest improvements in cognition, and some of them were approved by the FDA. Unfortunately, side effects such as nausea, vomiting, diarrhoea or even hepatotoxicity have been detected. Moreover, cholinesterase inhibitors stabilise symptoms for 1-3 years but do not interfere with the progress of the pathology.[113]

A different strategy consists in the compensation of the condition of oxidative stress by the administration of neuroprotective antioxidants.[112] This class of medication includes vitamin E, a fat-soluble free-radical scavenger; selegiline, which is also used as anti-depressive and in early stages of PD; and Ginkgo Biloba, whose leaves are rich in neuroprotective biomolecules.[112,114] Despite a successful delay of the symptoms for some months and improvement of cognition, only weak effects were observed.

Activated microglia and astrocytes, which participate in tissue inflammation, are involved in AD.[117] Ibuprofen, prednisone or non-steroidal anti-inflammatory drugs have been associated with lower Aβ deposition and reduced risk of suffering AD. However, beneficial effects could not be proven for prednisone and celecoxib in large clinical trials.

ApoE, which is involved in processes such as immune modulation, cholesterol redistribution after injury, and nerve growth, is overexpressed in AD, and mutations in the apoE ε4 allele have been implicated with late-onset familial and sporadic AD (see above). Moreover, elimination of apolipoprotein E in transgenic mice resulted in decreased Aβ aggregation.[118] Statin drugs, which reduce lipid levels, have been found to reduce aggregated Aβ levels in animal models and have been associated with decreased risk of suffering AD in humans.[118]

Oestrogens have been found to reduce amyloidogenic cleavage of wildtype APP, whereas enhanced Aβ production has been observed for APP bearing the Swedish mutation.[53] Oestrogen administration has shown some improvement in cognitive performance in symptomatic recently menopausal women, and some data support protective effects.[53,112] Interaction with apoE and reduction of oxidative stress are additional proposed mechanisms.[53]

As a logical step, medications intended to inhibit the production of Aβ or its clearance from the brain have also been designed. Secretases have been the target of extensive research (see section **1.3.1** for the role of the different secretases). Stimulation of α-secretases, which promotes the non-amyloidogenic cleavage of Aβ, has been achieved *in vitro* with muscarinic agonists and oestrogen but their effect was minimal in clinical trials. Besides, side effects involving the cholinergic system were observed. In turn, inhibitors of β- (BACE-1) and γ-secretases have been found to reduce Aβ production *in vitro* and in transgenic mice.[113] It has been remarkably challenging to find inhibitors of β-secretases since BACE-1 possesses a particularly large catalytic site and thus cannot be blocked by small molecules. Moreover, both β- and γ-secretases have many substrates. A number of inhibitors of γ-secretases are currently undergoing clinical trials.[113] Yet, they are associated with severe toxicity, and investigation has shifted towards modulators, which move the cleavage position to produce non-toxic fragments.[115]

The antibody-assisted clearance of Aβ has received remarkable attention.[119] Mice administered with topical Aβ antibody for 3 days showed enhanced clearance of Aβ deposits, as shown by *in vivo* multiphoton microscopy, which rapidly encouraged research in the field.[120] The injection of pre-made antibodies is known as passive immunisation, whereas the administration of antigens (such as the Aβ peptide) is called active immunisation. Such antibodies are selective to specific monomeric or aggregated species. Currently, several active and passive immunotherapeutic approaches are undergoing clinical trials up to phase 3.[119]

Intercalating compounds that prevent the aggregation of Aβ or reverse amyloids back into monomers have also been developed. Unfortunately, none of the Aβ-targeting approaches that have been tested recently in phase 3 clinical trials has demonstrated relevant beneficial effects.[115]

The microtubule-associated tau protein, the main component of NFTs, has been subject of research as well. The main strategies targeting tau include the stabilisation of microtubules, inhibitors of phosphorylation or phosphatases (enzymes that reverse phosphorylation). *In vitro*, tau kinases have also been pointed to as potential targets. Finally, immunotherapy targeting tau has shown promising results in mice, but adverse effects have also been observed.[119]

1.6.4 Metal-protein attenuating compounds (MPACs)

In spite of the growing body of evidence that links the AD pathology with a dis-regulation in brain metal levels (see sections **1.4** and **1.5**), research in metal-targeting approaches has been scarce until recently. As can be observed in most common anti-AD approaches listed above, none of them include metal ions as their focus of action. Nonetheless, it is our belief that the metal hypothesis cannot remain unexplored.

Chelation might seem the first logical approach to ameliorate the metal-induced Aβ toxicity. However, the administration of traditional metal chelators could be toxic as they may sequester metal centres from essential metalloproteins. Besides, chelator-mediated elimination of Cu from AD brains might be detrimental since total copper levels are already reduced in the pathology.[121,122]

Accordingly, the focus has been set on ionophores, small molecules with the capacity to cross the BBB and displaying a moderate affinity towards metal ions.[122] Such molecules are called metal-protein attenuating compounds (MPACs) and are expected to dissociate metals from amyloids and redistribute them rather than removing them from the affected tissue, while blocking Cu- and Fe-induced ROS production.

In order to test the metal-targeted, ionophore approach, Bush and co-workers developed and evaluated two 8-hydroxyquinolines as potential anti-AD drugs in collaboration with the Australian company Prana Biotechnology Ltd.[122] Such compounds were 5-chloro-7-iodo-8-hydroxyquinoline, also known as **clioquinol**, and 2-(dimethylamino)methyl-5,7-dichloro-8-hydroxyquinoline, also called **PBT2** (**Figure 1.20**).

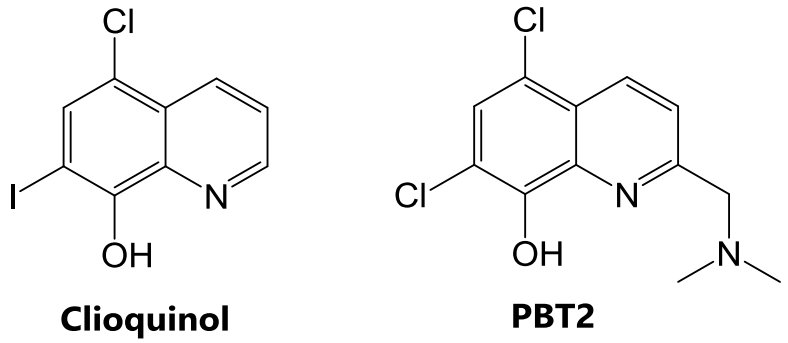

Figure 1.20: Metal-protein attenuating compounds (MPACs) clioquinol and PBT2.

Coordination of clioquinol and PBT2 to metal ions occurs through the deprotonated phenol oxygen and the quinoline nitrogen.[123] Neutral 2:1 clioquinol-metal species are

formed with either Cu(II) and Zn(II). The zinc complex presents a trigonal bipyramid environment with a water molecule as the fifth ligand. The copper-clioquinol species displays a square-planar geometry. On the other hand, PBT2 generates 1:1 complexes with copper, whereas PBT2-Zn species are very versatile and can be generated as 2:1 (cationic or neutral) or 1:1 (anionic) ligand/metal complexes, square-pyramidal or trigonal bipyramids.

Clioquinol was first sold as a topical antiseptic and an oral intestinal amebicide in 1934, but it was banned from the market in the early 70s due to its relationship with myelo-optic neuropathy, which causes sensory and motor disturbances and visual changes.[124,125] Such adverse effect has been related to reduced vitamin B_{12} absorption, which has been overcome by administration of vitamin supplements. Clioquinol is metabolised to glucoronate and sulphates, and in humans it presents a half-life of 11-14 h.[125]

Clioquinol reached AD clinical trials some years ago. In 2003, AD patients with different degrees of severity were treated with clioquinol for 36 weeks in a double-blind phase 2 clinical trial.[126] In these assays, the drug was well tolerated and inhibited cognitive decline, whereas patients receiving placebo experienced deterioration. Moreover, levels of Aβ(1-42) decreased in patients treated with clioquinol but increased in those untreated. Plasma zinc levels rose in patients treated with clioquinol, while no effect was observed on copper levels. However, beneficial effects were only observed in severely-affected patients. Additionally, two patients with familial early-onset AD were treated in 2005 with clioquinol for 9 and 14 months, respectively.[124] The treatment led to improved glucose metabolism in both patients; one of the patients showed progressed cognition while the other one remained stable.

Despite such encouraging clinical results, the large-scale synthesis of clioquinol was hampered by the concomitant generation of toxic 5,7-di-iodo-8-hydroxy quinoline, which prevented further clinical trials. As a result, interest was shifted towards PBT2, whereas clioquinol was abandoned. PBT2 is devoid of iodine, hence solving the contamination issue; it is a better Cu and Zn ionophore than clioquinol and displays superior solubility and BBB permeability.[121] Two types of transgenic mice expressing human Aβ were treated orally with PBT2 and clioquinol. PBT2 outperformed the latter by reducing Aβ levels in hours and improving cognitive performance within days.

In a first phase IIa clinical study, 75 patients over 55 years old with mild AD were treated with PBT2 in a double-blind, randomised placebo-controlled trial for 12 weeks (**PBT2-201 EURO study**).[127,128] Those receiving 250 mg of PBT2 daily presented a 13% decrease in CSF Aβ(1-42), which originates mainly in the brain, but not in plasma Aβ(1-42), suggesting that PBT2 promotes central Aβ clearance. In contrast, serum metal levels were unaltered. Remarkably, they showed an improvement in several cognitive markers compared to those treated with a placebo, although no relationship between changes in CSF Aβ or tau protein levels and cognitive variations were detected. Regarding copper and zinc, no effects on total plasma levels, nor on the levels of protein-bound or exchangeable metal ions, were detected, suggesting that the peripheral metal metabolism was not disturbed.[128]

Subsequently, a larger, 12-month study with 42 patients called **PBT2-204 IMAGINE study** was carried out.[129] In this study, the patients were administered with a placebo or 250 mg of PBT2 and the levels of amyloid were visualised using PiB by PET imaging. The drug showed negligible toxicity over the period of study, but no significant differences were observed between the PBT2 and placebo groups. The authors attributed such results to the "large individual variances over a relatively small number of subjects". A longer (over 18 months) clinical trial with more than 90 subjects per arm (PBT2/placebo) will be required in order to ascertain the beneficial effects of the drug.

It is worth mentioning that the safety and efficacy of PBT2 against HD, another protein-misfolding pathology featuring increased levels of copper and iron, has been tested in the phase II **REACH2HD study**.[130] Promising results have been obtained and phase III studies are awaiting approval.

The therapeutic activity of 8-hydroxyquinolines is not totally clear, but it seems to emerge from different contributions: sequestering metal ions from Aβ peptide, redistributing metal ions (*e.g.* transporting copper back to neurons) and upregulating matrix metalloproteases, which degrade Aβ.[121,125,131] Additionally, Ryan *et al.* found that clioquinol and PBT2 interfere with the aggregation of the Aβ peptide even in the absence of metal ions, by stabilising nontoxic dimers and suppressing the formation of high molecular-weight oligomers.[132]

1.7 Peptides as potential copper-chelating drugs

Peptides can be highly efficient and specific ligands for several metal ions. The peptide backbone possesses multiple donor groups, including the α-amino group, the carbonyl and amide groups and the α-carboxylate. Moreover, the side chains of most amino acids can act as further ligands. Regardless of the multiple binding groups, the binding mode is determined by the peptide sequence, which also contributes to the overall stability of the complex through hydrophobic interactions and pi-pi stacking forces.[133] Therefore, small peptides represent a valuable platform for the discovery of new drugs with easily tunable metal-chelating properties, appropriate solubility in water and low toxicity.

In particular, it is well known that the imidazole rings of histidine residues are good ligands for copper ions.[133,134] Multi-histidinic peptides and proteins with copper-chelating properties are frequently found in nature. The presence of a histidine residue in position 3 allows the simultaneous chelation of copper by three fused rings, resulting in the saturation of its equatorial square-planar coordination and in the most stable peptidic complexes.

In our group we have evaluated the copper-binding capacity of tripeptides of sequence His-His-Xaa, His-Xaa-His and Xaa-His-His, where Xaa is an amino acid residue other than histidine. In these studies, we found that the His-Xaa-His sequence is the most efficient one at chelating copper(II) ions. Such motif has been observed in a number of proteins, including APP (His-Leu-His-Trp-His), SOD5 (His-Val-His) or amyloid-like protein 2 (APLP2, His-Gln-His).[94] Besides, the sequence and the relative position of the histidine residues are key in the electrochemical properties of the resulting copper complexes.[135]

1.8 Aim of the PhD project

Despite the extensive work made so far, the metal-targeted anti-AD approach is vastly unexplored. In particular, the rich coordination chemistry of copper should allow for the design of innumerable compounds with potential Cu-chelating properties, which may ameliorate the copper-induced toxicity of Aβ peptide. Indeed, copper represents a potential therapeutic target which cannot be overlooked, considering its increasingly evidenced implication in the aggregation of Aβ into toxic oligomers and the generation of oxidative stress. Copper-targeting therapies in combination with those previously mentioned, such as cholinergic therapy and promotion of Aβ clearance might produce improved beneficial effects.

In this context, peptides offer a great opportunity for the design of versatile multifunctional metal-chelating drugs with high biocompatibility. Peptide synthesis is straightforward and widely developed, and high-water solubility can be achieved.

This work aims to use short (3-4 amino acids) peptides containing the motif His-Xaa-His as potential copper-chelating agents and evaluate their *in vitro* capacity to remove Aβ-bound copper ions, lessen the copper-induced ROS production and prevent the copper-induced generation of oligomeric Aβ. Such peptides were rationally designed for their additional application in the detection of copper ions or Aβ aggregates and to be transported grafted onto gold nanoparticles to improve their properties *in vivo*. The implication of copper in the formation of dityrosine cross-links and in the aggregation of Aβ, and how the chelating peptides affect these processes have also been assessed. Thus, the following objectives were defined and pursued in **Chapters 2-6**, respectively:

Objective 1: Synthesis of copper-chelating peptides with different emissive properties.

Objective 2: Evaluation of the copper-chelating properties of commercial (custom-made) and newly synthesised peptides and their effect against Cu-induced Aβ toxicity.

Objective 3: Assessment of the impact of dityrosine cross-links on the aggregation of Aβ peptide, and the effect of copper-chelating peptides in this process.

Objective 4: Attachment of Cu-chelating peptides to gold nanocarriers and *in vitro* studies with Aβ peptide.

Objective 5: Design of fluorescent probes for the detection of aggregated Aβ.

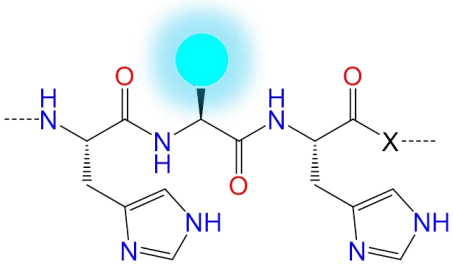

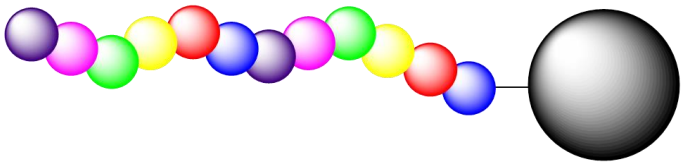

2. Synthesis of emissive chelating peptides

2. Synthesis of emissive chelating peptides

2.1 Introduction

2.1.1 Design of the peptides

As mentioned in **Chapter 1**, metal ions have received scarce attention as therapeutic targets in Alzheimer's disease (AD) in spite of the growing evidence of imbalanced metal homeostasis in AD brains. In this regard, we have found that peptides containing the *N*-terminal His-Xaa-His sequence (Xaa = randomly-chosen amino acid) are efficient copper(II) ligands.[135] Based on this finding, we decided to use short (3-4 L-amino acids) peptides containing the *N*-terminal His-Xaa-His motif for the evaluation of copper chelation as a therapeutic strategy in Alzheimer's disease. Additionally, fluorescent amino acids displaying different emissive properties were included, for their potential utilisation as sensors.

The peptides herein prepared presented the sequence His-Xaa-His (Xaa = Lys, Nle) and His-Lys-His-Lys. Besides, they are either *C*-terminal acids or amides, since the presence of a carboxylic acid was disadvantageous for some applications and had to be amide-protected. Moreover, amide protection confers additional stability against peptidases (also called proteases), which are peptide-degrading enzymes. Likewise, the *N*-terminal amino group was in some cases protected by acetylation.

The introduction of the fluorescent probes was achieved in some cases by the derivatisation of Fmoc-lysine and its subsequent incorporation into the growing peptide, and in other cases, by direct tagging of the previously formed peptide. The probes used in this chapter are listed below:

*2.1.1.1 Coumarin-3-carboxylic acid (**Coum**)*

Coumarins (benzopyran-2-ones, also called α-benzopyrones) are structurally diverse compounds found, for example, in fruits, vegetables, coffee, wine and nuts (**Figure 2.1**). For many years, such natural products have attracted considerable attention since they exhibit remarkable pharmacological properties.[136] Indeed, antioxidant, anti-inflammatory, anti-cancer and even anti-HIV effects have been attributed to coumarinic compounds.[137-140]

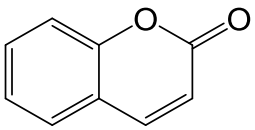

Figure 2.1: Benzopyran-2-one (coumarin).

Moreover, coumarins display fluorescent properties which are dramatically dependent on the substituents present in the aromatic ring, also varying with the solvent used.[141,142] Their photophysical behaviour has thus been the subject of intense research for applications as dyes, molecular switches and memories.[143] Here, we have used the carboxylic acid derivative of the parent coumarin moiety (coumarin-3-carboxylic acid, **Coum**) to label Fmoc-Lys-OH for its incorporation into peptides; its optical properties are described in **Chapter 3**.

*2.1.1.2 4-*N,N*-dimethylamino-1,8-naphthalimide (**4DMN**)*

Fluorescent probes that are sensitive to the polarity of their environment are extremely useful tools for different applications. Such fluorophores usually present a change in their emission intensity, the excitation/emission wavelengths or both. If introduced into a peptide, they can be used to study protein dynamics, determine protein-protein interactions and affinity constants, among other examples.

The 4-*N,N*-dimethylamino-1,8-naphthalimido (**4DMN**) probe is a component of this family which shows remarkable photophysical properties and chemical stability (**Figure 2.2**). Recently, Loving and Imperiali designed a method to prepare a 4DMN derivative of Fmoc-alanine, which was used to study the recognition between two peptides.[144] In this work, we have adapted the procedure developed by the Imperiali's group to the synthesis of Fmoc-Lys(4DMN)-OH for its subsequent introduction into peptides.

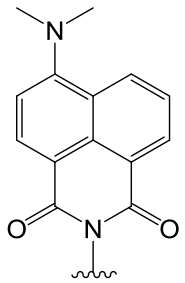

Figure 2.2: 4-*N,N*-dimethylamino-1,8-naphthalimido (4DMN) probe.

*2.1.1.3 Fluorescein (**Fluo**) and Rhodamine B (**RhoB**)*

Fluorescein and rhodamines are other popular fluorophores frequently used in biochemistry and biotechnology. Fluorescein and some rhodamines (such as rhodamine B, which was used in this work) exhibit strong emissive properties and can be used separately or in tandem as Förster resonance energy transfer (**FRET**) pairs, which can be used as ratiometric probes for many applications in the field of sensing and detection of different molecules and ions (**Figure 2.3**). In FRET systems, a fluorophore called donor transfers non-radiative energy to a second nearby (<100 Å) fluorophore, the acceptor. Hence, upon irradiation of the probe at the excitation wavelength of the donor, fluorescence at the emission wavelength of the acceptor is observed.

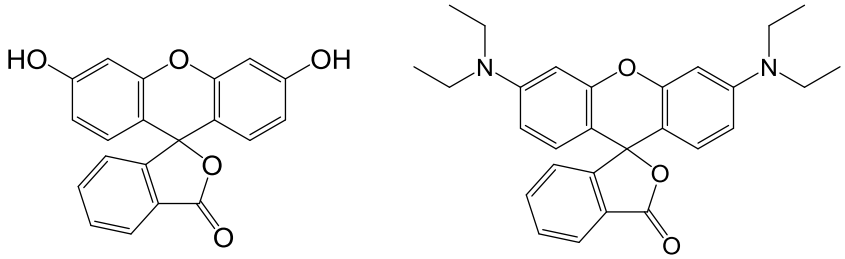

Fluorescein **Rhodamine B**

Figure 2.3: Fluorescein (**Fluo**) and rhodamine B (**RhoB**).

2.1.1.4 Applications of the peptides

The Cu(II)-chelating peptides were rationally designed for different applications, such as metal-protein attenuating compounds (MPACs) -to reduce the toxicity that derives from copper-Aβ interaction-, detection of Aβ aggregates and grafting onto gold nanoparticles to improve their delivery into the central nervous system (CNS, **Figure 2.4**). Accordingly, a toolbox of peptides was necessary to deal with the different properties required in this work (**Figure 2.4**). The peptides containing natural, unmodified amino acid residues were purchased, while peptides containing synthetic fluorescent probes were prepared by conventional Fmoc solid-phase chemistry. The synthesis of such fluorescently-labelled peptides is described in this chapter.

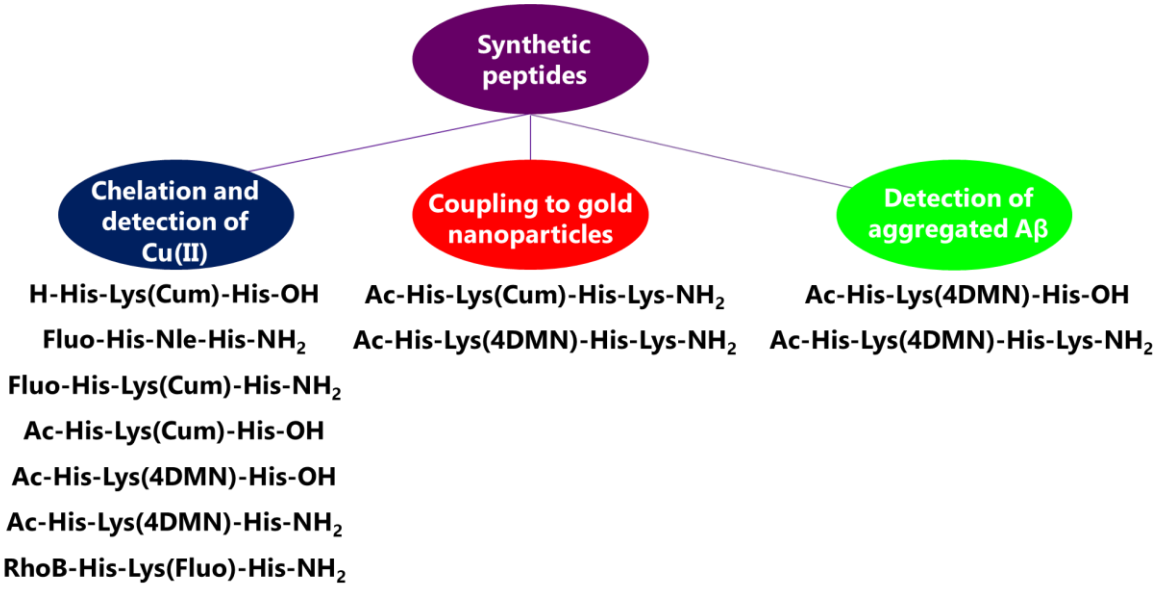

Figure 2.4: Application of the different peptides synthesised.

Once the building blocks and the structures of the multifunctional peptides were defined, the synthesis of the chelating agents was addressed by solid-phase peptide synthesis (**SPPS**), a methodology which has been the subject of immense efforts and optimisation over the years since its first description, more than 50 years ago.

2.1.2 A brief history of peptide synthesis

Peptides and proteins are biological polymeric chains of amino acids (average of 300 amino acid residues) that are involved in numerous cellular functions. The amino acids are linked through peptidic bonds, which are formed by the alpha amino group of an amino acid and the carboxylic acid of the next monomer of the biomolecule (**Figure 2.5**). Peptides and proteins exert many diverse functions in living organisms, such as antioxidant, opioid, antimicrobial, antithrombotic, enzymatic, structural or metal transport, among others.[145]

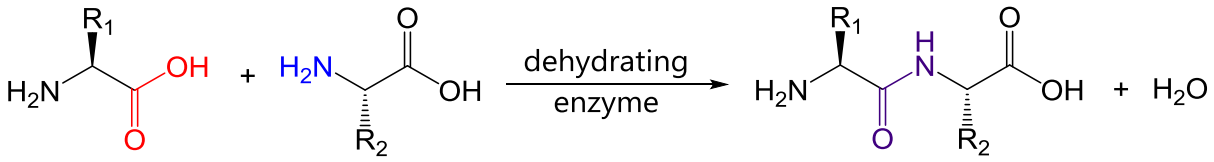

Figure 2.5: Enzyme-catalysed generation of a peptide bond in living organisms.

The properties and functions of peptides/proteins are directly determined by their three-dimensional structure, which is ultimately defined by the amino acid sequence: the interactions among the different amino acid residues render the folding of the peptide into the most thermodynamically favourable conformations. The biochemical information for the synthesis of peptides is encoded in DNA, which is then transcripted into RNA. This RNA is finally used to incorporate and assemble the amino acids in a sequential fashion, from the *N*-terminus to the *C*-terminus.

Although peptides are naturally occurring substances, the amount that can be extracted from nature is limited, and much lower than the quantities that modern society requires to fulfil the necessities in the different industrial fields. Indeed, applications of peptides include drug development,[146,147] drug delivery,[148] diagnostics,[149] biomaterials,[150] cosmetics[151] or nutrition.[152] The chemical synthesis of peptides and proteins was hence one of the greatest challenges of the 20th century.[153]

It was the bright German organic chemist Emil Fischer who set the first stone for the development of the organic synthesis of peptides (**Figure 2.6**). The principles and techniques designed by Fischer and his colleagues, which used side chain-protected amino acids and organic solvents as the reaction media, led to the eventual preparation of fully functional human insulin, a 51 amino acid residue protein.

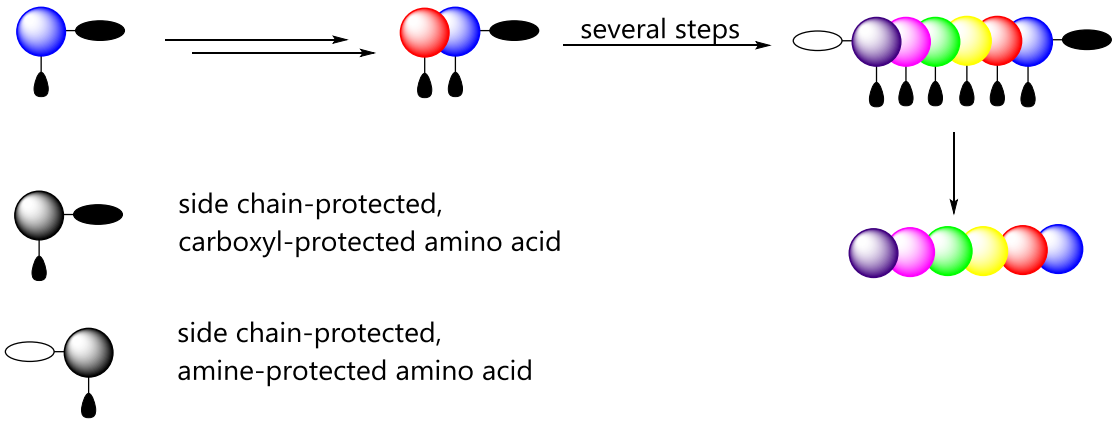

Figure 2.6: Classical peptide synthesis in solution.

Nevertheless, these procedures were far from efficient. The poor solubility of the protected amino acids resulted in slow and incomplete reactions, as well as elevated side-product generation. Moreover, the purification of the crude products by recrystallisation often did not result in sufficiently pure peptides, and the chiral information was frequently lost during the several synthetic steps.

Thus, it is not surprising that the apparition of recombinant DNA engineering in *Escherichia coli* was received with overwhelming enthusiasm by researchers, who started to discard common chemical peptide synthesis as a viable approach. In this technique, which was developed about 40 years ago, recombinant DNA encoding the information for the peptide of choice is introduced into the bacteria. The desired peptide is then expressed by the microorganisms, and subsequently isolated and purified. However, despite the importance and the significant impact of this approach, it presents some limitations. First, only the twenty natural amino acids can be used; second, post-transcriptional modifications are extremely complicated or even impossible.

In 1963, Robert Bruce Merrifield reported the strategy known as solid-phase peptide synthesis (SPPS), which earned him the Nobel Prize in Chemistry in 1984. This strategy would ultimately lead to a great renaissance of the chemical synthesis of peptides.[154] In the approach developed by Merrifield, N^{α}-, side chain-protected amino acids are sequentially bound to an insoluble polymeric support or resin, usually copolymers of styrene with low percentages of divinylbenzene (**Figure 2.7**). Contrary to natural synthesis, the peptide chains in SPPS grow from the *C*-terminus to *N*-terminus.

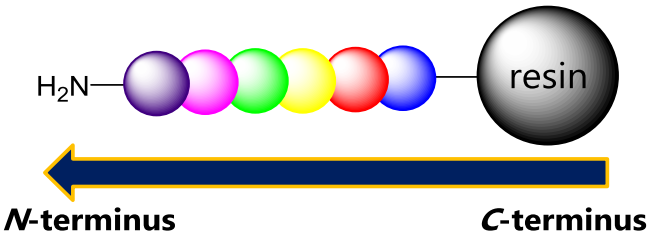

Figure 2.7: *C*-terminal to *N*-terminal growth of peptide chains in SPPS.

Although it is called "solid-phase" synthesis, the reactions take place in a gel phase where solvents are added. Once the reaction is finished, the solvents, excess of reagents and soluble by-products are eliminated by filtration, while the growing chains remain bound to the polymeric support. Therefore, this novel approach greatly facilitated the purification of the peptide. Moreover, this approach allows the use of high excesses of amino acids, which ultimately leads to quantitative or nearly-quantitative coupling yields. Finally, the peptide product is released from the resin and the protecting groups of the side chains are eliminated simultaneously.

Since its origins, SPPS has evolved considerably and has been optimised with the design of a number of polymeric supports, protecting groups and coupling agents,

which have been used, not only to connect natural amino acids, but also non-natural amino acids, fluorescent tags or other specific chemical groups, with good specificity.[155,156] Other synthetic strategies based on SPPS, such as the side chain anchoring to the resin, have been developed as alternatives to the standard binding through the α-carboxylic group.[157] Moreover, the easy sequential assembly of the peptide chain has allowed the development of automatic SPPS, which is nowadays routinely used by companies or even research groups. Finally, microwave-assisted SPPS is emerging as a useful tool to accelerate both the deprotection and coupling steps.[158]

Yet, although solid-phase synthesis has provided a much easier approach for the preparation of peptides, the maximum length that can be efficiently produced in a sequential manner includes up to about 50 amino acid residues. In this context, the convergent synthesis consisting in the coupling of preformed peptide fragments, either in solid phase or in solution, has been applied (**Figure 2.8**).[159,160]

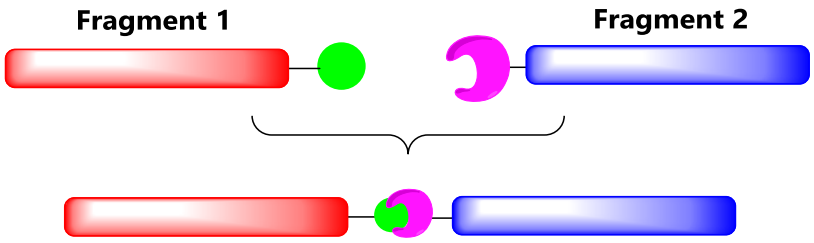

Figure 2.8: Convergent peptide synthesis by coupling of preformed fragments.

This coupling can be performed via conventional peptide bond formation or by the methodology known as *chemical ligation*, which uses complementary chemical functionalities that react specifically with each other. Nonetheless, some researchers were critical about the fact that the link thus generated was not a natural connection and then the resulting proteins were not appropriate for their utilisation. Accordingly, an alternative approach was developed, which was called *native chemical ligation* (**Figure 2.9**).

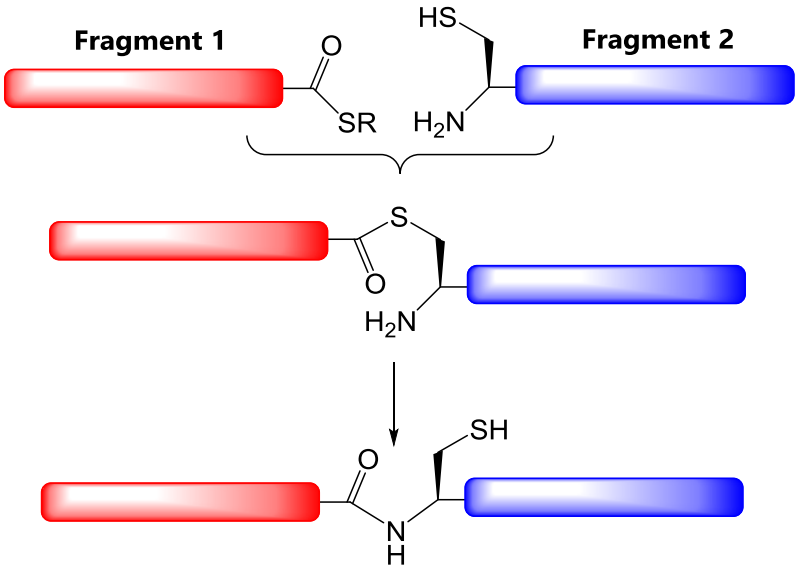

Figure 2.9: Native chemical ligation of two preformed fragments.

In native chemical ligation protocols, the *C*-terminal thioester function of one fragment reacts with the thiol group of the *N*-terminal cysteine residue of the second fragment, affording a thioester-connected intermediate. Then, the *N*-terminal α-amino group of the second fragment undergoes an intramolecular nucleophilic attack to the labile thioester bond to generate the natural amide bond. This approach has allowed the synthesis of proteins larger than 200 amino acid residues.[153]

In conclusion, the solid-phase approach designed by Merrifield revolutionised the field of peptide synthesis, and the progressive advances in the methodology have turned SPPS into a truly powerful tool for chemists. Every year, a great number of articles on SPPS are published worldwide, and massive amounts of money are invested in the solid-phase synthesis of peptides. Hence, SPPS has a deep impact on modern chemistry.

2.1.3 Boc/Bzl and Fmoc/tBu strategies in SPPS

Two main synthetic strategies are used in SPPS to assemble peptide chains depending on the kind of protecting groups (**PG**) presented by the amino acids at their α-amino function and their side chains: Boc/Bzl and Fmoc/tBu strategies (**Figure 2.10**). In the Boc/Bzl approach, the α-amino groups of the amino acids are protected with *tert*-butoxycarbonyl (Boc) groups -labile to trifluoroacetic acid (TFA)-, whereas their side chains are protected with benzyl-type (Bzl) groups -labile to fluorhydric acid (HF)-,

which also cleaves the peptide from the resin. This synthetic approach requires careful handling due to the hazards associated to HF, and it is partially orthogonal.[161,162]

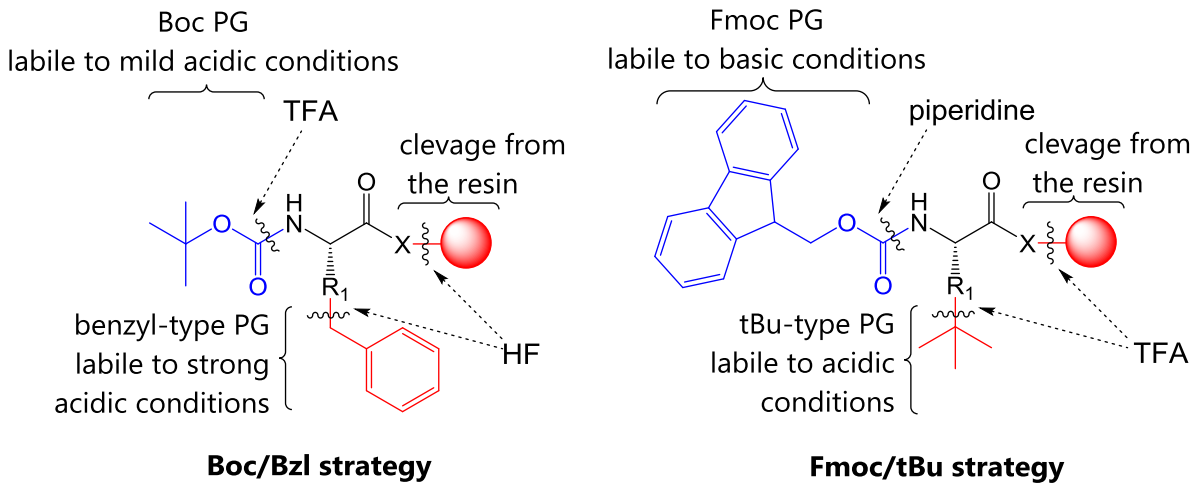

Figure 2.10: Boc/Bzl and Fmoc/tBu strategies in solid-phase peptide synthesis.

In contrast, the Fmoc/tBu strategy is carried out using amino acids bearing a 9-fluorenylmethoxycarbonyl (Fmoc) group at their α-amino function, which is labile to bases such as piperidine, and TFA sensitive *tert*-butyl (tBu) type moieties as the protecting groups for the side chains.[163] The Fmoc strategy is considered totally orthogonal, and it was the strategy of choice for this work.

2.1.4 Polymeric supports

In the present study, two different polymeric supports, namely 2-chlorotrityl chloride resin (2-CTC, also called Barlos resin) and Rink amide AM resin (RA AM), were used for the solid-phase synthesis of the peptides (**Figure 2.11**).[164-168] The former affords carboxylic *C*-terminal peptides whilst the latter gives *C*-terminal carboxamide peptides, as a result of their different functionalities. Besides, the RA AM resin presents a norleucine residue which serves as an internal standard for amino acid quantification.

N,N-dimethylformamide (DMF) and dichloromethane (DCM) are generally used to shrink and swell the resin, respectively, and thus achieve a better washing and conditioning of the support. These solvents are also added to the resins in order to generate the gel phase where the Fmoc chemistry takes place.

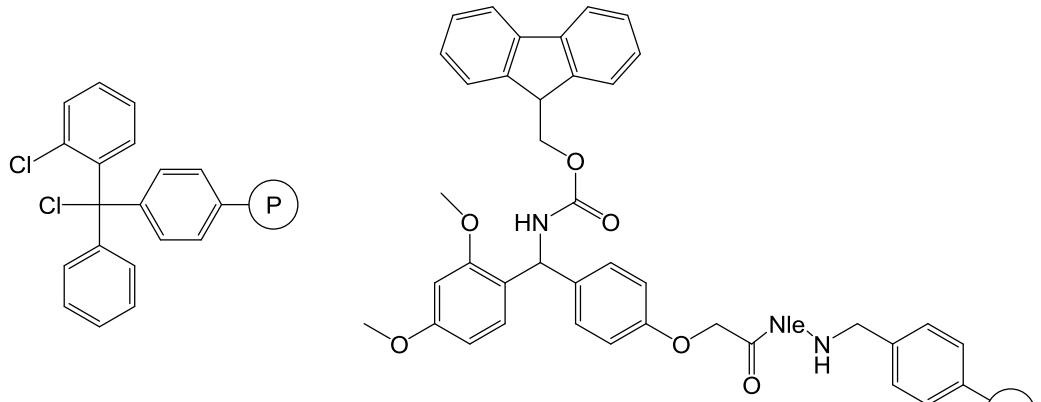

2-Chlorotrityl chloride
2-CTC
1.6 mmol/g

Rink amide AM
RA AM
0.69 mmol/g

Figure 2.11: 2-CTC and RA AM for resins used solid-phase synthesis. The extent of labelling (mmol of active sites per g of resin) is given under the names of the resins.

In addition, such polymeric supports avoid the formation of 2,5-diketopiperazines (DKPs), important side products in Fmoc chemistry, which are generated *via* intramolecular aminolysis of the peptide-resin bond.[169,170] The unprotected α-amino group of the second amino acid bound to the resin can undergo nucleophilic attack of the dipeptide-resin bond (an ester bond in general), producing DKP, as shown in **Figure 2.12**.

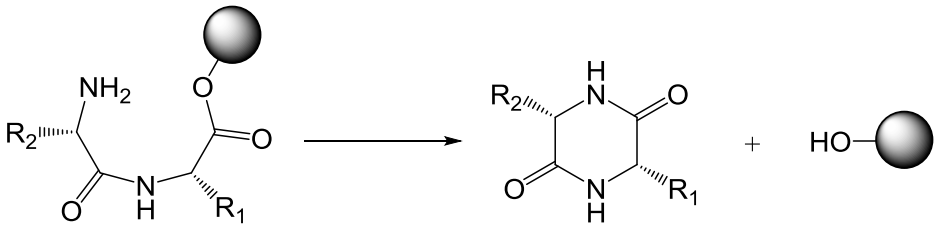

Figure 2.12: Solid-phase generation of a 2,5-diketopiperazine (DKP).

Indeed, the steric hindrance of the bulky polymeric supports such as 2-CTC or the low reactive amide bonds afforded by resins such as RA AM prevent the formation of DKPs.

Histidine is particularly prone to epimerise upon activation. The basic imidazolic π nitrogen can subtract the α proton to form an enolate-like intermediate that leads to the undesired epimerised residue and the formation of diastereomeric mixtures of peptides (**Figure 2.13**). This side reaction can be avoided by temporarily protecting the π nitrogen, or by protecting the τ nitrogen with bulky or electron-withdrawing groups

that reduce the basicity of the imidazole ring. The 2-CTC resin can also prevent the epimerisation of the *C*-terminal histidine since its anchoring takes place in the absence of any activated species, as will be explained later.

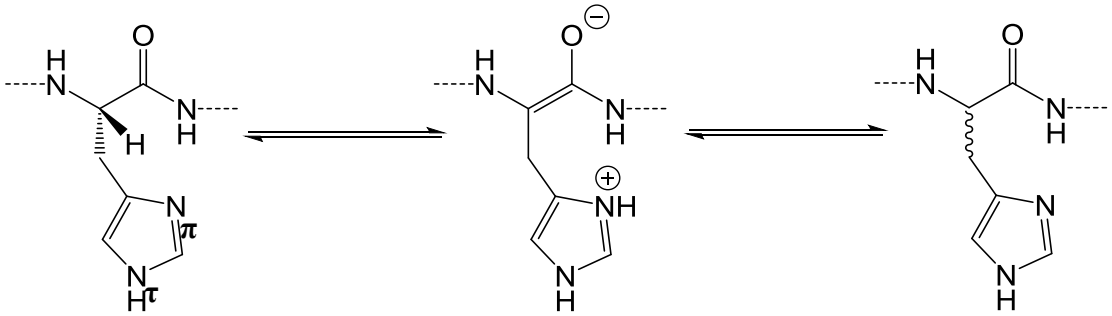

Figure 2.13: Epimerisation of histidine residues.

2.1.5 Coupling agents

Carbodiimides have been used in solid-phase peptide synthesis since its early stages, as carboxylic acid activators. Such compounds generally allow the formation of amide bonds under mild conditions and at room temperature. *N,N'*-dicyclohexylcarbodiimide (DCC) and *N,N'*-diisopropylcarbodiimide (DIC) are probably the most popular agents, although DCC is less frequently used as it is a powerful allergen and yields highly insoluble *N,N'*-dicyclohexylureas (**Figure 2.14**).

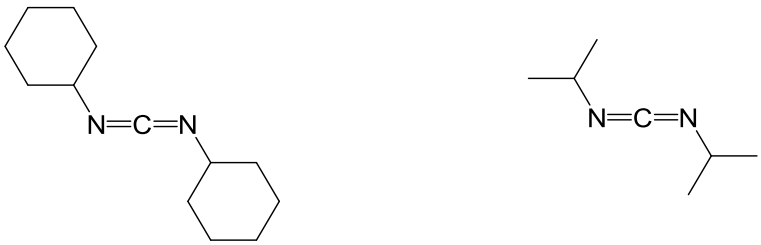

DCC *N,N'*-Dicyclohexylcarbodiimide

DIC *N,N'*-Diisopropylcarbodiimide

Figure 2.14: Carbodiimides DCC and DIC.

Nonetheless, side reactions can occur during the coupling of the amino acids. One of the most frequent ones is racemisation through the intramolecular cyclisation into 5(4*H*)-oxazolones (**Figure 2.15**). The chiral configuration is lost *via* the generation of the enol tautomer, thus leading to the racemic amino acid.

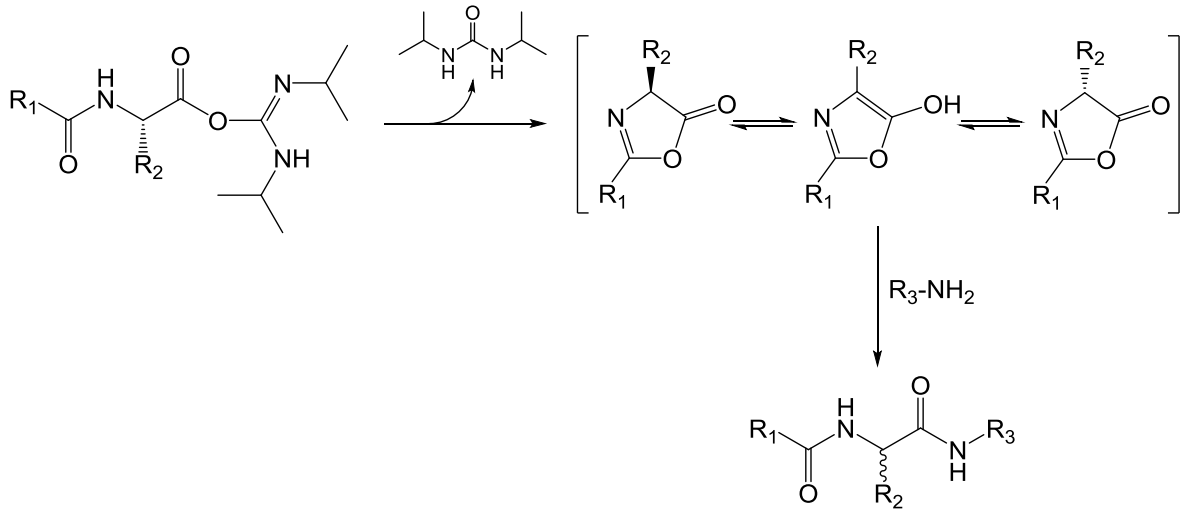

Figure 2.15: Racemisation of amino acids *via* oxazolone formation.

To avoid such undesired processes, additives are used in the coupling mixture. In that context, 1-hydroxybenzotriazole (HOBt) and aza-1-hydroxybenzotriazole (HOAt) have been extensively used in SPPS for several years. These additives generate an active ester of the amino acid that is less reactive but also less prone to undergo side reactions such as racemisation or the formation of *N*-acylureas.

Recently, the new additive ethyl 2-cyano-2-(hydroxyimino)acetate, also called Oxyma, was developed.[171] Oxyma is added to the reaction mixture in the presence of a carbodiimide in order to minimise racemisation and accelerate the coupling of the amino acid, while presenting a lower risk of explosion and being much cheaper than most HOBt derivatives. The structures of HOBt, HOAt and Oxyma are shown in **Figure 2.16**.

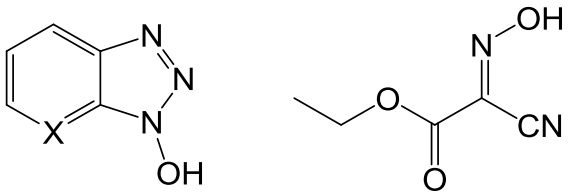

HOBt: X = CH
HOAt: X = N

Oxyma

Figure 2.16: Additives for the coupling of amino acids HOBt, HOAt and Oxyma.

Carbodiimides activate N^{α}-protected amino acids by generating the *O*-acylisourea derivative, which can further react either with another molecule of amino acid or with

Oxyma, affording the symmetrical anhydride or the active Oxyma ester, respectively (**Figure 2.17**). Both species can then be attacked by a free amino group, thus yielding an amide bond.[172] If the formation of the peptide bond is not fast enough, the irreversible generation of *N*-acylurea can take place. Therefore, Oxyma is used to accelerate the coupling reaction and avoid the production of such side products.

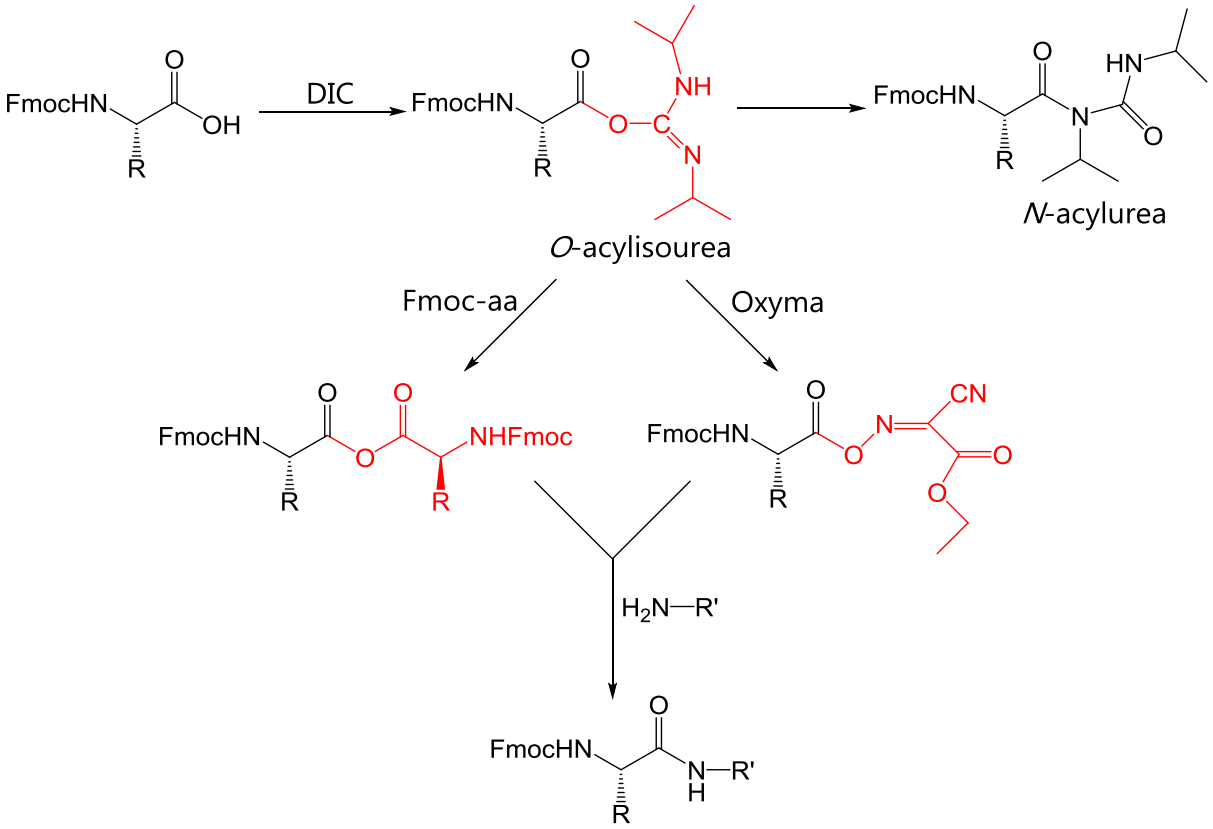

Figure 2.17: Mechanism of the coupling of Fmoc amino acids using DIC and Oxyma.

Other coupling agents more efficient than carbodiimides have been developed, phosphonium (which include PyBOP and PyAOP) and uronium (or amidinium, including HATU, HBTU and HCTU) salts being the most popular ones (**Figure 2.18**).[173] These salts are HOBt/HOAt derivatives and present improved reaction times even for intricate couplings, especially in the case of HATU. All of them require basic media (generally DIPEA) to perform the coupling.

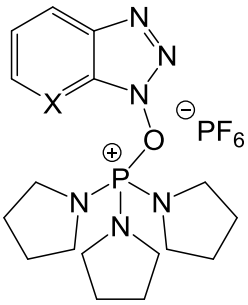

PyBOP: X = CH
PyAOP: X = N

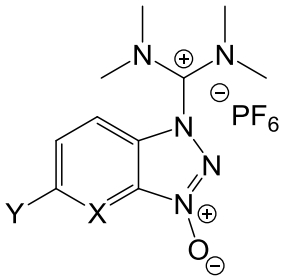

HATU: X = N, Y = H
HBTU: X = CH, Y = H
HCTU: X = CH, Y = Cl

Figure 2.18: Coupling agents in SPPS.

HATU is rather expensive so its use is somewhat limited. Instead, HCTU has been reported to be almost as efficient as HATU and is much cheaper.[174] In addition, many other coupling agents and coupling procedures have been described in the literature.[175,176]

Since the peptides prepared in this work are short (3-4 amino acid residues), expensive, more efficient coupling agents were not required; hence, DIC and Oxyma were selected for the preparation of the different fluorescent chelating peptides.

In the following sections, the general synthetic procedure applied in the present work is described, followed by the specific approach for each peptide. Finally, the yields and chromatographic purities of the products are given.

2.2 Objectives

- Synthesis and characterisation of the non-natural amino acid *N*$^{\alpha}$-Fmoc-*N*$^{\varepsilon}$-(Coumarin-3-ylcarbonyl)-*L*-lysine (Fmoc-Lys(Coum)-OH).
- Synthesis and characterisation of the non-natural amino acid *N*-α-Fmoc-(4-*N,N*-dimethylamino-1,8-naphthalimido)-*L*-lysine (Fmoc-Lys(4DMN)-OH).
- Solid-phase synthesis of peptides (3-4 amino acids) containing the sequence His-Xaa-His and 1-2 fluorescent probes; characterisation by ^{1}H, ^{13}C-NMR and MS, and evaluation of their chromatographic purity.

2.3 Results and discussion

2.3.1 General solid-phase synthetic approach

2.3.1.1 Coupling of the first amino acid

The first step for the preparation of the peptides consisted in the anchoring of the *C*-terminal amino acid to the polymeric support. The loading of the first amino acid onto 2-CTC resin is achieved through a unimolecular nucleophilic substitution (S_N1) assisted by a non-nucleophilic base, such as DIPEA, in DCM (**Figure 2.19**). Due to the extent of labelling of this polymeric support (1.6 mmol/g), optimised conditions (1.5 equivalents of amino acid, 1.5 h) were used in order to obtain 40-60% loading yields as, an excessively crowded resin could difficult the proper growing of the peptide chains.

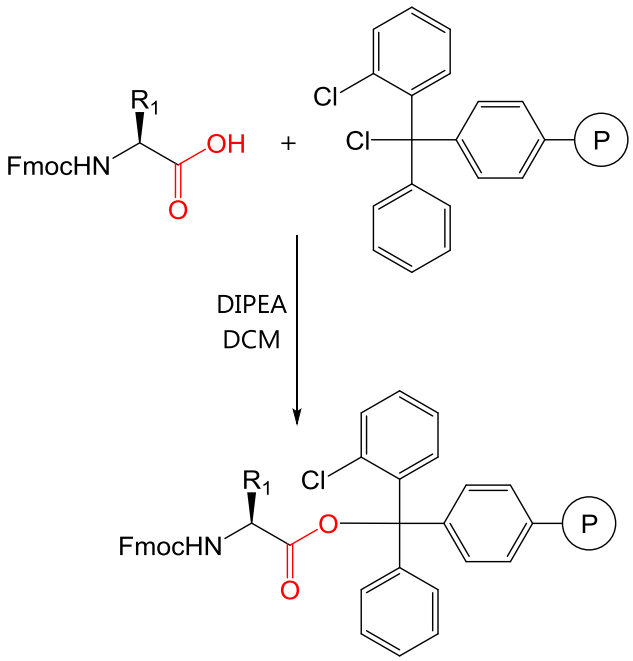

Figure 2.19: Anchoring of the first amino acid residue onto the 2-CTC resin through an ester bond.

Once the first amino acid was anchored, the remaining binding sites had to be blocked in order to avoid the incorporation of the following amino acids of the sequence, which would lead to the formation of deletion peptides. The capping of these sites was achieved by reacting the amino acyl-resin with MeOH through an analogous S_N1 mechanism to yield the unreactive methyl ether function.

For the RA AM resin (0.69 mmol/g), the loading of the first amino acid follows a completely different pathway. The amino binding sites present in this resin are protected with Fmoc groups. Hence, a deprotection step with piperidine was required before the coupling reaction. Bases such as piperidine cleave the Fmoc group, yielding a dibenzofulvene-piperidine adduct and the unprotected amino function, as shown in **Figure 2.20**.[172]

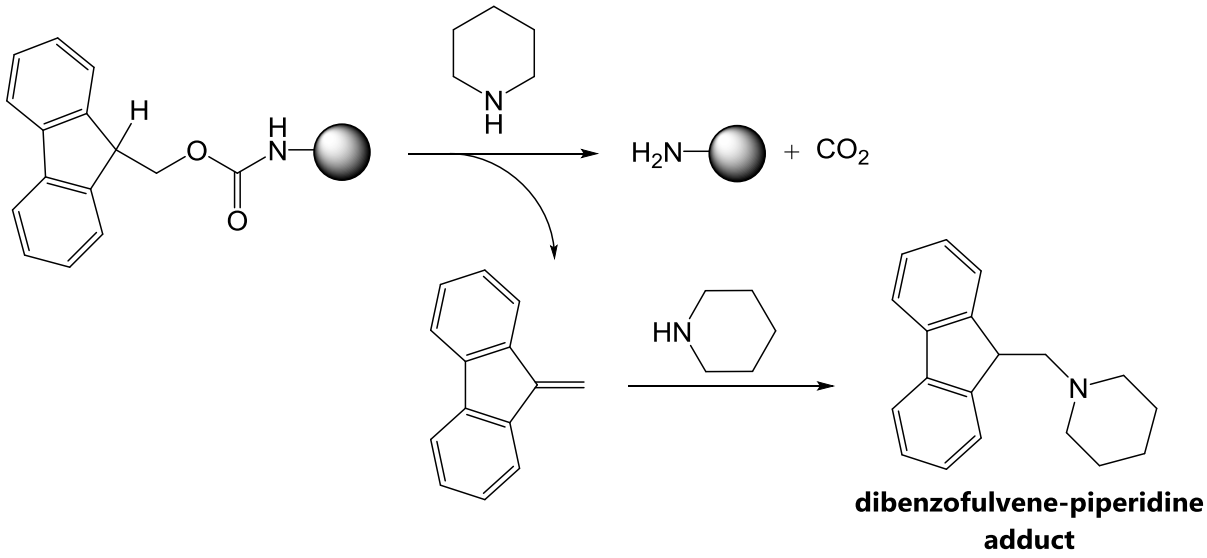

Figure 2.20: Deprotection of Fmoc-(RA AM) and formation of the dibenzofulvene-piperidine adduct.

Then, the free amino group can undergo a nucleophilic attack of the amino acid activated with DIC to afford an amide bond (**Figure 2.21**). The anchoring reaction was performed twice using 3 eq of the amino acid and the coupling agents in order to achieve nearly-quantitative yields.

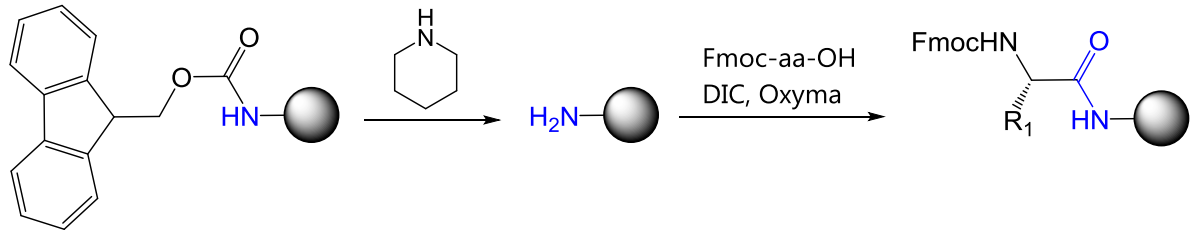

Figure 2.21: Anchoring of the first amino acid residue onto the RA AM resin.

Analogously to the 2-CTC resin, the binding sites that remained unreacted had to be capped. An acetic anhydride/DIPEA mixture in DMF was used to block the amino

functions with acetyl groups, preventing them to react with the following activated Fmoc amino acids.

Information about the yield of the coupling of the first amino acid to the polymeric support and the elongation steps can be obtained by quantifying the amount of the temporary protecting group Fmoc present in the resin through UV-Vis absorbance analysis of the dibenzofulvene-piperidine adduct formed (**Figure 2.22**). The concentration of Fmoc groups is determined by using the Lambert-Beer law (**Equation 2.1**):

$$\boldsymbol{A = \varepsilon \times c \times l} \qquad \textbf{(2.1)}$$

where $\boldsymbol{\varepsilon}$ is 7800 $M^{-1} \times cm^{-1}$ at 301 nm, $\boldsymbol{c}$ is the concentration of the adduct in mol × dm^{-3}, which corresponds to the concentration of the bound amino acid, and $\boldsymbol{l}$ is the optical path length of the cuvette, usually 1 cm.

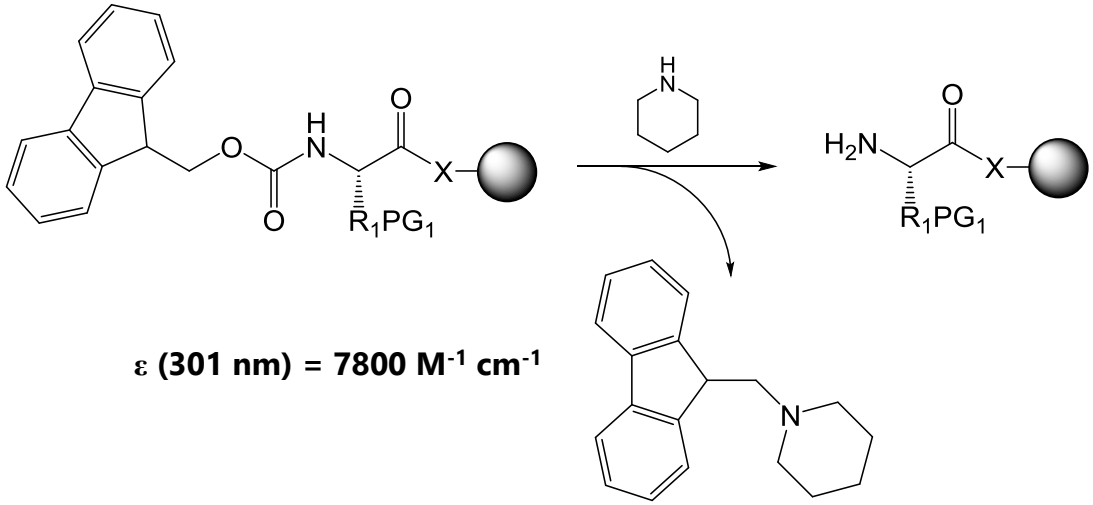

Figure 2.22: Elimination of the Fmoc protecting group and quantification of the dibenzofulvene-piperidine adduct.

The Fmoc quantification analysis was carried out to determine (i) the yields of the loading of the first amino acid of every sequence and (ii) the on-resin yields after the coupling of the last amino acid.

2.3.1.2 Elongation steps

Once the amount of amino acid bound to the resin is determined, the peptide chain is progressively grown through successive coupling/deprotection cycles. An excess (3 eq) of Fmoc amino acids, the coupling agent (DIC) and the additive (Oxyma) were used for the coupling reactions in order to achieve quantitative elongation.

Despite the fact that carbodiimide activation proceeds more efficiently in DCM, the subsequent nucleophilic attack of the amino groups is performed in polar solvents such as DMF because it is faster. DMF/DCM mixtures were employed to achieve optimal results.

After the coupling reaction is complete, the Fmoc group of the amino acid just incorporated to the growing chain is eliminated, and the coupling-deprotection cycle is repeated until the targeted peptide sequence is obtained (**Figure 2.23**).

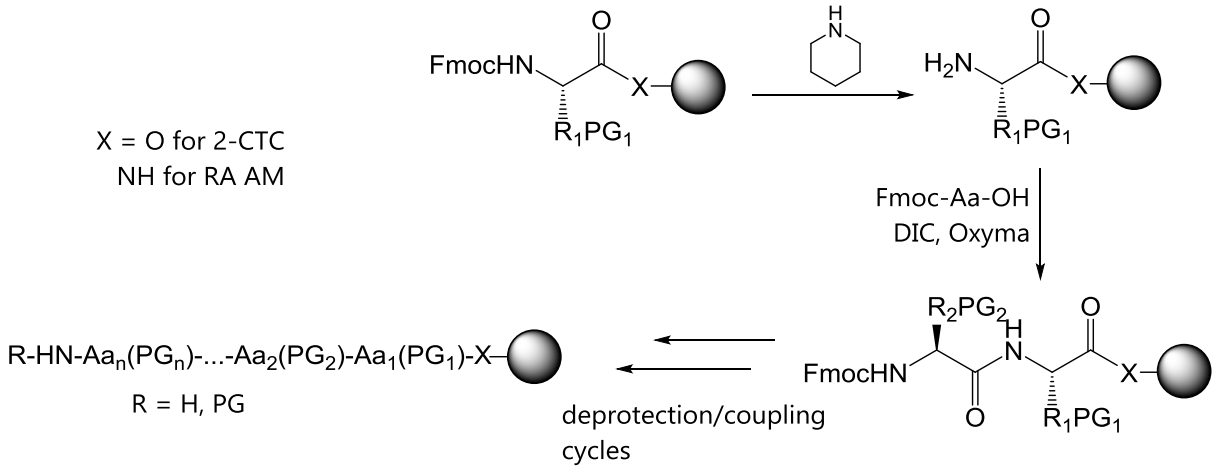

Figure 2.23 Elongation steps in Fmoc peptide synthesis using DIC and Oxyma.

The ninhydrin test, also called Kaiser Test, is a qualitative colorimetric experiment that is used for the detection of free primary amino groups, thus providing information about the completeness of the coupling steps. In this assay, ninhydrin reacts with primary amines to yield a dark blue compound called *Ruhemann's blue* (**Figure 2.24**).[172]

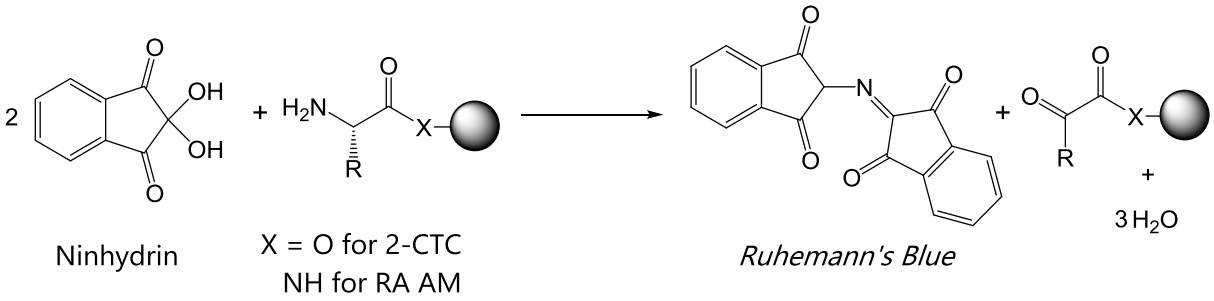

Figure 2.24: Ninhydrin or Kaiser test for the detection of primary amines.

Hence, the persistence of the initial yellow colour indicates the absence of free α-amino groups and a complete coupling reaction, while a change into a pale to dark blue colour means that the coupling step should be repeated.

When the desired peptide chain is finished, the *N*-terminal α-amino group can be either left unprotected or functionalised (*e.g.* with a fluorescent dye or with a protecting group). The derivatisation of the *N*-terminus is very versatile as many different functional units can be bound, providing the peptide with special properties. However, it must be considered that the molecule will present different coordination modes to copper or other metal ions depending on the presence/absence of these units, as will be described in **Chapter 3**.

2.3.1.3 Cleavage of the peptide from the resin

Once the elongation process is finished, the target peptide was recovered from the resin through treatments with TFA, which cleaves the peptide-resin bond as well as the protecting groups of the side chains. The concentration of TFA in the cleavage mixture depends on the resin; thus, 60% TFA was used for 2-CTC resin whereas 95% TFA was necessary to cleave the peptidyl-Rink amide resin, as the former is more labile to acidic conditions. Longer reaction times were also generally required with the Rink amide resin.

During the cleavage process, highly undesirable reactive carbocations (for example, trityl cations) are generated, which may sometimes turn the purification of the crude precipitate into a challenging process, due to the presence of by-products. To avoid that, the carbocation scavenger triisopropylsilane (TIPS) was added to the cleavage mixture (**Figure 2.25**).

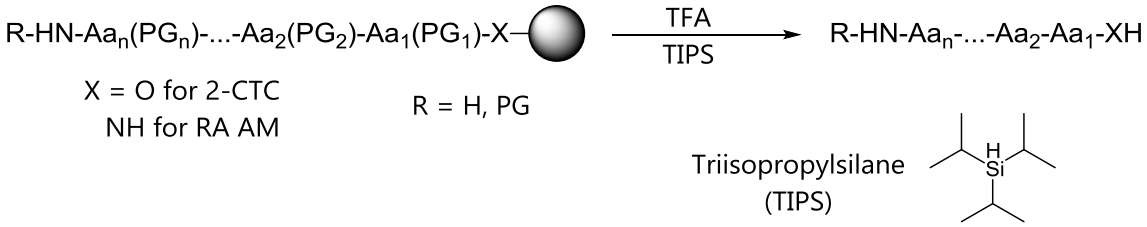

Figure 2.25: Release of the free peptide from the polymeric support using TFA in the presence of TIPS.

Depending on the peptidyl-resin, higher TFA concentrations and/or longer reaction times may be necessary to achieve a complete deprotection and release of the peptide from the resin. However, the stability of the peptidyl-resin is compromised under these aggressive acidic conditions if prolonged treatments are used.

The resin was filtered after the cleavage and the filtrates were poured onto Et_2O to induce the precipitation of the peptide, which was recovered by centrifugation of the suspension and washed with additional amounts of Et_2O. Finally, the solid was analysed by high performance liquid chromatography coupled to mass spectrometry (HPLC-MS), to identify the desired peptide and evaluate its chromatographic purity. The peptide was subsequently characterised by NMR spectroscopy.

2.3.2 Solid-phase synthesis of the peptides studied in this work

2.3.2.1 H-His-Lys(Coum)-His-OH

Previous to the synthesis of the peptide, the preparation of Fmoc-Lys(Coum)-OH was carried out following the procedure described by Katritzky and coworkers for the preparation of coumarin derivatives of amino acids and dipeptides.[177] First, the carboxylic group of coumarin-3-carboxylic acid was activated with thionyl chloride in THF; the reaction of the resulting acid chloride with 1*H*-benzotriazole yielded the intermediate in good yields (**Figure 2.26**).

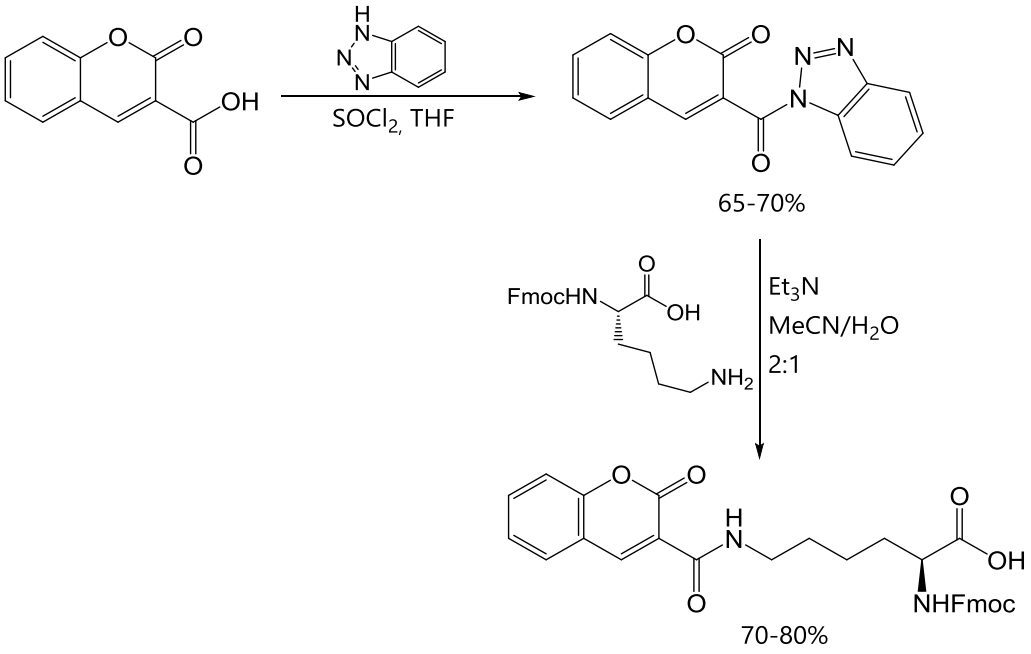

Figure 2.26: Synthesis of Fmoc-Lys(Coum)-OH.

Next, the coumarinic intermediate was treated with Fmoc-Lys-OH and the cumarin-labelled amino acid derivative was produced through a base-assisted nucleophilic attack of the side chain amino group. Upon recrystallisation from CH_2Cl_2-hexane mixtures, the Fmoc amino acid derivative was obtained in high purity and good yields, ready for its utilisation in SPPS.

Once the unnatural Fmoc amino acid was available, the tripeptide of sequence H-His-Lys(Coum)-His-OH (**Figure 2.27**) was prepared using the 2-CTC resin. This peptide includes a carboxylic group at the *C*-terminus and a free *N*-terminal amino group and was used as an ATCUN copper chelator as well as a ROS scavenger, as described in **Chapter 3**.

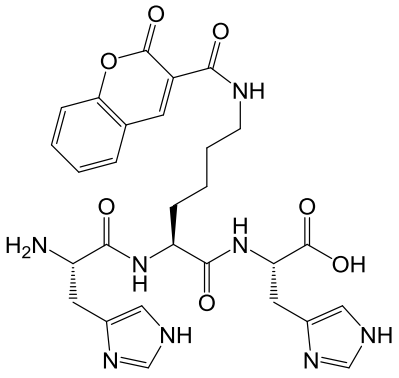

Figure 2.27: Structure of H-His-Lys(Coum)-His-OH.

For the incorporation of the histidine residues to the peptide, the *N*α-Fmoc-*N*τ-trityl protected histidine (Fmoc-His(Trt)-OH) was used (**Figure 2.28**). Such protecting group of the imidazole ring is labile to acids and can thus be eliminated during the final cleavage of the peptide from the resin.

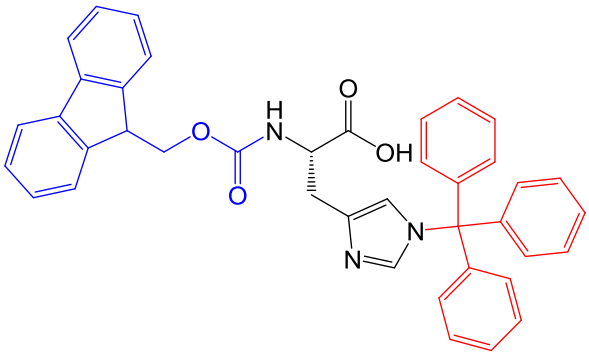

Figure 2.28: Fmoc-His(Trt)-OH.

The synthetic strategy is shown in **Figure 2.29**. First, Fmoc-His(Trt)-OH was anchored to the 2-CTC resin in the presence of DIPEA (10 eq). After a capping step with MeOH, the elimination and quantification of the Fmoc group was carried out. Next, Fmoc-Lys(Coum)-OH and Fmoc-His(Trt)-OH were coupled sequentially using DIC and Oxyma. Ninhydrin tests were positive and recoupling steps were therefore required. A final Fmoc elimination-quantification step was performed and, finally, the peptide was released from the resin with 60% TFA in the presence of TIPS. The crude product was obtained with a purity of 85%, determined by analytical HPLC, and was finally purified by preparative HPLC to a final purity of 94%, high enough to use the peptide in (biological) experiments.

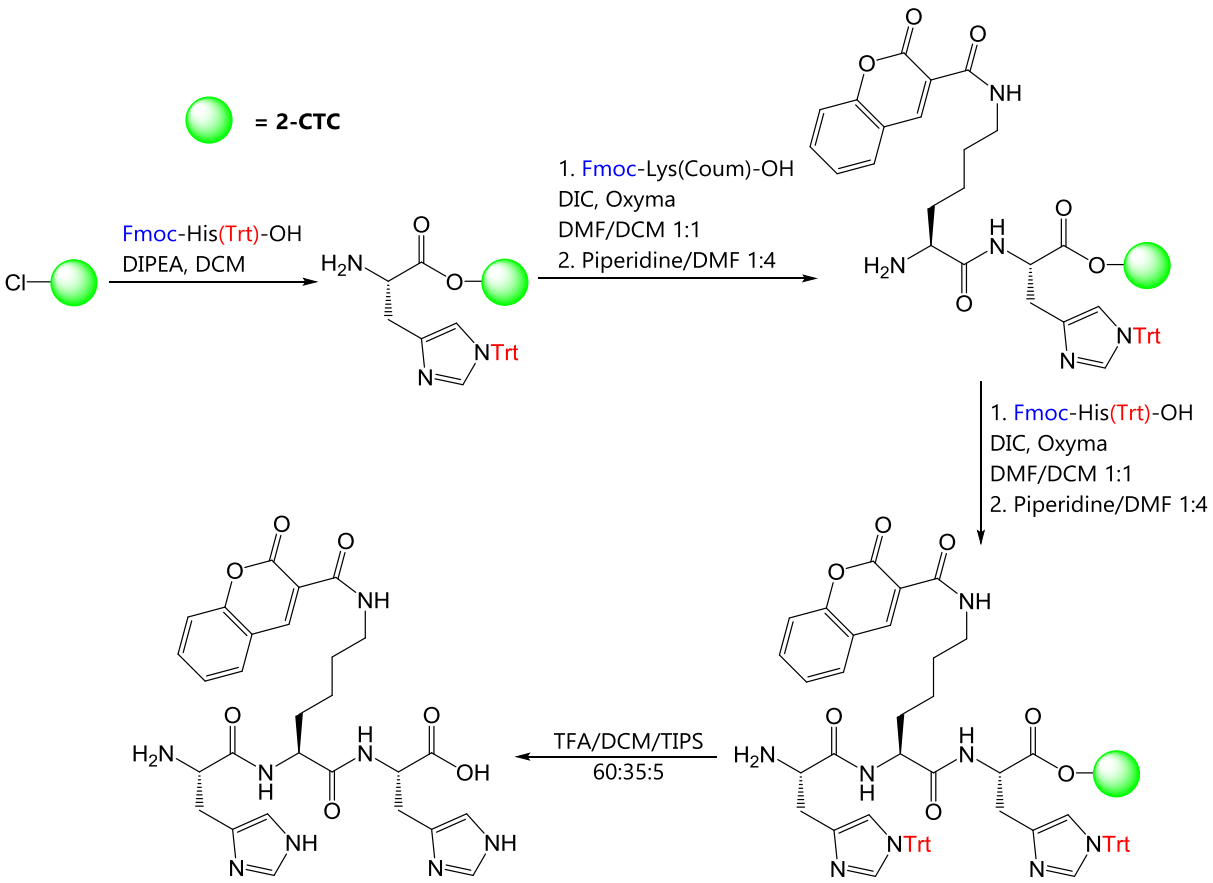

Figure 2.29: Synthesis of H-His-Lys(Coum)-His-OH.

2.3.2.2 Fluo-His-Xaa-His-NH_2 peptides

Next, the synthesis of tripeptides labelled with fluorescein was carried out. Such peptides, namely Fluo-His-Lys(Coum)-His-NH_2 and Fluo-His-Nle-His-NH_2, were tagged at the *N*-terminal amino group and were prepared using the RA AM resin (**Figure 2.30**). The two fluorescent probes present in Fluo-His-Lys(Coum)-His-NH_2 are expected to behave as a FRET pair, used for the detection of copper, while Fluo-His-Nle-His-NH_2 was designed for comparison purposes. The application of both peptides is described in **Chapter 3**.

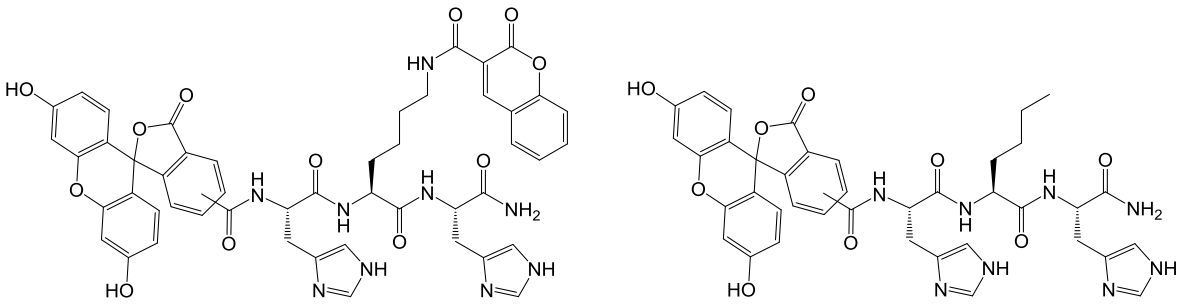

Fluo-His-Lys(Coum)-His-NH_2 **Fluo-His-Nle-His-NH_2**

Figure 2.30: Fluo-His-Xaa-His-NH_2 peptides.

The fluorescein tag was incorporated to the resin once the peptide chain was completed; 5(6)-carboxyfluorescein was coupled via its carboxylic group at position 5/6 of fluorescein to the *N*-terminal amino function of the His residue. The reagent used in this study (**Figure 2.31**) consists of a mixture of two regioisomers differing in the position of the carboxylic group responsible of the coupling (the pure 6-carboxyfluorescein isomer is about 100 times more expensive).[178]

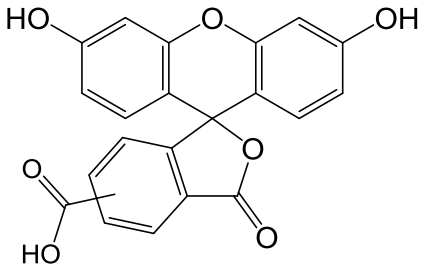

Figure 2.31: 5(6)-carboxyfluorescein.

In a first attempt, the synthesis of the peptide was carried out using the 2-CTC resin, following a protocol similar to that described for H-His-Lys(Coum)-His-OH, which also required a recoupling. However, the reaction mixture became a viscous gel and the peptide chains were not released from the resin upon TFA treatment. The RA AM resin was then used, and two treatments with smaller amounts (2 eq) of 5(6)-carboxyfluorescein, DIC and Oxyma were done (**Figure 2.32**).

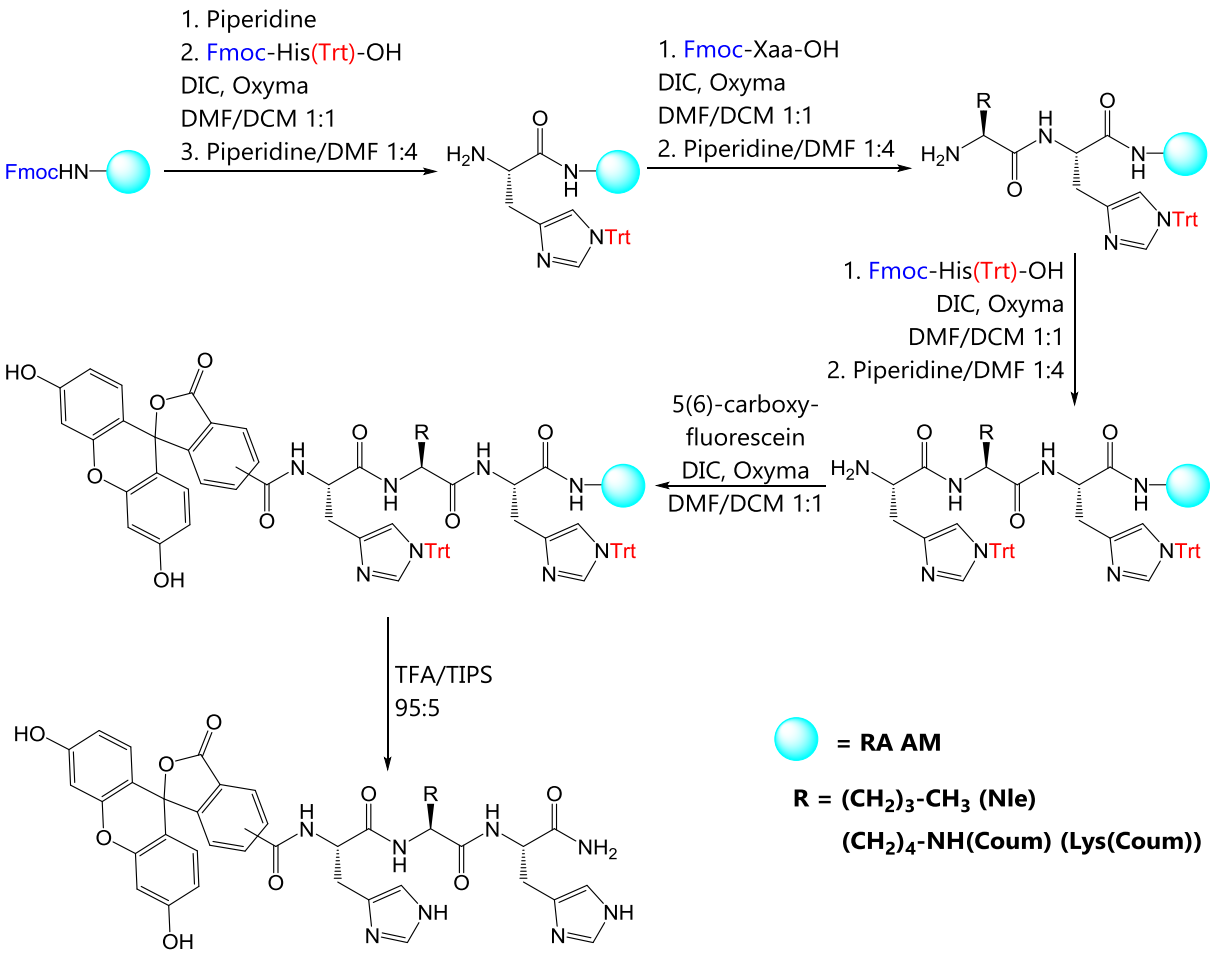

Figure 2.32: General synthesis of the Fluo-His-Xaa-His-NH_2 peptides.

The corresponding reaction mixture presented the usual appearance and viscosity. Excess of 5(6)-carboxyfluorescein may have interacted in a non-covalent manner with the resin, thus modifying the physical properties of the peptidyl-resin.

A sample of peptidyl-resin was thus treated with TFA and analysed by HPLC-MS. The chromatogram obtained presented three different peaks, as shown in **Figure 2.33**; the peaks observed at retention times t_R = 9.95 and 10.2 min belong to species with a m/z value of 950, which were attributed to the 5(6)-isomers of the target Fluo-His-Lys(Coum)-His-NH_2 peptide.

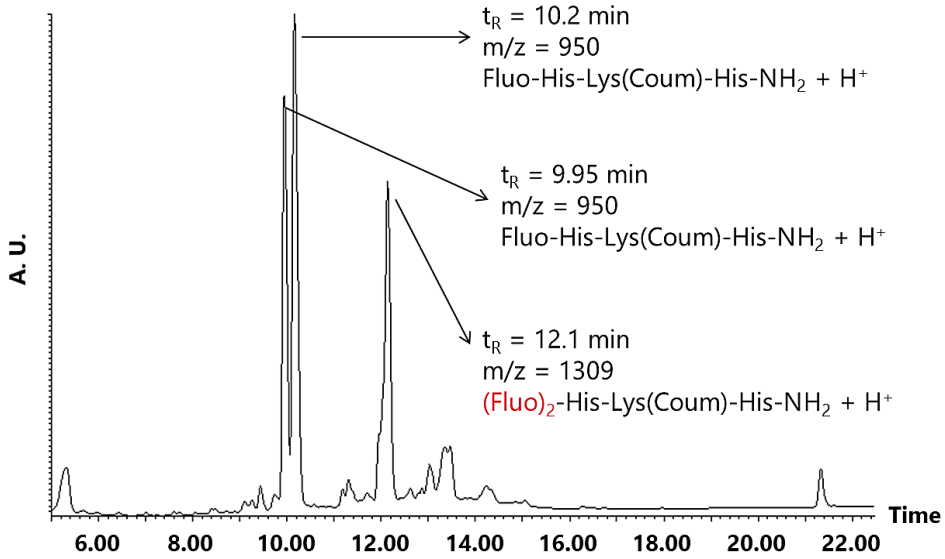

Figure 2.33: Chromatogram of the acidolytic crude containing Fluo-His-Lys(Coum)-His-NH_2.

The peak with t_R = 12.1 min presented a m/z value of 1309 and was attributed to the target peptide with an additional 5(6)-carboxyfluorescein molecule. Interestingly, when the peptidyl-resin was treated with 20% piperidine in DMF (5 × 5 mL × 10 min), this peak disappeared, suggesting that the second fluorescein molecule was reversibly bound to the peptide, and that its elimination could be provoked by the nucleophilic attack of piperidine (**Figure 2.34**).

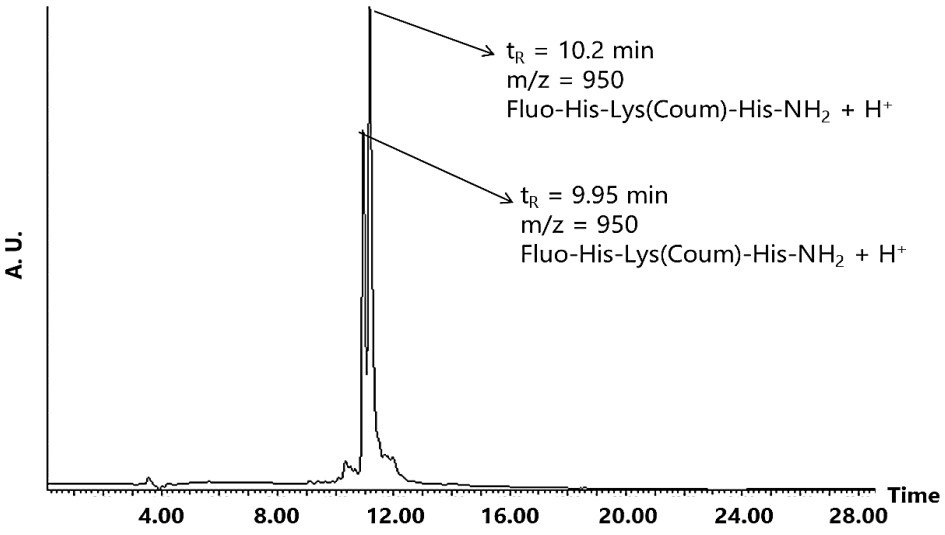

Figure 2.34: Chromatogram of the acidolytic crude of Fluo-His-Lys(Coum)-His-NH_2 after treatment with piperidine.

The synthesis of the peptide Fluo-His-Nle-His-NH_2 under similar experimental conditions could be carried out without any remarkable incidence; one sole coupling reaction was sufficient for the incorporation of the different amino acids. These disparities suggest a specific reactivity of the coumarin moiety. The generation of unexpected side products when preparing coumarin-containing peptides was noticed in other cases, as will be discussed later.

2.3.2.3 Ac-His-Lys(Fp)-His-Lys-NH_2 peptides

Fluorophore- (Fp) containing tetrapeptides of sequence His-Lys-His-Lys were then prepared (**Figure 2.35**). Such peptides, namely Ac-His-Lys(Coum)-His-Lys-NH_2 (see **Chapter 5**) and Ac-His-Lys(4DMN)-His-Lys-NH_2 (see **Chapter 6**), contained an unprotected lysine residue for subsequent connection to gold nanoparticles. Moreover, the peptides include Coum and 4DMN probes, respectively, attached to the side chain of the internal Lys residue.

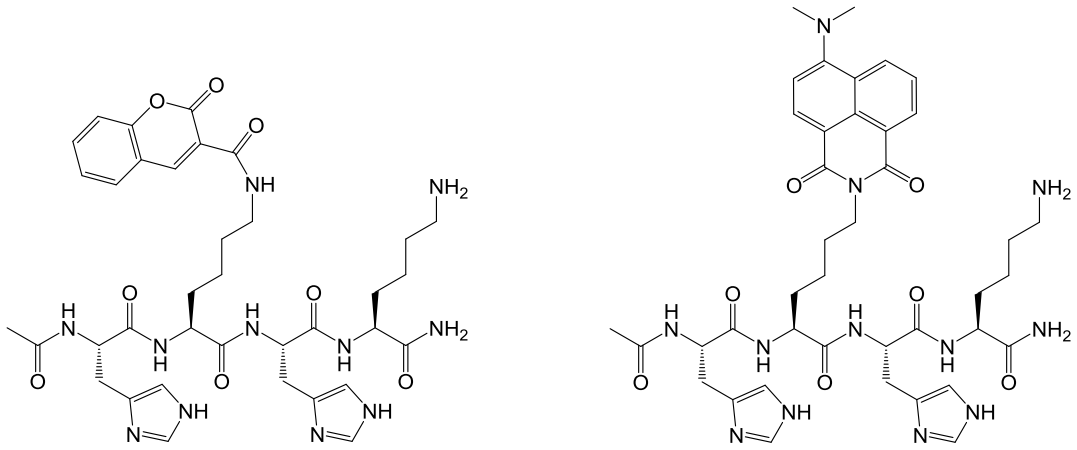

Ac-His-Lys(Coum)-His-Lys-NH_2 **Ac-His-Lys(4DMN)-His-Lys-NH_2**

Figure 2.35: The Ac-His-Lys(Fp)-His-Lys-NH_2 peptides.

The peptides were *C*-terminal amides and *N*-terminal acetylated to avoid any side reactions upon attachment to the gold nanocarriers. Fmoc-Lys(Boc)-OH was used for the incorporation of the Lys residue with the unfunctionalised side chain (Lys4) because the Boc group can be easily eliminated upon final TFA treatment (**Figure 2.36**). Fmoc-Lys(Coum)-OH and Fmoc-Lys(4DMN)-OH were used as the fluorophore-bearing amino acids, and the preparation of the latter amino acid is described below.

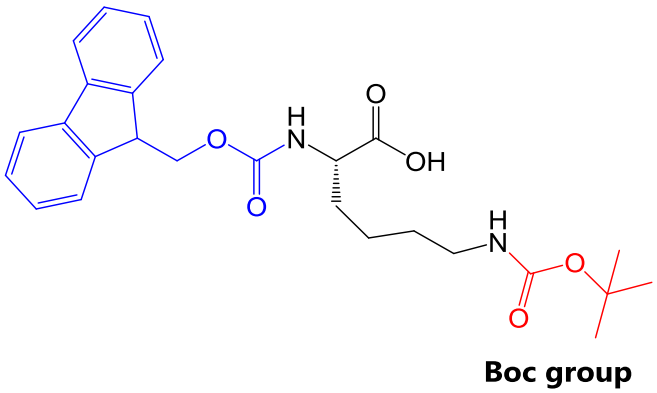

Figure 2.36: Fmoc-Lys(Boc)-OH.

The synthesis starts with the derivatisation of the precursor 4-bromo-naphthalic anhydride with the donating dimethylamino function that confers the bright orange colour and the unique emissive features to the conjugated aromatic system (**Figure 2.37**). The starting anhydride was refluxed in 3-methyl-1-butanol (isoamyl alcohol) in the presence of 3-dimethylaminopropionitrile to produce the dimethylamino anhydride as an orange solid in high yield.[179]

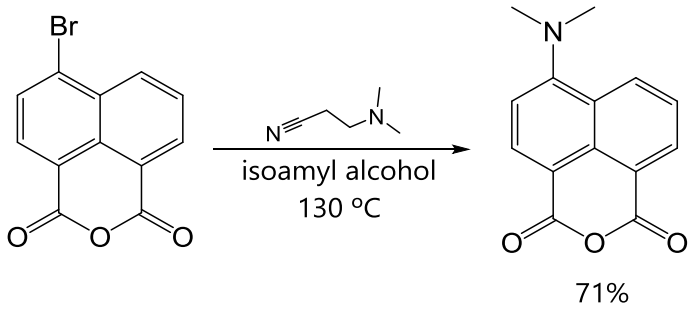

Figure 2.37: Synthesis of 4-*N,N*-Dimethylamino-1,8-naphthalic anhydride.

Second, the probe was incorporated into the side chain of Boc-Lys-OH under basic conditions by refluxing both the amino acid and the anhydride in a 1,4-dioxane/H_2O solvent mixture.[144] Finally, the Boc protecting group was replaced by a Fmoc group to allow conventional Fmoc solid-phase chemistry; Boc was removed using TFA and reaction of the resulting amino acid with *N*-(9-fluorenylmethoxycarbonyloxy)-succinimide (Fmoc-OSu) yielded the desired Fmoc-Lys(4DMN)-OH (**Figure 2.38**).

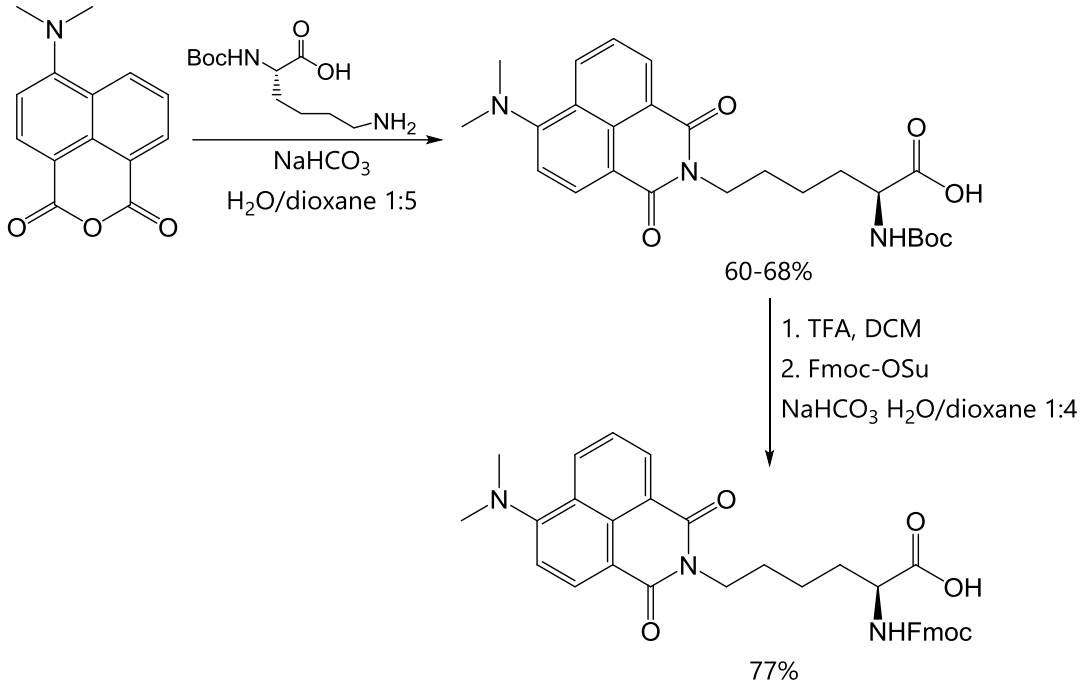

Figure 2.38: Synthesis of Fmoc-Lys(4DMN)-OH.

The 4DMN Fmoc amino acid was obtained as a yellow solid, soluble in a wide range of organic solvents and in neutral or alkali aqueous solutions and exhibited a solvent-dependent fluorescent emission. The properties and potential applications of such extremely interesting probe are described in **Chapter 6**.

After having prepared all the Fmoc amino acids, the peptides were subsequently synthesised. The synthetic approach for the Ac-His-Lys(Fp)-His-Lys-NH_2 peptides is depicted in **Figure 2.39**. First, Fmoc-Lys(Boc)-OH was anchored to the resin and then Fmoc-His(Trt)-OH was coupled. Next, Coum- or 4DMN-lysine derivatives were incorporated and Fmoc-His(Trt)-OH was added again to complete the peptide sequence. Recoupling was not required for any of the two peptides. After removing the Fmoc group of the last amino acid residue, the peptidyl resins were treated with 30 eq of Ac_2O and DIPEA to acetylate the *N*-terminal amino group.

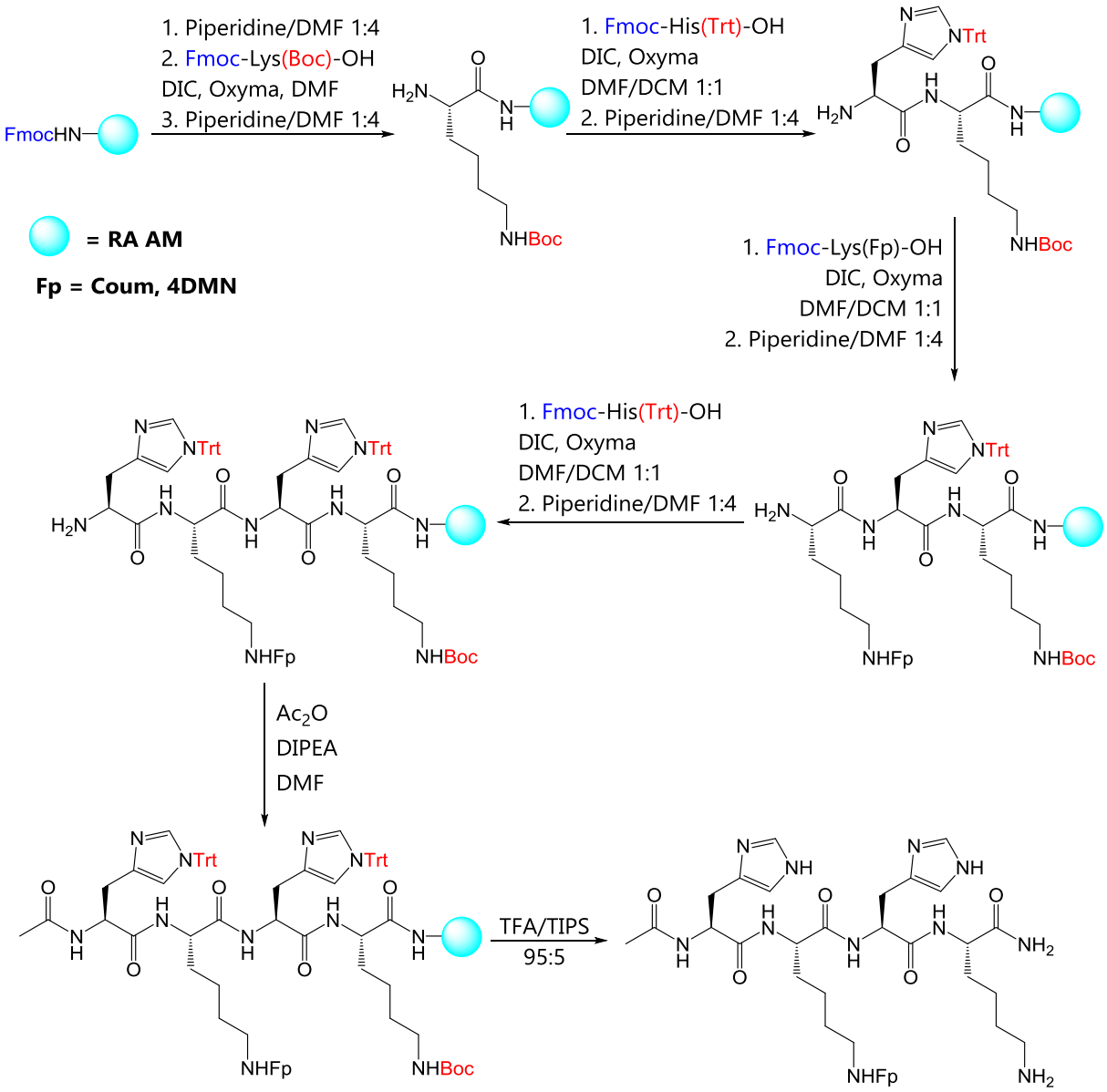

Figure 2.39: General synthesis of the Ac-His-Lys(Fp)-His-Lys-NH_2 peptides.

After treating the Ac-His-Lys(Coum)-His-Lys-NH_2 peptidyl-resin with 95% TFA, the cleaved product was precipitated in Et_2O, and subsequently analysed by HPLC-MS. Two main peaks of approximately the same intensity appeared in the chromatogram (**Figure 2.40**). The peak at t_R = 8.73 min was associated to the target peptide (m/z = 762), while that at t_R = 9.98 min was ascribed to a polyacylated product, in accordance with its m/z value (889).

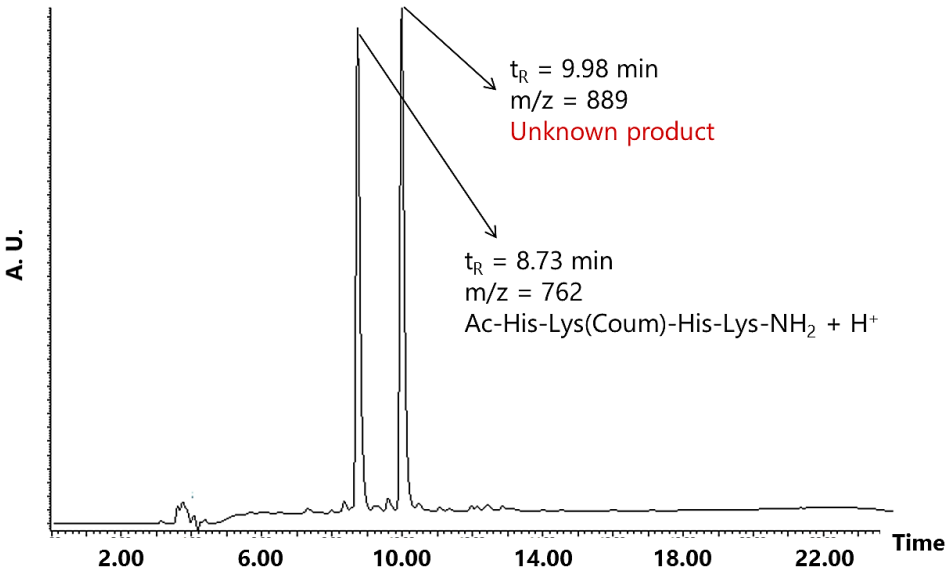

Figure 2.40: Chromatogram of the acidolytic crude containing Ac-His-Lys(Coum)-His-Lys-NH_2.

In an attempt to eliminate potential reversibly bound groups to the peptide chain (e.g. extra acetyl groups), the same strategy followed for the Fluo-His-Lys(Coum)-His-NH_2 peptide was used. Thus, the peptidyl-resin was treated with 20% piperidine in DMF (5 × 5 mL × 10 minutes), and only the desired peptide was obtained, as shown in **Figure 2.41**. Any poly-acetylation reaction was therefore reversed through the addition of piperidine.

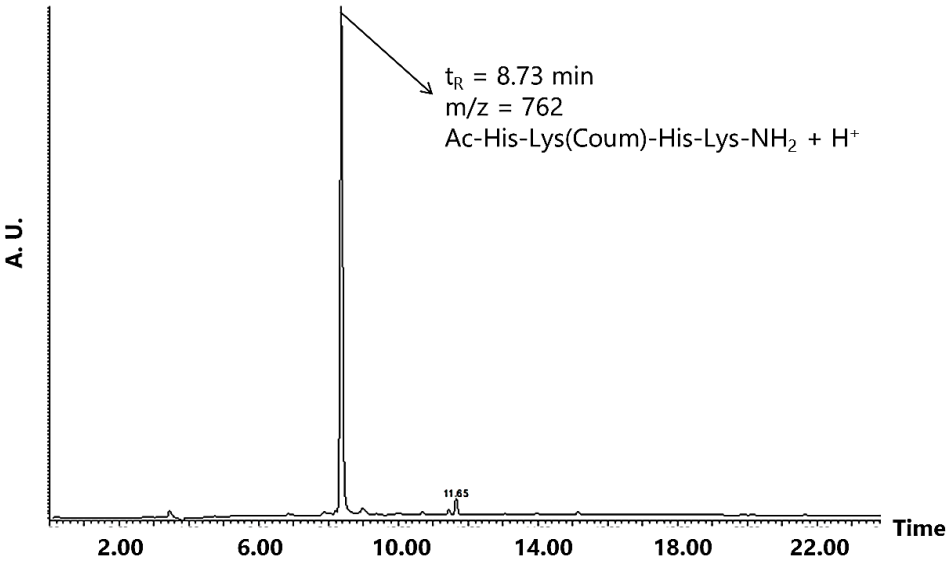

Figure 2.41: Chromatogram of the acidolytic crude of Ac-His-Lys(Coum)-His-Lys-NH_2 after treatment of the peptidyl-resin with piperidine.

For the synthesis of the Ac-His-Lys(4DMN)-His-Lys-NH_2 under similar conditions, no side products were observed. This fact supports the hypothesis that the preparation of coumarin-containing peptides also generates (coumarin-assisted) secondary products. These unwanted side products can be eliminated by treating the peptidyl-resin with piperidine; the wanted peptides were obtained with high purity. It can be pointed out that neither the nature of the side products nor the mechanism through which they were formed were investigated.

2.3.2.4 Ac-His-Lys(Fp)-His-XH peptides (Fp = Coum, 4DMN; X = O, NH)

The peptides with sequence Ac-His-Lys(Fp)-His-XH, namely Ac-His-Lys(Coum)-His-OH (**Chapter 3**), Ac-His-Lys(4DMN)-His-OH (**Chapters 3 and 6**) and Ac-His-Lys(4DMN)-His-NH_2 (**Chapter 3**) represent the fourth group of synthetic copper ionophores (**Figure 2.42**). These chelating agents were designed as models to study the copper-binding properties of Ac-His-Lys(Fp)-His-Lys-NH_2 peptides that will be attached to gold nanocarriers. Besides, the 4DMN peptides were used for the fluorescent detection of aggregated Aβ.

The Ac-His-Lys(Coum)-His-OH and Ac-His-Lys(4DMN)-His-OH peptides were prepared with the 2-CTC resin and, therefore, presented a *C*-terminal carboxylic group. Conversely, the Ac-His-Lys(4DMN)-His-NH_2 peptide was synthesised with the RA AM resin and was thus *C*-terminal amide-protected. The three peptides contained an acetylated *N*-terminal amino group, which was expected to affect their coordination mode to Cu(II) ions.

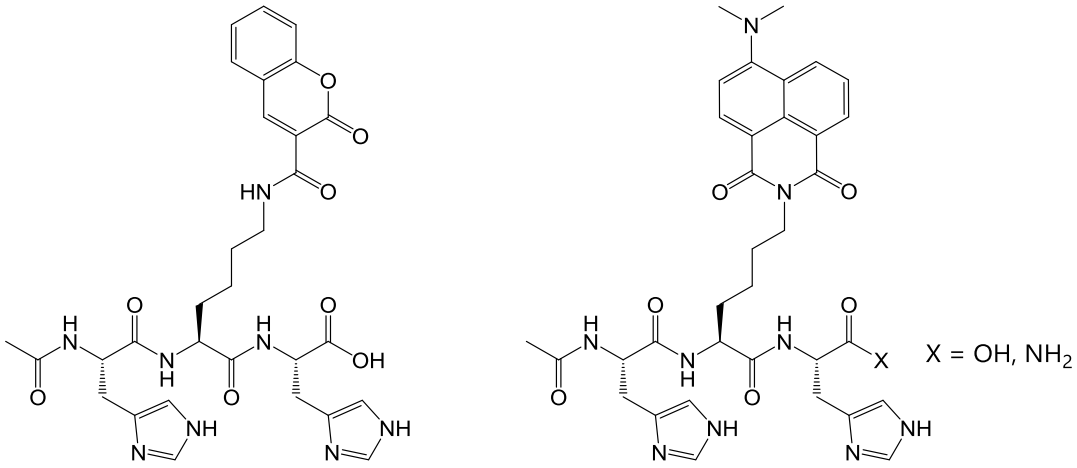

Ac-His-Lys(Coum)-His-OH **Ac-His-Lys(4DMN)-His-OH/NH_2**

Figure 2.42: Ac-His-Lys(Fp)-His-OH/NH_2 peptides.

The general synthetic pathway of the peptides is shown in **Figure 2.43**. Fmoc-His(Trt)-OH was first loaded onto 2-CTC or RA AM resins. Once the coupling of the Fmoc-Lys(Fp)-OH and Fmoc-His(Trt)-OH was performed and the Fmoc was removed, the *N*-terminal amino group was acetylated using Ac_2O (30 eq) in the presence of DIPEA (30 eq). Single coupling reactions were sufficient for the complete amino acid incorporation for Ac-His-Lys(Coum)-His-OH and Ac-His-Lys(4DMN)-His-OH; however, recoupling was necessary for Ac-His-Lys(4DMN)-His-NH_2. The cleavage from the 2-CTC resin was then performed using 60% TFA and 5% TIPS in DCM, while the Ac-His-Lys(4DMN)-His-NH_2 peptide was released from the RA AM resin using TFA/TIPS 95:5. For Ac-His-Lys(Coum)-His-OH, a final treatment with piperidine (5 × 3 mL × 10 min) was performed to prevent the isolation of polyacetylated products, as discussed above. All peptides were synthesised under conditions similar to those described before and were obtained with high purities without additional purification steps.

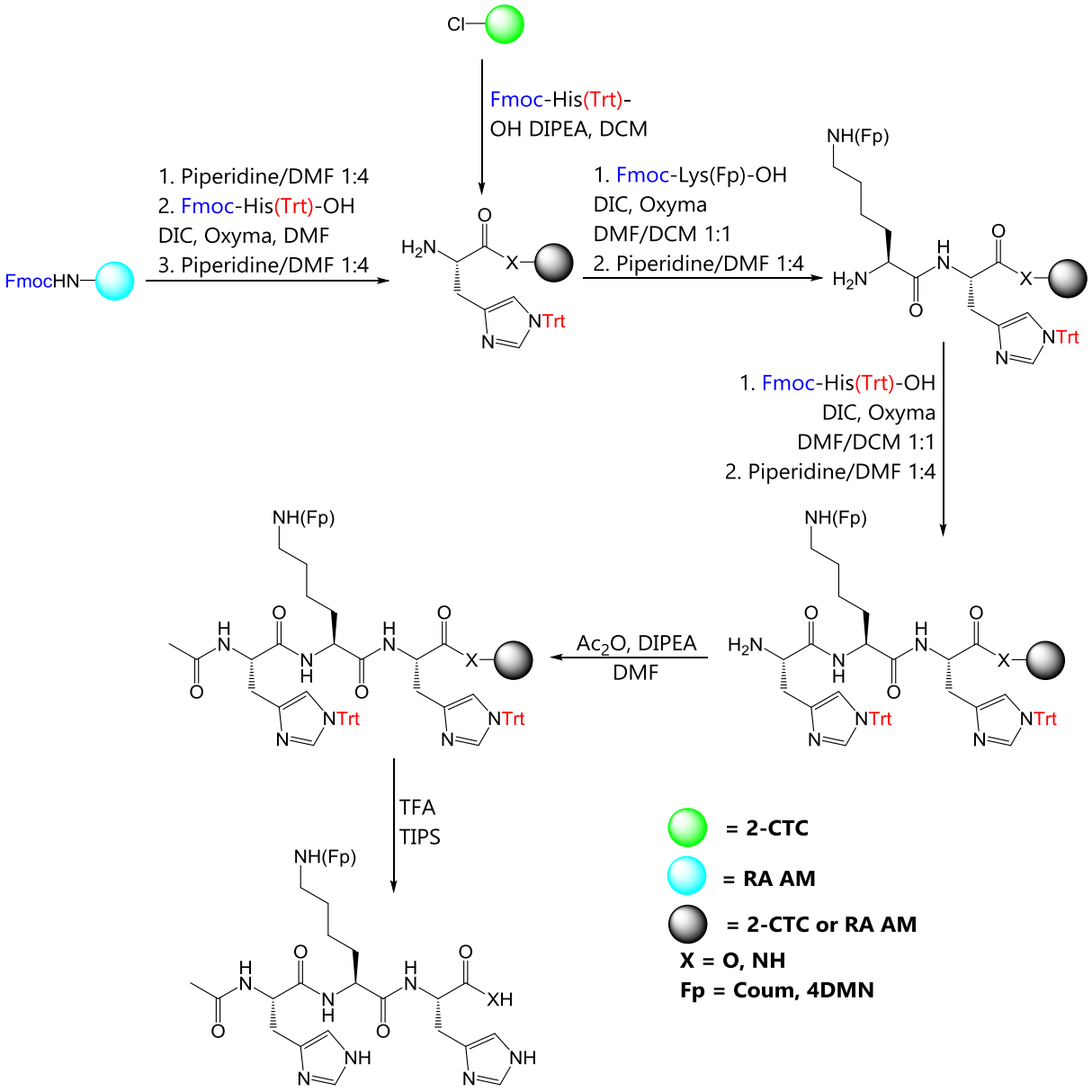

Figure 2.43: General synthesis of the Ac-His-Lys(Fp)-His-XH peptides.

2.3.2.5 RhoB-His-Lys(Fluo)-His-OH peptide

Finally, the synthetic approach of a peptide containing the Rhodamine B-Fluorescein FRET pair was designed (**Figure 2.44**). As mentioned previously, a ratiometric FRET probe would be useful for the highly sensitive detection of copper ions, thanks to the remarkable emission of both fluorescent probes and the overlapping of their emission and excitation spectra (allowing a FRET phenomenon).

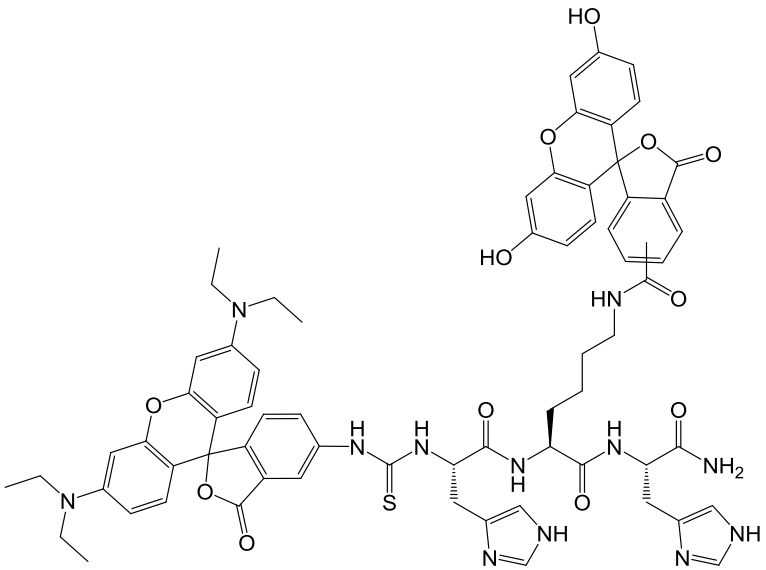

Figure 2.44: Fluorescein- and rhodamine B-tagged RhoB-His-Lys(Fluo)-His-NH_2 peptide.

Rhodamine B isothiocyanate (see **Figure 2.45**) and 5(6)-carboxyfluorescein were used to introduce the rhodamine B and the fluorescein dyes, respectively. Rhodamine B was planned to be tagged at the *N*-terminal amino group through a thiourea bond, whereas fluorescein would be connected at the side chain of the lysine residue.

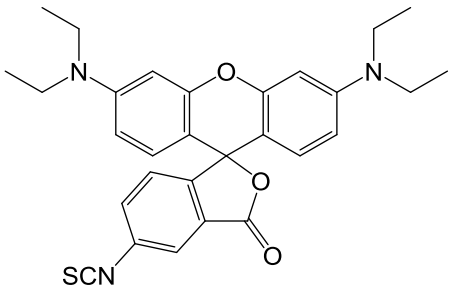

Figure 2.45: Rhodamine B isothiocyanate.

For the preparation of the peptide, the side chain of the Lys residue had to be removed while keeping the peptide anchored to the resin and the trityl protecting groups of the His residues intact. The experimental conditions to remove the Lys protecting group had to be orthogonal to those used for the remaining protecting groups, *viz*. acids or bases had to be avoided. With this aim, Fmoc-Lys(alloc)-OH was selected, where alloc is the allyloxycarbonyl protecting group (**Figure 2.46**).

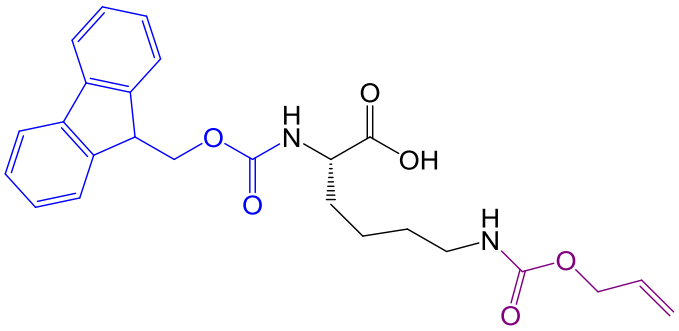

Figure 2.46: Fmoc-Lys(alloc)-OH.

Unlike the protecting groups described previously, the removal of this function is only promoted by [Pd(PPh$_3$)$_4$] under neutral conditions (**Figure 2.47**); [Pd(PPh$_3$)$_4$] is a common Pd^0 catalyst used in many important organic reactions, such as the Suzuki cross-coupling reaction that allows to generate carbon-carbon bonds.[180,181] The addition of a suitable scavenger is required to avoid allyl back alkylation. In this sense, nucleophiles such as PhSiH$_3$, which was the scavenger of choice in this work, are compatible with the SPPS procedure.

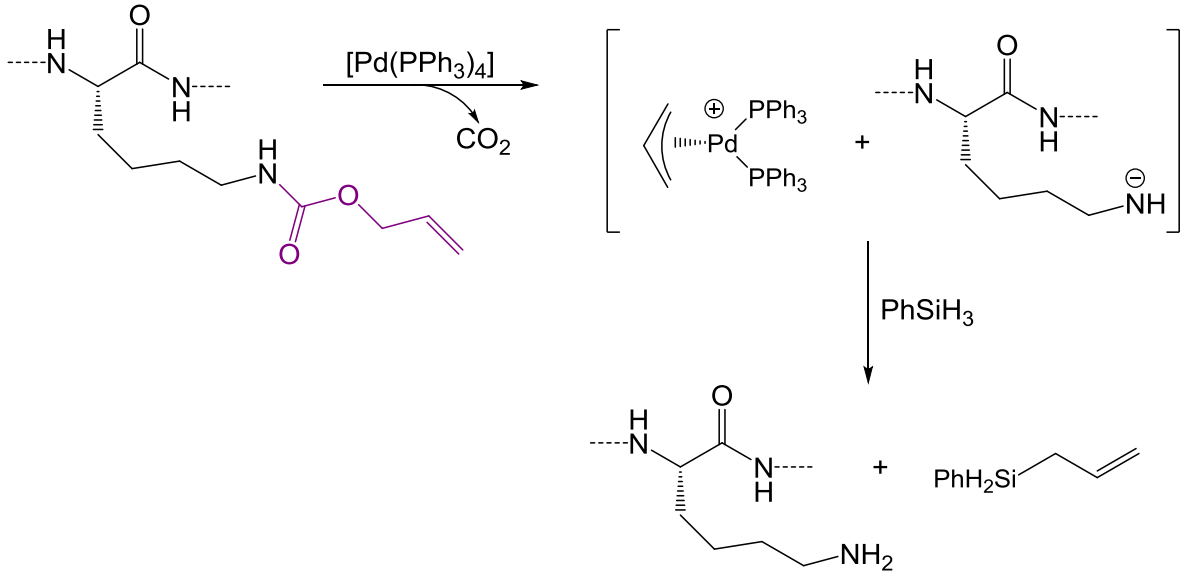

Figure 2.47: Alloc group elimination under neutral conditions.

Upon treatment with the palladium catalyst, decarboxylation takes place and a π allyl-Pd complex is generated, thus deprotecting the amino function. To avoid back-alkylation, it is necessary to treat the peptidyl-resin with an excess of the nucleophilic PhSiH$_3$, which binds the highly reactive allyl group. Finally, sodium *N,N*-

diethyldithiocarbamate trihydrate in DMF is used as a palladium chelator to wash the resin.[182]

The synthesis of the RhoB-His-Lys(Fluo)-His-NH_2 peptide was addressed as follows. First, Fmoc-His(Trt)-OH was anchored to the RA AM resin and Fmoc-Lys(alloc)-OH was subsequently coupled. Then, the *N*-terminal histidine residue was introduced and its Fmoc group was eliminated with piperidine/DMF 1:4; the resulting *N*-terminal amino function can hence be functionalised with rhodamine B isothiocyanate, as depicted in **Figure 2.48**.

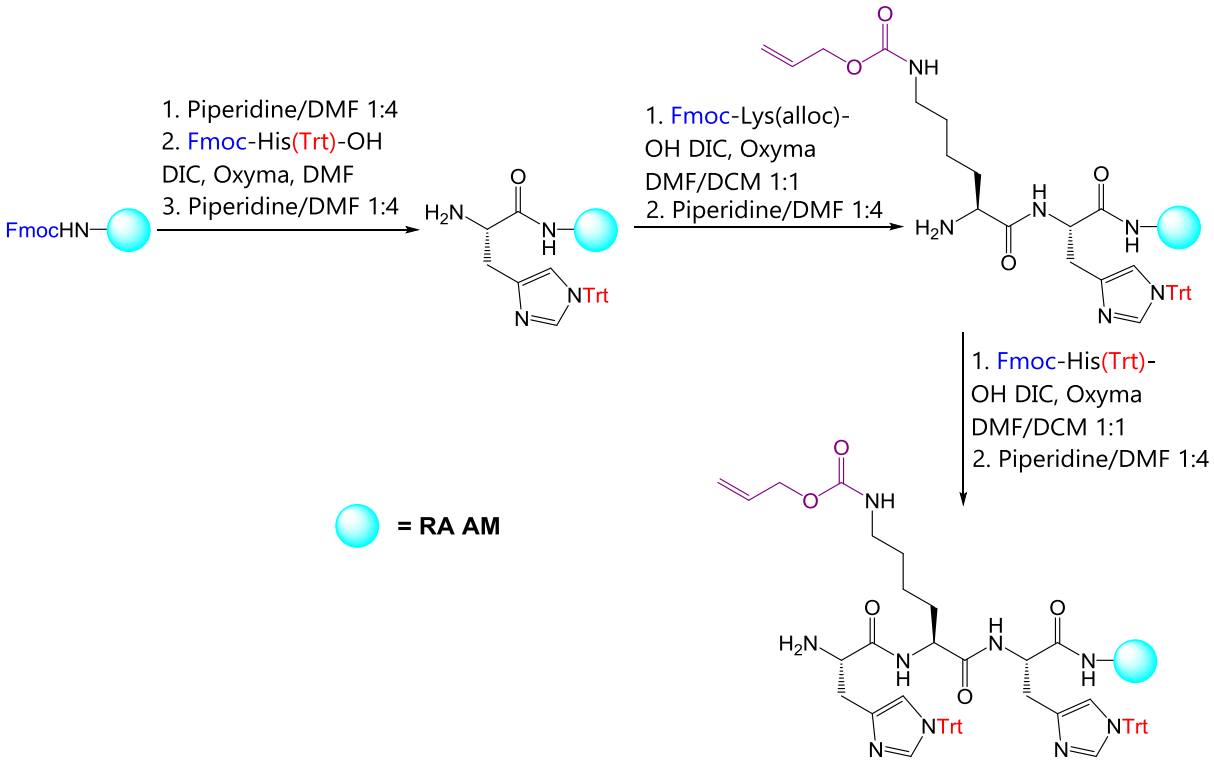

Figure 2.48: Synthesis of the RhoB-His-Lys(Fluo)-His-NH_2 peptide: Amino acid chain assembly on the resin.

The second part of the planned synthesis is shown in **Figure 2.49**. The initial strategy was to couple the rhodamine fluorophore in the presence of DIPEA to favour the nucleophilic attack of the amino group to form a thiourea bond. Then, Pd-mediated alloc group removal would be performed for further coupling of 5(6)-carboxyfluorescein under the same conditions than those used for the synthesis of the Fluo-His-Xaa-His-NH_2 peptides. Finally, cleavage with TFA would generate the fluorescein- and rhodamine-tagged peptides.

However, it was not possible to connect the rhodamine label to the peptide sequence. Neither successive additions of rhodamine B isothiocyanate nor longer reaction times (up to 5 days) were successful. A wide range of reaction conditions for the coupling of rhodamine isothiocyanates to amine functions is available in the literature, like sonication for 1 hour,[183] 5 hours stirring at room temperature,[184] 24 h reaction in the presence of DIPEA,[185] 4-day [186] or heating at 60 °C for 4 h followed by 3 additional hours at 90-100 °C[187] and so on.

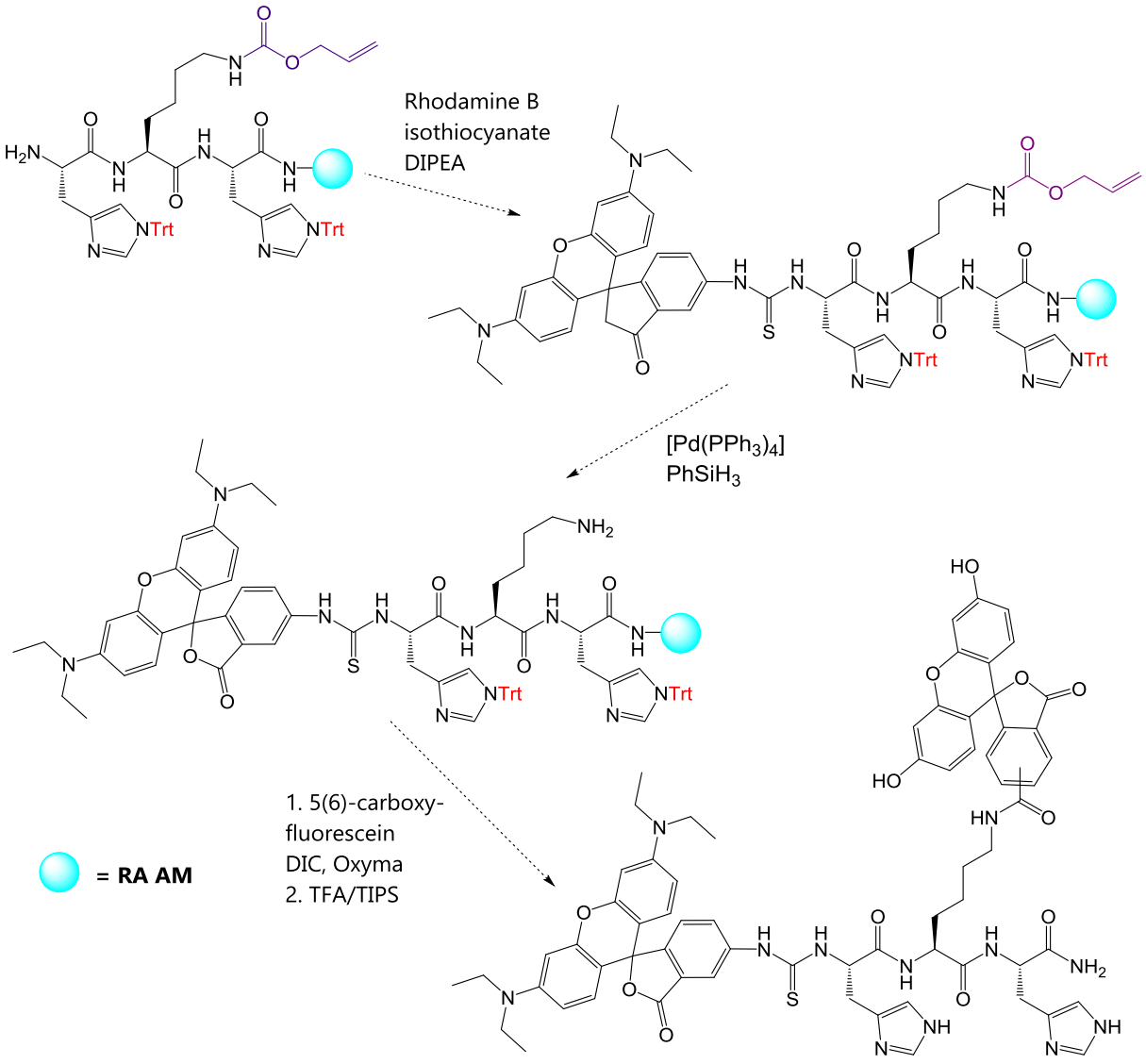

Figure 2.49: Continuation of Figure 2.48: Attempted procedure for the peptide functionalisation with Rhodamine B and corresponding steps to obtain RhoB-His-Lys(Fluo)-His-NH_2 peptide.

Accordingly, high temperatures might be required for the reaction to take place. Microwave-assisted coupling could also be a suitable approach to reach the temperature necessary to generate the thiourea bond. Future investigations are hence required for the preparation of this peptide.

2.3.2.6 Yields and purities of the peptides

The yields and the final purities of the peptides are summarised in **Table 2.1**. In general, the yields for the incorporation of the first amino acid using 2-CTC (typically 40-65%) were lower than those with the RA AM resin (80%-quantitative). The low loading on the 2-CTC resin was purposely achieved (using specific conditions) since a high functionalisation of this resin can result in deletion peptide sequences.

In contrast, the final yields were in general higher for the peptides prepared with 2-CTC (42%-95%). The low final yields obtained for the peptides prepared with RA AM (8-25%), except for Fluo-His-Lys(Coum)-His-NH_2 (44% yield) were in some cases a limiting factor for their applications. With the objective to improve the yields, successive acidic treatments and high TFA concentrations were used; unfortunately, no improvement was achieved.

The yields were calculated considering that the peptides were obtained as trifluoroacetate salts. Both the imidazole rings and the amino groups are positively charged after TFA treatment; therefore, there is one trifluoroacetate counterion per imidazole/amino function. Accordingly, H-His-Lys(Coum)-His-OH is obtained with three trifluoroacetate anions, whereas two trifluoroacetate anions are expected for Ac-His-Lys(Coum)-His-OH, Ac-His-Lys(4DMN)-His-OH and Ac-His-Lys(4DMN)-His-NH_2. In contrast to H-His-Lys(Coum)-His-OH, which had to be purified by preparative HPLC, the other peptides were always obtained with high purity; no further purification by HPLC was required.

Table 2.1: Yields (%) of the different steps and final purity of the peptides synthesised.

Peptide	Loading of the first amino acid[a]	Peptide on the resin[a]	Isolated peptide (purity)[b]
H-His-Lys(Coum)-His-OH	48	88	42 (94)
Fluo-His-Lys(Coum)-His-NH_2	86	quantitative	44 (92)
Fluo-His-Nle-His-NH_2	quantitative	quantitative	9 (96)
Ac-His-Lys(Coum)-His-Lys-NH_2	73	quantitative	25 (94)
Ac-His-Lys(4DMN)-His-Lys-NH_2	92	91	8 (94)
Ac-His-Lys(Coum)-His-OH	49	quantitative	95 (95)
Ac-His-Lys(4DMN)-His-OH	64	83	42 (95)
Ac-His-Lys(4DMN)-His-NH_2	86	quantitative	16 (97)

[a] Determined by Fmoc quantification

[b] Determined by weight (determined by HPLC)

The on-resin yields were calculated by Fmoc quantification using the Lambert-Beer law (λ_{abs} = 301 nm). It should be noted that the yields of peptide-chain assembly on 2-CTC were not quantitative, although negative ninhydrin tests were obtained. The fact that deletion peptides were not detected indicates that Fmoc quantification was not reliable for this resin. The final yields for all the peptides were thus determined by the corresponding isolated quantities. The on-resin yields for RA AM were always quantitative, except for Ac-His-Lys(4DMN)-His-Lys-NH_2 peptide, which was obtained with a yield of 91%.

2.4 Concluding remarks

Seven, potentially copper-chelating peptides, containing the sequence His-Xaa-His have been manually prepared by solid-phase synthesis. Two fluorescent non-natural amino acids, namely Fmoc-Lys(Coum)-OH and Fmoc-Lys(4DMN)-OH, were prepared to generate fluorescent peptidic probes, whose applications are described in the following chapters. Two of the peptides were tagged with the highly emissive fluorescein dye, giving a potential FRET pair with coumarin in one of them.

The fluorescent tri- and tetrapeptides were manually prepared by solid-phase synthesis using DIC and Oxyma as the coupling agents, and TFA-TIPS for both the cleavage of the peptide from the resin and the side chain deprotection. Unexpectedly, the synthesis of the coumarinic peptides gave by-products of high molecular weight, which were fortunately converted back to the desired products by final treatment of the peptidyl-resin with piperidine.

H-His-Lys(Coum)-His-OH, Ac-His-Lys(Coum)-His-OH and Ac-His-Lys(4DMN)-His-OH were prepared using the 2-chlorotrityl chloride resin (2-CTC) and were obtained with moderate to good yields of 42-95% and high chromatographic purities of 94-95%. On the other hand, Ac-His-Lys(4DMN)-His-NH_2, Fluo-His-Lys(Coum)-His-NH_2, Fluo-His-Nle-His-NH_2, Ac-His-Lys(Coum)-His-Lys-NH_2 and Ac-His-Lys(4DMN)-His-Lys-NH_2 were synthesised using the Rink amide aminomethyl resin (RA AM) and were obtained with low yields of 8-44% and high chromatographic purities of 92-97%. The products were characterised by ^{1}H and ^{13}C NMR spectroscopy and HPLC-MS. The *L*-peptides prepared in the lab and provided by commercial sources on a custom-based basis, represent a versatile toolbox for diverse applications such as the chelation of Cu(II) ions, the coupling to gold nanocarriers or the detection of Aβ aggregates, as will be illustrated in the following chapters.

Unfortunately, the FRET RhoB-His-Lys(Fluo)-His-NH_2 peptide could not be prepared since the solid-phase reaction of rhodamine B isothiocyanate with the *N*-terminal amino group of the peptide chain was unsuccessful. Microwaves or high temperatures may allow to successfully couple this dye to the peptide. Further experimental efforts are required to obtain such ratiometric copper detector.

2.5 Experimental section

2.5.1 Reagents, solvents and equipment

Table 2.2: Reagents and solvents used for the work described in this chapter.

Brand	Products
Acros Organics	1*H*-benzotriazole, $SOCl_2$, coumarin-3-carboxylic acid
Sigma Aldrich	$CDCl_3$, D_2O, d_6-DMSO, TIPS, Et_3N, Ac_2O, piperidine, Et_2O, 5(6)-carboxyfluorescein, 1,4-dioxane, 3-dimethylaminopropionitrile, Rhodamine B isothiocyanate
Fisher Scientific	DIPEA, MeCN (HPLC grade), TFA
Fluka	MeCN
Iris Biotech	2-CTC resin, Oxyma, Fmoc-His(Trt)-OH, Fmoc-Lys(Boc)-OH, Fmoc-Nle-OH
Jescuder	Anhydrous $MgSO_4$, $KMnO_4$, NaCl, $NaHCO_3$
Novabiochem	Boc-Lys-OH, Fmoc-Lys-OH, Fmoc-OSu, RA AM resin
Panreac	absolute ethanol, pyridine
Scharlau	acetone, AcOEt, AcOH, CH_2Cl_2, HCl 37%, hexanes, MeOH, 3-methyl-1-butanol, THF
Specialist des solvants	DMF
TCI	DIC, 4-bromo-1,8-naphthalic anhydride

Table 2.3: Equipment used for the synthetic work described in this chapter.

Instrument	Brand	Model
Gram-scale balance	Mettler	Toledo AB254 PJ360
Centrifuge	Hettich	Rotofix 32A
Vacuum lyophiliser	Christ	Alpha 2-4 LD plus
Rotatory evaporator	BUCHI	R-200
Sonicator	JP SELECTA S.A.	Ultrasons MEDI-II

Milli-Q H_2O (resistivity > 18 MΩ·cm) was produced by filtering deionised water with a Milli-Q Plus (Millipore) system. Anhydrous DCM was dried over CaH_2 under N_2 and was distilled just before its use. Anhydrous THF was kept over Na with benzophenone under N_2 and was also distilled prior to its utilisation. Dried Et_2O was stored over Na.

2.5.2 Syntheses and characterisation

Thin-Layer Chromatography (TLC)

TLC was performed on silica gel 60 F254 plates purchased from Merck. Exposure to UV light and $KMnO_4$ was used to reveal the spots.

Nuclear Magnetic Resonance (NMR)

NMR spectra were registered at the Centres Científics i Tecnològics of the Universitat de Barcelona (CCiTUB). The NMR data were analysed using MestReNova 9.1.0. Data are reported as follows: s, singlet; d, doublet; t, triplet; q, quartet; m, multiplet. ^{1}H NMR spectra were recorded at 400 MHz, while ^{13}C NMR spectra were registered at 100.6 MHz with proton decoupling. Coupling constants are given in Hz. 2D techniques (COSY, HSQC and HMBC) were used to fully characterise the products.

Fmoc amino acid derivatives and intermediates

All spectra were registered on a Varian Mercury-400 spectrometer. Chemical shifts are quoted in ppm downfield from TMS with the partially-deuterated solvent as the internal standard ($CDCl_3$ δ 7.26 and d_6-DMSO δ 2.50 for ^{1}H NMR; $CDCl_3$ δ 77.16 ± 0.06 and d_6-DMSO δ 39.52 ± 0.06 for ^{13}C NMR).

Peptides

1D and 2D NMR experiments were performed on a Bruker Avance III 400 MHz spectrometer, equipped with a 5 mm cryoprobe (Prodigy) broadband (CPPBBO BB-^{1}H/^{19}F/D) with gradients in Z. Solvent suppression for the 1D experiments was achieved

using a PRESAT pulse sequence. Solutions of 10 mM peptide in D_2O were adjusted to pH 7.4, and measured with an insert containing a 5 mg·mL^{-1} solution of [D_4]-3-(trimethylsilyl)propanoic acid (TSP) as an internal reference (D_2O δ 4.79 for ^{1}H NMR). It should be noted that, even though the measurements were made in D_2O, it was decided to use the notation pH.

Infrared (IR) spectroscopy

IR spectra of the solid products were registered using a Thermo Scientific Nicolet 6700 FT-IR spectrophotometer with an attenuated total reflectance (ATR) accessory.

UV-Vis spectroscopy

Spectra were recorded using a Varian Cary 100 spectrophotometer from 800 to 200 nm at room temperature. Quartz cuvettes (3 mL, 1 cm path length) were used.

Exact Mass Spectrometry (High Resolution Electrospray Ionisation, HR ESI)

High resolution electrospray ionisation mass spectrometry (HR ESI-MS) was performed using a LC/MSD-TOF spectrometer with an Agilent 1100 HPLC pumping system in either positive or negative-ion modes at the Centres Científics i Tecnològics of the Universitat de Barcelona (CCiTUB).

Liquid Chromatography

A Phenomenex® C18 reverse phase column (250 x 4 mm) with a particle size of 5.15 ± 0.30 μm and a pore size of 320 ± 40 Å was employed. The eluents were 0.045% TFA in H_2O (v/v) for eluent A and 0.036% TFA in MeCN (v/v) for eluent B, using the following gradient:

Table 2.4: HPLC gradient used in this work.

Time (min)	% Eluent A	% Eluent B
0	98	2
20	0	100
25	0	100
30	98	2
40	98	2

The flow rate was 1 mL/min and double detection at wavelengths 220 and 301 nm was used.

High Performance Liquid Chromatography (HPLC)

Analytical HPLC was carried out in a system consisting of a Shimadzu LC-20AD quaternary pump, a SIL-10Advp automatic injector, an SPD-20A variable dual wavelength detector and a DGU-20A5 online degas device.

High Performance Liquid Chromatography coupled to Mass Spectrometry (HPLC-MS)

A Waters Alliance HT system formed by a 2795 separation module, a PDA detector 2996 and a Micromass ZQ 2000 mass detector (Electrospray Ionisation, ESI-MS) was used.

Synthesis of the non-natural amino acids

3-(1H-Benzotriazol-1-ylcarbonyl)-2H-chromen-2-one

$SOCl_2$ (2.40 mL, 33.2 mmol) was added to a stirring solution of 1*H*-benzotriazole (6.00 g, 50.4 mmol) in freshly distilled THF (100 mL) at rt under N_2. After 20 min, coumarin-3-carboxylic acid (1.90 g, 9.99 mmol) was added and the reaction was stirred for 4 h. Then, the white precipitate formed was filtered off and the solvent was evaporated under reduced pressure. AcOEt (150 mL) was added to the crude solid and the remaining precipitate was filtered off. The resulting solution was washed with saturated aqueous Na_2CO_3 (3 × 50 mL) and brine (1 × 50 mL). The organic fraction was then dried

with anhydrous $MgSO_4$, filtered and evaporated under reduced pressure. The solid obtained was finally recrystallised from DCM-hexanes to yield 1.92-2.05 g (65-70% yield) of the desired product.

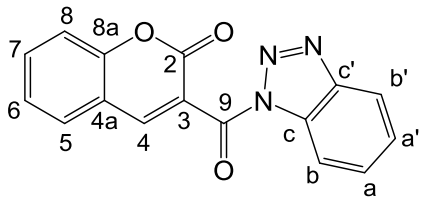

White solid. **R_f** (DCM/MeOH 9:1): 0.85. **^{1}H NMR** ($CDCl_3$, 400 MHz): δ 7.35-7.39 (m, 1H, H_6), 7.39-7.43 (m, 1H, H_8), 7.52-7.56 (m, 1H, $H_{a'}$), 7.63-7.65 (m, 1H, H_5), 7.66-7.68 (m, 1H, H_7), 7.68-7.72 (m, 1H, H_a), 8.12 (d, 1H, *J* = 8.3, $H_{b'}$), 8.30-8.33 (m, 2H, H_4 + H_b). **^{13}C NMR** ($CDCl_3$, 100.6 MHz): δ 114.3 (C_b), 117.1 (C_8), 117.6 (C_{4a}), 120.4 ($C_{b'}$), 121.8 (C_3), 125.2 (C_6), 126.7 ($C_{a'}$), 129.6 (C_5), 130.8 (C_a), 131.1 (C_c), 134.4 (C_7), 146.1 ($C_{c'}$), 146.9 (C_4), 154.8 (C_{8a}), 157.3 (C_2), 162.6 (C_9). **IR** (cm^{-1}): 756, 792, 938, 1201, 1383, 1610, 1713, 1731.

N^{α}-Fmoc-N^{ε}-(Coumarin-3-ylcarbonyl)-lysine (Fmoc-Lys(Coum)-OH)

Et_3N (0.56-1.40 mL, 4.02-10.0 mmol) was added to a stirring suspension of 3-(1*H*-Benzotriazol-1-ylcarbonyl)-2*H*-chromen-2-one (0.59-1.46 g, 2.02-5.03 mmol) and Fmoc-Lys-OH (0.75-1.86 g, 2.05-5.04 mmol) in 2:1 MeCN-H_2O (30-75 mL). The reaction mixture was then stirred for approximately 1 h, and HCl 4 N (2-5 mL) was added, giving rise to the formation of a white precipitate. Most of the MeCN was evaporated under reduced pressure. The solid thus obtained was dissolved in AcOEt (150-300 mL) and the resulting organic solution was washed with HCl 4 N (3 × 50 mL) and brine (1 × 50 mL). The organic fraction was then dried with anhydrous $MgSO_4$, filtered, and the solvent was eliminated by rotatory evaporation. The resulting white solid was recrystallised from DCM-hexanes to afford **2** in 70-80% yields.

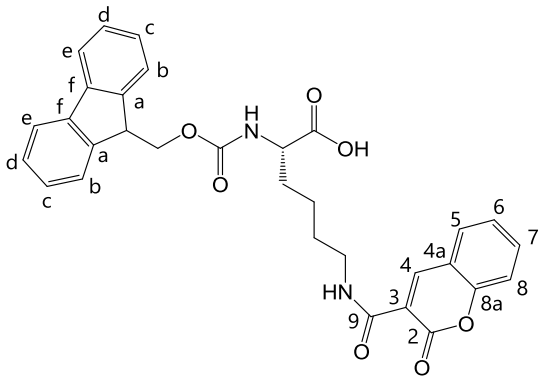

White solid. **R_f** (DCM/MeOH 9:1): 0.23. **^{1}H NMR** (DMSO-d_6, 400 MHz): δ 1.32-1.44 (m, 2H, Hγ), 1.47-1.57 (m, 2H, Hδ), 1.60-1.79 (m, 2H, Hβ), 3.27-3.34 (m, 2H, Hε), 3.90-3.97 (m, 1H, Hα), 4.16-4.20 (m, 1H, CH-Fmoc), 4.21-4.30 (m, 2H, CH_2-Fmoc), 7.26-7.32 (m, 2H, H_c), 7.34-7.38 (m, 2H, H_d), 7.39-7.40 (m, 1H, H_6), 7.44 (d, 1H, *J* = 8.4, H_8), 7.63 (d, 1H, *J* = 8.1, NHα), 7.67-7.69 (m, 2H, H_b), 7.69-7.71 (m, 1H, H_7), 7.83 (dd, 2H, *J* = 3.0, *J* = 7.5, H_e), 7.91 (dd, 1H, *J* = 1.3, *J* = 7.8, H_5), 8.68 (t, 1H, *J* = 5.7, NHε), 8.80 (s, 1H, H_4). **^{13}C NMR** (DMSO-d_6, 100.6 MHz): δ 23.56 (Cγ), 28.98 (Cδ), 30.88 (Cβ), 47.09 (CH-Fmoc), 54.17 (Cα), 66.04 (CH_2-Fmoc), 116.5 (C_8), 118.9 (C_{4a}), 119.4 (C_3), 120.5 (C_e), 125.5 (C_6), 125.7 (C_b), 127.5 (C_c), 128.1 (C_d), 130.6 (C_5), 134.4 (C_7), 141.1 (C_f), 144.2 (C_a), 147.7 (C_4), 154.2 (C_{8a}), 156.6 (CO-Fmoc), 160.8 (C_2), 161.5 (C_9), 174.4 (COOH). **IR** (cm^{-1}): 743, 1027, 1174, 1245, 1526, 1726, 3319, 3377.

4-N,N-Dimethylamino-1,8-naphthalic anhydride

A stirred solution of 4-bromo-1,8-naphthalic anhydride (2.72 g, 9.83 mmol) in 3-methyl-1-butanol (55 mL) was refluxed and 3-dimethylamino-propionitrile (4.44 mL, 39.3mmol) was subsequently added. The initial white suspension progressively turned into a bright orange solution which was refluxed overnight. The orange solid formed upon cooling at room temperature was filtered out and washed with cold water and cold isohexane to afford 1.69 g (71%) of the dimethylamino anhydride precursor.

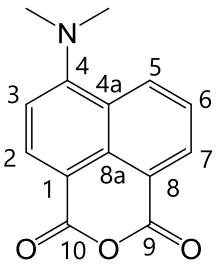

Orange solid. **R_f** (AcOEt with 0.5% AcOH): 0.75. **^{1}H NMR** ($CDCl_3$, 400 MHz): δ 3.11 (s, 6H, N$\underline{Me}_2$), 7.08 (d, 1H, *J* = 8.4, H_3), 7.65 (dd, 1H, *J* = 7.3, *J* = 8.5, H_6), 8.39 (d, 1H, *J* = 8.3, H_2), 8.46 (dd, 1H, *J* = 1.1, *J* = 8.5, H_5), 8.52 (dd, 1H, *J* = 1.1, *J* = 7.3, H_7). **^{13}C NMR** ($CDCl_3$, 100.6 MHz): δ 44.55 (N$\underline{Me}_2$), 109.2 (C_1), 113.1 (C_3), 119.1 (C_8), 124.7 (C_{4a}), 124.9 (C_6), 132.8 (C_5 + C_{8a}), 133.1 (C_7), 134.9 (C_2), 157.8 (C_4), 160.6 (C_{10}), 161.6 (C_9). **IR** (cm^{-1}): 747, 774, 996, 1014, 1339, 1566, 1584, 1717.

N^{α}-Boc-N^{ε}-(4-N,N-dimethylamino-1,8-naphthalimido)-lysine (Boc-Lys(4DMN)-OH)

A three-necked round-bottomed flask containing 4-*N,N*-dimethylamino-1,8-naphthalic anhydride (1.59 g, 6.60 mmol) and equipped with a magnetic bar, a reflux condenser and a dropping funnel was purged with N_2. Then, 1,4-dioxane (150 mL) was transferred to the flask with a syringe through the rubber septum and the resulting brown suspension was refluxed under stirring. Simultaneously, an aqueous solution (30 mL) of Boc-Lysine-OH (1.49 g, 6.03 mmol) and $NaHCO_3$ (2.52 g, 30.0 mmol) was prepared and transferred to the dropping funnel. The amino acid solution was added dropwise, and the resulting yellow mixture was stirred for further 2.5 h. Then, the yellow suspension was allowed to cool to rt and most of the solvent mixture was evaporated under reduced pressure. The crude product was diluted with distilled water (150 mL) and acidified under stirring with 4 N HCl to pH 7-8 in the presence of DCM (50 mL). The aqueous phase was further extracted with DCM (3 × 50 mL) and the combined organic extracts were dried with anhydrous $MgSO_4$, filtered and evaporated under reduced pressure. The resulting bright orange solid (1.71 g, 60 %) was used in the next step without further purification.

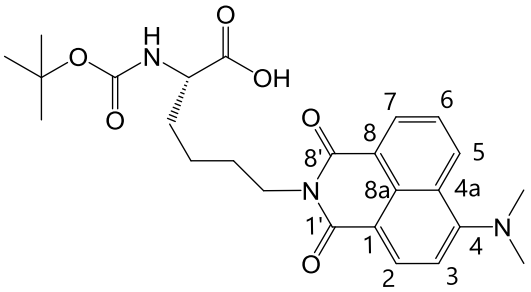

Orange solid. **R_f** (AcOEt with 0.5% AcOH): 0.55. **MS (HR ESI+): *m/z*** calculated for $[C_{25}H_{31}N_3O_6 + H]^+$ 470.2291, found 470.2282. **^{1}H NMR** ($CDCl_3$, 400 MHz): δ 1.41 (s, 9H, $\underline{Me}$-^{t}Bu), 1.45-1.55 (m, 2H, Hγ), 1.68-1.79 (m, 2H, Hδ), 1.80-1.99 (m, 2H, Hβ), 3.07 (s, 6H, N$\underline{Me}_2$), 4.08-4.20 (m, 2H, Hε), 4.23-4.31 (m, 1H, Hα), 7.06 (d, 1H, *J* = 8.2, H_3), 7.62 (t_{app},

1H, J_{app} = 8.0, H_6), 8.38 (d, 1H, J = 8.4, H_5), 8.43 (d, 1H, J = 8.2, H_2), 8.52 (d, 1H, J = 7.2, H_7). **^{13}C NMR** ($CDCl_3$, 100.6 MHz): δ 22.68 (Cγ), 27.61 (Cδ), 28.32 (Me-^{t}Bu), 31.61 (Cβ), 39.48 (Cε), 44.74 (NMe_2), 53.48 (Cα), 79.90 (C-^{t}Bu), 113.3 (C_3), 114.7 (C_1), 122.9 (C_8), 124.8 (C_6), 125.1 (C_{4a}), 130.2 (C_{8a}), 131.1 (C_7), 131.2 (C_5), 132.8 (C_2), 155.9 (CO-^{t}Bu), 157.0 (C_4), 164.2 ($C_{1'}$), 164.7 ($C_{8'}$), 176.5 (COOH). **IR** (cm^{-1}): 752, 792, 1161, 1361, 1570, 1637, 1682, 2856, 2928.

N^{α}-Fmoc-N^{ε}-(4-N,N-dimethylamino-1,8-naphthalimido)-lysine (Fmoc-Lys(4DMN)-OH)

Cold TFA (40 mL) was slowly added to a solution of Boc-Lys(4DMN)-OH (1.64 g, 3.48 mmol) in DCM (40 mL) and the reaction was stirred for 2 h at rt. Next, the solution was dried using a rotatory evaporator and an azeotrope with $CHCl_3$ to eliminate residual TFA; the resulting crude product was left under vacuum overnight. The resulting oil was diluted with an aqueous solution (20 mL) of $NaHCO_3$ (1.62 g, 19.2 mmol), generating a basic mixture (as checked by measuring the pH). Then, a solution of Fmoc-OSu (1.41 g, 4.18 mmol) in 1,4-dioxane (95 mL) was added dropwise with a dropping funnel and the mixture was stirred at rt for 2.5 h. Afterwards, dioxane was evaporated under reduced pressure. The crude product was diluted in distilled water (150 mL), acidified with 4 N HCl and extracted with DCM (3 × 50 mL). The combined organic phases were dried with anhydrous $MgSO_4$, filtered and the solvent was evaporated under reduced pressure. The resulting oil was finally purified by flash column chromatography (EtOAc/DCM 1:1 to EtOAc with 0.5% of AcOH); the fractions containing the target compound were evaporated using an azeotrope with toluene (3 × 50 mL) to remove residual AcOH. A bright orange solid (1.58 g, 77%) was obtained.

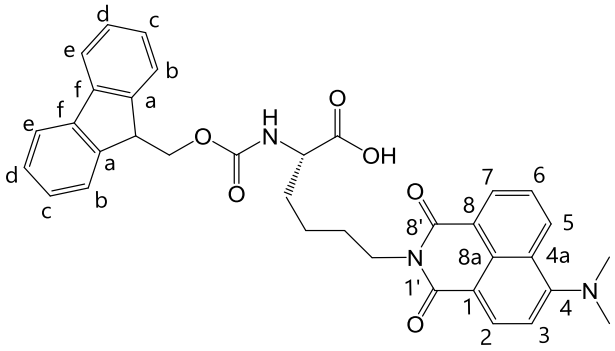

Orange solid. **R_f** (AcOEt with 0.5% AcOH): 0.50. **MS (HR ESI+):** ***m/z*** calculated for $[C_{35}H_{33}N_3O_6 + H]^+$ 592.2448, found 592.2448. **^{1}H NMR** ($CDCl_3$, 400 MHz): δ 1.42-1.56

(m, 2H, Hγ), 1.67-1.85 (m, 2H, Hδ), 1.86-2.05 (m, 2H, Hβ), 3.01 (s, 6H, N$\underline{Me_2}$), 4.08-4.20 (m, 3H, Hε + $\underline{CH}$-Fmoc), 4.25-4.35 (m, 2H, $\underline{CH_2}$-Fmoc), 4.35-4.44 (m, 1H, Hα), 6.96 (d, 1H, *J* = 8.2, H_3), 7.20-7.26 (m, 2H, H_c), 7.31-7.36 (m, 2H, H_d), 7.51-7.54 (m, 1H, H_6), 7.55 (d, 2H, *J* = 7.3, H_b), 7.67 (d, 2H, *J* = 7.5, H_e), 8.32 (d, 1H, *J* = 8.4, H_5), 8.41 (d, 1H, *J* = 8.2, H_2), 8.51 (d, 1H, *J* = 7.0, H_7). **^{13}C NMR** ($CDCl_3$, 100.6 MHz): δ 22.59 (Cγ), 27.50 (Cδ), 31.44 (Cβ), 39.41 (Cε), 44.68 (N$\underline{Me_2}$), 47.12 ($\underline{CH}$-Fmoc), 53.82 (Cα), 67.02 ($\underline{CH_2}$-Fmoc), 113.2 (C_3), 114.5 (C_1), 120.0 (C_e), 122.8 (C_8), 124.8 (C_{4a}), 125.0 (C_6), 125.2 (C_b), 127.0 (C_c), 127.4 (C_d), 130.2 (C_{8a}), 131.2 (C_7), 131.3 (C_5), 132.9 (C_2), 141.3 (C_f), 143.8 (C_a), 156.4 ($\underline{CO}$-Fmoc), 157.0 (C_4), 164.4 ($C_{1'}$), 164.8 ($C_{8'}$), 175.8 (COOH). **IR** (cm^{-1}): 729, 760, 1205, 1245, 1348, 1375, 1575, 1633, 1682, 1717, 2861, 2945.

Solid-phase synthesis and characterisation of the peptides

The solid-phase synthesis of the peptides described in this Thesis was carried out manually in 12 mL or 20 mL polypropylene syringes including porous polyethylene filters. The reaction mixtures were stirred with a Teflon rod and the excess of reagents was eliminated by filtration under reduced pressure.

Loading of the first amino acid and capping of the resin

For the coupling of the first amino acid, the resin was previously washed with DMF (3 x 30 s), DCM (3 x 30 s) and DMF again (3 x 30 s). Different pathways were followed for the loading of the amino acid to the 2-chlorotrtyl chloride resin (2-CTC) and to the Rink amide AM resin (RA AM):

$\underline{2\text{-CTC resin:}}$ 1.5 eq of amino acid were transferred to the syringe, after which DIPEA (6.7 eq) and DCM (2 mL) were added. The mixture was regularly stirred for 10 min and more DIPEA (3.3 eq) was added. The mixture was left for 1.5 h with recurrent stirring and MeOH (1 mL) was added. The solvents and the excess of regents were filtered off after 10 min, and the yields were determined by spectrophotometric Fmoc quantification (see protocol *Fmoc quantification/elimination* in this chapter).

$\underline{\text{RA AM resin:}}$ the Fmoc group of the resin was previously removed following the protocol already described and the resin was washed (1 mL of solvent per 100 mg of resin) with DMF (3 x 30 s), DCM (3 x 30 s) and DMF (3 x 30 s). Then, the corresponding

Fmoc amino acid (3 eq), Oxyma (3 eq) and DIC (3 eq) were added and dissolved in the minimum amount of DMF/DCM 1:1 to allow a proper stirring of the reaction mixture. The reaction was carried out for 1 h with regular stirring, and the resin was subsequently washed with DMF (3 x 30 s); the coupling of the amino acid was then repeated with the same quantities of reagents. The resin was washed with DMF (3 x 30 s), DCM (3 x 30 s) and DMF (3 x 30 s), and then Ac_2O (30 eq) and DIPEA (30 eq) in DMF (up to 1 mL of mixture per 100 mg of resin) were added. The mixture was left to react for 45 min with intermittent stirring and the reagents were finally filtered off and the resin was washed (1 mL of solvent per 100 mg of resin) again with DMF, CH_2Cl_2 and DMF.

Peptide chain elongation

After the elimination/quantification of the Fmoc group, 3 eq of the Fmoc amino acid, Oxyma and DIC were added in the minimum amount of DMF/CH_2Cl_2 1:1 to allow (occasional) stirring of the reaction mixture. The resulting suspension was left to react for 1 h and a ninhydrin test was performed to assess the completeness of the elongation step. Then, the solvents were filtered off and the resin was washed with DMF (3 x 30 s) if the reaction had to be repeated (positive test), or with DMF (3 x 30 s), DCM (3 x 30 s) and DMF (3 x 30 s) when the coupling was quantitative (negative test). This process was repeated one or two more times with the same quantities of reagents, if required.

Ninhydrin Test

Two solutions were required for this test:

Reagent A: A solution of phenol (40 g) was prepared in absolute EtOH (10 mL). Simultaneously, 2 mL of a KCN aqueous solution (65 mg in 100 mL of H_2O) were added to pyridine (98 mL), freshly distilled over ninhydrin. Then, these two solutions were stirred independently with 4 g of Amberlite MB-3 for 45 min, after which they were filtered and combined.

Reagent B: Ninhydrin (2.5 g) was dissolved in absolute EtOH (50 mL) and the resulting solution was stored, protected from light.

The test was performed as follows: first, the peptidyl-resin was washed with DCM (3 x 30 s) to remove potential traces of primary amines formed by decomposition of DMF. Then, a small portion of the peptidyl-resin was introduced into a test tube, where it was washed three times with MeOH to avoid false-positive results. Once the last fraction of MeOH was removed with a Pasteur pipette, 6 drops of reagent A and 2 drops of reagent B were added. After that, the solution was heated at 110 ºC for 3 min. A blank was prepared in parallel to compare colours.

A blue colour of the solution (positive test) indicated remaining free α-amino groups, suggesting an incomplete coupling step, whereas an unchanged yellow colour (negative test) indicated the absence of primary amines, suggesting that above 99.5% of the growing chains had incorporated the amino acid.

Fmoc quantification/elimination

The Fmoc quantification analysis was carried out to determine the yields of the loading of the first amino acid of every sequence and on-resin yields after the coupling of the last amino acid (the analysis was carried out after the coupling of the second-to-last amino acid when the *N*-terminal Fmoc group had to be kept).

To perform the analysis, the peptidyl-resin was previously washed with DMF (3 x 30 s) and treated with 25 mL of piperidine/DMF 1:4 in portions of 5 mL (5 x 5 min), which were then filtered and collected in a 100 mL volumetric flask (the filtrates were directly discarded if no quantification was required). The *N*-terminal-deprotected peptidyl-resin was washed with 25 mL of DMF in portions of 5 mL (5 x 30 s) that were collected in the same volumetric flask, and the resulting solution was diluted to the mark with DCM. An aliquot of 2 mL of this mixture was transferred to another 100 mL volumetric flask with 25 mL of piperidine/DMF 1:4 and 25 mL of DMF, and the final solution was diluted to the mark with DCM. A blank was also prepared in a 50 mL volumetric flask with 12.5 mL of piperidine/DMF 1:4 and 12.5 mL of DMF and diluted to the mark with DCM.

The absorbance of the dibenzofulvene-piperidine adduct formed was then measured and the concentration of Fmoc was determined by using the Lambert-Beer law (**Equation 2.1**),

$$\boldsymbol{A = \varepsilon \times c \times l} \qquad (\mathbf{2.1})$$

where ε is 7800 $M^{-1} \times cm^{-1}$ at 301 nm, ***c*** is the concentration of the adduct in mol × dm^{-3} and ***l*** is the optical path length of the cuvette, *viz*. 1 cm. The amount of Fmoc groups, equivalent to the quantity of amino acid incorporated, was then calculated.

Acetylation

The peptidyl-resin was treated with a mixture of Ac_2O (30 eq) and DIPEA (30 eq) diluted with DMF up to a total volume of 1 mL per 100 mg of resin. The resulting suspension was regularly stirred during 20 min, filtered and thoroughly washed with DMF (3 x 30 s), DCM (3 x 30 s) and DMF (3 x 30 s).

Cleavage of the peptide from the resin

The resin was first washed with DMF (1 x 30 s), DCM (3 x 30 s), MeOH (3 x 30 s) and DCM (3 x 30 s). Then, a mixture of 5% TIPS and 60% TFA in DCM (1 mL of mixture per 100 mg of resin) was added and the reaction performed during 45 min. Next, the mixture was filtered off and the filtrate was collected in a round-bottomed flask with Et_2O (15 mL per 100 mg of resin). The resin was washed with TFA/DCM 1:1 (1 mL of mixture per 100 mg of resin, 2 x 30 s) and TFA/Et_2O 1:1 (1 mL of mixture per 100 mg of resin, 2 x 30 s), the washing solutions being collected into the same round-bottomed flask. The precipitated peptide was then centrifuged and the Et_2O supernatant was poured and discarded. The peptide was washed 2-3 times with Et_2O, centrifuged and dried under reduced pressure (lyophilisation was sometimes necessary). Final yields were determined by weight.

H-His-Lys(Coum)-His-OH

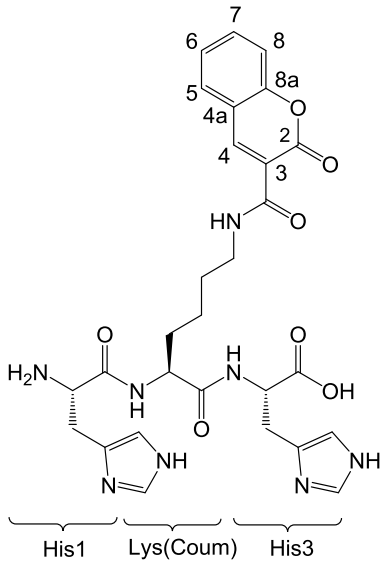

Anchoring of His3 (1 × 1.5 eq)	497 mg of 2-CTC resin 746 mg of Fmoc-His(Trt)-OH 930 + 460 μL of DIPEA
Yield	48%
Coupling of Lys(Coum) (2 × 3 eq)	629 mg of Fmoc-Lys(Coum)-OH 163 mg of Oxyma 180 μL of DIC
Coupling of His1 (2 × 3 eq)	713 mg of Fmoc-His(Trt)-OH 163 mg of Oxyma 180 μL of DIC
Yield on the resin	88%
Amount of peptide (purity)	370 mg (85%)
Amount of peptide after purification (mass yield)	150 mg (42%)
Chromatographic purity after purification	94%

White solid. **HPLC-MS:** t_R = 8.78 min; ***m/z*** 593.14 ($[C_{28}H_{32}N_8O_7 + H]^+$). **^{1}H NMR** ($D_2O$, pH = 7.4, 400 MHz): δ 1.18-1.34 (m, 2H, Hγ-Lys2), 1.49-1.60 (m, 2H, Hδ-Lys2), 1.60-1.78 (m, 2H, Hβ-Lys2), 2.80-3.10 (m, 4H, Hβ-His1 + Hβ-His3), 3.27-3.37 (m, 2H, Hε-Lys2), 3.84 (dd, 1H, *J* = 7.5, *J* = 5.7, Hα-His1), 4.21 (dd, 1H, *J* = 9.0, *J* = 5.3, Hα-Lys2), 4.33 (dd, 1H, *J* = 7.8, *J* = 5.1, Hα-His3), 6.81 (d, 1H, *J* = 1.2, H_5-His1), 6.89 (d, 1H, *J* = 1.2, H_5-His3),

7.30-7.39 (m, 2H, H_6 + H_8-Lys(Coum)), 7.60 (d, 1H, J = 1.2, H_2-His1), 7.64-7.70 (m, 2H, H_5 + H_7-Lys(Coum)), 7.85 (d, 1H, J = 1.2, H_2-His3), 8.62 (s, 1H, H_4-Lys(Coum)). **^{13}C NMR** (D_2O, pH = 7.4, 100.6 MHz): δ 25.16 (Cγ-Lys2), 30.74 (Cδ-Lys2), 31.20 (Cβ-His3), 33.04 (Cβ-His1), 33.24 (Cβ-Lys2), 42.28 (Cε-Lys2), 56.63 (Cα-Lys2), 56.69 (Cα-His1), 57.52 (Cα-His3), 119.2 (C_8-Lys(Coum)), 119.8 (C_5-His1), 120.3 (C_3-Lys(Coum)), 120.5 (C_5-His3), 121.1 (C_{4a}-Lys(Coum)), 128.5 (C_6-Lys(Coum)), 133.1 (C_5-Lys(Coum)), 134.2 (C_4-His1), 134.4 (C_4-His3), 137.5 (C_2-His3), 137.7 (C_7-Lys(Coum)), 138.7 (C_2-His1), 151.9 (C_4-Lys(Coum)), 156.7 (C_{8a}-Lys(Coum)), 165.1 (C_2-Lys(Coum)), 166.7 (CONH-Lys(Coum)), 175.6 (CO-Lys2), 175.9 (CO-His1), 179.6 (CO-His3).

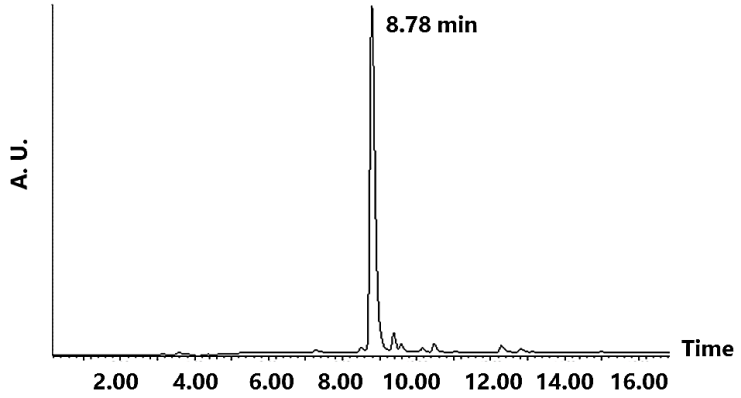

Figure 2.50: Chromatogram of H-His-Lys(Coum)-His-OH.

Fluo-His-Lys(Coum)-His-NH_2

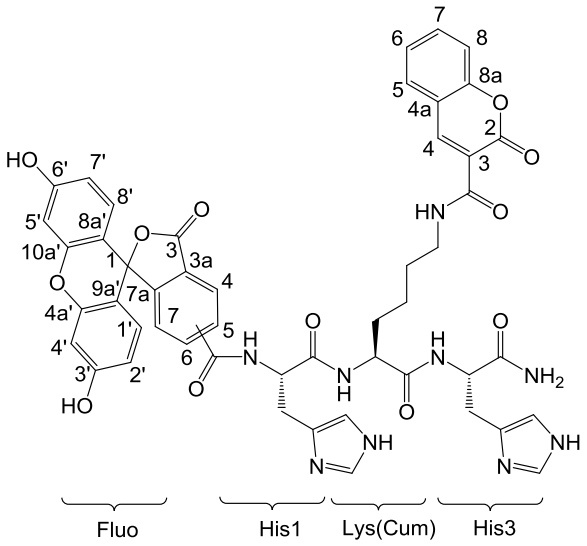

Anchoring of His3 (2 × 3 eq)	347 mg of Rink Amide resin 445 mg of Fmoc-His(Trt)-OH 102 mg of Oxyma 110 μL of DIC
Yield	86%
Coupling of Lys(Coum) (2 × 3 eq)	336 mg of Fmoc-Lys(Coum)-OH 88 mg of Oxyma 96 μL of DIC
Coupling of His1 (2 × 3 eq)	385 mg of Fmoc-His(Trt)-OH 88 mg of Oxyma 96 μL of DIC
Yield on the resin	quantitative
Coupling of 5(6)-carboxyfluorescein (2 × 2 eq)	156 mg of 5(6)-carboxyfluorescein 59 mg of Oxyma 64 μL of DIC
Purity	79%
Amount of peptide (mass yield)	107 mg (44%)
Chromatographic purity	92%

Orange solid. **HPLC-MS:** t_R = 11.0 + 11.2 min; ***m/z*** 950.2 ($[C_{49}H_{43}N_9O_{12} + H]^+$). **^{1}H NMR** ($D_2O$, pH = 7.4, 400 MHz): δ1.03-2.05 (m, Hβ + Hγ + Hδ-Lys2), 2.99-3.32 (m, Hβ-His1 + Hβ-His3 + Hε-Lys2), 4.39-4.50 (m, Hα-Lys2), 4.76-4.85 (m, Hα-His1 + Hα-His3), 6.38-6.50 (m, H_6 + H_8-Lys(Coum)), 6.61-6.68 (m, $H_{2'}$ + $H_{4'}$ + $H_{5'}$ + $H_{7'}$-Fluo), 6.84-7.02 (m, $H_{1'}$ + $H_{8'}$-Fluo), 7.17-7.23 (m, H_5-His1 + H_5-His3 + H_6-Fluo), 7.35 (d, *J* = 7.9, H_7-Fluo), 7.52-7.66 + 7.97-8.17 (m, H_5 + H_7-Lys(Coum)), 7.77 (d, *J* = 1.7, H_7-Fluo), 7.86 (s, H_2-His1/3), 7.88 (s, H_2-His1/3), 8.04-8.09 (m, H_4 + H_5-Fluo), 8.27 (d, *J* = 1.7, H_4-Fluo), 8.40-8.44 (m, H_4-Lys(Coum)).

The low solubility of this peptide in D_2O prevented the proper integration of the proton signals and a complete characterisation with ^{13}C and 2D NMR.

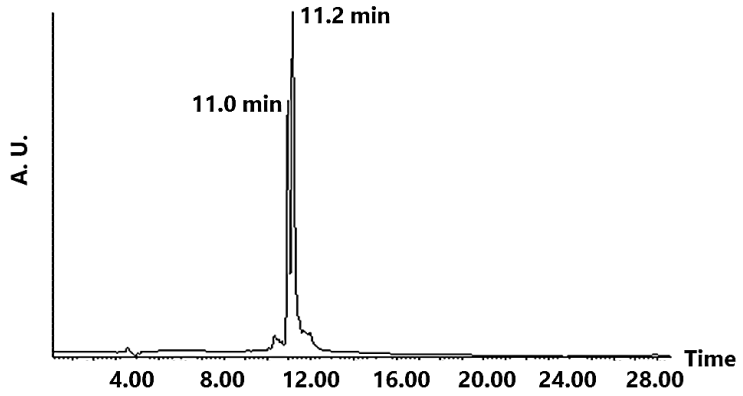

Figure 2.51: Chromatogram of Fluo-His-Lys(Coum)-His-NH_2.

Fluo-His-Nle-His-NH_2

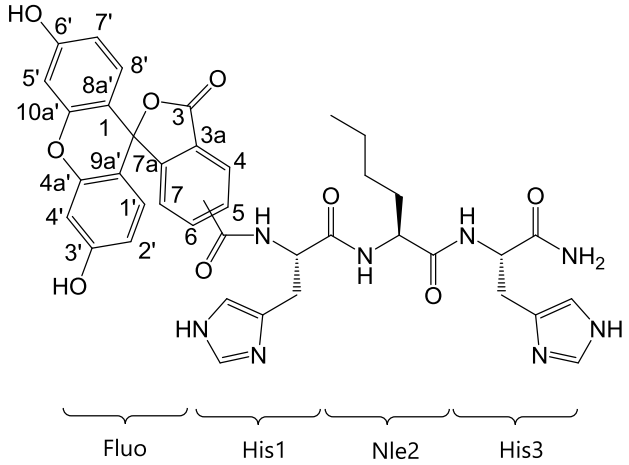

Anchoring of His3 (2 × 3 eq)	224 mg of Rink Amide resin 287 mg of Fmoc-His(Trt)-OH 66 mg of Oxyma 71 μL of DIC
Yield	quantitative
Coupling of Nle2 (3 eq)	164 mg of Fmoc-Nle-OH 66 mg of Oxyma 71 μL of DIC
Coupling of His1 (3 eq)	287 mg of Fmoc-His(Trt)-OH 66 mg of Oxyma 71 μL of DIC

Yield on the resin	quantitative
Coupling of 5(6)-carboxyfluorescein (1.5 eq)	87 mg of 5(6)-carboxyfluorescein 66 mg of Oxyma 71 μL of DIC
Amount of peptide (mass yield)	14 mg (9%)
Chromatographic purity	96%

Orange solid. **HPLC-MS:** t_R = 10.4 + 10.5 min; ***m/z*** 763.1 ($[C_{39}H_{38}N_8O_9 + H]^+$).

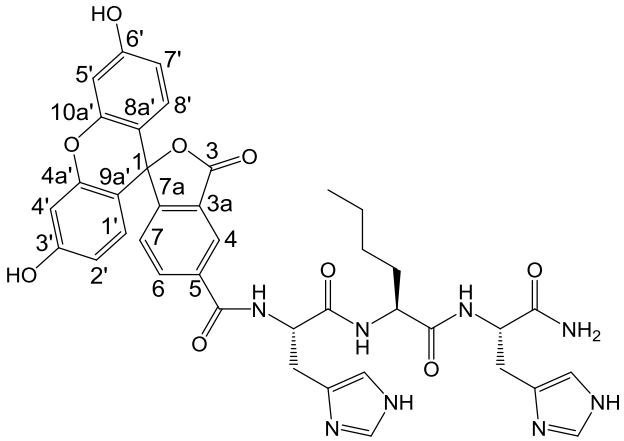

^{1}H NMR (D_2O, pH = 7.4, 400 MHz): δ 0.79 (t, 3H, *J* = 7.2, Hε-Nle2), 1.09-1.27 (m, 4H, Hγ + Hδ-Nle2), 1.61-1.71 (m, 2H, Hβ-Nle2), 3.01-3.20 (m, 2H, Hβ-His3), 3.16-3.27 (m, 2H, Hβ-His1), 4.22-4.27 (m, 1H, Hα-Nle2), 4.59-4.64 (m, 1H, Hα-His3), 4.77-4.84 (m, 1H, Hα-His1), 6.50-6.56 (m, 2H, $H_{4'}$ + $H_{5'}$-Fluo), 6.57-6.61 (m, 2H, $H_{2'}$ + $H_{7'}$-Fluo), 6.98 (s, 1H, H_5-His3), 7.00-7.06 (m, 2H, $H_{1'}$ + $H_{8'}$-Fluo), 7.06-7.08 (s, 1H, H_5-His1), 7.24 (d, 1H, *J* = 7.9, H_7-Fluo), 7.85 (d, 1H, *J* = 1.3, H_2-His3), 7.86-7.87 (m, 1H, H_6-Fluo), 7.89 (d, 1H, *J* = 1.1, H_2-His1), 8.15 (d, 1H, *J* = 1.8, H_4-Fluo). **^{13}C NMR** (D_2O, pH = 7.4, 100.6 MHz): δ 16.02 (Cε-Nle2), 24.43 (Cδ-Nle2), 29.83 (Cγ-Nle2), 30.88 + 30.93 (Cβ-His1 + Cβ-His3), 33.14 (Cβ-Nle2), 56.00 (Cα-His3), 57.15 (Cα-Nle2), 57.37 (Cα-His1), 106.5 ($C_{4'}$ + $C_{5'}$), 115.4 ($C_{8a'}$ + $C_{9a'}$), 119.8 (C_5-His1 + C_5-His3), 125.5 ($C_{2'}$ + $C_{7'}$), 130.2 (C_4-Fluo), 130.9 (C_6-Fluo), 133.3 (C_7-Fluo), 134.0 ($C_{1'}$ + $C_{8'}$), 135.0 (C_4-His3), 135.1 (C_4-His1), 136.8 (C_5-Fluo), 138.3 (C_2-His3), 138.4 (C_2-His1), 138.5 (C_{7a}-Fluo), 142.9 (C_{3a}-Fluo), 160.5 (C_1-Fluo), 161.3 ($C_{4a'}$ + $C_{10a'}$), 172.4 ($CONH_2$-Fluo), 176.1 (CO-His1), 176.3 (C_3-Fluo), 176.9 (CO-Nle2), 178.1 (CO-His3), 182.4 ($C_{3'}$ + $C_{6'}$-Fluo).

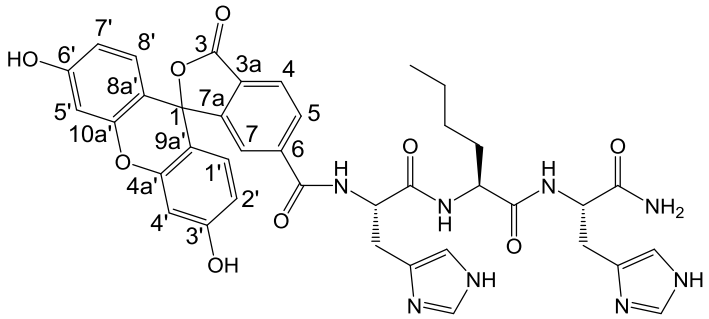

^{1}H NMR (D_2O, pH = 7.4, 400 MHz): δ 0.72 (t, 2H, *J* = 7.2, Hε-Nle2), 0.98-1.16 (m, 4H, Hγ + Hδ-Nle2), 1.51-1.63 (m, 2H, Hβ-Nle2), 2.86-3.09 (m, 2H, Hβ-His3), 3.09-3.20 (m, 2H, Hβ-His1), 4.14-4.19 (m, 1H, Hα-Nle2), 4.49-4.54 (m, 1H, Hα-His3), 4.77-4.84 (m, 1H, Hα-His1), 6.50-6.56 (m, 2H, $H_{4'}$ + $H_{5'}$-Fluo), 6.57-6.61 (m, 2H, $H_{2'}$ + $H_{7'}$-Fluo), 6.85 (d, 1H, *J* = 1.2, H_5-His3), 6.99 (d, 1H, *J* = 1.1, H_5-His1), 7.00-7.06 (m, 2H, $H_{1'}$ + $H_{8'}$-Fluo), 7.59 (d, 1H, *J* = 1.7, H_7-Fluo), 7.73 (d, 1H, *J* = 1.3, H_2-His3), 7.78 (d, 1H, *J* = 1.1, H_2-His1), 7.89-7.91 (m, 1H, H_4-Fluo), 7.93-7.97 (m, 1H, H_5-Fluo). **^{13}C NMR** (D_2O, pH = 7.4, 100.6 MHz): δ 15.95 (Cε-Nle2), 24.34 (Cδ-Nle2), 29.79 (Cγ-Nle2), 30.88 + 30.93 (Cβ-His1 + Cβ-His3), 32.97 (Cβ-Nle2), 56.07 (Cα-His3), 57.08 (Cα-Nle2), 57.50 (Cα-His1), 106.5 ($C_{4'}$ + $C_{5'}$), 115.4 ($C_{8a'}$ + $C_{9a'}$), 119.6 (C_5-His1 + C_5-His3), 125.5 ($C_{2'}$ + $C_{7'}$), 131.4 (C_5-Fluo), 131.6 (C_4-Fluo), 131.8 (C_7-Fluo), 134.0 ($C_{1'}$ + $C_{8'}$), 134.8 (C_4-His3), 135.1 (C_4-His1), 135.1 (C_6-Fluo), 136.4 (C_{7a}-Fluo), 138.1 (C_2-His3), 138.3 (C_2-His1), 145.9 (C_{3a}-Fluo), 160.0 (C_1-Fluo), 161.3 ($C_{4a'}$ + $C_{10a'}$), 172.4 ($CONH_2$-Fluo), 176.1 (CO-His1), 176.8 (C_3-Fluo), 176.9 (CO-Nle2), 178.0 (CO-His3), 182.4 ($C_{3'}$ + $C_{6'}$-Fluo).

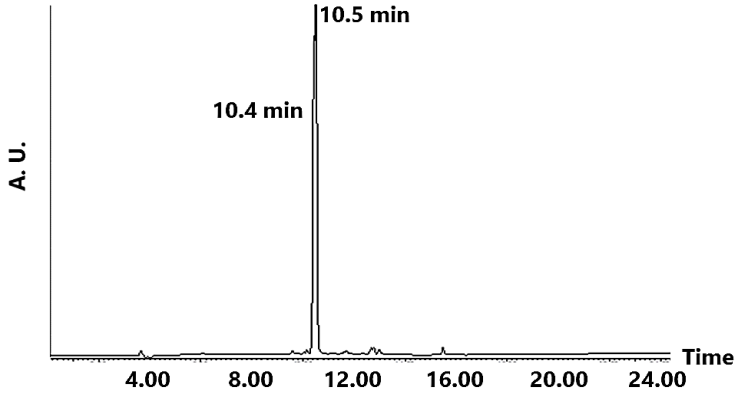

Figure 2.52: Chromatogram of Fluo-His-Nle-His-NH_2.

Ac-His-Lys(Coum)-His-Lys-NH_2

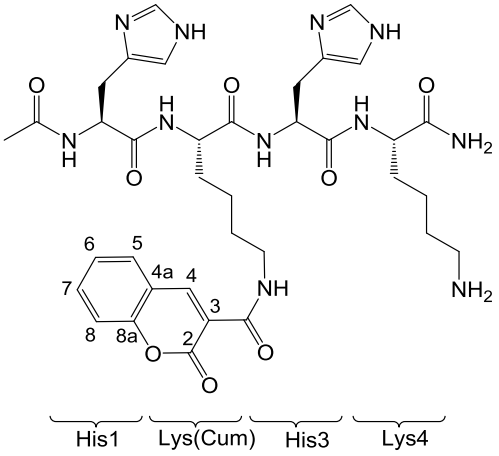

Anchoring of Lys4 (2 × 3 eq)	498 mg of Rink Amide resin 483 mg of Fmoc-Lys(Boc)-OH 146 mg of Oxyma 160 μL of DIC
Yield	73%
Coupling of His3 (3 eq)	465 mg of Fmoc-His(Trt)-OH 107 mg of Oxyma 116 μL of DIC
Coupling of Lys(Coum) (3 eq)	406 mg of Fmoc-Lys(Coum)-OH 107 mg of Oxyma 116 μL of DIC
Coupling of His1 (3 eq)	465 mg of Fmoc-His(Trt)-OH 107 mg of Oxyma 116 μL of DIC
Yield on the resin	quantitative
Acetylation	970 μL of acetic anhydride 1.80 mL of DIPEA
Treatment with piperidine/DMF 1:4	5 × 10 min × 5 mL
Amount of peptide (mass yield)	70 mg (25%)
Chromatographic purity	94%

White solid. **HPLC-MS:** t_R = 8.37 min; ***m/z*** 762.3 ($[C_{36}H_{47}N_{11}O_8 + H]^+$). **^{1}H NMR** ($D_2O$, pH = 7.4, 400 MHz): δ 1.20-1.30 (m, 4H, Hγ-Lys2 + Hγ-Lys4), 1.49-1.59 (m, 4H, Hδ-Lys2 + Hδ-Lys4), 1.60-1.72 (m, 4H, Hβ-Lys2 + Hβ-Lys4), 1.84 (s, 3H, Me-Ac), 2.74-2.84 (m,

2H, Hβ-His1), 2.84-2.90 (m, 2H, Hε-Lys4), 2.91-3.02 (m, 2H, Hβ-His3), 3.28-3.41 (m, 2H, Hε-Lys2), 4.08-4.13 (m, 1H, Hα-Lys4), 4.15-4.20 (m, 1H, Hα-Lys2), 4.37 (dd, 1H, J = 8.4, J = 5.8, Hα-His1), 4.46 (t, 1H, J = 7.4, Hα-His3), 6.75 (s, 1H, H_5-His1), 6.81 (s, 1H, H_5-His3), 7.32 (d, 1H, J = 8.7, H_8-Lys(Coum)), 7.36 (t_{app}, 1H, J_{app} = 7.6, H_6-Lys(Coum)), 7.49 (s, 1H, H_2-His1), 7.56 (s, 1H, H_2-His3), 7.65-7.66 (m, 1H, H_7-Lys(Coum)), 7.67-7.68 (m, 1H, H_5-Lys(Coum)), 8.64 (s, 1H, H_4-Lys(Coum)). **^{13}C NMR** (D_2O, pH = 7.4, 100.6 MHz): δ 21.58 (Me-Ac), 21.91 (Cδ-Lys4), 22.09 (Cδ-Lys2), 26.14 (Cγ-Lys4), 27.83 (Cγ-Lys2), 28.45 (Cβ-His3), 28.89 (Cβ-His1), 30.14 (Cβ-Lys2 + Cβ-Lys4), 39.10 (Cε-Lys4), 39.29 (Cε-Lys2), 53.07 (Cα-Lys2), 53.57 (Cα-Lys4), 53.82 (Cα-His3), 54.17 (Cα-His1), 116.3 (C_8-Lys(Coum)), 116.7 (C_5-His1 + C_5-His3), 117.4 (C_3-Lys(Coum)), 118.1 (C_{4a}-Lys(Coum)), 125.6 (C_6-Lys(Coum)), 130.1 (C_5-Lys(Coum)), 132.7 (C_4-His1 + C_4-His3), 134.9 (C_7-Lys(Coum)), 135.9 (C_2-His1), 135.9 (C_2-His3), 149.0 (C_4-Lys(Coum)), 153.8 (C_{8a}-Lys(Coum)), 162.2 (C_2-Lys(Coum)), 163.8 (CONH-Lys(Coum)), 172.6 (CO-His3), 173.4 (CO-Lys2), 173.5 (CO-His1), 174.1 (CO-Ac), 176.1 (CO-Lys4).

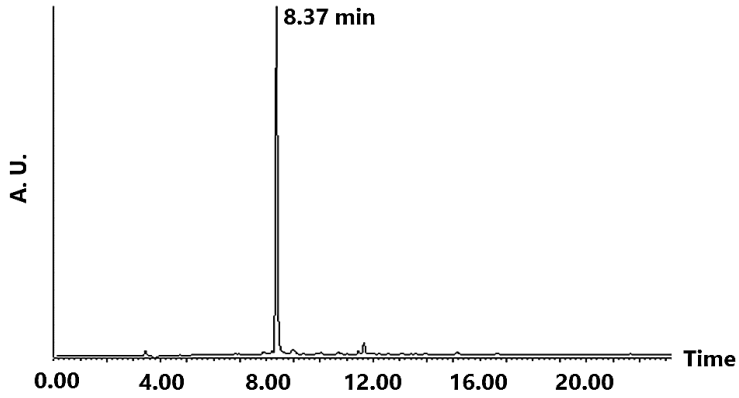

Figure 2.53: Chromatogram of Ac-His-Lys(Coum)-His-Lys-NH_2.

Ac-His-Lys(4DMN)-His-Lys-NH_2

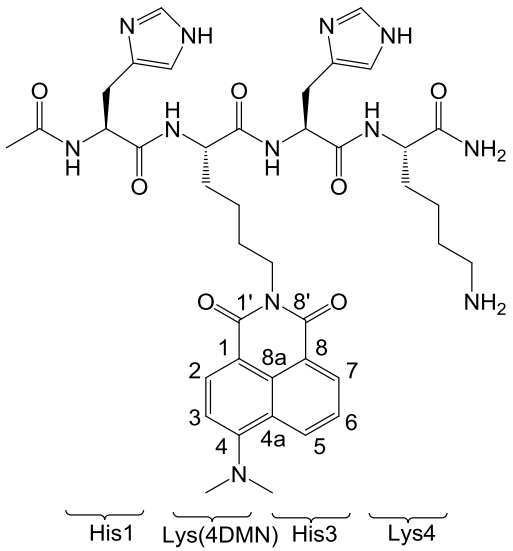

Anchoring of Lys4 (2 × 3 eq)	248 mg of Rink Amide resin 241 mg of Fmoc-Lys(Boc)-OH 73 mg of Oxyma 80 μL of DIC
Yield	89%
Coupling of His3 (3 eq)	282 mg of Fmoc-His(Trt)-OH 65 mg of Oxyma 70 μL of DIC
Coupling of Lys(4DMN) (3 eq)	270 mg of Fmoc-Lys(4DMN)-OH 65 mg of Oxyma 70 μL of DIC
Coupling of His1 (3 eq)	282 mg of Fmoc-His(Trt)-OH 65 mg of Oxyma 70 μL of DIC
Yield on the resin	89%
Acetylation	430 μL of acetic anhydride 790 μL of DIPEA
Amount of peptide (mass yield)	14 mg (8%)
Chromatographic purity	94%

Yellow solid. **HPLC-MS:** t_R = 9.58 min; ***m/z*** 813.3 ($[C_{40}H_{52}N_{12}O_7 + H]^+$). **^{1}H NMR** ($D_2O$, pH = 7.4, 400 MHz): δ 1.12-1.24 (m, 2H, Hγ-Lys2), 1.24-1.38 (m, 2H, Hγ-Lys4), 1.46-1.55

(m, 2H, Hδ-Lys2), 1.56-1.78 (m, 6H, Hδ-Lys4 + Hβ-Lys2 + Hβ-Lys4), 1.90 (s, 3H, Me-Ac), 2.63-2.79 (m, 2H, Hβ-His1), 2.89-3.03 (m, 2H, Hβ-His3), 2.93 (t, 2H, *J* = 7.7, Hε-Lys4), 2.99 (s, 6H, N$\underline{Me_2}$), 3.76 (t, 2H, *J* = 8, Hε-Lys2), 4.06 (dd, 1H, *J* = 5.2, *J* = 9.3, Hα-Lys4), 4.22 (dd, 1H, *J* = 5.8, *J* = 8.2, Hα-Lys2), 4.40 (dd, 1H, *J* = 5.8, *J* = 8.5, Hα-His1), 4.50 (t, 1H, *J* = 7.4, Hα-His3), 6.66 (d, 1H, *J* = 8.6, H_3-Lys($\underline{4DMN}$)), 6.75 (s, 1H, H_5-His1), 6.87 (d, 1H, *J* = 1.1, H_5-His3), 7.29 (dd, 1H, *J* = 7.5, *J* = 8.4, H_6-Lys($\underline{4DMN}$)), 7.63 (d, 1H, *J* = 1.2, H_2-His1), 7.66 (d, 1H, *J* = 1.2, H_2-His3), 7.70 (d, 1H, *J* = 8.5, H_2-Lys($\underline{4DMN}$)), 7.93 (dd, 1H, *J* = 1.0, *J* = 7.3, H_7-Lys($\underline{4DMN}$)), 8.02 (dd, 1H, *J* = 1.0, *J* = 8.7, H_5-Lys($\underline{4DMN}$)). **^{13}C NMR** (D_2O, pH = 7.4, 100.6 MHz): δ 24.48 (Me-Ac), 24.79 (Cγ-Lys4), 25.15 (Cγ-Lys2), 29.04 (Cδ-Lys4), 29.61 (Cδ-Lys2), 31.29 (Cβ-His3), 31.56 (Cβ-His1), 32.95 (Cβ-Lys4), 33.31 (Cβ-Lys2), 41.98 (Cε-Lys4), 42.74 (Cε-Lys2), 46.90 (N$\underline{Me_2}$), 55.89 (Cα-Lys4), 56.36 (Cα-Lys2), 56.64 (Cα-His3), 56.93 (Cα-His1), 113.4 (C_1-Lys($\underline{4DMN}$)), 115.0 (C_3-Lys($\underline{4DMN}$)), 119.6 (C_5-His1 + C_5-His3), 123.2 (C_8-Lys($\underline{4DMN}$)), 125.7 (C_{4a}-Lys($\underline{4DMN}$)), 127.0 (C_6-Lys($\underline{4DMN}$)), 131.9 (C_{8a}-Lys($\underline{4DMN}$)), 133.9 (C_7-Lys($\underline{4DMN}$)), 135.2 (C_5-Lys($\underline{4DMN}$)), 135.5 (C_4-His1), 135.6 (C_4-His3), 135.8 (C_2-Lys($\underline{4DMN}$)), 138.6 (C_2-His1), 138.8 (C_2-His3), 159.7 (C_4-Lys($\underline{4DMN}$)), 167.2 ($C_{1'}$-Lys($\underline{4DMN}$)), 168.1 ($C_{8'}$-Lys($\underline{4DMN}$)), 175.4 (CO-His3), 176.1 (CO-His1), 176.3 (CO-Lys2), 176.9 (CO-Ac), 178.9 (CO-Lys4).

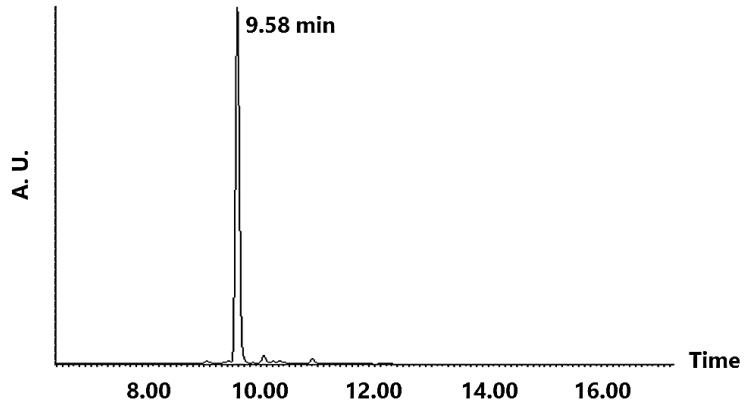

Figure 2.54: Chromatogram of Ac-His-Lys(4DMN)-His-Lys-NH_2.

Ac-His-Lys(Coum)-His-OH

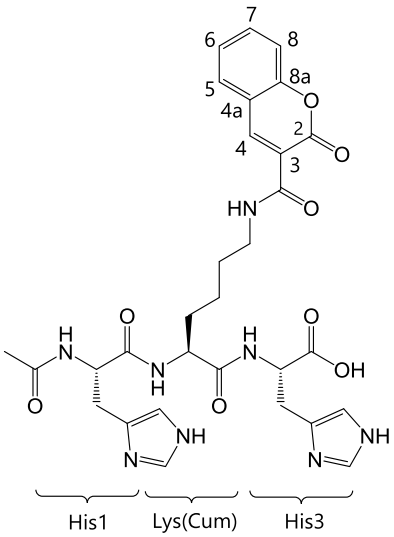

Anchoring of His3 (1 × 1.5 equiv)	248 mg of 2-CTC resin 369 mg of Fmoc-His(trt)-OH 460 + 230 μL of DIPEA
Yield	49%
Coupling of Lys(Coum) (3 equiv)	319 mg of Fmoc-Lys(Coum)-OH 84 mg of Oxyma 91 μL of DIC
Coupling of His1 (3 equiv)	365 mg of Fmoc-His(trt)-OH 84 mg of Oxyma 91 μL of DIC
Acetylation	550 μL of acetic anhydride 1.03 mL of DIPEA
Treatment with piperidine/DMF 1:4	5 × 10 min × 3 mL
Yield on the resin	quantitative
Amount of peptide (mass yield)	168 mg (95%)
Chromatographic purity	95%

White solid. **HPLC-MS:** t_R = 8.55 min; ***m/z*** 635.2 ($[C_{30}H_{34}N_8O_8 + H]^+$). **^{1}H NMR** ($D_2O$, pH = 7.4, 400 MHz): δ 1.29-1.44 (m, 2H, Hγ-Lys2), 1.57-1.67 (m, 2H, Hδ-Lys2), 1.67-1.88 (m, 2H, Hβ-Lys2), 1.91 (s, 3H, Me-Ac), 2.83-3.18 (m, 4H, Hβ-His1 + Hβ-His3), 3.37-3.49 (m, 2H, Hε-Lys2), 4.31 (dd, 1H, *J* = 9.5, *J* = 4.5, Hα-Lys2), 4.41 (dd, 1H, *J* = 8.0, *J* = 5.1, Hα-His3), 4.50 (dd, 1H, *J* = 8.6, *J* = 5.5, Hα-His1), 6.86 (s, 1H, H_5-His1), 7.00 (s, 1H, H_5-His3), 7.39-7.48 (m, 2H, H_6 + H_8-Lys(Coum)), 7.57 (d, 1H, *J* = 1.2, H_2-His1), 7.74-7.79 (m, 2H, H_5 + H_7-Lys(Coum)), 8.00 (d, 1H, *J* = 1.2, H_2-His3), 8.73 (s, 1H, H_4-Lys(Coum)). **^{13}C**

NMR (D_2O, pH = 7.4, 100.6 MHz): δ 24.42 (Me-Ac), 25.07 (Cγ-Lys2), 30.66 (Cδ-Lys2), 31.12 (Cβ-His3), 31.54 (Cβ-His1), 33.21 (Cβ-Lys2), 42.20 (Cε-Lys2), 56.35 (Cα-Lys2), 56.70 (Cα-His1), 57.44 (Cα-His3), 119.1 (C_3 + C_8-Lys(Coum)), 119.7 (C_5-His1), 120.3 (C_5-His3), 121.0 (C_{4a}-Lys(Coum)), 128.5 (C_6-Lys(Coum)), 133.0 (C_5-Lys(Coum)), 134.1 (C_4-His3), 134.9 (C_4-His1), 137.4 (C_2-His3), 137.7 (C_7-Lys(Coum)), 138.4 (C_2-His1), 151.9 (C_4-Lys(Coum)), 156.7 (C_{8a}-Lys(Coum)), 165.1 (C_2-Lys(Coum)), 166.7 (CONH-Lys(Coum)), 175.6 (CO-Lys2), 175.8 (CO-His1), 176.8 (CO-Ac), 179.6 (CO-His3).

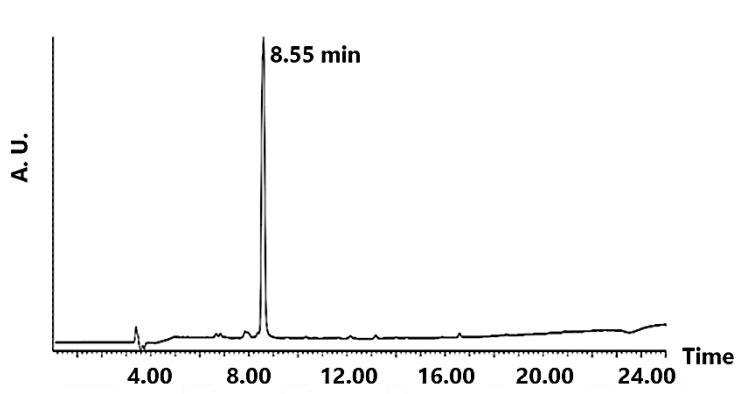

Figure 2.55: Chromatogram of Ac-His-Lys(Coum)-His-OH.

Ac-His-Lys(4DMN)-His-OH

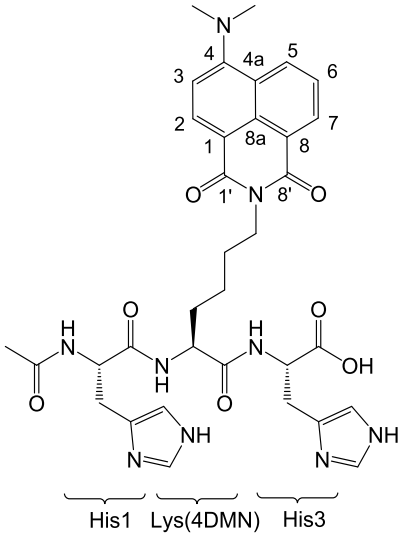

Anchoring of His3 (1 × 1.5 eq)	255 mg of 2-CTC resin 380 mg of Fmoc-His(Trt)-OH 480 + 230 μL of DIPEA
Yield	64 %
Coupling of Lys(4DMN) (3 eq)	460 mg of Fmoc-Lys(4DMN)-OH 110 mg of Oxyma 120 μL of DIC
Coupling of His1 (3 eq)	482 mg of Fmoc-His(Trt)-OH 110 mg of Oxyma 120 μL of DIC
Yield on the resin	83%
Acetylation	730 μL of acetic anhydride 1.35 mL of DIPEA
Amount of peptide (mass yield)	100 mg (42%)
Chromatographic purity	95%

Yellow solid. **HPLC-MS:** t_R = 10.6 min; ***m/z*** 686.1 ($[C_{34}H_{39}N_9O_7 + H]^+$). **^{1}H NMR** ($D_2O$, pH = 7.4, 400 MHz): δ 1.13-1.32 (m, 2H, Hγ-Lys2), 1.37-1.54 (m, 2H, Hδ-Lys2), 1.60-1.82 (m, 2H, Hβ-Lys2), 1.88 (s, 3H, Me-Ac), 2.64-2.84 (m, 2H, Hβ-His1), 2.91 (s, 6H, N<u>Me$_2$</u>), 2.95-3.16 (m, 2H, Hβ-His3), 3.64 (t, 2H, *J* = 6.8, Hε-Lys2), 4.26 (dd, 1H, *J* = 4.8, *J* = 9.5, Hα-Lys2), 4.41 (dd, 1H, *J* = 5.0, *J* = 7.9, Hα-His3), 4.46 (dd, 1H, *J* = 5.5, *J* = 8.6, Hα-His1), 6.51 (d, 1H, *J* = 8.6, H_3-Lys(<u>4DMN</u>)), 6.79 (s, 1H, H_5-His3), 6.99 (s, 1H, H_5-His1), 7.16 (t_{app}, 1H, J_{app} = 7.9, H_6-Lys(<u>4DMN</u>)), 7.53 (d, 1H, *J* = 8.4, H_2-Lys(<u>4DMN</u>)), 7.75-7.80 (m, 2H, H_7-Lys(<u>4DMN</u>) + H_2-His3), 7.86 (d, 1H, *J* = 8.3, H_5-Lys(<u>4DMN</u>)), 8.04 (d, 1H, *J* = 1.0, H_2-His1). **^{13}C NMR** (D_2O, pH = 7.4, 100.6 MHz): δ 24.48 (Me-Ac), 25.33 (Cγ-Lys2), 29.52 (Cδ-Lys2), 31.08 (Cβ-His3), 31.25 (Cβ-His1), 33.38 (Cβ-Lys2), 42.71 (Cε-Lys2), 46.85 (N<u>Me$_2$</u>), 56.32 (Cα-Lys2), 56.47 (Cα-His1), 57.38 (Cα-His3), 113.2 (C_1-Lys(<u>4DMN</u>)), 114.8 (C_3-Lys(<u>4DMN</u>)), 119.9 (C_5-His3), 120.3 (C_5-His1), 123.0 (C_8-Lys(<u>4DMN</u>)), 125.4 (C_{4a}-Lys(<u>4DMN</u>)), 126.8 (C_6-Lys(<u>4DMN</u>)), 131.7 (C_{8a}-Lys(<u>4DMN</u>)), 133.7 (C_7-Lys(<u>4DMN</u>)), 134.0 (C_4-His3), 134.6 (C_4-His1), 135.0 (C_2-Lys(<u>4DMN</u>)), 135.6 (C_5-Lys(<u>4DMN</u>)), 137.2 (C_2-His1), 138.2 (C_2-His3), 159.4 (C_4-Lys(<u>4DMN</u>)), 166.9 ($C_{1'}$-Lys(<u>4DMN</u>)), 167.8 ($C_{8'}$-Lys(<u>4DMN</u>)), 175.6 (CO-Lys2), 175.6 (CO-His1), 176.6 (CO-Ac), 179.5 (CO-His3).

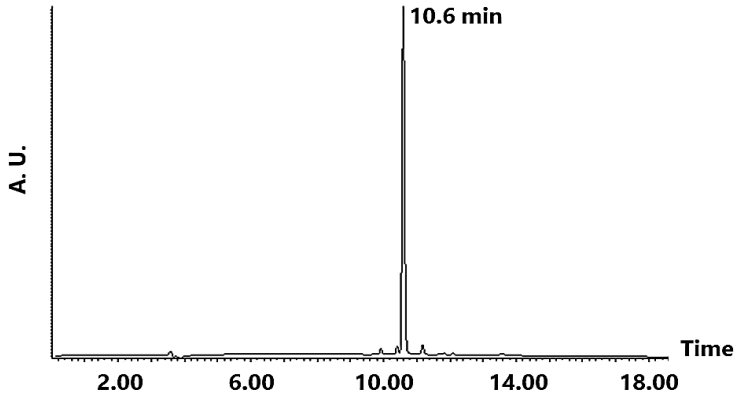

Figure 2.56: Chromatogram of Ac-His-Lys(4DMN)-His-OH.

Ac-His-Lys(4DMN)-His-NH_2

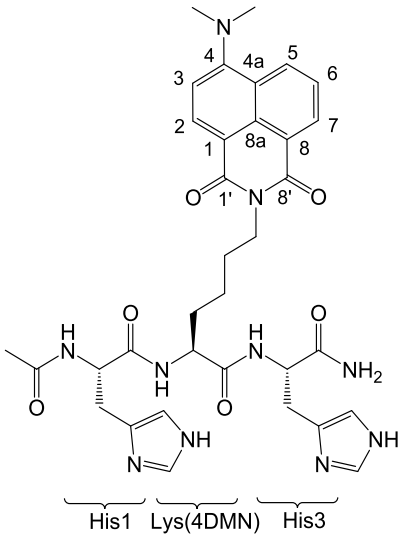

Anchoring of His3 (2 × 3 eq)	220 mg of Rink Amide resin 282 mg of Fmoc-His(trt)-OH 65 mg Oxyma 70 μL DIC
Yield	86%
Coupling of Lys(4DMN) (2 × 3 eq)	232 mg of Fmoc-Lys(4DMN)-OH 56 mg of Oxyma 61 μL of DIC
Coupling of His1 (2 × 3 eq)	244 mg of Fmoc-His(trt)-OH 56 mg of Oxyma

	61 μL of DIC
Yield on the resin	quantitative
Acetylation	370 μL of acetic anhydride 690 μL of DIPEA
Amount of peptide (mass yield)	20 mg (16%)
Chromatographic purity	97%

Yellow solid. **HPLC-MS:** t_R = 10.2 min; ***m/z*** 685.2 ($[C_{34}H_{40}N_{10}O_6 + H]^+$). **^{1}H NMR** ($D_2O$, pH = 4.5, 400 MHz): δ 1.22-1.38 (m, 2H, Hγ-Lys2), 1.50-1.63 (m, 2H, Hδ-Lys2), 1.67-1.83 (m, 2H, Hβ-Lys2), 1.88 (s, 3H, Me-Ac), 2.79-3.01 (m, 2H, Hβ-His1), 3.04 (s, 6H, N$\underline{Me_2}$), 3.08-3.26 (m, 2H, Hβ-His3), 3.79 (t, 2H, *J* = 6.5, Hε-Lys2), 4.23-4.29 (m, 1H, Hα-Lys2), 4.51-4.56 (m, 1H, Hα-His1), 4.60-4.65 (m, 1H, Hα-His3), 6.74 (d, 1H, *J* = 8.5, H_3-Lys(4DMN)), 7.12 (s, 1H, H_5-His1), 7.25 (s, 1H, H_5-His3), 7.36 (t_{app}, 1H, J_{app} = 7.9, H_6-Lys(4DMN)), 7.78 (d, 1H, *J* = 8.4, H_2-Lys(4DMN)), 8.00 (d, 1H, *J* = 7.3, H_7-Lys(4DMN)), 8.09 (d, 1H, *J* = 8.4, H_5-Lys(4DMN)), 8.52 (s, 1H, H_2-His1), 8.56 (s, 1H, H_2-His3). **^{13}C NMR** (D_2O, pH = 4.5, 100.6 MHz): δ 24.43 (Me-Ac), 25.31 (Cδ-Lys2), 29.26-29.33 (Cβ-His1 + Cβ-His3), 29.53 (Cγ-Lys2), 33.35 (Cβ-Lys2), 42.76 (Cε-Lys2), 46.95 (N$\underline{Me_2}$), 55.15 (Cα-His3), 55.40 (Cα-His1), 56.49 (Cα-Lys2), 113.5 (C_1-Lys(4DMN)), 115.1 (C_3-Lys(4DMN)), 120.0 (C_5-His1 + C_5-His3), 123.3 (C_8-Lys(4DMN)), 125.7 (C_{4a}-Lys(4DMN)), 127.2 (C_6-Lys(4DMN)), 131.5-131.6 (C_4-His1 + C_4-His3), 132.0 (C_{8a}-Lys(4DMN)), 134.0 (C_7-Lys(4DMN)), 135.3 (C_5-Lys(4DMN)), 135.9 (C_2-Lys(4DMN)), 136.4-136.5 (C_2-His1 + C_2-His3), 159.8 (C_4-Lys(4DMN)), 167.4 ($C_{1'}$-Lys(4DMN)), 168.2 ($C_{8'}$-Lys(4DMN)), 174.8 (CO-His1), 176.5 (CO-Lys2), 176.7 (CO-His3), 176.8 (CO-Ac).

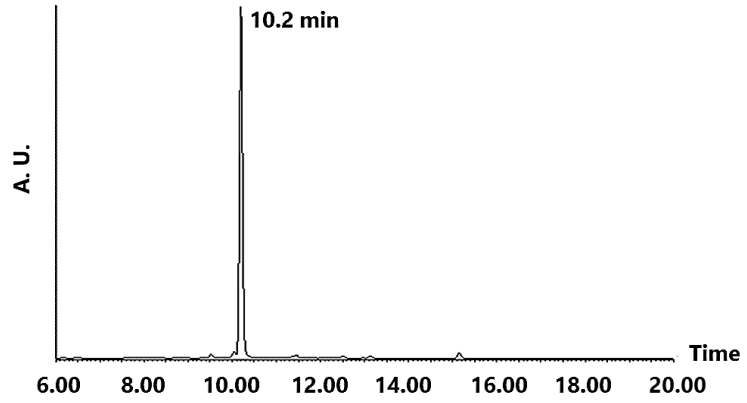

Figure 2.57: Chromatogram of Ac-His-Lys(4DMN)-His-NH_2.

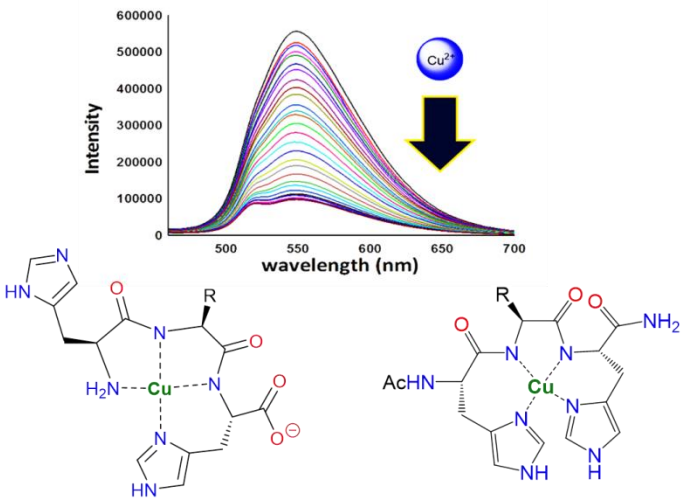

3. Chelation and detection of Cu(II)

3. Chelation and detection of Cu(II)

3.1 Introduction

3.1.1 Peptides containing the His-Xaa-His sequence as Cu(II)-chelators/probes

The potential copper-chelating properties of the peptides described in **Chapter 2** were then examined and compared with those of commercial peptides, obtained in a custom-made manner. Aβ(1-40/42) have been reported to be more neurotoxic in the presence of Cu(II) ions, as the result of their involvement in oligomer stabilisation and ROS production.[38,39,62,66] Thus, the design of compounds presenting the ability to remove copper ions bound to Aβ represents a strategy that should be explored.

The metal-induced toxicity is thought to be closely related to the flexibility of the Aβ copper-binding domain, the lability of the Cu(II) ions and the ill-defined three-dimensional structure of the Cu(II)-Aβ complex (see **Chapter 1**).[18,71] The facile copper exchange has been proposed to favour the metal-mediated aggregation of the peptide; copper(II) ions can indeed bring two peptide molecules into close proximity, then dissociate and so on.[18,27,42] The coordination by readily exchangeable ligands is believed to easily re-accommodate both Cu(I)/(II) ions upon reduction/oxidation, concomitantly producing reactive oxygen species (**ROS**).[86,89,93]

Therefore, chelating agents are aimed at lessening copper-induced Aβ toxicity by blocking the redox activity of this metal ion. The Cu(II)-binding affinity of such agents should be higher than that of Aβ peptide (to allow the extraction of copper) but yet lower than those of essential metalloproteins (not to disturb the cellular metabolism). In other words, they should act as metal-protein attenuating compounds, (**MPACs**) and transport metal ions back into neurons, rather than as classical chelators, which eliminate metals from the organism, which would then lead to a severe metal depletion.[121,122]

Moreover, the detection and quantification of copper in AD brains is attracting increasing interest. Indeed, the spatio-temporal monitoring of copper ions in neuronal tissue would provide invaluable information about for instance its interaction with Aβ peptide (*e.g.* where and at what rates this interaction takes place in living cells) or its distribution in brain tissue. Fluorescence spectroscopy has emerged as a very popular technique for the detection and imaging of metal ions, including copper, as it is very

sensitive (with detection limits in the range of parts per billion/trillion), inexpensive, methodologically straightforward, and it presents high spatial resolution and fast response (even in the range of picoseconds).[188,189]

As discussed in **Chapter 1**, peptides presenting the His-Xaa-His motif are efficient Cu(II)-chelating agents and represent potential candidates for the attenuation of the copper-associated toxicity of Aβ peptide *in vitro*. Besides, peptides either containing naturally fluorescent amino acids or wisely labelled with fluorophores may be exploited for the detection of Cu(II) ions through their paramagnetic quenching effect or by fluorescence resonance energy transfer (FRET).

In this chapter, the Cu(II)-coordination mode and binding affinity of several His-Xaa-His tripeptides, as well as their prospective capacity to prevent Cu(II)-induced Aβ aggregation or/and to inhibit ROS production, are described. Hence, different techniques, including UV-vis, fluorescence and NMR spectroscopies, were used. The peptides were classified into two series, namely the *N*-terminal free and *N*-terminal protected peptides. The protection of the *N*-terminal amino function with an acetyl group was expected to result in distinct coordination modes, copper-binding affinities and redox activities. The free/protected peptides were therefore analysed separately. Finally, the Fluo-His-Lys(Coum)-His-NH_2 peptide, containing the coumarin-fluorescein FRET pair, was evaluated as a ratiometric probe candidate for the detection and visualisation of Cu(II) ions by fluorescence spectroscopy.

3.1.2 N-terminal free peptides

Three different *N*-terminal unprotected tripeptides were chosen for the evaluation of their Cu(II)-chelating properties: the custom-made H-His-Ala-His-OH (**HAH**) and H-His-Trp-His-OH (**HWH**), containing natural amino acids, and H-His-Lys(Coum)-OH (**HK^{c}H**), including a non-natural coumarin-labelled lysine residue (whose synthesis was described in **Chapter 2**; see **Figure 3.1**). Both HWH and HK^{c}H present fluorescent probes (namely the Trp indole and the coumarin rings, respectively), whose emissive properties can be exploited for the monitoring of possible Cu(II)-exchange processes between Aβ and the peptides. The non-emissive HAH peptide was chosen as a reference.

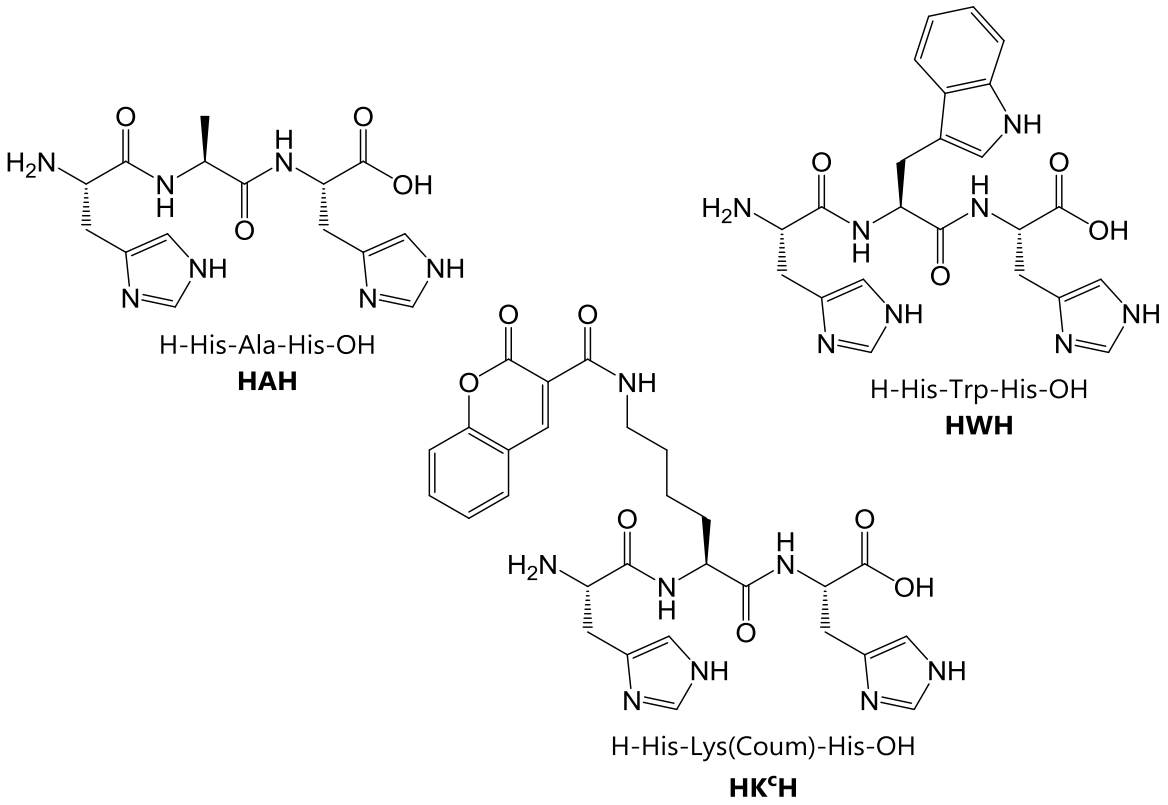

Figure 3.1: *N*-terminal free tripeptides used.

The copper binding by these tripeptides can take place through the *N*-terminal amino group, the imidazole ring(s), the terminal carboxylate and the amide functions. Amide nitrogen deprotonation is energetically costly (pK_a around 15) and is only achieved when the resulting complex is highly stable.[135,190]

Peptides presenting both a free *N*-terminal amino group and a His residue in position 3 can bind Cu(II) ions *via* the amino-terminal copper and nickel (**ATCUN**) binding motif.[191] This motif is also known as the albumin-like coordination mode since human albumin binds copper in this fashion through its H-Asp-Ala-His-Lys (DAHK) sequence.[192,193] In ATCUN coordination, copper binding occurs via the *N*-terminal amino group, two amide functions and the imidazole ring of His3, producing a highly stable and rigid square-planar conformation. Accordingly, copper blocking by formation of a highly stable ATCUN complex represents a potential approach to decrease the toxicity associated with copper in AD.

3.1.3 N-terminal protected peptides

The study of copper coordination by *N*-terminal protected peptides was carried out for Ac-His-Lys(Coum)-His-OH (**AcHK^{c}H**), Ac-His-Lys(4DMN)-His-OH (**AcHK^{d}H**) and *C*-terminal protected Ac-His-Lys(4DMN)-His-NH_2 (**AcHK^{d}H-NH_2**), which are depicted in **Figure 3.2**. All three peptides were synthesised as described in **Chapter 2**. The protection of the *N*-terminal amino function with an acetyl group impedes its participation in the binding of Cu(II) ions. Therefore, a different coordination mode was expected. The imidazole ring(s), one or two amide functions (depending on the stability of the Cu(II)-complex formed) and carbonyl/carboxylate oxygen atoms represent the putative donors for Cu(II) chelation by these peptides.

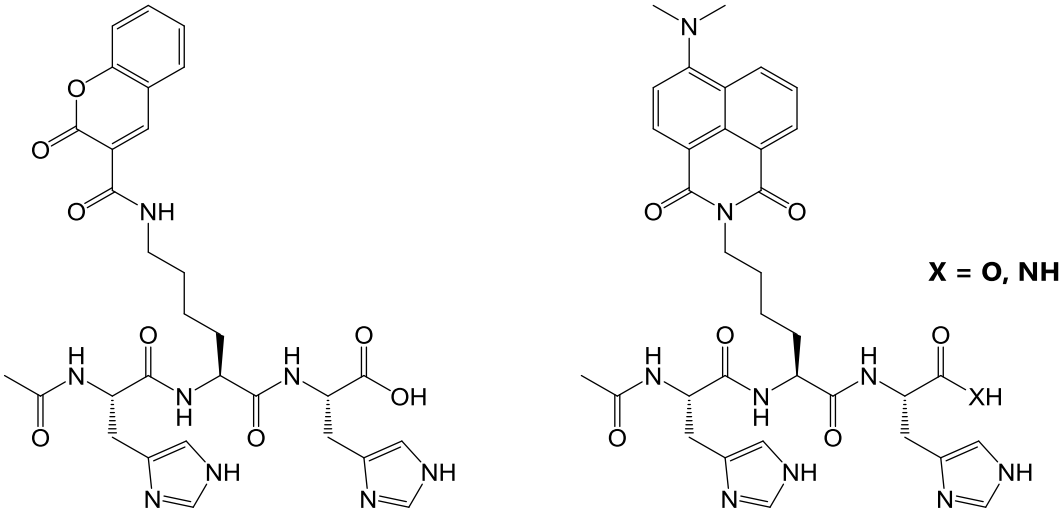

Ac-His-Lys(Coum)-His-OH
AcHK^{c}H

Ac-His-Lys(4DMN)-His-XH
AcHK^{d}H (X = O)
AcHK^{d}H-NH_2 (X = NH)

Figure 3.2: *N*-terminal protected peptides studied.

The different coordination modes may obviously affect the consequent copper-binding affinity of the peptides, as well as the respective redox activity of the resulting Cu(II)-peptide complexes. For instance, a more flexible wrapping of the metal ion may result in a higher reduction potential, owing to an easier accommodation of the Cu(I/II) ions upon electron transfer, hence resulting in higher ROS production (see section **3.1.1**).

Ac-His-Lys(Coum)-His-Lys-NH_2 (**AcHK^{c}HK**) and Ac-His-Lys(4DMN)-His-Lys-NH_2 (**AcHK^{d}HK**) were designed with the objective to couple them to gold nanoparticles, as explained in **Chapter 5** (**Figure 3.3**). These tetrapeptides may be connected to gold

nanocarriers through the free side chain of the additional lysine residue (Lys4). The His-Lys(Fp)-His motif (where Fp = fluorescent probe) is the binding unit of these peptides.

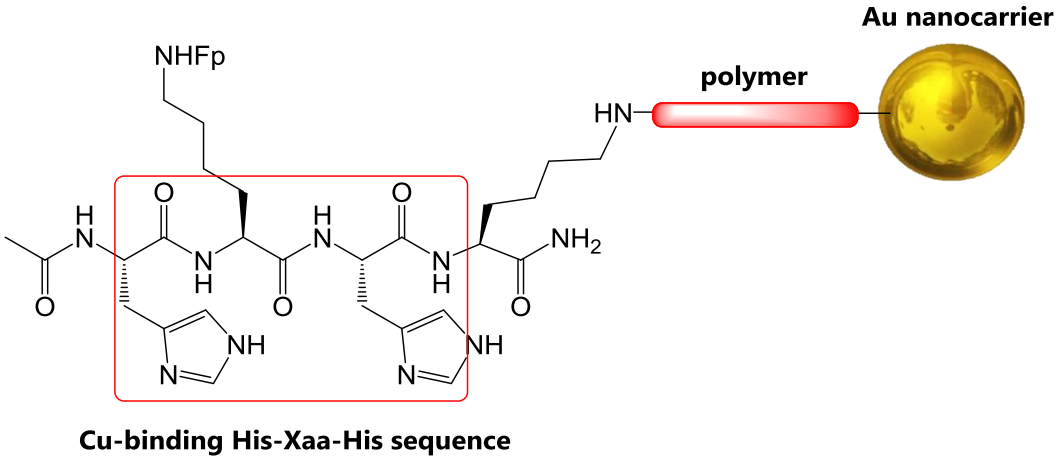

Figure 3.3: Ac-His-Lys(Fp)-His-Lys-NH_2 peptides linked to gold nanoparticles.

3.1.4 FRET-based Cu(II)-sensing with Fluo-His-Lys(Coum)-His-NH_2

Copper is the third most abundant transition metal in humans, after zinc (second) and iron (first), and it is crucial for a proper functioning of the organism.[194,195] This is evidenced by the severity of the disorders where copper homeostasis is disturbed, like for instance, Wilson (Cu accumulation) and Menkes (Cu deficiency) diseases, and neurodegenerative pathologies such as Alzheimer's or Parkinson's disease where Cu-induced ROS production is implicated. In addition, the way(s) in which copper is trafficked and localised in cells is still poorly understood. It is not surprising then that the design of copper-selective (fluorescent) probes has received considerable attention.

Turn-off probes exhibit intensity decrease upon interaction with Cu(II) ions (due to paramagnetic quenching). In contrast, turn-on probes display an enhanced emission upon Cu(II)-binding, which is usually triggered by a chemical reaction or a conformational change.[189,194,196] Such probes are inappropriate for *in vivo* sensing since their output (*i.e.* their fluorescent intensity) is dependent on the concentration of the probe.

Fluorescent ratiometric probes rely on the ratio of the emission intensities at two different emission wavelengths.[188] These probes contain either one dye, which

undergoes a shift in its emission wavelength, or two different dyes of varying intensities. As a result, they present a higher sensitivity and a built-in correction for environmental effects (*e.g.* artefacts caused by variations on the concentration of the probe).[188,197,198] Unfortunately, ratiometric probes for the visualisation of Cu(I/II) in living cells are scarce.[195,199-201]

Most ratiometric probes are based on the Förster (or fluorescence) resonance energy transfer (**FRET**) phenomenon.[202-206] FRET is a non-radiative energy-transfer process from an excited donor towards an acceptor, which takes place through long-range dipole-dipole and/or short-range multipolar interactions.[202,207] The energy-transfer process depends on several parameters, such as the extent of the emission(donor)-excitation(acceptor) spectral overlap, the relative orientation of the transition dipole moments and the donor-acceptor distance (usually 10-100 Å).[142,189,202,207,208] Hence, if FRET takes place, the emission of the acceptor is observed upon excitation of the donor.

In this chapter, the potential application as a FRET-based ratiometric Cu(II)-probe of Fluo-His-Lys(Coum)-His-NH_2 (**FluoHK^{c}H**), which encompasses a coumarin and a fluorescein dye, is reported (**Figure 3.4**). Although fluorescein and functionalised coumarins have been extensively used in biology and biomedicine, fluorescein and the parent, unfunctionalised coumarin have not been reported as a FRET pair before.[202] Since the emission spectrum of coumarin is close to the excitation spectrum of fluorescein, the emission at the λ_{em} of fluorescein was supposed to occur upon excitation of the fluorescent peptide at the λ_{exc} of coumarin.

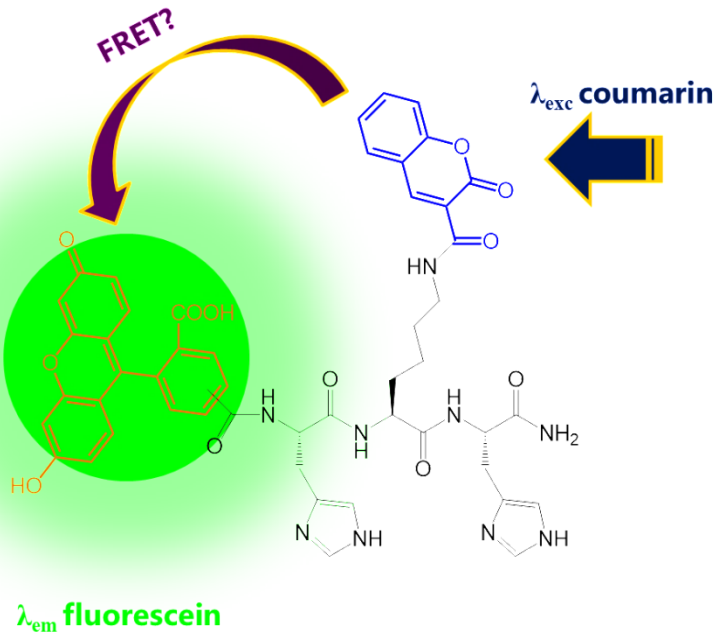

Figure 3.4: Potential FRET-based peptidic Cu(II)-probe Fluo-His-Lys(Coum)-His-NH_2 (**FluoHK^{c}H**).

For this peptide to become a ratiometric probe candidate for Cu(II) detection/imaging, the emission of the dyes should be differently quenched by Cu(II), or the FRET process should be altered. Thus, the effect of the addition of Cu(II) ions on the emission of coumarin and fluorescein in the peptide was assessed.

3.2 Objectives

- Evaluation of the copper-chelating properties (stoichiometry, coordination mode and binding affinity) of several *N*-terminal protected and unprotected His-Xaa-His peptides.
- Assessment of the prevention of copper-induced aggregation of Aβ and of the production of reactive oxygen species by the copper-chelating His-Xaa-His peptides.
- Evaluation of Fluo-His-Lys(Coum)-His-NH_2 as a FRET-based Cu(II)-ratiometric probe.

3.3 Results and discussion

3.3.1 Chelating properties of the N-terminal free peptides

3.3.1.1 Determination of the Cu(II)-binding mode of N-terminal unprotected peptides

The stoichiometry of the Cu(II) complexes of the unprotected peptides was first analysed. The peptides were incubated with 2 equivalents of $CuCl_2$ in Milli-Q water and the mixtures were analysed by electrospray ionisation (ESI) mass spectrometry. The formation of 1:1 Cu(II)-peptide species was evidenced by the presence of peaks with m/z values corresponding to $[Cu(peptide) + H]^+$ species showing the isotopic distribution of copper. In spite of the excess of Cu(II) ions, no 2:1 Cu(II)-peptide species were detected, nor were 1:2 metal complexes.

To further confirm the 1:1 copper-peptide stoichiometry, the changes in turbidity upon addition of copper to the tripeptide solutions were registered. This experiment is based on the precipitation of the peptide complex with increasing concentrations of $CuCl_2$, which leads to an increased baseline absorbance (the absorbance was observed at 405 nm).[209] No significant changes were observed until a Cu-peptide ratio superior to 1:1 (**Figure 3.5**, top).[210] Analogously, the formation of the Cu(II) complex was monitored through the absorption of the metal ion d-d transition bands: $\lambda_{d\text{-}d}$ (CuHAH) = 520 nm (ε = 113 $M^{-1}cm^{-1}$), $\lambda_{d\text{-}d}$ (CuHWH) = 515 nm (ε = 105 $M^{-1}cm^{-1}$) and $\lambda_{d\text{-}d}$ (CuHK^{c}H) = 515 nm (ε = 94 $M^{-1}cm^{-1}$) (**Figure 3.5**, bottom). An inflection point in the absorbance was observed at 1:1 Cu/peptide ratio.

Such relatively low wavelength values for d-d transitions are indicative of strong-field ligands, and deprotonated amide nitrogen atoms are the strongest field ligands that these peptides may provide.[190] The empirical equation described by Sigel and Martin for square-planar Cu(II) complexes can be used to determine the ligands forming the coordination sphere (**Equation 3.1**).[211] Hence, the values obtained suggest that there are four equatorial nitrogen atom donors.[212] The predicted $\lambda^{d\text{-}d}$ value for a [NH_2, N^-, N^-, N_{Im}] ATCUN coordination motif is about 530 nm; ATCUN Cu(II) complexes have been described with $\lambda^{d\text{-}d}$ values ranging from 510 to 530 nm.[213,214] The spectroscopic properties of the three Cu(II) complexes obtained with HAH, HWH and HK^{c}H fall within this range and, hence, suggest an ATCUN coordination environment (see section **3.1.2**).

$$\lambda^{max} = 10^3/[0.294(n^o \text{ carbonyls}) + 0.346(n^o \text{ carboxylates}) + 0.434(n^o \text{ imidazoles}) + 0.460(n^o \text{ amino groups}) + 0.494\ (n^o \text{ deprotonated amides})] \quad (3.1)$$

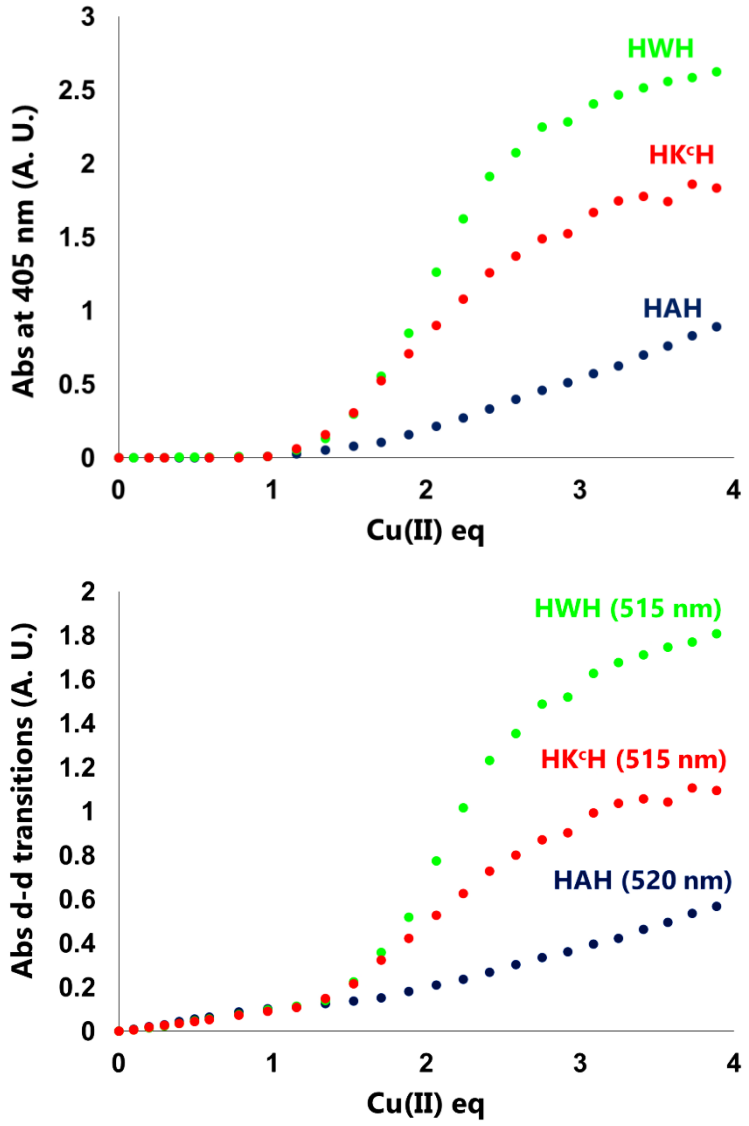

Figure 3.5: Changes of absorbance (at 405 nm, **top**; and d-d transition, **bottom**) of the *N*-terminal free tripeptides upon addition of increasing amounts of $CuCl_2$ (in 100 mM HEPES, pH 7.4).

Next, the interaction of the tripeptides with copper was studied by circular dichroism (CD). CD is based on the differential absorption of left-handed and right-handed circularly polarised light by chiral molecules. As a result, CD spectra are very sensitive to changes in the secondary structure of molecules like peptides.

The CD spectra of the peptides at increasing amounts of $CuCl_2$ were registered at pH 7.4 (**Figure 3.6**).[210] A broad band appeared at λ = 310, 321 and 338 nm upon addition of Cu(II) to HAH, HWH and HK^{c}H, respectively; these bands characterise an $N_{amide} \rightarrow$Cu(II) charge-transfer transition.[215] The shoulder bands detected at about 350

nm for HAH and HWH most likely arise from $N_{imidazole}$→Cu(II) charge-transfer transitions.[216,217] Intense negative bands at 265 (HAH and HWH) and 288 nm (HK^cH) were attributed to intraligand imidazole and N_{amine}→Cu(II) charge-transfer transitions.[218]

Two rising d-d bands, due to the Cotton effect, are observed, one negative at around 560 nm and another positive at about 485 nm for all the Cu-peptide complexes. The fact that the two d-d bands are considerably below 600 nm indicates that a 4N species involving deprotonated amide nitrogen atoms are present.[218] These results, together with those of the UV-Vis experiments, are typical for an albumin-like (ATCUN) coordination environment. It is also worth mentioning that no shifting of the bands was noticed for both 1:2 or 2:1 Cu/peptide ratios, suggesting that only the 1:1 complex is formed.

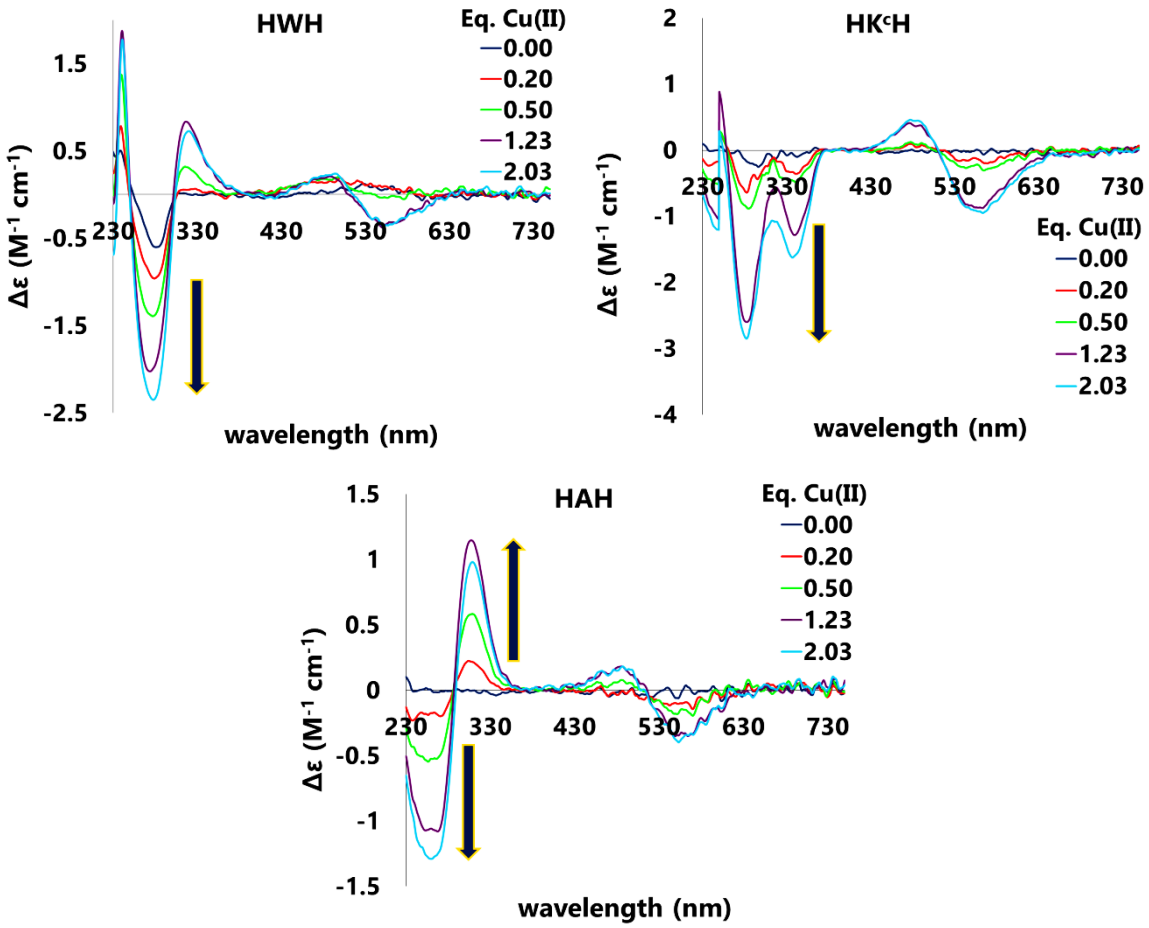

Figure 3.6: Circular dichroism spectra of the *N*-terminal free peptides at different Cu(II)-peptide ratios. 100 mM HEPES (pH 7.4).

Nuclear magnetic resonance (NMR) experiments were carried out to obtain further information about the coordination of the peptides, taking advantage of the paramagnetism of Cu(II). Addition of 0.01 equivalents of Cu(II) to the tripeptides gave rise to the broadening of the signals of the ^{1}H and ^{13}C nuclei located in the proximity of bound copper ions.[219] Similar results were obtained for all three peptides, as evidenced in **Figure 3.7**.[210] Purple dots symbolise highly affected NMR signals (thus close to the copper centre), dark blue dots illustrate a medium degree of broadening, and light-blue dots indicate a slight or no alteration of the signals (indicating that the corresponding atoms are far from the paramagnetic ion).

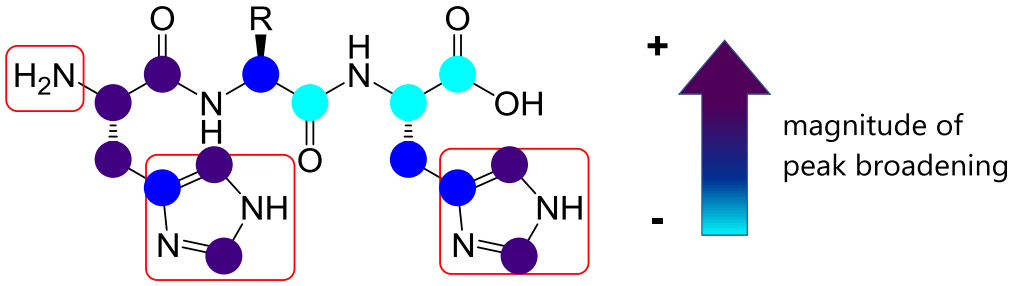

Figure 3.7: Schematic representation (using a range of color) of the magnitude of peak broadening in ^{1}H and ^{13}C NMR of *N*-terminal free tripeptides in the presence of 0.01 eq of $CuCl_2$ (D_2O solutions).

Unexpectedly, the results obtained disagreed with those achieved with UV-Vis and CD experiments. The NMR spectra suggest that coordination takes place through the *N*-terminal amino group, the first amide function and the two imidazole rings; an ATCUN coordination mode would involve the *N*-terminal amino group, both amide functions and only the imidazole ring of His3.

The strong broadening of the signals upon addition of only 1 mol% Cu(II) indicates a fast ligand exchange, superior to the NMR time scale. These data contradict earlier ones for histidine-containing peptides, for which at least 10 mol% copper was required to achieve a comparable signal broadening.[193,220]

Electron paramagnetic resonance (EPR) experiments were subsequently performed to elucidate the origin of the opposing results obtained by UV-Vis/CD and NMR spectroscopies. EPR is based on the interaction of unpaired electrons (namely from Cu(II) ions) with nearby (ligand) nuclei, and provides information on the coordination sphere of the metal ion.

EPR spectra of frozen solutions of the three Cu-peptide complexes were recorded at Cu/peptide ratios of 1:1.1 and 1:100. Representative spectra of the Cu-HAH species are shown in **Figure 3.8**.[210] At 1:1.1 ratio, axial symmetry was indicated by the order of the g tensors, namely $g_{\parallel} > g_{\perp} > g_e$ (**Figure 3.8**, left).[221] These values are indicative of a square-planar, square-pyramidal or axially elongated octahedral geometry. More specifically, the values $g_{\parallel}$ = 2.18, $g_{\perp}$ = 2.05 and $A_{\parallel}$ = 601 MHz (205 G) are indicative of a 4N square-planar albumin-like coordination sphere.[222]

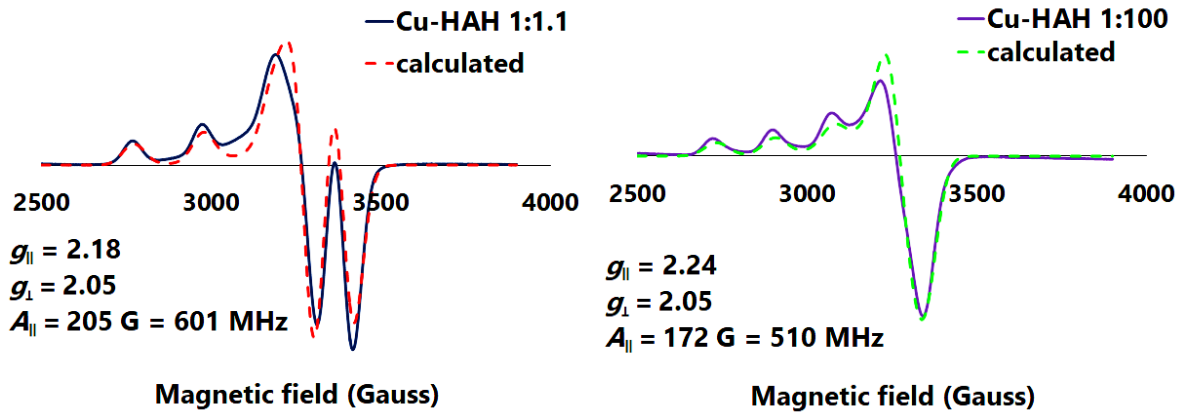

Figure 3.8: EPR spectra of 1:1.1 (**left**) and 1:100 (**right**) Cu(II)-HAH samples. 100 mM HEPES (pH 7.4), 77 K.

At a Cu/peptide ratio of 1:100 (that is, at the conditions used for the NMR experiments), the corresponding EPR spectra were totally different to those previously obtained (**Figure 3.8**, right). Indeed, the $g_{\parallel}$ value increased to 2.24, suggesting an increase of the electron-withdrawing character of the ligands , and the hyperfine parallel constant $A_{\parallel}$ decreased notably to 510 MHz (172 G).[223] The combination of these two features indicates that one or two nitrogen atoms have been replaced with oxygen atoms; the poor resolution of the superhyperfine structure does not allow to determine the exact number of O atoms. Furthermore, the colour change observed, from pink (1:1.1 ratio) to blue (1:100 molar ratio), corroborates the replacement of nitrogen donors by oxygen atoms.

As discussed previously, the NMR results suggested the coordination of the *N*-terminal amino group, the first amide function and the two imidazole rings of the peptides. The EPR results for the 1:100 Cu/peptide ratio characterise a Cu(II)-3N2O square-pyramidal coordination sphere, with an oxygen atom at the apical position; this oxygen may belong to a water molecule (O_w) or a carboxylate group (O_{COO^-}). Consequently, a [NH_2,

N^-, $N_{Im1/3}$, $O_{w/COO-}$, $O_{w/COO-}$] donor set was proposed when 1:100 Cu/peptide ratio was used. The coordinated amide most likely is from the central amino acid (*i.e.* Ala, Trp or Lys(Coum)), which is more acidic – because it is closer to the *N*-terminal amino group and can generate a 5-membered ring upon coordination. The imidazole ligand can belong either to a His residue of the chelating peptide or to a second peptide molecule. Since there is a marked excess of peptide (100-fold) with respect to copper, the imidazole ligand is probably from a second peptide molecule and can equally be from a His1 or His3 residues.

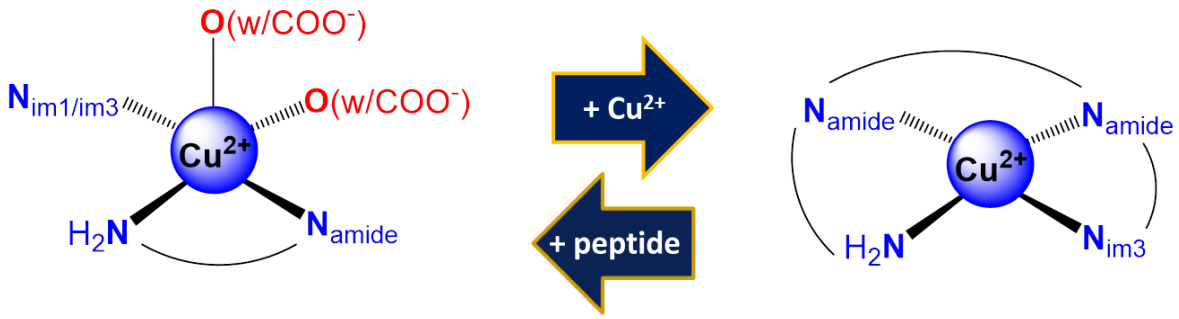

Figure 3.9: Proposed coordination modes and geometries for the Cu(II)-peptide species in the case of Cu(II)/peptide = 1:100 (**left**) and Cu(II)/peptide = 1:1.1 (**right**).

The highly stable ATCUN motif is therefore generated at equimolar or nearly equimolar Cu(II)-peptide ratios, whereas the intermolecular binding of a histidine residue from a second peptide molecule takes place in the presence of a high excess of peptide (**Figure 3.9**). Interestingly, such coordination-sphere variation with the Cu(II)/peptide ratio was not observed for Xaa-Xaa-His peptides like H-Gly-Trp-His-OH (**GWH**, **Figure 3.10**), for which the ATCUN motif was generated, even when using a Cu(II)-peptide ratio of 1:100.

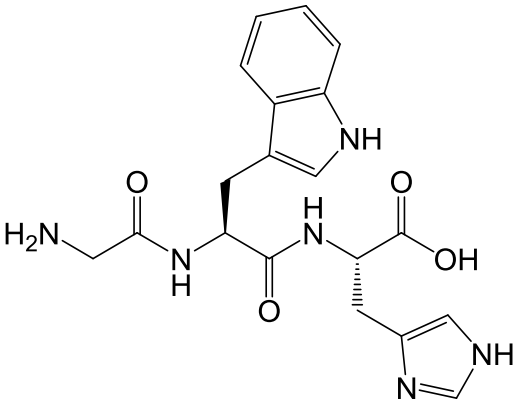

Figure 3.10: Representation of H-Gly-Trp-His-OH (**GWH**).

A schematic representation of a Cu(II) ATCUN complex generated from *N*-terminal free His-Xaa-His peptides is shown in **Figure 3.11**. Cu(II) binding occurs through the free amino group of His1, the amide nitrogen atoms of Xaa2 and His3, and the imidazole ring of His3, generating a square-planar geometry with 3 (5,5,6)-membered fused rings.[210] The coordination of the imidazole ring takes place through the δ nitrogen atom, since this binding mode allows the formation of a 6-membered ring and a more efficient σ donation to the metal centre.[133,135,192] Such a rigid conformation was expected to result in a high copper-binding affinity and low redox activity, as will be discussed below.

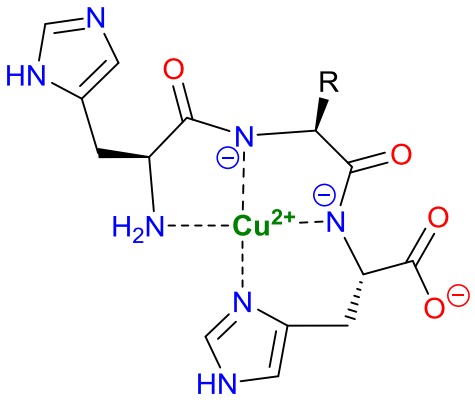

Figure 3.11: Albumin-like copper coordination sphere (ATCUN motif) of Cu(II) complexes from *N*-terminal free His-Xaa-His peptides.

3.3.1.2 Determination of Cu(II)-affinity constants for the unprotected peptides by fluorescence spectroscopy

ATCUN peptides and proteins present high copper affinities, with log *K* values in the range of 11.0-14.6, which are much higher than those of Aβ(1-40) and Aβ(1-42).[224] In fact, the *N*-terminal truncated Aβ(4-16) fragment binds Cu(II) through its *N*-terminal Phe-Arg-His domain with high affinity (log *K* = 13.5), in an ATCUN coordination mode that blocks the copper redox cycle, therefore inhibiting ROS production.[224-226] Aβ(4-16) contains a second copper binding site involving the His13 and His14 residues (using the numbering for Aβ(1-x)) with an affinity of about 7 orders of magnitude lower.[224,225] The Aβ(4-42) fragment, which exhibits the same Cu(II)-binding domains, has been found in brain tissue and is believed to act as a synaptic copper scavenger, especially under oxidising conditions.[224,225] Hence, the ATCUN tripeptides herein described may be capable of extracting Aβ-bound Cu(II) ions.

Measurements of the copper-induced fluorescence quenching were performed for HWH and HK^{c}H. Complete quenching was achieved with HWH upon addition of 1 equivalent of $CuCl_2$, while 88% quenching was obtained with HK^{c}H.[210] This incomplete quenching may be due to the longer distance between the coumarin probe and the Cu(II)-binding site. The fluorescence-quenching data, using up to 1 equivalent of Cu(II), were fitted to the Stern-Volmer equation (**Equation 3.2**):

$$\frac{I_0}{I} = 1 + K_{sv}[\text{Cu(II)}] \qquad (3.2)$$

where I_0 is the fluorescent intensity of the free peptides, I is their intensity in the presence of Cu(II) ions, K_{sv} is the Stern-Volmer constant and *[Cu(II)]* is the concentration of Cu(II) ions. The Stern-Volmer plots obtained were not linear, thus indicating a second-order dependence on [Cu(II)] and, the participation of both dynamic and static quenching processes.[227] K_{sv} values of 1.7 × 10^5 M^{-1} and 1.3 × 10^5 M^{-1} were obtained for HWH and HK^{c}H, respectively (r^2 > 0.99 in both cases).

The determination of the apparent and conditional Cu(II)-affinity constants of the emissive HWH and HK^{c}H tripeptides were carried out from fluorescence quenching data in HEPES-buffered solutions (100 mM, pH 7.4). The apparent affinity constants, K^{app}, are given at a particular buffer and salt concentration and a fixed pH, while the conditional affinity constants, K^{cond}, are corrected from the binding of the buffer.[71] HEPES is a weak competitor for copper and it is known that it does not form ternary complexes.[228,229]

The apparent affinity constants were obtained by fitting the intensity values to **Equation 3.3**:[228,230]

$$I = I_0 + \frac{I_{lim} - I_0}{2[\text{L}]}\left([\text{L}] + [\text{Cu}^{2+}] + \frac{1}{K^{app}} - \sqrt{\left([\text{L}] + [\text{Cu}^{2+}] + \frac{1}{K^{app}}\right)^2 - 4[\text{L}][\text{Cu}^{2+}]}\right) \qquad (3.3)$$

where [L] is the concentration of peptide, which was maintained constant at 10 μM, [Cu^{2+}] is the concentration of copper, K^{app} is the apparent affinity constant, and I_{lim} and I_0 are the intensity of the fully Cu-complexed and the free peptide, respectively.

The corresponding plots are shown in **Figure 3.12**.[210] Upon addition of copper, the fluorescent intensity decreases gradually until an equimolar amount of Cu and peptide is reached, which supports the formation of 1:1 species. The determination coefficients (r^2) were > 0.99 in all cases.

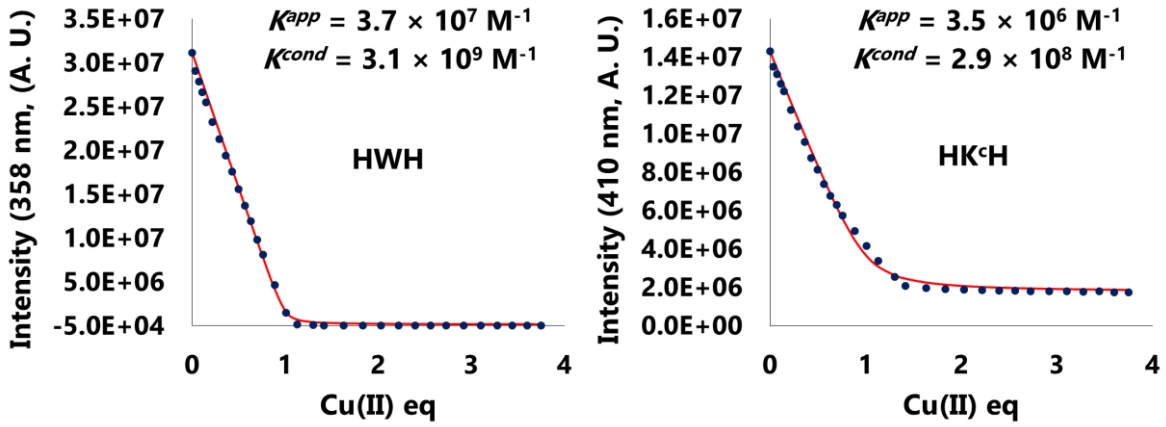

Figure 3.12: Fluorescence Cu(II)-titration data and fitting using **Equation 3.3**, for HWH (**left**) and HK^{c}H (**right**) in 100 mM HEPES buffer (pH 7.4).

The K^{app} values obtained were 3.7 × 10^{7} for HWH and 3.5 × 10^{6} M^{-1} for HK^{c}H. The contribution of the HEPES buffer was subsequently subtracted to obtain the conditional affinity constants, K^{cond}, using **Equation 3.4**:

$$\log K^{cond} = \log K^{app} + \log\left(1 + \beta_{Cu\text{-}buffer} \times \frac{[buffer]}{1 + 10^{-pH+pK_a}}\right) \qquad (3.4)$$

where $\beta_{Cu\text{-}buffer}$ is the dissociation constant of the Cu-HEPES complex (log $\beta_{Cu\text{-}buffer}$ = 3.22), [buffer] is the concentration of HEPES (100 mM) and K_a is the acidity constant of HEPES (pK_a = 7.41).[228,229]

Conditional affinity constants K^{cond} of 3.1 × 10^{9} M^{-1} and 2.9 × 10^{8} M^{-1} were determined for HWH and HK^{c}H, respectively.[210] Remarkably, these values are two and one order of magnitude higher, respectively, than the affinity constant, *viz.* 2.9 × 10^{7} M^{-1}, which Tõugu *et al.* obtained for Aβ(1-40) using the same methodology.[228] Both HWH and HK^{c}H should therefore be able to displace Aβ(1-40)-bound copper ions and hence prevent copper-induced Aβ toxicity.

It has to be mentioned that the Aβ(1-40) affinity constant obtained from Tõugu *et al.* is three orders of magnitude lower than the widely accepted value of 10^{10} M^{-1}.[231,232] Accordingly, this methodology does not seem to be adequate for the determination of K values for such strong Cu(II)-chelators for which the equilibrium is strongly displaced towards the formation of the Cu(II)-complexes. Hence, the affinity constants herein presented should only be taken as relative values; potentiometric analyses are required to accurately determine the correct binding affinities. However, the simplicity and

reproducibility of this method, which avoids the use of competitive binders, is sufficient for rapid comparative analyses of potential copper-chelating agents.

Since HAH is non-emissive, competitive binding studies with HWH and HK^{c}H (monitored by their emission changes) were conducted to determine its relative Cu-binding affinity. The addition of increasing amounts of HAH to either (1:1) Cu(II)-HWH or Cu(II)-HK^{c}H resulted in a partial (50%) recovery of the fluorescent intensity in both cases (**Figure 3.13**).[210] The fact that the initial intensity was not totally recovered may be explained by an incomplete extraction of the Cu(II) ions by HAH, or by quenching produced by intermolecular interactions between aromatic rings (*viz.* indole/coumarin-imidazole). Actually, blank experiments (that is without copper) showed emission quenching upon addition of HAH.

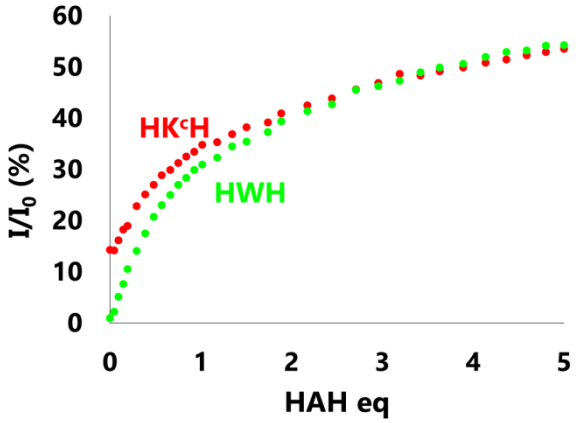

Figure 3.13: Fluorescence titration data of 1:1 Cu(II)-HWH and 1:1 Cu(II)-HK^{c}H with increasing amounts of HAH in 100 mM HEPES (pH 7.4).

Therefore, the Cu-binding affinity followed the trend HAH > HWH > HK^{c}H. In light of these results, the stabilising effect of the aromatic central residues in the complexation can be excluded as the driving factor of this trend;[233] instead, a higher peptidic flexibility might explain a stronger interaction.

In order to elucidate the influence of His1 on the binding affinity, the Cu(II)-binding affinity constants for GWH (see **Figure 3.10**), for which His1 is substituted with a glycine residue, were determined (**Figure 3.14**). 70% fluorescence quenching was observed upon addition of 1 equivalent of Cu(II), associated with a K_{sv} value of 7.7×10^4 M^{-1} (**Equation 3.2**; $r^2 = 0.931$).[210] **Equations 3.3** and **3.4** were used to obtain the apparent and conditional values of affinity constants of respectively 1.5×10^6 and 1.2×10^8 M^{-1} ($r^2 = 0.984$). These values are one order of magnitude lower than those of HWH;

although these data should be confirmed by potentiometric analyses, the difference/tendency observed suggests that the imidazole ring, although it does not participate in the binding of copper, has a stabilising role.

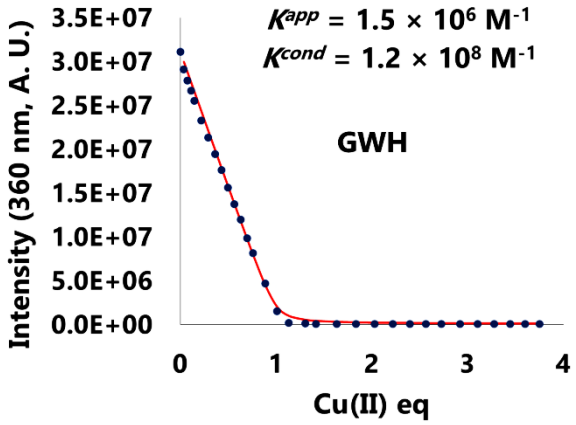

Figure 3.14: Fluorescence Cu(II)-titration data and fitting using **Equation 3.3** for GWH in 100 mM HEPES buffer (pH 7.4).

As already mentioned, the tripeptides should be able to compete with Aβ(1-40) for copper binding. Competition studies were therefore carried out using the Aβ(1-16) fragment. This non-aggregating fragment of Aβ contains the sequence responsible for copper binding as well as an emissive Tyr10 residue, which can be used to follow the metal interaction through spectrofluorimetry (see **Chapter 1**). The coumarinic HK^{c}H peptide was selected for such experiments to avoid excitation/emission overlapping with the tyrosine residue (λ_{exc} = 275, 280 and 300 nm; λ_{em} = 305, 360 and 410 nm for tyrosine, tryptophan and coumarin, respectively).

First, increasing amounts of HK^{c}H were added to a 1:1 Cu(II)-Aβ(1-16) solution and the Cu(II)-extraction process was followed by the changes in Tyr10 emission (**Figure 3.15**, top). The fluorescent intensity of Aβ(1-16), decreased by 40% upon Cu(II) binding, was recovered up to 90% upon addition of 1 equivalent of HK^{c}H, therefore indicating that the tripeptide was extracting Aβ-bound Cu(II) ions.[210] Further HK^{c}H additions resulted in a linear emission decrease. A similar effect was observed for a blank experiment containing Aβ(1-16) and HK^{c}H, but without copper. This can be explained by an energy transfer effect (FRET, see section 3.1.4) between the two chromophores, the emission of tyrosine (λ_{em} = 305 nm) being very close to the excitation of coumarin (λ_{exc} = 300 nm). This effect was not observed upon titration with non-emissive HAH, where 100%

of the emission was recovered and no decrease was observed for > 1 equivalent of added HAH.

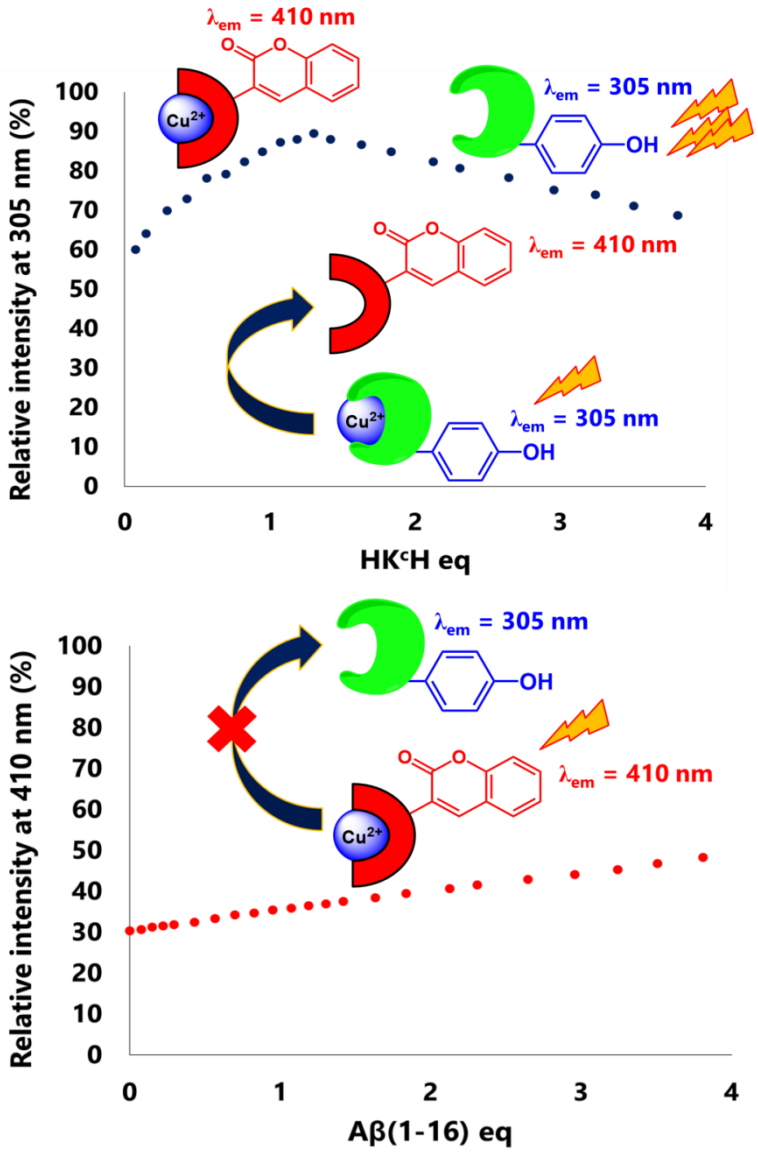

Figure 3.15: Cu(II)-competitive titration studies between HK^{c}H and Aβ(1-16): addition of increasing amounts of HK^{c}H to Cu(II)-Aβ(1-16), monitored by the emission at 305 nm (**top**); addition of Aβ(1-16) to Cu(II)-HK^{c}H, monitored by the emission at 410 nm (**bottom**). 10 mM HEPES (pH 7.4).

A reverse experiment was subsequently carried out where increasing amounts of Aβ(1-16) were added to a solution containing equimolar amounts of Cu(II) and HK^{c}H (**Figure 3.15**, bottom). The emission increased linearly but in a less pronounced fashion than in the previous assay, and no slope change was observed this time.[210] Again, the

intensity increase can be explained by a FRET phenomenon, and blank experiments (namely without copper) showed a similar profile. The contribution to the intensity increase due to Cu(II) extraction by Aβ(1-16) was negligible, further supporting the high stability of the Cu(II)-tripeptide complexes, even in the presence of a 4-fold excess of Aβ(1-16). HK^{c}H presented the lowest affinity, compared with those of HWH and HAH.

In conclusion, the three ATCUN tripeptides exhibit Cu(II)-binding affinities that are high enough to allow them to extract Aβ-bound Cu(II) ions. ATCUN peptidic sequences might thus represent promising synthons for the design of Cu(II)-ionophores for copper redistribution in AD.

3.3.1.3 Inhibition of Cu-induced Aβ(1-40) aggregation and ROS production by unprotected peptides

The aggregation of monomeric Aβ(1-40) in the presence and absence of copper, and the effect of the Cu-chelating tripeptides on this process was then followed by thioflavin T (ThT) fluorescence, which is a procedure commonly applied to monitor amyloid formation (see **Chapter 1**).[108,109] Free ThT exhibits a weak fluorescent emission at 445 nm upon excitation at 385 nm. In the presence of amyloids, though, the excitation and emission wavelengths shift to 445 and 482 nm, respectively, and the emission intensity increases dramatically.[108] ThT is selective towards amyloids and is unresponsive to aggregated species without β-sheet structures, low-order oligomers or amorphous precipitates.

The data achieved for these aggregation studies are shown in **Figure 3.16**.[210] Freshly prepared monomeric Aβ(1-40) induced low ThT emission intensity during the first 10-15 minutes, due to the lack of β-sheet content in this nucleation phase.[30] After this lag time, the elongation phase (in which nuclei rapidly incorporate peptide molecules to generate β-sheet-containing protofibres) took place, resulting in an abrupt increase of ThT emission.[32] Finally, the emission reaches saturation during the maturation phase, where large amyloids are generated. The aggregation process is thus characterised by a sigmoidal curve, common feature for amyloidogenic proteins.[109]

The incubation of the protein with an equimolar amount of Cu(II) ions (copper is known to stabilise Aβ(1-40) oligomers) resulted in a weak and slow increase of ThT emission, consistent with the presence of low quantities of fibrillary Aβ(1-40).[66-68] However, ThT

emission began to increase after 3 hours of incubation, reaching an intensity similar to that obtained for metal-free Aβ(1-40); thus, Cu(II) ions delayed the formation of fibres.

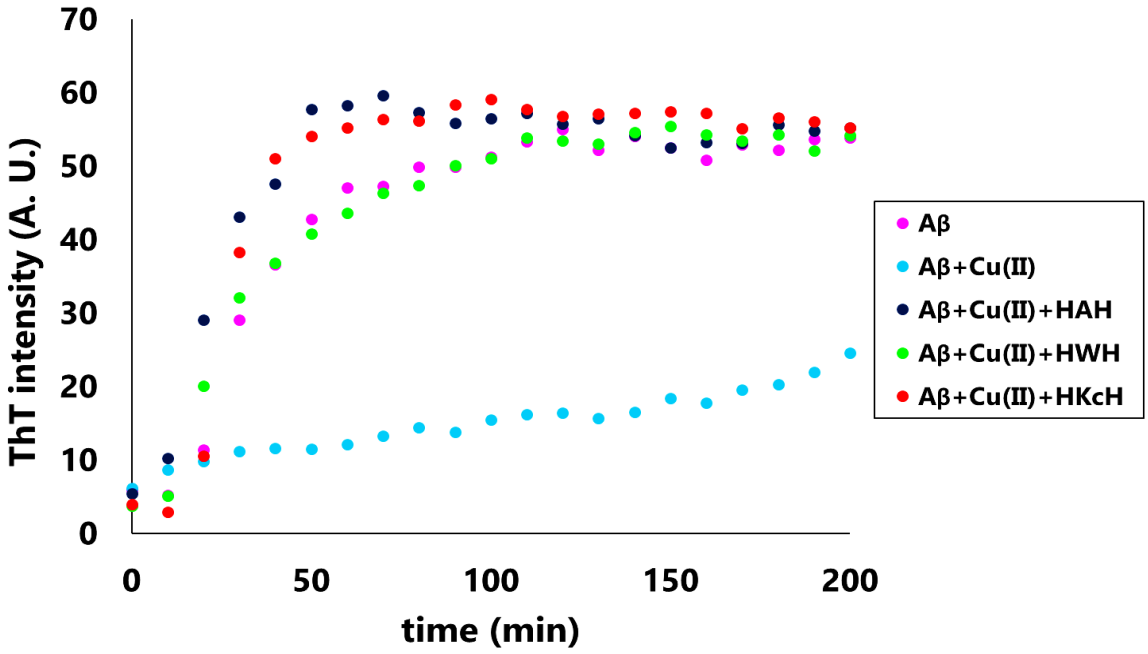

Figure 3.16: Aggregation of Aβ(1-40) (pink dots), Aβ(1-40) in presence of $CuCl_2$ (light-blue dots) and Aβ(1-40) in presence of $CuCl_2$ and the different ATCUN tripeptides, namely HAH (dark-blue dots), HWH (green dots) and HKcH (red dots). The concentration of Aβ(1-40) was 20 μM in all cases. ThT emission; λ_{exc} = 440 nm, λ_{em} = 490 nm. 10 mM Tris-HCl (pH 7.4), 37 ºC.

To evaluate the ability of the tripeptides to prevent the copper-induced stabilisation of oligomeric species, the emission of ThT was followed for Aβ(1-40) incubated with 1 equivalent of Cu(II) and 2 equivalents of each chelating agent (**Figure 3.16**). Remarkably, characteristic sigmoidal curves were obtained for the three tripeptides, indicating that they are able to sequester the copper ions, giving rise to a normal aggregation of Aβ(1-40).[210]

The aptitude of the ATCUN tripeptides to inhibit copper-catalysed ROS production was next investigated. As explained in **Chapter 1**, the interaction of copper with Aβ peptide induces the formation of oxidising species, which are responsible of oxidative stress and contribute to neuronal death in AD. The uncontrolled production of ROS is implicated in several pathologies including AD, amyotrophic lateral sclerosis, Huntington's and Parkinson's diseases or cancer.

When coordinated to Aβ, the redox potential of the Cu(II)/Cu(I) pair rises significantly (from +150 for free copper to +550 mV in the case of Cu-Aβ(1-42)).[85] Therefore, Cu(II) is easily reduced to Cu(I) by endogenous reductants such as ascorbate (with a midpoint potential of +280 mV), which is highly abundant in cells (its concentration being of about 100 μM).[85,234] Cu(I)-Aβ can then react with dioxygen and be re-oxidised to Cu(II) through a one-electron transfer, regenerating Cu(II)-Aβ species and producing highly damaging species like the superoxide radical (**Figure 3.17**).[86,234]

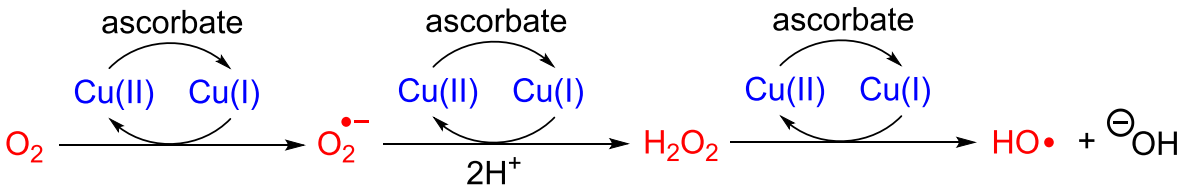

Figure 3.17: Copper-catalysed ROS production in the presence of ascorbate.

This catalytic one-electron process can further proceed and superoxide can be reduced to dihydrogen peroxide (first) and ultimately to the highly oxidising hydroxyl radical.[234] These ROS damage cell membranes, lipids and nucleic acids, leading to cell death.[86] The production of ROS is more efficient for [copper-oligomeric Aβ] complexes; the rearrangement of the coordination environment required during the successive oxidation-state changes of copper is easier (*viz.* a lower energy cost is involved) with soluble Aβ oligomers.[76] The design of copper-chelating agents capable of blocking this catalytic cycle and inhibiting ROS production therefore represents a promising approach to diminish the oxidative stress observed in AD.

The capacity of the chelating tripeptides to prevent Cu-catalysed ROS generation was then evaluated under aerobic conditions, following the consumption of ascorbate (100-fold excess compared to copper) through the decrease of its absorbance at 265 nm during 30 min experiments.[235] For these studies, the phosphate buffer used was pre-treated with Chelex 100 resin to remove any traces of metal present.

The inhibition rates of the *N*-terminal unprotected tripeptides were calculated using **Equation 3.5**:

$$\textbf{\% inhibition} = \left(1 - \frac{\textbf{Abs} - \textbf{Abs}_{\textbf{blank}}}{\textbf{Abs}_{\textbf{freeCu}} - \textbf{Abs}_{\textbf{blank}}}\right) \qquad \textbf{(3.5)}$$

where Abs_{blank} and Abs_{freeCu} are the absorbance values of ascorbate in the absence and presence of $CuCl_2$, respectively.

After 30 minutes, 73% of the initial amount of ascorbate was consumed in the presence of Cu(II) ions (light-blue dots in **Figure 3.18**).[210] Surprisingly, the addition of 1.1 equivalents (with respect to copper) of Aβ(1-40) resulted in 62% inhibition of the ascorbate consumption (pink dots in **Figure 3.18**). Such antioxidant properties of Aβ are apparently contradictory with the extended idea that Cu-Aβ species generate ROS. However, it is reasonable to consider that the coordination of Cu(II) to Aβ may affect its redox cycling (compared with that of the "free" metal ion), leading to a decrease of ROS production. In turn, the presence of the ATCUN tripeptides (1.1 equivalents) yielded higher inhibition rates; 85, 95 and 97% inhibition of ascorbate consumption was observed for HAH, HWH and HK^{c}H, respectively (see dark-blue, green and red dots in **Figure 3.18**).[210]

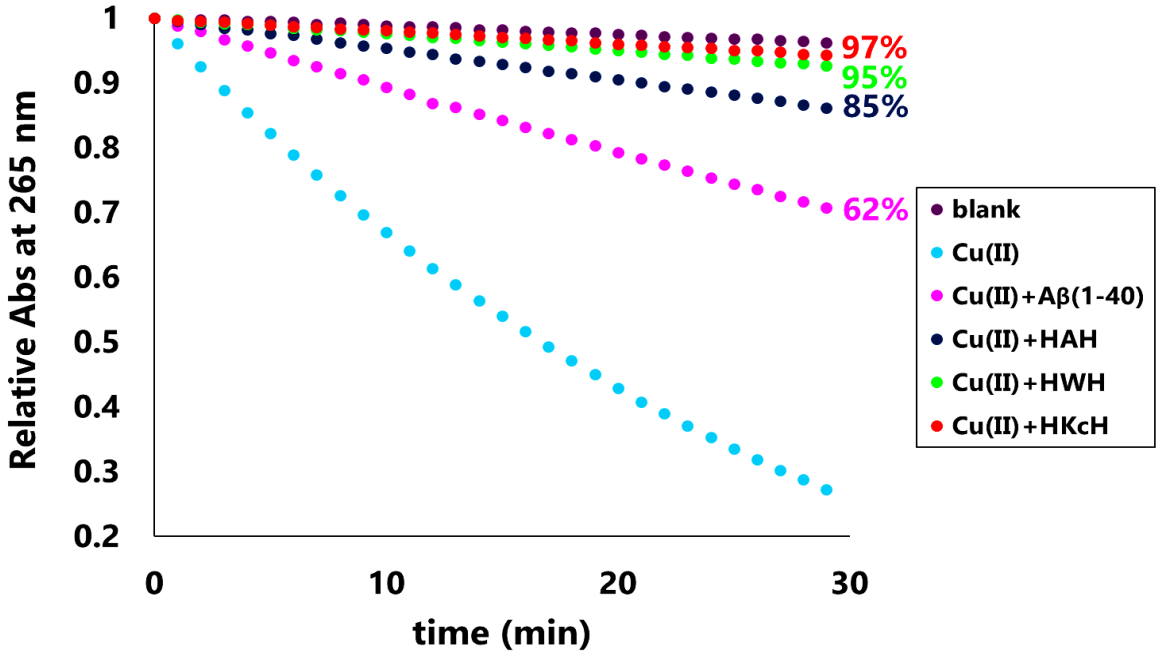

Figure 3.18: Cu(II)-induced generation of ROS monitored through the consumption of ascorbate using its absorbance at 265 nm, in the presence and absence of the *N*-terminal free tripeptides. The inhibition rates of ROS production are indicated as percentages in relation to free copper (light-blue dots; 0% inhibition). Phosphate buffer 100 mM (pH 7.4).

In agreement with the results here demonstrated, Mena *et al.* found that Cu(II) reduction for the complexes Cu(II)-HAH and Cu(II)-HWH could not be achieved applying potentials up to -1.2 V.[135] DFT calculations actually showed reduction potentials of around -1.7 V for such ATCUN complexes. The rigidity of the ATCUN binding mode and the coordination of the two negatively charged amide functions

account for the very low reduction potential and hinder reduction of the metal centre. With such highly negative potentials, the reduction of Cu(II) with ascorbate cannot occur and therefore the production of ROS is prevented.

The inhibition of the production of hydroxyl radicals was subsequently studied using coumarin-3-carboxylate as a radical scavenger. Coumarin-3-carboxylate reacts with hydroxyl radicals to yield the highly emissive 7-hydroxycoumarin-3-carboxylate (**7-OHCCA**), which displays excitation and emission wavelengths of λ_{exc} = 385 nm and λ_{em} = 500 nm, respectively (**Figure 3.19**). The effect of the peptides on the production of such highly damaging radicals was thus assessed by monitoring the emission at 500 nm using ascorbate as the reducing agent (initially 300 μM), under aerobic conditions. Coumarin-3-carboxylate was added in a high excess, compared to the peptides (1 mM and 1.1 μM, respectively), so that any contribution of the hydroxylated coumarinic moiety of HK^{c}H peptide would be negligible.

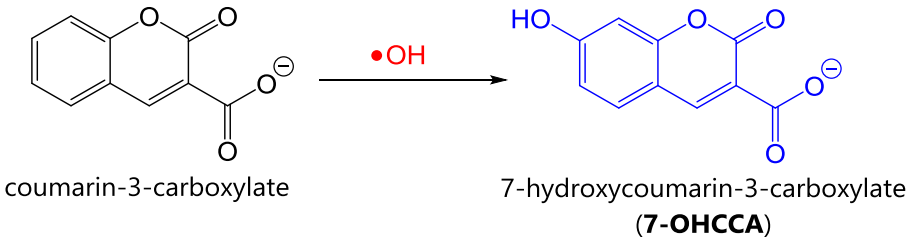

Figure 3.19: Generation of 7-OHCCA (λ_{exc} = 385 nm, λ_{em} = 500 nm) by reaction of coumarin-3-carboxylate with the hydroxyl radical.

The results obtained are shown in **Figure 3.20**, and the inhibition rates were calculated using **Equation 3.6**:

$$\% \text{ inhibition} = \left(1 - \frac{I - I_{blank}}{I_{freeCu} - I_{blank}}\right) \qquad (3.6)$$

where I_{blank} and I_{freeCu} are the intensity values of ascorbate-coumarin-3-carboxylate in the absence and presence of $CuCl_2$, respectively. The fluorescent intensity when copper was incubated with ascorbate in the presence of coumarin-3-carboxylate rapidly increased after the first 3 minutes, suggesting that hydroxyl radicals were produced. When copper was incubated with 1.1 equivalents of Aβ(1-40), 12% inhibition of the emission of 7-OHCCA was observed. In contrast, the ATCUN tripeptides (1.1 equivalents) showed remarkable inhibition properties, as reflected by the values of 67%, 70% and 76% for HAH, HWH and HK^{c}H, respectively.[210]

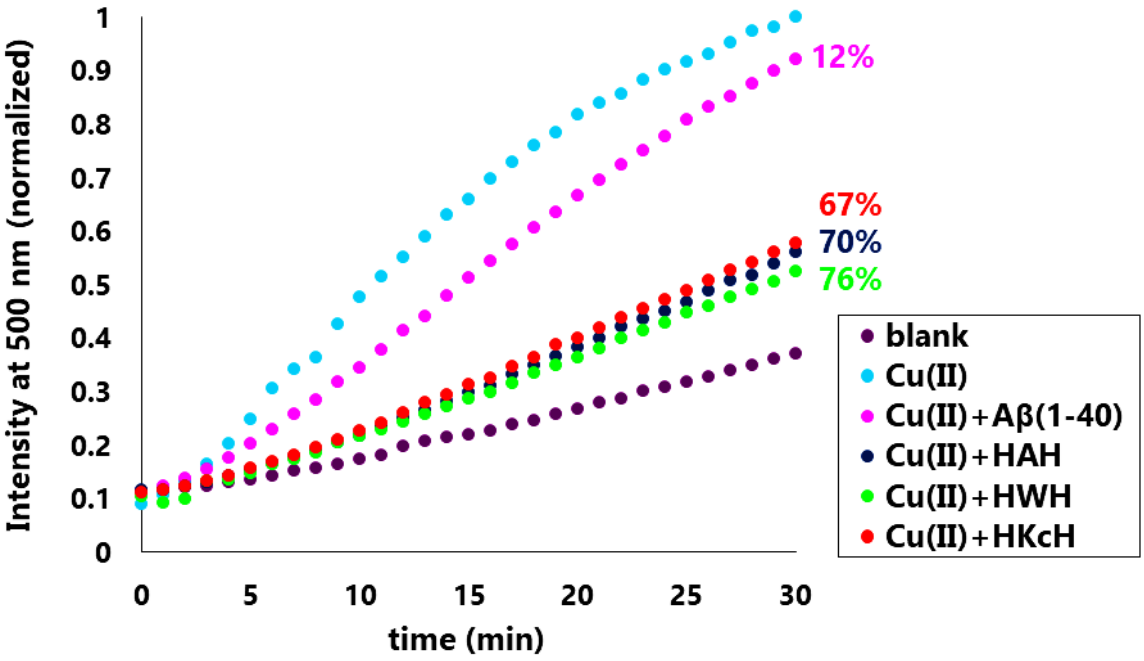

Figure 3.20: Cu(II)-induced production of hydroxyl radicals followed by the emission of 7-OHCCA (λ_{exc} = 385 nm, λ_{em} = 500 nm) in the presence and absence of the *N*-terminal free tripeptides. The inhibition rates of hydroxyl production are indicated as percentages, in relation to free copper (light-blue dots that are defined as 0% inhibition). Phosphate buffer 100 mM (pH 7.4).

In summary, the three chelating agents described above possess two of the crucial properties required for a potential ionophore drug, namely, upon Cu(II) chelation, they are able to 1) prevent the copper-induced stabilisation of toxic oligomers, and 2) inhibit the copper-catalysed production of ROS in the presence of high concentrations of a reducing agent (like ascorbate).

3.3.2 Chelating properties of the N-terminal protected peptides

3.3.2.1 Determination of the Cu(II)-binding mode of the N-terminal protected peptides

The characterisation of the Cu(II)-binding properties of the protected peptides and of their ability to inhibit the copper-induced Aβ(1-40) oligomer formation and ROS production was next addressed. The tripeptides AcHK^{c}H and AcHK^{d}H were first incubated with 2 equivalents of $CuCl_2$ at pH 7.4 and the resulting solutions were analysed by ESI-MS. As for the ATCUN peptides (*viz.* the peptides with unprotected *N*-terminus), only the 1:1 Cu(II)-peptide species were detected; *i.e.* the 1:2 or 2:1 species

were not observed. The intensity of the peaks was remarkably lower than that obtained for the ATCUN peptides under similar experimental conditions, which might be indicative of a weaker Cu(II)-peptide interaction.

Subsequently, the changes in absorbance upon titration with $CuCl_2$ were analysed.[209] For AcHK^{c}H, precipitation of the Cu(II)-peptide complex started with substoichiometric copper amounts; the actual stoichiometry could not be determined. The colour of the precipitate was bluish green, which indicated absorption in the orange-red region. Addition of $CuCl_2$ to AcHK^{d}H produced an even less soluble metal-peptide adduct.

The suspensions were then centrifuged, and the precipitates were analysed by diffuse reflectance spectroscopy (**Figure 3.21**). Absorption maxima were found at 704 and 701 nm for AcHK^{c}H and AcHK^{d}H, respectively. These significantly red-shifted d-d bands compared with those of the ATCUN peptides (515-520 nm, violet solutions, see section **3.3.1**) suggested the replacement of strong-field ligands, such as the *N*-terminal amino group or deprotonated amides, by weak-field donors, like carbonyl oxygen and imidazole nitrogen atoms.

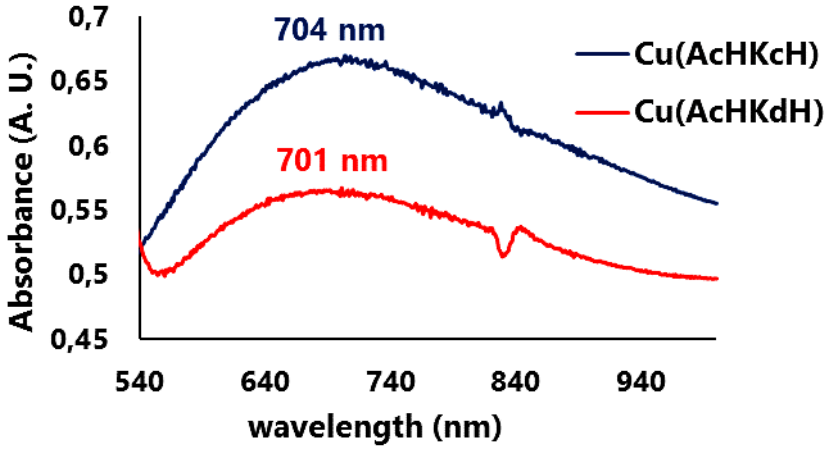

Figure 3.21: Diffuse reflectance spectra of CuAcHK^{c}H (blue) and CuAcHK^{d}H (red).

Using **Equation 3.1** for a [N_{Im}, N^-, N^-, N_{Im}] donor set, a $\lambda^{d\text{-}d}$ value of 540 nm is expected, whereas this transition band is estimated at around 600 nm for a [N_{Im}, N^-, CO, N_{Im}] one.[211] Both values were far from the experimental ones obtained for the Cu(II)-complexes of the *N*-acetylated peptides. Such a discrepancy may be due to the fact that **Equation 3.1** is not valid when the coordination sphere includes donors at the apical positions (which could be the carboxylate group of His3 in the present case).

The interaction of the *N*-protected tripeptides with copper was subsequently studied by CD using Cu(II)/peptide ratios ranging from 0 to 2. Intense negative bands at λ = 290 nm (AcHK^{c}H) and 285 nm (AcHK^{d}H) were detected, which were attributed to N_{amide}→Cu(II) charge-transfer transitions, together with intraligand imidazole charge-transfer processes (**Figure 3.22**).[215,216,218,236] Shoulders were observed at about 330 and 320 nm for AcHK^{c}H and AcHK^{d}H, respectively, which were attributed to $N_{imidazole}$→Cu(II) charge-transfer transitions. Unfortunately, the d-d bands were poorly defined, especially for AcHK^{c}H. For AcHK^{d}H, a possible positive band centred at about 550 nm was noticed.

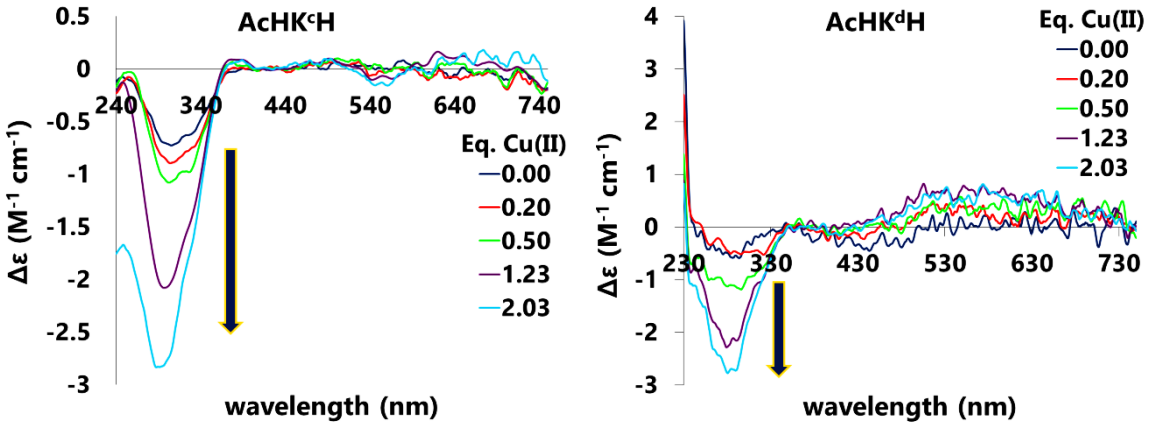

Figure 3.22: Circular dichroism spectra of the AcHK^{c}H (**left**) and AcHK^{d}H (**right**), using different Cu(II)-peptide ratios (in 100 mM HEPES pH 7.4).

The coordination of the peptides to Cu(II) was further investigated by NMR.[219] Addition of 0.5 mol% Cu(II) to AcHK^{c}H resulted in a broadening of the signals corresponding to the first amide function, the carbonyl oxygen of Lys2 and the two imidazole rings (**Figure 3.23**, purple dots). These results are consistent with those obtained for AcHWH.[135] Remarkably, the signals of the carboxylic group were also significantly affected, suggesting its participation in Cu(II) binding, probably in an apical position.

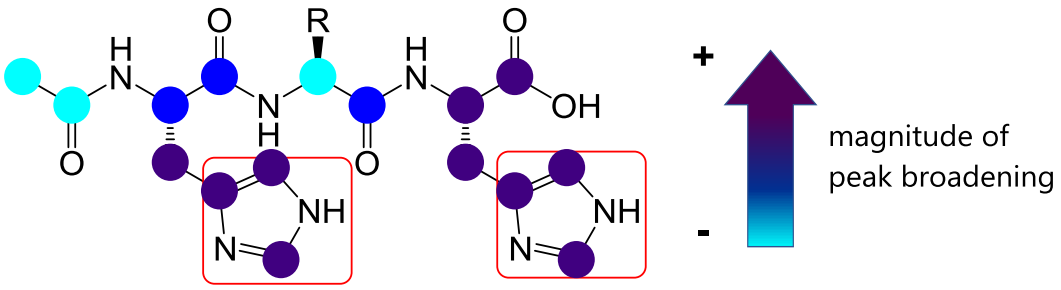

Figure 3.23: Colour-based representation of the magnitude of NMR peak broadening (^{1}H and ^{13}C NMR experiments) observed for the *N*-terminal protected tripeptides in the presence of 0.01 eq of $CuCl_2$ (D_2O solutions, pH 7.4).

Finally, EPR spectra of frozen 1:1.1 Cu-peptide solutions were recorded. It can be pointed out that some precipitation occurred upon mixing the metal with the chelating agent. The spectra of the major species for both peptides are shown in **Figure 3.24**. As for the ATCUN peptides, the order of the *g* tensor ($g_{\parallel} > g_{\perp} > g_e$) indicated a complex with axial symmetry.[221] Similar values were obtained for both peptides, namely $g_{\parallel}$ = 2.27, $g_{\perp}$ = 2.09 and $A_{\parallel}$ = 511 MHz (170 G) for AcHK^{c}H, and $g_{\parallel}$ = 2.26, $g_{\perp}$ = 2.06 and $A_{\parallel}$ = 521 MHz (175 G) for AcHK^{d}H. Such values characterise a square-planar geometry with a [$2N_{Im}$, N^-, CO/COO^-] donor set.[236-238] The $g_{\parallel}$ values were higher than that obtained for Cu(II)-HAH (*viz.* $g_{\parallel}$ = 2.07), whereas the value of the hyperfine parallel constant $A_{\parallel}$ was significantly lower ($g_{\parallel}$ Cu-HAH = 205 G = 601 MHz, see section **3.3.1**), pointing towards an increase of the electron-withdrawing behaviour of the ligands.[223] Hence, oxygen donor atoms (*e.g.* from carbonyl groups of the amide backbone and/or the His3 carboxylic group) most likely participate in the binding of Cu(II) ions.

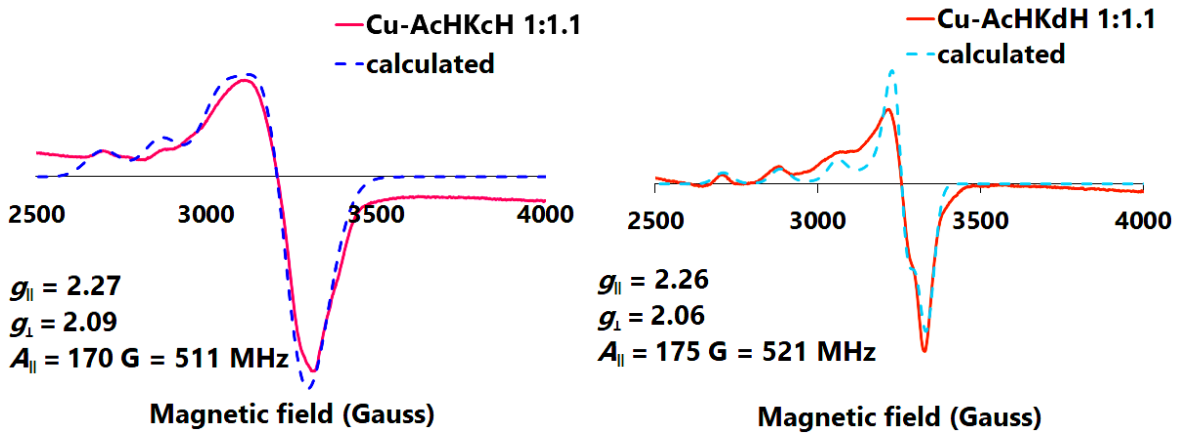

Figure 3.24: EPR spectra of 1:1.1 Cu(II)-AcHK^{c}H (**left**) and Cu(II)-AcHK^{d}H (**right**) solutions. 100 mM HEPES (pH 7.4), 77 K.

In summary, the characterisation data achieved using various techniques suggested the formation of a 3N1O coordination sphere, in agreement with computational studies described in the literature.[135] The precipitation of Cu(II)-peptide adducts in some cases may be explained by the formation of neutral, hydrophobic species, involving a deprotonated amide function and the carboxylate group of His3. Accordingly, the two imidazole rings, the carbonyl oxygen atom of Lys2 and the amide nitrogen atom of Lys2 appear to be involved in the binding of copper, producing a three-(7,5,8)-membered fused ring, as depicted in **Figure 3.25**.[135] The participation of the carboxylate group of a second peptide molecule might also take place (indeed, the intramolecular binding of the carboxylate moiety would require high conformational strain), at an apical position of the 3N1O square plane.

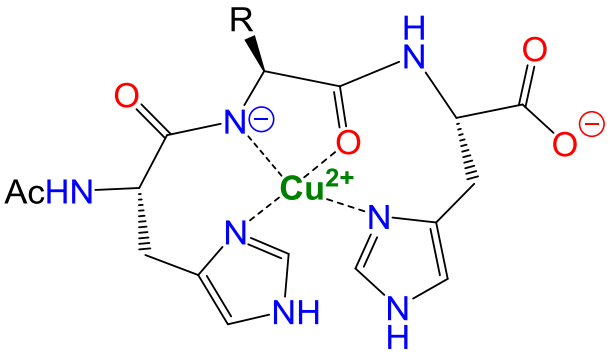

Figure 3.25: Proposed copper-coordination mode for the *N*-terminal protected His-Xaa-His peptides.

It has been reported that, when both the *C*- and *N*-terminus are protected, a different binding is operating as the binding of only one deprotonated amide function is not sufficiently stable when the *C*-terminal carboxylate function is not available.[237] For instance, 4N coordination, involving the two imidazole rings and the two deprotonated amide functions of Xaa2 and His3, has been reported for Ac-His-Xaa-His-NH_2 peptides (**Figure 3.26**).[237,238] In that context, it was envisaged to study the copper binding of AcHK^{d}H-NH_2 since it represents a "model compound" of a *C*-protected tripeptide connected to gold nanoparticles through its *N*-terminus (see section **3.1.3**). Unfortunately, AcHK^{d}H-NH_2 was poorly soluble and therefore could not be studied by UV-Vis or EPR spectroscopy.

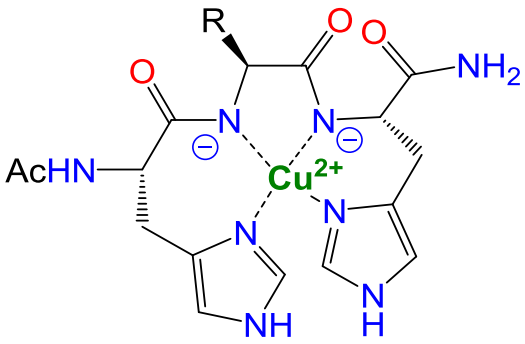

Figure 3.26: Proposed Cu(II)-binding mode for *C*- and *N*-terminal protected His-Xaa-His peptides.

3.3.2.2 Determination of the Cu(II)-affinity constants of the N-protected peptides by fluorescence spectroscopy

Fluorescence-quenching experiments were next carried out with the *N*-acetylated peptides to determine their Cu(II)-binding affinities. For AcHK^{c}H, 31% quenching of the emission was observed upon addition of 1 equivalent of $CuCl_2$. Such a low quenching effect may indicate a low affinity of this peptide for copper or that the distance between the coumarin (fluorescent) probe and the Cu(II)-binding site is too long. Unfortunately, the intensity data could not be fitted to the Stern-Volmer equation (**Eq. 3.2,** see section **3.3.1**). 84% quenching of the emission of the 4DMN probe was observed for AcHK^{d}H, with a K_{sv} value of 2.9 × 10^5 M^{-1} (r^2 = 0.981), that is in the same order of magnitude than those obtained for HWH and HK^{c}H (see section **3.3.1**).

The intensity data were fitted to **Equation 3.3** to determine the corresponding, apparent Cu(II)-affinity constants, K^{app} (see section **3.3.1**).[228,230] The conditional affinity constants, K^{cond}, were calculated using **Equation 3.4**. The plots obtained are shown in **Figure 3.27**. A decrease of the emission intensity was noticed, for both AcHK^{c}H and AcHK^{d}H, upon addition of up to 1 equivalent of $CuCl_2$; afterwards, the emission intensity remained relatively constant. Such a change of slope at a Cu(II)-peptide molar ratio of 1:1 indicated a 1:1 stoichiometry, as already observed with the ATCUN peptides.

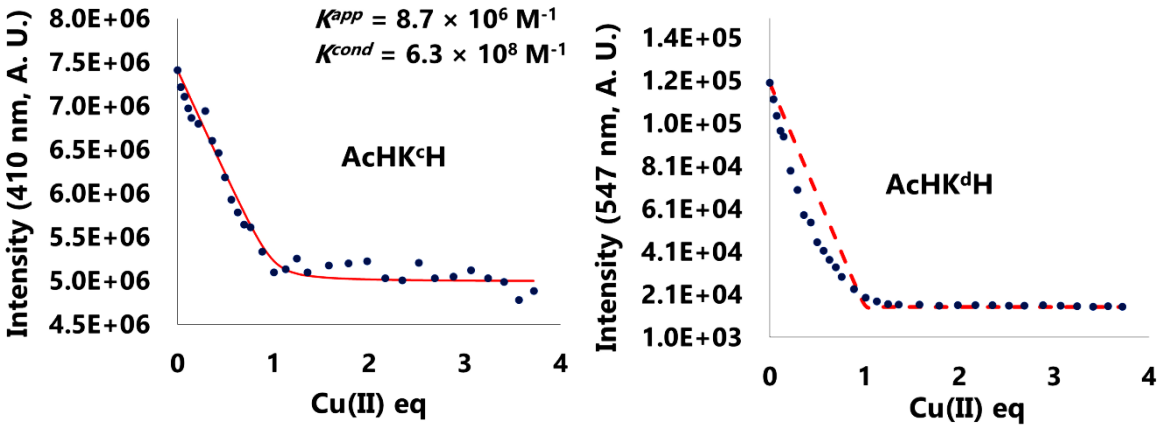

Figure 3.27: Cu(II) titration data obtained by fluorescence quenching (dark-blue dots) and fitting of the results (red curves) using **Equation 3.3**. **Left:** AcHK^{c}H; **right:** AcHK^{d}H. 100 mM HEPES buffer (pH 7.4).

For AcHK^{c}H, a poor fitting of the data to **Equation 3.3** was achieved (r^2 = 0.971), which gave K^{app} = 3.0 × 10^6 M^{-1} and K^{cond} = 2.2 × 10^8 M^{-1} (**Figure 3.27**, left). Unexpectedly, these values were similar to those found for the *N*-terminal free analogue HK^{c}H (*viz.* K^{app} = 3.5 × 10^6 M^{-1}, K^{cond} = 2.9 × 10^8 M^{-1}, see section **3.3.1**). The conditional affinity constant is one order of magnitude larger than that of Aβ(1-40), namely 2.9 × 10^7 M^{-1}; AcHK^{c}H should therefore be able to displace Cu(II)-ions bound to Aβ(1-40).[228] For AcHK^{d}H, the titration data could not be fitted to **Equation 3.3**; a, most likely, overestimated K^{cond} value of 9.0 × 10^{10} M^{-1} (r^2 = 0.902) was obtained (**Figure 3.27**, right).

The Cu(II)-binding affinity of the doubly protected peptide AcHK^{d}H-NH_2 was then investigated; it should be stressed here that the concentrations needed for fluorescence-quenching studies are very low (10 μM), which allowed to study the affinity of this poorly soluble peptide. The addition of 1 equivalent of Cu(II) ions to AcHK^{d}H-NH_2 gave rise to 80% quenching of its emission intensity; applying **Equation 3.2**, a K_{sv} value of 3.8 × 10^5 M^{-1} (r^2 = 0.974) was obtained. The intensity data points and their fitting to **Equation 3.3** are shown in **Figure 3.28**.

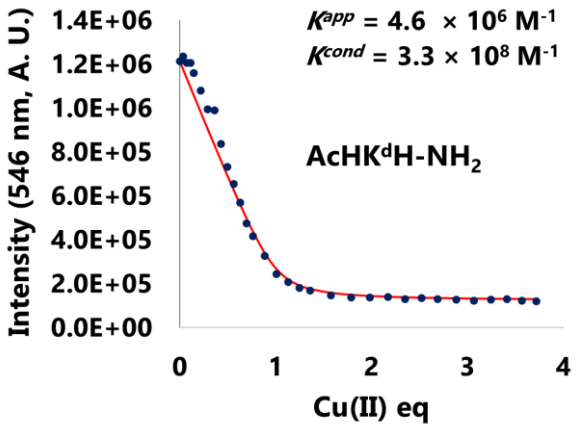

Figure 3.28: Fluorescence Cu(II)-titration data for AcHK^{d}H-NH$_2$, obtained by fluorescence quenching and corresponding fitting using **Equation 3.3**. 100 mM HEPES buffer (pH 7.4).

The reasonable fitting (r^2 = 0.985; **Figure 3.28**) gave an apparent and a conditional affinity constant K^{app} = 4.6 × 10^6 M^{-1} and K^{cond} = 3.3 × 10^8 M^{-1}, respectively. Thus, like AcHK^{c}H, AcHK^{d}H-NH$_2$ should be capable of abstracting Cu(II) ions bound to Aβ(1-40).

Competitive binding studies with Aβ(1-16) were subsequently conducted. In a first instance, a solution of Cu(II)-Aβ(1-16) 1:1 was titrated with AcHK^{c}H or AcHK^{d}H, following the Cu(II)-displacement process by the emission of Tyr10 at 305 nm (see section **3.3.1**). Unfortunately, the addition of the tripeptides resulted in the formation of precipitates that impeded to carry out the investigation.

The reverse experiments, namely the addition of increasing amounts of Aβ(1-16) to 1:1 Cu(II)-tripeptide solutions, were then performed to assess whether the Aβ fragment could displace Cu(II) ions previously bound to the *N*-acetylated peptides. For AcHK^{c}H, the emission at 410 nm (corresponding to the emission of the coumarin probe) increased linearly up to the addition of 0.22 equivalents of Aβ(1-16) (**Figure 3.29,** top). Then, the emission intensity remained relatively constant, which suggested that the displacement of Cu(II) ions did not proceed further. Addition of Aβ(1-16) to AcHK^{c}H without copper generated a precipitate with concomitant decrease of the fluorescent intensity.

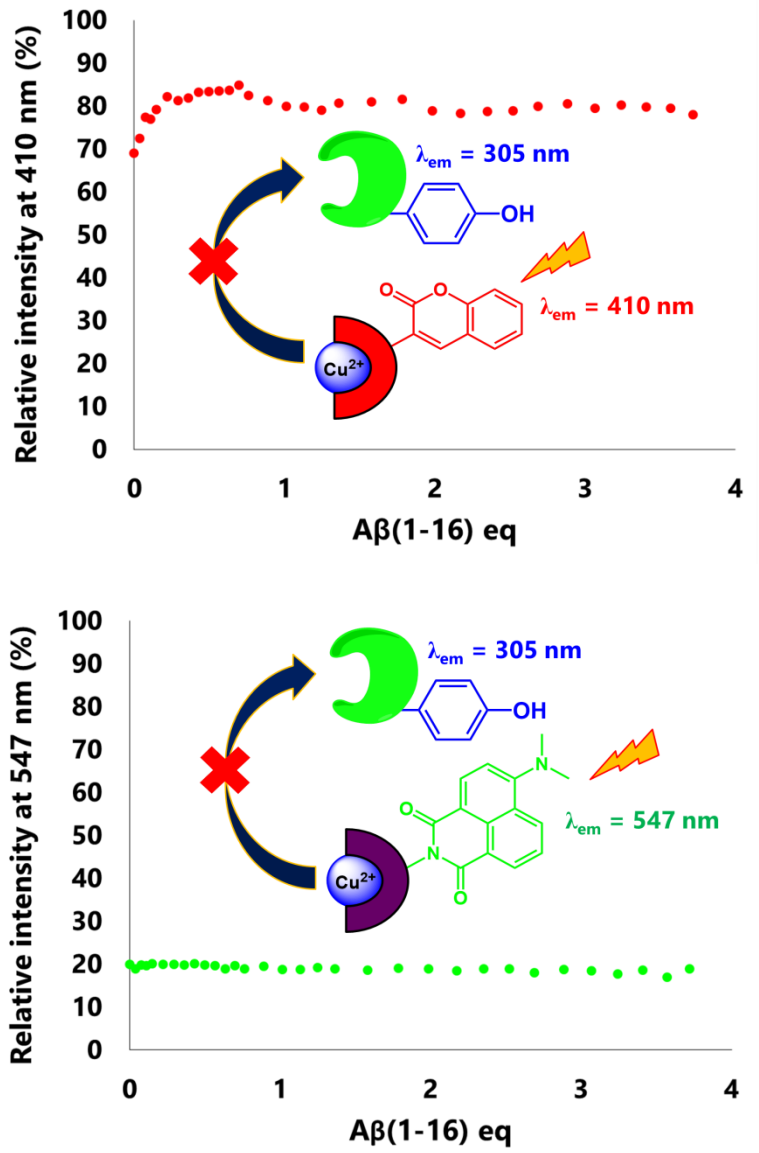

Figure 3.29: Competitive Cu(II)-binding studies between Aβ(1-16) and AcHK^{c}H (**top**) or AcHK^{d}H (**bottom**). The experiments were carried out by in 10 mM HEPES (pH 7.4) adding increasing amounts of Aβ(1-16) to a solution of Cu(II)-tripeptide solution 1:1, which was monitored by the respective emissions, *i.e.* at 410 nm and 547 nm.

The same procedure was carried out for AcHK^{d}H, with λ_{exc} = 441 nm and λ_{em} = 547 nm. When a solution of Cu(II)-AcHK^{d}H 1:1 was titrated with Aβ(1-16), the emission of the 4DMN probe did not vary, suggesting that Aβ(1-16) could not remove copper bound to AcHK^{d}H (**Figure 3.29**, bottom). As observed for AcHK^{c}H, precipitation also occurred when Aβ(1-16) was added to a copper-free solution of AcHK^{d}H.

In summary, in the case of CuAcHK^{c}H, the initial increase of the fluorescent intensity could be due to the generation of AcHK^{c}H-Cu-Aβ(1-16) ternary species. In contrast, no alteration of the fluorescence was observed for CuAcHK^{d}H, hence implying that Aβ(1-16) did not interact with this Cu(II)-tripeptide species.

3.3.2.3 Effect of the N-acetylated peptides on the Cu-induced aggregation of Aβ(1-40) and ROS production

The potential inhibition properties of the *N*-protected tripeptides towards the copper-induced formation of oligomeric Aβ(1-40) species was examined; thus, Aβ(1-40) aggregation in the presence of $CuCl_2$ and the tripeptides was followed by ThT (see section **3.3.1**).[108,109] The ATCUN peptide HAH, which was shown to efficiently act as an inhibitor of the copper-induced formation of oligomers (see above), was used as a reference.

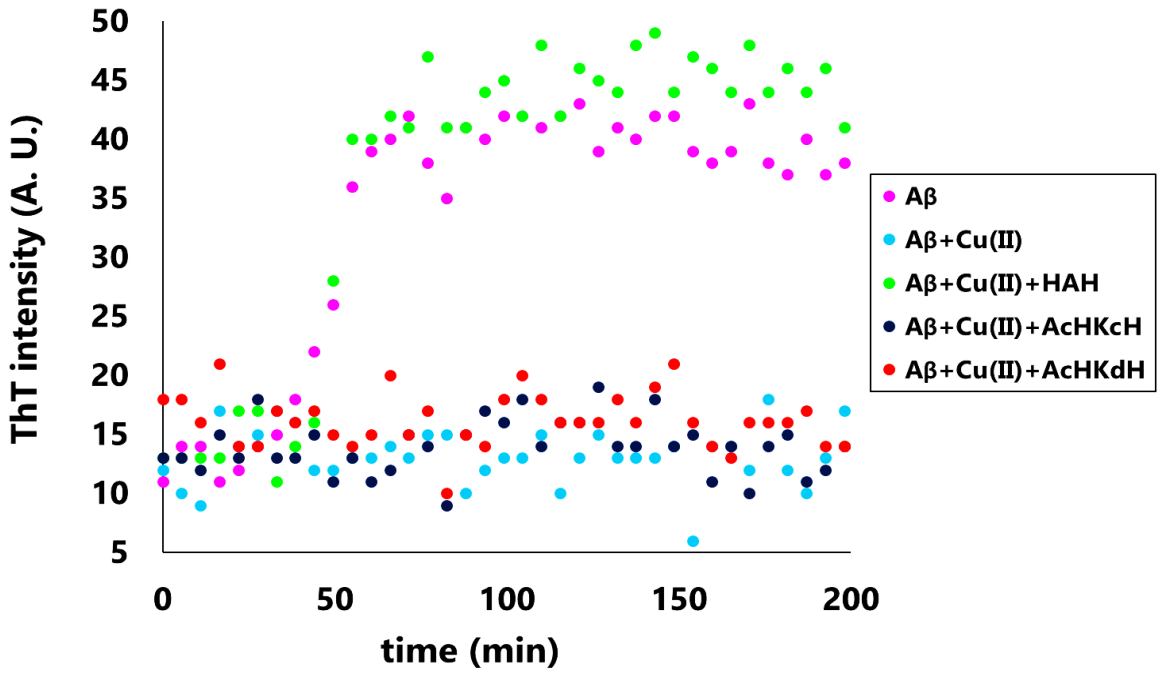

Figure 3.30: Aggregation of Aβ(1-40) (pink dots), Aβ(1-40) in presence of $CuCl_2$ (light-blue dots), and Aβ(1-40) in presence of $CuCl_2$ and 2 eq of HAH (green dots), AcHK^{c}H (dark-blue dots) or AcHK^{d}H (red dots). Aβ(1-40) aggregation was followed by ThT fluorescence emission. 1X PBS (pH 7.4).

The corresponding aggregation plots are depicted in **Figure 3.30**. The characteristic sigmoidal curve, indicative of amyloid formation, was obtained without copper (purple dots). Contrarily, with stoichiometric amounts of $CuCl_2$, ThT fluorescence did not increase due to the stabilisation of oligomeric species;[66-68] the formation of amyloid was delayed.

When 2 equivalents of HAH were added to the Cu(II)-Aβ(1-40) system, the sigmoidal aggregation profile and thus the formation of fibrillary Aβ(1-40) was restored, indicating that HAH sequestered the Cu(II) ions, as previously observed (see section **3.3.1**). Such effect was not observed for the *N*-terminal protected tripeptides AcHK^{c}H and AcHK^{d}H, suggesting that they were not able to (sufficiently) displace Cu(II) ions from Aβ(1-40), and thus to restore the fibrillation process. Aggregation studies without copper showed that the formation of Aβ(1-40) fibres was slightly delayed by AcHK^{c}H and AcHK^{d}H, but eventually took place.

The data achieved contradicted the results of the fluorescence-quenching studies (see above), which indicated that these tripeptides had a better Cu(II)-binding affinity than Aβ(1-16). The fluorescence analyses as those described earlier, are therefore not accurate for the determination of the Cu(II)-affinity constants of strong chelating agents; competitive binding experiments with a weak Cu(II)-competitor such as glycine may be more appropriate for the study of AcHK^{c}H and AcHK^{d}H.[231] In the case of AcHK^{d}H, the preformed Cu-Aβ(1-40) oligomers remained stable and soluble after addition of 2 eq of the peptide. The addition of Aβ(1-40) to a solution of preformed Cu(II)-AcHK^{d}H complex generated a ThT-silent precipitate (amorphous aggregates).

Considering the results obtained with the non-aggregating Aβ(1-16) and aggregating Aβ(1-40) fragments, a series of specific features can be proposed for the interaction between the *N*-acetylated peptides, copper ions and Aβ, which are listed in **Table 3.1**.

Table 3.1: Summary of the results of the competitive Cu(II)-binding studies between Aβ and the *N*-acetylated peptides AcHK^{c}H and AcHK^{d}H. TC: ternary complex. BC: binary complex.

Experiment	Aβ(1-16)	Aβ(1-40)
Aβ-Cu(II) + tripeptide	Insoluble TC	Does not compete
tripeptide-Cu(II) + Aβ	Does not compete (soluble TC with AcHK^{c}H?)	Amorphous Aβ aggregates
tripeptide + Aβ	Insoluble BC	Aβ fibrils

Aβ(1-16) most likely forms ternary Cu(II)-peptide-Aβ or binary peptide-Aβ complexes, whereas Aβ(1-40) does not. Such behaviour has not been previously reported with other tripeptides.[210] The *N*-acetylated tripeptides cannot displace Aβ-bound copper, and copper previously bound to the peptides cannot be removed by Aβ. Interestingly, the Cu(II)-peptide complexes inhibit Aβ fibrillation, probably inducing instead the formation of amorphous aggregates.

The redox properties of the *N*-acetylated tripeptides-Cu(II) complexes in the presence of an excess of ascorbate (*i.e.* 100-fold) were then examined by following the consumption of the reducing agent (see section **3.3.1**).[235] In absence of copper (blank experiment), the ascorbate absorbance remained almost unaltered (green dots in **Figure 3.31**). In the absence of peptides, the $CuCl_2$ salt consumed 66% of the initial amount of ascorbate within the first 5 minutes, and 97% had reacted after 15 minutes (light-blue dots). Incubation of $CuCl_2$ with the *N*-terminal protected tripeptides (1.1 equivalents) resulted in slower rates of ascorbate consumption. After the first 15 minutes, AcHK^{c}H (dark-blue dots) and AcHK^{d}H (red dots) inhibited the consumption of ascorbate by 17% and 34% (calculated using **Equation 3.5**, see section **3.3.1**), respectively, but only a slight inhibition was achieved after 30 min.

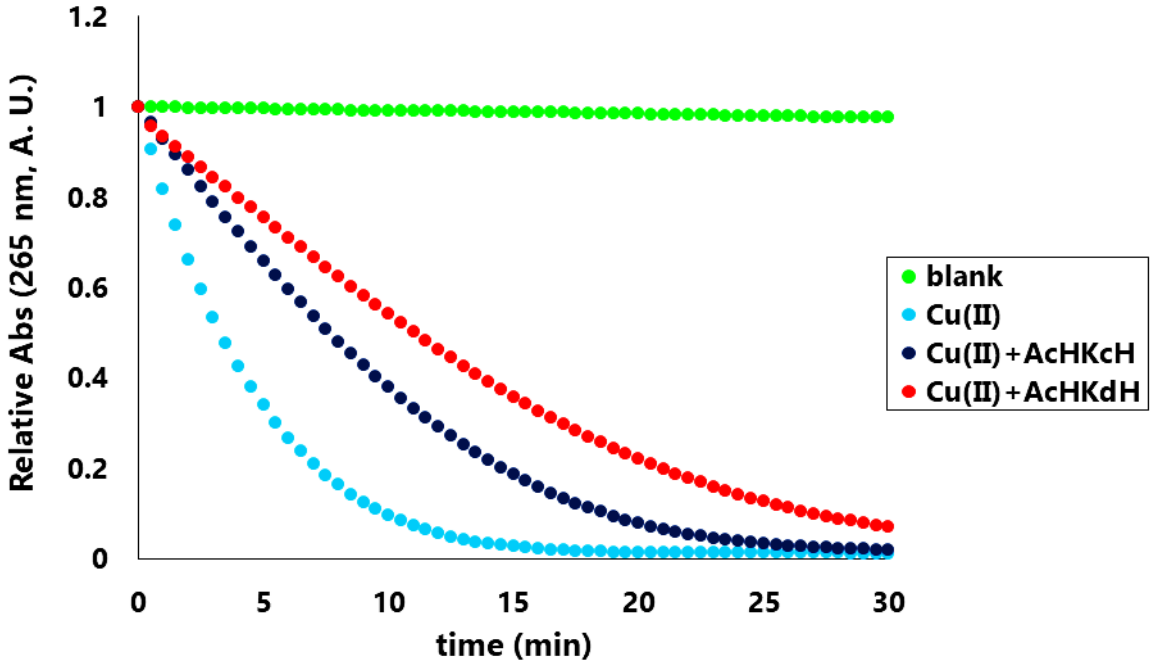

Figure 3.31: Cu(II)-induced ROS generation monitored by the consumption of ascorbate through its absorbance at 265 nm, in the presence and absence of the *N*-terminal protected tripeptides. Phosphate buffer 100 mM (pH 7.4).

As reported by Mena *et al.*, a potential of -0.24 V was found for the reduction of Cu(II)-AcHWH to Cu(I)-AcHWH, whereas the potential for the oxidation of Cu(I)-AcHWH to Cu(II)-AcHWH, was found to be 0.22 V.[135] Such a large difference was indicative of an irreversible one-electron transfer involving critical changes in the conformation of the metal complex, coupled with the protonation of the amide function bound to the Cu(II) ion. The reduction potential predicted by DFT analyses was -0.23 V, in good agreement with the experimental results. The *N*-terminal protected peptides thus present remarkably higher reduction potentials than those of ATCUN peptides; this difference can be explained by their less rigid conformation and the binding of only one amide function (see section **3.3.1**). Although the potential is still negative, the reduction of the corresponding Cu(II)-complexes can be achieved in the presence of high amounts of ascorbate or other reducing agents, with concomitant production of ROS.

Finally, the capacity of the chelating agents to prevent the production of hydroxyl radicals in the presence of ascorbate (300 μM) was assessed through the emission of the hydroxylated product 7-OHCCA (λ_{exc} = 385 nm, λ_{em} = 500 nm; see section **3.3.1**) of coumarin-3-carboxylate; the results obtained are shown in **Figure 3.32**. For the ascorbate-Cu(II) system (light-blue dots in **Figure 3.32**), the characteristic emission of 7-OHCCA increased linearly during the first 15 minutes, indicating that hydroxyl radicals were produced. Then, the emission reached a plateau and subsequently started to decrease, probably as the result of the oxidation of 7-OHCCA.

Upon incubation of copper with 1.1 equivalents of AcHK^{c}H and AcHK^{d}H, inhibition rates of 11% (dark-blue dots) and 47% (red dots) were respectively observed (calculated using **Equation 3.6**, see section **3.3.1**). Thus, both the UV-Vis and fluorescence data indicate that AcHK^{d}H is a more effective hydroxyl-radical inhibitor than AcHK^{c}H. However, these *N*-terminal protected tripeptides display poorer ROS-inhibition properties than ATCUN chelating agents, which may be explained by their higher flexibility and/or the involvement of only one negatively-charged amide function for copper binding.[135]

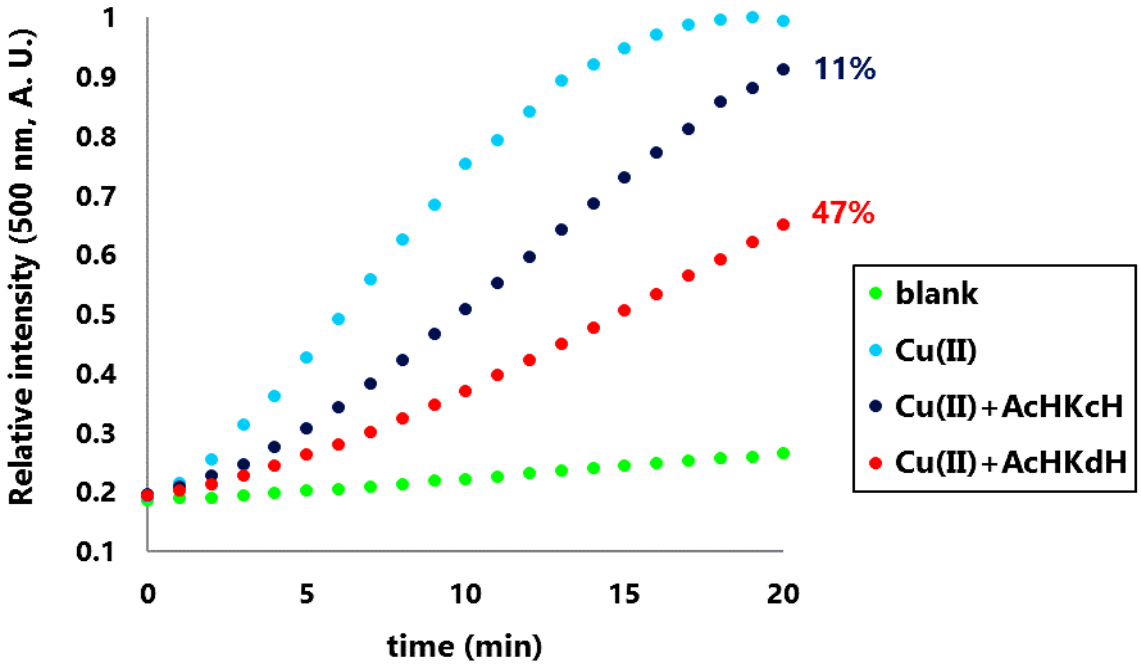

Figure 3.32: Cu(II)-induced production of hydroxyl radicals followed by the emission of 7-OHCCA (λ_{exc} = 385 nm, λ_{em} = 500 nm; green dots = free 7-OHCCA) in the presence and absence of the *N*-terminal protected tripeptides (dark-blue dots = AcHK^{c}H; red dots = AcHK^{d}H). The inhibition rates of the production of hydroxyl radicals are indicated as percentages, in relation to free copper (light-blue dots that are defined as 0% inhibition). Phosphate buffer 100 mM (pH 7.4).

3.3.3 Fluorescent properties of Fluo-His-Lys(Coum)-His-NH_2 (FluoHK^{c}H) in the presence and absence of Cu(II)

As discussed in section **3.1.4**, since copper and its regulation are essential for living organisms, the development of Cu-sensitive fluorescent probes has received worldwide attention. In that context, the potential Cu(II)-probe, namely Fluo-His-Lys(Coum)-His-NH_2 (**FluoHK^{c}H**), containing both a coumarin and a fluorescein unit, was designed and synthesised (see **Chapter 2**). In this section, the analysis of its possible Förster resonance energy transfer (FRET) properties and their variation in the presence of Cu(II) is described.

Coumarins and fluorescein derivatives are very commonly used for biological, pharmaceutical and biomedical applications. Coumarin compounds display fluorescent properties that can be (fine-)tuned using different substituents.[141,142] Furthermore, they

may exhibit interesting pharmacological activities (see **Chapter 2**).[137-140] Fluorescein is used for the labelling of proteins,[239] imaging,[240] the detection of liposome lysis[241,242] or for the design of fluorescent probes.[202] Fluorescein displays an intense fluorescent emission, a high water solubility and can easily be bioconjugated; moreover, it can be excited with a standard argon-ion laser.[202,243] Nevertheless, fluorescein can suffer from photobleaching effects and can self-quench.[202]

The two pH-dependent isomers depicted in **Figure 3.33** are usually considered in aqueous solutions of fluorescein.[243] At low pH, fluorescein is non-emissive, whilst a bright green-emissive isomer including a lactone ring is present in neutral or alkali solutions. Such pH-dependent behaviour has been exploited for its application as an acid-base indicator.[202,243]

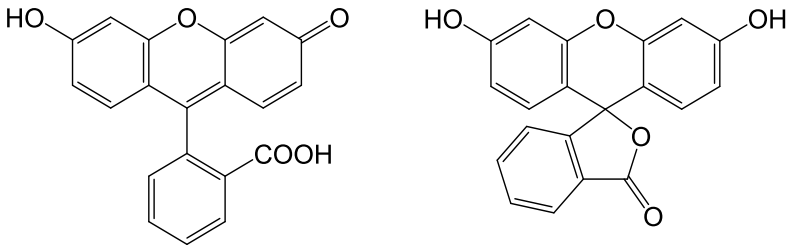

low pH neutral or high pH

Figure 3.33: Tautomeric forms of fluorescein at acidic (**left**) or neutral/alkali pH (**right**).

The maximum absorption wavelength of carboxyfluorescein is 492 nm (ε_{492} = 5.86 × 10^4 $M^{-1}cm^{-1}$), which is associated with an emission wavelength of 521 nm.[208] These spectroscopic data were also found for FluoHK^{c}H.

Although the difference between the maximum emission wavelength of coumarin (410 nm, acting as the donor) and the excitation wavelength of fluorescein (492 nm, acting as the acceptor) is significant (*viz.* 82 nm difference), a certain overlap is though expected. Hence, upon excitation of the fluorescent peptide at 300 nm (λ_{exc} of coumarin), fluorescence emission at 521 nm (the λ_{em} of fluorescein) is anticipated.

The potential FRET properties of FluoHK^{c}H was investigated by comparison with H-His-Lys(Coum)-His-OH (**HK^{c}H**) and Fluo-His-Nle-His-NH_2 (**FluoHJH**) (**Figure 3.34**). These peptides, whose synthesis is described in **Chapter 2**, indeed contain only one dye of the FRET pair, namely coumarin for HK^{c}H and fluorescein for FluoHJH, and therefore cannot undergo any FRET process. Accordingly, the emission at 410 nm should be weaker for FluoHK^{c}H than for HK^{c}H due to a non-radiative energy transfer from the

coumarin donor to the fluorescein acceptor. In contrast, the emission at 521 nm for FluoHK^{c}H should be enhanced compared to that of FluoHJH, in which no energy transfer can take place.

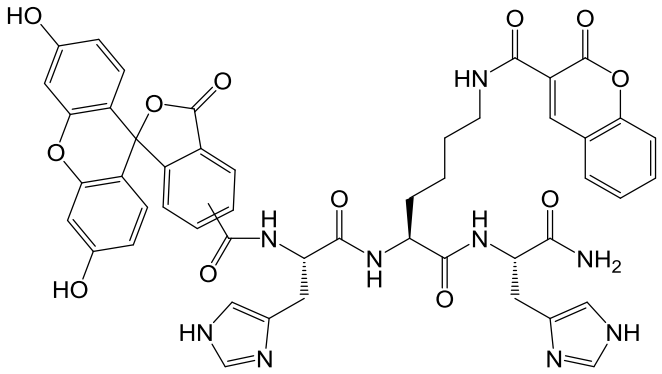

Fluo-His-Lys(Coum)-His-OH
(**FluoHK^{c}H**)

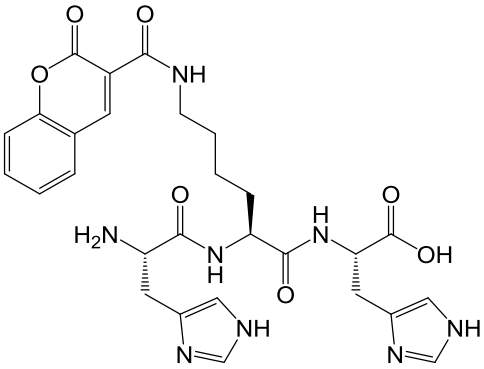

H-His-Lys(Coum)-His-OH
(**HK^{c}H**)

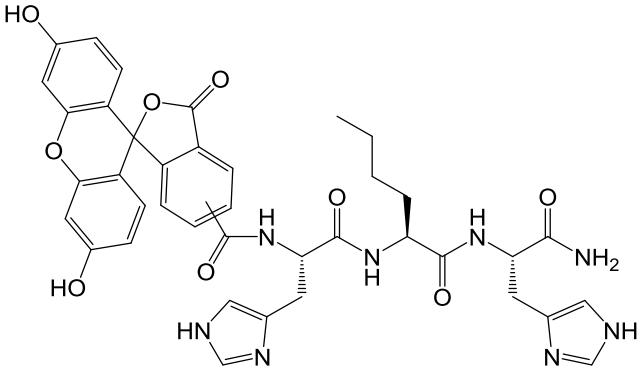

Fluo-His-Nle-His-NH_2
(**FluoHJH**)

Figure 3.34: Peptides containing one or two fluorescent dyes (coumarin - Coum and/or fluorescein - Fluo).

For these studies, HEPES solutions (pH 7.4) of the peptides were excited at 300 nm (the excitation wavelength of the coumarin donor), and the emission of either the coumarin or the fluorescein moiety was registered. Expectedly, the intensity of HK^{c}H at 410 nm (the emission wavelength of coumarin) was 8.7-fold higher than that of FluoHK^{c}H (**Figure 3.35**).

However, the emission intensity at 521 nm (corresponding to the emission of fluorescein) was 1.4-time higher for FluoHJH than for FluoHK^{c}H. A control experiment with 5(6)-carboxyfluorescein and coumarin-3-carboxylic acid showed no significant effect (for instance quenching) on the emission of the fluorescein dye.

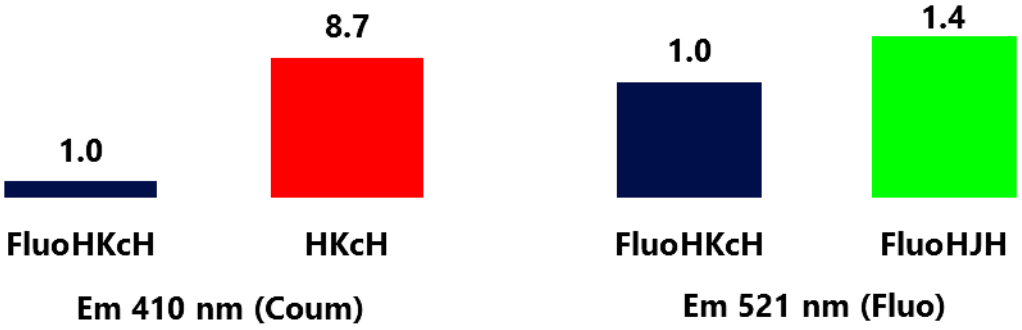

Figure 3.35: Relative intensities of **left**: FluoHK^{c}H and HK^{c}H (λ_{em} = 410 nm); **right**: FluoHK^{c}H and FluoHJH (λ_{em} = 521 nm). 10 mM HEPES (pH 7.4); λ_{exc} = 300 nm.

Moreover, the fluorescein emission of FluoHJH was 18 times higher than that of coumarin for HK^{c}H, as the result of the much larger quantum yield of fluorescein compared with that of coumarin (**Figure 3.36**).[208] Consequently, FluoHK^{c}H was not appropriate for its use as a ratiometric probe as similar intensities are desirable for the two FRET-pair dyes.

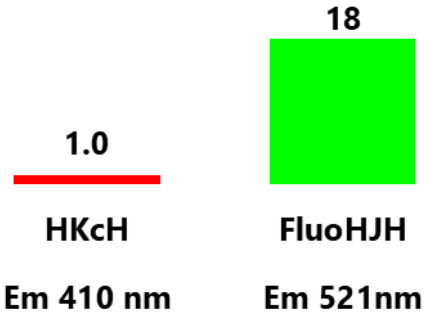

Figure 3.36: Relative intensities of HK^{c}H (λ_{em} = 410 nm) and FluoHJH (λ_{em} = 521 nm) in 10 mM HEPES (pH 7.4). λ_{exc} = 300 nm was used for both peptides

The variation of the emission intensities of FluoHK^{c}H upon addition of Cu(II) was then studied. A HEPES-buffered solution (pH 7.4) of the peptide was titrated with $CuCl_2$, by registering the fluorescence intensities at 410 and 521 nm upon excitation at 300 nm. **Figure 3.37** represents the variation of the ratio of the intensities at 410 and 521 nm (I_{410}/I_{521}) with respect to the number of equivalents of added Cu(II). I_{410}/I_{521} increased gradually up to 4.2-times the initial value. This intensification of the fluorescence signal was due to 184% intensity increase at 410 nm associated with 46% intensity decrease at 521 nm. This could be explained by *i)* the (partial) deactivation of a FRET-like energy transfer process or *ii)* a differential Cu(II)-quenching effect, *viz.* the metal had a stronger quenching effect on fluorescein. The apparent lower copper influence on coumarin

might be due to its longer distance from the metal binding site, compared to fluorescein.

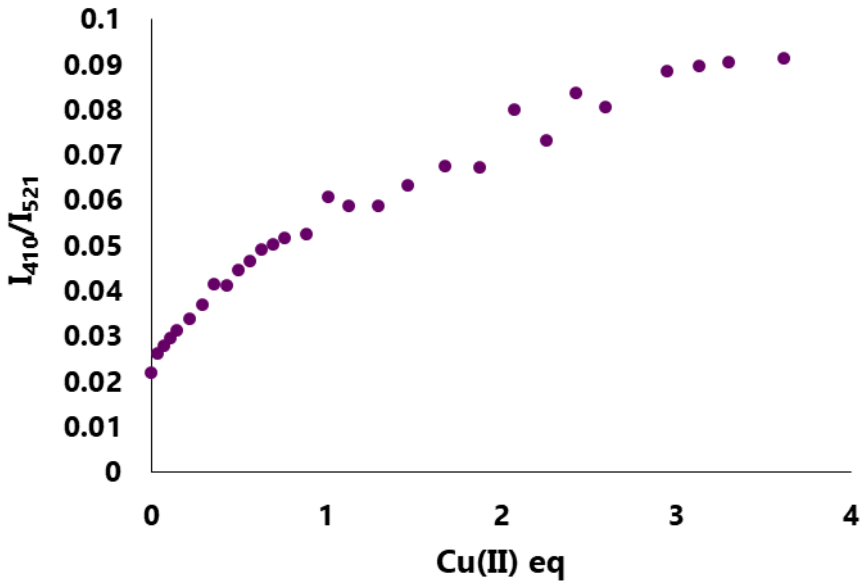

Figure 3.37: Variation of the ratio of the intensities at 410 and 521 nm (I_{410}/I_{521}) for FluoHK^{c}H upon addition of increasing amounts of Cu(II) in 100 mM HEPES (pH 7.4); λ_{exc} = 300 nm.

Despite the unfavourable fluorescence properties (namely the lack of intensity enhancement for the fluorescein acceptor, the low fluorescent emission of the coumarin dye and unconfirmed FRET) of FluoHK^{c}H, these results are encouraging for the future design of two-fluorophore probes using the His-Lys-His scaffold. Ratiometric fluorescent probes containing two non-interacting dyes (*viz.* an analyte-sensitive reporter and an analyte-insensitive reference) represent an alternative to FRET-based sensors for different ions or other analytes,[188] for instance Pb(II),[244] protons,[245] glucose[246] or dioxygen.[247]

3.4 Concluding remarks

Cu(II) coordination of both *N*-terminal free and *N*-terminal protected peptides was investigated by mass spectrometry, UV-Vis, circular dichroism, nuclear magnetic resonance and electron paramagnetic resonance spectroscopies.[210] The Cu(II)-binding affinities of the peptides were studied by fluorescence spectroscopy and compared with that of Aβ(1-40); competitive binding studies with the non-aggregating Aβ(1-16) fragment, which contains the Cu(II)-binding sequence, were also carried out. The capacity of the tripeptides to prevent the Cu(II)-induced formation of oligomeric Aβ(1-40) was examined by ThT kinetic measurements. Finally, the inhibition of the copper-catalysed production of reactive oxygen species (ROS) was assessed through the consumption of ascorbate; the formation of hydroxyl radicals was assessed by the emission of 7-hydroxycoumarin-3-carboxylate (7-OHCCA).

The *N*-terminal free peptides HAH, HWH and HK^{c}H bind one Cu(II) ion through the *N*-terminal amino group, two amide functions (that of the central amino acid and of His3) and the imidazole ring of His3, generating a 4N ATCUN coordination environment.[210] This rigid and highly stable motif provides Cu(II)-binding affinity constants that are 1 to 2 orders of magnitude higher than that of Aβ(1-40) and of the promising anti-AD ionophore clioquinol.[122,228,248] Moreover, it has been demonstrated that the presence of a His1 in an ATCUN peptide enables a completely different binding mode (with lower affinity) at very high peptide/copper ratios.

HK^{c}H was able to remove Cu(II) ions bound to Aβ(1-16), while the addition of up to 4 equivalents of Aβ(1-16) to the Cu(II)-HK^{c}H complex did not result in metal displacement.[210] Interestingly, the presence of a His residue in position 1, although not participating directly in copper binding, was found to increase the affinity of the peptides towards Cu(II); for instance, GWH exhibited an affinity constant one order of magnitude lower than that of HWH.

The addition of 2 equivalents of the ATCUN tripeptides prevented the Cu(II)-induced stabilisation of Aβ(1-40) oligomeric forms, restoring the natural aggregation of the peptide, as deduced from ThT assays.[210] Moreover, all tripeptides efficiently inhibited the production of ROS (85-97% inhibition), and particularly of the generation of very harmful hydroxyl radicals. Hence, the ATCUN His-Xaa-His tripeptides possess two of the major properties required for drugs aimed at reducing the toxicity associated to the interaction of Aβ with copper: *i)* the removal of Cu(II) ions bound to Aβ and *ii)* the

inhibition of ROS production. Furthermore, it is not expected that the ATCUN His-Xaa-His tripeptides can remove copper from the strong Cu-chelating metalloproteins found in cells (which is essential for their biological activity). The ATCUN His-Xaa-His sequence thus represents a promising building block for the design and development of drugs against AD oxidative stress.

At high Cu(II)-peptide ratios, the *N*-terminal free peptides formed a different, 3N2O square-pyramidal coordination sphere. Such species are likely to present different electronic features and therefore their redox properties should be carefully investigated.

The *N*-terminal protected (acetylated) peptides AcHK^{c}H and AcHK^{d}H generated 1:1 Cu(II) complexes in a 3N1O coordination environment, which involved both imidazole rings (of His1 and His3), an amide function and the carbonyl oxygen of the central amino acid. A Cu(II)-binding affinity constant one order of magnitude higher than that of Aβ(1-40) was determined for AcHK^{c}H. For AcHK^{d}H, the emission intensity data could not be fitted. Competitive binding studies to evaluate the ability of the protected tripeptides to displace Cu(II) from Aβ(1-16) were unsuccessful, due to precipitation. Aβ(1-16) was not able to extract Cu(II) ions bound to AcHK^{d}H, even at high concentrations; the formation of other (ternary) species between AcHK^{c}H and Aβ(1-16) most likely takes place. 2 equivalents of the acetylated tripeptides were not able to restore the normal fibrillation of Aβ(1-40) in solutions containing Cu(II) ions. More in-depth studies, for instance using the weak copper-binding glycine or by potentiometry, are needed to determine the actual Cu(II)-chelating affinities of AcHK^{c}H and AcHK^{d}H; the mechanism upon which they promote the precipitation of Aβ(1-16) should also be thoroughly investigated.

The *N*-protected tripeptides were weak inhibitors of the Cu-mediated generation of ROS, suggesting a high copper reduction potential (upon binding). Such remarkable difference in the redox properties highlighted the significant impact of the ligands involved in the coordination of copper on the electronic properties of the Cu(II)-peptide complexes. Important redox activities and ROS productions have been reported for Cu(II)-complexes from other ATCUN tripeptides; these features depended markedly on the stereochemistry of the amino acid residues and the surrounding charge density.[249]

Finally, FluoHK^{c}H was studied as a potential FRET-based fluorescent probe for Cu(II). FluoHK^{c}H contains a coumarin (λ_{exc} = 300 nm, λ_{em} = 410 nm) and a fluorescein (λ_{exc} = 492 nm, λ_{em} = 521 nm) groups. Upon addition of $CuCl_2$, the I_{410}/I_{521} intensity ratio increased 4.2-fold through a combined increase of the emission at 410 nm and decrease of the intensity at 521 nm.

A FRET process could not be confirmed for FluoHK^{c}H. Upon exciting the coumarin moiety of FluoHK^{c}H, the fluorescein emission at 521 nm was lower than that of FluoHJH, which only possessed fluorescein; an enhancement of the emission intensity due to the energy transfer from the coumarin donor to the fluorescein acceptor was expected. Besides, fluorescein emission was much higher than that of coumarin, hence discarding the potential application of this peptide as a FRET-based probe. The utilisation of an acceptor non-absorbing at the excitation wavelength of the donor would also be more adequate.

A tripeptide like RhoB-His-Lys(Fluo)-His-NH_2 (RhoB = rhodamine B), whose synthesis has been attempted with no success (see **Chapter 2**) would probably be a more suitable FRET-based probe candidate. Fluorescein and rhodamine derivatives represent another widely employed FRET pair, fluorescein acting as the donor and rhodamine as the acceptor; fluorescein and rhodamine present similar and highly intense fluorescence emissions.[202,208]

Alternatively, substituted coumarins may provide efficient donors for fluorescein, with much higher intensities than that afforded by the parent unsubstituted coumarin described in this chapter.[141,142] In addition, a larger overlap between the emission of the donor and the excitation of the acceptor is desirable. However, the dependence of I_{410}/I_{521} on the concentration of Cu(II) found for FluoHK^{c}H is encouraging and validates the approach combining two different fluorophores in a single chelating peptide.

3.5 Experimental section

3.5.1 Reagents, solvents and equipment

Table 3.2: Reagents and solvents used for the work described in this chapter.

Brand	Products
Acros Organics	coumarin-3-carboxylic acid
Sigma Aldrich	ascorbate, D_2O, HEPES, HFIP, ThT, Tris-HCl, TSP
Fisher Scientific	DMSO, PBS
Panreac	$CuCl_2 \cdot 2H_2O$
Scharlau	acetone

Table 3.3: Instrumentation used for the work described in this chapter.

Instrument	Brand	Model
Analytical balance	A & D Instruments	GR-200-EC
Gram-scale balance	Sartorius	Basic BA 110
Sonicator	Fisherbrand	FB15051
Shaking Block Heater	Eppendorf	ThermoMixer C

Milli-Q H_2O (resistivity > 18 MΩ·cm) was produced by filtering deionised water with a Milli-Q Plus (Millipore) system. $CuCl_2 \cdot 2H_2O$ was used as the source of copper for all the studies.

H-His-Ala-His-OH (HAH), H-His-Trp-His-OH (HWH), H-His-Lys(Coum)-His-OH (HK^cH) and H-Gly-Trp-His-OH (GWH) peptides were purchased from GeneCust (Luxembourg) as hydrochloride salts and were used as received. Ac-His-Lys(Coum)-His-OH ($AcHK^cH$), Ac-His-Lys(4DMN)-His-OH ($AcHK^dH$), Ac-His-Lys(4DMN)-His-NH_2 ($AcHK^dH$-NH_2), Fluo-His-Nle-His-NH_2 (FluoHJH) and Fluo-His-Lys(Coum)-His-NH_2 ($FluoHK^cH$) were synthesised as described in **Chapter 2**, and obtained as trifluoroacetate salts. Aβ(1-40) was acquired from Bachem as a trifluoroacetate salt, while Aβ(1-16) was purchased from Innovagen. Chelex® 100 resin (200-400 mesh, sodium form) was purchased from Bio-Rad.

The concentrations of the stock solutions of all peptides were determined spectrophotometrically in buffer at pH 7.4 using the molar extinction coefficients ε(Trp, 280 nm) = 5690 M^{-1} cm^{-1}, ε(Lys(Coum), 300 nm) = 12300 M^{-1} cm^{-1}, ε(Lys(4DMN), 441 nm) = 8400 M^{-1} cm^{-1} and ε(Fluo, 492 nm) = 58600 M^{-1} cm^{-1}.

3.5.2 Procedures, instrumentation and techniques

Electrospray ionisation mass spectrometry (ESI-MS)

ESI mass spectra were recorded on an LC/MSD-TOF spectrometer from Agilent Technologies equipped with an electrospray ionisation (ESI) source at the Serveis Cientificotècnics of the Universitat de Barcelona (CCiTUB). The spectra were acquired in positive-ion mode at a voltage of either 175 or 215 V. The peptide solutions with 2 eq of $CuCl_2$ (250 μM and 500 μM, respectively) were prepared in Milli-Q water, and the pH was adjusted to 7.4 using NaOH.

UV-Vis spectroscopy

Absorbance spectra were recorded on a Varian Cary 100 Scan spectrophotometer using a quartz cuvette (1 cm pathlength) at rt.

Determination of the stoichiometry of the Cu(II)-peptide complexes

Peptide solutions (1 mM) in HEPES (100 mM, pH 7.4) were titrated with aqueous $CuCl_2$ (50 mM). The spectra were registered from 800 to 200 nm. The data at 405 nm and the absorbance values corresponding to the d-d bands of the Cu(II)-peptide complexes were separately plotted against the number of eq of Cu(II). The concentration of peptide was kept constant by adding a 3 mM peptide solution (prepared in 100 mM HEPES, pH 7.4).

Ascorbate consumption

The ascorbate consumption reactions were performed in 100 mM phosphate buffer (pH 7.4) pre-treated with Chelex 100 resin (Bio-Rad). The stock solutions of the peptides and of $CuCl_2$ were prepared in Milli-Q H_2O. The ascorbate solutions were freshly prepared in Chelex-treated phosphate buffer, prior to each measurement. The final concentrations were 1 μM $CuCl_2$, 1.1 μM peptide and 100 μM ascorbic acid. Absorbance measurements were done from 350 to 200 nm under aerobic conditions, during a period of 30 min. The absorbance data obtained at 265 nm were plotted against time. The inhibition rates were calculated applying **Equation 3.5** (see section **3.3.1**).

Circular Dichroism (CD)

CD experiments were run from 750 to 240 nm using a JASCO J-815 circular dichroism spectropolarimeter and 1 cm quartz cuvettes, with a scanning speed of 200 nm per minute. Peptide solutions (125 μM) were prepared in 100 mM HEPES (pH 7.4) and were subsequently titrated with aqueous $CuCl_2$ (2.5 mM). The concentration of peptide was kept constant along the titration.

Diffuse reflectance UV-Vis spectroscopy

1 mM suspensions of CuAcHK^{c}H and CuAcHK^{d}H were prepared and centrifuged (13300 rpm, 30 min). The supernatants were discarded, and the solids were dispersed in Al_2O_3. The resulting mixture was homogenised, and the UV-Vis spectra were registered. Al_2O_3 was used as a blank.

Nuclear Magnetic Resonance (NMR)

^1H and ^{13}C NMR experiments were performed on a Bruker Avance III 400 MHz spectrometer equipped with a 5 mm cryoprobe (Prodigy) broadband (CPPBBO BB-$^1H/^{19}F$/D) with gradients in Z at the Centres Científics i Tecnològics of the Universitat de Barcelona (CCiTUB). ^1H NMR spectra were recorded at 400 MHz, while ^{13}C NMR spectra were registered at 100.6 MHz with proton decoupling. Solvent suppression was achieved using a PRESAT pulse sequence. The NMR data were analysed using

MestReNova 9.1.0. Solutions of 10 mM peptide with 0.5-1% $CuCl_2$ in D_2O were adjusted to pH 7.4, and measured with an insert containing a 5 mg·mL^{-1} solution of [D_4]-3-(trimethylsilyl)propanoic acid (TSP) as an internal reference (D_2O δ 4.79 ppm for ^1H NMR). It should be noted that, even though the measurements were made in D_2O, it was decided to use the notation pH.

EPR studies

$CuCl_2$-peptide samples in 1:1.1 (5 mM Cu^{2+}) or 1:100 (2 mM Cu^{2+}) ratios were used in 100 mM HEPES buffer (pH 7.4). X-band EPR spectra of frozen solutions were registered at 77 K on a Bruker ESP300E spectrometer. Processing and simulation of the spectra were carried out using Bruker WINEPR 2.11 software.

Fluorescence spectroscopy

Fluorescence experiments were performed at rt using a HORIBA Jobin–Yvon iHR320 spectrofluorometer under aerobic conditions. The instrument excitation and emission slits were set at 5 nm.

Determination of the conditional binding constants:

Peptide solutions (10 μM) were titrated with $CuCl_2$ (150 μM); the peptide concentration was kept constant at 10 μM by adding a 30 μM solution of the peptide. All solutions were prepared in 100 mM HEPES buffer (pH 7.4). The emission spectra were registered using the following excitation and emission wavelengths (voltage of the photomultiplier detector = 950 V): λ_{exc} = 280 nm, λ_{em} = 300-600 nm for HWH and GWH; λ_{exc} = 300 nm, λ_{em} = 320-570 nm for HK^{c}H and AcHK^{c}H; λ_{exc} = 441 nm, λ_{em} = 460-700 nm for AcHK^{d}H and AcHK^{d}H-NH_2. The apparent affinity constants, K^{app}, of the Cu(II) complexes were calculated by fitting the fluorescence data (at λ_{em} = 360, 410 and 547 nm for the peptides containing indole, coumarin or 4DMN probes, respectively) to **Equation 3.3** (see section **3.3.1**). The conditional affinity constants, K^{cond}, were then determined by using **Equation 3.4** (see section **3.3.1**).

Evaluation of the Cu(II)-binding affinity of HAH by competitive studies with HWH/HK^{c}H:

Cu(II)-HWH or Cu(II)-HK^{c}H solutions (10 μM) were titrated with HAH (200 μM); the concentrations of HWH/HK^{c}H and of Cu(II) were kept constant at 10 μM by adding a 30 μM Cu(II)-HWH or Cu(II)-HK^{c}H solution, respectively. All solutions were prepared in 100 mM HEPES buffer (pH 7.4). The emission spectra were registered using the following excitation and emission wavelengths (voltage of the photomultiplier detector = 950 V): λ_{exc} = 280 nm, λ_{em} = 300-600 nm for HWH; λ_{exc} = 300 nm, λ_{em} = 320-570 nm for HK^{c}H. The emission values at λ_{em} = 360 nm (HWH) and λ_{em} = 410 nm (HK^{c}H) were plotted against the number of eq of HAH.

Competitive binding studies with Aβ(1-16):

Preparation of the Aβ(1-16) stock solution: solid Aβ(1-16) (1 mg) was dissolved in 10 mM HEPES (pH 7.4), and the resulting solution was sonicated for 30 min. The concentration was determined spectrophotometrically using the molar extinction coefficient ε(Abs_{276} – Abs_{296} = 1410 M^{-1} cm^{-1}).

Titration of Cu(II)-Aβ(1-16) with the chelating peptides: Cu(II)-Aβ(1-16) (10 μM) was titrated with the chelating peptides (HK^{c}H, AcHK^{c}H or AcHK^{d}H, 150 μM); the concentration of Aβ(1-16) and of Cu(II) were kept constant at 10 μM by adding a 30 μM Cu(II)-Aβ(1-16) solution. All solutions were prepared in 10 mM HEPES buffer (pH 7.4). The emission spectra were registered using λ_{exc} = 275 nm from 280 to 450 nm (voltage of the photomultiplier detector = 950 V). The emission intensities at λ_{em} = 305 nm (Tyr) were plotted against the number of eq of HK^{c}H.

Titration of Cu(II) complexes of the chelating peptides with Aβ(1-16): the Cu(II) complexes of the chelating peptides (HK^{c}H, AcHK^{c}H and AcHK^{d}H, 10 μM) were titrated with Aβ(1-16) (150 μM); the concentration of the chelating peptides and of Cu(II) were kept constant at 10 μM by adding a 30 μM Cu(II)-peptide solution. All solutions were prepared in 10 mM HEPES buffer (pH 7.4). The emission spectra were registered using the following excitation and emission wavelengths (voltage of the photomultiplier detector = 950 V): λ_{exc} = 300 nm, λ_{em} = 320-570 nm for HK^{c}H and AcHK^{c}H; λ_{exc} = 441 nm, λ_{em} = 460-700 nm for AcHK^{d}H. The emission intensities at λ_{em} = 410 nm (HK^{c}H and AcHK^{c}H) and λ_{em} = 547 nm (AcHK^{d}H) were plotted against the number of eq of Aβ(1-16).

Inhibition of the generation of hydroxyl radicals monitored by the emission of 7-hydroxycoumarin-3-carboxylate (7-OHCCA):

Single-point fluorescence measurements were carried out at rt in phosphate buffer (100 mm, pH 7.4), pre-treated with Chelex 100 resin (Bio-Rad). The emission of 7-OHCCA (λ_{exc} = 385 nm, λ_{em} = 500 nm, voltage of the photomultiplier detector = 950 V) was registered during a period of 30 min under aerobic conditions. A coumarin-3-carboxylate stock solution (5 mM) was prepared in phosphate buffer as described previously. The stock solutions of the peptides and of $CuCl_2$ were prepared in Milli-Q H_2O. The ascorbate solutions were freshly prepared in Chelex-treated phosphate buffer, immediately prior to each measurement. The final concentrations were 1 μM $CuCl_2$, 1.1 μM peptide, 300 μM ascorbic acid, and 1 mM coumarin-3-carboxylate. The inhibition rates were calculated applying **Equation 3.6** (see section **3.3.1**).

Study of the fluorescence properties of FluoHK^{c}H:

Comparative analyses of the emission intensities of FluoHK^{c}H, HK^{c}H and FluoHJH: FluoHK^{c}H, HK^{c}H and FluoHJH solutions (5 μM) were prepared in 10 mM HEPES buffer (pH 7.4) and their emission intensity was measured from 320 to 700 nm using λ_{exc} = 300 nm with the photomultiplier detector set at 700 V.

Titration of FluoHK^{c}H with $CuCl_2$: A 10 μM FluoHK^{c}H solution in 100 mM HEPES buffer (pH 7.4) was titrated with $CuCl_2$ (150 μM); the peptide concentration was kept constant at 10 μM by adding a 30 μM solution of the peptide. The sample was excited at 300 nm and the emission was registered from 320 to 600 nm with the voltage of the photomultiplier detector set at 700 V. The ratio of the intensities at 410 and 521 nm was plotted against the number of eq of Cu(II).

In vitro Aβ(1–40) aggregation kinetics

Preparation of aggregate-free amyloid-β peptide:

Aβ(1-40) (5 mg) was dissolved in 1,1,1,3,3,3-hexafluoro-2-propanol (HFIP; 500 μL) under vigorous shaking at rt for 1 h, after which it was sonicated for 30 min. The solution was further shaken for 1 h and subsequently kept at 4 ºC for 30 min to avoid solvent evaporation during aliquoting. Aliquots of soluble Aβ(1-40) were collected and HFIP was evaporated in air. The resulting solid Aβ(1-40) aliquots were stored at –20 ºC, and the amount of protein per sample was calculated spectrophotometrically, dissolving one aliquot in 100 mM HEPES (pH 7.4) and using the molar extinction coefficient ε(Tyr, 280 nm) = 1490 M^{-1} cm^{-1}.

Aggregation studies:

Aliquots of monomeric Aβ(1-40) were dissolved in DMSO (20-50 μL) using sonication for 10 min. Stock solutions containing Aβ(1–40) and ThT in the appropriate concentrations were prepared just before the preparation of the samples. The final samples contained 20 μM Aβ(1–40), 25 μM ThT, 20 μM $CuCl_2$ and 40 μM tripeptide.

For the experiments with HAH, HWH and HK^{c}H, the final solutions were prepared in 10 mM Tris-HCl (pH 7.4) and contained 5% DMSO. The samples were stirred at 1400 rpm at 37 ºC, and the aggregation process was then followed by ThT fluorescence (λ_{exc} = 445 nm; λ_{em} = 480 nm), using an Aminco Bowman Series 2 luminescence spectrometer. Emission measurements were performed every 10 min.

For the experiments with HAH, AcHK^{c}H and AcHK^{d}H, the final solutions were prepared in 96-well plates (Clearline® 131012C) using 1X PBS buffer (pH 7.4) and contained 1.4% DMSO. The measurements were carried out using a BMG Labtech FLUOstar Omega plate reader in bottom optics configuration with 440/490 nm excitation/emission optics (700 rpm shaking, 37 ºC). Endpoint measurements were performed in the plate reader immediately after sample preparation and were performed every 6 min for 20 h.

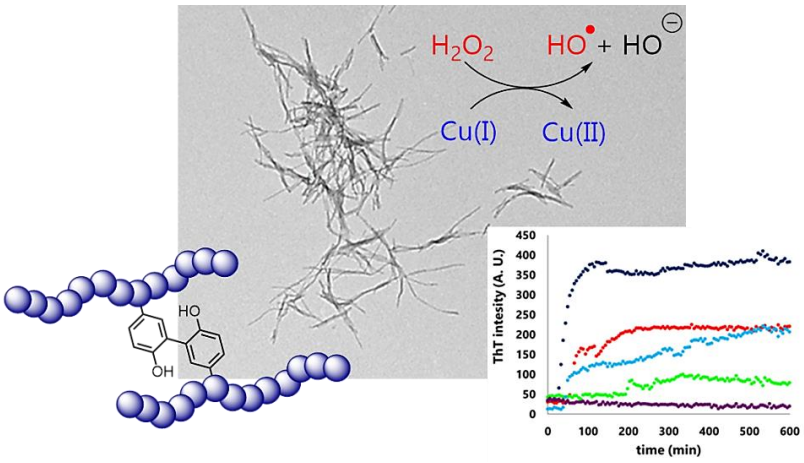

4. Copper-induced oxidative formation of dityrosine cross-links in β-amyloid

4. Copper-induced oxidative formation of dityrosine cross-links in β-amyloid

4.1 Introduction

4.1.1 Oxidation products of Aβ peptide: dityrosine cross-links

As described in **Chapter 3**, the Cu-Aβ complex is able to catalyse the reduction of atmospheric O_2 and produce reactive oxygen species (ROS) in the presence of ascorbate. The generation of ROS may lead to oxidative stress *in vivo*. Oxidative damage to biomolecules includes lipid peroxidation, protein carbonylation and DNA cleavage, among other deleterious effects.

The Aβ peptide itself can also be the target of oxidative ROS. The Cu-Aβ complex has been described by some authors as a radical cage, where most of the radical species react directly with the Aβ peptide and hence do not reach the solution.[250] The amino-acid residues that are most susceptible to oxidation are those involved in copper binding, namely the histidines 6, 13 and 14 (which are oxidised to 2-oxohistidine), and aspartate 1 (which yields pyruvate). The cleavage of Aβ at different positions can also occur.[250]

Another relevant protein oxidation mechanism is the metal-catalysed oxidation (**MCO**). In the presence of an electron acceptor, metal ions can catalyse the oxidation of proteins.[251] For this reason, MCO systems have been used to mimic biological oxidations.

Although the Aβ tyrosine residue (Tyr10) is not directly involved in copper binding, it is one of the amino-acid residues that is most sensitive to oxidation. Indeed, it can undergo MCO to give a number of oxidised derivatives (**Figure 4.1**): nitrotyrosine, dityrosine, 3,4-dihydroxyphenylalanine (DOPA), 2,4,5-trihydroxyphenylalanine (TOPA), dopamine, dopamine quinone, isodityrosine, pulcherosine and so on.[252] Among them, dityrosine and isodityrosine are the most stable oxidation products.

Dityrosine is generated through the formation of an interpeptidic bond. Inter-amino acid cross-links have been found in various enzymes and proteins, where they provide novel motifs and structures.[253] Besides, dityrosine-containing materials, such as

collagen and spider silk, display remarkable mechanical properties like strength or elasticity.[254,255]

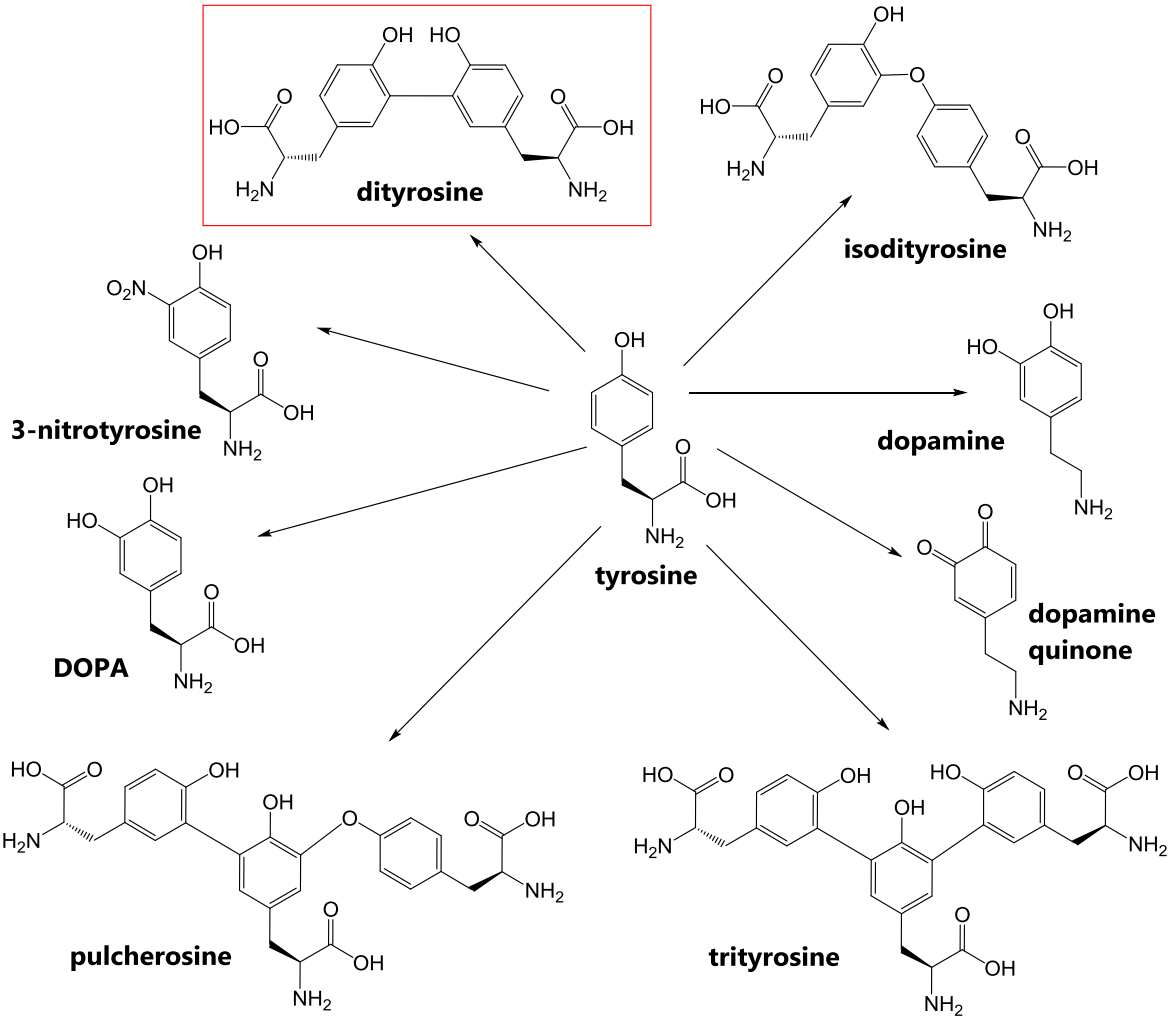

Figure 4.1: Examples of tyrosine oxidation products.

Importantly, covalent dityrosine cross-links of Aβ have been found in cerebrospinal fluid (CSF) of AD brains, while such connections are rarely detected in age-matched (healthy) controls.[90,256] The high concentration of copper ions co-localised with Aβ is thought to trigger the formation of dityrosine cross-links via an MCO pathway, as well as other oxidation products. The source of H_2O_2 required for the oxidation is also a matter of debate. H_2O_2 might be generated by microglia, from impaired mitochondrial function or from the Cu-Aβ redox activity itself, as described in **Chapter 3**. Dityrosine has been proposed as a potential biomarker for oxidative stress and for some diseases, as it has also been found in Parkinson's disease and atherosclerosis.[257-260]

4.1.2 Mechanism of the formation of dityrosine cross-links by MCO systems

Both dityrosine and covalently-linked dimers of Aβ peptide have been produced and studied *in vitro* using MCO systems, as well as other oxidation procedures. The generation of dityrosine is known to occur through a long-lived tyrosyl radical, which is delocalised over the whole aromatic ring. Condensation of two tyrosyl radicals yields the irreversible C-C covalent bond at the ortho position, producing the dityrosine scaffold (**Figure 4.2**).

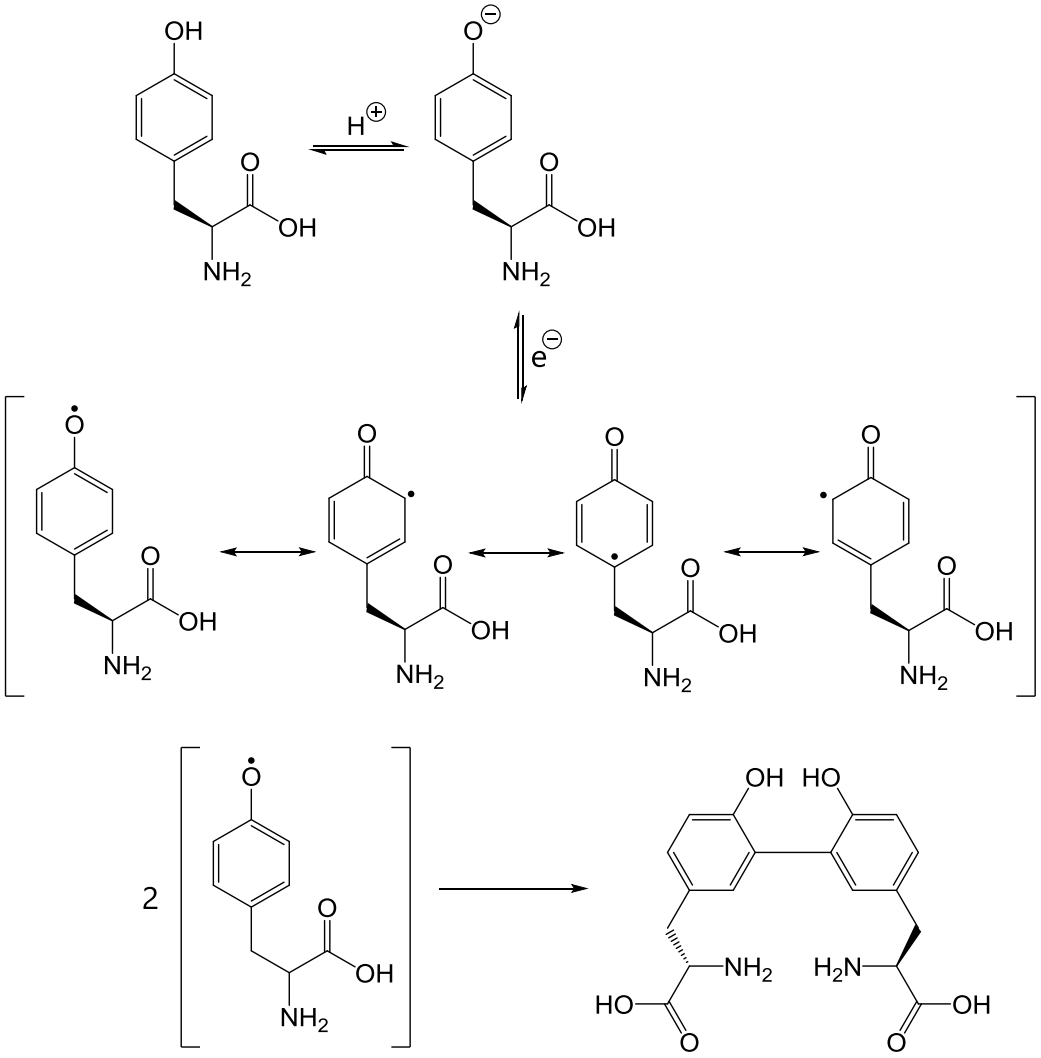

Figure 4.2: Condensation of tyrosyl radicals.

The mechanism of the copper-catalysed oxidation of tyrosine to dityrosine is not well understood as many different products are formed. Kato and Kitamoto reported that the production of cross-links in lens proteins was specific for the Cu(II)-H_2O_2 system.[251] Furthermore, Atwood and collaborators demonstrated that both copper ions and H_2O_2

were required for the production of dityrosine in Aβ, since Cu(II) or H_2O_2 alone did not produce dityrosine cross-linking.[261] Besides, they found that addition of a copper chelator inhibited dityrosine generation.

A plausible mechanism for the copper-catalysed dityrosine formation is depicted in **Figure 4.3.** First, Cu(II) is reduced by a tyrosine residue to Cu(I), while tyrosine is oxidised to a tyrosyl radical. Then, H_2O_2 re-oxidises Cu(I) to Cu(II) with concomitant production of a hydroxyl radical. If two tyrosyl radicals come into close proximity, they can condense and generate the covalently linked protein dimer.

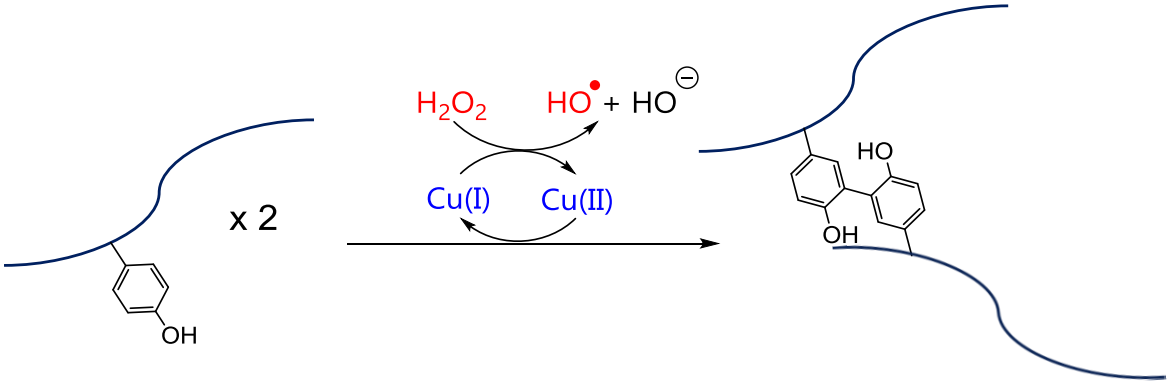

Figure 4.3: Copper-catalysed protein dimerisation by dityrosine cross-linking.

Despite the generation of hydroxyl radicals, they are arguably not involved in dityrosine cross-linking. Kato and Kitamoto reported in the work cited above that the production of dityrosine cross-links was not affected by the addition of the hydroxyl radical scavenger mannitol. As a matter of fact, the formation of hydroxyl radicals was associated with the generation of polyhydroxylated derivatives, especially DOPA.[252]

4.1.3 Physiological relevance of the dityrosine cross-links

Controversy regarding the nature and the impact of such irreversible connections on the toxicity of Aβ and its self-assembly has also arisen. Dityrosine cross-links are believed to provide fibrillary Aβ with enhanced stability to proteolysis, oxidation and low pH, and thus present reduced clearance levels.[90,256]

Furthermore, dityrosine cross-linked oligomers have been extracted from AD brains. These oligomers are resistant to harsh conditions such as formic acid, sodium dodecyl sulphate (SDS) or urea treatment. Very recently, Carulla and co-workers reported the

utilisation of synthetic dityrosine cross-linked dimers of full-length Aβ to optimise the isolation and characterisation of such bridged species.[262] In this study, they were able to unequivocally confirm the presence of covalent dityrosine links in Aβ dimers directly extracted from AD brain tissue.

Importantly, Selkoe and collaborators showed that soluble Aβ oligomers extracted directly from the affected cortex of AD patients and injected into the brain of adult rats affected learning and decreased dendritic spine density.[41] Most remarkably, the dimers resistant to lithium dodecyl sulphate (and therefore covalently bound) were the only oligomeric forms that impaired synaptic plasticity. The authors proposed amyloid plaques as reservoirs of Aβ dimers, although the release of dimers was not detected upon incubation at 37 ºC for 24 h.

Such results were in agreement with those reported by Barnham *et al.* in which a mutant Aβ, whose tyrosine residue was substituted by alanine, did not present neurotoxicity.[44] These findings suggest that covalently bound Aβ dimers rather than oligomers are the toxic species. It is possible that covalently-bound Aβ presents restricted conformations that are more toxic (because of enhanced production of ROS, membrane disruption, etc.), and that such dimers exhibit extended life-times.

Finally, some authors have suggested that dityrosine cross-linked Aβ dimers might nucleate the aggregation of the peptide, for instance into higher-order oligomeric forms or Aβ fibres; dityrosine-bridged Aβ may be amyloidogenic.[90,91] Thus, inhibition of dityrosine formation can be a novel possible strategy for the development of anti-AD therapeutics.

Due to the potential high relevance of Aβ dityrosine cross-links, their quantification in Aβ(1-40) peptide under MCO conditions was performed, using their characteristic fluorescent emission. The impact of cross-links on the aggregation behaviour of Aβ(1-40) was also assessed. Finally, the inhibitory effect of the strong Cu(II)-chelating H-His-Ala-His-OH (**HAH**) peptide on the formation of dityrosine cross-links was evaluated.

4.2 Objectives

- Synthesis of a dityrosine standard for fluorescence measurements (reference compound).
- Generation of copper-induced dityrosine cross-links.
- Identification and quantification of dityrosine cross-linking by fluorescence spectroscopy.
- Evaluation of the impact of the formation of dityrosine cross-links on the aggregation and morphology of Aβ(1-40).

4.3 Results and discussion

4.3.1 Synthesis of a dityrosine standard and of cross-linked dimeric peptides

The synthesis of a dityrosine standard was necessary for the quantification of copper-induced dityrosine cross-links by fluorescence spectroscopy. The procedure described by Ahn and co-workers was first attempted.[263] The strategy consisted in the oxidation of tyrosine with $Mn(AcO)_3$ in phosphate buffer at pH 2.1 (**Figure 4.4**).

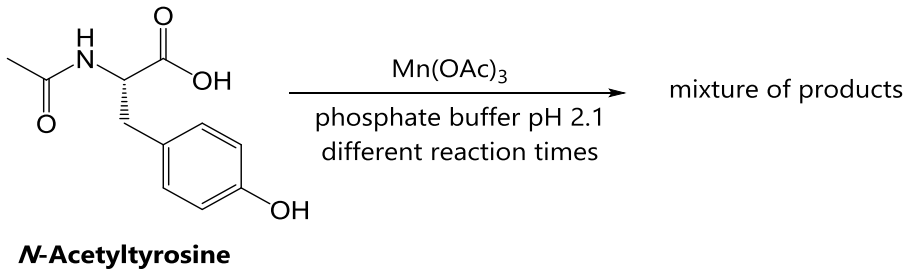

Figure 4.4: Reaction of tyrosine with $Mn(OAc)_3$.

Different reaction times (varying from 30 s to 10 min) and tyrosine/$Mn(AcO)_3$ ratios (1:1 and 1:2) were tried. However, both tyrosine and the Mn(III) salt were poorly soluble and no dityrosine was detected in the crude products, unreacted tyrosine being mostly recovered. A tyrosine-Cu(II)-H_2O_2 mixture of 1:1:20 was then used, but a complex mixture of oxidised products was obtained, most likely resulting from an uncontrolled oxidation reaction.

Hutton reported the preparation of dityrosine and other polymeric tyrosine products using 3-iodotyrosine and tyrosine-3-boronic acid derivatives as the starting

reagents.[264] The generation of dityrosine by enzymatic catalysis using peroxidases has also been widely used.[265-268] Although the yields reported by Hutton were in general higher than those obtained by peroxidase catalysis, the latter approach was more straightforward and it was therefore chosen.

Peroxidases catalyse the degradation of peroxides into water (if the substrate is H_2O_2) or to the corresponding alcohols (if the substrate is an organic peroxide) in the presence of an electron donor. Several peroxidases have been described, such as cytochrome c peroxidase, soybean peroxidase, lactoperoxidase, myeloperoxidase, thyroid peroxidase and horseradish peroxidase.[266] Also, different electron donors are accepted by these enzymes.

The active centre of most peroxidases consists of a Fe(III) heme group, which is the catalytic species.[267,268] The Fe(III) centre of the heme group is first oxidised by H_2O_2 to Porphyrin*-Fe(IV)=O, which presents a highly unstable porphyrin* π-cation radical (Compound I, **Figure 4.5**). Then, Compound I accepts one electron from a substrate (in this case, tyrosine) and is subsequently reduced to Porphyrin-Fe(IV)=O (Compound II). Finally, Compound II undergoes a second one-electron reduction with another molecule of substrate to return to the initial Porphyrin-Fe(III) resting state.

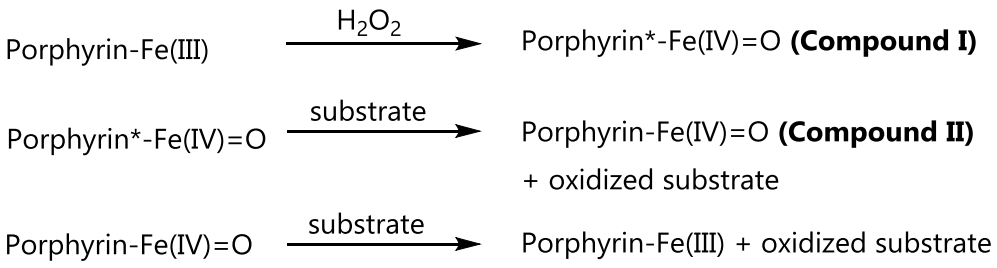

Figure 4.5: Redox cycle of the active centre of peroxidases.

The active site of horseradish peroxidase (**HRP**) is more accessible and therefore accepts several substrates, *e.g.* tyrosine and *N*-acetyltyrosine. Accordingly, HRP was chosen for the enzymatic preparation of the dityrosine standard (*i.e.* reference compound). HRP can be used to oxidise two equivalents of tyrosine or tyrosine-containing peptides using dihydrogen peroxide as the electron acceptor.[269]

In order to improve solubility, *N*-acetyl-L-tyrosine was used to avoid the formation of water-insoluble zwitterionic species (**Figure 4.6**). Besides, if L-tyrosine is used as the substrate of HRP, the rate of dityrosine formation is decreased by the presence of a positive charge in the vicinity of the phenol ring, which undergoes repulsion with a

functional arginine residue.[270,271] The *N*-acetyldityrosine (**NAdT**) dimer obtained is subsequently deprotected under acidic conditions producing dityrosine.

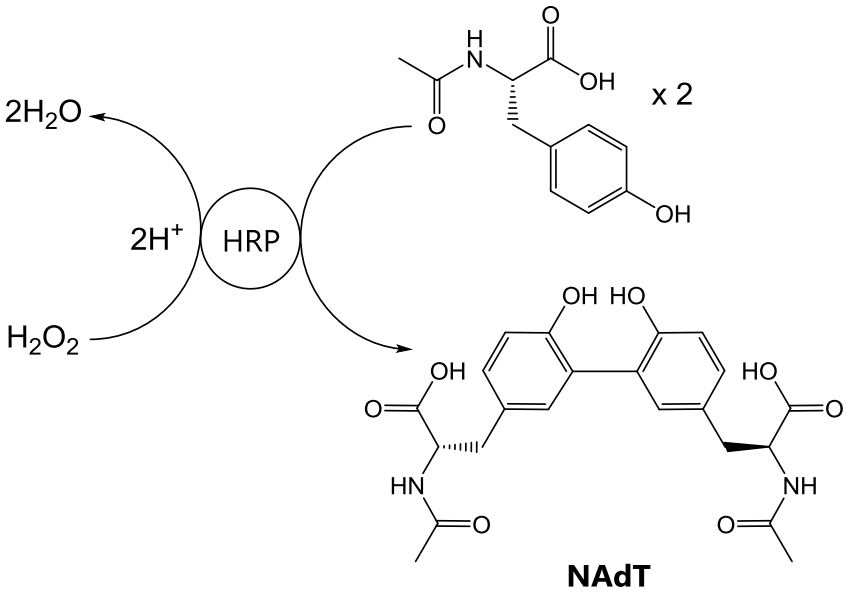

Figure 4.6: NAdT formation by HRP catalysis.

The synthesis of NAdT was optimised through a number of modifications of established protocols (**Figure 4.7**). Hence, the reaction was carried out using catalytic amounts of HRP in borate buffer (pH 9.4) at 37 ºC under an inert N_2 atmosphere, and a slight excess of H_2O_2 (related to the amount of *N*-acetyltyrosine).

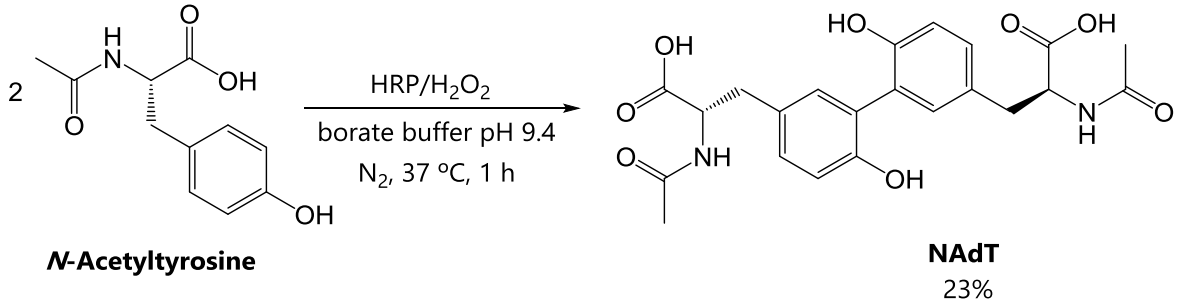

Figure 4.7: Enzymatic synthesis of NAdT.

After freeze-drying, NAdT was purified by preparative thin-layer chromatography (TLC) and obtained with a yield of 23% with a chromatographic purity of 97%. Although low, the yield is comparable with those reported for the HRP-catalysed preparation of dityrosine. Moreover, the quantity obtained was sufficient for the projected studies. The product was characterised by HPLC-MS and ^{1}H NMR; the aromatic region of the NMR spectrum showed characteristic signals of the dityrosine moiety NAdT.

Next, the α-amino groups were deprotected (**Figure 4.8**). Harsh conditions in highly acidic media were necessary to remove the acetyl groups. Hence, NAdT was refluxed in 6 M HCl for 20 h under N_2. The reaction was quantitative and dityrosine was obtained with a chromatographic purity of 92%, sufficient for its use as reference (fluorescent) compound.

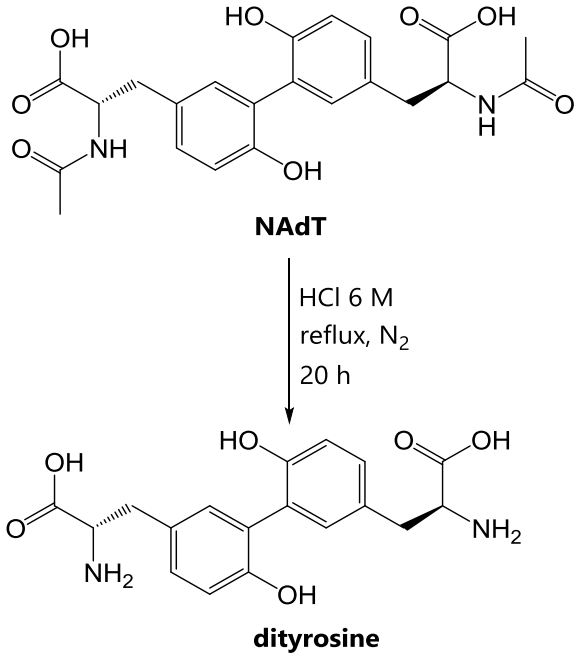

Figure 4.8: Acidic deprotection of NAdT.

Both NAdT and dityrosine presented a maximum absorption at 286 nm in acidic media (ε_{acid} = 4850 $M^{-1}cm^{-1}$), while it absorbed at 320 nm under neutral or basic conditions (ε_{alkali} = 8300 $M^{-1}cm^{-1}$); these data are consistent with the values reported elsewhere.[272] Upon excitation at the corresponding absorption wavelength, both products presented a characteristic emission around 410-415 nm.

The same synthetic procedure was applied to the tyrosine-containing peptides H-His-Ala-His-Tyr-NH_2 (**HAHY**) and H-Lys-Asp-Tyr-Asp-OH (**KDYD**), which are depicted in **Figure 4.9**. In principle, dityrosine cross-linked dimeric peptides may behave as more efficient copper chelators and may also represent an interesting scaffold for the preparation of bioactive peptidic drugs. Unfortunately, the synthesis of such peptidic dimers was unsuccessful (solely the starting materials were detected at the end of the reaction).

It is known that the efficiency of the peroxidase-catalysed formation of the dityrosine link is dependent on the molecular weight of the substrate; indeed, the enzymatic active site may not be accessible for large peptides. Besides, the tyrosine side chain (in peptides) is sometimes not appropriately exposed to the solvent, although this is rather unlikely for such small peptides. The position of the tyrosine residue may also affect the rate of cross-linking.[265,270]

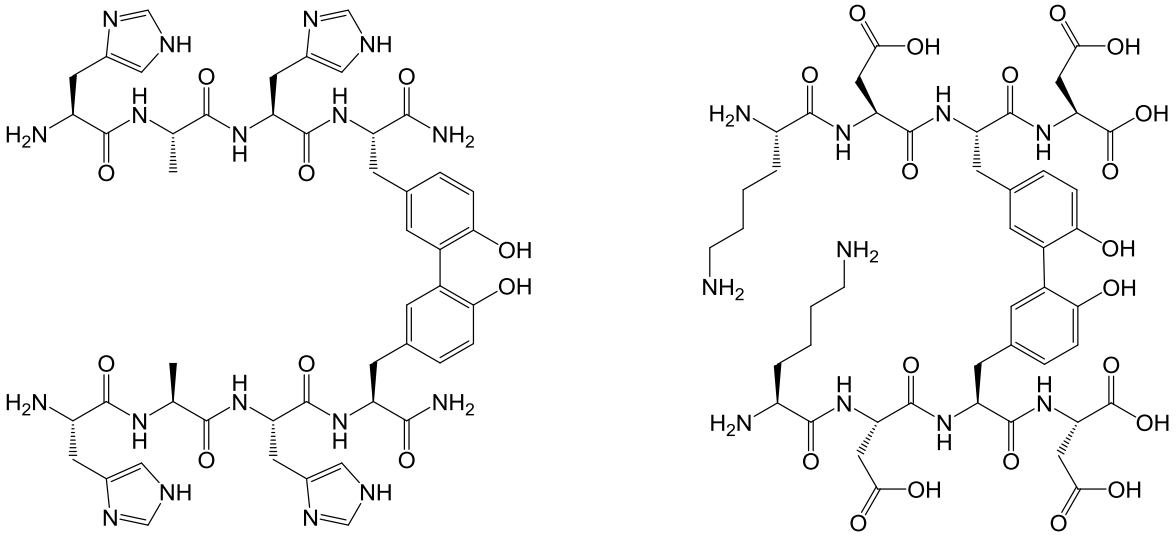

Figure 4.9: Dityrosine cross-linked dimers of H-His-Ala-His-Tyr-NH_2 and H-Lys-Asp-Tyr-Asp-OH.

It is also possible that the effective conditions used for *N*-acetyldityrosine were not suitable for the aforementioned peptides. Alternatively, the manganese-dependent peroxidase (MnP) of the fungus *Phanerochaete chrysosporium* could be used. Such peroxidase proceeds through indirect catalysis: the active species is a freely diffusing manganese complex, which is released and acts as the oxidising agent; thus, the binding of tyrosine to the enzyme is not required with this enzyme.[254] This strategy would require a complex optimisation of the reaction conditions; due to the lack of time, the preparation of cross-linked dimeric peptides was abandonned.

4.3.2 UV-Vis kinetics study of the generation of dityrosine and tyrosyl radical

The reaction to produce NAdT was next monitored by UV-Vis spectroscopy. The generation of NAdT was followed by the increase in its absorbance at 320 nm. Simultaneously, the kinetics of the tyrosyl radical were monitored by the variation in absorbance at 417 nm (**Figure 4.10**).[273]

N-acetyltyrosine (25 mM) and catalytic amounts of HRP were dissolved in borate buffer and purged with N_2. The solution was quickly transferred into a cuvette and H_2O_2 was immediately added.

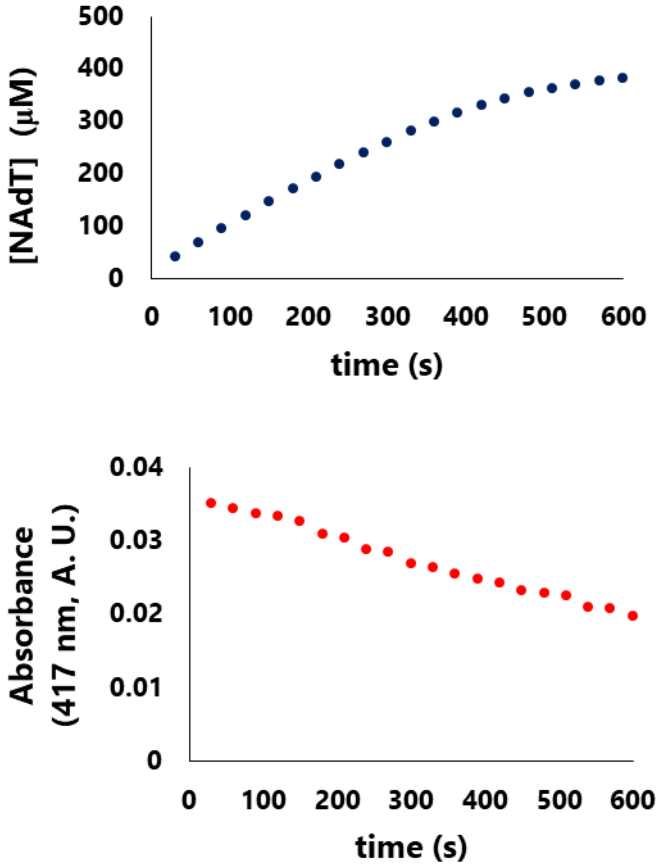

Figure 4.10: Top: Formation of NAdT monitored by the increase of absorbance at 320 nm. **Bottom:** Disappearance of tyrosyl radical evidenced by the decrease in absorbance at 417 nm.

The NAdT concentration with time was determined at 320 nm using Lambert-Beer law (ε_{alkali} = 8300 $M^{-1}cm^{-1}$, see above). The concentration of NAdT increased linearly until a plateau was reached after approximately 10 min, indicating reaction saturation. The

concentration at this plateau was 380 nM, which corresponded to a yield in NAdT of 3%.

The formation of dityrosine trimers and tetramers can also take place and once formed they behave as competitive inhibitors.[265,270,271] Nonetheless, they are restricted by steric hindrance, and the oxidation of dimers to give higher order oligomers is much slower than the formation of dityrosine.

The absorbance at 417 nm due to the tyrosyl radical decreased in a linear fashion, suggesting that it was consumed. This decrease continued during 10 min, *viz*. after the plateau observed for the production of NAdT; this suggests that the tyrosyl radicals quenched back to tyrosine or/and generated other by-products. It is known that radicals rapidly react, much faster than their production, the rate-limiting step being the reduction of Compound I back to the resting state (**Figure 4.5**).[270,271]

4.3.3 Generation of dityrosine cross-links in Aβ

The possible generation of dityrosine cross-links in full-length Aβ was then investigated. The formation of the dityrosine moiety (and any other oxidation product(s)) was monitored by fluorescence spectroscopy in the range 330-600 nm. The kinetic experiments were performed at a fixed emission wavelength, namely 410 nm, using a plate reader. In both cases, the samples were excited at λ_{exc} = 320 nm. Calibration curves with the dityrosine standard (using concentrations from 62.5 nM to 2 μM) were generated with the spectrofluorometer and the plate reader (**Figure 4.11**).

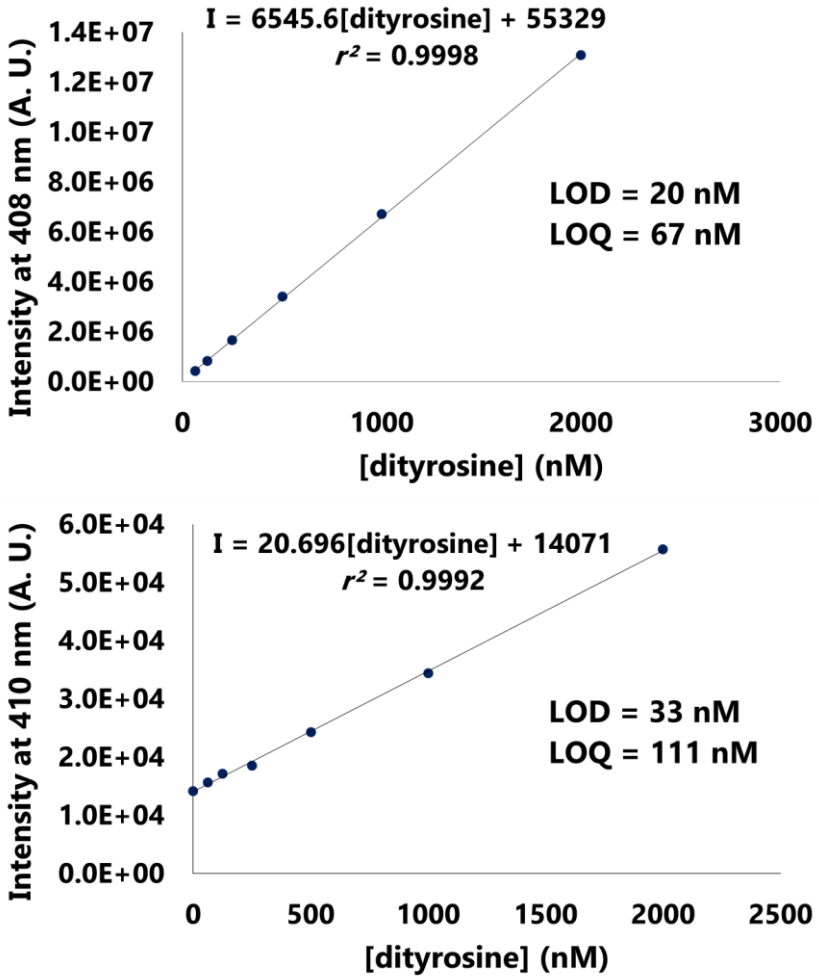

Figure 4.11: Calibration curves of dityrosine in 100 mM HEPES buffer (pH 7.4) using the spectrofluorometer (**top**) and the plate reader (**bottom**). λ_{exc} = 320 nm.

Excellent calibration curves were obtained in both cases (r^2 > 0.999). The limits of detection (**LOD**) were 20 nM with the spectrofluorometer and 33 nM with the plate reader. The limits of quantification (**LOQ**) were 67 and 111 nM, respectively. Therefore, fluorescence spectroscopy allows the determination of dityrosine even in the nanomolar range.

Next, Aβ(1-40) was treated with copper(II) and H_2O_2 to induce protein cross-links. A 1:1:20 mixture of Aβ(1-40)-Cu(II)-H_2O_2 in 1X PBS buffer (protein concentration of 30 μM) was selected, as reported in the literature.[39,66] It can be stressed that these concentrations and ratios are comparable to those found in the synaptic cleft.

However, no detectable levels of dityrosine cross-links were found. Since Cu(II) may precipitate as its phosphate salt in PBS, the buffer was changed to 100 mM HEPES,

which is a weaker copper-coordinating agent (see **Chapter 3**). As a matter of fact, the characteristic emission of the dityrosine motif was detected within some hours; these experimental conditions were thus used for subsequent studies.

Next, the full emission spectra were registered over time to follow the potential generation of Aβ(1-40) dityrosine cross-links. Samples of 30 μM Aβ(1-40) in the presence of Cu(II) and H_2O_2, and the corresponding blanks were incubated at 37 ºC, and fluorescence spectra were recorded every 24 h for 3 days. In addition, the possible inhibition of dityrosine production by the ATCUN copper-chelator peptide H-His-Ala-His-OH (**HAH**) was examined. The results obtained are shown in **Figure 4.12**.

Free Aβ(1-40) (panel **A**) displayed low-intensity band(s) with a maximum emission at 412 nm. This emission at 412 nm may be indicative of the formation of low amounts of dityrosine; the presence of a shoulder around 426 nm suggests that various (oxidation) products were produced. Van Vranken and collaborators reported that fibrillary Aβ(1-40) is prone to dityrosine formation; therefore, its cross-linking may have occurred upon aggregation, together with other undetermined (oxidation) products.[255]

Panel **B** shows the spectra obtained for Aβ(1-40) with an equimolar amount of Cu(II). No significant fluorescence bands were observed after 72 h, indicating that, as already described in the literature, copper ions alone cannot induce the formation of dityrosine formation.[250,261] In contrast to previous reports, it was found that H_2O_2 was able to oxidise Aβ(1-40), as evidenced by the appearance of a broad, low-intensity band with maximum emission at 424 nm (panel **C**). Several amino-acid residues are susceptible to oxidative modifications in the presence of H_2O_2 or other ROS. However, the yields of such alterations are likely to be very low; therefore, their detection by mass spectrometry may not be possible and can explain that the authors of the previous studies have not seen them.[89,250] In contrast, the highly sensitive methodology used in the present investigation has allowed to detect them.

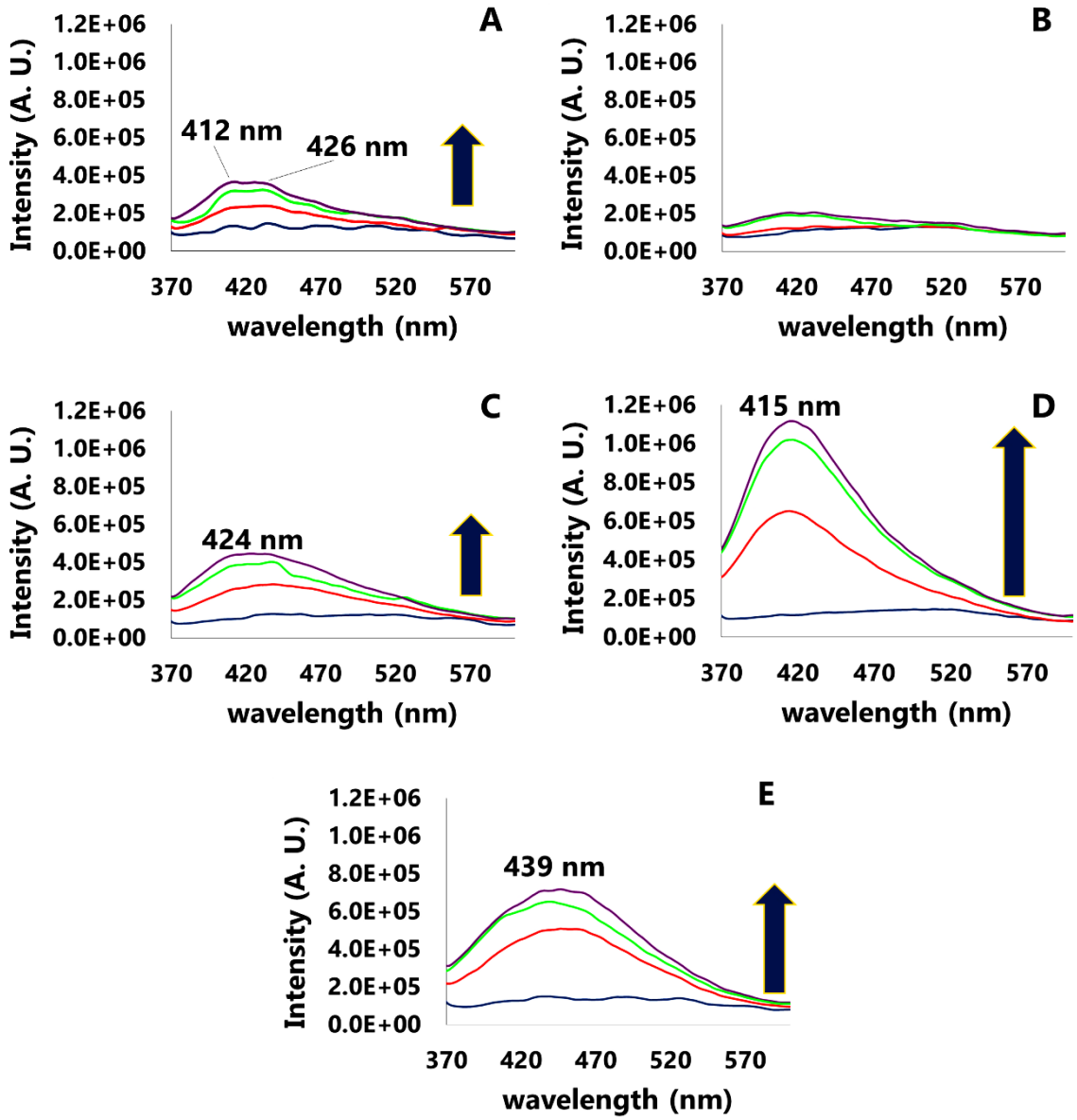

Figure 4.12: Fluorescent emission spectra (370−570 nm), of samples incubated for 3 days at 37 °C containing **A:** Aβ(1-40); **B:** Aβ(1-40)-Cu(II), 1:1; **C:** Aβ(1-40)-H_2O_2, 1:20; **D:** Aβ(1-40)-Cu(II)-H_2O_2, 1:1:20; **E:** Aβ(1-40)-HAH-Cu(II)-H_2O_2, 1:1:1:20. Blue line: 0 h; red line: 24 h; green line: 48 h; purple line: 72 h. λ_{exc} = 320 nm. 100 mM HEPES (pH 7.4).

Panel **D** shows the fluorescence spectra recorded for Aβ(1-40) in the presence of both Cu(II) and H_2O_2 in a molar ratio of 1:20. The formation of dityrosine cross-links was evidenced by the appearance of an increasing intense band centred at 415 nm. The amount (yield) of dityrosine was evaluated using the emission data at λ_{em} = 408 nm. The maximum concentration of dityrosine that could be generated was 15 μM since 30 μM Aβ(1-40) was used (two molecules of protein are required to generate a dityrosine

motif). Blank experiments with dityrosine and copper allowed to determine a Cu(II)-induced paramagnetic quenching of 16% in dityrosine emission. Thus, the corrected dityrosine concentrations (and yields) generated after 24, 48 and 72 h were 103 (0.68%), 167 (1.1%) and 183 nM (1.3%), respectively. Such low values are consistent with those previously reported for both tyrosine and the Aβ protein.[252,261]

Finally, the emission spectra obtained for Aβ(1-40)-Cu(II)-H_2O_2 in the presence of the copper-chelating peptide HAH are shown in panel **E**. A broad (multi)band with maximum emission at 439 nm, suggesting the presence of various products, was observed (see **Figure 4.1** for the more frequent derivatives resulting from tyrosine oxidation). The oxidation of other amino-acid residues (namely other than tyrosine) is also possible, including the HAH peptide. Actually, histidine residues have been reported to be particularly prone to oxidation, for instance giving 2-oxohistidine.[250]

To determine whether the emission observed was due to HAH oxidation products, the ATCUN chelating peptide was treated with $CuCl_2$ (1 eq) and H_2O_2 (20 eq). A fluorescent band centred at 425 nm was obtained after 3 days (**Figure 4.13**). Since a shoulder band was observed for the Aβ(1-40)-Cu(II)-H_2O_2 system at this wavelength (see **Figure 4.12**, panel **E**), it appears that oxidation products of HAH were also generated.

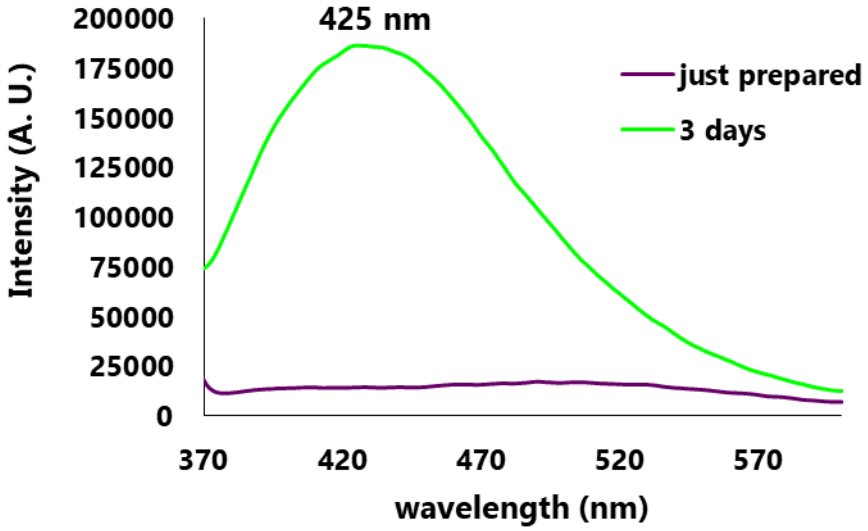

Figure 4.13: Emission spectra of HAH-Cu-H_2O_2 1:1:20. λ_{exc} = 320 nm.

The appearance of significantly red-shifted band(s) (439 nm and above; see **Figure 4.12**, panel **E**), compared with the emission of dityrosine at 410-415 nm, suggests that the formation of the cross-links may have been inhibited, but other species were

produced. It would be interesting to determine the nature/structure of these new species, for example by HPLC-MS. However, one may expect such characterisation to be difficult because individual species are usually generated in extremely low quantities. Moreover, the resolution by HPLC of different products with similar polarities is not straightforward.

4.3.4 Impact of dityrosine cross-linking on the aggregation of Aβ(1-40)

The implications of the presence of cross-linked Aβ on the aggregation process of the protein were subsequently studied. Oxidative stress is believed to occur in the early stages of AD; therefore, cross-linked Aβ may play a key role in self-assembly processes.

Aggregation studies were carried out with a plate reader that allows a great number of simultaneous, temperature-controlled experiments over extended periods of time. First, the formation of dityrosine cross-links was followed during 3 days (at 410 nm) for the different systems.

The results obtained are shown in **Figure 4.14**. The intensity values for all samples were below the **LOQ** (see section **4.3.3**), except for the Aβ-Cu-H_2O_2 system, in agreement with the data achieved in the previous section. Free Aβ (dark blue spots) showed relatively constant emission values over the 3 days, indicating that covalent dimers were not formed. Aβ in the presence of H_2O_2 (20 eq; red spots) gave slightly higher intensity values, suggesting low levels of protein oxidation. In contrast, the presence of copper (1 eq; green spots) had no effect on the emission, as reflected by intensity data similar to those of control Aβ (as observed previously).

For the Aβ-Cu-H_2O_2 system (pink spots), higher intensity values were obtained, due to the formation of dityrosine cross-links. Serpell and collaborators found significant levels of dityrosine bridges as early as 10 min after the beginning of the reaction; therefore, dityrosine may be expected to affect the aggregation process in its early stages.[90] The initial emission lied below the quantification limit and was comparable to that obtained for the other samples. After 24, 48 and 72 h, measurable intensities were achieved, which were attributed to the formation 2.1, 2.9 and 2.4% yield of dityrosine, respectively. It can be observed that, in all cases, the formation of dityrosine reached a maximum after 2 days (**Figure 4.14**); the subsequent reduction of the emission

intensity may be due to precipitation of dityrosine-containing aggregates or to further oxidation of the protein dimer.

Importantly, adding 2 eq of HAH peptide to the Aβ-Cu-H_2O_2 system drastically reduced the formation of dityrosine (compare light-blue and pink spots in **Figure 4.14**); actually, the fluorescent intensities with added HAH match those of Aβ-H_2O_2 (**Figure 4.14**; red spots), therefore indicating a very efficient chelation of the copper ions by the tripeptide. These data support the idea of administrating copper ionophores to decrease the oxidative stress and toxicity associated to Aβ oxidation.

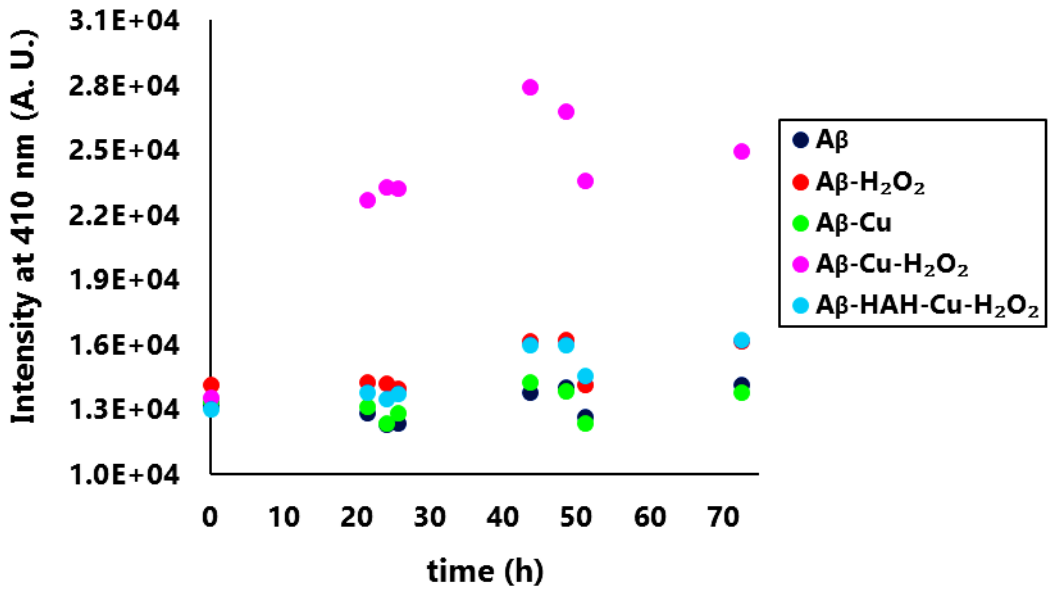

Figure 4.14: Formation of dityrosine-bridged Aβ(1-40) dimers under different experimental conditions (illustrated by distinct colours). The generation of the cross-links was monitored at 37 ºC during 3 days by fluorescence at 410 nm, using a plate reader. λ_{exc} = 320 nm.

Next, the aggregation of Aβ applying the same experimental conditions (as above) was followed for 3 days by ThT fluorescence, with the objective to assess whether dityrosine cross-linking has an effect on the aggregation properties of the protein. The results obtained during the first 10 hours are shown in **Figure 4.15**. After 10 hours (up to 3 days), the emission remained constant (in all cases) or progressively decreased due to precipitation of insoluble fibres.

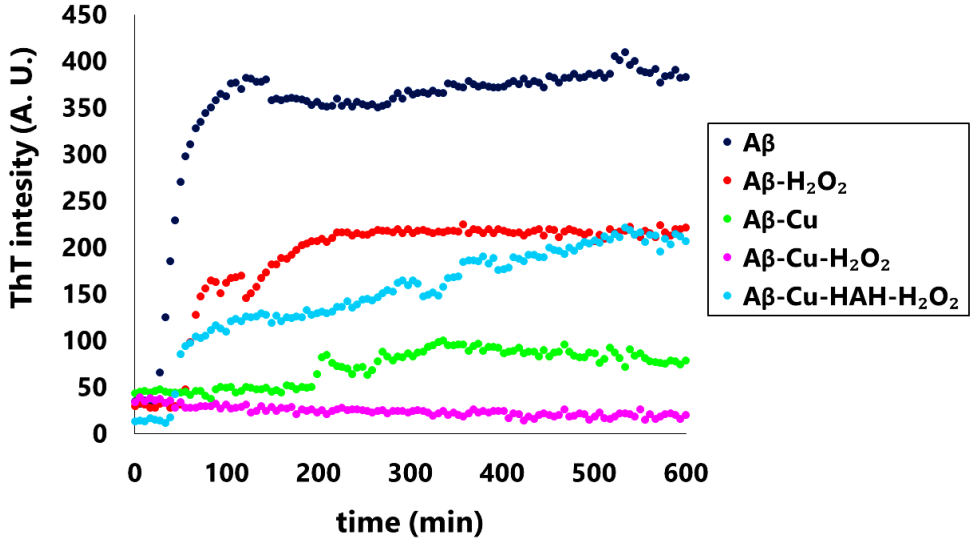

Figure 4.15: Aggregation of Aβ(1-40) under different oxidative conditions (illustrated by different colours), followed by ThT emission (λ_{exc} = 440 nm, λ_{em} = 490 nm) at 37 ºC. 100 mM HEPES buffer (pH 7.4).

The aggregation of free Aβ (dark-blue dots in **Figure 4.15**) followed the typical sigmoidal shape, with an abrupt increase in ThT fluorescence after 20-30 min, indicative of the formation of fibres. In the presence of H_2O_2 (20 eq, red dots), the aggregation of Aβ was delayed by approximately 30 min and reduced compared with free Aβ. H_2O_2 thus affects both the nucleation and elongation steps, probably as the result of protein oxidation. For the Aβ-Cu 1:1 system (green dots in **Figure 4.15**), no fluorescence increase was observed, in accordance with the expected metal-mediated stabilisation of oligomeric Aβ. After approximately 200 min, low levels of fibrillary Aβ started to be detected.

In the presence of both copper (1 eq) and H_2O_2 (20 eq), Aβ aggregation was totally inhibited during the 3-days-long measurements (pink dots in **Figure 4.15**). As previously mentioned, the potential role of dityrosine cross-linked Aβ dimers as aggregation nuclei is still a matter of debate. Serpell and collaborators hypothesised that covalent dimerisation of the aggregation-prone Aβ(1-42) serves as nucleus for the self-assembly/aggregation of the protein. However, they noticed remarkably reduced ThT fluorescence compared to that of non-oxidised Aβ; moreover, they did not observe fibrillary species by TEM before 48 h.[90] Galeazzi *et al.* also suggested that the formation of dityrosine bridging might trigger amyloidogenesis.[91]

Conversely, van Vranken and co-workers found that dityrosine cross-links did not induce the formation of β-sheet structures in the Aβ(8-14) fragment.[255] Assuming that this can be extrapolated to the full-length peptide, it is quite unlikely that such a small oligomeric form, lacking the required β-sheet conformation, can serve as a template for the generation of the highly ordered fibrillary structure.

Hutton reported the synthesis of dityrosine cross-linked Aβ(1-40) and Aβ(1-42) dimers by SPPS.[274] These dimers self-assembled in higher-order soluble aggregates, but did not lead to the formation of fibres until 7 days. In fact, the synthetic dimers resulted in long-lived oligomers with enhanced toxicity.

The pathophysiological relevance of such synthetic dimers, though, has been a matter of debate. Williams *et al.* reported the isolation of cross-linked Aβ oligomers generated by the naturally-occurring Cu-H_2O_2 system in concentrations similar to those found *in vivo*.[39] Such cross-linked oligomeric species, which are thus biologically relevant, did not produce amyloids, in agreement with the aforementioned works. Moreover, these cross-linked oligomers were toxic as they induced membrane disruption.

It is important to consider that the inhibitory effects found in the present study may arise from the combination of the formation of dityrosine bridges and the stabilisation of oligomeric species by copper. Further experiments are required to investigate separately the effects of copper and dityrosine cross-linking on the aggregation of Aβ. Nonetheless, these results suggest that, if such conditions take place *in vivo*, dityrosine cross-linked Aβ species bound to copper do not lead to the formation of fibrillary Aβ. In fact, the stabilisation of potentially toxic oligomeric species may occur.

When 2 eq of the copper-chelating peptide HAH were added simultaneously to Cu(II) and H_2O_2, the sigmoidal shape of the aggregation process was recovered (light-blue dots in **Figure 4.15**). After a lag phase of 40-50 min, the ThT intensity rose abruptly; then, a progressive slow increase was observed until reaching a plateau at the same intensity to that of Aβ-H_2O_2 (see red and light-blue dots in **Figure 4.15**). These data suggest that the chelating agent efficiently prevented the copper-induced formation of dityrosine and the stabilisation of oligomers, restoring the native aggregation of the protein (in the presence of H_2O_2).

TEM images were then taken for the different systems described above, after an incubation of 24 h. The samples were negatively stained with uranyl acetate and subsequently visualised (**Figure 4.16**). As expected, fibres are observed for Aβ(1-40)

(**Figure 4.16**; panels **A** and **B**). Deposits with high amounts of closely associated protein fibres were found in some sections of the image shown in panel **A**. Fibres were also observed for Aβ-H_2O_2 (**Figure 4.16**; panels **C** and **D**).

Remarkably, no fibrillary species were found for the Aβ-Cu sample (**Figure 4.16**; panels **E** and **F**). This is not surprising since stoichiometric amounts of copper are known to stabilise oligomeric species.[66-68] For instance, ThT fluorescence was much weaker for this sample (see above), whose maximum was only reached after 200 min; these spectroscopic data suggested that very low amounts of fibrillary Aβ were generated. It cannot be precluded that the fluorescence intensities observed are due high-order oligomers with a certain degree of β-sheet content. For Aβ-Cu-H_2O_2 (**Figure 4.16**; panels **G** and **H**), the microscopy data are in line with those observed by fluorescence spectroscopy, namely the absence of ThT emission agrees with the absence of fibres, confirming the inhibited generation of Aβ fibrils.

In the case of Aβ-HAH-Cu-H_2O_2 (**Figure 4.16**; panels **I** and **J**), abundant fibres were observed, suggesting that the fibrillation-inhibitory effects of copper and/or dityrosine cross-links were blocked. Therefore, the ATCUN copper-chelating peptide HAH, possessing an ATCUN motif, is highly efficient against metal-mediated stabilisation of oligomers and oxidation (dimerisation) of Aβ. To date, it is still not clear if dityrosine covalent bridges are related to Aβ toxicity; in the plausible event that they indeed are, the present study suggests that copper chelation can be a promising strategy to lessen toxicity due to covalently-linked oligomeric Aβ, favouring the formation of fibrillary aggregates, which are considered less toxic.

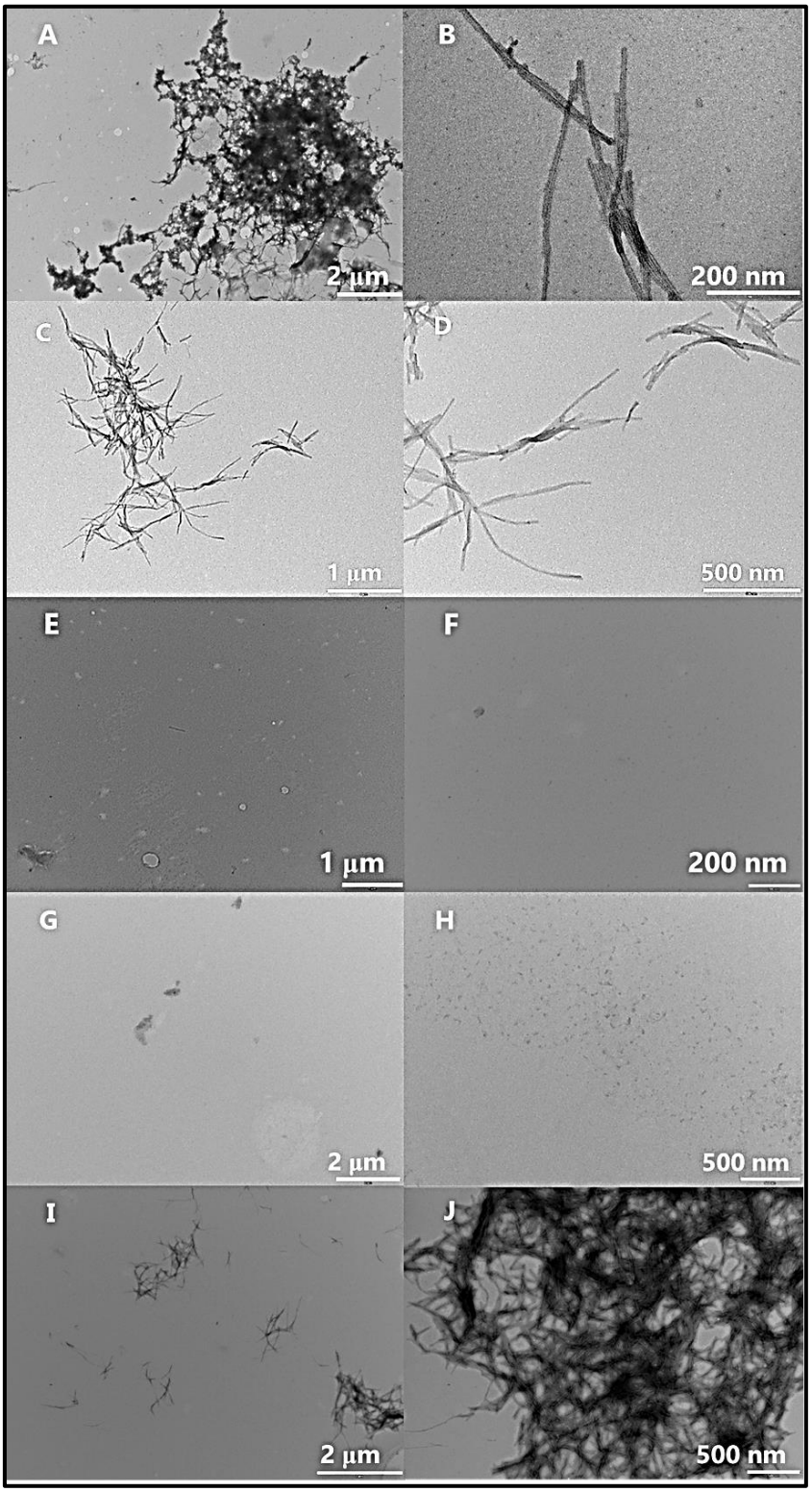

Figure 4.16: TEM images taken after 24 h incubation at 37 ºC of Aβ under different experimental conditions. Panels **A** and **B**: Aβ(1-40); **C** and **D**: Aβ(1-40)-H_2O_2 1:20; **E** and **F**: Aβ(1-40)-Cu 1:1; **G** and **H**: Aβ(1-40)-Cu-H_2O_2 1:1:20; **I** and **J**: Aβ(1-40)- HAH-Cu-H_2O_2 1:1:1:20.

4.4 Concluding remarks

The two-step synthesis of dityrosine (reference compound for the quantification of dityrosine crosslinking by fluorescence) from *N*-acetyltyrosine has been carried out. The first synthetic step, consisting in an enzymatic reaction, was followed spectrophotometrically, tracking the formation of dityrosine at λ_{abs} = 320 nm, and the disappearance of the tyrosyl radical at λ_{abs} = 417 nm. Fluorescence calibration curves (λ_{exc} = 320 nm, λ_{em} = 410 nm) were then generated with the as-synthesised standard, which allowed to quantify the generation of dityrosine cross-links in Aβ(1-40) peptide under various experimental conditions. The Aβ-Cu-H_2O_2 1:1:2 MCO system was found to generate covalent dityrosine links, although in very low amounts (< 3% after 3 days).

Under conditions of dityrosine formation, complete inhibition of the generation of fibres was observed. This inhibition of amyloid production is probably the result of the combined effects of both copper (which stabilises oligomeric species) and the covalent dimers. The spectroscopic results were supported by TEM studies, which showed the presence of abundant fibres in free Aβ(1-40), H_2O_2-treated Aβ and Aβ-HAH-Cu-H_2O_2; for Aβ in the presence of Cu(II) or Cu(II)-H_2O_2, no fibrillary aggregates were detected.

Although additional, in-depth studies are required to investigate separately the two effects, *viz.* from copper and from the dityrosine-bridged dimers, the results herein obtained suggest that cross-linked Aβ is not a nucleus for fibrillation, and actually does not evolve towards amyloids. Comparison of the structure of aggregates obtained from covalent and non-covalent oligomers would be of interest.

The low yields achieved for the preparation of cross-linked Aβ most likely have not allowed the isolation of sufficient amounts of covalent dimers, which would allow to accurately study their aggregation. Improvements in the preparation of synthetic models of the protein have certainly increased the knowledge of the properties of dityrosine-containing Aβ, but the pathophysiological relevance of these species remains unclear.[274] Recently, the generation of dityrosine-bridged Aβ oligomers using physiologically relevant conditions, *i.e.* Cu(II)-H_2O_2 system, has been reported.[39] The so-formed covalent oligomers displayed attenuated fibre formation and extended toxicity due to membrane disruption, which may represent a key mechanism of neurotoxicity.

We have found that cross-linked Aβ is not amyloidogenic in the presence of copper ions. If the conditions necessary for the copper-induced production of covalent dimers

are met in the early stages of AD, as some authors suggest, then long-lived oligomeric Cu-Aβ species with enhanced stability may form, potentially leading to increased oxidative stress and membrane permeation. Importantly, the addition of the ATCUN copper-chelating peptide HAH efficiently arrested the production of dityrosine cross-links and restored the natural aggregation of the protein. As mentioned earlier, amyloids are considered to be less toxic than oligomeric Aβ species, and cross-linked Aβ has been reported to impair cognitive performance. Therefore, the inhibition of cross-link formation with chelating agents (such as the oligopeptides described herein) may be beneficial. This chelation approach is expected to be more effective at the early stages of AD, that is, when ROS production and Aβ oxidation start.

4.5 Experimental section

4.5.1 Reagents, solvents and equipment

Table 4.1: Reagents and solvents used.

Brand	Products
Acros Organics	$Mn(AcO)_3 \cdot 2H_2O$
Sigma Aldrich	boric acid, $CHCl_3$, D_2O, H_2O_2 30%, HEPES, HFIP, ThT
Fisher Scientific	DMSO, MeCN (HPLC grade), MeOH, MeOH (HPLC grade), PBS
Alfa Aesar	*N*-acetyltyrosine
Panreac	$CuCl_2 \cdot 2H_2O$
Scharlau	acetone, HCl 37%

Table 4.2: Equipment used for the work described in this chapter.

Instrument	Brand	Model
Analytical balance	A & D Instruments	GR-200-EC
Gram-scale balance	Sartorius	Basic BA 110
UV lamp	Asahi Spectra	Max-303
Vacuum lyophiliser	Christ Alpha	2-4 LD plus
Rotatory evaporator	BUCHI	R-200
Sonicator	Fisherbrand	FB15051
Shaking Block Heater	Eppendorf	ThermoMixer C

Milli-Q H_2O (resistivity > 18 MΩ·cm) was produced by filtering deionised water with a Milli-Q Plus (Millipore) system. $CuCl_2 \cdot 2H_2O$ was used as the source of copper for all the studies.

Horseradish peroxidase (HRP, lyophilised powder, 179.2 units per mg of solid; solubility: 5 mg/mL in 50 mM potassium phosphate buffer pH 6.0 with 0.1% bovine serum albumin) was purchased from Sigma Aldrich. The solid HRP was dissolved in 50 mM phosphate buffer pH 7.6, and the resulting solution (final concentration 2.5 mM) was aliquoted (50 μL per aliquot) and kept frozen.

H-His-Ala-His-OH (HAH), H-His-Ala-His-Tyr-OH (HAHY) and H-Lys-Asp-Tyr-Asp-OH (KDYD) peptides were purchased from GeneCust (Luxembourg) as their hydrochloride salts and were used without further purification. Aβ(1-40) was acquired from Bachem as a trifluoroacetate salt.

4.5.2 Syntheses and characterisation

Nuclear Magnetic Resonance (NMR)

^{1}H NMR spectra were registered on a Varian Mercury-400 spectrometer at 400 MHz at the Centres Científics i Tecnològics of the Universitat de Barcelona (CCiTUB). Chemical shifts are given in ppm with the residual non-deuterated solvent as the internal standard. Coupling constants are given in Hz. The NMR data were analysed using MestReNova 9.1.0. Data are reported as follows: app, apparent; s, singlet; d, doublet; t, triplet; q, quartet; m, multiplet.

Liquid Chromatography

A Phenomenex® C18 reverse phase column (250 x 4 mm) with a particle size of 5.15 ± 0.30 μm and a pore size of 320 ± 40 Å was employed. The eluents were 0.045% TFA in H_2O (v/v) for eluent A, and 0.036% TFA in MeCN (v/v) for eluent B, using the following gradient:

Table 4.3: HPLC gradient used in this work.

Time (min)	% Eluent A	% Eluent B
0	98	2
20	0	100
25	0	100
30	98	2
40	98	2

The flow rate was 1 mL/min and double detection at wavelengths of 220 and 320 nm was used.

High Performance Liquid Chromatography (HPLC)

Analytical HPLC was carried out in a system consisting in a Shimadzu LC-20AD quaternary pump, a SIL-10Advp automatic injector, an SPD-20A variable dual wavelength detector and a DGU-20A5 online degas device.

High Performance Liquid Chromatography coupled to Mass Spectrometry (HPLC-MS)

A Waters Alliance HT system formed by a 2795 separation module, a PDA detector 2996 and a Micromass ZQ 2000 mass detector (Electrospray Ionisation, ESI-MS) was used.

Synthesis of the dityrosine standard

N-acetyldityrosine (NAdT)

A 25 mM *N*-acetyltyrosine solution (20 mL) in 200 mM borate buffer (pH 9.4) was heated at 37 ºC in a round-bottomed flask until it dissolved completely. The solution was then purged with N_2 and a 2.5 mM HRP solution (24 μL, final concentration 3 μM) was added. Immediately after, 30% H_2O_2 (50 μL, final concentration 24.5 mM) was added under N_2 and the reaction mixture was left stirring for 1 h, protected from light. The pale red solution was immediately frozen and subsequently lyophilised. The resulting solid was then dissolved in MeOH (1.5 mL) and purified by preparative thin-layer chromatography (TLC, silica gel matrix 60/F254 on glass support with fluorescent indicator as adsorbent material from Sigma Aldrich, 20 cm × 20 cm, 60 Å medium pore size) using H_2O/$CHCl_3$/MeOH 5:30:65 as the eluent. The bands were revealed under a UV lamp and subsequently scrapped off. The silica containing the product was suspended in MeOH (20 mL) and the procedure was repeated. After 15 min stirring, the mixture was filtered, and the solution was evaporated under reduced pressure. The yield was 23% (determined by UV-Vis spectroscopy) and the chromatographic purity was 92%.

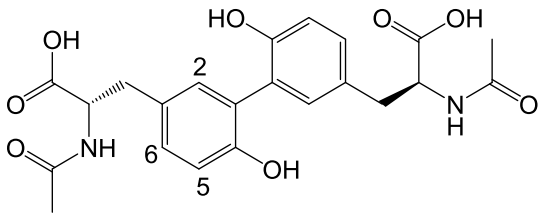

White solid. **R_f** (MeOH/$CHCl_3$/H_2O 65:30:5): 0.33. **HPLC-MS:** t_R = 8.65 min; ***m/z*** 445.1 ($[C_{22}H_{24}N_2O_8 + H]^+$). **^{1}H NMR** ($D_2O$, 400 MHz): δ 1.79 (s, 6H, Me-Ac), 2.71-3.05 (m, 4H, Hβ), 4.28 (dd, 2H, *J* = 4.8, *J* = 8.6, Hα), 6.81 (d, 2H, *J* = 8.3, H_5), 6.94 (d, 2H, *J* = 2.0, H_2), 7.05 (dd, 2H, *J* = 2.0, *J* = 8.3, H_6).

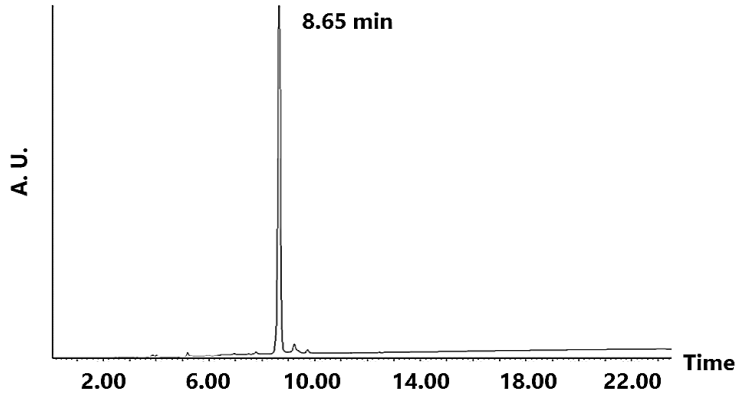

Figure 4.17: Chromatogram of NAdT.

Dityrosine

N-acetyldityrosine was dissolved in Milli-Q H_2O (1.5 mL) in a small round-bottomed flask under N_2. Concentrated HCl (1.5 mL) was then added and the mixture was refluxed for 20 h under stirring in an N_2 atmosphere. The solution was subsequently freeze-dried. Dityrosine was thus obtained as a white solid of high purity (92%).

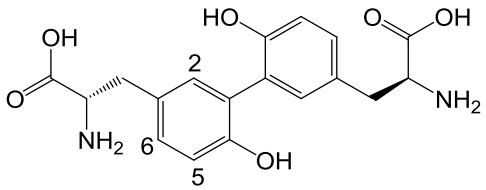

White solid. **HPLC-MS:** t_R = 5.67 min; ***m/z*** 361.2 ($[C_{22}H_{24}N_2O_8 + H]^+$). **^{1}H NMR** ($D_2O$, 400 MHz): δ 3.17-3.34 (m, 4H, Hβ), 4.25 (t_{app}, 2H, J_{app} = 6.3, Hα), 7.02 (d, 2H, *J* = 8.3, H_5), 7.16 (d, 2H, *J* = 1.9, H_2), 7.25 (dd, 2H, *J* = 1.9, *J* = 8.3, H_6).

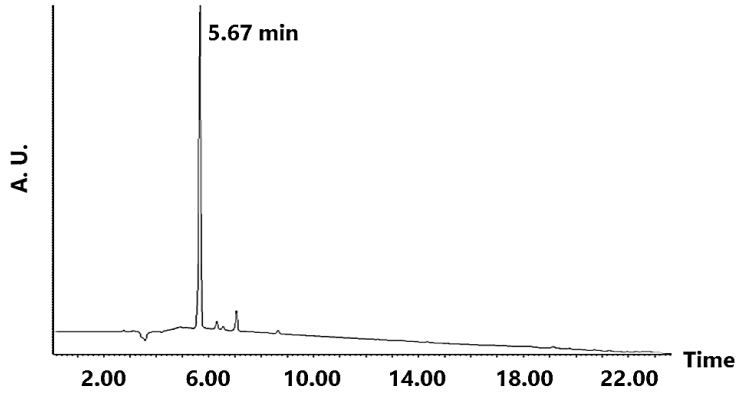

Figure 4.18: Chromatogram of dityrosine.

Preparation of dityrosine cross-linked H-His-Ala-His-Tyr-NH₂ (HAHY) and H-Lys-Asp-Tyr-Asp-OH (KDYD) homodimers

A 25 mM solution (2 mL) of either HAHY or KDYD in 200 mM borate buffer pH 9.4 was prepared. The concentration was checked spectrophotometrically using the molar extinction coefficient ε(Tyr, 280 nm) = 1490 M^{-1} cm^{-1}. The solution was then heated at 37 ºC in a round-bottomed flask and purged with N_2. Next, a 2.5 mM HRP solution (2.4 μL, final concentration 3 μM) was added under N_2, followed by 30% H_2O_2 (5 μL, final concentration 24.5 mM); the resulting reaction mixture was stirred for 1 h protected from light. The solution was immediately frozen and subsequently lyophilised. The solid obtained was then dissolved in MeOH (1.5 mL) and purified by preparative TLC using H_2O/$CHCl_3$/MeOH 5:30:65 as the eluent. The silica containing the different bands was scrapped off and the fractions were suspended in MeOH (20 mL). After 15 min stirring, the mixtures were filtered, and the solutions were evaporated in the rotatory evaporator. The crude products were analysed by ^1H NMR in D_2O and MS.

4.5.3 Procedures, instrumentation and techniques

UV-Vis kinetics study of dityrosine and tyrosyl radical

N-acetyltyrosine (16.7 mg) was dissolved in 200 mM borate buffer pH 9.4 (3 mL, final *N*-acetyltyrosine concentration 25 mM) and the solution was subsequently heated at 37 ºC under N_2. The solution was then transferred into a quartz cuvette (1 cm pathlength) and 2.5 mM HRP (3 μL, final concentration 2.5 μM) and 30% H_2O_2 (7.5 μL,

final concentration 24.5 mM) were added. The measurement was immediately initiated using a Varian Cary 100 Scan spectrophotometer, and endpoint absorbance measurements at 320 and 417 nm were performed every 30 s during a period of 10 min.

Preparation of Aβ(1-40) samples

For the preparation of aggregate-free Aβ(1-40) aliquots, solid Aβ(1-40) (5 mg) was dissolved in 1,1,1,3,3,3-hexafluoro-2-propanol (HFIP, 1 mL) under vigorous shaking at rt for 1 h, after which it was sonicated for 30 min. The solution was further shaken for 1 h and subsequently kept at 4 ºC for 30 min to avoid solvent evaporation. Aliquots of soluble Aβ(1-40) were collected and HFIP was evaporated in air. The resulting solid Aβ(1-40) samples were stored at –20 ºC, and the amount of protein per sample was determined by spectrophotometry using the molar extinction coefficient ε(Tyr, 280 nm) = 1490 M^{-1} cm^{-1}.

Detection and quantification of dityrosine cross-links in Aβ(1-40)

Spectrofluorometer: A HORIBA Jobin–Yvon iHR320 spectrofluorometer and a 200 μL quartz cuvette with 1 cm pathlength were employed. The excitation wavelength was 320 nm and the emission was registered from 340 to 600 nm. The photomultiplier detector voltage was set at 950 V and the instrument excitation and emission slits were both set at 5 nm.

Plate reader: A BMG Labtech FLUOstar Omega plate reader with 320/410 nm excitation/emission filters (10 nm bandwidth) in bottom optics configuration was used. The final samples (200 μL) were prepared and measured in UV-transparent 96-well plates (Corning Incorporated 3635).

Dityrosine calibration curves

Dityrosine standards of concentrations 2 μM, 1 μM, 500 nM, 250 nM, 125 nM and 62.5 nM were prepared by successive dilutions in 100 mM HEPES buffer (pH 7.4) and subsequently measured. The resulting emission data were used to generate the

calibration curves. In the plate reader, duplicates of each standard were measured, and the calibration curve was generated using the average values of the duplicates.

Limits of detection (***LOD***) and of quantification (***LOQ***) were determined using the following equations:

$$LOD = 3 \times S_a / b \quad (4.1)$$

$$LOQ = 10 \times S_a / b \quad (4.2)$$

where S_a is the standard deviation of the intercept and b is the slope.

Detection and quantification of dityrosine cross-links

$CuCl_2$ and H_2O_2 stock solutions were prepared in Milli-Q H_2O, while HAH was prepared in 100 mM HEPES (pH 7.4). The H_2O_2 stock solutions were prepared just before use. Solid monomeric Aβ(1-40) aliquots were dissolved in 20 μL of DMSO and sonicated for 1 h. Then, a 250 μM stock solution of Aβ(1-40) was prepared in 100 mM HEPES (pH 7.4).

Final samples were prepared adding the required reagents in the following order: first, the corresponding amount of 100 mM HEPES buffer pH 7.4, then HAH, $CuCl_2$, Aβ(1-40) and finally H_2O_2. The samples containing copper and Aβ(1-40) or copper and HAH were incubated at 37 ºC for 10 min previous to the addition of the remaining reagents. **Spectrofluorometer:** final concentrations were 30 μM Aβ(1-40), 30 μM $CuCl_2$, 30 μM HAH and 600 μM H_2O_2. **Plate reader:** final concentrations were 50 μM Aβ(1-40), 50 μM $CuCl_2$, 100 μM HAH and 1 mM H_2O_2. All samples contained 5% DMSO.

The measurements were performed immediately after sample preparation, after 24 h, after 48 h and after 72 h. The samples were incubated at 37 ºC between the measurements. For the measurements in the plate reader, the samples were shaken at 700 rpm between the measurements.

Aggregation studies of Aβ(1-40) in the presence of ThT

ThT stock solutions were prepared in 100 mM HEPES (pH 7.4). The required number of solid Aβ(1-40) aliquots were dissolved in 20 μL of DMSO and sonicated for 1 h. Then, a 250 μM stock solution of Aβ(1-40) was prepared in 100 mM HEPES (pH 7.4), which contained 312.5 μM ThT.

The final samples (200 μL) were prepared in 96-well plates (Clearline® 131012C) adding the required reagents in the following order: first, the corresponding amount of 100 mM HEPES buffer (pH 7.4), then H-His-Ala-His-OH (HAH), $CuCl_2$, Aβ(1-40)-ThT and finally H_2O_2. The samples containing copper and HAH peptide were incubated at rt for 10 min previous to Aβ(1-40)-ThT addition. The final concentrations were: 50 μM Aβ(1-40), 62.5 μM ThT, 50 μM $CuCl_2$, 100 μM HAH and 1 mM H_2O_2. The samples contained 5% DMSO.

A BMG Labtech FLUOstar Omega plate reader in bottom optics configuration was used. Kinetic measurements were initiated immediately after sample preparation. Endpoint measurements were performed at 37 ºC every 6 min during a period of 3 days, with continuous shaking (700 rpm). 440/490 nm excitation/emission filters with 10 nm bandwidth were used.

Evaluation of the morphology of aggregated Aβ(1-40) by transmission electron microscopy (TEM)

Formvar-coated copper grids of 200 mesh were activated by exposure to UV light for 5 min. Next, the samples were deposited for 1 min, after which the grids were washed with Milli-Q H_2O (3 × 20 s). Finally, the grids were treated with 2% uranyl acetate for 1 min and dried at rt.

The samples were visualised using a Tecnai Spirit TWIN (FEI) 120 kV TEM microscope equipped with a LaB6 emitter and a Megaview 1k×1k CCD at the Centres Científics i Tecnològics of the Universitat de Barcelona (CCiTUB).

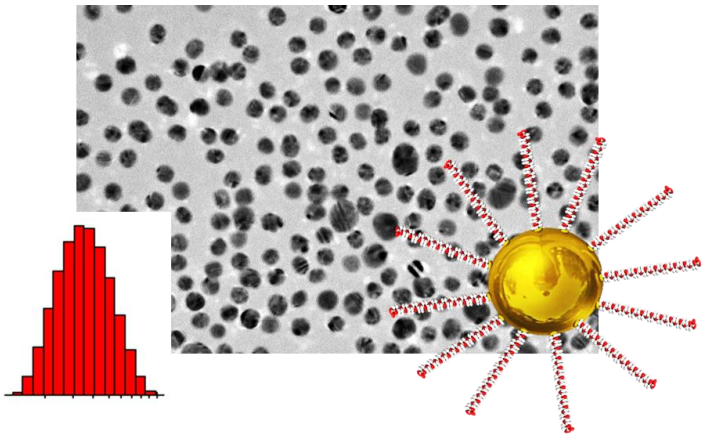

5. Conjugation of Cu(II)-chelating peptides to gold nanoparticles

5. Conjugation of Cu(II)-chelating peptides to gold nanoparticles

5.1 Introduction

5.1.1 The blood-brain barrier (BBB): the great challenge for CNS drug discovery

The ability of Cu(II)-chelating peptides to extract copper ions from Aβ, to prevent its copper-induced aggregation, and to inhibit ROS production and protein cross-linking, has been described in **Chapters 3** and **4**.[210] Such peptides thus represent potential synthons for the design of drugs that may lessen the copper-associated toxicity of Aβ. However, as explained in **Chapter 1**, any CNS drug candidate that is to be administered by conventional routes, must be able to cross the blood-brain barrier (**BBB**). This natural barrier is constituted by layers of pericytes, endothelial cells and by astrocyte endfeet.[95-97,275,276] BBB cells are tightly assembled, providing the brain with the impermeability required to maintain its highly controlled environment that is necessary for neural signalling.

Although the BBB is not completely impenetrable, as the brain also needs to be supplied with nutrients and to excrete metabolites, the search of substances capable of reaching the brain represents an important challenge.[99,101] To date, over 98% of the small molecules and all large molecules tested as drug candidates were unable to cross the BBB.[95-97] A certain lipophilicity is also necessary, which is often detrimental to water solubility. Therefore, it is rather unlikely that the polar and charged peptides herein presented can penetrate the BBB.

In recent years, it was shown that some nanoparticulate systems are able to reach the brain, which has generated a great impact on the field of biomedicine.[98] Among all available materials, gold nanoparticles (**Au NPs**) display a number of interesting properties that make them very promising materials: they are more stable than other types of nanoparticles; the fine-tuning of their size and shape has been extensively studied; their surface functionalisation is easy and versatile; they present a high degree of biocompatibility; their optical properties lie in the visible-infrared range.[99,100,277-279] Au NPs accumulate in several organs, including the brain.[99-102,280-283] Moreover, the introduction of appended ligands that activate mechanisms of brain uptake, such as

peptides that interact with the transferrin receptors of endothelial cells, has been described.[101,102]

5.1.2 The advent and evolution of Au NPs

Fascination for gold, possibly the most paradigmatic noble metal, comes from ancient times. First evidence of gold extraction comes from Bulgaria, more specifically Varna, in the 5th millennium BC.[284] Metallic gold has been used for thousands of years as a form of money and for jewellery. However, what was called "soluble gold" (that is, gold finely dispersed and suspended in a liquid) appeared in the 5th-4th centuries BC in China and Egypt. Roman and Greek civilisations attributed powerful curative properties to soluble gold against heart and venereal diseases, as well as tumours.[284] Its use for the diagnosis of syphilis (currently considered not completely reliable) was not abandoned until the 20th century.[285]

Gold dispersions provide glass and ceramics with ruby-red colours, and mankind has taken advantage of these properties in architecture and ornamentation.[284] The Lycurgus Cup is probably the most famous artistic example of such application. This cup represents the Thracian king Lycurgus being killed by the nymph Ambrosia, transformed in grapevine. When it is illuminated from behind or the inside, transmitted light makes the cup look red. When the light source is frontal, though, the reflected light makes the cup look green.

Already in the 19th century, Michael Faraday prepared a dark-red suspension of gold in CS_2 by means of the reduction of aqueous tetrachloroaurate(III), $AuCl_4^-$, with phosphorus.[284] He was the first person to study the optical properties of films prepared from liquid-gold dispersions. The term colloid, which refers to the fine dispersion of a phase into another continuous phase, appeared a few years later.

The more modern term "nanoparticle" is normally used nowadays to describe particles with sizes between 1 and 100 nm.[286] Within this range, the mean free path of electrons is comparable to the size of the particle; also, a high percentage of the atoms are arranged in the surface of the material.[278,287] This gives rise to unique properties, unprecedented for molecules and for bulk systems, which already have an impact on today's technology.[278,279,287-290]

In the last decades, chemists have developed very efficient synthetic pathways to prepare different types of nanoparticles, thanks to the discovery of their stabilisation and functionalisation with surfactants and ligands.[277,291,292] Further control on their shape has also been achieved, unveiling novel and exciting properties; hence, the number of publications involving nanoparticles has increased exponentially since then.[293,294] The interaction of anisotropic nanoparticulate building blocks, which has not been extensively studied yet, may afford complex structures and open the door to new and unexpected applications.[294-297] For instance, Wang and colleagues decorated polystyrene nanoparticles with gold nanodots arranged in linear, trigonal, tetrahedral or right-pyramidal dispositions, resembling the *sp*-hybridisation of carbon or silicon atoms.[298] Such nanoparticles with "valences" can potentially self-assemble through aurophilic interactions of the gold nanodots, generating so called "supraparticles" (**Figure 5.1**).

Figure 5.1: Polystyrene nanoparticles decorated with gold nanodots in linear, trigonal, tetrahedral and right-pyramidal arrangements.

5.1.3 Au NPs as drug carriers/delivery agents

Au NPs have attracted enormous interest as drug carriers or delivery platforms.[286,299] Colloidal gold provides enhanced stability and solubility, longer circulation times, improved cellular uptake and biodistribution, and high local drug concentration (one single Au NP can carry hundreds or thousands of appended ligands depending on the nanoparticle size).[286,299-302] Biomolecules such as proteins (*e.g.* insulin), nucleic acids and lipids can be adsorbed onto the nanoparticle surface and circumvent enzymatic degradation.[299,302]

For example, anticancer drugs can benefit from gold nanocarriers. The use of platinum-based drugs (cisplatin, oxaliplatin and carboplatin) is limited by their severe side-effects, and their connection to gold nanoscaffolds may improve their efficacy because of the extension of their circulation time and an enhanced penetration in tumour

cells.[300] Similarly, anti-HIV drugs have been connected to Au NPs with promising results.[301]

Cargos can be covalently attached to the carriers or bound through electrostatic interactions. To exert their activity, they can either remain connected or be released by different stimuli.[299,302] These stimuli can be internal, such as reduction by the highly abundant intracellular glutathione, or external, such as light activation, which can provide spatio-temporal control.[303,304]

In healthy tissues, passive uptake of nanoparticles takes place mainly via endocytosis, that is, they are engulfed by an invagination of the cell membrane and transfected into the cytosol inside a vesicle.[305,306] Importantly, nanoparticulate systems accumulate more in cancer cells due to the enhanced permeation and retention effect (EPR effect).[100,286,307] The vasculature of tumour tissues is generally much more leaky due to the overexpression of growth factors. This effect is supposed to facilitate the supply of macromolecules as well as tumour growth and expansion, but it may also bring an opportunity for nanoparticle-based therapeutics.[307]

BBB inflammation and disruption of the tight junctions have been observed in AD, which result in the permeation of this membrane.[275,276,308,309] Such feature might be advantageous for an enhanced access and accumulation of nanoparticles in the brain (similarly to the EPR effect).

On the other hand, specific uptake can be achieved by adding particular targeting ligands to the nanoconjugates.[101,102,302,310] Small molecules, peptides and antibodies have been attached with the aim of improving internalisation and selectivity in different tissues. For example, folic acid or the tumour necrosis factor (TNF) have been used for improved uptake by tumour cells.[302] BBB permeation has been improved by conjugating Au NPs with peptides targeting BBB receptors (for instance, transferrin, insulin or apolipoprotein receptors) or cell-penetrating peptides.[101,102]

The nanoparticle size has a great impact on the biodistribution.[280,281,283] Although some general trends have been observed, a screening of nanoparticles of different sizes is usually required to determine their biodistribution profiles. It is still not possible to predict the final destination, *i.e.* the target organ(s) and/or organelle(s), of a certain nanoparticulate system (characterised by several features such as the size, the charge or the presence of appended ligands).

In this chapter, Au NPs with core diameters of 5 nm (**5Au**) and 14-15 nm (**15Au**) are described, including their preparation, functionalisation and characterisation. The two different sizes of the NPs were selected because it has been shown that 5 nm[100] and 14-15 nm[99,280] Au NPs (and more generally nanoparticles with core sizes below 20 nm)[102,281,283,311] accumulate in the brain.

5.1.4 PEGylation of Au NPs

Under certain conditions, nanoparticles and other colloids tend to form aggregates through either reversible (flocculation) or irreversible processes (coagulation) to reduce their surface tension. According to the theory developed by Derjaguin, Verwey, Landau and Overbeek in 1940 (DVLO theory), the stability of a colloidal system depends on the balance between attractive van der Waals interactions and repulsive electrostatic forces.[312-314] Hence, if two particles collide with sufficient energy to overcome the electrostatic repulsion, they will adhere irreversibly together due to the attractive van der Waals interactions.

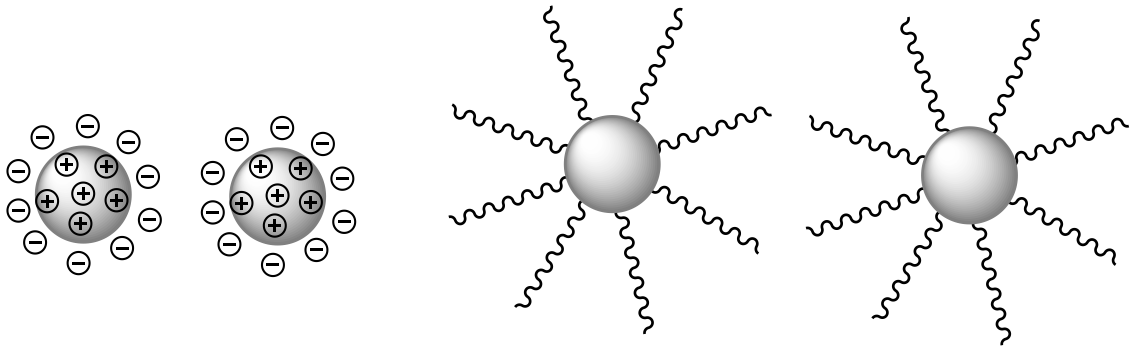

Figure 5.2: Electrostatic and steric stabilisation of nanoparticles that prevent aggregation.

To prevent the aggregation of nanoparticles, two main methodologies are commonly used, which are schematised in **Figure 5.2**: functionalisation with charged species (electrostatic functionalisation) or with polymers (steric stabilisation).[312-314] Both strategies are based on osmotic phenomena and do not allow the particles to be in close contact so that adhesion cannot occur.[313] Electrostatic stabilisation is often inexpensive and the colloid can be stabilised or flocculated by altering the concentration of the ionic species in the medium; however, this is not suitable for concentrated or electrolyte-sensitive systems. The functionalisation with polymers is

usually simple and allows the re-dispersion of the agglomerated particles. Though, this method may be expensive and the presence a polymeric shell is sometimes inconvenient.[292]

The coating of nanoparticles with polyethylene glycol (PEG), also known as PEGylation, is a common, FDA-approved strategy for the improvement of the pharmacokinetic properties and efficacy of nanoparticles or any other drug in general.[315-317] PEG polymers are water soluble, non-toxic, and simply eliminated through the liver and kidneys. Importantly, the lack of electric charge prevents nonspecific adsorption of proteins as well as macrophage recognition and clearance, which leads to extended blood circulation times.[282,286,292,306,316]

Due to the aforementioned advantages, this approach has been extended to other systems such as dendrimers and nanoparticles for biomedical applications.[315,318] Additionally, PEG chains terminated with different functionalities such as carboxylate, amino or thiol groups allow the covalent coupling of targeting ligands, peptides and drugs.[311,318-320] Therefore, PEGylation can also be regarded as a tool for the design and preparation of multifunctional systems.

Thus, the Au NPs of 5 and 14-15 nm, prepared in the present study, were treated with poly(ethylene glycol) 2-mercaptoethyl ether acetic acid (**HS-PEG$_{2100}$-COOH**) to afford the respective PEGylated nanoparticles **5Au-COOH** and **15Au-COOH**. This polymer presents a thiol group at one end for the interaction with Au NPs through a strong Au-S bond, and a carboxylic group on the other side, which can be used for the connection to peptides *via* the formation of an amide bond (**Figure 5.3**).[311,319,320]

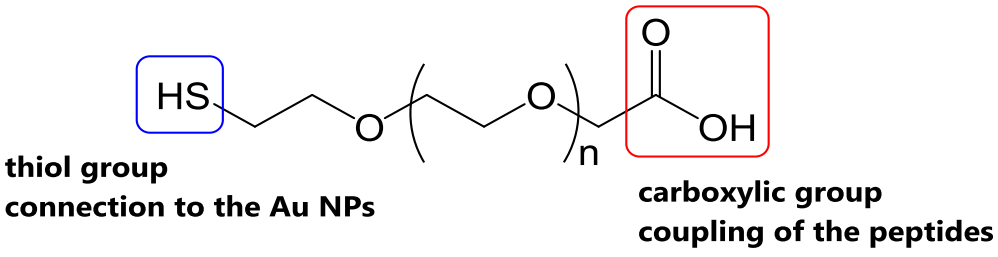

Figure 5.3: Poly(ethylene glycol) 2-mercaptoethyl ether acetic acid (**HS-PEG$_{2100}$-COOH**) for the coating of the Au NPs.

5.1.5 Preparation of Ac-His-Lys(Coum)-His-Lys-NH_2 (AcHK^{c}HK) and its subsequent coupling to Au NPs

Ac-His-Lys(Coum)-His-Lys-NH_2 (**AcHK^{c}HK**), whose synthesis was described in **Chapter 2**, was selected to couple it to Au NPs. AcHK^{c}HK indeed exhibits interesting properties/features (**Figure 5.4**); it includes *i)* an His-Xaa-His unit, responsible for the binding of Cu(II) ions (see **Chapter 3**); *ii)* a coumarinic fluorescent probe for the quantification of the peptide bound to the nanocarriers; *iii)* an ε amino group from the side chain of Lys4 allowing its connection to the Au NPs through the carbodiimide-assisted generation of an amide bond with the carboxylate of the PEG chains, and *iv)* carboxamide-protected *N*-terminal amino and *C*-terminal carboxylic functions to solely connect it to the nanoparticles through the ε amino group of Lys4.

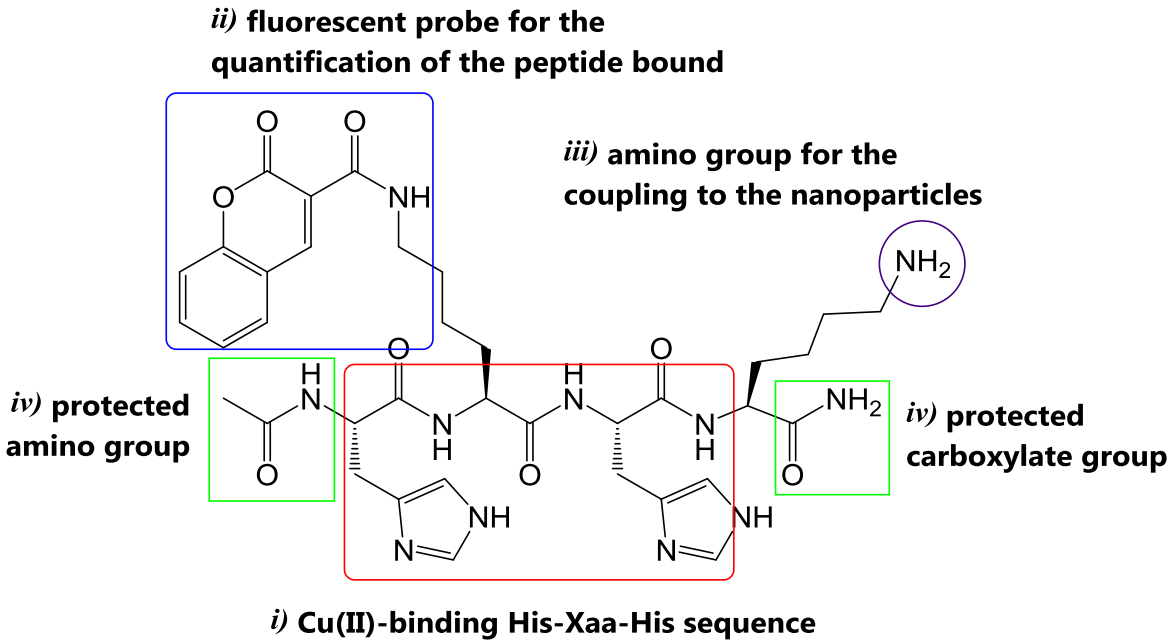

Figure 5.4: Structural and functional features of Ac-His-Lys(Coum)-His-Lys-NH_2 (AcHK^{c}HK).

In this chapter, the preparation of the AcHK^{c}HK-functionalised nanoparticles **5Au-HK^{c}HK** and **15Au-HK^{c}HK** is described. The evaluation of the Cu(II)-chelating properties of the nanoconjugates and preliminary cell-survival studies for 15Au-COOH and 15Au-HK^{c}HK are presented as well. The peptides coupled to the Au NPs were expected to retain their Cu(II)-binding capacities, improved BBB-permeability (thanks to the Au NPs) and resistance to proteolysis (see section **5.1.4**).

5.2 Objectives

- Synthesis of Au NPs of sizes 5 and 15 nm, subsequent functionalisation with HS-PEG_{2100}-COOH and coupling of $AcHK^cHK$.
- Characterisation of the different nanomaterials obtained and quantification of the amount of peptide linked to the NPs.
- Evaluation of the Cu(II)-chelating properties of the peptide-functionalised nanomaterials.
- Viability study using neuronal embryo cells of wildtype mice in the presence of $AcHK^cHK$, 15Au-COOH and 15Au-HK^cHK.

5.3 Results and discussion

5.3.1 Synthesis and functionalisation of Au NPs

The synthetic procedures for the preparation of solid nanoparticles are usually classified into two groups (**Figure 5.5**):[321-323]

- **Top-down approaches.** These use bulk starting materials, which are reduced in size by techniques that include mechanical methods (trituration, grinding) and laser or chemically-driven lithography.
- **Bottom-up approaches.** The source materials consist in atoms, ions and molecules, which self-assemble into nanometric structures through a sol process, hydrothermal synthesis, pyrolysis or vapour deposition, among many others.

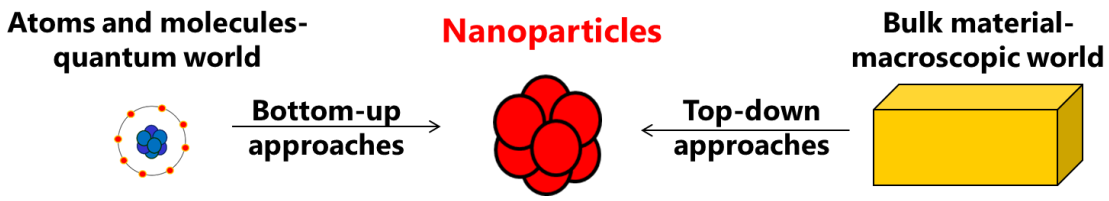

Figure 5.5: Bottom-up and top-down strategies for the synthesis of nanoparticles.

The Au NPs described herein were synthesised following the bottom-up sol process, which relies on the rapid generation of a supersaturated solution of the precursor

material, namely Au(0).[287,324] In a first step (nucleation), Au(III) is quickly reduced to Au(0) and small nuclei are formed (**Figure 5.6**).[277,287,291,324] The source of Au(III) ions is usually tetrachloroauric(III) acid, $HAuCl_4$, which is industrially obtained by reaction of metallic gold with *aqua regia*.[288] The nuclei under a critical size value, also called embryos, will redissolve, whereas the bigger ones will be stable.[277,287,291,324] In a second step (growth), the seeds further grow to form the final material. The ultimate maturation of the colloid occurs through diffusion and other mechanisms such as Ostwald ripening, in which large nanoparticles grow in expense of small ones.[277,287,291]

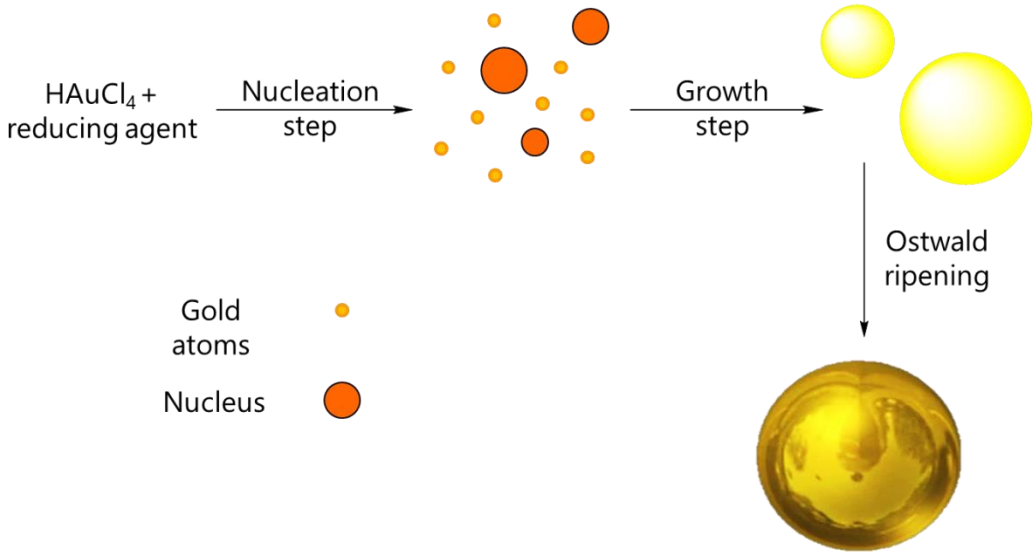

Figure 5.6: Steps in the generation of Au NPs by the sol process.

The most popular methodology for the aqueous preparation of Au NPs consists in variations of the approach reported by Turkevich in 1951, in which sodium citrate was used as the reducing agent for the preparation of 20 nm Au NPs.[325] Citrate ions have a double function; they reduce Au(III) to Au(0) and cap the resulting gold nanospheres, conferring a high colloid stability. In 1973, Frens published a method to customise the size of the nanoparticulate material by modifying the ratio of the reducing/stabilising agents.[326,327]

Other methodologies involving phase-transfer systems, membranes and reversed micelles have also been developed.[287] Physical approaches such as laser irradiation, ultrasounds or pyrolysis are alternative strategies available.

The size of the nanoparticles is determined by several factors:[327]

- **Temperature:** higher temperatures promote the formation of bigger nuclei and, hence, larger nanoparticles;
- **Reaction time:** longer reaction times lead to the formation of bigger nanoparticles due to an extended growth step;
- **Strength of the reducing agent:** strong reducing agents rapidly generate a great number of small nuclei, leading to smaller nanoparticles;
- **Other parameters:** the concentration of reagents and their relative amounts, the pH and the presence of surfactants modulate the size as well as the morphology of the particles.

The 5 nm Au NPs (**5Au**) were obtained using sodium borohydride as the reducing agent (**Figure 5.7**). When a basic solution of $NaBH_4$ was added to an acidic solution of $HAuCl_4$, under nitrogen and at room temperature, the colour immediately turned from pale yellow to bright orange, indicating the generation of colloidal gold.[328] The 5Au nanoparticles were subsequently functionalised with PEG chains, which improved their stability, up to several months (see below).

Next, the preparation of 15 nm Au NPs (**15Au**) was performed applying a modification of Turkevich's method in which aqueous sodium citrate was added to a boiling and stirred solution of $HAuCl_4$ in Milli-Q H_2O (**Figure 5.7**).[329] Sodium citrate is a weaker reducing agent than sodium borohydride and thus yields bigger Au NPs. The reaction mixture quickly changed from pale yellow to colourless and then to reddish-purple. The 15Au nanoparticles obtained were stable for months.

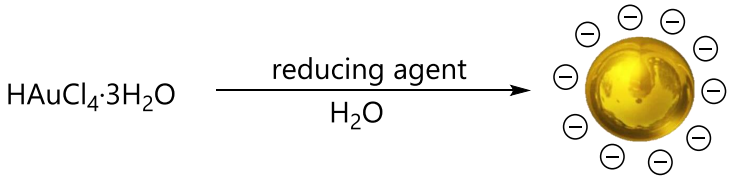

⊖ = borohydride for 5Au; citrate for 15Au

Figure 5.7: Synthesis of Au NPs with different core sizes using sodium borohydride (**5Au**) or sodium citrate (**15Au**) as the reducing agents.

The precursor nanoparticles were then functionalised with HS-PEG_{2100}-COOH (**Figure 5.8**). To cover the surface of the nanoparticles with a dense, brush-like monolayer of PEG, it should be considered that each PEG chain occupies 0.35 nm^2.[318,330] For the

calculation of the surface of the Au NPs, they were assumed to be perfect spheres.[331] Hence, the surface of a spherical nanoparticle, S_{NP}, can be calculated using **Equation 5.1**:

$$S_{NP} = 4\pi(R_{NP})^2 \qquad (5.1)$$

where R_{NP} is the radius of the nanoparticle, namely 2.5 nm for 5Au and 7.5 nm for 15Au. Thus, the surface of a 15 nm Au NP is 706.9 nm^2, whereas the surface of a 5 nm NP is 79 nm^2. Since the reported footprint of a thiol-terminated PEG molecule in an Au NP is about 0.35 nm^2, the number of PEG chains per nanoparticle, N_{PEG}, can be determined using **Equation 5.2**:

$$N_{PEG} = S_{NP}/0.35 \qquad (5.2)$$

Therefore, each 5 nm or 15 nm nanoparticle can accommodate up to 224 or 2020 PEG molecules, respectively. The PEGylation reaction was performed in Milli-Q H_2O by adding a 25% excess of HS-PEG_{2100}-COOH related to the total coverage of the surface. The exact size and concentration of the Au NPs were determined by transmission electron microscopy (**TEM**), as explained in section **5.3.2**.

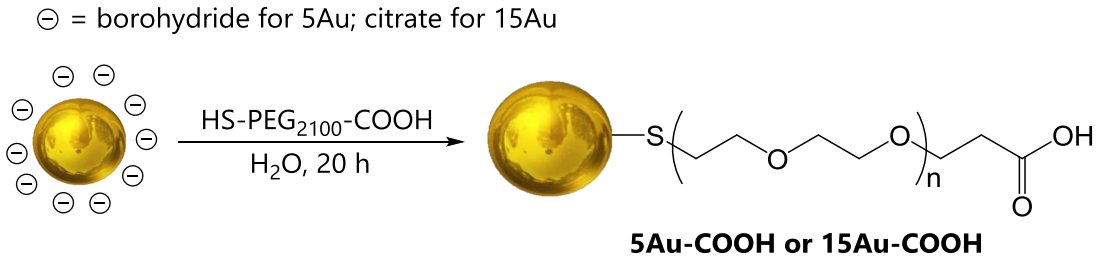

Figure 5.8: Functionalisation of Au NPs with HS-PEG_{2100}-COOH.

The 5Au nanoparticles were PEGylated immediately after preparation due to their lower stability (as a result of the higher surface/volume ratio), while the functionalisation of 15Au could be carried out even 2 months after their synthesis. The PEGylated nanoparticles of 5 (**5Au-COOH**) and 15 nm (**15Au-COOH**) were resistant to irreversible aggregation in the presence of high concentrations of salts, and upon heating or centrifugation.

Once PEGylated, the NPs were functionalised with AcHK^{c}HK through the activation of the PEG carboxylate groups (**Figure 5.9**). Such activation was achieved using the water-soluble coupling agent 1-ethyl-3-(3-dimethylaminopropyl)carbodiimide (**EDC**; see

Chapter 2 for the mechanism of the generation of amide bonds between amino and carboxylate groups using carbodiimides). EDC has been successfully employed for the coupling of proteins and antibodies to different nanoparticulate systems.[311,319,320,332,333] Upon nucleophilic attack of the ε amino group of AcHK^{c}HK to the carbodiimide-activated carboxylate groups, an amide bond connecting the peptide and the nanoparticle-bound PEG chains was produced, generating the nanoconjugates **5Au-HK^{c}HK** and **15Au-HK^{c}HK**.

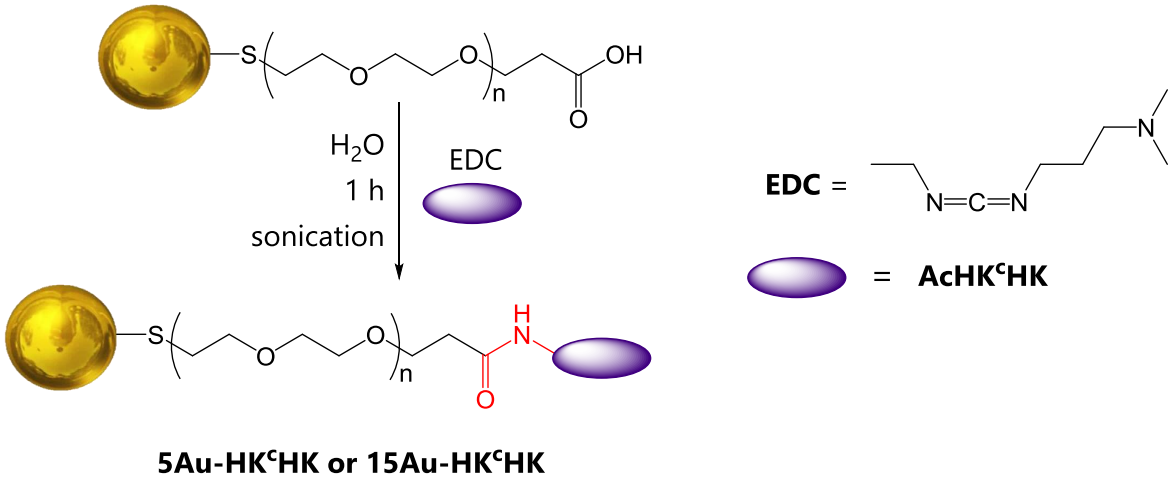

Figure 5.9: Coupling of AcHK^{c}HK to the Au NPs using the water-soluble carbodiimide EDC.

The reaction was carried under sonication for 1 h, and freshly prepared solutions of EDC were rapidly added to avoid the reaction of water molecules with the *O*-acylisourea produced, which would inactivate EDC.[319] Although such reaction has been reported in buffered media, the coupling of AcHK^{c}HK to Au-COOH had to be performed in pure Milli-Q H_2O.[319] Indeed, the reaction in either borate (10 or 200 mM) or 0.1X PBS buffers was unsuccessful, most likely due to the side reaction of borate or phosphate with EDC.

The nanomaterials were differently purified depending on their size. 15Au-COOH and 15Au-HK^{c}HK were purified by applying 3 cycles of centrifugation and resuspension in 0.1X PBS. 5Au-COOH and 5Au-HK^{c}HK were purified by dialysis using semipermeable membranes as sedimentation through centrifugation could not be achieved with these small NPs.

5.3.2 Characterisation of the Au NPs

5.3.2.1 Nanoparticle core size and concentration

The high electron density of gold atoms allows the direct visualisation of their NPs by transmission electron microscopy (TEM). The carbon-based appending ligands (*viz.* the PEG chains and the chelating peptides) display much lower electron densities and cannot therefore be observed by this technique, unless they are stained (*e.g.* with uranyl acetate).

TEM images and size distributions of 5Au-HK^{c}HK and 15Au-HK^{c}HK NPs are shown in **Figure 5.10**. The metallic core of 5Au-HK^{c}HK presented an average size of 4.50 ± 0.70 nm, most nanoparticles being in the range of 3.5-5.0 nm. The average size of 15Au-HK^{c}HK was 14.5 ± 1.7 nm, with most nanoparticles in the range of 13.0-15.0 nm. The core size dispersities obtained for both 5Au-HK^{c}HK$^{100,334\text{-}336}$ and 15Au-HK^{c}HK^{99,280,334} were comparable to those reported in the literature.

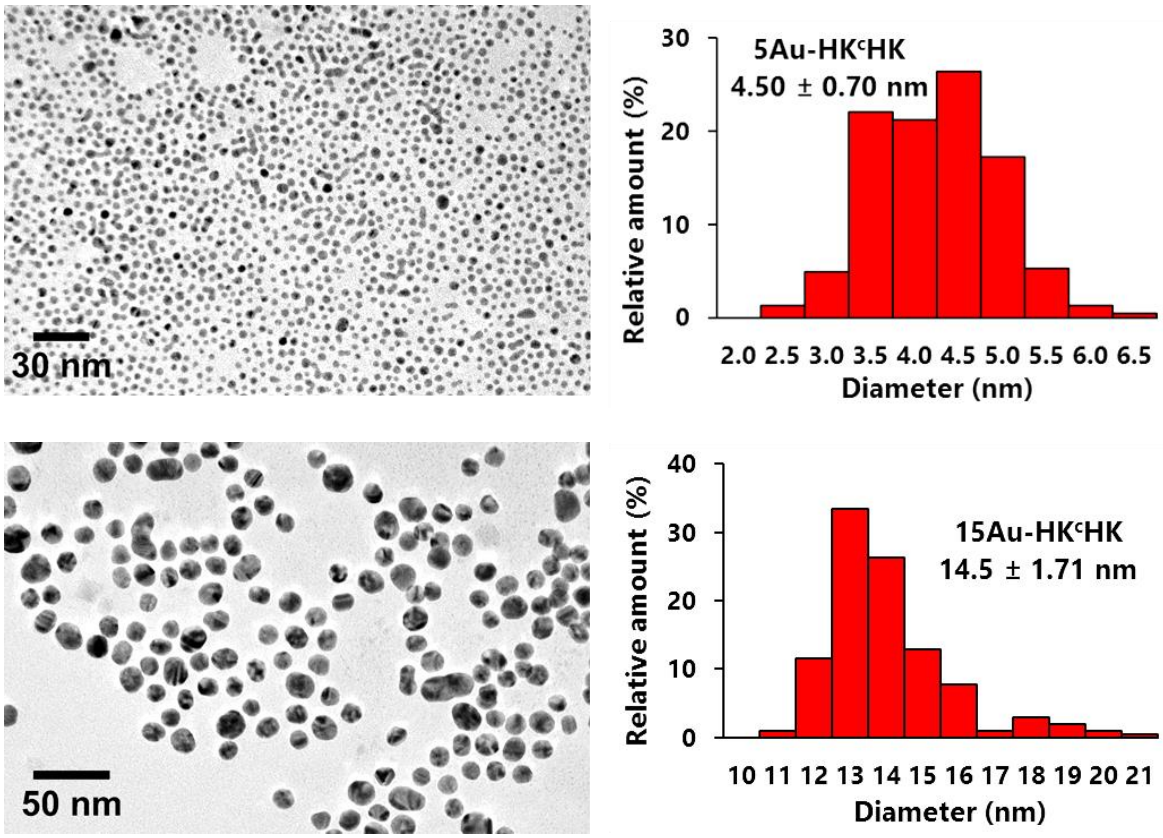

Figure 5.10: TEM images and metallic core-size distributions of 5Au-HK^{c}HK (**top**) and 15Au-HK^{c}HK (**bottom**).

The initial concentration of Au NPs was estimated once the mean size of the nanoparticles was determined from the TEM images. First, the number of total gold atoms in the solution, N_{Au}, was obtained using **Equation 5.3**:[331]

$$N_{Au} = N_A \times V_{Au} \times [HAuCl_4] \qquad (5.3)$$

where N_A is Avogadro's number, and V_{Au} and $[HAuCl_4]$ are the volume and the concentration of the solution of $HAuCl_4$, respectively. Then, the number of gold atoms per nanoparticle, *i.e.* N, was obtained using **Equation 5.4**:

$$N = (R_{NP} / R_{Au})^3 \qquad (5.4)$$

where R_{NP} is the mean radius of the nanoparticles, obtained by TEM, and R_{Au} is the atomic radius of gold (*viz.* 137 pm).[331] Next, the number of nanoparticles, N_{NP}, is obtained using **Equation 5.5**:

$$N_{NP} = N / N_{Au} \qquad (5.5)$$

Finally, the concentration of nanoparticles in the colloid, namely $[NP]$, was obtained using **Equation 5.6**:

$$[NP] = N_{NP} / (N_A \times V) \qquad (5.6)$$

where V is the final volume of the suspension. Hence, the initial concentration of Au NPs was determined to be 113 nM and 6.14 nM for the 4.5 and 14.5 nm nanoparticles, respectively (see section **5.5.2** for experimental details).

5.3.2.2 Monitoring the functionalisation by UV-Visible spectroscopy

For particles with sizes below the Bohr radius, electron motion is confined in the particle, in contrast to bulk metals where the electrons can travel throughout the material.[278] This results in higher band-gap energies and in the quantisation of the energy levels and, thus, to characteristic absorption phenomena. The optical properties of nanometric semiconductors, such as CdSe nanoparticles, are dramatically dependent on the particle size due to the different quantisation and separation of the energy levels.[278,297,337]

Among the unique optical phenomena arising from the quantum confinement effect, the surface plasmon resonance (**spr**) is one of the most important and exploited

ones.[278,337,338] The surface plasmon resonance is caused by the oscillation of electrons in the conduction band. When nanoparticles are irradiated with light with the adequate frequency, the electron density on the surface is polarised and oscillates in resonance with the electromagnetic wave, as schematised in **Figure 5.11**.[278,337,338]

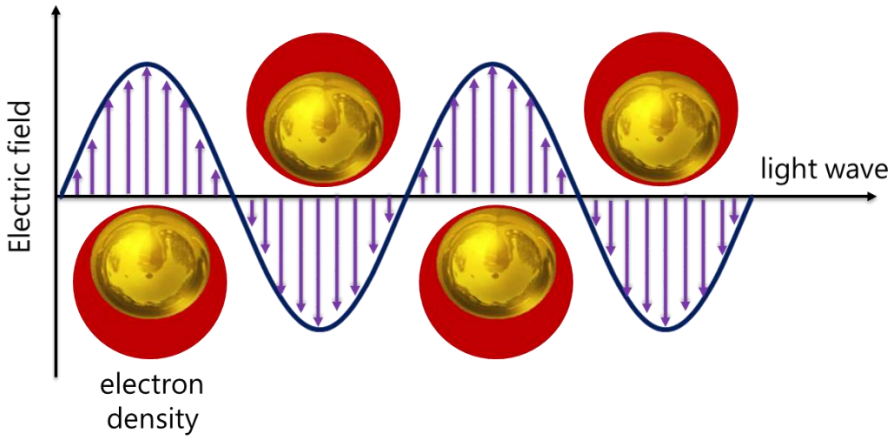

Figure 5.11: Radiation-induced oscillation of electron density giving rise to the spr effect.

The frequency of the plasmonic oscillation is dependent on the dielectric constant of the surroundings of the nanoparticle. Different solvents and capping ligands cause a variation in the dielectric constant, and therefore induce a shift of the spr absorption wavelength.[278,279] In addition, molar extinction coefficients of spr absorption bands are orders of magnitude higher than those of the best organic chromophores; they are even larger for anisotropic particles.[278,279,297,337,339] The spr phenomenon has found a vast number of sensing and imaging applications in different fields;[340] in biology and biomedicine, this phenomenon is used for the detection and imaging of relevant biomolecules.[290,339,341] Furthermore, differently-shaped anisotropic nanoparticles can provide additional, more sophisticated effects.[296,297,342]

Metal nanospheres present small variations of their absorption depending on their diameters. For example, gold nanospheres are typically red-coloured and their tone changes with their size.[278,297,337] Anisotropic nanoparticles (*e.g.* nanorods, nanocages, core-shell structures, etc.) display huge changes and particular features.[278,341,342] For instance, gold nanorods present two plasmonic absorptions: a weak transversal (≈ 520 nm) and a strong longitudinal ones at wavelengths that can be located at the near-infrared (NIR) range, depending on their length-to-width ratio.[278,296,297,342]

The spr band of 5Au-COOH nanoparticles appeared at 509 nm, which increased to 512 nm upon functionalisation with AcHK^{c}HK (**Figure 5.12**, left). The spr band of 15Au appeared at 519 nm, a value that red-shifted to 522 nm upon reaction with HS-PEG$_{2100}$-COOH (**Figure 5.12**, right). No further variation was observed upon reaction of 15Au-COOH with AcHK^{c}HK.

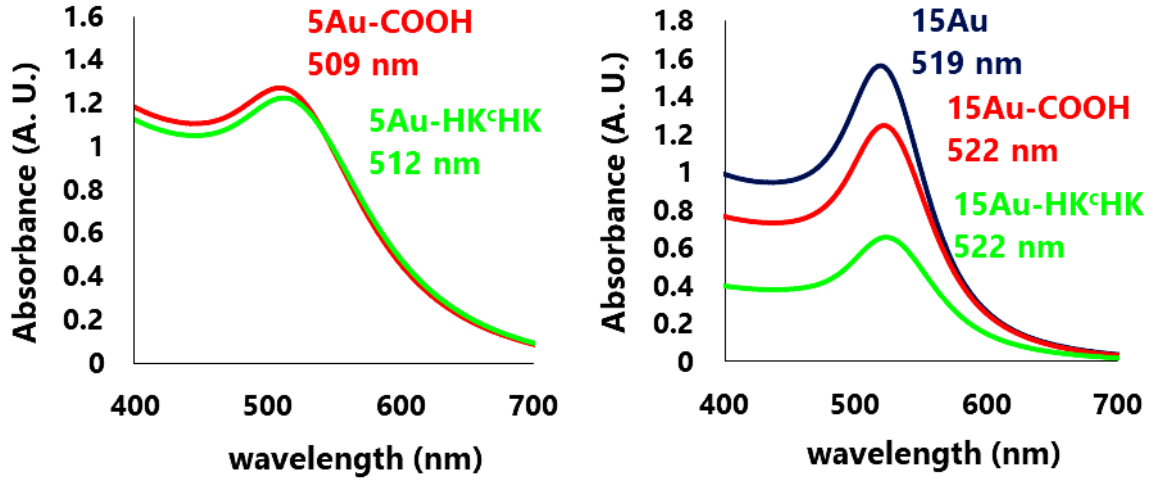

Figure 5.12: Surface plasmon resonance (spr) bands of the different nanomaterials, determined by UV-Vis spectroscopy. 5-Au-COOH (95 nM), 5Au-HK^{c}HK (92 nM), 15Au-COOH (2.27 nM) and 15Au-HK^{c}HK (1.20 nM) were analysed in 0.1X PBS, while 15Au (3.07 nM) was studied in Milli-Q H_2O.

The spr values obtained for the 5 nm (509-512 nm) and the 15 nm nanoparticles (519-522 nm) were similar to those reported elsewhere.[279,297,328,334-337,343] The red-shift of the spr bands with the increase of the nanoparticle size is due to a reduction of the energy bandgaps.[278] It is worth mentioning that, for 15Au nanoparticles, the addition of a high excess of HS-PEG$_{2100}$-COOH (25-fold the amount required for a complete covering of the surface) only resulted in a slight deviation of the spr absorption.

The spr absorptions were used to estimate the concentration of the different batches. The molar absorptivity of 5Au-COOH and 15Au-COOH was calculated from the spr absorption values of the samples before purification, as their concentration was directly related to that of the precursor sample (whose concentration was calculated from the initial [$HAuCl_4$] and the size of the NPs determined by TEM; see above). The purification steps, especially those involving centrifugation, led to a decrease of the final [Au NP].

5.3.2.3 PEGylation density

Thermogravimetric analysis (**TGA**), in which the weight loss of a sample (thermal decomposition) is monitored as a function of the temperature, was carried out to quantify the amount of HS-PEG_{2100}-COOH bound to the surface of 15Au-COOH.[330] PEGylated Au NPs are known to decompose at about 320 ºC, losing the PEG chains.[330] TGA requires high amounts of sample, namely about 5 mg; for the 5Au-COOH nanoparticles, this would correspond to 50-60 L of solution. Therefore, TGA could not be performed with these NPs.

As explained in section **5.3.1**, the footprint of a thiolate-PEG chain connected to an Au NP in a brush-like conformation is 0.35 nm^2.[318,330] Using **Equations 5.1** and **5.2**, the number of PEG chains per Au NP having an average size of 14.4 nm (as determined by TEM; see below) was found to be 1861.

The number of gold atoms per nanoparticle was 1.45×10^5 according to **Equation 5.4**; considering the molar masses of HS-PEG_{2100}-COOH (average molar mass of 2100 g/mol) and Au (196.967 g/mol), the mass percentage corresponding to the PEG chains, $\%_{PEG(m/m)}$, can be determined using **Equation 5.7**:

$$\%_{PEG\,(m/m)} = mass_{PEG} / (mass_{PEG} + mass_{Au}) \times 100 \quad (5.7)$$

where $mass_{PEG}$ and $mass_{Au}$ are the mass of PEG and the mass of gold per mol of nanoparticle, respectively. The calculated value of $\%_{PEG(m/m)}$ (and hence the expected loss of mass) was 12.0%.

The TGA results obtained for 15Au-COOH are shown in **Figure 5.13**. About 10 % mass loss occurred upon heating the sample from 30 to 460 ºC. An abrupt weight decrease was observed at around 350 ºC, which corresponded to the loss of approximately 1540 PEG chains per nanoparticle, namely 83% coverage of the total surface of the nanoparticle.

Such surface coverage was sufficient to prevent the aggregation of the nanomaterials and provided a high number of functional carboxylic end groups for the coupling of $AcHK^cHK$. Furthermore, such high-density PEG-brushes would prevent the undesired adsorption of large (bio)molecules.

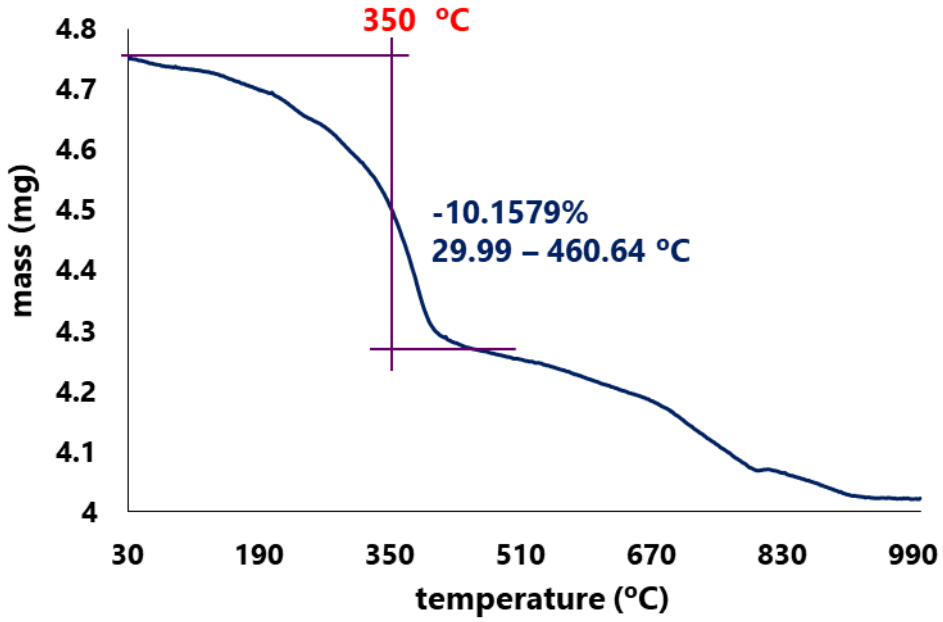

Figure 5.13: Thermogravimetry curve obtained for 15Au-COOH nanoparticles with an average size of 14.4 nm.

5.3.2.4 Hydrodynamic size

The Au NPs were subsequently characterised by dynamic light scattering (**DLS**, also called Quasi-Elastic Light Scattering or Photon Correlation Spectroscopy). DLS detects the Brownian motion of colloidal particles in the submicron range (that is, the random motion of particles in a liquid caused by the collision with the solvent molecules surrounding them) and relates it with their size.[344-346] The diameter determined by DLS is called the hydrodynamic size since it refers to the motion of the particles in a fluid (typically a liquid). Since this motion is affected by the size of both the metallic core and the surface ligands, this technique provides information about the total size of the functionalised particles (*viz.* the PEGylated Au NPs).

To determine their hydrodynamic size, the Brownian motion of the particles is detected using a laser. Then, the fluctuation rate of the light scattered by the colloid is measured and correlated to the hydrodynamic size of the particles by using the Stokes-Einstein equation (**Equation 5.8**):[344-346]

$$d(H) = \frac{kT}{3\pi\eta D} \qquad (5.8)$$

where ***d(H)*** is the hydrodynamic size, ***k*** is the Boltzmann's constant, ***T*** is the temperature of the system, ***η*** is the viscosity of the fluid at the temperature of measurement and ***D*** is the translational diffusion coefficient, which defines the velocity of the Brownian motion. Large particles exhibit a slow Brownian motion, whereas small ones are pushed further in the liquid phase and move faster. The translational diffusion coefficient is affected by several other factors, such as a non-spherical shape, the ionic strength of the medium or the presence of polymers on the particle surface.[344,345]

According to the Rayleigh theory, when the diameter of the particles, ***d***, is notably smaller than the wavelength of the incident light ($d \leq \lambda/10$), then the intensity of the scattered light is proportional to d^6.[346] For instance, the intensity of the light scattered by a 50 nm particle is 10^6 times higher than that scattered by a 5 nm particle.

The distribution of the size of the species can be expressed in terms of number, volume or intensity of scattered light (**Figure 5.14**).[346] If we consider a system composed by equal amounts of nanoparticles of size 5 and 50 nm, the distribution number will be 1:1, while the volume distribution will be $1:10^3$ since it is proportional to d^3. When the data are converted into an intensity distribution, the ratio is $1:10^6$ as the intensity of scattered light is proportional to d^6.

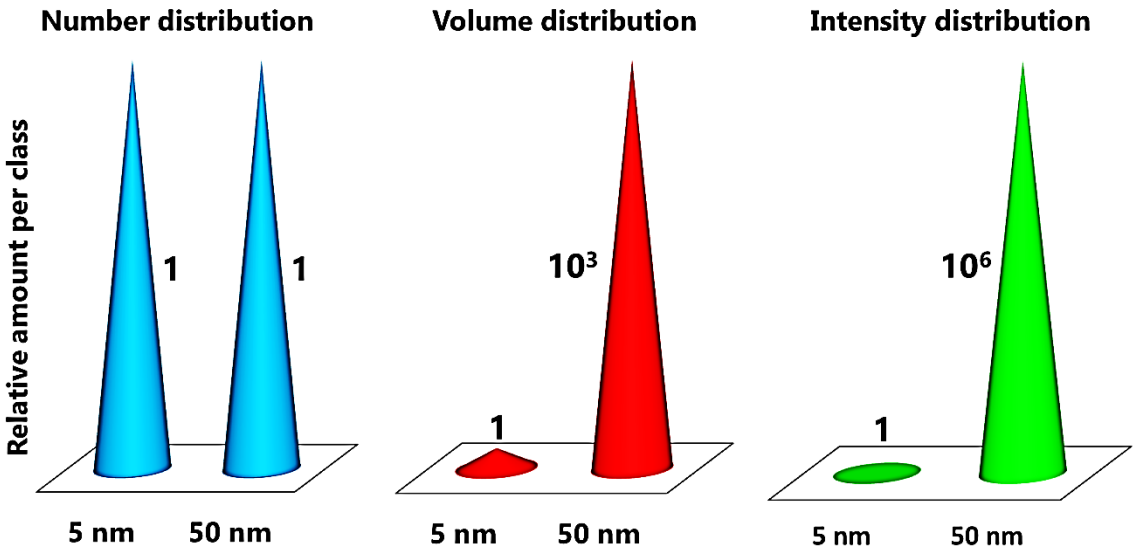

Figure 5.14: Number, volume and intensity distributions of a 50/50 mixture of nanoparticles with 5 and 50 nm diameters.

The DLS histrograms (intensity distribution) obtained for the 5 nm Au NPs in 0.1X PBS are shown in **Figure 5.15**. Characteristic peaks centred at 19 and 17 nm were observed

for 5Au-COOH and 5Au-HK^{c}HK, respectively. The smaller size observed for 5Au-HK^{c}HK (compared to 5Au-COOH) might be due to its less charged surface, giving rise to a somewhat folded peptide-PEG corona. It should be stressed that the hydrodynamic size of the initial 5Au NPs could not be measured due to their poor stability; hence, the size increase upon functionalisation with HS-PEG$_{2100}$-COOH could not be determined.

In addition, peaks centred at 250-300 nm appeared, which might be due to agglomerated nanoparticles, particularly large nanoparticles or artefacts that originated during the measurements or the subsequent mathematical treatment. Under the above-discussed considerations, larger nanoparticles scatter much more light, meaning that the number of large nanoparticles or aggregates should be negligible compared to that of 5Au. It should be mentioned that the samples were filtered through 0.2 μm filters prior to their measurement and that no large particles were observed by TEM. Such peaks might arise from reversible aggregation (flocculation) of the Au NPs; longer sonication times previous to DLS measurements might be required.

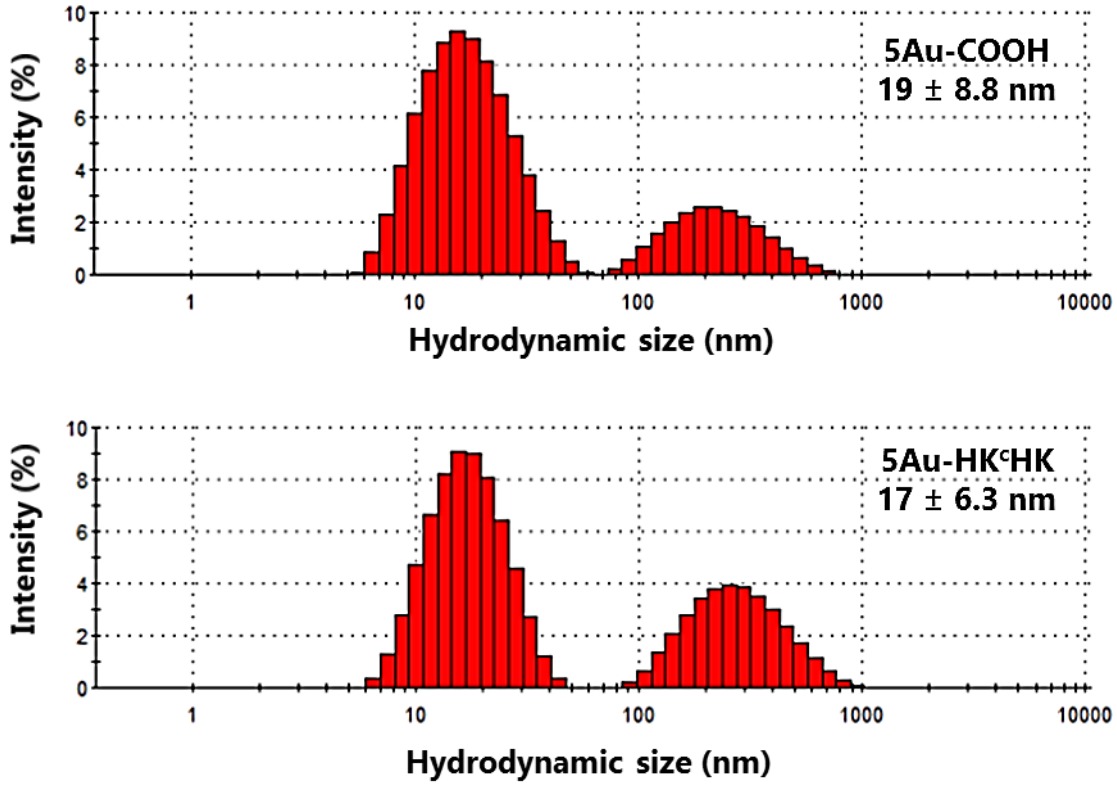

Figure 5.15: Intensity distributions of the hydrodynamic size of 5Au-COOH (**top**) and 5Au-HK^{c}HK (**bottom**) in 0.1X PBS (pH 7.4).

Figure 5.16 shows the DLS spectra (intensity distribution) obtained for the 15 nm Au NPs in 0.1X PBS. The hydrodynamic size increased with respect to 15Au upon coating with PEG (from 30 to 38 nm). It should be pointed out here that, as the 15Au samples were (necessarily) studied in Milli-Q H_2O, the difference observed might be incorrect; indeed, in ultrapure water, 2-10 nm larger values for hydrodynamic sizes are usually obtained compared to buffered solutions because the absence of ions impedes the shielding of long-distance interparticle interactions.[346]

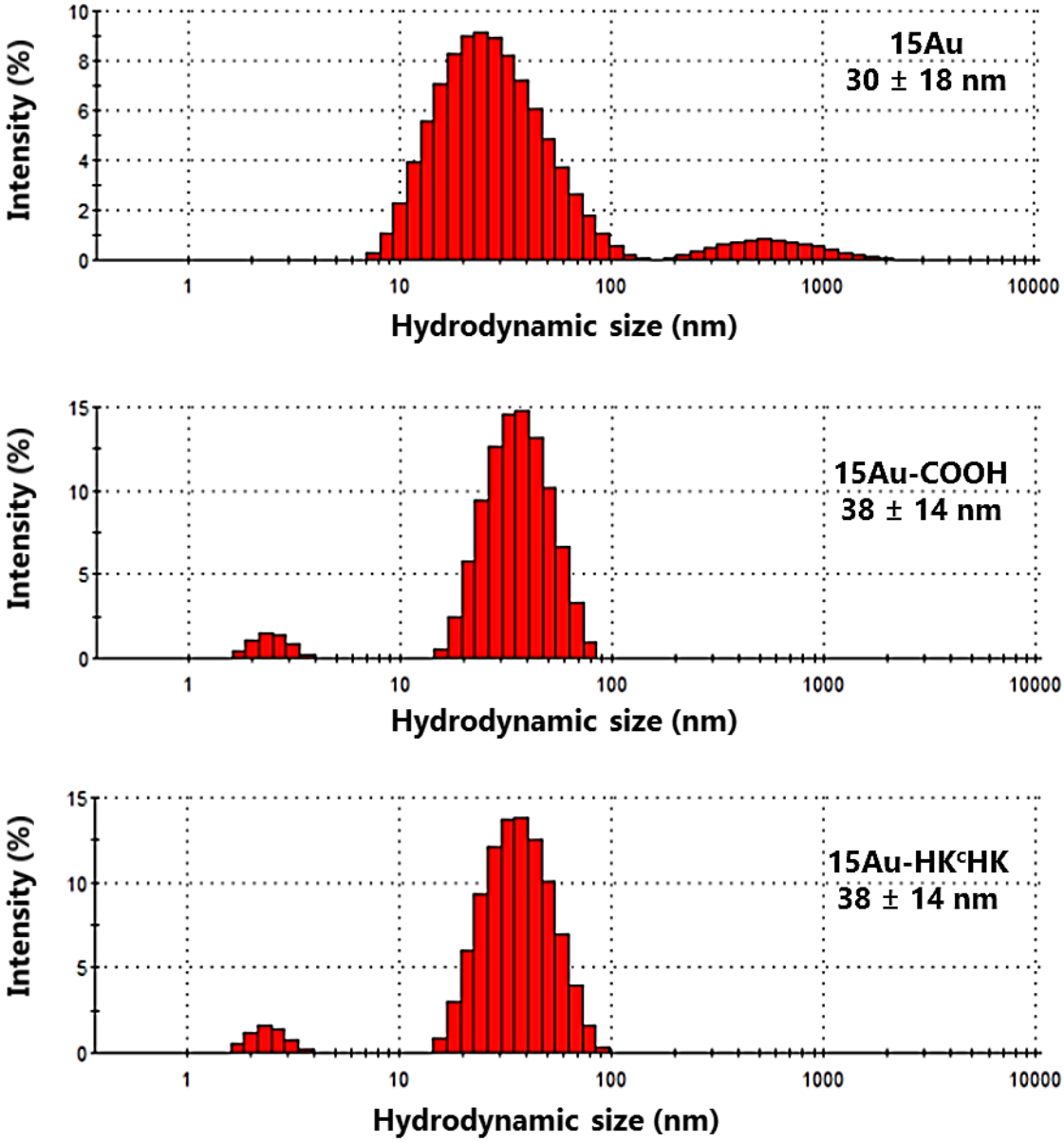

Figure 5.16: Intensity distributions of the hydrodynamic size of 15Au in Milli-Q H_2O (**top**), 15Au-COOH (**middle**) in 0.1X PBS (pH 7.4) and 15Au-HK^{c}HK (**bottom**) in 0.1X PBS (pH 7.4).

The 15Au (citrate) samples had to be prepared in Milli-Q H_2O since aggregation rapidly occurred in buffered solutions; in contrast, the 15Au-COOH and 15Au-HK^{c}HK samples were measured in 0.1X PBS, and no significant size variation was detected upon coupling of AcHK^{c}HK to 15Au-COOH.

Small peaks randomly centred at around 1-5 nm were often observed, especially for 15Au-COOH and 15Au-HK^{c}HK, which were due to the rotational diffusion of the nanoparticles.[346] When such peaks were not seen, polydispersity index (**PDI**) values of about 0.2 were obtained, which were indicative of moderately polydisperse samples.[346]

5.3.2.5 Surface effective charge

As mentioned in section **5.1.4**, the balance between attractive and repulsive interactions determines the stability of colloidal nanoparticles.[312-314,346] The repulsive interactions depend on the Z potential, ζ, which is the potential at the slipping/shear plane.[346,347] The greater is ζ (either positive or negative), the more stable is the system.[346,347] The occurrence of surface charges can have different origins, such as the ionisation of surface groups (*e.g.* acid and basic groups), the loss of ions from a crystal lattice or the adsorption of charged species.[346,347]

Charged particles are surrounded by two layers of ions which move with them. The inner layer, called Stern layer, contains ions which are tightly bound to the particle surface (**Figure 5.17**).[313,346,347] The ions within the outer layer, also called diffuse, are more loosely attached. Beyond the boundary of the double layer, which is called the slipping or shear plane, the ions remain in the bulk solvent rather than moving with the particle.[313,346,347]

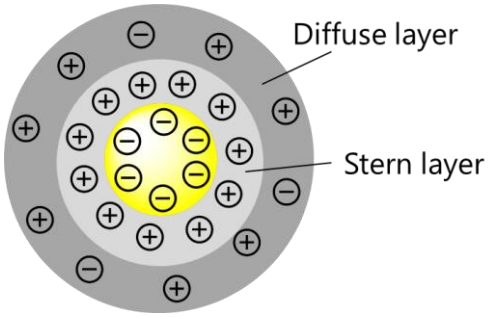

Figure 5.17: Electric double layer surrounding a nanoparticle with a negatively-charged surface.

The Z potential value of the as-obtained nanoparticles was measured in 0.1X PBS. The Z potential value of 5Au-HK^{c}HK was higher (less negative) than that of 5Au-COOH (**Figure 5.18**); this feature was consistent with a decrease in the number of negatively-charged carboxylates, as the result of the formation of neutral amide bonds through coupling with AcHK^{c}HK.

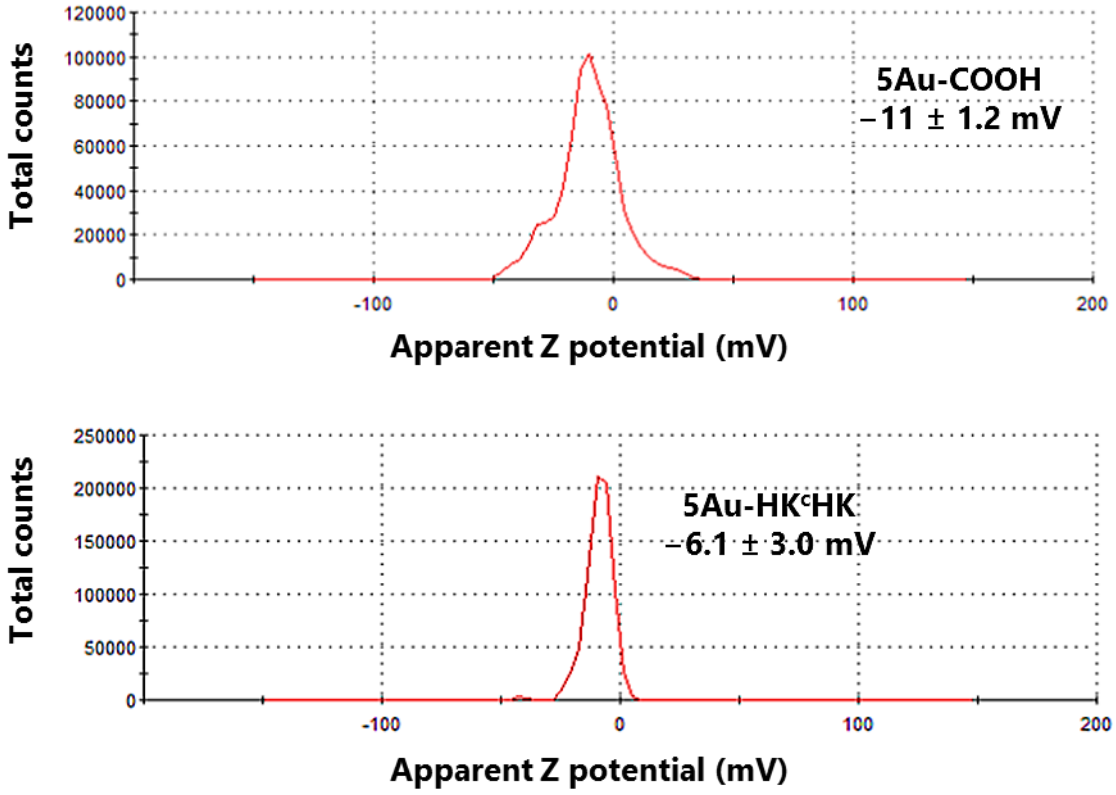

Figure 5.18: Z potential values of 5Au-COOH (**top**) and 5Au-HK^{c}HK (**bottom**).

The Z potentials obtained for 15Au-COOH and 15Au-HK^{c}HK are shown in **Figure 5.19**. The value observed for 15Au-HK^{c}HK was only 3 mV higher than that of 15Au-COOH. Considering their respective SD values, the difference in ζ is not conclusive regarding the effective coupling of AcHK^{c}HK; further studies by gel electrophoresis had to be carried out to confirm the functionalisation (see section **5.3.2.7**). The Z potential of 15Au could not be determined due to aggregation of the nanoparticles in the measurement media (0.1X PBS).

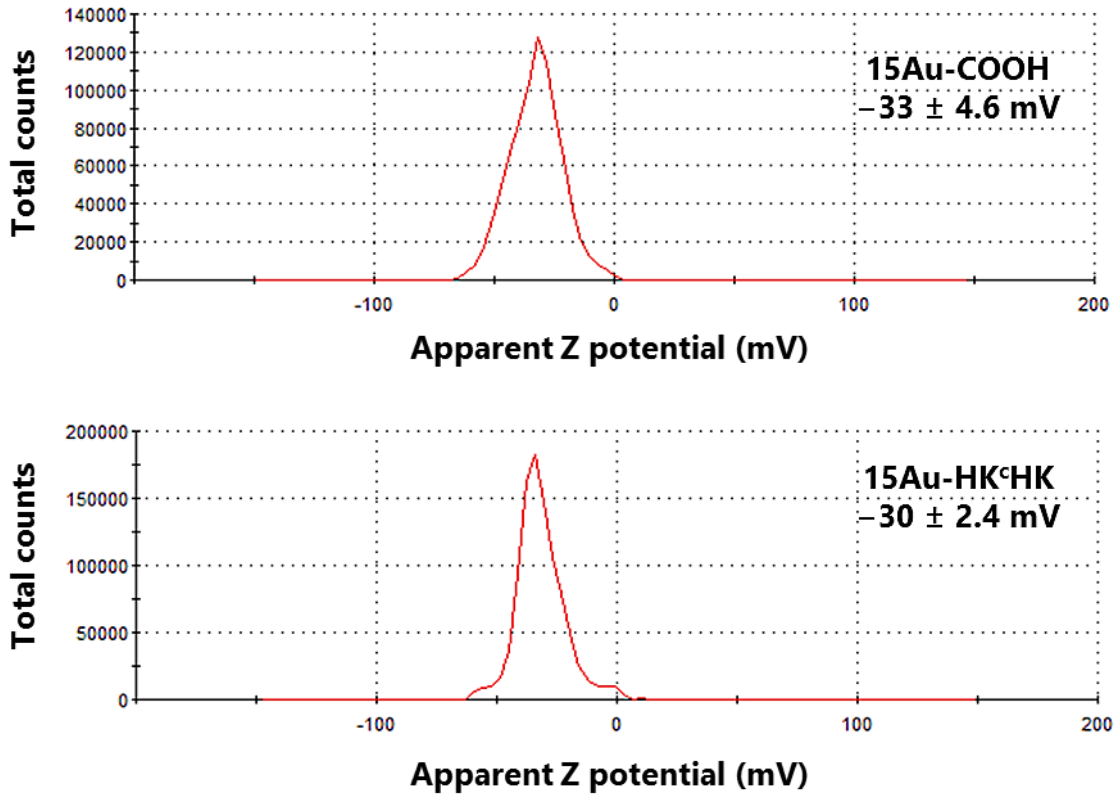

Figure 5.19: Z potentials of 15Au-COOH (**top**) and 15Au-HK^{c}HK (**bottom**).

It should be mentioned that well-defined and reproducible peaks were often not obtained; the zeta potential is affected by several factors such as the pH of the solution, its conductivity, the concentration of nanoparticles or the presence of components of the formulation that can adsorb on the surface.[346,347] All measurements were performed in 0.1X PBS; therefore, all samples presented similar pH and conductivity values. A better control of the parameters that may affect the measurements will clearly be required for future characterisations of the nanomaterials.

5.3.2.6 Summary of the physical characteristics of the Au NPs prepared

The main physical features of the Au NPs are summarised in **Table 5.1**. Unsurprisingly, the metallic core sizes were not altered by the different synthetic steps. The spr band of the orange-brown, 5 nm nanoparticles experienced a greater change than the 15 nm red ones.

Table 5.1: Core sizes (determined by TEM), spr bands, hydrodynamic sizes (determined by DLS) and zeta potentials for the different gold nanomaterials.

Nanomaterial	Core size (nm)[a]	spr band (nm)	Hydrodynamic size (nm)[a]	Zeta potential (mV)[a]
5Au-COOH	4.8 ± 0.83	509	19 ± 8.8	−11 ± 1.2
5Au-HK^{c}HK	4.5 ± 0.70	512	17 ± 6.3	−6.1 ± 3.0
15Au	14.1 ± 1.96	519	30 ± 18	n.d.
15Au-COOH	14.4 ± 1.62	522	38 ± 14	−33 ± 4.6
15Au-HK^{c}HK	14.5 ± 1.71	522	38 ± 14	−30 ± 2.4

[a] Values are expressed as mean ± standard deviation

The hydrodynamic sizes increased upon functionalisation with HS-PEG$_{2100}$-COOH; no significant variation occurred upon AcHK^{c}HK coupling. The Z potential values were more negative for the 15 nm nanoparticles than for 5 nm ones, in accordance with their higher amount of negative charges. Whereas the Z potential of 5Au-COOH became significantly less negative upon coupling of AcHK^{c}HK, the corresponding variation for 15Au-COOH was negligible.

5.3.2.7 Peptide coupling characterised by agarose-gel electrophoresis

Upon application of an electric field, negatively-charged species such as the pegylated nanoparticles described herein migrate towards the positive electrode. The coupling of AcHK^{c}HK to the PEG chains reduces the overall negative charge of the particle surface; therefore, the migration distance of the Au-HK^{c}HK NPs is expected to be shorter.[319]

The gels obtained are shown in **Figure 5.20**. As anticipated, both 15Au-HK^{c}HK and 5Au-HK^{c}HK migrated slower than the corresponding 15Au-COOH and 5Au-COOH nanoparticles, hence confirming the peptide coupling. Gel electrophoresis experiments confirmed (see section **5.3.1**) that AcHK^{c}HK could not be coupled to Au-COOH, both in borate (10 or 200 mM) or 0.1X PBS.

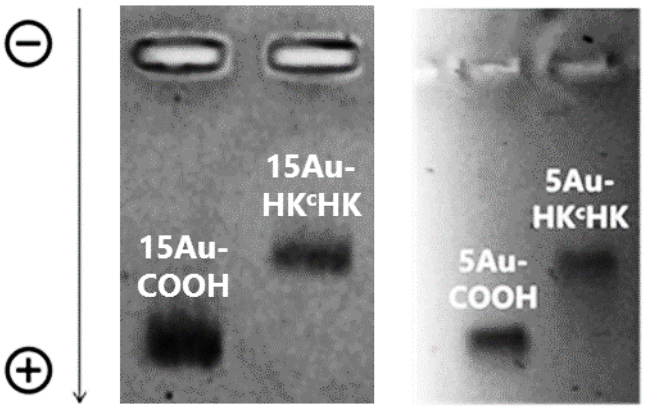

Figure 5.20: Agarose gels of 15Au-COOH/15Au-HK^{c}HK (**left**) and 5Au-COOH/5Au-HK^{c}HK (**right**).

5.3.2.8 Quantification of peptide content

a) By fluorescence spectroscopy

In principle, the coumarinic probe present in AcHK^{c}HK would allow the quantification of the peptide by fluorescence spectroscopy; however, its emission was quenched by its proximity to the gold surface, hence impeding a direct assessment. Quenched emission has been reported for fluorophores within a distance of 5 nm or shorter from the nanoparticle surface; this quenching is due to donation of the fluorophore electrons to the nanoparticle and subsequent non-radiative relaxation.[278,339] Conversely, 100-fold enhanced fluorescent intensities have been observed for fluorophores within distances of at least 10 nm, which result from constructive interactions with the electric field of the nanoparticle.[278,348] Surprisingly, although a distance of about 13 nm (fully extended length of PEG_{2100}) from the coumarinic moiety to the gold surface was expected according to the high density of PEG chains (brush-like conformation) determined by thermogravimetric analysis,[349] fluorescence quenching was observed. TEM experiments using uranyl acetate staining should therefore be carried out to appropriately determine the actual length of the PEG corona.

To quantify the amount of peptide grafted onto the nanoparticles, their cleavage from the gold surface was carried out (**Figure 5.21**). To do so, the nanoconjugates were treated with concentrated HCl (50 µL) and stirred for 3 days at rt. After subsequent

centrifugation to remove the gold nanoparticles, the supernatants were collected, and the pH of the solution was brought back to 7-8 using $NaHCO_3$.

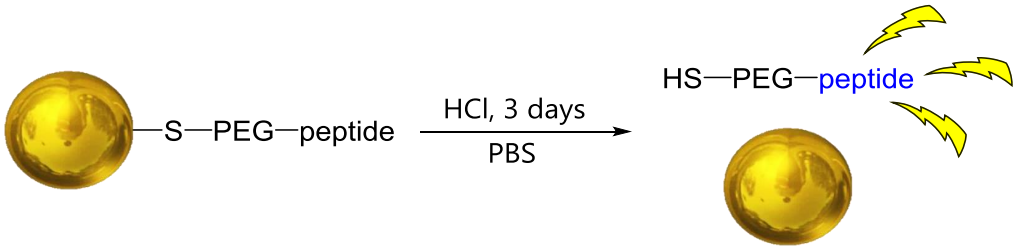

Figure 5.21: Cleavage of the Au-S bond by treatment with HCl at rt.

A calibration curve was created for AcHK^{c}HK using a set of standard solutions of the peptide; the corresponding plot is shown in **Figure 5.22**. The percentages of coupling were calculated considering the number of PEG chains per nanoparticle (see TGA results for 15Au-COOH); a PEG coverage of 100% was assumed for 5Au-HK^{c}HK even though it was not confirmed experimentally (see section **5.3.2.3**).

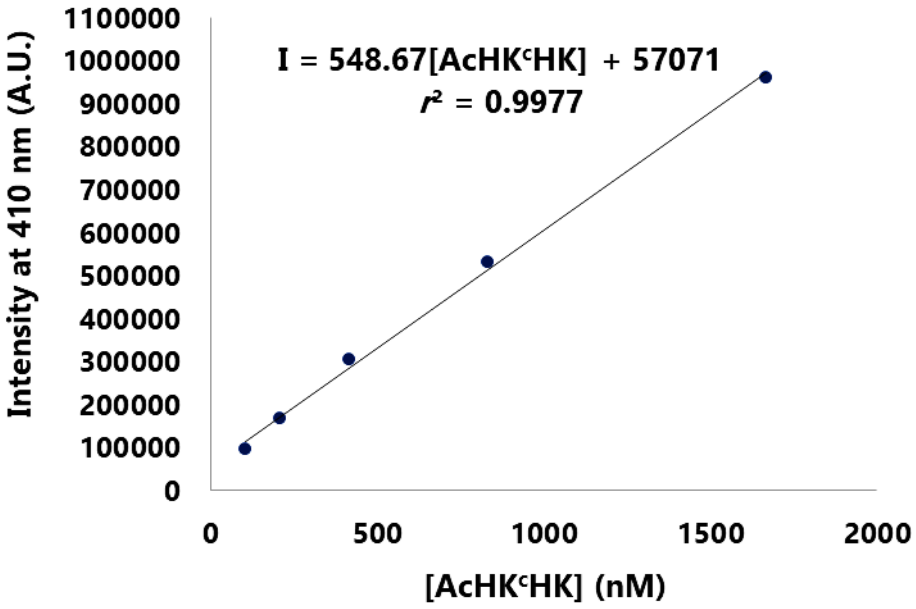

Figure 5.22: Calibration curve of fluorescence intensity for AcHK^{c}HK in 0.1X PBS (pH 7.4). Excitation wavelength λ_{exc} = 300 nm and λ_{em} = 410 nm.

Coupling efficiencies of 84% (corresponding to 152 AcHK^{c}HK molecules per nanoparticle) and 61% (*viz.* 937 AcHK^{c}HK molecules per nanoparticle) were obtained for 5Au-HK^{c}HK and 15Au-HK^{c}HK, respectively. Very low fluorescent intensities were observed when the coupling reaction was performed in borate or PBS buffers,

indicating poor coupling yields, and confirming the results obtained by agarose gel electrophoresis.

b) Amino-acid quantification by pre-column derivatisation

To validate the quantification results obtained by fluorescence spectroscopy, amino-acid quantification was carried out for 15Au-HK^{c}HK. In this method, the samples are digested with 6 M HCl at 110 ºC for 48 h and the resulting hydrolysed amino acids are subsequently reacted with the chromophore 6-aminoquinolyl-*N*-hydroxysuccinimidyl carbamate, which is used for their detection (λ_{abs} = 254 nm). The amino acid derivatives are then analysed by high-performance liquid chromatography and the quantification of the amino acids is obtained by comparison of the area responses with those of an internal standard (*i.e.* α-aminobutyric acid and norleucine).

The chromatogram showed various peaks that did not correspond to either His or Lys, thus suggesting that the peptide was degraded during its digestion. Therefore, acidic treatment of 15Au-HK^{c}HK with HCl for 3 days without thermal digestion was performed to release the peptide chains. After purification by centrifugation, the analysis gave similar results, ruling out any possible Au-induced degradation of the peptide. Several unidentified peaks were observed for a sample solely containing AcHK^{c}HK.

Accordingly, 15Au-HK^{c}HK was treated with HCl at a final concentration of 300 mM, at 60 ºC for 3 h. After centrifugation, the emission of the supernatant (containing, in principle, free AcH^{c}HK) using λ_{exc} = 300 nm (coumarin) was recorded. A blue-shift of the emission was observed compared with that of the original, non-treated peptide, indicating that the peptide is most likely thermally degraded in an acidic medium. These observations are consistent with features discussed in **Chapter 2**, where side reactions involving peptides containing the coumarin probe were described.

Further research is required to both elucidate the reactivity of the coumarin-containing peptides and to validate the coupling percentages obtained by fluorescence spectroscopy. Alternatively, a peptide bearing a more chemically and thermally stable fluorescent probe may be used.

5.3.3 Evaluation of the Cu(II)-chelating properties of the nanoconjugates and their cell toxicity

5.3.3.1 Cu(II)-chelating efficacy of the nanoconjugates against Aβ

Fluorescence competition studies were carried out to evaluate the Cu(II)-chelating properties of the Au-HK^{c}HK nanoparticles. As mentioned in **Chapter 3**, the *N*-protected peptides Ac-His-Lys(Coum)-His-OH (**AcHK^{c}H**), Ac-His-Lys(4DMN)-His-OH (**AcHK^{d}H**) and Ac-His-Lys(4DMN)-His-NH_2 (**AcHK^{d}H-NH$_2$**), which were studied as models of AcHK^{c}HK coupled to Au NPs, exhibited higher Cu(II)-binding affinities than Aβ(1-16). Therefore, Au-HK^{c}HK NPs were expected to extract Cu(II) ions from this non-aggregating, short fragment of Aβ.

Preformed Aβ(1-16)-Cu(II) complex was treated with the Au NPs and the copper-exchange process was followed by measuring the changes of the emission of the Tyr10 residue (λ_{exc} = 275 nm, λ_{em} = 305 nm) of Aβ(1-16), initially quenched by the Cu(II) ions (see **Chapter 3**). The emission of Aβ(1-16)-Cu(II) was measured immediately after addition of the Au NPs, and after 2 and 24 h of incubation at 37 ºC. In the presence of the Au NPs, the emission of Tyr10 further decreased due to the quenching induced by gold (**Figure 5.23**).[348]

The fluorescence decrease observed was lower for Au-HK^{c}HK than for Au-COOH, indicating that Cu(II) was partially displaced by the Au NPs functionalised with the Cu(II)-chelating peptide AcHK^{c}HK. This difference of emission intensity was observed at all incubation times. The greater alteration of the emission with the 15 nm Au NPs might be explained by the lower concentrations used, compared with those of the 5 nm Au NPs (namely 0.73 nM for 15Au-COOH/15Au-HK^{c}HK and 52 nM 5Au-COOH/5Au-HK^{c}HK); hence, quenching due to gold is lesser in the case of the 15 nm.

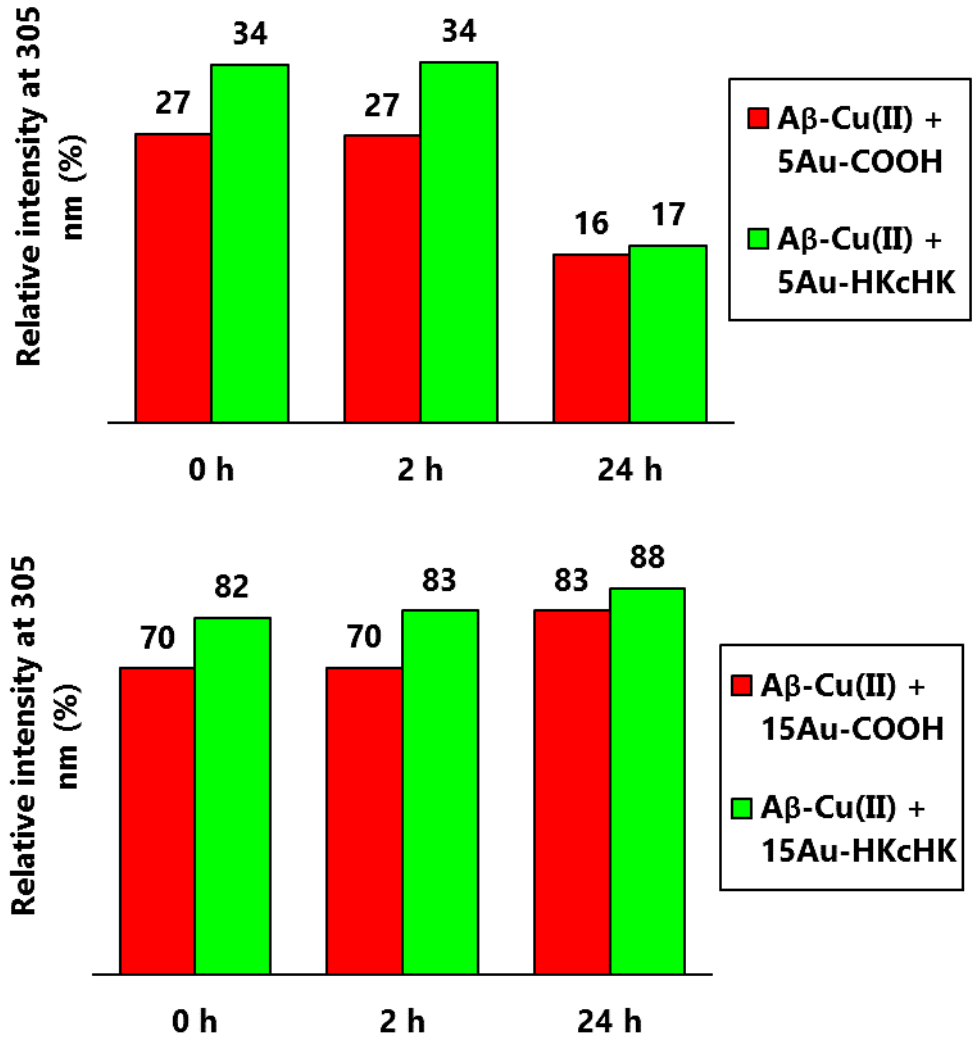

Figure 5.23: Relative fluorescence emission (%) of Aβ(1-16)-Cu(II) , in the presence of 15Au-COOH (red) and 15Au-HK^{c}HK (green) after 0, 2 and 24 h of incubation at 37 ºC. The fluorescence is relative to that of Aβ(1-16)-Cu(II). **Top:** 10 μM Aβ(1-16)-Cu(II) and 52 nM 5Au-COOH or 5Au-HK^{c}HK (8.0 μM AcHK^{c}HK, 0.80 eq). **Bottom:** 5 μM Aβ(1-16)-Cu(II) and 0.73 nM 15Au-COOH or 15Au-HK^{c}HK (688 nM AcHK^{c}HK, 0.14 eq). λ_{exc} = 275 nm, 10 mM HEPES (pH 7.4).

Next, the potential chelating activity of the peptide-functionalised Au NPs was evaluated by competitive studies with Cu(II)-containing Aβ(1-40) oligomers (generated through incubation of Aβ monomers with stoichiometric amounts of Cu(II), see section **5.5**). The Aβ(1-40)-Cu(II) oligomers were treated with Au-HK^{c}HK NPs and ThT fluorescence emission (which is related to fibrillation) was monitored over time to evaluate the ability of the peptide-functionalised nanoparticles to prevent the copper-induced stabilisation of oligomeric species (see **Chapter 3**). The characteristic

sigmoidal curve (indicative of the formation of fibres) was obtained for non-treated Aβ(1-40) monomers (**Figure 5.24**, dark-blue dots), while no variation was observed for the Aβ(1-40)-Cu(II) oligomers, thus confirming the stabilisation of ThT-silent species (**Figure 5.24**, light-blue dots).

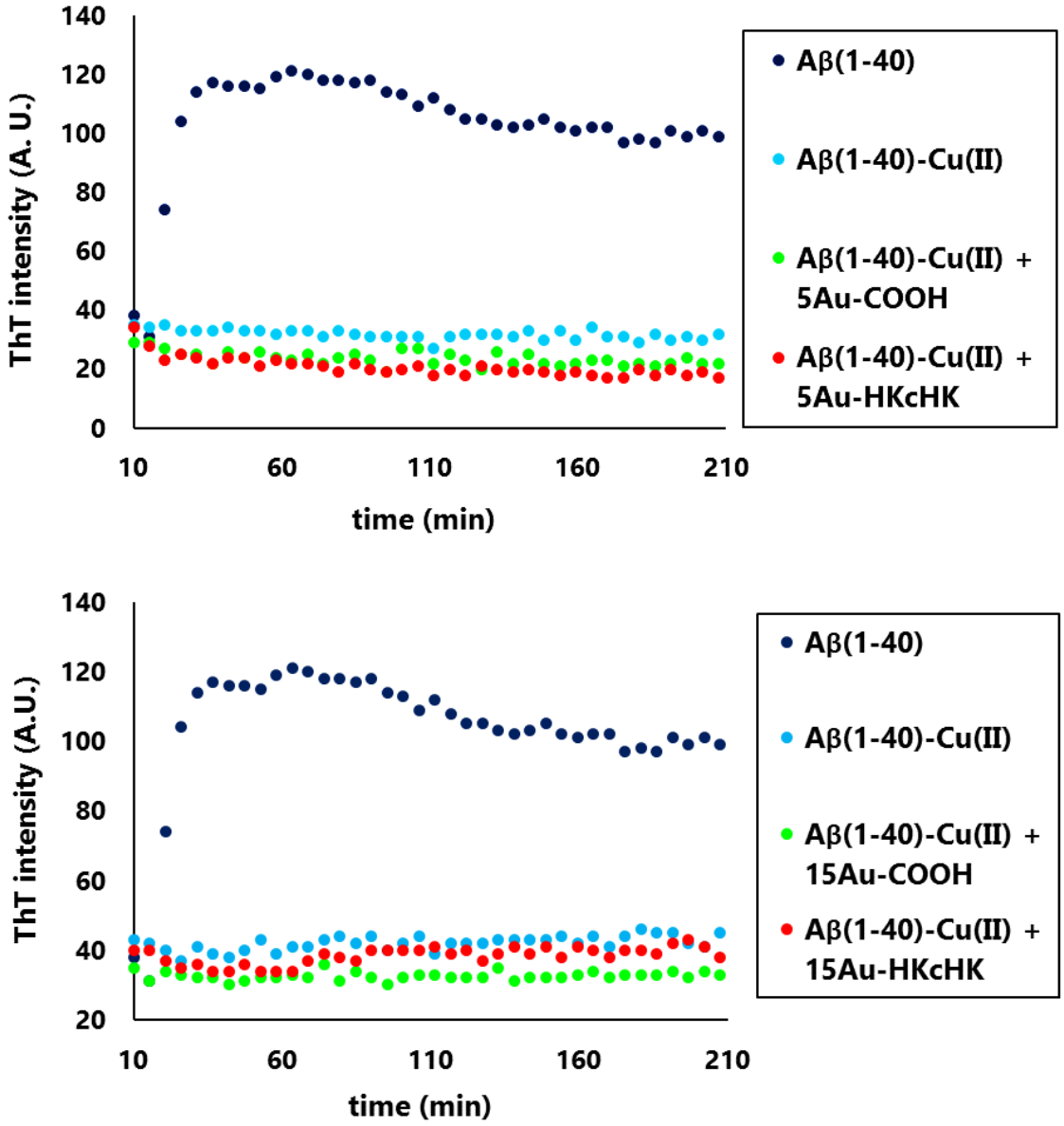

Figure 5.24: Aggregation studies of a 25 μM solution of Aβ(1-40) monomers (dark-blue dots), a 25 μM solution of Aβ(1-40)-Cu(II) oligomers (light-blue dots), and of Aβ(1-40)-Cu(II) oligomers in the presence of Au-COOH (green dots) or Au-HK^{c}HK (red dots). **Top:** 80.7 nM 5Au-COOH and 78.2 nM 5Au-HK^{c}HK (11.9 μM AcHK^{c}HK, 0.48 eq); **bottom:** 2.10 nM 15Au-COOH and 1.12 nM 15Au-HK^{c}HK (1.05 μM AcHK^{c}HK, 0.042 eq). ThT emission; λ_{exc} = 440 nm, λ_{em} = 490 nm. 1X PBS (pH 7.4), 37 ºC.

The addition of Au-COOH NPs to Aβ(1-40)-Cu(II) (**Figure 5.24**, green dots) did not lead to the recovery of the typical sigmoidal ThT-emission curve that depicts fibrillation, which was expected for these poorly-chelating NPs. The addition of 5Au-HK^{c}HK (0.48 eq of AcHK^{c}HK in relation to Aβ(1-40)-Cu(II)) or 15Au-HK^{c}HK (0.042 eq of AcHK^{c}HK in relation to Aβ(1-40)-Cu(II)) did not restore Aβ(1-40) fibrillation either (see red dots in **Figure 5.24**, top and bottom). It is possible that amorphous, ThT-silent species may have precipitated upon (partial) extraction of Cu(II) ions and interaction with the Au NPs. The extremely low amounts of peptide used in these experiments should be noted.

The adsorption of peptides and proteins onto the surface of (Au) NPs is a well-known phenomenon;[350] actually, Au NPs with different surface charges have successfully been tested in the group as modulators of Aβ(1-40) aggregation. Therefore, the Au NPs might have impeded the fibrillation of Aβ(1-40) even after extraction of Aβ-bound Cu(II) ions. Aggregation studies with Aβ(1-40) monomers in the absence of copper were thus carried out to evaluate the effect of the Au-HK^{c}HK NPs on Aβ fibrillation; the results achieved are shown in **Figure 5.25**.

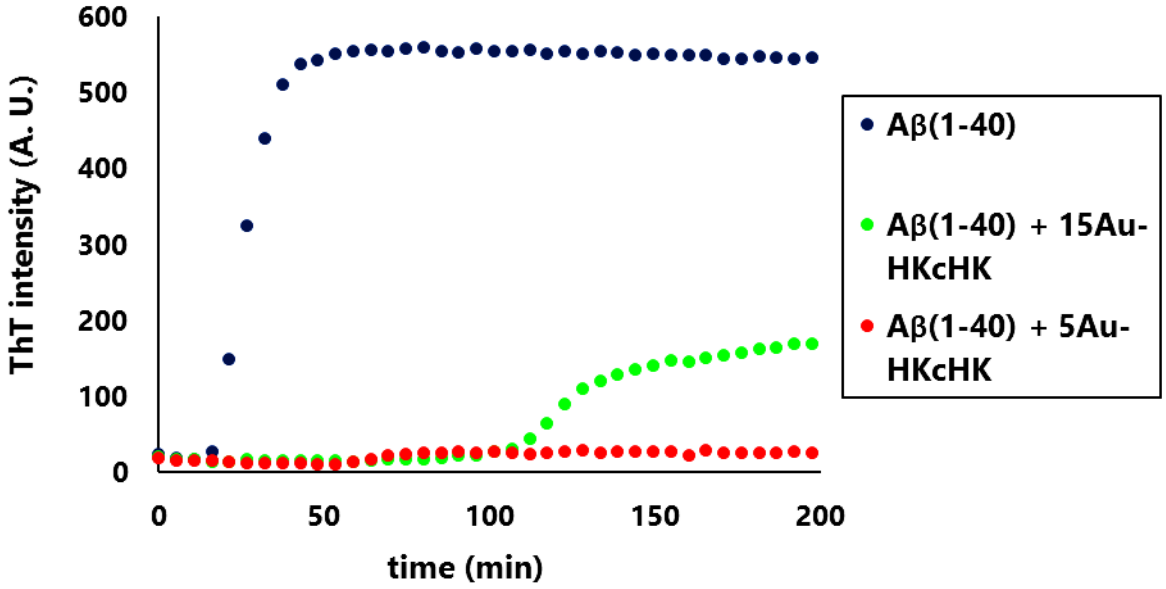

Figure 5.25: Aggregation of Aβ(1-40) (blue dots), Aβ(1-40) in the presence of 78.2 nM 5Au-HK^{c}HK (red dots) and Aβ(1-40) in the presence of 1.12 nM 15Au-HK^{c}HK (green dots). ThT emission; λ_{exc} = 440 nm, λ_{em} = 490 nm. [Aβ] = 25 μM, 1X PBS (pH 7.4), 37 ºC.

A typical lag time of 15 minutes was observed for Aβ(1-40) (blue dots), followed by an abrupt increase of the emission intensity of ThT, characterising the generation of fibres;

the final plateau was reached after 48 minutes. Aβ(1-40) aggregation was delayed by 95 minutes in the presence of 15Au-HK^{c}HK (green dots), which induced 69% inhibition. The lag time was shorter for 5Au-HK^{c}HK (red dots), namely 55 minutes, but 95% inhibition of the fibrillation process was achieved (the stronger inhibitory effect of 5Au-HK^{c}HK probably arises from their higher concentration compared with that of 15Au-HK^{c}HK). The adsorption of Aβ(1-40) onto the surface of Au-HK^{c}HK NPs most likely justifies the inhibition of the generation of fibres. Thus, the inhibition of Aβ fibrillation in the presence of copper was apparently induced both by the Au NPs (due to adsorption) and the non-displaced Cu(II) ions (due to stabilisation of oligomers).

Very recently, small differences in salt concentrations have been found to significantly affect the Aβ(1-40) aggregation kinetics. This aspect must be considered in future studies given that in our tests, 10-fold less saline NP solutions were added to the protein.

TEM experiments may be helpful to identify the nature of the aggregated species that form upon interaction of Cu(II)-oligomeric Aβ with Au-HK^{c}HK NPs. The use of longer PEG linkers and/or more emissive peptide derivatives, or isotopically labelled copper, may be more appropriate to monitor the Cu(II)-exchange process.

5.3.3.2 Viability of mouse neuronal cells in the presence of AcHK^{c}HK, 15Au-COOH and 15Au-HK^{c}HK

Au NPs are generally considered non-toxic and biocompatible; however, some studies demonstrating harmful effects on cells or biomolecules have brought controversy to the field. There are many parameters that can affect their cellular uptake, biodistribution and cell response, and thus explain contrasting results regarding the potential hazardous properties of Au nanoparticles that have been reported. For instance, the particle size, shape, surface charge, capping ligands, presence of cell penetrating peptides, or exposure times may affect the pharmacokinetic and toxic properties of Au NPs (**Figure 5.26**).

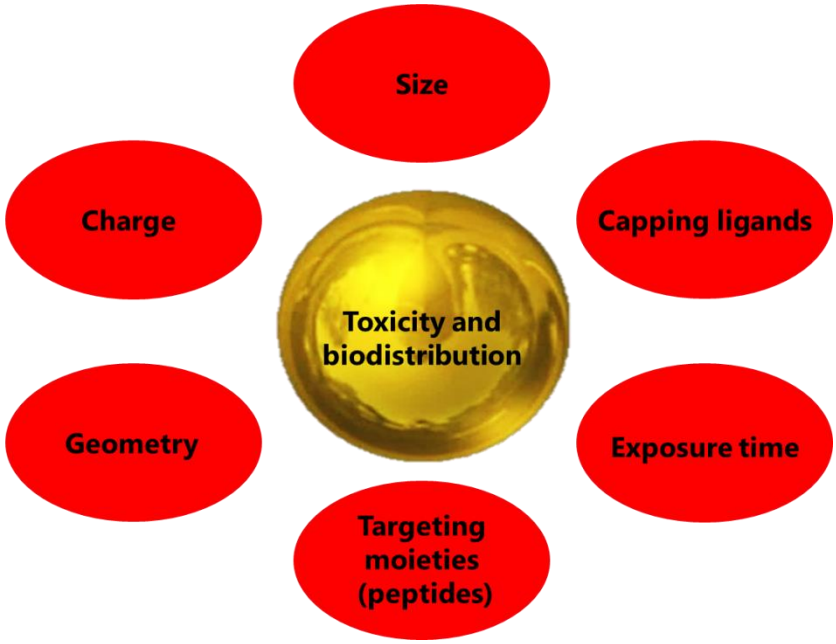

Figure 5.26: Features potentially affecting the toxicity and biodistribution of the Au NPs.

Therefore, each case should be thoroughly studied individually. Citrate-capped Au NPs are cytotoxic towards some cell lines;[286,351] some unfunctionalised Au NPs of 60 nm size were shown to be non-toxic in microglial and both undifferentiated and differentiated SH-SY5Y cells.[352] Small nanoparticles, which display a higher cell-penetrating ability, are in general more toxic than bigger ones. Cationic nanoparticles, which may disrupt cell membranes and accumulate more than negative ones of the same size, are more cytotoxic.[286,299,305,311,351,353]

In another study, methoxy-terminated nanoparticles of 10 to 15 nm size were non-toxic against human breast carcinoma xenograft cells and harmless to mice,[354,355] while nanoparticles of size 10, 13 and 60 nm were reported to induce acute inflammation and apoptosis in the liver of mice.[356,357] Au NPs (having a hydrodynamic size of 38.5 nm) functionalised with carboxy-terminated PEG chains were non-toxic against different lung epithelial and colon cancer cell lines.[300]

The potential toxicity of AcHK^{c}HK and the 15 nm Au NPs againts neuronal embryo cells of wildtype mice was evaluated in collaboration with the Molecular and Cellular Neurobiotechnology group at the Institute for Bioengineering of Catalonia (IBEC).

Cell viability assays were conducted using a slightly modified propidium iodide uptake method.[358] Propidium iodide is impermeable to cells with an intact plasma membrane;

when cells are damaged or dead, it permeates and binds to DNA through intercalation between the base pairs; this intercalation gives rise to high fluorescence.[359,360]

The viability of the neuronal cells was tested in the presence of AcHK^{c}H (5, 10 and 20 μM), 15Au-COOH (10, 25 and 50 nM) or 15Au-HK^{c}HK (5, 10, and 25 nM, estimated concentrations of AcHK^{c}HK 4.7, 9.4 and 23 μM, respectively). The percentage of dead cells (in triplicate studies) was determined through the fluorescence intensity of propidium iodide, after incubation during 1, 8, 24, 30 and 48 h. The results obtained are represented in **Figure 5.27**.

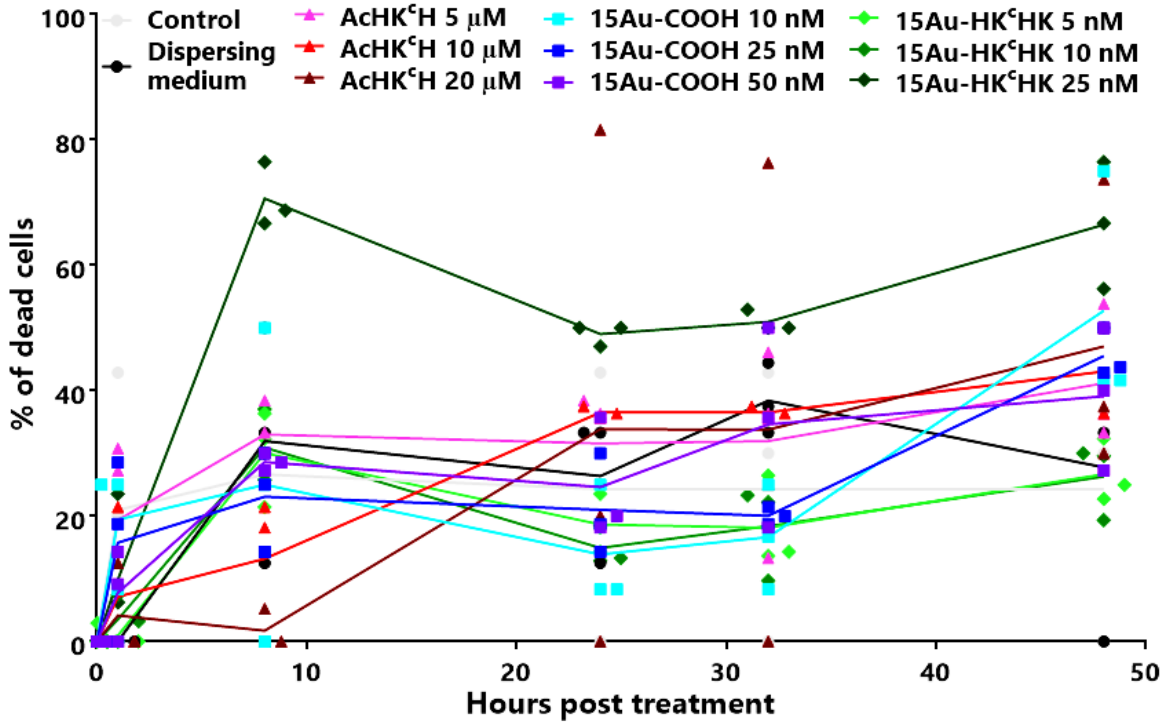

Figure 5.27: Viability results obtained for neuronal embryo cells of wildtype mice in the presence of AcHK^{c}HK, 15Au-COOH and 15Au-HK^{c}HK determined by the fluorescence intensity of propidium iodide.

All compounds tested were non-toxic within a normal range of concentration; the cell-viability values were comparable to those of the control and the dispersing medium (0.1X PBS), except for the 15Au-HK^{c}HK nanoparticles at a concentration of 25 nM. However, it should be stressed that the concentrations studied are much higher than those commonly used for biomedical applications.[311,353]

Considering such encouraging results, studies on the cell uptake of these nanoconjugates and their inhibition ability against Aβ production and effect on the

oxidative stress are now envisaged. Furthermore, experiments involving artificial BBB models (*e.g.* the parallel artificial membrane permeability assay, PAMPA,[361-366] or the immobilised artificial membrane chromatography, IAMC[366,367]), will assess the potential capacity of the nanomaterials to permeate biological membranes. The unique spectroscopic properties of Au NPs can also be exploited to investigate their penetration into cells applying microscopy techniques.[286,296,299,310,368] Besides, the toxicity of 5Au-COOH and 5Au-HK^{c}HK should be investigated as well.

5.4 Concluding remarks

Gold nanoparticles (**Au NPs**) of average core sizes of 4.8 and 14.4 nm were prepared by reduction of an aqueous solution of $HAuCl_4$ with sodium borohydride or citrate, respectively, and subsequently functionalised with HS-PEG_{2100}-COOH. AcHK^{c}HK was coupled to the resulting Au-COOH nanoparticles by EDC-mediated generation of amide bonds between the PEG carboxylate groups and the free amino function of the Lys4 residue of the peptide. Both the Au-COOH and Au-HK^{c}HK nanoparticles were stable for several months.

The nanomaterials were characterised by TEM, UV-Vis spectroscopy, DLS and Z potential measurements. The Au NPs presented moderate polydispersity as evidenced by the corresponding mean metal core sizes and hydrodynamic sizes. Characteristic spr bands at 509-512 nm (5 nm Au NPs) and 519-523 nm (15 nm Au NPs) were obtained and the negative Z potential and gel electrophoresis measurements were consistent with the functionalisation of the gold surface with the negatively-charged HS-PEG_{2100}-COOH coating and confirmed the further attachment of the AcHK^{c}HK peptide. TGA analyses revealed that 83% of the gold surface of 15Au-COOH was covered with PEG chains; such densely-packed PEG coating provided improved stability against aggregation. TGA analyses could not be carried out for 5Au-COOH due to the too high amount of sample required.

The PEG-AcHK^{c}HK chains were cleaved from the nanoparticles by treating Au-HK^{c}HK with concentrated HCl to quantify the amount of coupled peptide by fluorescence spectroscopy; 61% and 84% of the COOH active groups of respectively 5Au-HK^{c}HK and 15Au-HK^{c}HK were functionalised with AcHK^{c}HK (assuming that 100% of the gold surface was covered with PEG chains). The coupling yields obtained by this methodology could not be confirmed by amino acid quantification by HPLC; this is most likely due to the thermal degradation of the peptide upon its digestion. A thermally stable and acid-proof peptide with a fluorescent tag would therefore circumvent this issue.

Competitive binding studies with Aβ(1-16) were performed using fluorescence spectroscopy to evaluate the Cu(II)-binding properties of the Au-HK^{c}HK nanoparticles. The emission of Tyr10, initially quenched by Cu(II), further decreased upon addition of the different nanomaterials. The decrease was lower for Au-HK^{c}HK than for Au-COOH due to the partial intensity recovery arising from the binding of copper ions to the Au-

HK^{c}HK NPs. Preliminary results obtained for Au NPs functionalised with Ac-His-Lys(4DMN)-His-Lys-NH_2 (**AcHK^{d}HK**) have shown similar Cu(II)-binding properties. The Au-HK^{c}HK NPs were however unable to restore the fibrillation process of Cu(II)-bound Aβ(1-40) oligomers at the tested concentrations; aggregation studies in the absence of copper showed that Au-HK^{c}HK NPs inhibited the aggregation of Aβ(1-40) with different rates. Au NPs with different surface polarities (negative, neutral and positive) have been tested in our group, which show promising aggregation-modulating activity. Therefore, it may be expected that Au-HK^{c}HK can exhibit copper-chelating, anti-oligomerisation and anti-fibrillation properties, thus acting as efficient species against Aβ toxicity.

The potential cytotoxicity of AcHK^{c}HK, 15Au-COOH and 15Au-HK^{c}HK was evaluated against neuronal embryo cells of wildtype mice. AcHK^{c}HK and 15Au-COOH were non-toxic at the different concentrations tested, while 15Au-HK^{c}HK induced significant cell death at a concentration of 25 nM; nevertheless, this concentration is above the common therapeutic dosages used for brain disorders. Further cytotoxicity studies should be performed with neuronal embryo cells of APPPS1 mice, which bear the Swedish mutation of APP and the L166P mutation of PSEN1.[369-371] These mutations induce the overproduction of human Aβ peptides (especially Aβ(1-42)); therefore, APPPS1 mice are commonly used as models of AD. The prospective toxicity of 5Au-COOH and 5Au-HK^{c}HK remains to be assessed; the capacity of the different nanomaterials to cross the BBB must also be investigated.

The results described in this chapter are encouraging and validate the proposed approach to graft anti-AD compounds onto Au NPs. The functionalisation of Au NPs with bioactive compounds thus represents a versatile approach for the preparation of hydrophilic, non-toxic materials for a wide range of biomedical applications.

5.5 Experimental section

5.5.1 Reagents, solvents and equipment

Table 5.2: Reagents and solvents used for the work described in this chapter.

Brand	Products
Acros Organics	sodium citrate
Alfa Aesar	$HAuCl_4 \cdot 3H_2O$
Sigma Aldrich	HEPES, HFIP, HS-PEG_{2100}-COOH, ThT
Ecogen	agarose
Fisher Scientific	DMSO, NaN_3, PBS, TBE
Fluka	$NaBH_4$
ICN Biomedicals	glycerine
Malvern	polystyrene latex standard for Z potential
Panreac	$CuCl_2 \cdot 2H_2O$, absolute ethanol
Scharlau	HCl 37%
TCI	EDC

Table 5.3: Equipment used for the work described in this chapter.

Equipment	Brand	Model
Analytical balance	A & D	GR-200-EC
Gram-scale balance	Sartorius	Basic BA 110
Vacuum lyophiliser	Christ Alpha	2-4 LD plus
Microcentrifuge	ThermoFisher Scientific	Sorvall Legend Micro 17
Sonicator	Fisherbrand	FB15051

Milli-Q H_2O (resistivity > 18 MΩ·cm) was produced by filtering deionised water with a Milli-Q Plus (Millipore) system. $CuCl_2 \cdot 2H_2O$ was used as the source of copper for the competitive studies.

5.5.2 Syntheses

All glassware used for the synthesis of the gold nanoparticles (**Au NPs**) was carefully washed with aqua regia. The solutions of $HAuCl_4$ and the dispersions of Au NPs were kept protected from light.

5Au-COOH

100 μL of a 50 mM $HAuCl_4$ stock solution in 50 mM HCl were added to 9.6 mL of Milli-Q water in a Schlenk flask. The resulting solution was purged with N_2 and 300 μL of a freshly prepared 50 mM $NaBH_4$ solution in 50 mM NaOH were subsequently added under stirring at rt. The colour changed immediately from pale yellow to dark orange. The pH of the solution was 8-9. The solution was further stirred for 5 min protected from light. Next, a solution of HS-PEG_{2100}-COOH (0.61 mg, 0.29 μmol) in Milli-Q water (200 μL) was slowly added with constant stirring and the mixture was allowed to react for 20 h at rt. The nanoparticles were purified using Spectra-Por Float-A-Lyzer dialysis membranes of MWCO 100 kDa in 50 mM phosphate buffer (pH 7.2, 100 mL per mL of colloid), replacing the buffer every 12 h, thrice. The sample was finally filtered through a cellulose acetate membrane filter of 0.2 μm pore size.

15Au

100 mL of a 1 mM solution of $HAuCl_4$ in Milli-Q H_2O were rapidly refluxed under vigorous stirring in a 250 mL round-bottomed flask equipped with a condenser. Then, 10 mL of a 38.8 mM solution of sodium citrate in Milli-Q H_2O were rapidly added to the vortex of the mixture and the reaction was allowed to proceed for 10 minutes, during which the colour changed from pale yellow to colourless, and finally to intense reddish-purple. The heating mantle was removed, and the suspension was stirred for 15 minutes, after which it was allowed to reach ambient temperature. The Au colloid was finally filtered through a 0.7 μm glass fibre membrane filter. The pH was 5-6.

15Au-COOH

A solution of 15Au was diluted 2-fold with Milli-Q water in an Erlenmeyer flask. Next, a freshly-prepared solution of HS-PEG_{2100}-COOH (0.79 mg/mL, 2500 equivalents) in Milli-Q water was slowly added with constant stirring and the resulting mixture was allowed to react for 20 h. Then, the solution was divided into microcentrifuge vials, centrifuged and resuspended in 0.1X PBS (pH 7.4) or Milli-Q H_2O (30 min, 13300 rpm, 3 purification cycles). Finally, the fractions were combined, and the resulting solution was filtered through a cellulose acetate membrane filter of 0.2 μm pore size.

Coupling of Ac-His-Lys(Coum)-His-Lys-NH_2 (AcHK^{c}HK) to 5Au-COOH

A 15 mM solution of AcHK^{c}HK (10^3 equivalents) in 50 mM phosphate buffer (pH 7.2) was introduced in a glass vial containing 5Au-COOH suspended in Milli-Q H_2O. Next, a freshly-prepared 1.6 M solution of EDC (10^5 equivalents) in Milli-Q H_2O was immediately added to the vial. The reaction mixture was sonicated for 1 h protected from light. The resulting solution was purified using Spectra-Por Float-A-Lyzer dialysis membranes of MWCO 100 kDa in 50 mM phosphate buffer (pH 7.2, 100 mL per mL of colloid), replacing thrice the buffer every 12 h. The sample was finally filtered through a cellulose acetate membrane filter of 0.2 μm pore size.

Coupling of Ac-His-Lys(Coum)-His-Lys-NH_2 (AcHK^{c}HK) to 15Au-COOH

A 15 mM solution of AcHK^{c}HK (10^4 equivalents) in 50 mM phosphate buffer (pH 7.2) was added to a glass vial containing 15Au-COOH suspended in Milli-Q H_2O. Next, a freshly-prepared 300 mM solution of EDC (10^6 equivalents) in Milli-Q H_2O was immediately added to the vial. The reaction mixture was sonicated for 1 h, protected from light. The solution was then divided into microcentrifuge vials, centrifuged and resuspended in 0.1X PBS (pH 7.4) or Milli-Q H_2O (30 min, 13300 rpm, 3 purification cycles). Finally, the fractions were combined, and the resulting solution was passed through cellulose acetate membrane filters of 0.2 μm pore size.

5.5.3 Procedures, instrumentation and techniques

Transmission electron microscopy (TEM) imaging

The samples (10 μL) were deposited onto holey carbon- or Formvar-coated copper grids (300-mesh) and subsequently washed with absolute ethanol (10 μL). The samples were visualised with a JEOL2100 200 keV TEM microscope equipped with a Gatan multiscan camera using Digital Micrograph 1.8 (Gatan, CA, USA) at the Centres Científics i Tecnològics of the Universitat de Barcelona (CCiTUB). The images were analysed using ImageJ. The core size distributions were obtained by measuring the diameters of at least 200 nanoparticles per sample.

UV-Vis measurements

Absorbance spectra were recorded using a Varian Cary 100 Scan spectrophotometer with a quartz cuvette (1 cm pathlength) at rt. The solution of 15Au nanoparticles was diluted 2-fold prior to the measurement, and the value of its surface plasmon absorption (typically at 519-520 nm) was used to determine the approximate concentrations of the functionalised nanoparticles.

Thermogravimetric Analysis (TGA)

100 mL of 15Au-COOH were freeze-dried and the resulting solid (4.7507 mg) was heated from 30 to 1000 ºC (at a rate of 10 ºC/min) under 100% N_2 (50 mL/min) using a Mettler Toledo TGA/SDTA851e thermobalance, equipped with an alumina crucible, at the Centres Científics i Tecnològics of the Universitat de Barcelona (CCiTUB). The data were acquired and treated using the STARe SW 8.10 software.

Dynamic Light Scattering (DLS) and Z-potential measurements

DLS and Z-potential measurements were performed at 20 ºC using a Malvern Zetasizer NanoZS instrument at the Parc Científic of the Universitat de Barcelona. The DLS measurements (≥ 3 measurements per sample) were carried out in plastic disposable cuvettes with the detector set at 173º. The samples were previously passed through

cellulose acetate membrane filters (0.2 μm pore size) and sonicated for 5 min. The Z potential analyses (≥ 3 measurements per sample) were performed in disposable folded capillary cells (Malvern Zetasizer Nano Series); polystyrene latex nanoparticles in pH 9 aqueous solution (−42 ± 4.2 mV, Malvern Instruments) were used as standard.

Agarose gel electrophoresis

The samples were prepared by mixing 16 μL of Au NPs (1-2.5 nM and 60-100 nM for the 5Au and 15Au nanoparticles, respectively) with 4 μL of loading buffer (30% (v/v) glycerol in Milli-Q H_2O). The samples were subsequently electrophoresed on agarose gel (0.5% agarose in 0.5X Tris/borate/EDTA buffer) using a BIORAD horizontal tank connected to a Consort EV231 variable potential power supply, applying a voltage of 160 V during 30 min. The gels were visualised with a BIO-RAD Gel Doc EZ Imager using ImageLab software.

Amino acid quantification by pre-column derivatisation

3 mL of a solution of 15Au-HK^{c}HK (1.20 nM) were first freeze-dried. This solution was then treated with concentrated HCl (50 μL) and stirred for 3 days. The resulting mixture was centrifuged (13300 rpm, 15 min) and the pH of the supernatant was brought to 7-8 with $NaHCO_3$. The solution was subsequently freeze-dried. The resulting solid was analysed by amino acid quantification at the Centres Científics i Tecnològics of the Universitat de Barcelona (CCiTUB). The internal standards α-aminobutyric acid and norleucine were added to the samples and the mixtures were incubated with HCl 6 M at 110 ºC for 48 h. Then, the solutions were evaporated to dryness and redissolved in 100 μL of water. The hydrolysed amino acids were subsequently derivatised with 6-aminoquinolyl-*N*-hydroxysuccinimidyl carbamate (Waters AccQ-Fluor®) in borate buffer. Finally, 20 μL of the derivatised samples were analysed by HPLC with detection in the UV range.

The measurements were carried out with a Waters Delta 600 chromatographic module equipped with a Waters 2487 Dual λ Absorbance Detector, a Waters 717plus autosampler and a column temperature-controlled at 37 ºC by a Waters TCM II module. A Waters Nova-Pak column (C18 4 μm, 3.9 × 150 mm) was used. The derivatised amino

acids were separated by gradient elution using the eluents and conditions described in the Waters AccQTag method protocol and were detected at 254 nm.

The amino acid peaks were identified according to the retention times of the corresponding standards (Pierce Amino Acid Standard H, Thermo Scientific). The concentration of the amino acids was calculated by comparing the area responses of the analytes with those of the internal standards (2.5 mM α-aminobutyric acid or Norleucine, Sigma-Aldrich). The data were acquired and treated using the Empower 2 Software.

Fluorescence spectroscopy

Fluorescence spectroscopy experiments were performed at rt using a HORIBA Jobin–Yvon iHR320 spectrofluorometer. The instrument excitation and emission slits were set at 5 nm and the voltage of the photomultiplier detector was 950 V. The emission of AcHK^{c}HK was analysed using an excitation wavelength λ_{exc} = 300 nm and the emission was registered from 320 to 570 nm.

Quantification of AcHK^{c}HK coupled to the Au NPs

AcHK^{c}HK standards (concentrations in the range 104 nM-3.33 μM) were prepared by successive dilutions in 0.1X PBS (pH 7.4) and analysed by fluorescence spectroscopy. A calibration curve was generated by plotting the intensity data at 410 nm against the concentration of AcHK^{c}HK.

Concentrated HCl (50 μL) was added to a 1 mL fraction of an Au-HK^{c}HK suspension in 0.1X PBS and the resulting mixture was stirred for 3 days. The solution was then centrifuged (13300 rpm, 15 min) and the pH of the supernatant was brought to 7-8 using $NaHCO_3$. The resulting solution was analysed by fluorescence spectroscopy using a 1 mL quartz cuvette and the intensity value at 410 nm was used to determine the amount of AcHK^{c}HK coupled to the Au NPs.

Binding studies with Aβ(1-16)-Cu(II)

Preparation of the stock solution of Aβ(1-16): solid Aβ(1-16) (1 mg) was dissolved in 10 mM HEPES pH 7.4 and the resulting solution was sonicated for 30 min. The concentration was determined spectrophotometrically using the molar extinction coefficient $\varepsilon(Abs_{276} - Abs_{296})$ = 1410 M^{-1} cm^{-1}.

Cu(II)-Aβ(1-16) was incubated with Au-COOH or Au-HK^{c}HK. **5 nm Au NPs:** the final samples contained 10 μM Cu(II)-Aβ(1-16) and 52 nM 5Au-COOH or 5Au-HK^{c}HK (8 μM AcHK^{c}HK, 0.80 eq). **15 nm Au NPs:** the final samples contained 5 μM Cu(II)-Aβ(1-16) and 0.73 nM 15Au-COOH or 15Au-HK^{c}HK (688 nM AcHK^{c}HK, 0.14 eq). All solutions were prepared in 10 mM HEPES buffer (pH 7.4). The emission spectra were registered in 200 μL quartz cuvettes immediately after sample preparation, after 2 h and finally after 24 h. The samples were incubated at 37 ºC between each measurement. The intensity values at λ_{em} = 305 nm (Tyr) were plotted against time.

In vitro Aβ(1–40) aggregation kinetics

Preparation of aggregate-free amyloid-β peptide:

Aβ(1-40) (5 mg) was dissolved in 1,1,1,3,3,3-hexafluoro-2-propanol (HFIP; 1000 μL) under vigorous shaking at rt for 1 h, after which it was sonicated for 30 min. The solution was further shaken for 1 h and subsequently kept at 4 ºC for 30 min to avoid solvent evaporation. Aliquots of soluble Aβ(1-40) were collected and HFIP was evaporated in air. The resulting solid Aβ(1-40) aliquots were stored at –20 ºC, and the amount of protein per sample was determined spectrophotometrically, dissolving one aliquot in PBS (pH 7.4) and using the molar extinction coefficient ε(Tyr, 280 nm) = 1490 M^{-1} cm^{-1}.

Aggregation studies:

Aliquots of monomeric Aβ(1-40) were dissolved in DMSO (30 μL) using sonication for 10 min. Aβ(1–40) was preincubated with 1 eq of $CuCl_2$ at 37 ºC with continuous shaking (1400 rpm) for 2 h and subsequently freeze-dried; solutions of ThT and Au NPs were added to the dry residues and the resulting samples were sonicated for 5 min. The final concentrations were 25 μM Aβ(1–40), 32 μM ThT, 25 μM $CuCl_2$ and 80.7 nM 5Au-COOH,

78.2 nM 5Au-HK^{c}HK (11.9 μM AcHK^{c}HK), 2.10 nM 15Au-COOH or 1.12 nM 15Au-HK^{c}HK (1.05 μM AcHK^{c}HK). The controls containing Aβ(1–40)-ThT, Aβ(1–40)-ThT-$CuCl_2$ or Aβ(1–40)-ThT-Au NPs were prepared in a similar manner. All samples were prepared in 1X PBS.

The final solutions were transferred into 96-well plates (Clearline® 131012C). The measurements were carried out using a BMG Labtech FLUOstar Omega plate reader in bottom optics configuration with 440/490 nm excitation/emission optics (700 rpm shaking, 37 °C). Endpoint measurements were initiated in the plate reader immediately after sample preparation and data were recorded every 5 min for 60 h.

Assessment of the viability of mouse neuronal cells by propidium iodide uptake

The viability of neuronal embryo cells of wildtype mice (extracted from E16.5 mouse (CD1) embryo brains) in the presence of AcHK^{c}HK (5, 10 and 20 μM), 15Au-COOH (10, 25 and 50 nM) and 15Au-HK^{c}HK (5, 10, and 25 nM) was assessed using the propidium iodide uptake method. The fluorescence emission of propidium iodide was measured in 24-well plates using an Infinite M200 PRO scanner (TECAN Group, Männedorf, Switzerland) with 530-nm excitation (25-nm band pass) and 645-nm (40-nm band pass) emission filters. The fluorescence baseline F_1 was measured 1 h after addition of propidium iodide (30 μM) as an index of cell death not related to the treatment. Subsequently, the fluorescence intensity was recorded after 8, 24, 30 and 48 h following the onset of each treatment. At the end of the experiment, the cells were permeabilised for 10 min with 500 μM digitonin at 37 °C to obtain the maximum fluorescence corresponding to 100% of cell death (F_{max}). The percentage of cell death was calculated using **Equation 5.9**:

$$\textbf{\% cell death} = 100 \times (F_n - F_1) / (F_{max} - F_1) \qquad (5.9)$$

where F_n is the fluorescence intensity at any given time. The experiments were performed in triplicates and the cells were kept in the incubator between the measurements.

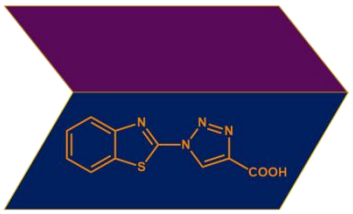

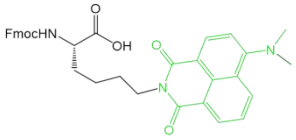

6. Detection of aggregated Aβ with fluorescent probes

6. Detection of aggregated Aβ with fluorescent probes

6.1 Introduction

6.1.1 Sensing of Aβ fibrillation: the mechanism of thioflavin T (ThT)

In the previous chapters, the use of chelating peptides to prevent the copper-induced formation of oligomeric Aβ, to extract copper ions bound to the protein and to inhibit the production of ROS and oxidation catalysed by this metal ion has been described.

The development of fluorescent probes for the detection of aggregated Aβ species and/or monitoring of the self-assembly process are crucial for a better understanding of the pathological events of the amyloid cascade, which would allow to design potential aggregation-inhibitory drugs.

As mentioned in **Chapter 1**, the most widely used and reliable fluorescent tool for the detection of Aβ aggregates is thioflavin T (**ThT**). ThT presents an excitation wavelength λ_{exc} of 385 nm and an emission wavelength λ_{em} of 445 nm.[108] Upon staining of amyloids, both the excitation and emission wavelengths of the dye red shift to 450 and 482 nm, respectively, with a concomitant increase of the fluorescent intensity.

ThT contains a cationic, *N*-methylated benzothiazole moiety, which makes it soluble in water, and a hydrophobic phenyl ring functionalised with a dimethylamino group (**Figure 6.1**). These two parts of the molecule are connected by a freely rotating C-C bond. The dimethylamino function is an electron donor which transfers electron density to the rest of the molecule.

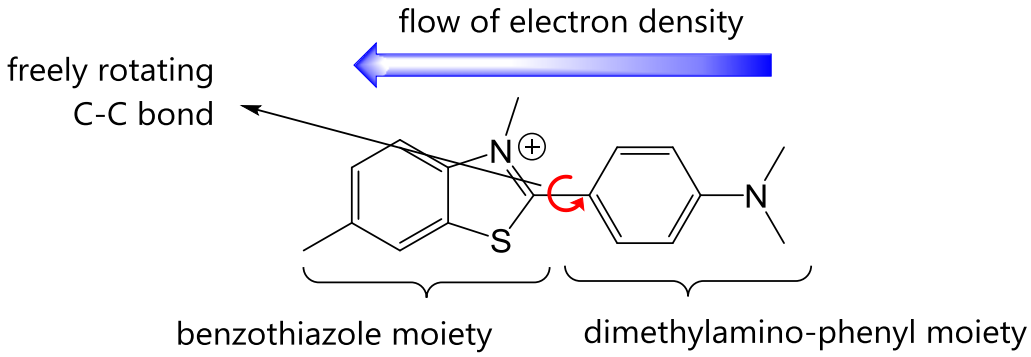

Figure 6.1: Structural and electronic features rationalising the mechanism of ThT emission.

Although ThT has been extensively used in the last decades, its mechanism of action and binding mode remain controversial.[372] In 2005, Krebs provided the first data regarding the arrangement of ThT molecules in amyloid fibrils.[373,374] Using polarised fluorescence microscopy, he concluded that ThT is regularly arranged parallel to the fibril long-axis in close proximity to the protein side chains. Therefore, ThT is accommodated in the channels among the cross-strand ladders.

Alternative models subsequently appeared, but none of them fully explained the behaviour of ThT. Khurana and collaborators suggested the importance of the formation of ThT micelles, which then bind to amyloid fibrils, giving rise to fluorescence enhancement.[375] However, other authors have pointed out that, in many experiments, the concentration of ThT used is lower than the critical micelle concentration. On the other hand, Groenning and co-workers have highlighted the presence of cavities capable of accommodating two ThT molecules in some proteins, which may indicate that the mechanism is based on excited dimers, also called "excimers".[376,377] ThT molecules, though, are often found individually in other binding sites.

Electrostatic interactions are also considered important: the positive charge in the benzothiazole scaffold may play a role in the binding process, as suggested by the low affinity towards proteins with a high content of basic residues and/or at low pH values, that is, when proteins present a high overall positive charge.[378]

In the last decade, experimental studies in solvents of different viscosities, supported by quantum-chemical calculations, have been reported, which strongly suggest that ThT behaves like a molecular rotor.[379-381] In its ground state, ThT exhibits minimal energy when the torsional angle of the benzothiazole moiety relative to the dimethylaminobenzene ring is 37º. However, the energy barrier for this rotation in low viscosity solvents is easily overcome.

Upon irradiation, ThT reaches a locally excited (LE) state from which fluorescent emission occurs (**Figure 6.2**).[379,381] Nevertheless, the transition from the fluorescent locally excited state to a non-fluorescent twisted internal charge transfer (TICT) state quenches the radiative process. This transition is concomitant to a change in the torsional angle from 37º to 90º. In the presence of amyloid fibrils, the rotation of the two fragments is sterically hindered and the charge transfer quenching mechanism is thus blocked, which explains the dramatic increase in fluorescent intensity.

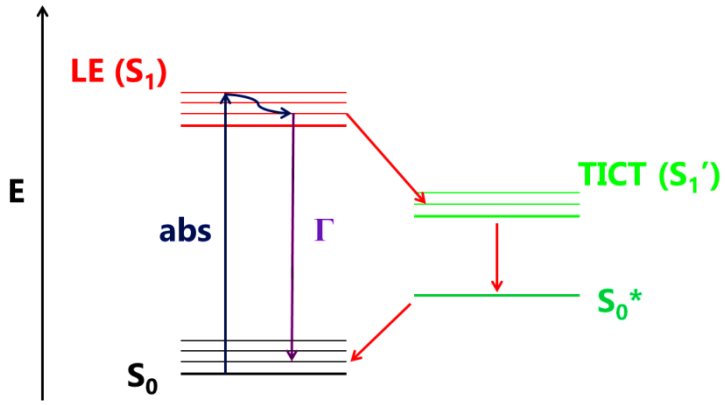

Figure 6.2: Energy level diagram of ThT.

However, as discussed in **Chapter 1**, ThT is not able to cross the BBB due to its cationic nature. For this reason, it is mainly used *in vitro*, in tissues and *ex vivo*. Besides, ThT can only detect fibrillary, β-sheet-rich protein aggregates; hence, the toxic oligomeric species are not detected by ThT.

Such drawbacks have spurred the search for new Aβ probes with improved biodistribution and selectivity toward different aggregated states.[104] Novel fluorescent probes include derivatives of ThT and of Congo red, luminescent conjugated polyelectrolytes, oxazines and other conjugated scaffolds.[107,382,383] Moderate success has been achieved in the detection of oligomeric species, and dyes emitting in the near infrared (NIR) window, much more suitable for *in vivo* applications due to the deeper tissue penetration of IR light, have been prepared.[383,384] Additionally, innovative methodologies, which do not require the utilisation of labels or probes, such as atomic force microscopy (AFM), surface plasmon resonance or mechanical transducers, are being used.[385]

In this chapter, our efforts on the search and utilisation of emissive probes for the detection of aggregated Aβ species are described. The strategy, schematised in **Figure 6.3**, relies on low-emitting molecules that, upon interaction with the aggregated forms of Aβ, show an increase of their fluorescent intensity. The newly-developed probes are intended not to present fluorescence enhancement in the presence of monomeric Aβ, and to be able to discriminate between oligomers, fibres and amorphous aggregates.

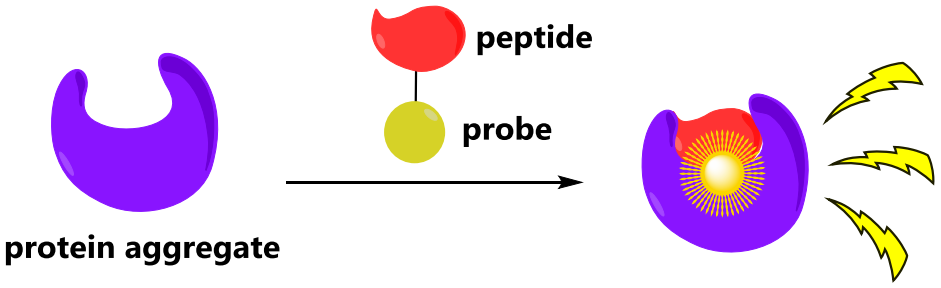

Figure 6.3: Proposed mechanism for the fluorescent detection of Aβ aggregates presented in this chapter.

Two different strategies were followed: first, a potential analogue of ThT, which can be connected to peptides, was synthesised by the so-called ***click chemistry***. Second, peptides containing the environment-sensitive 4DMN probe, whose synthesis was described in **Chapter 2**, were used as bimodal detectors of Aβ aggregates.

6.1.2 Synthesis of a potential ThT analogue by click chemistry

A dye with properties similar to those of ThT, but with the additional capacity to bind to peptidic structures, was thus designed. This compound (which was called **BzTz**) and the retrosynthetic analysis for its preparation are represented in **Figure 6.4**. BzTz contains a benzothiazole moiety, a triazole ring and a carboxylic group for its possible connection to peptides through the generation of an amide function. The azide of the benzothiazole and propiolic acid (also called propargylic acid) were chosen as the building blocks for the synthesis of BzTz, applying click chemistry.

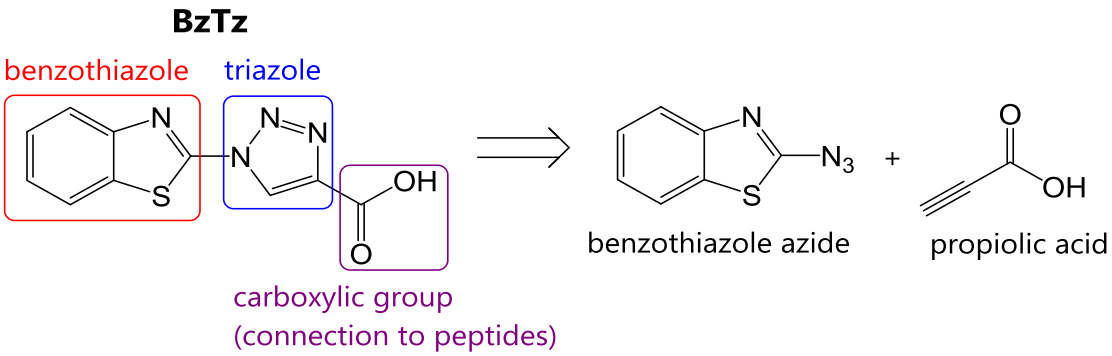

Figure 6.4: Retrosynthetic analysis and structure of BzTz.

Azides and alkynes are commonly used in click chemistry. Thus, the combination of two rationally designed building blocks through click chemistry allowed to obtain a

molecule containing the benzothiazole moiety found in ThT and the carboxylic acid group required for its subsequent use in peptide chemistry. Benzothiazole derivatives have been reported to present high binding affinities towards Aβ aggregates.[386,387] The two functional groups, namely benzothiazole and triazole, were connected to each other by a single C-C bond, similarly to ThT.

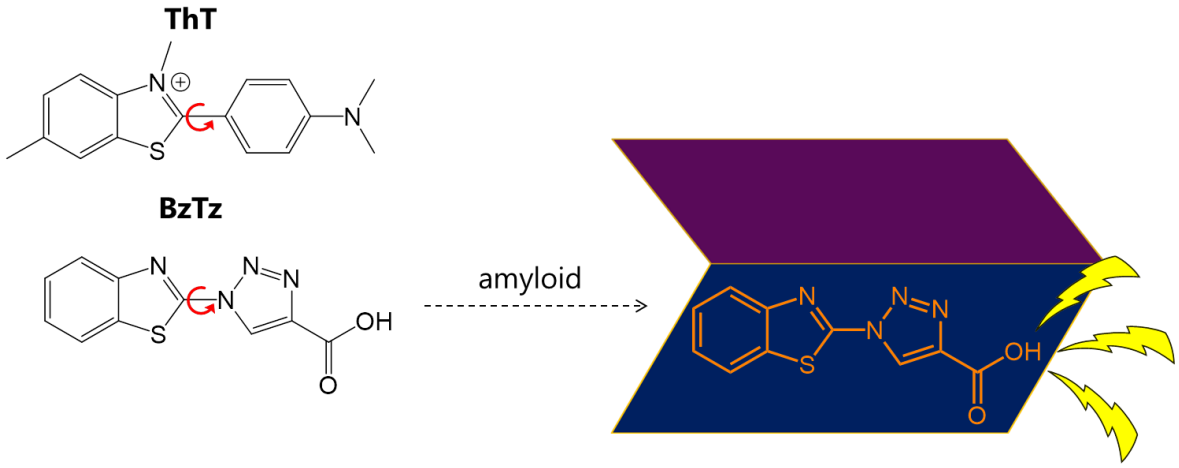

Figure 6.5: Potential ThT-like detection of Aβ amyloids by BzTz.

BzTz was expected to display fluorescence enhancement in the presence of fibrillary Aβ, as the result of the restriction of the C-C bond rotation (between the two functional moieties), producing an extension of the conjugated system, analogously to ThT (**Figure 6.5**). The possibility to connect BzTz to peptides could potentially lead to the development of molecules with low toxicity displaying ThT-like properties. Furthermore, the simple benzothiazole scaffold can be functionalised with electron-withdrawing or electron-donating groups, allowing a fine-tuning of the emissive features of the corresponding probe.

6.1.3 4DMN peptides as bimodal fluorescent probes for the detection of aggregated Aβ

Crucial biological processes such as cell replication, protein synthesis or cell differentiation are driven by groups of a few biomolecules, or even single molecules.[388,389] Therefore, our understanding of the processes involved in cellular biochemistry is highly depending on the ability of scientists to visualise the interactions of individual proteins, nucleic acids and other biomolecules.[388]

However, many common techniques are not suitable to study phenomena of such dynamic nature as they cannot provide real-time data, and often require the death of the cell. Among the different techniques available, fluorescence spectroscopy has emerged as a powerful approach for time-resolved, non-invasive visualisation, due to its intrinsic high sensitivity and spatial resolution.[390-392]

The FRET phenomenon (which only becomes active when the substrates are in close proximity; see **Chapter 3**) has been widely exploited in studies involving living cells during the last years. The most popular strategy consists in expressing the target proteins or peptides fused to the green fluorescent protein (GFP), and its blue, cyan, yellow or red mutants.[390,393] However, such proteins are large and may disrupt the natural folding, recognition and aggregation properties of the conjugates.

Environment-sensitive fluorescent probes (*i.e.*, emissive moieties whose photophysical behaviour changes upon variations of the polarity or the viscosity of the solvent, orientation to electric fields, etc.) have proved to be powerful tools in the field of biology.[394] In particular, dimethylamino-containing probes have been reported that exhibit remarkable properties: their emission quantum yields are much higher in non-polar than in polar solvents, and they show red-shifted emissions in non-polar solvents, with $\Delta\lambda$ of up to 100 nm. Such probes can thus be considered as bimodal probes, since two different parameters are affected upon protein interaction, namely the fluorescent intensity and emission wavelength.

One of the first reported examples was 6-propionyl-2-(dimethylamino)naphthalene, PRODAN, which has extensively been applied, especially to study lipid bilayers.[395-398] Nevertheless, its use was limited by its difficulty to be incorporated into a protein, until its Fmoc-alanine derivative DANA/ALADAN was prepared by Imperiali and co-workers.[399] More recently, solvatochromic fluorophores of the dimethylaminophthalimide family 4DMAP and 6DMN, as well as their respective Fmoc

amino acid derivatives 4DAPA and 6DMNA, have been prepared and incorporated into peptides (**Figure 6.6**).[400,401]

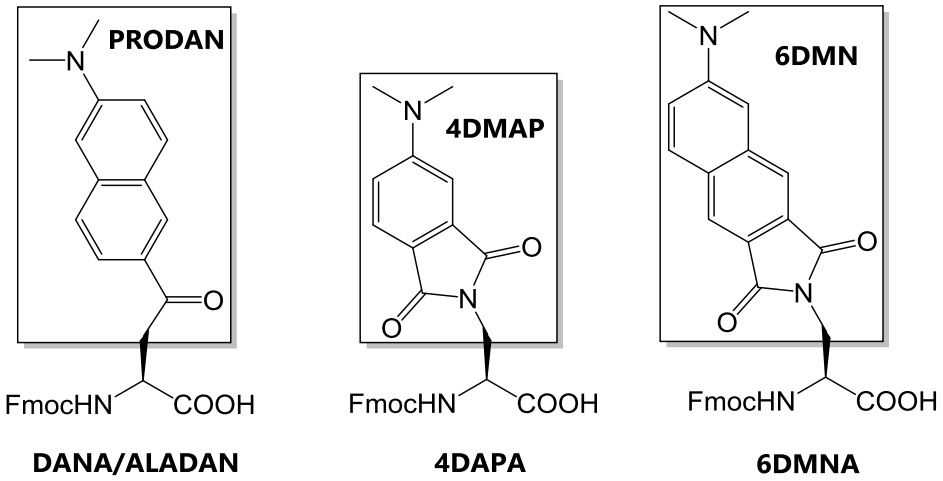

Figure 6.6: Environment-sensitive probes (shown in the rectangles) and their Fmoc-alanine derivatives DANA/ALADAN, 4DAPA and 6DMNA.

In an aqueous solution, peptides labelled with the aforementioned amino acids are poorly emissive. However, upon addition of the target protein, interaction with its hydrophobic domain occurs, and the fluorescence intensity increases in a concentration-dependent fashion, providing a much higher signal-to-noise ratio.[400-402] Hence, the binding dynamic process can be monitored, and affinity constants can be obtained. Moreover, they are similar in size to tryptophan; thus, the structure of the native peptide is not significantly altered.[402]

In 2008, Loving and Imperiali reported the synthesis of a new solvatochromic probe, *viz*. 4-*N,N*-dimethylamino-1,8-naphthalimide (4DMN) and its Fmoc-alanine derivative 4-*N,N*-dimethylamino-1,8-naphthalimidoalanine (4DMNA, **Figure 6.7**).[144] The 1,8-naphthalimide family has been extensively exploited to design DNA-targeting agents and for fluorescence cellular imaging.[403] A straightforward synthesis, improved chemical stability and longer excitation wavelengths are some of the advantages of 4DMNA, compared with 4DAPA and 6DMNA. Many applications of the 4DMN probe have been published, but only a few of them in the field of biology; for instance, it was used for the determination of the affinity of protein-protein interactions or for labelling cell receptors and nucleotides.[144,404,405]

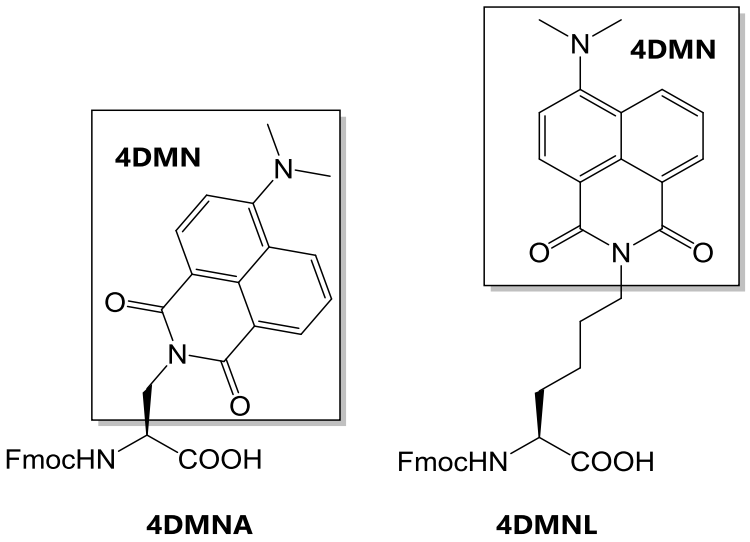

Figure 6.7: 4DMN probe (shown in rectangles), and their Fmoc-amino acid derivatives 4DMNA and 4DMNL.

We prepared a lysine residue labelled with the 4DMN probe, namely **4DMNL** (**Figure 6.7**), which was subsequently incorporated into two peptides (**Figure 6.8**, see **Chapter 2**): Ac-His-Lys(4DMN)-His-OH (**AcHK^{d}H**) and Ac-His-Lys(4DMN)-His-Lys-NH_2 (**AcHK^{d}HK**). Such peptides were expected to interact with Aβ aggregates and to present distinct fluorescence intensity and emission wavelength, depending on the structure of the aggregate. Hence, such peptides may potentially be used as sensors of Aβ oligomers and/or senile plaques. The 4DMNL probe was used instead of 4DMNA, because the longer side chain of lysine, compared to that of alanine, was expected to facilitate the accommodation of the 4DMN moiety into the hydrophobic domain of Aβ.

The metal-chelating His-Xaa-His sequence, exhibited by the two peptides, has been selected as Cu(II)-binding unit (and possibly Zn(II)-binding moiety as well) to subtract this(ese) metal(s) from the aggregates. It is hypothesised that metal removal (from the fibrils) could lead either to disaggregation or to structural changes, which may result in lower toxicity. The AcHK^{d}H peptide presents a free *C*-terminal carboxylic group and is thus negatively charged at physiological pH 7.4. On the contrary, AcHK^{d}HK is amide-protected and therefore presents a positive charge located at the side-chain amino group of Lys4. Such different charges are expected to lead to distinct affinities and interactions with the negatively-charged Aβ peptide.

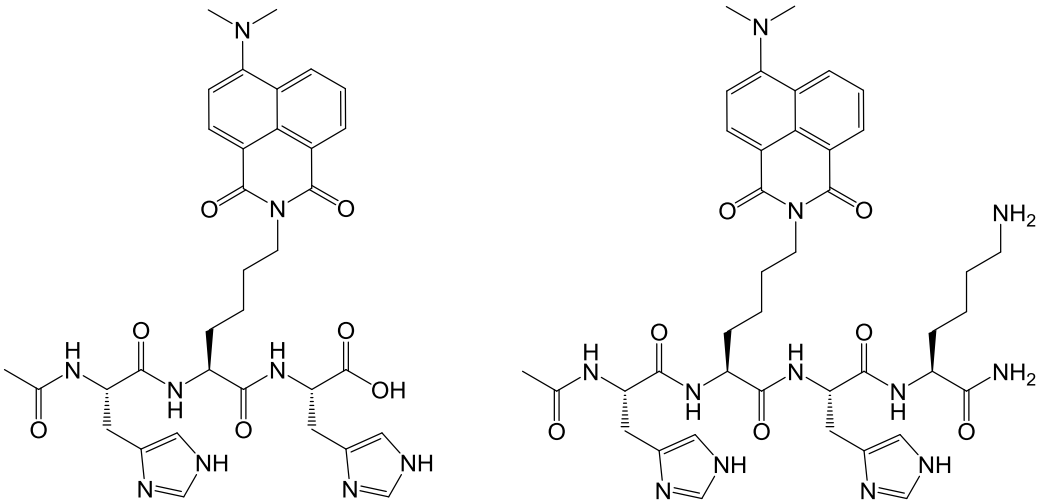

Ac-His-Lys(4DMN)-His-OH (AcHK^{d}H)

Ac-His-Lys(4DMN)-His-Lys-NH$_2$ (AcHK^{d}HK)

Figure 6.8: Representation of the 4DMN-containing peptides AcHK^{d}H and AcHK^{d}HK.

6.2 Objectives

- Synthesis of the ThT analogue BzTz by click chemistry.
- Study of the environment-sensitive fluorescent properties of the 4DMN compounds.
- Evaluation of the capacity of the fluorescent probes to detect aggregated Aβ(1-40) species formed in the presence and absence of metal ions.
- Competition with ThT and evaluation of the sensing capacities of the new probes.

6.3 Results and discussion

6.3.1 Synthesis of the ThT analogue BzTz by click chemistry

6.3.1.1 Definition and applications of click chemistry

The concept of "click chemistry" was first introduced by Sharpless in 2001 as a set of powerful and selective reactions through which heteroatom links are generated.[406,407] Numerous synthetic works involving click-chemistry steps were increasingly published, showing that this reaction became one of the most popular synthetic strategies worldwide.[407] Its simplicity, versatility and tolerance towards diverse functional groups allow to connect virtually any building blocks.

To be categorised as a click-chemistry reaction, a process should meet all the following requirements:

- Give excellent yields
- Be modular, wide in scope and stereospecific
- Generate harmless side products or no side products at all
- Use no solvent or benign ones (*e.g.* water)
- Available starting materials, physiologically stable products
- Non-chromatographic purification (if purification is required)

Click-chemistry reactions must present a high thermodynamic driving force (≥ 20 kcal·mol^{-1}), so that they can achieve the aforementioned requirements. Hence, highly energetic starting materials are typically utilised.[407]

The most common synthetic processes that fall under the umbrella of click chemistry are nucleophilic substitution reactions (especially those which involve the opening of strained heterocycles), non-aldol carbonyl chemistry, additions to C-C multiple bonds and cycloadditions of unsaturated reactants. Within the latter category, the Huigsen 1,3-dipolar cycloaddition reactions of organic azides and alkynes are probably the most popular and paradigmatic click-chemistry processes.

Alkynes and azides are, in general terms, stable under most organic and biological conditions; they are inert towards atmospheric oxygen, water and most common

synthetic conditions. This stability is due to kinetic factors rather than to thermodynamic ones. However, such stability is responsible for the observed slow reaction rates; hence, this type of cycloadditions often requires high temperatures and long reaction times. Furthermore, although reactions involving terminal, highly electron-deficient alkynes present a good regioselectivity, most processes with other alkynes yield mixtures of the 1,4- and 1,5-regioisomers (see **Figure 6.9**).

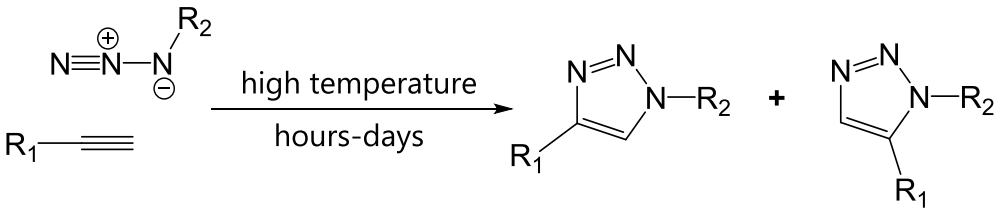

Figure 6.9: Huigsen 1,3-dipolar cycloaddition reaction between organic azides and alkynes.

In 2001, the development of Cu(I)-catalysed alkyne-azide cycloadditions (**CuAAC**) gained worldwide attention (**Figure 6.10**). This copper-mediated procedure, which exclusively yields the corresponding 1,4-disubstituted 1,2,3-triazoles under mild conditions and with much shorter reaction times, was independently published by Sharpless and Fokin in the United States and by Meldal in Denmark. The former group developed the CuAAC reaction in solution with protic polar solvents, while the latter reported it in the solid phase. Since then, different catalysts based on other metals such as ruthenium, silver, gold, zinc or nickel have been described; however, copper is still the most efficient metal.[408]

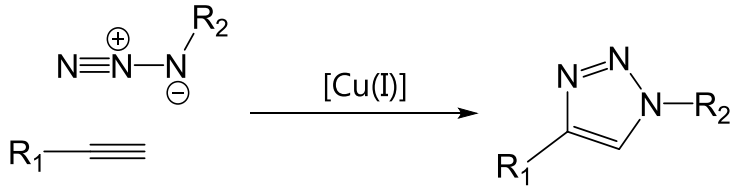

Figure 6.10: Cu(I)-catalysed alkyne-azide cycloaddition (CuAAC).

The CuAAC reaction is extremely powerful for the solid-phase preparation of peptides, nucleotides, peptoids, supramolecular assemblies, etc.[409] For instance, the completion of the reaction can be conveniently assessed by monitoring the disappearance of the organic azide by infrared spectroscopy. Besides, shorter reaction times and often quantitative yields can be achieved by using microwaves.

The mechanism of copper-catalysed alkyne-azide cycloadditions has been a matter of debate. Although the first mechanisms proposed, based on DFT calculations, involved a mononuclear copper acetylide moiety, further experimental and computational studies on the kinetics of the reaction suggested the participation of dinuclear copper species.[410]

Recently, Fokin, Worrell and Malik elegantly demonstrated the presence of a dinuclear active species by heat-flow reaction calorimetry.[411] They treated a preformed, stable Cu^{I}-acetylide with an organic azide in presence or absence of a Cu(I) catalyst. When no copper catalyst was used, no conversion was observed, whereas the copper-catalysed reaction was completed within 20 minutes (see **Figure 6.11**).

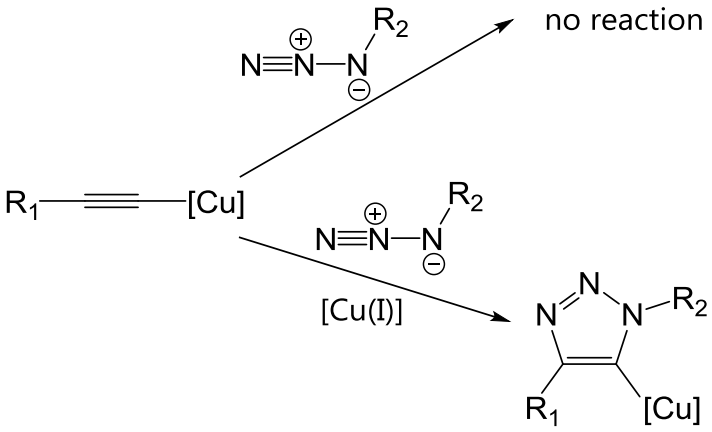

Figure 6.11: Role of Cu(I) species in CuAAC.

Additional experiments with an isotopically enriched exogenous copper source allowed them to propose a mechanism for the catalytic cycle, which is shown in **Figure 6.12**. First, a copper(I) ion binds to an alkyne molecule through a π bond (step *i*), and a second copper is subsequently coordinated through a σ bond, generating a dinuclear copper acetylide (step *ii*). This dinuclear complex is thought to be the catalytically active species, which next coordinates the azide, in a reversible manner (step *iii*). Then, the nucleophilic attack of the β-carbon to the terminal nitrogen atom of the azide produces the first C-N bond (step *iv*). At this point, the two copper atoms undergo a rapid exchange of ligands and become equivalent. Finally (step *v*), the second C-N bond is generated, completing the annellation process, and the triazole is released by protonation (step *vi*).

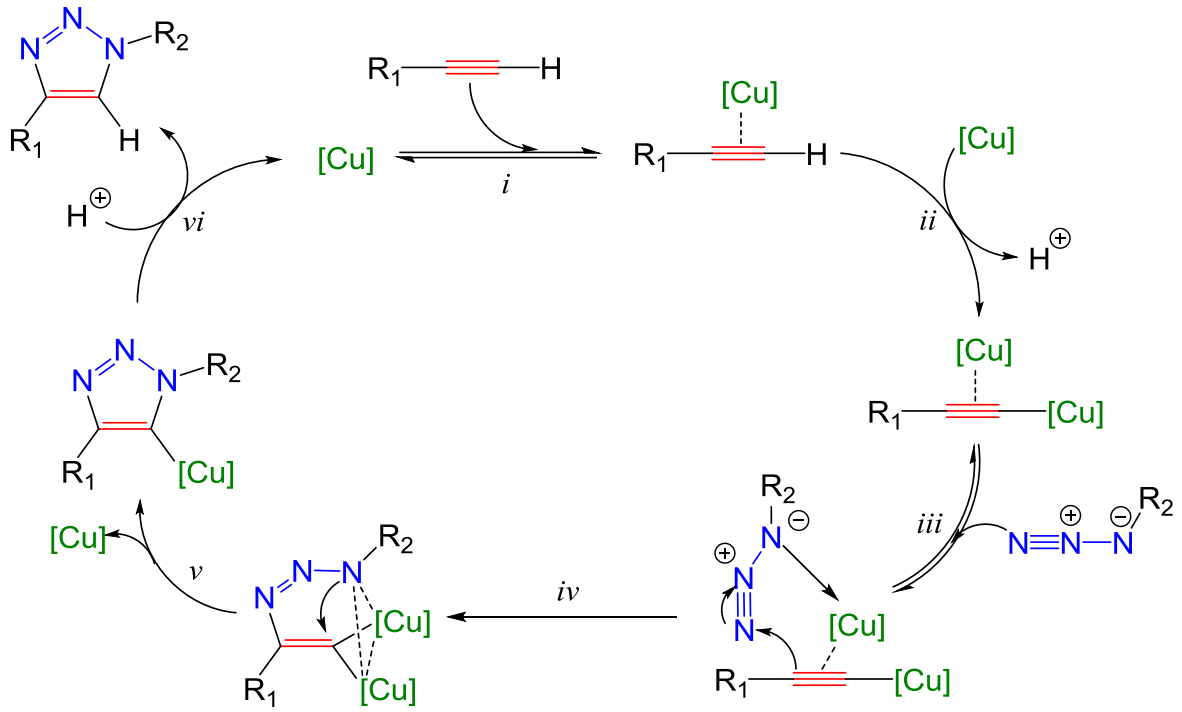

Figure 6.12: Catalytic cycle of the CuAAC reaction.

The ease of connection of the different building blocks has, as already mentioned, attracted a lot of interest in chemical synthesis. Click chemistry has found its most relevant applications in materials science (for example, in nanotechnology, supramolecular chemistry or for the preparation of dendrimers), bioconjugation (usually to incorporate (fluorescent) labels to biomolecules) and drug discovery.[412-415]

The particular properties of the 1,4-disubstituted triazole generated by the CuAAC reaction may be valuable for medicinal and biological applications.[416] Indeed, the triazole ring possesses a strong dipole moment, which may enhance the hydrophilicity of the product, and displays hydrogen bond-accepting ability and aromaticity, which may favour its interaction with a wide variety of biomolecules. Furthermore, the triazole architecture may act as a pseudo-peptide bond (in a peptide sequence), more resistant to hydrolytic cleavage and metabolic degradation. A number of 1,2,3-triazole derivatives exhibit promising biological activities, and have been used as anti-fungal,[417,418] anti-bacterial,[419,420] anti-cancer,[421-423] anti-histamine or anti-HIV agents.[424-427] In the last few years, reports on the modulation of Aβ aggregation by compounds containing the 1,2,3-triazole ring have also been published.[428-430]

6.3.1.2 Preparation of BzTz by click chemistry

The synthesis of this potential analogue of ThT started with the preparation of an organic azide containing the benzothiazole moiety found in the original dye. The commercially available 2-aminobenzo[*d*]thiazole may be converted into the target building block through a diazotisation reaction, followed by a nucleophilic substitution with sodium azide.

The generation of diazonium salts from primary aromatic amines using sodium nitrite in acidic media is known for many years. Diazonium salts readily react with nucleophiles with concomitant release of N_2 (acting as the leaving group). In the present case, different conditions were tested, which are summarised in **Table 6.1**:

Table 6.1: Tested conditions for the preparation of the 2-benzothiazole azide precursor.

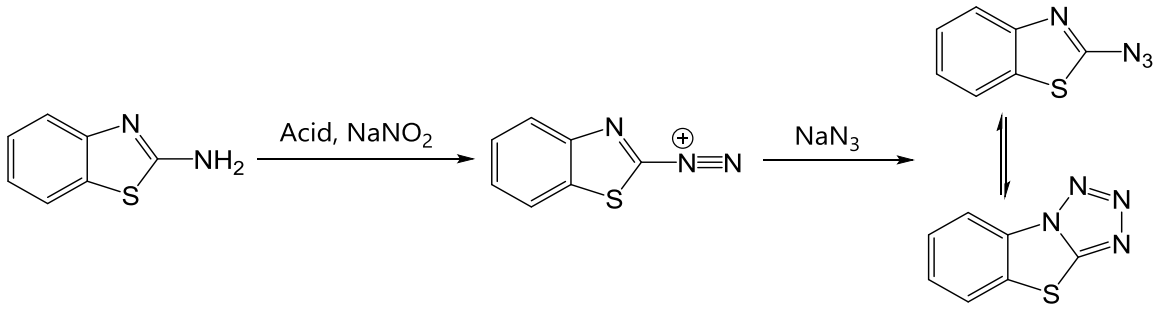

Entry	Solvent	Acid	Eq of $NaNO_2$/ NaN_3	Time (1 + 2)	T (ºC)	Yield
1[431]	H_2O/THF	H_2SO_4	2/3	30 min + 2 h	rt	-
2	H_2O/EtOH	H_2SO_4	20/30	30 min + 2 h	rt	-
3	H_2O/EtOH	H_2SO_4	20/30	30 min + 2 h	0	-
4[432]	H_2O	HCl	1/1	0 min + 20 h	0 to rt	-
5	H_2O/EtOH	HCl	20/30	10 + 15 min	2-3	-
6[433]	H_2O	H_3PO_4	1/1.5	30 + 60 min	0 to rt	75%

The presence of the benzothiazole azide was assessed by IR spectroscopy, *via* the characteristic band of organic azides at around 2120 cm^{-1}. Solely the use of H_3PO_4 yielded appreciable amounts of benzothiazole azide (**Entry 6**). Successful nucleophilic

aromatic substitutions involving diazonium salts greatly depend on the stability of the ionic pair; hence, a higher stabilising effect of the dihydrogen phosphate counterion may explain the results achieved with phosphoric acid.

The benzothiazole azide exists as two species in equilibrium, namely benzo[4,5]thiazolo[3,2-*d*]tetrazole and 2-azidobenzo[*d*]thiazole (See **Table 6.1**). This well-known equilibrium was slow enough to be observed by thin-layer chromatography, HPLC and NMR spectroscopy (**Figure 6.13**).[433-440]

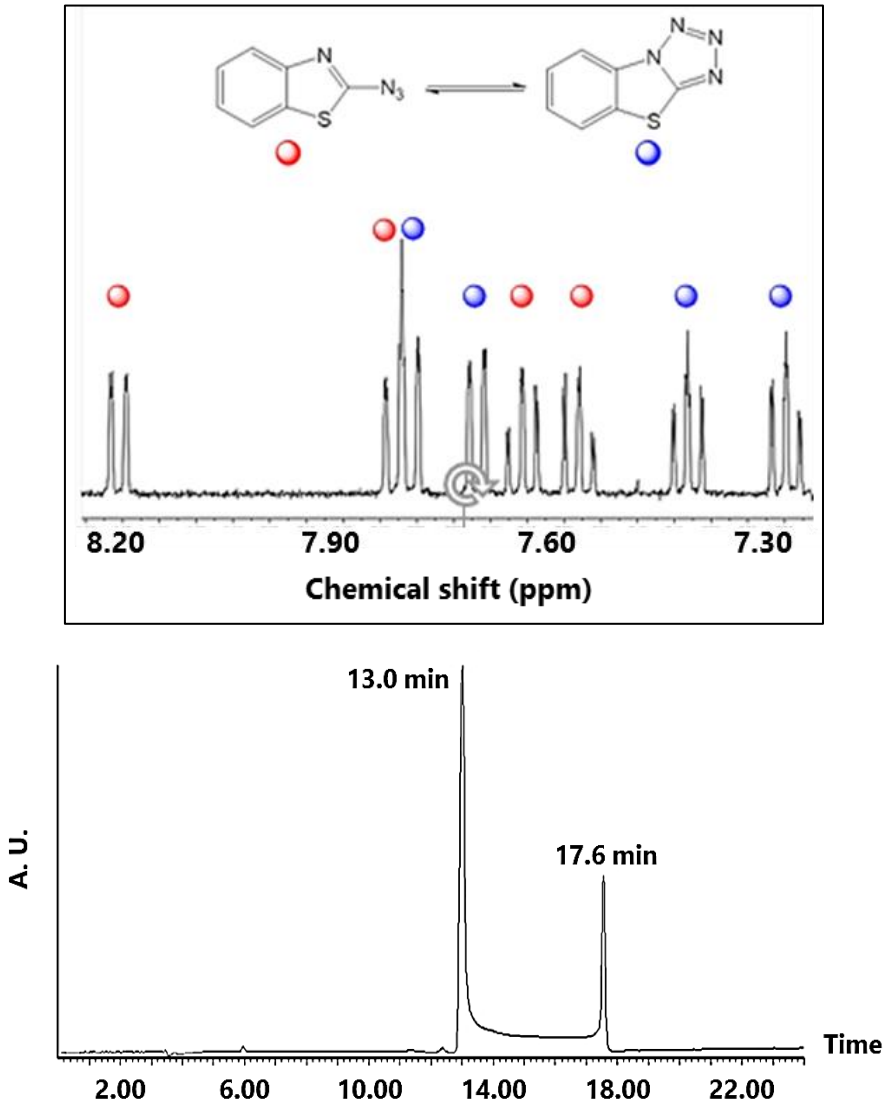

Figure 6.13: Presence of benzo[4,5]thiazolo[3,2-*d*]tetrazole and 2-azidobenzo[*d*] thiazole in equilibrium, revealed by ^{1}H NMR (**top**) and HPLC chromatogram (**bottom**).

The predominant form will be dictated by various factors; for instance, the presence of an electron-withdrawing group, will favour the azide, while an electron-donating group, will favour the tetrazole tautomer. The polarity of the solvent, the temperature and the physical state (*viz.* in the solid state or in solution) will also affect this equilibrium. Under the conditions applied, the integration of the corresponding ^{1}H NMR signals in $CDCl_3$ suggests that the two forms exist in a ratio of approximately 1:1.

Next, the azide was used to perform the copper-catalysed 1,3-dipolar cycloaddition with propiolic acid. Alternatively, the target compound may be obtained through the reaction of the benzothiazole azide with ethyl propiolate, followed by the hydrolysis of the resulting ester using lithium hydroxide (**Figure 6.14**).

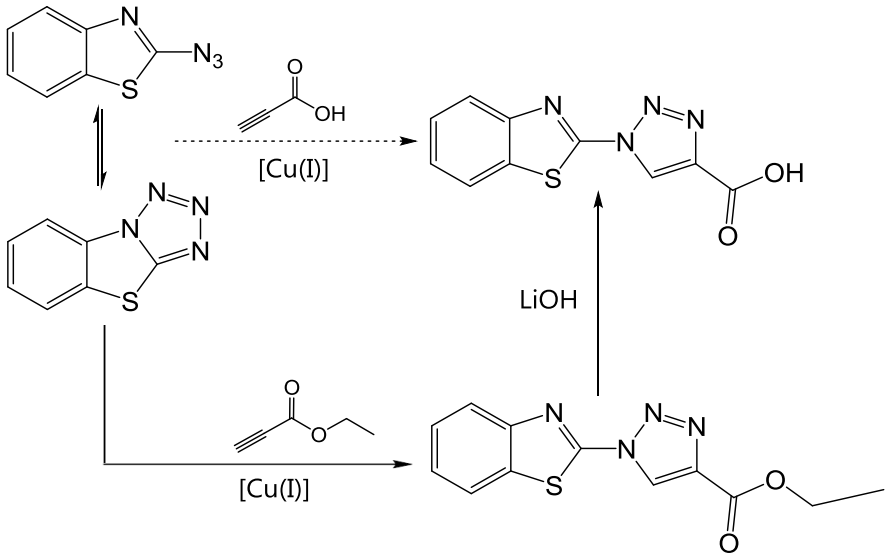

Figure 6.14: Synthetic scheme for the preparation of BzTz using propiolic acid or ethyl propiolate.

Universal experimental conditions (that would work for any substrate) are not available for CuAAC. The nature of the substrate(s) requires the tuning of reaction parameter(s), and various reaction conditions have been reported, the copper source being an important factor.[441] The most common ways to generate the copper catalyst are by:

- *In situ* reduction of copper(II) salts with sodium ascorbate
- Using a copper(I) salt in the presence of a base (typically DIPEA)
- The generation of Cu(I) species by oxidation of metallic copper

The ligands or counterions of the copper species also have an influence on the rate of the reaction. Very recently, Bertrand and co-workers studied the rates of a *L*Cu(I)*X* complex, where *L* was a cyclic (alkyl)-(amino)carbene and *X* a triflate, chloride, acetate, phenolate or *tert*-butoxide counterion (*X* of increasing basicities).[442] It was found that, whereas basic species promote the initial metalation of a terminal alkyne, they disfavour the subsequent formation of the active σ,π-bis(copper) acetylide (step *ii* in **Figure 6.12**). Thus, the acetate anion was found to be the best compromise; furthermore, AcO^- assists the proton transfer that eliminates the copper atom in the final step (step *vi* in **Figure 6.12**).

In our study, three different Cu(I) sources were evaluated, which are listed in **Table 6.2**. These are copper(II) sulphate (**Entries 1**, **2** and **3**), copper(II) acetate (**Entry 4**) and copper(I) iodide (**Entries 5** and **6**). The crudes of the corresponding cycloaddition reactions were analysed by HPLC.

Table 6.2: Experimental conditions tested for the preparation of BzTz from the benzothiazole azide using propiolic acid as the alkyne.

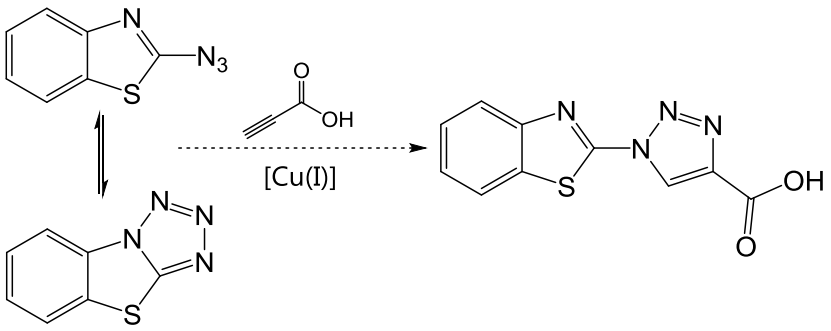

Entry	Propiolic acid (eq)	Cu source (eq)	Additive (eq)	Solvent	T (°C)	Time (h)	HPLC purity (%)
1	1	$CuSO_4$ (0.1)	ascorbate (0.1)	*t*-BuOH/H_2O	rt	24	-
2	2.5	$CuSO_4$ (0.1)	ascorbate (0.2)	*t*-BuOH/H_2O	rt	5	-
3[443]	2.5	$CuSO_4$ (0.1)	ascorbate (0.2)	*t*-BuOH/H_2O	60	5	32
4[444]	1.2	$Cu(AcO)_2$ (0.02)	ascorbate (0.02)	MeCN	45	24	5
5	1.5	CuI (1)	DIPEA (3)	THF	rt	5	-
6[433]	1.5	CuI (0.1)	DIPEA (3)	THF	rt	5	58

For the $CuSO_4$-ascorbate system, BzTz was only detected when the reaction was heated at 60 ºC (**Entry 3**), although the chromatographic purity was low (32%). The $Cu(AcO)_2$-ascorbate system (**Entry 4**) yielded very low amounts of BzTz (chromatographic purity of 5%). Finally, the CuI(catalytic)-DIPEA system (**Entry 6**, chromatographic purity of 58%) was the most efficient, whereas the CuI(equimolar)-DIPEA system (**Entry 5**) was completely ineffective. Purification of the crude mixtures gave very low yields of BzTz and with poor purities, insufficient for its subsequent characterisation and use as fluorescent probe.

Reaction with ethyl propiolate was therefore alternatively carried out, applying the conditions described in **Entry 6**, that is, using catalytic amounts of CuI in presence of DIPEA. The ester precursor was obtained in excellent yield (95%) after a reaction time of only 40 min (**Figure 6.15**). A simple purification step consisting of acidic washings afforded a highly pure product (chromatographic purity of 95%), which was used as the starting material for the next step.

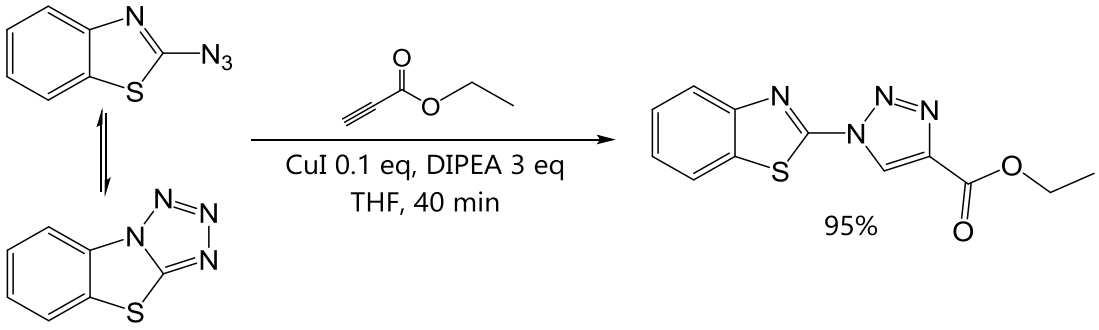

Figure 6.15: Synthesis of the ester precursor of BzTz.

The ester precursor was hydrolysed with lithium hydroxide and subsequently protonated with hydrochloric acid (**Figure 6.16**). BzTz was obtained by precipitation in moderate yield (50%), but with a high chromatographic purity (96%), allowing the study of its interaction with Aβ(1-40) peptide by fluorescence.

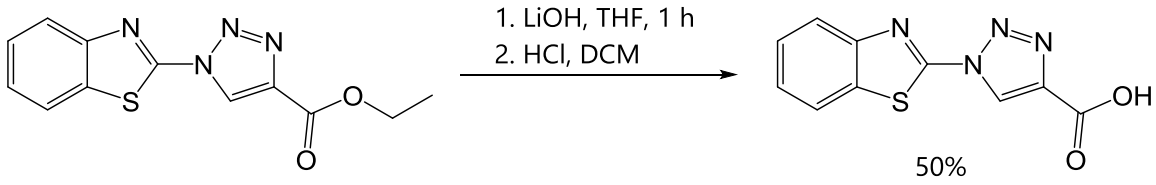

Figure 6.16: Hydrolysis of the ester precursor to afford BzTz.

6.3.1.3 Detection of Aβ(1-40) fibres with BzTz compounds

The fluorescent properties of BzTz and its potential ThT-like behaviour were subsequently evaluated. To become an alternative candidate to ThT, the excitation and emission wavelengths of BzTz should vary upon addition of proteins with β-sheet structure. The absorption and emission of free BzTz in 100 mM HEPES were first determined. Under these conditions, BzTz presented an absorption band centred at 290 nm (1.02×10^4 M^{-1} cm^{-1}) and, upon excitation at this wavelength, it emitted at 390 nm.

Next, the fluorescent properties of BzTz in the presence of fibres of Aβ(1-40) were evaluated. The presence of fibres was verified by using ThT with increasing amounts of the protein (**Figure 6.17**).

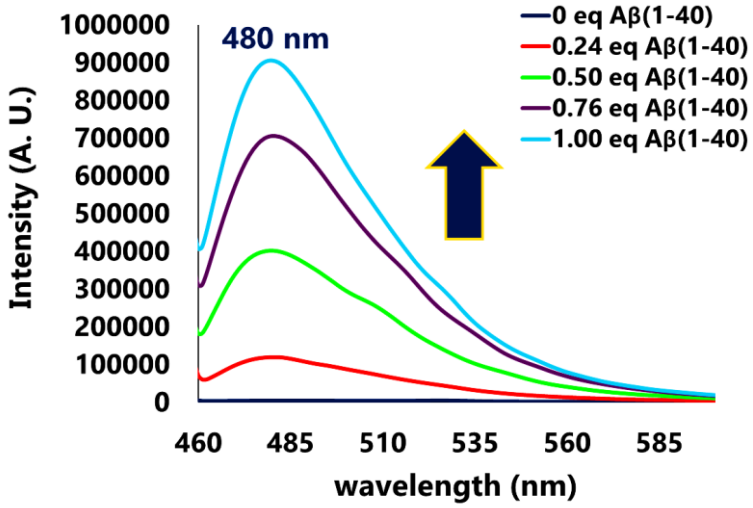

Figure 6.17 Fluorescence spectra of ThT in the presence of increasing amounts of Aβ(1-40) fibres. λ_{exc} = 447 nm. HEPES 10 mM (pH 7.4).

Unfortunately, no fluorescence changes were detected for BzTz with similar amounts of Aβ(1-40) fibres. Its emission intensity indeed remained unaltered, so as its excitation/emission wavelengths (**Figure 6.18**). This lack of (fluorescence) activity of BzTz may be due to a poor interaction with the fibres or/and to inadequate electronic and rotational features.

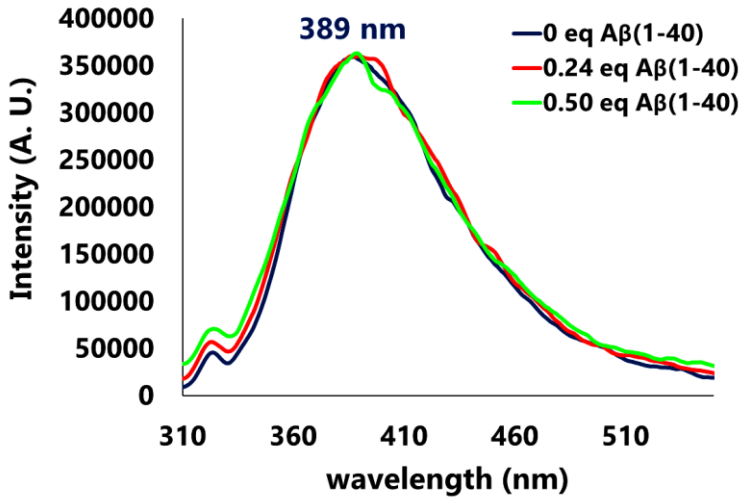

Figure 6.18: Fluorescence spectra of BzTz in the presence of increasing amounts of Aβ(1-40) fibres. Excitation wavelength λ_{exc} = 290 nm. HEPES 10 mM (pH 7.4).

As mentioned above, it is generally accepted that the positive charge of ThT is important for its interaction with proteins. Aβ(1-40) presents three aspartate and three glutamate residues (negatively charged), and one arginine and two lysine residues (positively charged), providing an overall charge of -3. Therefore, it is plausible that negatively charged BzTz was electrostatically repelled by the protein fibres.

Accordingly, a lysine derivative, *i.e.* BzTz-Lys-NH_2, was prepared *via* solid-phase synthesis following the scheme shown in **Figure 6.19**. Such derivative was prepared using a Rink amide AM resin; therefore, its carboxylic group was protected as a carboxamide moiety. It can be noticed here that BzTz was coupled through its α-amino group. The side chain of BzTz-Lys-NH_2 is positively charged at physiological pH, which might favour a better interaction with the negatively charged amyloids.

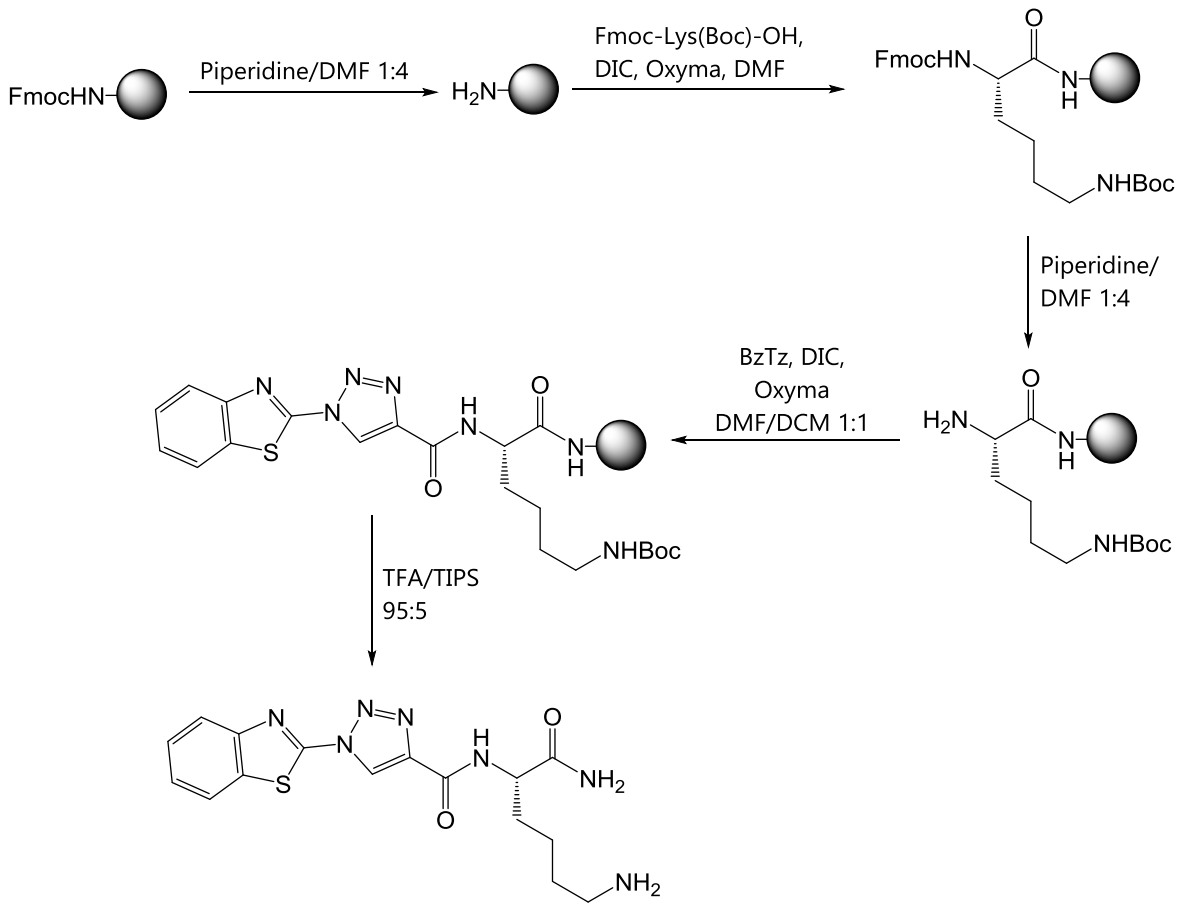

Figure 6.19: Solid-phase synthesis of BzTz-Lys-NH_2.

The derivative was obtained in high yield (83%) and very high chromatographic purity (99%). As expected, BzTz-Lys-NH_2 presented good solubility in water at pH 7.4 and kept the fluorescent properties of the (parent) BzTz group. Treatment of BzTz-Lys-NH_2 with increasing amounts (0.24-1.00 eq) of Aβ(1-40) fibres, however, did not give rise to the alteration of the fluorescence emission (**Figure 6.20**).

This absence of ThT-like behaviour may arise from a deficient electron conjugation throughout the dye, which is necessary for the variation of the emissive properties taking place upon restriction of the rotation. A push-pull system, in which an electron-rich part of the molecule would transfer electron density to an electron-deficient part, is certainly required for an efficient fluorescence, and BzTz and its lysine derivative most likely do not fulfil these structural and electronic features. Computational studies may help to assess whether the electronic structure of BzTz is appropriate or not to build a ThT analogue.

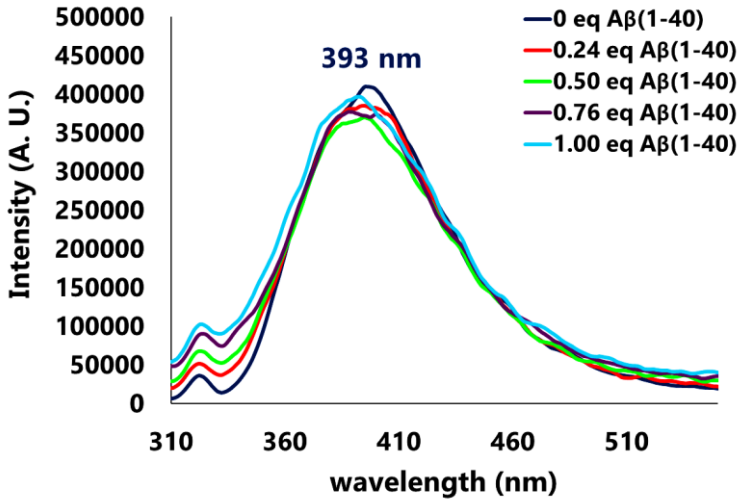

Figure 6.20: Fluorescence spectra of BzTz-Lys-NH_2 in the presence of increasing amounts of Aβ(1-40) fibres. λ_{exc} = 290 nm. HEPES 10 mM (pH 7.4).

6.3.1.4 Inhibition of the aggregation of Aβ(1-40) peptide by BzTz compounds

BzTz and BzTz-Lys-NH_2 were also tested as potential inhibitors of Aβ aggregation. Several triazole-containing compounds with anti-aggregation properties have been reported.[428-430] Moreover, the benzothiazole moiety is known to bind amyloids with high affinity.[386,387] The aggregation of Aβ(1-40) into fibres in the presence of 0.05 equivalents of the BzTz compounds was thus followed by ThT fluorescence at 37 ºC with constant shaking, and the results obtained are shown in **Figure 6.21**.

Control Aβ (non-treated) presented the typical abrupt increase in ThT fluorescence after 20-25 min (see previous chapters), indicative of the formation of amyloid fibrils. The plateau was reached 40 min after the beginning of the experiment. In the presence of BzTz, the increase in ThT emission was gradual until 50 min from the start, suggesting that BzTz affected the nucleation step. In addition, the final ThT fluorescence (at the plateau) was about 30% lower than that of the control (**Figure 6.21**). BzTz-Lys-NH_2 practically did not delay the increase of ThT fluorescence (compared to the control), and the intensity of ThT emission at the final phase (plateau) was lower by approximately 25%.

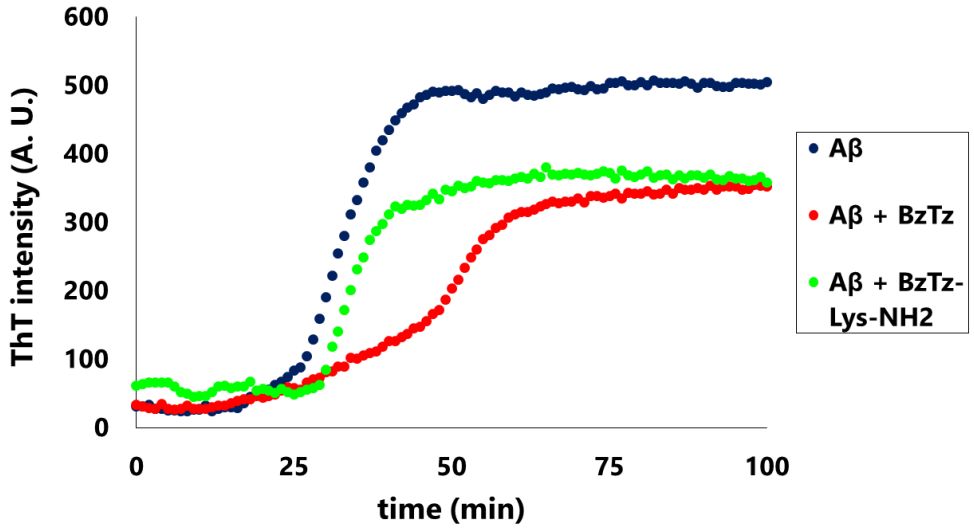

Figure 6.21: Aggregation kinetics of Aβ(1-40) in the presence of 0.05 eq of BzTz (red dots) and BzTz-Lys-NH_2 (green dots) followed by ThT emission (λ_{exc} = 440 nm, λ_{em} = 490 nm) in 1X PBS (pH 7.4) at 37 ºC.

Although inhibition of the fibrillation by BzTz compounds cannot be ruled out, partial displacement of ThT by BzTz and BzTz-Lys-NH_2 might have occurred as well, explaining the emission decrease observed at the final phase; the benzothiazole moiety of the compounds, also present in ThT, may direct them to the same Aβ binding sites. BzTz produced a slight delay in amyloid formation, which might arise from repulsion of the negatively charged peptides. The opposite effect, that is, the acceleration by attractive interactions, was not observed for the positively charged Lys derivative.

Although the results achieved were not exciting, it is nonetheless believed that the development of benzothiazole-based molecules, which can be coupled to a variety of different functional groups *via* an amide bond, opens the possibility to enhance the properties of known Aβ-aggregation inhibitors. For example, BzTz may be coupled to the KLVFF peptide or its analogues LPFFD, LPYFD and RDLPFYPVPID, which are all potent inhibitors, known as *β-sheet breakers*.[116]

6.3.2 Development of environment-sensitive peptides for the detection of Aβ aggregates

6.3.2.1 Evaluation of the environment-sensitive properties of the 4DMN probe

Research efforts were then directed towards the use of the polarity-sensitive 4-*N,N*-dimethylamino-1,8-naphthalimido (**4DMN**) probe. The mechanism of action of this probe is different from that of ThT; 1,8-naphthalimido probes rely on the dependence of the relaxation rates on the polarity of the solvent, while ThT works as a molecular rotor.[401,405]

The polarisation of the 4DMN molecule upon irradiation induces an electron transfer from the dimethylamino function to the carbonyl groups, resulting in high quantum yields.[405] In protic solvents, though, hydrogen-bonding with the carbonyl groups of the 4DMN imide favours the non-radiative relaxation of the fluorophore, producing a dramatic decrease of the fluorescence intensity.[394,405] Furthermore, the band gap between the ground and the excited states greatly depends on the solvent polarity, thus presenting shorter/longer excitation and emission wavelengths in low/high polarity solvents, respectively.

The spectroscopic properties of the Boc amino acid were first investigated. Boc-Lys(4DMN)-OH (**Boc-K^d**) is soluble in a wide range of solvents, which allowed to study the variation of its emissive properties with the polarity of the solvent. First, the excitation and emission wavelengths and the molar extinction coefficients of Boc-K^d in a polar medium, namely 100 mM HEPES, and in a low polar solvent, namely DCM, were determined. The spectroscopic features obtained, which are in agreement with those found in the bibliography for other derivatives, are summarised in **Table 6.3**.[144,404]

Table 6.3: Excitation and emission wavelengths and molar extinction coefficients of Boc-K^d in 100 mM HEPES (pH 7.4) and in DCM.

	HEPES pH 7.4	DCM
ε ($M^{-1}·cm^{-1}$)	8400 (441 nm)	10500 (420 nm)
λ_{exc} (nm)	441	420
λ_{em} (nm)	546	510

As anticipated, both the maximum excitation and emission wavelengths were shorter in low polar DCM, and the molar extinction coefficient was higher (than in HEPES). Moreover, the fluorescence intensity of Boc-K^d was three orders of magnitude higher

in DCM than in HEPES at the same amino-acid concentration (**Figure 6.22**). Actually, DCM solutions displayed a very bright green colour, while aqueous solutions were dim yellow.

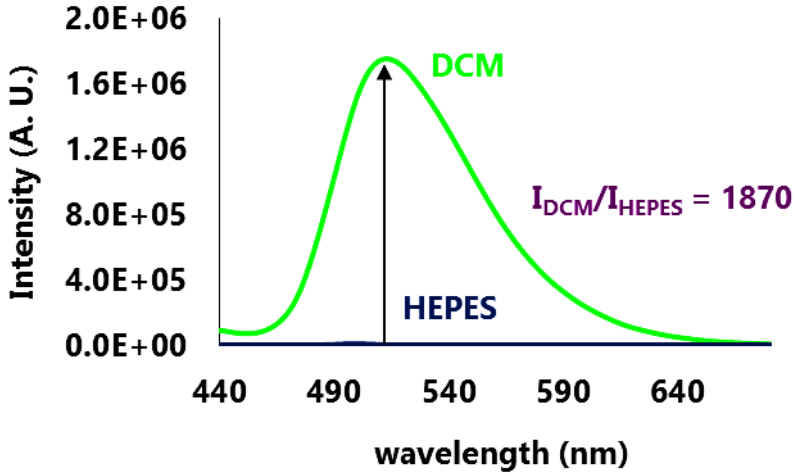

Figure 6.22: Fluorescent emission of Boc-K^d in DCM and in 100 mM HEPES (pH 7.4). The excitation wavelengths were 420 and 441 nm in DCM and HEPES, respectively.

To further assess the solvatochromism of the fluorescent amino acid, the maximum emission wavelength in different solvents was plotted against their corresponding dielectric constants (**Figure 6.23**). The optimal excitation wavelength in DCM (420 nm) was used for all the measurements.

The less polar the solvent, the shorter the emission wavelength of Boc-K^d was. This effect was more pronounced for the solvents with the lowest dielectric constants. The emission intensity also decreased as the polarity increased. The inset image in **Figure 6.23** qualitatively illustrates this difference in the emissive properties: when exposed to UV radiation, the Boc amino acid presented a bright green-blue emission in toluene, a less intense green fluorescent emission in DCM and almost no fluorescence in MeOH (dielectric constant: toluene < DCM < MeOH).

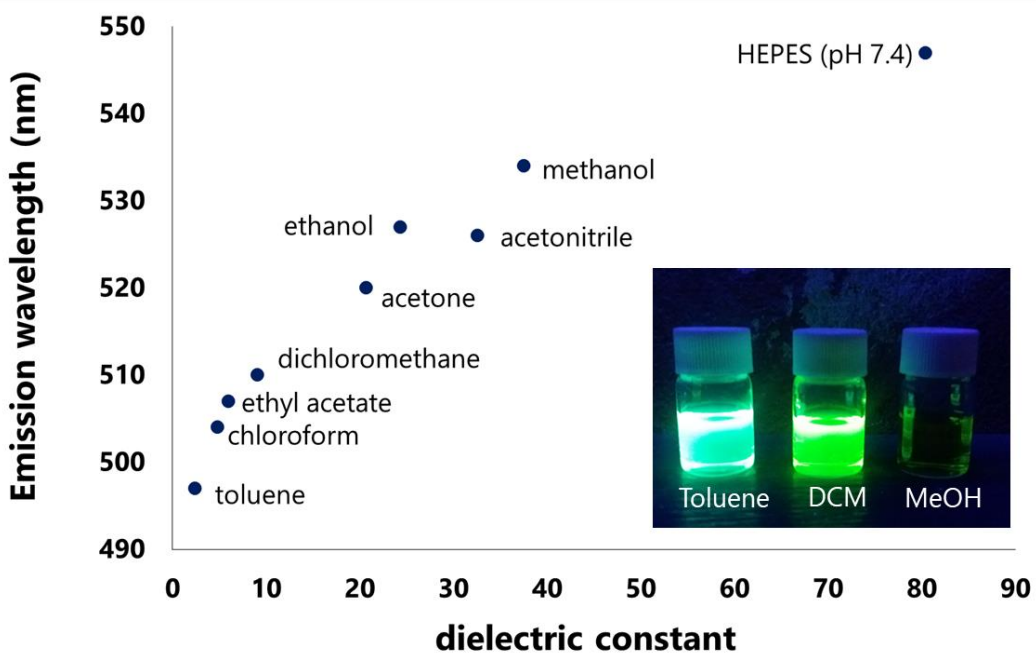

Figure 6.23: Variation of the maximum emission wavelength of Boc-K^{d} with the dielectric constant of the solvent (λ_{exc} = 420 nm). Inset image: solutions of Boc-K^{d} in toluene, DCM and MeOH that were exposed to UV radiation.

6.3.2.2 Detection of Aβ(1-40) fibrils

Once the environment-sensitive behaviour of the 4DMN probe was investigated, its ability to detect aggregated Aβ was examined. The fluorescent emission of Boc-K^{d} in the presence and absence of 2 equivalents of fibrillary Aβ(1-40) was recorded for 5 days at 37 ºC. The results obtained, exciting the samples at 420 nm, are shown in **Figure 6.24**.

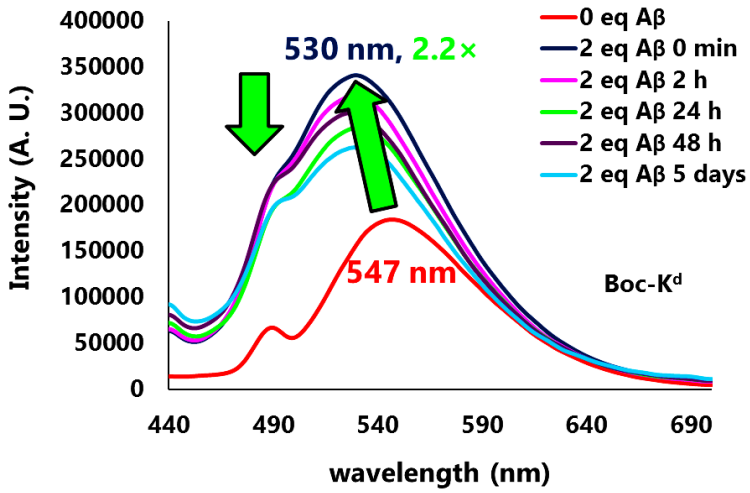

Figure 6.24: Emission spectra of free Boc-K^d (red spectrum) and Boc-K^d in the presence of 2 eq of fibrillary Aβ(1-40) during 5 days. The concentration of Aβ(1-40) was 10 μM. λ_{exc} = 420 nm, 100 mM HEPES (pH 7.4).

Immediately after sample preparation, the maximum emission wavelength blue-shifted from 547 to 530 nm, as the result of the more hydrophobic environment. In addition, Boc-K^d exhibited a 2.2-fold intensity increase at 530 nm in the presence of amyloids, compared with the free amino acid. During the 5 days experiment, the emission gradually decreased without shifting the maximum but still remained markedly higher than that in the absence of beta-amyloid aggregates. A progressive degradation of the probe and/or the precipitation of the peptide with aggregated Aβ may explain such diminution of the emission intensity.

Following these promising results, similar studies were carried out with the 4DMN peptides AcHK^{d}H and AcHK^{d}K. Enhanced interaction with the amyloids compared to the Boc-amino acid was expected due to the possibility to generate hydrogen bonds with the amide backbones. As a matter of fact, a 3.7- and 3.5-fold increase in the fluorescence intensity at 530 nm was observed for the AcHK^{d}H and AcHK^{d}HK peptides, respectively, upon treatment with preformed Aβ(1-40) fibres (2 eq) (**Figure 6.25**). In contrast, the changes in the emission wavelengths (*i.e.* a decrease from 547-548 to 530 nm) were similar to those observed for the Boc-amino acid.

Different behaviours were noticed for the two peptides. For AcHK^{d}H, after the immediate increase upon incubation with the protein aggregates, the fluorescence intensity continued to increase during the 5-days experiment. For AcHK^{d}HK, the maximum emission was reached immediately upon addition of the fibres. These distinct

comportments may arise from their different charge, which affect their interaction with the fibres; the positively charged AcHK^{d}HK may interact through electrostatically attractive forces with the aggregates whereas the interaction is less favoured with the negatively charged AcHK^{d}H.

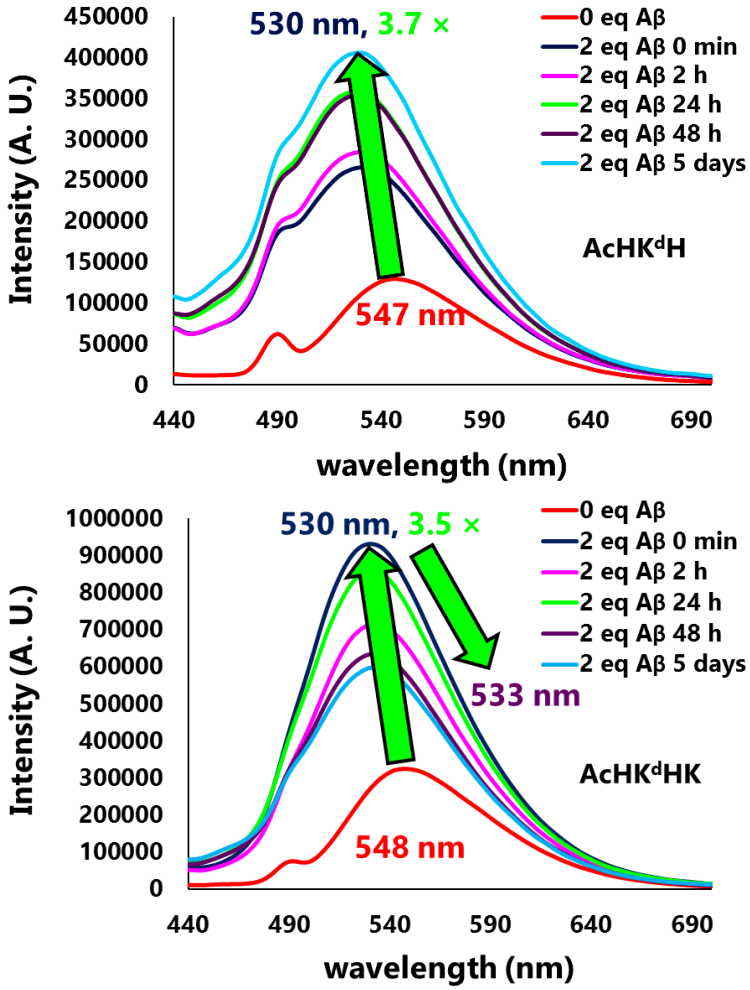

Figure 6.25: Emission spectra of free AcHK^{d}H (**top**; red spectrum) and AcHK^{d}HK (**bottom**; red spectrum); and in the presence of 2 eq of fibrillary Aβ(1-40). The concentration of Aβ(1-40) was 10 μM. λ_{exc} = 420 nm, 100 mM HEPES (pH 7.4).

Similarly to the Boc-amino acid, AcHK^{d}HK suffered a decrease in intensity with time, from 350% (initial value) at 530 nm to 240% after 48 h. In order to investigate the nature of this intensity decrease, the emission of free AcHK^{d}HK was recorded for 5 days. As seen in **Figure 6.26**, the fluorescence emission decreased by 43% during the 5-days period, while the emission wavelength did not vary. The reduction in intensity was therefore independent of the presence or absence of Aβ fibres. Hence, the loss of emission might be caused by the degradation of the 4DMN probe or the precipitation

of the peptide, driven by stacking forces of the highly planar, conjugated probe. In contrast, the emission of AcHK^{d}H remained almost constant during the 5 days.

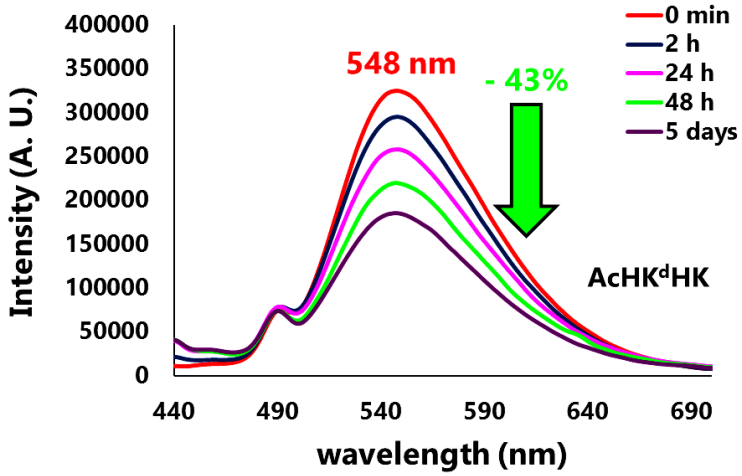

Figure 6.26: Emission spectra of 5 μM AcHK^{d}HK in 100 mM HEPES (pH 7.4). λ_{exc} = 420 nm.

6.3.2.3 Competition with ThT using Aβ(1-40) aggregates

ThT-displacement studies were next performed with the 4DMN compounds. The 4DMN amino acid and its peptidic derivatives were first added to a solution containing ThT previously bound to Aβ(1-40) fibres. A decrease of the ThT-characteristic band at 482 nm with concomitant appearance of the Aβ-bound 4DMN band would suggest ThT displacement, the 4DMN compounds thus occupying its binding site.

The addition of the 4DMN compounds (1 and 5 eq in relation to the amount of ThT) reduced the intensity of the band attributed to amyloid-bound ThT in all cases (**Figure 6.27**). Simultaneously, a band overlapping that of ThT, appeared at 525-530 nm. As described earlier, such a band corresponded to 4DMN bound to fibrillary Aβ(1-40). The most remarkable change was observed for the AcHK^{d}HK peptide, especially upon addition of 5 eq of it. This apparently stronger interaction may result from attractive electrostatic interactions between positively charged AcHK^{d}HK and negatively charged Aβ(1-40).

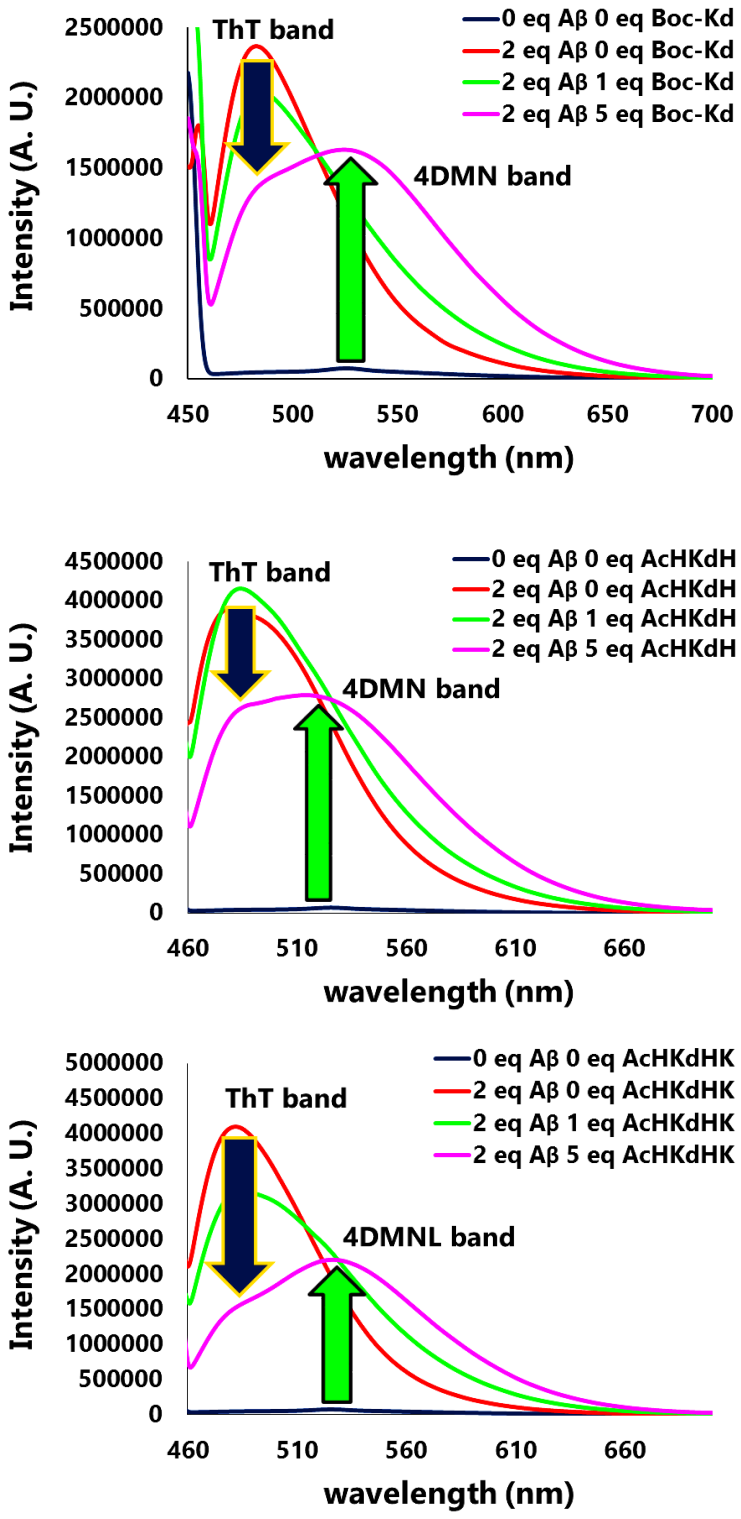

Figure 6.27: Emission spectra upon addition of Boc-K^{d} (**top**), AcHK^{d}H (**centre**) and AcHK^{d}HK (**bottom**) to ThT-bound fibrillary Aβ(1-40). The concentration of Aβ(1-40) was 10 μM. λ_{exc} = 447 nm, 100 mM HEPES (pH 7.4).

Next, reverse experiments, namely the addition of ThT to amyloid-bound to 4DMN compounds, were performed. Unfortunately, the high emission intensity of bound ThT masked the low emission of the free 4DMN compounds; hence, no valuable information could be obtained. Thus, to overcome this drawback, the amyloid samples with bound 4DMN were centrifuged and the supernatants were analysed before and after addition of ThT.

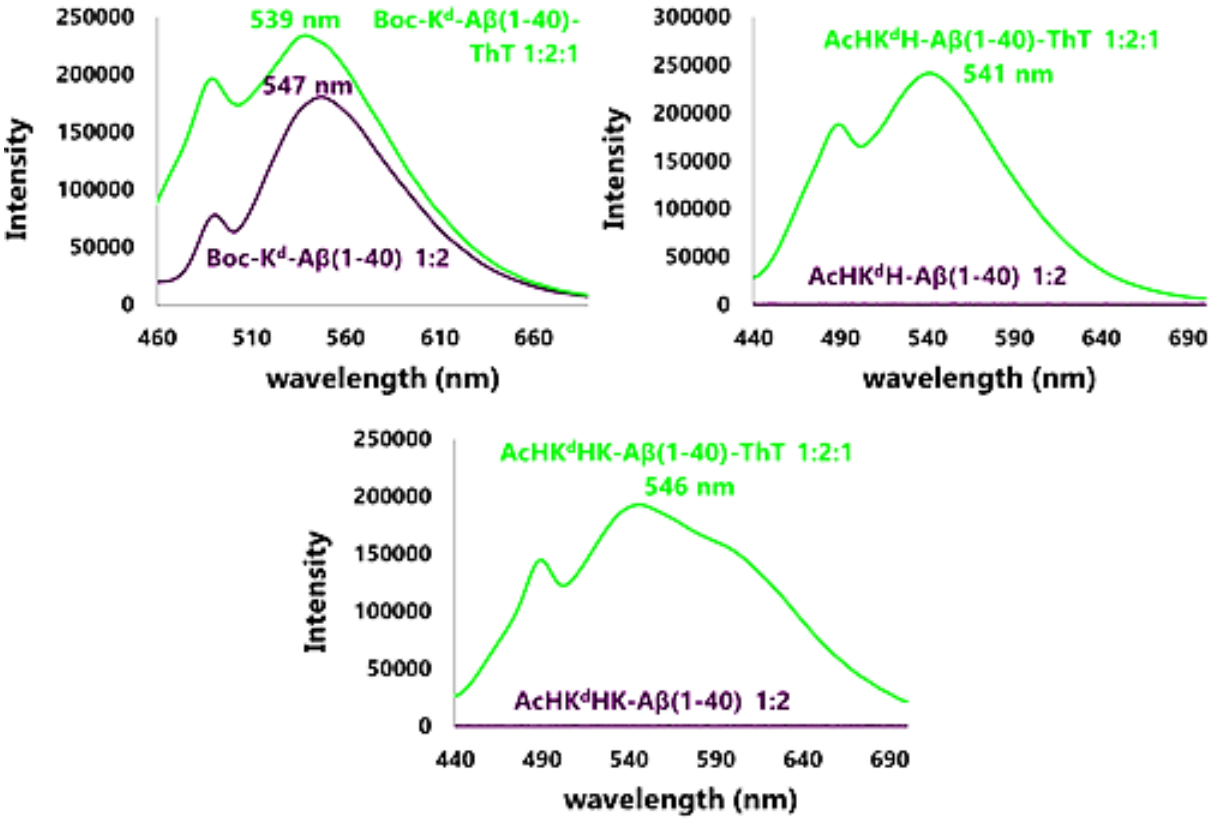

Figure 6.28: Fluorescence spectra of the supernatants of centrifuged solutions of 1:2 4DMN-fibrillary Aβ(1-40) (purple spectra) and centrifuged solutions of 4DMN-fibrillary Aβ(1-40) after addition of 1 eq ThT (green spectra). The concentration of Aβ(1-40) was 10 μM λ_{exc} = 420 nm. 100 mM HEPES (pH 7.4).

For the supernatants of centrifuged solutions of 4DMN compounds incubated with Aβ(1-40) fibres (purple spectra in **Figure 6.28**), fluorescence was only detected for the Boc-amino acid (**Figure 6.28**, top). The 4DMN peptides most likely interact more strongly with Aβ(1-40) amyloids than Boc-K^d, which corroborated the earlier experiments of fibre detection (see above). In contrast, after addition of ThT (1 eq in relation to 4DMN compounds) to previously incubated 4DMN-Aβ(1-40) samples, a similar and significant 4DMN emission was observed in all cases for the different

supernatants (green spectra in **Figure 6.28**), indicating that ThT was also able to displace the peptidic probes. The fluorescence bands presented slightly different shapes compared to those of the free compounds. Moreover, these featured shorter maximum emission wavelengths and slightly higher intensities. These minor differences could be due to the presence of some residual amounts of fibres or smaller aggregates in the supernatants.

It is worth mentioning that 1 eq of ThT was able to fully displace the 4DMN compounds; a 5-fold 4DMN excess could only achieve partial ThT displacement. Thus, ThT clearly exhibits a higher affinity towards Aβ fibres than the 4DMN compounds.

6.3.2.4 Monitoring the aggregation of monomeric Aβ(1-40)

The 4DMN peptides, showing a higher affinity for Aβ than Boc-K^d, were further investigated. Since the 4DMN probes showed the ability to detect preformed Aβ aggregates, their potential use to monitor the aggregation of the monomeric protein was examined. For that purpose, their spectroscopic behaviour in the presence of the non-aggregating Aβ(1-16) fragment was first evaluated. This fragment lacks the hydrophobic region of Aβ(1-40), which drives the aggregation process. If the intensity and emission wavelengths of the 4DMN peptides do not vary upon incubation with Aβ(1-16), then they might discriminate aggregated species, hence allowing their detection.

The emissions of AcHK^{d}H and AcHK^{d}HK in the presence of Aβ(1-16) (peptide-Aβ ratio of 1:2) were recorded during 5 days (**Figure 6.29**). For AcHK^{d}H, a 6 nm-decrease of the emission wavelength was observed, and the emission intensity at 541 nm progressively increased up to 1.7 times its initial value. The direct observation of the sample revealed that the observed increase was most probably due to the co-aggregation of the peptides with the protein; such co-aggregation had already been observed in the Cu(II)-competitive studies (see **Chapter 3**). For AcHK^{d}HK, the initial emission remained unaltered (contrary to AcHK^{d}H); after 2 hours, the emission wavelength decreased of about 8 nm and the intensity dropped, reaching a value of about 22% lower at 540 nm. The data achieved for both compounds were thus not sufficient to propose them as viable candidate probes for the monitoring of Aβ aggregation.

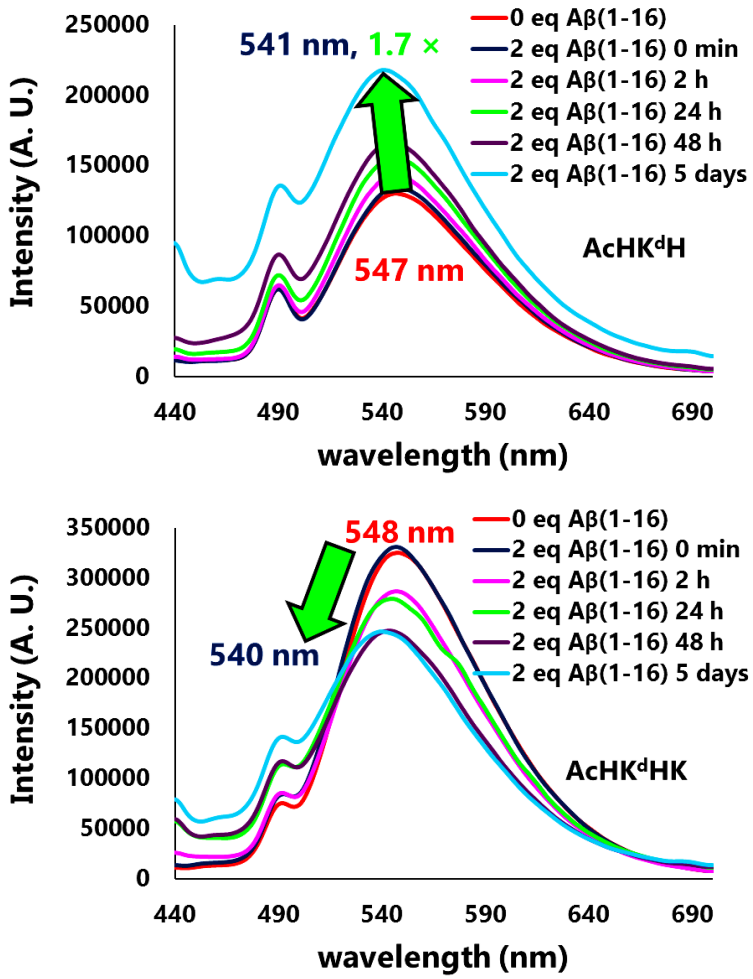

Figure 6.29: Emission spectra of free AcHK^{d}H (**top**; red spectrum) and AcHK^{d}HK (**bottom**; red spectrum), and in the presence of 2 eq of Aβ(1-16). The concentration of monomeric Aβ(1-40) was 10 μM. λ_{exc} = 420 nm, 100 mM HEPES (pH 7.4).

Experiments with monomeric Aβ(1-40) were subsequently carried out. First, the aggregation process was followed by using ThT (ThT-Aβ 1:2). Fluorescence spectra (λ_{exc} = 447 nm) were recorded during a period of 5 days (immediately after sample preparation, and after 2 h, 24 h, 48 h and 5 days).

After 2 h incubation at 37 ºC, the ThT emission increased by 22-fold, as the result of fibrillation, and it continued to augment reaching a value corresponding to 58-fold the initial one, after 48 h (**Figure 6.30**). Then, the emission increased slightly (60-fold the value for the free dye) after 5 days, illustrating the end of the fibrillation.

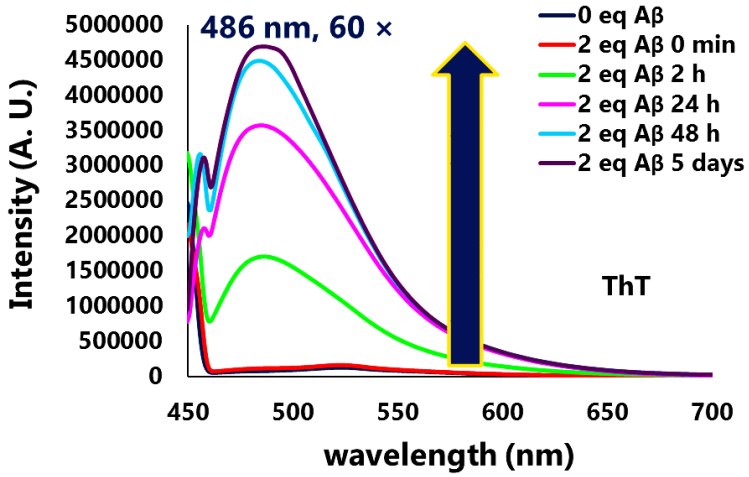

Figure 6.30: Emission spectra of free ThT (dark-blue spectrum) and in the presence of 2 eq of monomeric Aβ(1-40). The concentration of monomeric Aβ(1-40) was 10 μM. λ_{exc} = 447 nm. 100 mM HEPES (pH 7.4).

The emission of AcHK^{d}H and AcHK^{d}HK in the presence of 2 eq of monomeric Aβ(1-40) was then monitored, and the corresponding data obtained are shown in **Figure 6.31**. The fluorescence intensity of both peptides increased slightly (23% for AcHK^{d}H and 40% for AcHK^{d}HK) upon addition of monomeric Aβ(1-40). This immediate increase was attributed to preformed aggregates or small aggregates generated during the time between sample preparation and measurement. Again, distinct characteristics were observed for the two peptides. For AcHK^{d}H, the intensity increased moderately (47%) during the first 2 h, and the maximum emission wavelength decreased from 547 to 540 nm. This value further decreased to 526 nm. The emission intensity reached its maximum at 526 nm after 24 h, corresponding to 3.2-fold the initial value.

The emission of AcHK^{d}HK increased progressively during the first 24 h, up to 8.8-fold the initial intensity at the new maximum emission wavelength of 522 nm. Subsequently, however, the intensity decreased to 6.4-fold the intensity of the free peptide, as observed in previous experiments (see above). No further significant blue-shift of the emission wavelength occurred. Attractive electrostatic interactions may justify the remarkable difference of intensity increase compared with that noticed with AcHK^{d}H. The intensity enhancement is also notably higher than that of the experiments with preformed fibres. This might be due to a better accommodation of AcHK^{d}HK within the hydrophobic structure of Aβ(1-40) aggregates. A template effect, in which Aβ(1-40) monomers self-assemble around the positively-charged peptide, is also conceivable. The distinct aggregation rates with the two peptides may thus arise from their different

electrostatic charges and consequent interaction with the protein; one may thus favour the self-assembly process whereas the other one hampers it.

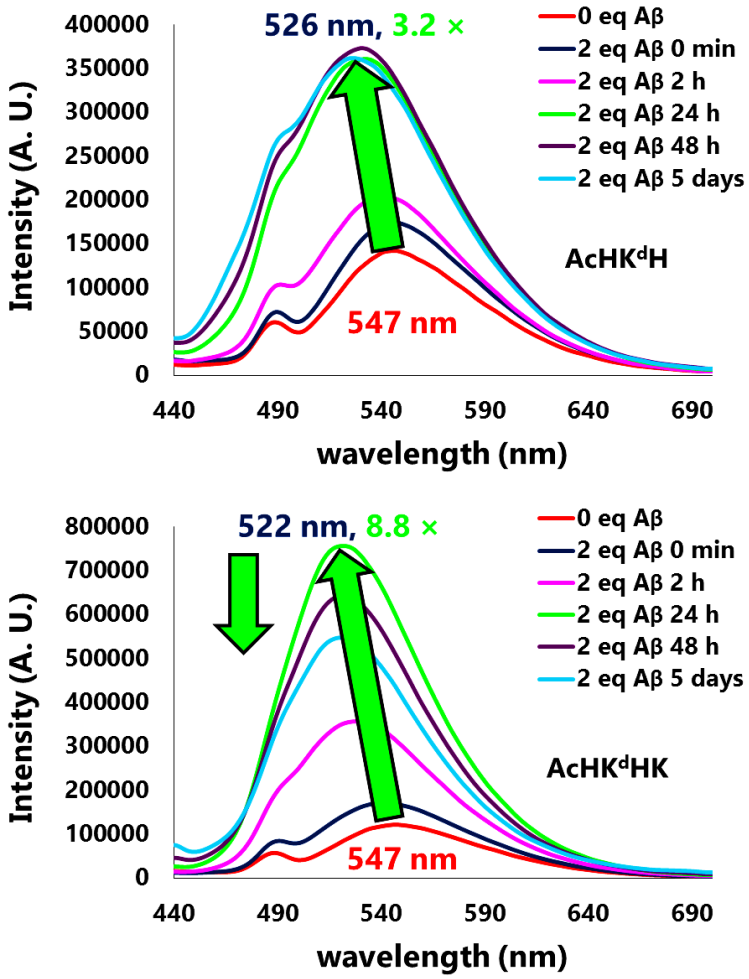

Figure 6.31: Emission spectra of free AcHK^{d}H (**top**; red spectrum) and AcHK^{d}HK (**bottom**; red spectrum) and of the peptides in the presence of 2 eq of monomeric Aβ(1-40). The concentration of monomeric Aβ(1-40) was 10 μM. λ_{exc} = 420 nm, 100 mM HEPES (pH 7.4).

The aggregation of Aβ(1-40) in the presence of the 4DMN compounds under constant shaking was finally followed using ThT, with the objective to determine any alterations of the self-assembly process (4DMN-ThT-Aβ ratio of 1:1.8:2 with constant shaking at 37 °C). As seen in **Figure 6.32**, only slight differences during the elongation phase (that is, when the fibrils are growing). It seems that the shaking of the samples reduced the contribution of the electrostatic interactions, giving rise to comparable nucleation times.

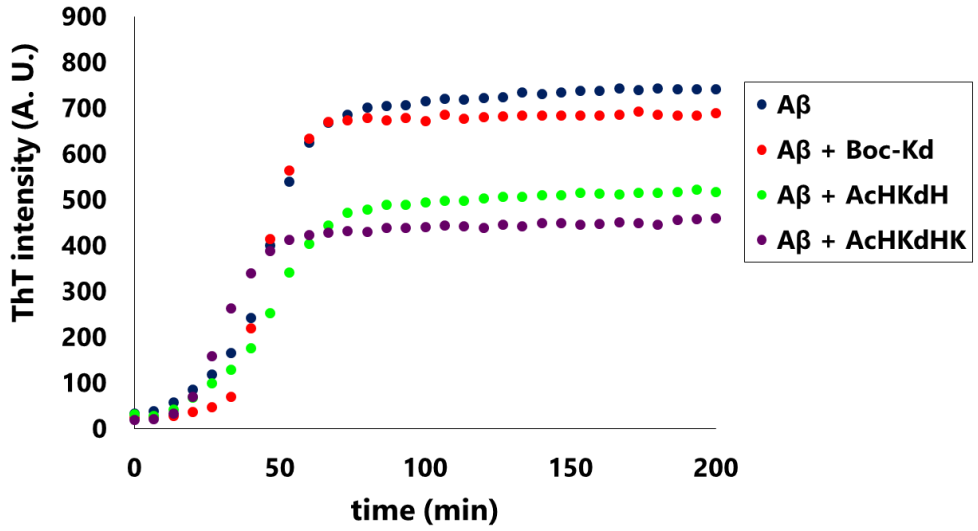

Figure 6.32: Aggregation of Aβ(1-40) in the presence of the 4DMN compounds (4DMN-Aβ ratio of 1:2), followed by ThT (λ_{exc} = 440 nm, λ_{em} = 490 nm) in 1X PBS (pH 7.4) at 37 ºC. The concentration of monomeric Aβ(1-40) was 25 μM.

The 4DMN peptides (green and purple dots in **Figure 6.32**) induced a significant decrease of the final ThT fluorescence. These lower emission intensities may be attributed to some inhibition of the fibrillation process, as well as to partial displacement of ThT by the 4DMN compounds. The latter factor is evidenced by the reduction of ThT fluorescence following the order Boc-K^d << AcHK^{d}H < AcHK^{d}HK, which is in agreement with the order of the affinities obtained in the displacement studies (see above). These data suggest that the 4DMN compounds might be efficient probes for the monitoring of Aβ(1-40) aggregation.

Finally, the capability of Boc-K^d to monitor the fibrillation of Aβ(1-40) under agitation by fluorescence was explored. To do so, the aggregation process was first followed by the commonly used ThT as the control experiment (**Figure 6.33**). Fibre formation started after 30-40 minutes, as indicated by the intensity increase at λ_{em} = 493 nm. The emission rose progressively until a plateau was reached after 75-80 minutes with a fluorescent intensity 21-fold higher than the initial value.

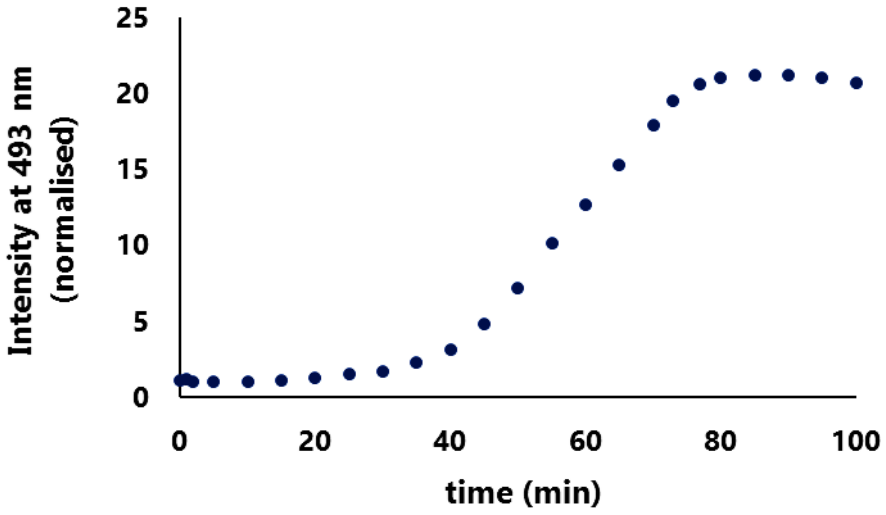

Figure 6.33: Aggregation of Aβ(1-40) followed by ThT emission (ThT-Aβ ratio of 1:2) at 493 nm (λ_{exc} = 440 nm). The concentration of monomeric Aβ(1-40) was 20 μM. 1X PBS (pH 7.4).

Next, the same aggregation process was monitored using Boc-K^d emission (**Figure 6.34**). The exponential phase took place after 10 minutes and the emission rose up to 1.64-fold the value of free Boc-K^d. After 45 minutes, the intensity remained constant and, after 1 h, decreased to 1.34-fold the initial value due to the precipitation of large fibres. The formation of fibres was simultaneously followed by the variation of the maximum emission wavelength of the environment-sensitive Boc-K^d (**Figure 6.34**). Initially, the maximum emission wavelength was 545 nm and remained almost unaltered for 30 minutes, after which it blue-shifted abruptly to 526 nm. Then, it remained almost constant and, after 80 min, it red-shifted to 535-532 nm as precipitation of fibres occurred. It is worth noting that the blue-shift occurred 20 minutes after the onset of the intensity increase. Therefore, the generation of oligomers and protofibrils (which form after the lag phase) was characterised by an augmented intensity with unaltered emission wavelength, while the fibres induced both an intensity enhancement and a shortening of the emission wavelength. These distinct effects on the Boc-K^d emission intensity and its respective wavelength may allow distinguishing between different Aβ(1-40) aggregates that may form during the fibrillation process. Such information could be particularly relevant to unravel the mechanism of amyloid misfolding of proteins like Aβ(1-40).

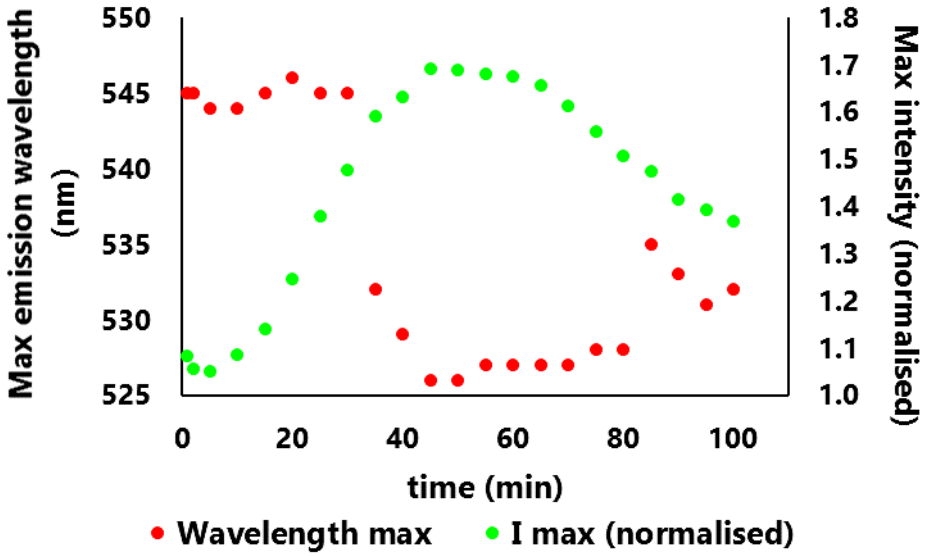

Figure 6.34: Aggregation of Aβ(1-40) followed by the maximum emission intensity (green dots) and by the maximum emission wavelength (red dots) of Boc-K^d (Boc-K^d-Aβ ratio of 1:2, λ_{exc} = 420 nm). The concentration of monomeric Aβ(1-40) was 20 μM. 1X PBS (pH 7.4).

Interestingly, significantly different lag times were observed for ThT and Boc-K^d: the lag time of Aβ(1-40) is three-fold longer when ThT is used (**Figure 6.35**). The use of extrinsic fluorophores (like ThT) can disturb the aggregation kinetics of Aβ(1-40), which may hinder the fibrillation in some degree.[445,446] Indeed, it has been assumed rather than proved that ThT does not affect the aggregation kinetics of Aβ;[372] as a matter of fact, some dyes structurally-related to ThT, such as Congo red, are known to affect the aggregation of Aβ.[105,106] Boc-K^d (which presents a lower affinity towards Aβ than ThT) may cause a lower disturbance, thus accounting for such difference. It should also be considered a possible detection of oligomeric species by Boc-K^d, which are ThT-silent, thus resulting in an earlier intensity increase when Boc-K^d is used to monitor the Aβ(1-40) aggregation.[447]

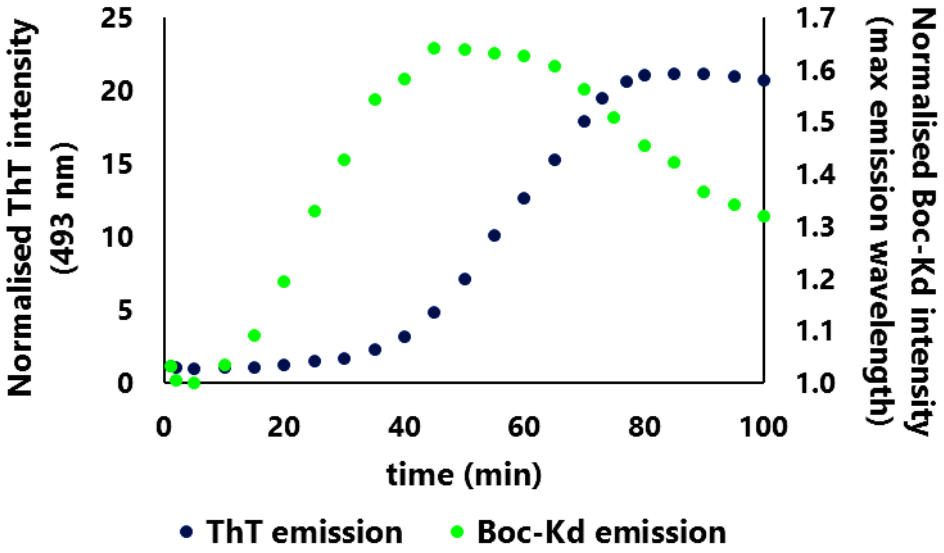

Figure 6.35: Aggregation of Aβ(1-40) followed by ThT emission at 493 nm (λ_{exc} = 440 nm) and by the maximum emission of Boc-K^d (λ_{exc} = 420 nm). The concentration of monomeric Aβ(1-40) was 20 μM (Boc-K^d/ThT-Aβ ratio of 1:2). 1X PBS (pH 7.4).

6.3.2.5 Detection of Cu(II)- and Zn(II)-induced Aβ(1-40) aggregates

Aβ(1-40) aggregation was next followed in the presence of Cu(II) and Zn(II) ions, which promote the formation of other aggregation species such as oligomers or amorphous aggregates. Whereas ThT is only able to detect amyloids, the 4DMN compounds might be sensitive towards other aggregated species, as the result of their different mechanism. The detection of such species is of paramount importance since aberrant interaction of Aβ with metal ions is thought to lead to neurotoxicity in AD brains.[16,18,66-68] Furthermore, the type/structure of the aggregates that form under specific conditions (like for instance in the presence of various metal-Aβ ratios) remains unknown.

Figure 6.36 shows the generation of Aβ(1-40) fibres in the presence of Cu(II) and Zn(II) ions (ThT-metal-Aβ ratio of 1:2:2). The addition of any of these metal ions remarkably reduced the amount of β-sheet-rich structures, as evidenced by the lower ThT intensity (compared with that of the metal-free experiment; **Figure 6.36**, top). Indeed, the emission only increased up to 26-fold and 12-fold in the presence of copper and zinc, respectively, while the augmentation is 60-fold for the metal-free aggregates.

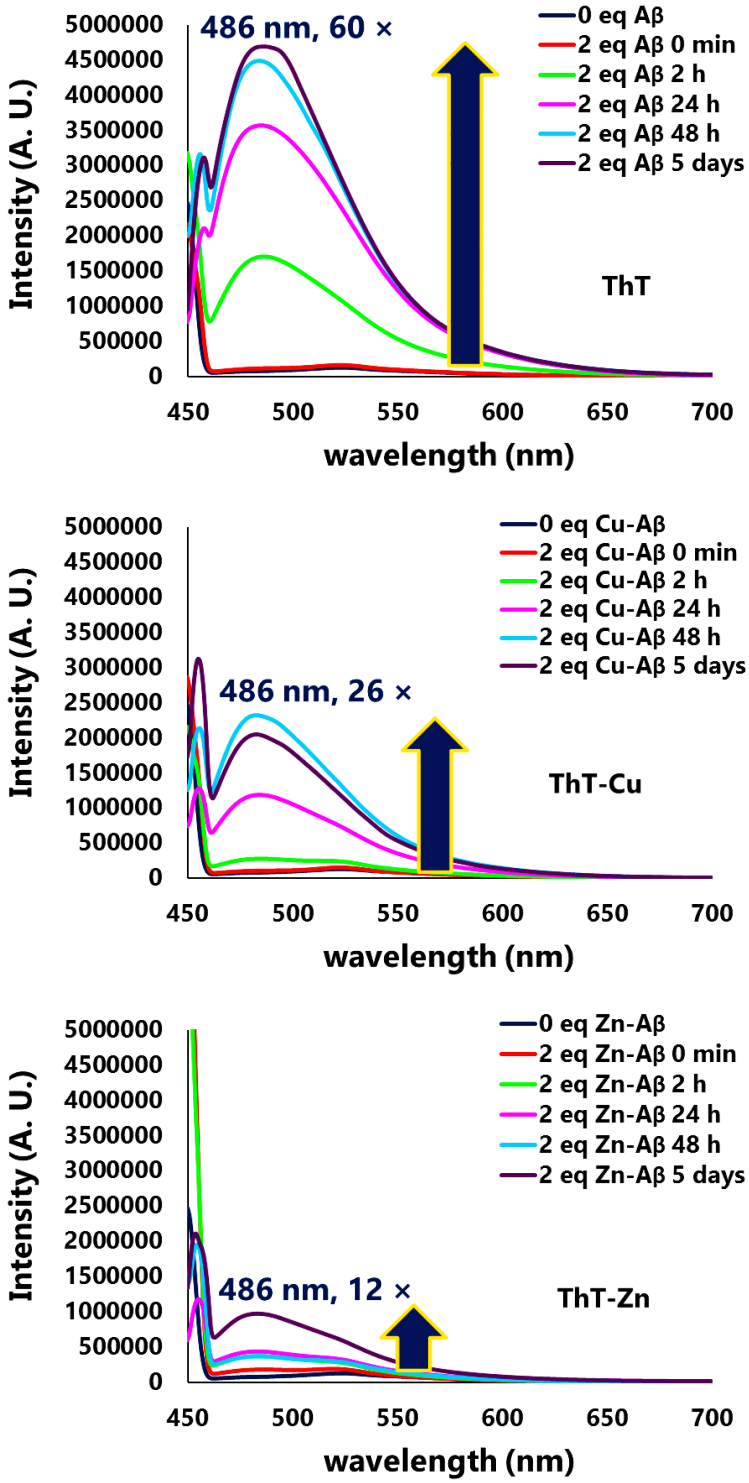

Figure 6.36: Emission spectra of ThT-Aβ(1-40) (**top**) and ThT-M^{2+}-Aβ(1-40) 1:2:2 systems (**middle:** M = Cu; **bottom :** M = Zn): The concentration of monomeric Aβ(1-40) was 10 μM. λ_{exc} = 447 nm, 100 mM HEPES (pH 7.4).

As mentioned earlier, equimolar or higher amounts of copper ions induce the formation of oligomeric species, which present several degrees of secondary structure and β-sheet content, depending on their size.[16,31,66] Zinc ions promote the generation of α-helical or amorphous aggregates (see **Chapter 1**).[42,68] It can be pointed out here that an equilibrium between such species and amyloids has been suggested by some authors;[18] such equilibrium may justify the delayed increase of ThT intensity observed.

Next, the effect of AcHK^{d}H and AcHK^{d}HK was assessed; despite the metal-chelating properties of the peptides, metal exchange between the 4DMN peptides and Aβ monomers was indeed expected.

The aggregation of Aβ(1-40) was first monitored in the presence of copper(II) ions (**Figure 6.37**). The emission wavelength of AcHK^{d}H immediately decreased by 14 nm, and the corresponding emission at 533 nm increased by 69%. After 5 days, the wavelength disminished down to 524 nm and the intensity increased further up to 2.9-fold the initial one. For AcHK^{d}HK, the emission wavelength immediately down-shifted to 529 nm with a concomitant increase of the intensity by 2.5-fold. Similarly to the case without metal ions (section **6.3.2.4**), the emission intensity of AcHK^{d}HK decreased within the next five hours while the emission wavelength remained unaltered.

The wavelength and intensity changes noticed under experimental conditions that promote the formation of oligomeric species suggest that the peptides can detect oligomers. Additional characterisation data are definitively required to confirm these important observations.

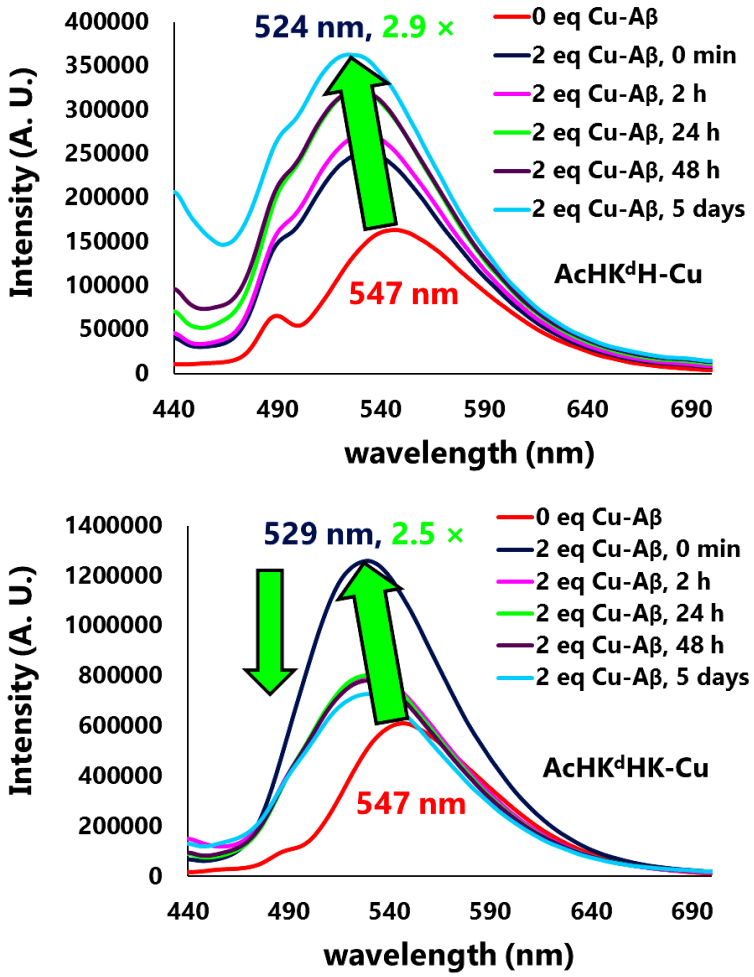

Figure 6.37: Emission spectra of AcHK^{d}H-Cu^{2+}-Aβ(1-40) (**top**) and AcHK^{d}HK-Cu^{2+}-Aβ(1-40) (**bottom**) using 1:2:2 ratios. λ_{exc} = 420 nm. The concentration of monomeric Aβ(1-40) was 10 μM. 100 mM HEPES (pH 7.4).

In the presence of Zn(II) ions (**Figure 6.38**), and unlike what happened with Cu(II), a dramatic increase of the emission intensity (9.0-fold at 522 nm) immediately occurred for AcHK^{d}H; after 5 days this peptide underwent the largest intensity enhancement observed in these studies (up to 16-fold the initial one at 519 nm). The emission wavelength experienced a down-shift of 25 nm immediately after sample preparation and of 28 nm after 5 days.

In the case of AcHK^{d}HK, the emission wavelength immediately moved from 547 to 521 nm (**Figure 6.38**), and the emission intensity reached a value 7.5-fold higher than that of the free peptide. After that, the intensity decreased slightly down to 6.8-fold the initial value after 5 days. As already stated, electrostatic effects may affect the interaction between the peptides and the aggregates; here, negatively-charged

AcHK^{d}H showed a stronger interaction with the metal-bound (and thus more positively-charged) Aβ than positively-charged AcHK^{d}HK.

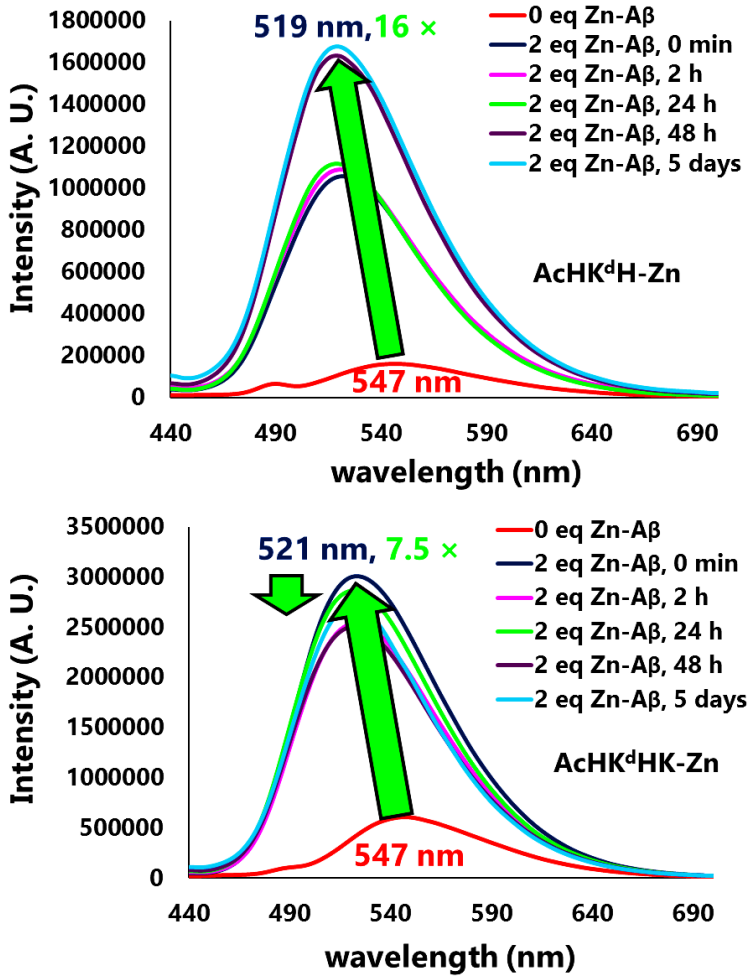

Figure 6.38: Emission spectra of AcHK^{d}H-Zn^{2+}-Aβ(1-40) (**top**) and AcHK^{d}HK-Zn^{2+}-Aβ(1-40) (**bottom**) using a ratio of 1:2:2. λ_{exc} = 420 nm. 100 mM HEPES (pH 7.4).

It is important to note that, whereas ThT is able to detect amyloid aggregates, the observed increase of emission intensities of AcHK^{d}H and AcHK^{d}HK in the presence of Zn(II) ions suggests that these 4DMN peptides are capable of detecting (highly hydrophobic) aggregated species other than of amyloid type.

6.3.2.6 Detection of Aβ(1-40) aggregates with the 4DMN compounds

In summary, the 4DMN compounds were used to detect Aβ aggregates and to follow aggregation through the increase of the fluorescence intensity and the blue-shifting of the emission wavelength. Boc-K^{d}, (and particularly) AcHK^{d}H and AcHK^{d}HK seem to act as bimodal probes, as the presence of aggregates may be sensed by both a blue-shift of the fluorescence emission associated with an increase of its intensity. Additionally, the 4DMN compounds herein presented appear to detect different types of Aβ aggregates, in contrast to ThT, which is restricted to amyloids or other β-sheet-containing species.

Environment-sensitive probes are commonly used in the field of biology. For instance, the incorporation of DANA/ALADAN and DAPA into peptides have been reported, whose subsequent binding to proteins resulted in hypsochromic effects as large as 80 and 104 nm, respectively. Increments of emission intensity ranging from 6 to 37-fold have been described for DAPA-containing peptides.[399,400,402] For peptides containing dimethylnaphthalimide moieties, emission enhancements of up to 106-fold associated with hypsochromic effects of 45 nm were obtained for the 4DMN probe, and 5-19-fold intensity increases together with blue-shifts of 64 nm have been reported for the 6DMN probe.[144,401] Finally, the interaction of a 6DMN-containing peptide with the major histocompatibility complex (MHC) protein produced a remarkable 1000-fold increase of the emission intensity and with a blue-shift of 115 nm; these drastic variations of the fluorescence parameters are due to the burying of the probe into a highly hydrophobic pocket of the protein.[402]

The spectroscopic changes (augmentation of the emission intensity and blue-shifts of the wavelength) provoked by the 4DMN compounds in the presence of the various "types" of Aβ aggregates are summarised in **Table 6.4**. Most data reported in the literature were obtained for native proteins such as the S-Protein, calmodulin or MHC proteins.[144,399,402] The study of the interaction of environment-sensitive probes with misfolding proteins has been barely explored.[448,449] The present study has allowed to assess, for the first time, the fluorescence behavior of a probe of the naphthalimido family upon interaction with fibrillary Aβ.

Table 6.4: Spectroscopic changes for the 4DMN compounds through their interaction with different forms of Aβ(1-40). The values shown correspond to the maximum increments of the intensity observed, and the values in parentheses are the maximum blue-shifts of the emission wavelength (in nm) that occurred.

		Aβ(1-40) species			
		Fibres	Monomers	Monomers-Cu(II)	Monomers-Zn(II)
4DMN compound	Boc-K^{d}	2.2 (17)	n. d.	n. d.	n. d.
	AcHK^{d}H	3.7 (17)	3.2 (21)	2.9 (23)	16 (28)
	AcHK^{d}HK	3.5 (18)	8.8 (25)	2.5 (18)	7.5 (26)

The results obtained for the 4DMN peptides are in general comparable in terms of emission-intensity enhancement with published data for native proteins. As far as the hypsochromic effect is concerned, the values obtained with Aβ are smaller than those achieved with native proteins. In fact, spectroscopic changes larger than those obtained for native proteins are not expected for the detection of Aβ(1-40) amyloids because of the intrinsically disordered nature of the peptide. Nevertheless, the optimisation of the sequence of the 4DMN-containing peptides may lead to the accommodation of the 4DMN probes into more hydrophobic environments, hence resulting in improved spectroscopic variations. The selectivity of the probes towards Aβ aggregates in front of non-fibrillary proteins, such as globular proteins, has to be evaluated.

6.4 Concluding remarks

The detection of aggregated Aβ(1-40) with novel fluorescent probes was investigated. First, a dye structurally analogous to ThT was synthesised applying click chemistry. This new dye, named BzTz, contains a carboxylic group allowing to connect it to peptide sequences through the formation of an amide (peptide) bond. BzTz was designed to present a sensing behaviour comparable to that of ThT, that is, to display enhancement of the fluorescence emission and/or a change in the excitation/emission wavelengths in the presence of β-sheet-rich protein structures.

Unfortunately, BzTz did not act as ThT, suggesting that it was not properly interacting with fibrillary Aβ(1-40), or/and that its photophysical properties were different from those of ThT. The positively-charged amino acid derivative BzTz-Lys-NH_2, prepared by solid-phase synthesis, was also not effective although it was expected to interact with the negatively-charged protein aggregates. A thorough investigation/examination of the electronic and structural properties of ThT would be interesting for the design of more adequate dyes; push-pull systems with extended conjugation throughout the molecule, and with the ability to act as molecular rotors, would probably be more efficient amyloid sensors.

The BzTz-based compounds affected in some extent the aggregation of monomeric Aβ(1-40), only slightly in the case of BzTz-Lys-NH_2. The development of other BzTz probes and their connection to different molecules, may allow to generating effective Aβ-targeting agents, thanks to the benzothiazole moiety, which is known to bind Aβ with high affinity.

The second approach was based on the environment-sensitive probe 4DMN, which presents higher quantum yields and shorter excitation/emission wavelengths in non-polar solvents than in polar ones. Hence, Boc-K^d, AcHK^{d}H and AcHK^{d}HK were successfully used to detect Aβ(1-40) amyloids, and the two 4DMN-containing peptides were employed to follow the aggregation of monomeric Aβ in the absence or presence of metal ions (*viz*. Cu and Zn ions). Upon interaction with the hydrophobic channels or other domains of Aβ aggregates, the 4DMN compounds exhibited fluorescence-emission increases ranging from 2.2- to 16-fold the original signal, and blue-shifts of 17-28 nm. The aggregation of Aβ(1-40), followed by ThT, was not significantly affected by the presence of the 4DMN compounds.

Displacement studies suggested that the 4DMN compounds and ThT might share a common binding site in amyloids; indeed, the addition of 4DMN-containing agents to ThT-containing fibres resulted in a decrease of the emission intensity of ThT, and an increase of the blue-shifted emission of the 4DMN probe. The studies also indicated that ThT presents a higher binding affinity, since 1 eq of ThT completely displaced the 4DMN-based peptides, while up to 5 eq of the new peptidic probes were required to partially displace ThT. Additional experiments would be useful to identify the binding sites of the interacting probes to the aggregates.

While ThT is only able to detect amyloids, which are β-sheet-rich, the 4DMN peptides can detect other Aβ structures. Future work should combine fluorescence experiments with microscopy techniques, with the objective to associate the nature, structure and amounts of aggregates formed with the spectroscopic changes of the 4DMN probe.

The environment-sensitive properties of the 4DMN fluorophore can be extremely useful for the bimodal detection of Aβ aggregates; the interaction-dependent variations of the emission intensity together with the associated hypsochromic effects may provide valuable information regarding the degree of aggregation and/or the structural differences between distinct forms of aggregates. The 4DMN probe was able to detect a structurally-disordered peptide, in a comparable manner to that reported with native proteins. Moreover, the study suggested that 4DMN-containing peptide sequences may recognize different regions of Aβ aggregates. Based on these pioneering results, future investigation may be to computationally design a series of 4DMN-containing peptides that would allow to detect diverse types/forms of Aβ aggregates.

Other misfolding proteins are involved in several neurodegenerative diseases; thus, huntingtin (Huntington disease) or α-synuclein (Parkinson disease) may also be studied using 4DMN-based peptidic probes bearing the appropriate sequence. The multi-dimensional monitoring of their aggregation processes may help to understand their self-assembly mechanism, which is key to design efficient drugs.

6.5 Experimental section

6.5.1 Reagents, solvents and equipment

Table 6.5: Reagents and solvents used for the experiments described in this chapter.

Brand	Products
Acros Organics	2-aminobenzothiazole, ascorbic acid, $Cu(AcO)_2$, ethyl propiolate, NaN_3, propiolic acid, $ZnCl_2$
Sigma Aldrich	Ac_2O, $CDCl_3$, CuI, D_2O, d_6-DMSO, Et_2O, HEPES, LiOH, piperidine, ThT, TIPS, TSP
Fisher Scientific	$CuSO_4$, DIPEA, DMSO, MeCN (HPLC grade), $NaNO_2$, TFA
Fluka	MeCN, *t*-BuOH
Iris Biotech	Fmoc-Lys(Boc)-OH, Oxyma
Jescuder	Anhydrous $MgSO_4$, $KMnO_4$
Novabiochem	RA AM resin
Panreac	absolute ethanol, $CuCl_2{\cdot}2H_2O$, H_3PO_4 85%, pyridine
Scharlau	acetone, DCM, HCl 37%, H_2SO_4 98%, MeOH, THF
Specialist des solvants	DMF
TCI	DIC

Table 6.6: Equipment used for the experiments described in this chapter.

Instrument	Brand	Model
Analytical balance	A & D Instruments	GR-200-EC
Gram-scale balance	1) Sartorius 2) Mettler	1) Basic BA 110 2) Toledo AB254 PJ360
UV lamp	Asahi Spectra	Max-303
Centrifuge	Hettich	Rotofix 32A
Vacuum lyophiliser	Christ	Alpha 2-4 LD plus
Rotary evaporator	BUCHI	R-200
Sonicator	1) JP SELECTA S.A. 2) Fisherbrand	1) Ultrasons MEDI-II 2) FB15051
Incubator	JP SELECTA S.A.	Conterm
Shaking Block Heater	Eppendorf	ThermoMixer C

Milli-Q H_2O (resistivity > 18 MΩ·cm) was produced by filtering deionised water with a Milli-Q Plus (Millipore) system. Anhydrous DCM was dried over CaH_2 under N_2 and was distilled just before its use. Anhydrous THF was kept over Na with benzophenone under N_2 and was distilled prior to its utilisation. Dried Et_2O was stored over Na.

Aβ(1-40) was acquired from Bachem as a trifluoroacetate salt, while Aβ(1-16) was purchased from Innovagen. $CuCl_2 \cdot 2H_2O$ and $ZnCl_2$ were used as the source of Cu and Zn, respectively, in the experiments in the presence of metal ions.

6.5.2 Syntheses and characterisation

Thin Layer Chromatography (TLC)

TLC was performed on silica gel 60 F254 plates purchased from Merck. Exposure to UV light and $KMnO_4$ was used to reveal the spots.

Nuclear Magnetic Resonance (NMR)

NMR spectra were recorded at the Centres Científics i Tecnològics of the Universitat de Barcelona (CCiTUB). The NMR data were analysed using MestReNova 9.1.0. The signals are reported as follows: *s*, singlet; *d*, doublet; *t*, triplet; *q*, quartet; *m*, multiplet. ^{1}H NMR spectra were recorded at 400 MHz, while ^{13}C NMR spectra were obtained at 100.6 MHz with proton decoupling. 2D techniques (COSY, HSQC and HMBC) were used to fully characterise the products.

BzTz and intermediates

All spectra were recorded on a Varian Mercury-400 spectrometer. Chemical shifts are quoted in ppm downfield from TMS with the partially-deuterated solvent as the internal standard ($CDCl_3$: δ 7.26 and d_6-DMSO: δ 2.50 for ^{1}H NMR; $CDCl_3$: δ 77.16 ± 0.06 and d_6-DMSO: δ 39.52 ± 0.06 for ^{13}C NMR). The partially-deuterated solvent was used as the internal standard for D_2O (D_2O: δ 4.79 for ^{1}H NMR).

BzTz-Lys-NH_2

1D and 2D NMR experiments were performed on a Bruker Avance III 400 MHz spectrometer, equipped with a 5 mm cryoprobe (Prodigy) broadband (CPPBBO BB-^{1}H/^{19}F/D) with gradients in Z. Solvent suppression for the 1D experiments was achieved

using a PRESAT pulse sequence. A 10 mM BzTz-Lys-NH_2 solution in D_2O was adjusted to pH 7.4, and measured with an insert containing a 5 mg·mL^{-1} solution of [D_4]-3-(trimethylsilyl)propanoic acid (TSP) as an internal reference (D_2O: δ 4.79 for ^1H NMR). It should be noted that, even though the measurements were made in D_2O, it was decided to use the notation pH.

Infrared (IR) spectroscopy

IR spectra of the solid products were registered using a Thermo Scientific Nicolet 6700 FT-IR spectrophotometer.

UV-Vis spectroscopy

Spectra were recorded using a Varian Cary 100 spectrophotometer from 800 to 200 nm, at rt. Quartz cuvettes (3 mL, 1 cm path length) were used.

High-resolution electrospray ionisation mass spectrometry (HR-ESI-MS)

High-resolution electrospray ionisation mass spectrometry (HR-ESI-MS) was performed using a LC/MSD-TOF spectrometer with an Agilent 1100 HPLC pumping system in either positive or negative-ion modes at the Centres Científics i Tecnològics of the Universitat de Barcelona (CCiTUB).

Liquid Chromatography

For BzTz and its intermediates, a Phenomenex® C18 reverse-phase column (250 x 4 mm) with a particle size of 50 μm and a pore size of 320 Å was used. The eluents were 0.045% TFA in H_2O (v/v) for eluent A, and 0.036% TFA in MeCN (v/v) for eluent B.

For BzTz-Lys-NH_2, a Jupiter 5u Phenomenex® C18 reverse-phase column (250 x 4.6 mm) with a particle size of 5 μm and a pore size of 300 Å was employed. The eluents were 10 mM NH_4HCO_3 in H_2O (v/v) for eluent A, and MeCN for eluent B. The following gradient was used for all compounds:

Table 6.7: HPLC gradient used in the present work.

Time (min)	% Eluent A	% Eluent B
0	98	2
20	0	100
25	0	100
30	98	2
40	98	2

The flow rate was 1 mL/min and the detection was performed at 220 nm.

High Performance Liquid Chromatography (HPLC)

Analytical HPLC was carried out in a system consisting in a Shimadzu LC-20AD quaternary pump, a SIL-10Advp automatic injector, a SPD-20A variable dual wavelength detector and a DGU-20A5 online degas device.

High Performance Liquid Chromatography coupled to Mass Spectrometry (HPLC-MS)

A Waters Alliance HT system formed by a 2795 separation module, a PDA detector 2996 and a Micromass ZQ 2000 mass detector (Electrospray Ionisation, ESI-MS) was used.

Synthesis of BzTz by click chemistry

2-Azidobenzo[d]thiazole / Benzo[4,5]thiazolo[3,2-d]tetrazole

A 100 mL round-bottom flask containing a magnetic stirring bar was placed in an ice bath; 2-aminobenzothiazole (1.28 g, 8.52 mmol) was added followed by concentrated H_3PO_4 (30 mL). An aqueous solution (13 mL) of sodium nitrite (730 mg, 10.6 mmol) was slowly added under vigorous stirring at 0 ºC for 25 min, and an aqueous solution (5.4 mL) of sodium azide (830 mg, 12.8 mmol) was added dropwise to the resulting brown suspension. Intense effervescence was observed, and the ice bath was removed after 5 min; the mixture was allowed to react at rt for 2 h. The resulting brownish solid was isolated by filtration, washed with water and dried under reduced pressure to afford 1.20 g of product (6.82 mmol, 84%).

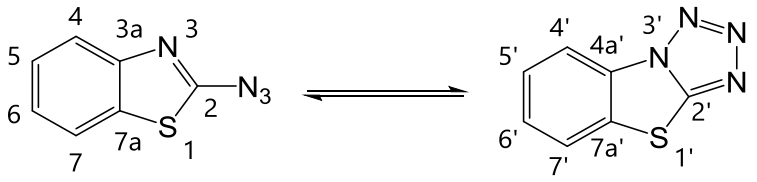

Brownish solid. **R_f** (DCM): 0.40 + 0.78. **HPLC-MS:** t_R = 13.0 + 17.6 min; ***m/z*** 176.9 ($[C_7H_4N_4S + H]^+$). **MS (HR ESI+):** ***m/z*** calculated for $[C_7H_4N_4S + H]^+$ 177.0235, found 177.0232. **^{1}H NMR** ($CDCl_3$, 400 MHz): δ 7.29-7.34 (m, 1H, H_{12}), 7.43-7.47 (m, 1H, H_{13}), 7.57-7.62 (m, 1H, H_6), 7.65-7.70 (m, 1H, H_5), 7.72-7.75 (m, 1H, H_{11}), 7.79-7.82 (m, 1H, H_{14}), 7.82-7.85 (m, 1H, H_7), 8.22 (dd_{app}, 1H, J_{app} = 0.88, J_{app} = 8.4, H_4). **^{13}C NMR** ($CDCl_3$, 100.6 MHz): δ 115.4 (C_4), 121.5 ($C_{7'}$), 121.6 ($C_{4'}$), 124.7 ($C_{5'}$), 125.3 (C_7), 126.7 ($C_{6'}$), 127.9 (C_5), 128.3 (C_6), 128.6 (C_{3a}), 132.8 (C_{7a}), 133.7 ($C_{3a'}$), 150.9 ($C_{7a'}$), 157.9 ($C_{2'}$), 162.9 (C_2). **IR** (KBr, cm^{-1}): 2122 (stretching N_3), 1496, 1423, 1255.

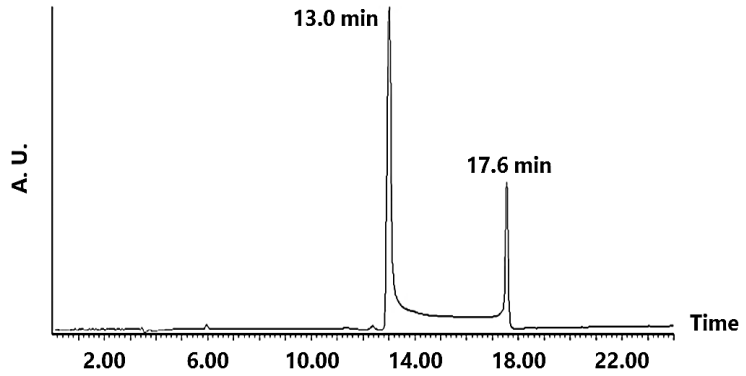

Figure 6.39: Chromatogram of 2-azidobenzo[*d*]thiazole/benzo[4,5]thiazolo[3,2-*d*]tetrazole.

*Ethyl-1-(benzo[*d*]thiazol-2-yl)-1*H*-1,2,3-triazole-4-carboxylate*

A 100 mL round-bottomed flask containing benzo[4,5]thiazolo[3,2-*d*]tetrazole/2-azidobenzo[*d*]thiazole (0.320-1.02 g, 1.82-5.79 mmol) and a magnetic stirring bar was purged with N_2, and THF (15-40 mL) was added. Next, ethyl propiolate (280-890 μL, 2.73-8.78 mmol), DIPEA (0.95-3.0 mL, 5.46-17.4 mmol) and CuI (35-110 mg, 0.18-0.58 mmol) were added in this order to the solution under stirring. The original orange solution turned brown within 5-10 min, and the reaction mixture was stirred at rt for 40 min; the solvent was eliminated under reduced pressure. The resulting brown residue was dissolved in DCM (20-50 mL) and washed with 1 M aqueous solution of HCl (3 × 20-50 mL), and the combined organic fraction was dried over anhydrous

$MgSO_4$ and filtered. Finally, the solvent was eliminated under reduced pressure to yield the ester precursor (0.47-1.56 g, 94-98%) as a light brown solid.

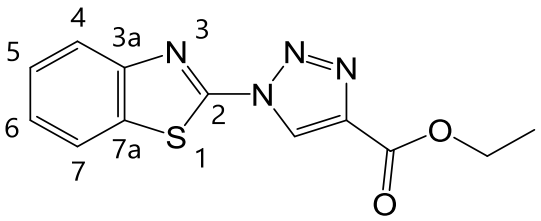

Light brown solid. **R_f** (DCM/AcOEt 9.8:0.2): 0.48. **HPLC-MS:** t_R = 17.2 min; ***m/z*** 275.0 ($[C_{12}H_{10}N_4O_2S + H]^+$). **MS (HR ESI+):** ***m/z*** calculated for $[C_{12}H_{10}N_4O_2S + H]^+$ 275.0603, found 275.0592. **^{1}H NMR** ($CDCl_3$, 400 MHz): δ 1.45 (t, 3H, *J* = 7.2, $COOCH_2\underline{CH_3}$), 4.49 (q, 2H, *J* = 7.1, $COO\underline{CH_2}CH_3$), 7.48-7.52 (m, 1H, H_6), 7.55-7.60 (m, 1H, H_5), 7.94 (d_{app}, 1H, J_{app} = 8.3, H_7), 8.02 (d_{app}, 1H, J_{app} = 8.2, H_4), 9.06 (s, 1H, $\underline{CH}$NNN). **^{13}C NMR** ($CDCl_3$, 100.6 MHz): δ 14.39 ($COOCH_2\underline{CH_3}$), 61.89 ($COO\underline{CH_2}CH_3$), 122.1 (C_7), 123.7 (C_4), 125.2 ($\underline{CH}$NNN), 126.7 (C_6), 127.4 (C_5), 133.4 (C_{7a}), 141.1 (NNN$\underline{C}$), 150.0 (C_{3a}), 155.4 (N=$\underline{C}$-S), 160.0 ($\underline{COO}CH_2CH_3$). **IR** (KBr, cm^{-1}): 1714, 1553, 1454, 1331, 1252, 1147, 1021, 960, 758, 720.

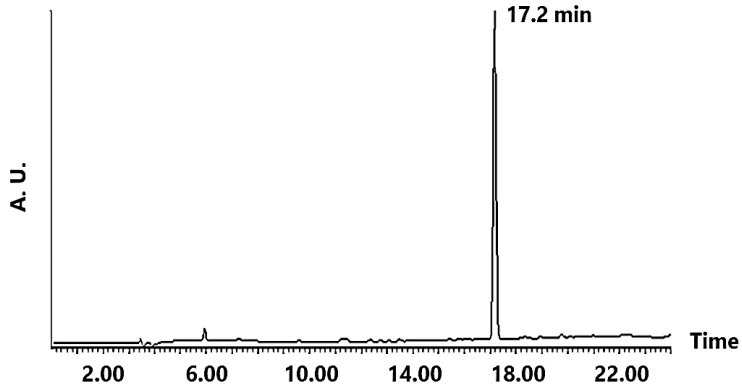

Figure 6.40: Chromatogram of ethyl-1-(benzo[*d*]thiazol-2-yl)-1*H*-1,2,3-triazole-4-carboxylate.

1-(benzo[d]thiazol-2-yl)-1H-1,2,3-triazole-4-carboxylic acid (BzTz)

LiOH (80 mg, 3.34 mmol) was dissolved in distilled water (4.5 mL) and the resulting solution was added, under stirring, to a solution of the ester precursor (765 mg, 2.76 mmol) in THF (37 mL). The reaction mixture was stirred at rt for 1 h, after which distilled water (30 mL) was added and most of the THF was eliminated by rotary evaporation. The aqueous suspension was then washed with DCM (3 × 50 mL) and acidified with a 4 M aqueous solution of HCl to reach a pH of 1-2. The resulting brownish precipitate was filtered and further washed with DCM to yield 360 mg (1.46 mmol, 52%) of **BzTz**.

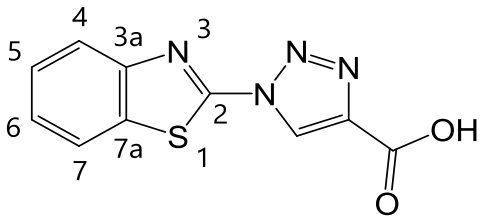

Light brown solid. **HPLC-MS:** t_R = 13.6 min; ***m/z*** 246.9 ($[C_{10}H_7N_4O_2S + H]^+$). **MS (HR ESI+):** ***m/z*** calculated for $[C_{10}H_6N_4O_2S + H]^+$ 247.0290, found 247.0284. **^{1}H NMR** (DMSO-d_6, 400 MHz): δ 7.57 (t_{app}, 1H, J_{app} = 7.6, H_5), 7.63 (t_{app}, 1H, J_{app} = 7.6, H_6), 8.07 (d, 1H, J = 8.0, H_7), 8.24 (d_{app}, 1H, J_{app} = 8.0, H_4), 9.45 (s, 1H, CHNNN). **^{13}C NMR** (DMSO-d_6, 100.6 MHz): δ 123.5 (C_4), 123.6 (C_7), 126.8 (CHNNN), 127.0 (C_5), 127.9 (C_6), 133.4 (C_{7a}), 141.7 (NNNC), 149.4 (C_{3a}), 156.3 (N=C-S), 161.3 (COOH). **IR** (KBr, cm^{-1}): 3440 (broad), 3148, 1701, 1537, 1448, 1356, 1249, 1230, 1030, 964, 767.

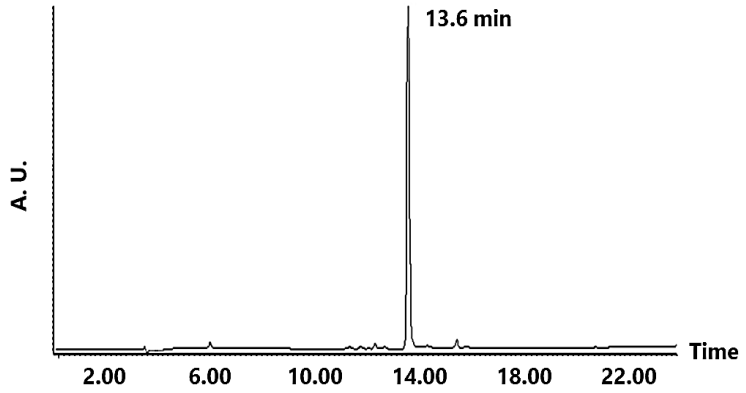

Figure 6.41: Chromatogram of 1-(benzo[*d*]thiazol-2-yl)-1*H*-1,2,3-triazole-4-carboxylic acid.

Solid-phase synthesis of BzTz-Lys-NH₂

BzTz-Lys-NH_2 was prepared following the procedures described in **Chapter 2**.

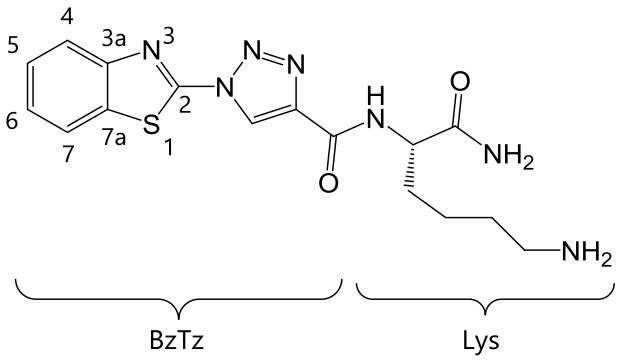

Anchoring of Lys_1 (3 eq)	500 mg of Rink Amide resin 485 mg of Fmoc-Lys(Boc)-OH 147 mg of Oxyma 160 μL of DIC
Yield	68%
Coupling of BzTz (3 eq)	174 mg of BzTz 101 mg of Oxyma 110 μL of DIC
Amount of compound (mass yield)	95 mg (83%)
Chromatographic purity	99%

White solid. **HPLC-MS:** t_R = 11.1 min; ***m/z*** 374.2 ($[C_{16}H_{19}N_7O_2S + H]^+$). **^{1}H NMR** ($D_2O$, pH = 7.4, 400 MHz): δ 1.50-1.65 (m, 2H, Hγ-Lys), 1.72-1.85 (m, 2H, Hδ-Lys), 1.90-2.07 (m, 2H, Hβ-Lys), 3.06 (t, 2H, *J* = 7.6, Hε-Lys), 4.54 (dd, 1H, *J* = 8.6, *J* = 5.7, Hα-Lys), 7.44 (t_{app}, 1H, J_{app} = 7.6, H_5), 7.51 (t_{app}, 1H J_{app} = 7.6, H_6), 7.85 (d_{app}, 1H, J_{app} = 8.0, H_7), 7.93 (d_{app}, 1H, J_{app} = 8.0, H_4), 8.88 (s, 1H, CHNNN). **^{13}C NMR** (D_2O, pH = 7.4, 100.6 MHz): δ 25.12 (Cγ-Lys), 29.24 (Cδ-Lys), 33.39 (Cβ-Lys), 42.09 (Cε-Lys), 56.43 (Cα-Lys), 125.2 (C_4), 125.5 (C_7), 126.9 (CHNNN), 129.7 (C_5), 130.4 (C_6), 135.3 (3a), 145.2 (NNNC), 151.5 (C_{7a}), 158.8 (C_2), 163.6 (CO-BzTz), 179.1 (CO-Lys).

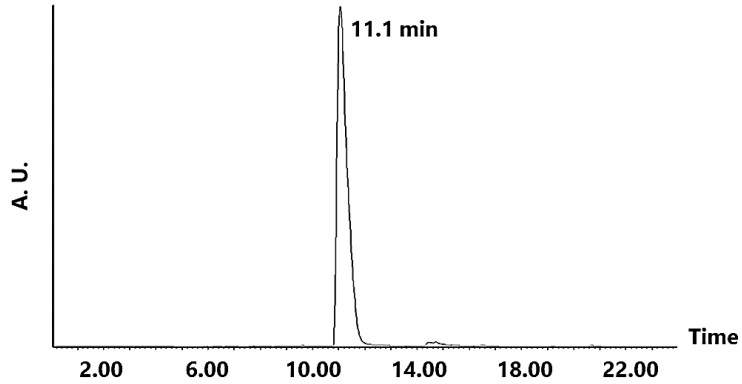

Figure 6.42: Chromatogram of BzTz-Lys-NH_2.

6.5.3 Procedures, instrumentation and techniques

Determination of the molar extinction coefficients by UV-Vis spectroscopy

Standard solutions of BzTz (concentrations of 15-90 μM) were prepared in 100 mM HEPES (pH 7.4). Standard solutions of Boc-Lys(4DMN)-OH (concentrations of 19-97 μM) were prepared in 100 mM HEPES pH 7.4 and in DCM. UV-Vis spectra of the different standards were registered using a Varian Cary 100 spectrophotometer and quartz cuvettes (3 mL, 1 cm path length) from 800 to 200 nm, at rt.

The respective calibration curves were constructed and the molar extinction coefficients, ε, were obtained from the slopes of the curves using Lambert-Beer equation (**Equation 6.1**):

$$A = \varepsilon \times c \times l \qquad (6.1)$$

where A is the absorbance value, c is the concentration of the standard and l is the optical path length of the cuvette (1 cm).

Preparation of Aβ samples

For the preparation of aggregate-free Aβ(1-40) aliquots, a 5 mg-vial of Aβ(1-40) was dissolved in 1,1,1,3,3,3-hexafluoro-2-propanol (HFIP, 1 mL) under vigorous shaking at rt for 1 h, after which it was sonicated for 30 min. The solution was further shaken for 1 h and subsequently kept at 4 ºC for 30 min to avoid solvent evaporation. Aliquots of

soluble Aβ(1-40) were collected and HFIP was evaporated in air. The resulting solid Aβ(1-40) aliquots were stored at –20 ºC, and the amount of protein per sample was checked by spectrophotometry dissolving one aliquot in 100 mM HEPES (pH 7.4) using the molar extinction coefficient ε(Tyr, 280 nm) = 1490 M^{-1} cm^{-1}.

Fibrillary Aβ was prepared by dissolving the required number of solid Aβ(1-40) aliquots in 50 μL of DMSO with sonication for 1 h. Then, a stock solution was prepared in 1X PBS (pH 7.4) and incubated at 37 ºC for 5 days with continuous shaking (1400 rpm). The formation of fibres was confirmed by ThT analysis (20 μM ThT, excitation at 447 nm, emission at 480 nm).

Monomeric Aβ(1-40) stock solutions were prepared in 10 mM NaOH from the solid peptide, sonicated for 30 min and centrifuged for 10 min. The supernatants were collected and the concentration was checked spectrophotometrically using the molar extinction coefficient ε(Tyr^{alkali}, 280 nm) = 2300 M^{-1} cm^{-1}.

Aβ(1-16) stock solutions were prepared in 10 mM HEPES (pH 7.4) from solid peptide, sonicated for 30 min and centrifuged for 10 min. The concentration was checked spectrophotometrically using the molar extinction coefficient ε(Abs_{276} – Abs_{296})= 1410 M^{-1} cm^{-1}. The Aβ stock solutions were kept frozen.

Study of the fluorescence properties of the BzTz and 4DMN compounds

Stock solutions of BzTz, BzTz-Lys-NH_2 and ThT were prepared in 10 mM HEPES (pH 7.4). Stock solutions of Boc-Lys(4DMN)-OH, Ac-His-Lys(4DMN)-His-OH, Ac-His-Lys(4DMN)-His-Lys-NH_2 and ThT were prepared in 100 mM HEPES (pH 7.4), while those of $CuCl_2$ and $ZnCl_2$ were prepared in Milli-Q H_2O. All stock solutions were always kept at 4 ºC.

Fluorescence measurements were made with a HORIBA Jobin–Yvon iHR320 spectrofluorometer at room temperature. The photomultiplier detector voltage was set at 725 V for the experiments with the BzTz compounds, and at 950 V for the 4DMN-containing amino acids and peptides. The instrument excitation and emission slits were both set at 5 nm. Detection was performed at 1 nm intervals and data acquisition was carried out at a scan rate of 120 nm/min. Spectra were collected in 200 μL quartz cuvettes (1 cm optical path length).

Detection of fibrillary Aβ(1-40) by BzTz and BzTz-Lys-NH_2

Samples (300 μL) with a final concentration of 5 μM were prepared in 10 mM HEPES (pH 7.4) and were subsequently titrated with increasing amounts of Aβ(1-40) fibres. The concentration of the compounds was kept constant at 5 μM by adding a 15 μM solution of BzTz compound. The samples were incubated at rt for 2 min after every addition of Aβ(1-40). Samples contained 5% DMSO.

The excitation wavelength for the binding experiments with BzTz and BzTz-Lys-NH_2 was 290 nm, and the emission was monitored from 310 to 600 nm. For amyloid-bound ThT, the excitation wavelength was 447 nm and the emission was monitored from 450 to 700 nm.

Emission of Boc-Lys(4DMN)-OH in DCM and HEPES buffer

Solutions of Boc-Lys(4DMN)-OH (100 nM) were prepared in DCM and 100 mM HEPES (pH 7.4). Emission in DCM was recorded from 440 to 700 nm using λ_{exc} = 420 nm, while emission in HEPES was recorded from 460 to 700 nm using λ_{exc} = 441 nm. The voltage was 950 V in both cases.

Emission of Boc-Lys(4DMN)-OH in different solvents

Solutions of Boc-Lys(4DMN)-OH (40 μM) were prepared in toluene, $CHCl_3$, AcOEt, DCM, acetone, EtOH, MeCN, MeOH and 100 mM HEPES (pH 7.4). Spectra were recorded from 440 to 700 nm using λ_{exc} = 420 nm and adjusting the voltage depending on the intensity of the band obtained.

Emissive properties of the 4DMN compounds in the presence of Aβ(1-16), monomeric Aβ(1-40) or fibrillary Aβ(1-40)

Final samples (260 μL) were prepared in 100 mM HEPES (pH 7.4) adding the required reagents in the following order: first, the corresponding amount of HEPES buffer, then the corresponding Aβ species and finally the 4DMN-containing compound. The samples were incubated at rt for 5 min. Final concentrations were 5 μM for the 4DMN

compound and 10 μM for Aβ. For monomeric Aβ(1-40), the same procedure was also carried out using ThT (5 μM) instead of the 4DMN compounds. Samples with fibrillary Aβ contained 5% DMSO.

Fluorescence spectra were registered immediately after sample preparation, after 2 h, 24 h, 48 h and 5 days. The excitation wavelength for the binding experiments with 4DMN compounds was 420 nm and the emission was monitored from 440 to 700 nm. The excitation wavelength for amyloid-bound ThT was 447 nm, and the emission was monitored from 450 to 700 nm. The samples were incubated at 37 ºC between each measurement.

Emissive properties in the presence of monomeric Aβ(1-40) and metal ions

Final samples (260 μL) were prepared in 100 mM HEPES (pH 7.4) adding the required reagents in the following order: first, the corresponding amount of HEPES buffer, then Aβ, the 4DMN compound and finally the metal. The samples were incubated at rt for 5 min. Final concentrations were: 5 μM for the 4DMN compound, 10 μM for the metal and 10 μM for Aβ. For monomeric Aβ(1-40), the same procedure was carried out but with ThT (5 μM) instead of the 4DMN compounds.

Fluorescence spectra were registered immediately after sample preparation, after 2 h, 24 h, 48 h and 5 days. The excitation wavelength for the binding experiments with the 4DMN compounds was 420 nm and the emission was monitored from 440 to 700 nm. The excitation wavelength for amyloid-bound ThT was 447 nm, and the emission was monitored from 450 to 700 nm. The samples were incubated at 37 ºC between each measurement.

Displacement studies between ThT and the 4DMN compounds

Displacement of ThT by the 4DMN compounds: First, the fluorescent spectrum of free ThT (5 μM, 260 μL) was registered. Next, samples of ThT bound to Aβ(1-40) fibres (260 μL; final concentrations 5 and 10 μM, respectively) were prepared and incubated during 2 min at rt; the fluorescence spectra were subsequently recorded. The Aβ(1-40) fibres were then treated with 1 eq and further 4 eq of 4DMN compound, and the emission was registered. The solutions were incubated at 37 ºC for 15 min after each addition. Emission measurements were performed from 450 to 700 nm using the excitation wavelength of amyloid-bound ThT (447 nm). All samples were prepared in 100 mM HEPES (pH 7.4).

Displacement of the 4DMN compounds by ThT: The 4DMN compounds were incubated with Aβ(1-40) fibres (300 μL, final concentrations 5 and 10 μM, respectively) at 37 ºC for 5 min. The solutions were subsequently treated with 1 eq of ThT and incubated at 37 ºC for further 5 min, after which they were centrifuged for 30 min. A fraction of the supernatants (100 μL) was collected and its fluorescent emission was measured. Emission measurements were performed from 460 to 700 nm using the excitation wavelength of bound 4DMN compounds (420 nm). All samples were prepared in 100 mM HEPES (pH 7.4).

Aβ(1-40) aggregation kinetics in the presence of the BzTz and 4DMN compounds followed by ThT emission

Stock solutions of BzTz, BzTz-Lys-NH_2 and ThT were prepared in 10 mM HEPES (pH 7.4). Stock solutions of Boc-Lys(4DMN)-OH, Ac-His-Lys(4DMN)-His-OH, Ac-His-Lys(4DMN)-His-Lys-NH_2 and ThT were prepared in 100 mM HEPES (pH 7.4). All stock solutions were always kept at 4 ºC. A BMG Labtech FLUOstar Omega plate reader in bottom optics configuration was used. Samples were prepared and measured in 96-well plates (Clearline® 131012C).

ThT kinetic measurements on the aggregation of Aβ(1-40) in the presence of BzTz compounds

Solid Aβ(1-40) aliquots were dissolved in 50 μL of DMSO and sonicated for 1 h. Then, a 133 μM stock solution of Aβ(1-40) was prepared in 100 mM HEPES (pH 7.4), which contained 147 μM ThT.

Final samples (200 μL) were prepared in plates adding the required reagents in the following order: first, the corresponding amount of 1X PBS buffer pH 7.4, then the BzTz compound and finally Aβ(1-40)-ThT. The final concentrations were: 20 μM Aβ(1-40), 22 μM ThT and 1 μM BzTz compound. Samples contained 4.4% DMSO.

Kinetic measurements were initiated in the plate reader immediately after sample preparation. Endpoint measurements were performed at 37 ºC every 1 min for 1000 min with continuous shaking (700 rpm). Excitation/emission of 440/490 nm optics were used.

Aggregation of Aβ(1-40) in the presence of 4DMN compounds

Solid Aβ(1-40) aliquots were dissolved in 50 μL of DMSO and sonicated for 1 h. Then, a 167 μM stock solution of Aβ(1-40) was prepared in 100 mM HEPES (pH 7.4), which contained 144 μM ThT.

Final samples (200 μL) were prepared in plates adding the required reagents in the following order: first, the corresponding amount of 1X PBS buffer pH 7.4, then the 4DMN compound and finally Aβ(1-40)-ThT. Final concentrations were: 25 μM for Aβ(1-40), 21.5 μM for ThT and 12 μM for the 4DMN compound. Samples contained 4.3% DMSO.

Kinetic measurements were initiated in the plate reader immediately after sample preparation. Endpoint measurements were performed at 37 ºC every 6 min for 5 days with continuous shaking (700 rpm). Excitation/emission optics of 440/490 nm were used.

Bimodal monitoring of Aβ(1-40) aggregation by Boc-Lys(4DMN)-OH (Boc-K^d)

Stock solutions (100 μM) of Boc-Lys(4DMN)-OH and ThT were prepared in 100 mM HEPES (pH 7.4) and kept at 4 °C. A solid Aβ(1-40) aliquot was dissolved in 50 μL DMSO and sonicated for 15 min, to which 100 μM ThT/Boc-K^d and 1X PBS (pH 7.4) were subsequently added. The final concentrations of the resulting solution (containing 0.5% DMSO) were 20 and 10 μM for Aβ(1-40) and ThT/Boc-K^d, respectively. Fluorescence measurements were made with an AMINCO-Bowman Series 2 luminescence spectrometer at 37 °C with vigorous and constant stirring. The photomultiplier detector voltage was set at 840 V (ThT) and 885 V (Boc-K^d). The instrument excitation and emission slits were both set at 5 nm. Detection was performed at 1 nm intervals and data acquisition was carried out at a scan rate of 2 nm/min. Spectra were collected in 1 mL quartz cuvettes (1 cm optical path length). Emission spectra (460-600 nm) were initiated immediately after sample preparation and recorded every 5 minutes; the excitation wavelengths for ThT and Boc-K^d were 440 and 420 nm, respectively. The emission intensity at 493 nm was plotted against time for ThT, while both the maximum intensity and the maximum emission wavelength were plotted against time for Boc-K^d.

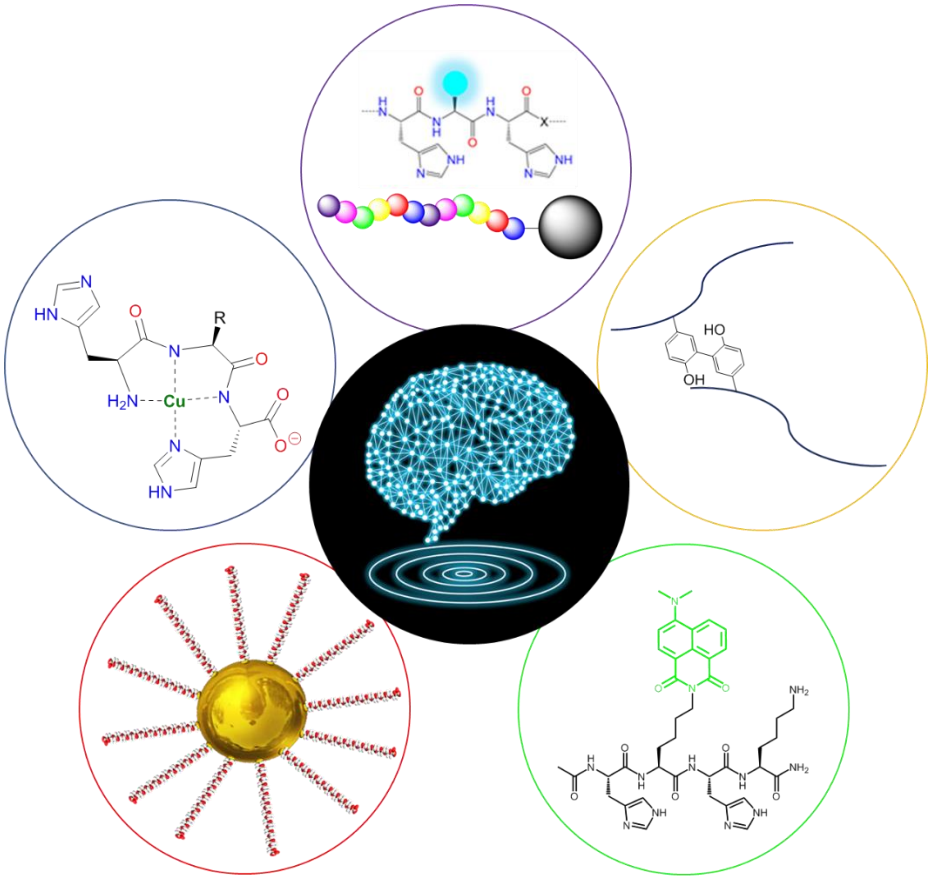

7. Final remarks

7. Final remarks

His-containing peptides have been designed that show great potential regarding their use as valuable synthons for the development of diagnosis tools and/or drugs to detect and/or treat Alzheimer's Disease (AD). The chelating peptides have been successfully applied *in vitro* to *i)* reduce the Cu(II)-mediated formation of oligomeric Aβ species and associated oxidative stress, *ii)* to inhibit the formation of long-lived toxic covalent dimers of Aβ and *iii)* to detect Aβ aggregates. In addition, the peptides could be conveniently grafted onto Au NPs with the objective to enhance their stability in biological media, their efficacy and their BBB permeability.

The results achieved applying a pioneering approach support the idea of using peptide-based compounds to address two of the major challenges of AD research, *viz.* the prevention of Aβ toxicity and the detection of different types of Aβ aggregates. Copper-targeting therapies (*e.g.* using peptides) in combination with more traditional strategies, such as cholinergic therapy or the promotion of Aβ clearance, may give rise beneficial synergistic effects.

Chapter 2: Synthesis of emissive chelating peptides

- Peptides of sequence His-Lys-His (HKH) or His-Lys-His-Lys (HKHK) were synthesised in high chromatographic purities (92-97%), by solid-phase synthesis using conventional Fmoc chemistry. These sequences were selected for their excellent Cu(II)-binding properties.
- The fluorophores coumarin (Coum) and 4-*N*,*N*-dimethylamino-1,8-naphthalimide (4DMN) were successfully incorporated into the peptides *via* the synthetic amino acid derivatives Fmoc-Lys(Coum)-OH and Fmoc-Lys(4DMN)-OH, respectively. Commercially available 5(6)-carboxyfluorescein was also used to label two of the peptides at their *N*-terminal ends. Some of the peptides were amide-protected at their *C*- and/or *N*-terminal ends for comparison purposes, to contrast their Cu(II)-chelating properties with ATCUN-type peptides or peptides connected to Au NPs (through their *C*- and/or *N*-terminal groups).
- The *C*-terminal amide-protected peptides were generally obtained in low yields, most likely as the result of a poorly efficient cleavage step. This issue should be

addressed in future studies as the low amounts of product obtained were a limiting factor in some cases; for instance, high amounts of peptide are required for their coupling to Au NPs. The use of a different (more labile) resin may help to address this limitation.

- High molecular weight by-products were generated during the syntheses of the coumarinic peptides, which could fortunately be converted back to the desired products using piperidine.
- RhoB-His-Lys(Fluo)-His-NH_2 could not be obtained by reaction of rhodamine B isothiocyanate with the *N*-terminal amino group of His1. An alternative future approach may be to use carboxyrhodamine B instead.

Chapter 3: Chelation and detection of Cu(II) ions

- The *N*-terminal free peptides HAH, HWH and HK^cH bind one Cu(II) ion through a [N_{amino}, N_{amide}, N_{amide}, $N_{imidazole}$] donor set, *i.e.* an ATCUN motif. These tripeptides present higher Cu(II)-binding affinity constants than that of Aβ(1-40) and of clioquinol. Such ATCUN peptides may therefore act as efficient chelating agents for therapeutic uses.
- HK^cH was able to extract Cu(II) ions previously bound to Aβ(1-16), while Aβ(1-16) could not displace Cu(II) ions bound to HK^cH; a similar effect is expected for HAH and HWH since they display higher Cu(II)-binding affinities than HK^cH.
- These ATCUN peptides efficiently prevent the Cu(II)-induced stabilisation of Aβ(1-40) oligomers and the production of ROS.
- The *N*-terminal protected (acetylated) peptides $AcHK^cH$ and $AcHK^dH$ generated 1:1 Cu(II) complexes with a [$N_{imidazole}$, N_{amide}, $O_{carbonyl}$, $N_{imidazole}$] coordination donor set. $AcHK^cH$ and $AcHK^dH$-NH_2 exhibited Cu(II)-binding affinity constants one order of magnitude higher than that of Aβ(1-40). The Cu(II)-binding affinity of $AcHK^dH$ could not be determined because the fluorescence-emission intensity data could not be fitted.
- The *N*-protected tripeptides were not able to restore normal Aβ(1-40) fibrillation in the presence of Cu(II) ions, probably owing to the formation of ternary

species. Moreover, AcHK^{c}H and AcHK^{d}H were weak inhibitors of the Cu(II)-mediated generation of ROS.

- The occurrence of FRET could not be confirmed for FluoHK^{c}H, which contains the fluorescein-coumarin pair. The fluorescein emission was much higher than that of coumarin, thus hampering the potential application of this peptide as a FRET-based probe for Cu(II) ions. Nevertheless, the I_{410}/I_{521} intensity ratio (between the two fluorophores) of FluoHK^{c}H increased by a factor of 4.2 upon addition of $CuCl_2$. This encouraging data stimulated the design and preparation of another potential (FRET-based) Cu(II) peptidic probe, *viz.* RhoB-His-Lys(Fluo)-His-NH_2 that may act as a more efficient ratiometric Cu(II)-sensor. Unfortunately, the preparation of this peptide containing the widely-used fluorescein-rhodamine B FRET pair was unsuccessful.

Chapter 4: Copper-induced oxidative formation of dityrosine cross-links in β-amyloid

- A dityrosine reference was synthesised from *N*-acetyltyrosine, which was used to quantify by fluorescence spectroscopy the generation of dityrosine Aβ(1-40) cross-links.
- Dityrosine Aβ(1-40) cross-links were generated in the presence of an equimolar amount of Cu(II) ions and an excess of H_2O_2. ThT and TEM studies evidenced the complete inhibition of the generation of Aβ(1-40) fibres after formation of dityrosine cross-links, even at very low concentration, namely < 3% of cross-linked Aβ. These results hence suggest that non-amyloidogenic, cross-linked Aβ(1-40) oligomers are produced.
- Addition of the ATCUN Cu(II)-chelating peptide HAH restored the fibrillation process of Aβ(1-40) in the presence of Cu(II) ions and H_2O_2, indicating that the copper-catalysed formation of dityrosine cross-links was prevented. Such an impediment of the generation of long-lived toxic oligomers may represent a good strategy to reduce Aβ toxicity.
- The formation, structure and toxicity of the Aβ oligomeric species generated through copper binding or *via* the generation dityrosine-bridged dimers should

be investigated separately. Both the coordination and covalent oligomers hinder Aβ(1-40) fibrillation.

Chapter 5: Coupling of Cu(II)-chelating peptides to gold nanoparticles

- AcHK^{c}HK was coupled to PEGylated gold nanoparticles (Au NPs) of 4.8 and 14.4 nm core sizes, with a yield of 61% and 84%, respectively. The nanomaterials were stable, moderately polydisperse and exhibited a negatively charged surface. 15Au-COOH NPs presented a surface coverage of 83%, which prevented their aggregation. The number of PEG chains grafted onto the surface of 5Au-COOH NPs could not be determined due to the high amounts of sample required.
- The experimental procedure for the DLS and Z potential measurements should be optimised to avoid the generation of poorly defined peaks.
- The Au NPs quenched the emission of AcHK^{c}HK, which impeded the direct determination of the coupling yields by fluorescence spectroscopy. Thus, the peptides were cleaved from the NPs using HCl, purified by centrifugation and subsequently quantified. Such quenching effect also prevented the monitoring of the Cu(II)-binding process. The coupling yields could not be confirmed by amino acid quantification as amino acid degradation occurred upon thermal digestion with HCl; such unexpected degradation might be induced by the coumarin moiety.
- Au-HK^{c}HK NPs seemed to (partially) extract Cu(II) ions from Aβ(1-16), and to inhibit Aβ(1-40) fibrillation. Hence, Au-HK^{c}HK NPs acted both as inhibitors of the formation of Cu(II)-induced oligomers (*via* the peptide groups) and of the fibrillation (*via* their PEG chains).
- Cell studies with neuronal embryo cells of wildtype mice showed that AcHK^{c}HK, 15Au-COOH and 15Au-HK^{c}HK were not cytotoxic at typical working concentrations; these highly promising results motivate future thorough *in vitro* and *in vivo* studies.

Chapter 6: Detection of aggregated Aβ with fluorescent probes

- A ThT-like molecule, namely BzTz, was synthesised using click chemistry, and its Lys derivative, *i.e.* BzTz-Lys-NH_2, was subsequently prepared by solid-phase synthesis.

- Contrary to ThT, BzTz did not show any spectroscopic changes (*e.g.* enhancement of fluorescence emission, shift in the excitation/emission wavelengths) in the presence of fibrillary Aβ(1-40). This suggests that the probe did not exhibit interaction with Aβ(1-40) fibres nor behaved as ThT (whose fluorescence increases upon intercalation between β-sheets that impedes its free rotation). Push-pull systems would probably be better scaffolds for the design of ThT-like Aβ-probes.

- The 4DMN-containing amino acid derivative Boc-K^d and the peptides AcHK^dH and AcHK^dHK were used to detect Aβ(1-40) fibres and to monitor the aggregation of Aβ(1-40). Cu(II)-stabilised oligomeric forms and Zn(II)-induced amorphous aggregates were detected. The 4DMN compounds presented hypsochromic effects and higher quantum yields in the presence of the different aggregated Aβ(1-40) species, and thus acted as bimodal probes. The compounds seemed to share a common binding site with ThT, and Aβ(1-40) aggregation was unaffected by their presence. For the first time, a 4DMN-based probe has been used to detect a structurally-disordered peptide.

- The use of the fluorophore 4DMN combined with other characterisation techniques such as TEM (or other microscopic methods), may help to discriminate different Aβ aggregated species (*viz.* oligomers, fibres and amorphous aggregates). The computational design of 4DMN-containing peptides showing potential selectivities for diverse types/forms of Aβ aggregates can also be envisaged. The multi-dimensional monitoring of the Aβ aggregation process may help to understand its self-assembly mechanism (which would allow to design more appropriate/efficient inhibitors).

- The pioneering results achieved with Aβ are highly promising; hence, they open the door to the use of the fluorophore 4DMN for the detection of aggregated species of other misfolding proteins.

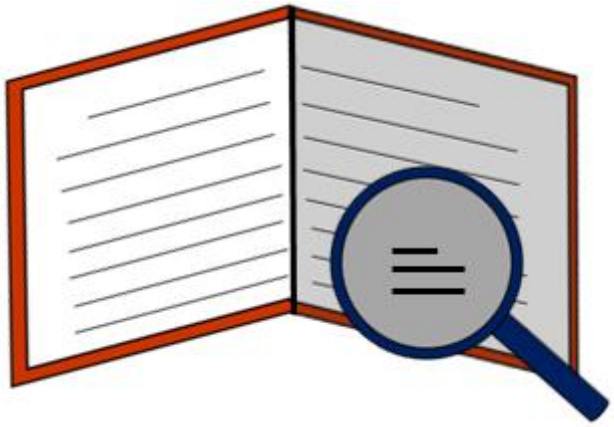

8. References

8. References

[1] B. Duthey. Background Paper 6.11 Alzheimer Disease and other Dementias. Priority Medicines for Europe and the World "A Public Health Approach to Innovation" World Health Organization, 2013.

[2] Dementia. A Public Health Priority. World Health Organization and Alzheimer's Disease International, 2012.

[3] Braak, H.; Braak, E. *Neurobiol. Aging* **1997**, *18*, 351–357.

[4] World Alzheimer Report 2015. The Global Impact of Dementia. An analysis of prevalence, incidence, cost and trends. Alzheimer's Disease International, 2015.

[5] Bateman, R.; Xiong, C.; Benzinger, T.; Fagan, A.; Goate, A.; Fox, N.; Marcus, D.; Cairns, N.; Xie, X.; Blazey, T.; Holtzman, D.; Santacruz, A.; Buckles, V.; Oliver, A.; Moulder, K.; Aisen, P.; Ghetti, B.; Klunk, W.; McDade, E.; Martins, R.; Masters, C.; Mayeux, R.; Ringman, J.; Rossor, M.; Schofield, P.; Sperling, R.; Salloway, S.; Morris, J. *N. Engl. J. Med.* **2012**, *367*, 795–804.

[6] Jack, C.; Knopman, D.; Jagust, W.; Shaw, L.; Aisen, P.; Weiner, M.; Petersen, R.; Trojanowski, J. *Lancet Neurol.* **2010**, *9*, 119–128.

[7] Price, J.; Morris, J. *Ann. Neurol.* **1999**, *45*, 358–368.

[8] Dubois, B.; Hampel, H.; Feldman, H.; Scheltens, P.; Aisen, P.; Andrieu, S.; Bakardjian, H.; Benali, H.; Bertram, L.; Blennow, K.; Broich, K.; Cavedo, E.; Crutch, S.; Dartigues, J.; Duyckaerts, C.; Epelbaum, S.; Frisoni, G.; Gauthier, S.; Genthon, R.; Gouw, A.; Habert, M.; Holtzman, D.; Kivipelto, M.; Lista, S.; Molinuevo, J.; O'Bryant, S.; Rabinovici, G.; Rowe, C.; Salloway, S.; Schneider, L.; Sperling, R.; Teichmann, M.; Carrillo, M.; Cummings, J.; Jack, C. *Alzheimers Dement.* **2016**, *12*, 292–323.

[9] Selkoe, D. *Physiol. Rev.* **2001**, *81*, 741–766.

[10] Selkoe, D. *Ann. Intern. Med.* **2004**, *140*, 627–638.

[11] Lambert, J.; Heath, S.; Even, G.; Campion, D.; Sleegers, K.; Hiltunen, M.; Combarros, O.; Zelenika, D.; Bullido, M.; Tavernier, B.; Letenneur, L.; Bettens, K.; Berr, C.; Pasquier, F.; Fiévet, N.; Barberger-Gateau, P.; Engelborghs, S.; De Deyn, P.; Mateo, I.; Franck, A.; Helisalmi, S.; Porcellini, E.; Hanon, O.; De Pancorbo, M.; Lendon, C.; Dufouil, C.; Jaillard,

C.; Leveillard, T.; Alvarez, V.; Bosco, P.; Mancuso, M.; Panza, F.; Nacmias, B.; Boss, P.; Piccardi, P.; Annoni, G.; Seripa, D.; Galimberti, D.; Hannequin, D.; Licastro, F.; Soininen, H.; Ritchie, K.; Blanché, H.; Dartigues, J.; Tzourio, C.; Gut, I.; Van Broeckhoven, C.; Alpérovitch, A.; Lathrop, M.; Amouyel, P.; Arosio, B.; Coto, E.; Del Zompo, M.; Deramecourt, V.; Epelbaum, J.; Forti, P.; Brice, A.; Ferri, R.; Scarpini, E.; Siciliano, G.; Solfrizzi, V.; Sorbi, S.; Spalletta, G.; Ravaglia, G.; Sahel, J.; Valdivieso, F.; Vepsäläinen, S.; Pilotto, A. *Nat. Genet.* **2009**, *41*, 1094–1099.

[12] Hamley, I. *Chem. Rev.* **2012**, *112*, 5147–5192.

[13] Xu, W.; Tan, L.; Wang, H.; Jiang, T.; Tan, M.; Tan, L.; Zhao, Q.; Li, J.; Wang, J.; Yu, J. *Neurol. Neurosurg. Psychiatry* **2015**, *86*, 1299–1306.

[14] Mandelkow, E.; Mandelkow, E. *Trends Cell Biol.* **1998**, *8*, 425–427.

[15] Haass, C.; Selkoe, D. *Nat. Rev. Mol. Cell Biol.* **2007**, *8*, 101–112.

[16] Bush, A. *Trends Neurosci.* **2003**, *26*, 207–214.

[17] Selkoe, D. *Trends Cell Biol.* **1998**, *8*, 447–453.

[18] Faller, P.; Hureau, C.; Berthoumieu, O. *Inorg. Chem*. **2013**, *52*, 12193–12206.

[19] Valensin, D.; Gabbiani, C.; Messori, L. *Coord. Chem. Rev.* **2012**, *256*, 2357–2366.

[20] Lewis, J.; Dickson, D.; Lin, W.; Chisholm, L.; Corral, A.; Jones, G.; Yen, S.; Sahara, N.; Skipper, L.; Yager, D.; Eckman, C.; Hardy, J.; Hutton, M.; Mcgowan, E. *Science* **2001**, *293*, 1487–1491.

[21] Götz, J.; Chen, F.; van Dorpe, J.; Nitsch, R. *Science* **2001**, *293*, 1491–1495.

[22] Jin, M.; Shepardson, N.; Yang, T.; Chen, G.; Walsh, D.; Selkoe, D. *Proc. Natl. Acad. Sci. USA* **2011**, *108*, 5819–5824.

[23] Roberson, E.; Scearce-Levie, K.; Palop, J.; Yan, F.; Cheng, I.; Wu, T.; Gerstein, H.; Yu, G.; Mucke, L. *Science* **2007**, *316*, 750–754.

[24] Goate, A.; Chartier-Harlin, M.; Mullan, M.; Brown, J.; Crawford, F.; Fidani, L.; Giuffra, L.; Haynes, A.; Irving, N.; James, L.; Mant, R.; Newton, P.; Rooke, K.; Roques, P.; Talbot, C.; Pericak-Vance, M.; Roses, A.; Williamson, R.; Rossor, M.; Owen, M.; Hardy, J. *Nature* **1991**, *349*, 704–706.

[25] Schmechel, D.; Saunders, A.; Strittmatter, W.; Crain, B.; Hulette, C.; Joo, S.; Pericak-Vance, M.; Goldgaber, D.; Roses, A. *Proc. Natl. Acad. Sci. USA* **1993**, *90*, 9649–9653.

[26] Sherrington, R.; Rogaev, E.; Liang, Y.; Rogaeva, E.; Levesque, G.; Ikeda, M.; Chi, H.; Lin, C.; Li, G.; Holman, K.; Tsuda, T.; Mar, L.; Foncin, J.; Bruni, A.; Montesi, M.; Sorbi, S.; Rainero, I.; Pinessi, L.; Nee, L.; Chumakov, I.; Pollen, D.; Brookes, A.; Sanseau, P.; Polinsky, R.; Wasco, W.; Da Silva, H.; Haines, J.; Pericak-Vance, M.; Tanzi, R.; Roses, A.; Fraser, P.; Rommens, J.; St George-Hyslop, P. *Nature* **1995**, *375*, 754–760.

[27] Gamez, P.; Caballero, A. *AIP Advances* **2015**, *5*, 092503/1–092503/12.

[28] Paravastu, A.; Leapman, R.; Yau, W.; Tycko, R. *Proc. Natl. Acad. Sci. USA* **2008**, *105*, 18349–18354.

[29] Naylor, R.; Hill, A.; Barnham, K. *Eur. Biophys. J.* **2008**, *37*, 265–268.

[30] Bieschke, J.; Zhang, Q.; Bosco, D.; Lerner, R.; Powers, E.; Wentworth, P.; Kelly, J. *Acc. Chem. Res.* **2006**, *39*, 611–619.

[31] Ono, K.; Condron, M.; Teplow, D. *Proc. Natl. Acad. Sci. USA* **2009**, *106*, 14745–14750.

[32] Bhak, G.; Choe, Y.; Paik, S. *BMB Rep.* **2009**, *42*, 541–551.

[33] Xue, W.; Homans, S.; Radford, S. *Proc. Natl. Acad. Sci. USA* **2008**, *105*, 8926–8931.

[34] Chiti, F.; Dobson, C. *Annu. Rev. Biochem.* **2006**, *75*, 333–366.

[35] Lue, L.; Kuo, Y.; Roher, A.; Brachova, L.; Shen, Y.; Sue, L.; Beach, T.; Kurth, J.; Rydel, R.; Rogers, J. *Am. J. Pathol.* **1999**, *155*, 853–862.

[36] Wang, J.; Dickson, D.; Trojanowski, J.; Lee, V. *Exp. Neurol.* **1999**, *158*, 328–337.

[37] McLean, C.; Cherney, R.; Fraser, F.; Fuller, S.; Smith, M.; Beyreuther, K.; Bush, A.; Masters, C. *Ann. Neurol*. **1999**, *46*, 860–866.

[38] Campioni, S.; Mannini, B.; Zampagni, M.; Pensalfini, A.; Parrini, C.; Evangelisti, E.; Relini, A.; Stefani, M.; Dobson, C.; Cecchi, C.; Chiti, F. *Nat. Chem. Biol.* **2010**, *6*, 140–147.

[39] Williams, T.; Serpell, L.; Urbanc, B. *Biochim. Biophys. Acta* **2016**, 1864, 249–259.

[40] Barham, K.; Ciccotosto, G.; Tickler, A.; Ali, F.; Smith, D.; Williamson, N.; Lam, Y.; Carrington, D.; Tew, D.; Kocak, G.; Volitakis, I.; Separovic, F.; Barrow, C.; Wade, J.; Masters, C.; Cherny, R.; Curtain, C.; Bush, A.; Cappai, R. *J. Biol. Chem.* **2003**, *278*, 42959–42965.

[41] Shankar, G.; Li, S.; Mehta, T.; Garcia-Munoz, A.; Shepardson, N.; Smith, I.; Brett, F.; Farrell, M.; Rowan, M.; Lemere, C.; Regan, C.; Walsh, D.; Sabatini, B.; Selkoe, D. *Nat. Med.* **2008**, *14*, 837–842.

[42] Barnham, K.; Bush, A. *Chem. Soc. Rev.* **2014**, *43*, 6727–6749.

[43] Ayton, S.; Lei, P.; Bush, A. *Free Radic. Biol. Med.* **2013**, *62*, 76–89.

[44] Barnham, K.; Haeffner, F.; Ciccotosto, G.; Curtain, C.; Tew, D.; Mavros, C.; Beyreuther, K.; Carrington, D.; Masters, C.; Cherny, R.; Cappai, R.; Bush, A. *FASEB J.* **2004**, *18*, 1427–1429.

[45] Osredkar, J.; Sustar, N. *J. Clinic. Toxicol.* **2011**, *s3*, 1–18.

[46] Greenough, M.; Volitakis, I.; Li, Q.; Laughton, K.; Evin, G.; Ho, M.; Dalziel, A.; Camakaris, J.; Bush, A. *J. Biol. Chem.* **2011**, *286*, 9776–9786.

[47] Adlard, P.; Parncutt, J.; Finkelstein, D.; Bush, A. *J. Neurosci.* **2010**, 30, 1631–1636.

[48] Cole, T.; Wenzel, H.; Kafer, K.; Schwartzkroin, P.; Palmiter, R. *Proc. Natl. Acad. Sci. USA* **1999**, *96*, 1716–1721.

[49] Lee, J.; Kim, J.; Hong, S.; Lee, J.; Cherny, R.; Bush, A.; Palmiter, R.; Koh, J. *J. Biol. Chem.* **2004**, *279*, 8602–8607.

[50] Aizenman, E.; Stout, A.; Hartnett, K.; Dineley, K.; McLaughlin, B.; Reynolds, I. *J. Neurochem.* **2000**, *75*, 1878–1888.

[51] Zhang, Y.; Wang, H.; Li, J.; Jimenez, D.; Levitan, E.; Aizenman, E.; Rosenberg, P. *J. Neurosci.* **2004**, *24*, 10616–10627.

[52] Lee, J.; Cole, T.; Palmiter, R.; Suh, S.; Koh, J. *Proc. Natl. Acad. Sci. USA* **2002**, *99*, 7705–7710.

[53] Callahan, M.; Lipinski, W.; Bian, F.; Durham, R.; Pack, A.; Walker, L. *Am. J. Pathol.* **2001**, *158*, 1173–1177.

[54] Kessler, H.; Bayer, T.; Bach, D.; Schneider-Axmann, T.; Supprian, T.; Herrmann, W.; Haber, M.; Multhaup, G.; Falkai, P.; Pajonk, F. *J. Neural. Transm.* **2008**, *115*, 1181–1187.

[55] Singh, I.; Sagare, A.; Coma, M.; Perlmutter, D.; Gelein, R.; Bell, R.; Deane, R.; Zhong, E.; Parisi, M.; Ciszewski, J.; Kasper, R.; Deane, R. *Proc. Natl. Acad. Sci. USA* **2013**, *110*, 14771–14776.

[56] Sparks, D.; Schreurs, B. *Proc. Natl. Acad. Sci. USA* **2003**, *100*, 11065–11069.

[57] Inestrosa, N.; Cerpa, W.; Varela-Nallar, L. *IUBMB Life* **2005**, *57*, 645–650.

[58] Bellingham, S.; Lahiri, D.; Maloney, B.; La Fontaine, S.; Multhaup, G.; Camakaris, J. *J. Biol. Chem.* **2004**, *279*, 20378–20386.

[59] Hung, Y.; Robb, E.; Volitakis, I.; Ho, M.; Evin, G.; Li, Q.; Culvenor, J.; Masters, C.; Cherny, R.; Bush, A. *J. Biol. Chem.* **2009**, *284*, 21899–21907.

[60] Huang, X.; Atwood, C.; Moir, R.; Hartshorn, M.; Tanzi, R.; Bush, A. *J. Biol. Inorg. Chem.* **2004**, *9*, 954–960.

[61] Jun, S.; Gillespie, J.; Shin, B.; Saxena, S. *Biochemistry* **2009**, *48*, 10724–10732.

[62] Sarell, C.; Wilkinson, S.; Viles, J. *J. Biol. Chem.* **2010**, *285*, 41533–41540.

[63] Mold, M.; Ouro-Gnao, L.; Wieckowski, B.; Exley, C. *Sci. Rep.* **2013**, *3*, 1256/1–1256/6.

[64] Yoshiike, Y.; Tanemura, K.; Murayama, O.; Akagi, T.; Murayama, M.; Sato, S.; Sun, X.; Tanaka, N.; Takashima, A. *J. Biol. Chem.* **2001**, *276*, 32293–32299.

[65] Huang, X.; Atwood, C.; Moir, R.; Hartshorn, M.; Vonsattel, J.; Tanzi, R.; Bush, A. *J. Biol. Chem.* **1997**, *272*, 26464–26470.

[66] Smith, D.; Ciccotosto, G.; Tew, D.; Fodero-Tavoletti, M.; Johanssen, T.; Masters, C.; Barnham, K.; Cappai, R. *Biochemistry* **2007**, *46*, 2881–2891.

[67] Pedersen, J.; Østergaard, J.; Rozlosnik, N.; Gammelgaard, B.; Heegaard, N. *J. Biol. Chem.* **2011**, *286*, 26952–26963.

[68] Bush, A.; Pettingell, W.; Paradis, M.; Tanzi, R. *J. Biol. Chem.* **1994**, *269*, 12152–12158.

[69] Pedersen, J.; Teilum, K.; Heegaard, N.; Østergaard, J.; Adolph, H.; Hemmingsen, L. *Angew. Chem. Int. Ed.* **2011**, *50,* 2532–2535.

[70] Alies, B.; Renaglia, E.; Rózga, M.; Bal, W.; Faller, P.; Hureau, C. *Anal. Chem.* **2013**, *85*, 1501–1508.

[71] Faller, P.; Hureau, C.; La Penna, G. *Acc. Chem. Res.* **2014**, *47*, 2252–2259.

[72] Drew, S.; Noble, C.; Masters, C.; Hanson, G.; Barnham, K. *J. Am. Chem. Soc.* **2009**, *131*, 1195–1207.

[73] Drew, S.; Kok, W.; Hutton, C.; Barnham, K. *Appl. Magn. Reson.* **2013**, *44*, 927–939.

[74] Shearer, J.; Szalai, V. *J. Am. Chem. Soc.* **2008**, *130*, 17826–17835.

[75] Furlan, S.; Hureau, C.; Faller, P.; La Penna, G. *J. Phys. Chem. B* **2010**, *114*, 15119–15133.

[76] Shearer, J.; Callan, P.; Tran, T.; Szalai, V. *Chem. Commun.* **2010**, *46*, 9137–9139.

[77] Peck, K.; Clewett, H.; Schmitt, J.; Shearer, J. *Chem. Commun.* **2013**, *49*, 4797–4799.

[78] Zawisza, I.; Rózga, M.¸Bal, W. *Coord. Chem. Rev.* **2012**, *256*, 2297–2307.

[79] Faller, P.; Hureau, C. *Dalton Trans.* **2009**, 1080–1094.

[80] Atwood, C.; Scarpa, R.; Huang, X.; Moir, R.; Jones, W.; Fairlie, D.; Tanzi, R.; Bush, A. *J. Neurochem.* **2000**, *75*, 1219–1233.

[81] Sarell, C.; Syme, C.; Rigby, S.; Viles, J. *Biochemistry* **2009**, *48*, 4388–4402.

[82] Feaga, H.; Maduka, R.; Foster, M.; Szalai, V. *Inorg. Chem.* **2011**, *50*, 1614–1618.

[83] Alies, B.; Badei, B.; Faller, P.; Hureau, C. *Chem. Eur. J.* **2012**, *18*, 1161–1167.

[84] La Penna, G.; Hureau, C.; Andreussi, O.; Faller, P. *J. Phys. Chem. B* **2013**, *117*, 16455–16467.

[85] Huang, X.; Cuajungco, M.; Atwood, C.; Hartshorn, M.; Tyndall, J.; Hanson, G.; Stokes, K.; Leopold, M.; Multhaup, G.; Goldstein, L.; Scarpa, R.; Saunders, A.; Lim, J.; Moir, R.; Glabe, C.; Bowden, E.; Masters, C.; Fairlie, D.; Tanzi, R.; Bush, A. *J. Biol. Chem.* **1999**, *274*, 37111–37116.

[86] Opazo, C.; Huang, X.; Cherny, R.; Moir, R.; Roher, A.; White, A.; Cappai, R.; Masters, C.; Tanzi, R.; Inestrosa, N.; Bush, A. *J. Biol. Chem.* **2002**, *277*, 40302–40308.

[87] Jiang, D.; Li, X.; Liu, L.; Yagnik, G.; Zhou, F. *J. Phys. Chem. B* **2010**, *114*, 4896–4903.

[88] Murakami, K.; Murata, N.; Noda, Y.; Tahara, S.; Kaneko, T.; Kinoshita, N.; Hatsuta, H.; Murayama, S.; Barnham, K.; Irie, K.; Shirasawa, T.; Shimizu, T. *J. Biol. Chem.* **2011**, *286*, 44557–44568.

[89] Cassagnes, L.; Hervé, V.; Nepveu, F.; Hureau, C.; Faller, P.; Collin, F. *Angew. Chem. Int. Ed.* **2013**, *52*, 11110–11113.

[90] Al-Hilaly, Y.; Williams, T.; Stewart-Parker, M.; Ford, L.; Skaria, E.; Cole, M.; Bucher, W.; Morris, K.; Sada, A.; Thorpe, J.; Serpell, L. *Acta Neuropathol. Commun.* **2013**, *1*, 83.

[91] Galeazzi, L.; Ronchi, P.; Franceschi, C.; Giunta, S. *Amyloid* **1999**, *6*, 7–13.

[92] Gunderson, W.; Hernández-Guzmán, J.; Karr, J.; Sun, L.; Szalai, V.; Warncke, K. *J. Am. Chem. Soc.* **2012**, *134*, 18330–18337.

[93] Tabner, B.; Mayes, J.; Allsop, D. *Int. J. Alzheimers Dis.* **2010**, *2011*, 546380/1–546380/6.

[94] Park, G.; Lee, J.; Himes, R.; Thomas, G.; Blackburn, N.; Karlin, K. *J. Am. Chem. Soc.* **2014**, *136*, 12532–12535.

[95] Abbott, N.; Patabendige, A.; Dolman, D.; Yusof, S.; Begley, D. *Neurobiol. Dis.* **2010**, *37*, 13–25.

[96] Pardridge, W. *Drug Discov. Today* **2007**, 12, 54–61.

[97] Malakoutikhah, M.; Teixidó, M.; Giralt, E. *Angew. Chem. Int. Ed.* **2011**, *50*, 7998–8014.

[98] Kreuter, J. *Adv. Drug Delivery Rev.* **2001**, *47*, 65–81.

[99] Sousa, F.; Mandal, S.; Garrovo, C.; Astolfo, A.; Bonificiacio, A.; Latawiec, D.; Menk, R.; Arfelli, F.; Huewel, S.; Legname, G.; Galla, H.; Krol, S. *Nanoscale* **2010**, *2*, 2826–2834.

[100] Cheng, Y.; Dai, Q.; Morshed, R.; Fan, X.; Wegscheid, M.; Wainwright, D.; Han, Y.; Zhang, L.; Auffinger, B.; Tobias, A.; Rincón, E.; Thaci, B.; Ahmed, A.; Warnke, P.; He, C.; Lesniak, M. *Small* **2014**, *10*, 5137–5150.

[101] Velasco-Aguirre, C.; Morales, F.; Gallardo-Toledo, E.; Guerrero, S.; Giralt, E.; Araya, E.; Kogan, M. *Int. J. Nanomedicine* **2015**, *10*, 4919–4936.

[102] Prades, R.; Guerrero, S.; Araya, E.; Molina, C.; Salas, E.; Zurita, E.; Selva, J.; Egea, G.; López-Iglesias, C.; Teixidó, M.; Kogan, M.; Giralt, E. *Biomaterials* **2012**, *33*, 7194–7205.

[103] Mathis, C.; Lopresti, B.; Klunk, W. *Nucl. Med. Biol.* **2007**, *34*, 809–822.

[104] Eckroat, T.; Mayhoub, A.; Garneau-Tsodikova, S. *Belstein J. Org. Chem.* **2013**, *9*, 1012–1044.

[105] Khurana, R.; Uversky, V.; Nielsen, L.; Fink, A. *J. Biol. Chem.* **2001**, *276*, 22715–22721.

[106] Frid, P.; Anisimov, S.; Popovic, N. *Brain Res. Rev.* **2007**, *53*, 135–160.

[107] Klunk, W.; Bacskai, B.; Mathis, C.; Kajdasz, S.; McLellan, M.; Frosch, M.; Debnath, M.; Holt, D.; Wang, Y.; Hyman, B. *J. Neuropathol. Exp. Neurol.* **2002**, *61*, 797–805.

[108] LeVine, H. *Protein Science*, **1993**, *2*, 404–410.

[109] Nielsen, L.; Khurana, R.; Coats, A.; Frokjaer, S.; Brange, J.; Vyas, S.; Uversky, V.; Fink, A. *Biochemistry* **2001**, *40*, 6036–6046.

[110] Ban, T.; Hamada, D.; Hasegawa, K.; Naiki, H.; Goto, Y. *Biol. Chem.* **2003**, *278*, 16462–16465.

[111] Ban, T.; Hoshino, M.; Takahashi, S.; Hamada, D.; Hasegawa, K.; Naiki, H.; Goto, Y. *J. Mol. Biol.* **2004**, *344*, 757–767.

[112] Irizarry, M.; Hyman, B. *J. Neuropathol. Exp. Neurol.* **2001**, *60*, 923–928.

[113] Frisardi, V.; Solfrizzi, V.; Imbimbo, B.; Capurso, C.; D'Introno, A.; Colacicco, A.; Vendemiale, G.; Seripa, D.; Pilotto, A.; Capurso, A.; Panza, F. *Curr. Alzheimer Res.* **2010**, *7*, 40–55.

[114] Emilien, G.; Beyreuther, K.; Masters, C.; Maloteaux, J. *Arch. Neurol.* **2000**, *57*, 454–459.

[115] Selkoe, D.; Hardy, J. *EMBO Mol. Med.* **2016**, *8*, 595–608.

[116] Bachurin, S. *Med. Res. Rev.* **2003**, *23*, 48–88.

[117] Hong, S.; Beja-Glasser, V.; Nfonoyim, B.; Frouin, A.; Li, S.; Ramakrishnan, S.; Merry, K.; Shi, Q.; Rosenthal, A.; Barres, B.; Lemere, C.; Selkoe, D.; Stevens, B. *Science* **2016**, *352*, 712–716.

[118] Choi, J.; Gao, J.; Kim, J.; Hong, C.; Kim, J.; Tontonoz, P. *Sci. Transl. Med.* **2015**, *7*, 314ra184/1–314ra184/12.

[119] Wisniewski, T.; Goñi, F. *Neuron* **2015**, *85*, 1162–1176.

[120] Bacskai, B.; Kajdasz, S.; Christie, R.; Carter, C.; Games, D.; Seubert, P.; Schenk, D.; Hyman, B. *Nat. Med.* **2001**, *7*, 369–372.

[121] Adlard, P. A.; Cherny, R. A.; Finkelstein, D. I.; Gautier, E.; Robb, E.; Cortes, M.; Volitakis, I.; Liu, X.; Smith, J. P.; Perez, K.; Laughton, K.; Li, Q.; Charman, S.; Nicolazzo, J.; Wilkins, S.; Deleva, K.; Lynch, T.; Kok, G.; Ritchie, C.; Tanzi, R.; Cappai, R.; Masters, C.; Barnham, K.; Bush, A. *Neuron* **2008**, *59*, 43–55.

[122] Bush, A. *J. Alzheimers Dis.* **2008**, *15*, 223–240.

[123] Nguyen, M.; Vendier, L.; Stigliani, J.; Meunier, B.; Robert, A. *Eur. J. Inorg. Chem.* **2017**, 600–608.

[124] Ibach, B.; Haen, E.; Marienhagen, J.; Hajak, G. *Pharmacopsychiatry* **2005**, *38*, 178–179.

[125] Bareggi, S.; Cornelli, U. *CNS Neurosci. Ther.* **2012**, *18*, 41–46.

[126] Ritchie, C.; Bush, A.; Mackinnon, A.; Macfarlane, S.; Mastwyk, M.; MacGregor, L.; Kiers, L.; Cherny, R.; Li, Q.; Tammer, A.; Carrington, D.; Mavros, C.; Volitakis, I.; Xilinas, M.; Ames, D.; Davis, S.; Beyreuther, K.; Tanzi, R.; Masters, C. *Arch. Neurol.* **2003**, *60*, 1685–1691.

[127] Lannfelt, L.; Blennow, K.; Zetterberg, H.; Batsman, S.; Ames, D.; Harrison, J.; Masters, C.; Targum, S.; Bush, A.; Murdoch, R.; Wilson, J.; Ritchie, C. *Lancet Neurol.* **2008**, *7*, 779–786.

[128] Faux, N.; Ritchie, C.; Gunn, A.; Rembach, A.; Tsatsanis, A.; Bedo, J.; Harrison, J.; Lannfelt, L.; Blennow, K.; Zetterberg, H.; Ingelsson, M.; Masters, C.; Tanzi, R.; Cummings, J.; Herd, C.; Bush, A. *J. Alzheimers Dis.* **2010**, *20*, 509–516.

[129] Villemagne, V.; Rowe, C.; Barnham, K.; Cherny, R.; Woodward, M.; Bozinosvski, S.; Salvado, O.; Bourgeat, P.; Perez, K.; Fowler, C.; Rembach, A.; Maruff, P.; Ritchie, C.; Tanzi, R.; Masters, C. *Alzheimers Dement. (N Y)* **2017**, *3*, 622–635.

[130] Angus, D.; Herd, C.; Stone, C.; Stout, J.; Wieler, M.; Reilmann, R.; Ritchie, C.; Dorsey, E.; Helles, K.; Kayson, E.; Oakes, D.; Rosas, H.; Vaughan, C.; Panegyres, P.; Ames, D.; Goh, A.; Agarwal, P.; Churchyard, A.; Murathodizic, M.; Chua, P.; Germaine, D.; Lim, D.; Mack, H.; Loy, C.; Griffith, J.; Mitchell, P.; Corey-Bloom, J.; Gluhm, S.; Goldstein, J.; Levi, L.; Margolis, R.; Yoritomo, N.; Janicki, S.; Marder, K.; Clouse, R.; Singer, C.; Moore, H.; Padron, N.; Kostyk, S.; Daley, A.; Segro, V.; Kumar, R.; Anderson, K.; Drazinic, C.; Hennig, B.; Nance, M.; Molho, E.; Criswell, S.; LeDoux, M.; Guyot, S.; Iannaccone, A.; Jennings, B.; Leavitt, B.; Feigin, A.; Evans, S.; Wray, S.; Casaceli, C.; Orme, C.; Gao, S.; Watts, A.; Baker, K.; Labuschagne, I.; El-Dairi, M.; Fekrat, S.; Hersch, S.; Moscovitch-Lopatin, M.; Tanzi, R.; Targum, S. *Lancet Neurol.* **2015**, *14*, 39–47.

[131] Matlack, K.; Tardiff, D.; Narayan, P.; Hamamichi, S.; Caldwell, K.; Caldwell, G.; Lindquist, S. *Proc. Natl. Acad. Sci. USA* **2014**, *111*, 4013–4018.

[132] Ryan, T.; Roberts, B.; McColl, G.; Hare, D.; Doble, P.; Li, Q.; Lind, M.; Roberts, A.; Mertens, H.; Kirby, N.; Pham, C.; Hinds, M.; Adlard, P.; Barnham, K.; Curtain, C.; Masters, C. *J. Neurosci.* **2015**, *35*, 2871–2884.

[133] Kozlowski, H.; Bal, W.; Dyba, M.; Kowalik-Jankowska, T. *Coord. Chem. Rev.* **1999**, *184*, 319–346.

[134] Matera, A.; Brasuń, J.; Cebrat, M.; Świątek-Kozłowska, J. *Polyhedron* **2008**, *27*, 1539–1555.

[135] Mena, S.; Mirats, A.; Caballero, A.; Guirado, G.; Barrios, L.; Teat, S.; Rodriguez-Santiago, L.; Sodupe, M.; Gamez, P. *Chem. Eur. J.* **2018**, *24*, 5153–5162.

[136] Borges, F.; Roleira, F.; Milhazes, N.; Santana, L.; Uriarte, E. *Curr. Med. Chem.* **2005**, *12*, 887–916.

[137] Kontogiorgis, C.; Xu, Y.; Hadjipavlou-Litina, D.; Luo, Y. *Free Radic. Res.* **2007**, *41*, 1168–1180.

[138] Fylaktakidou, K.; Hadjipavlou-Litina, D.; Litinas, K.; Nicolaides, D. *Curr. Pharm. Des.* **2004**, *10*, 3813–3833.

[139] Lacy, A.; O'Kennedy, R. *Curr. Pharm. Des.* **2004**, *10*, 3797–3811.

[140] Yu, D.; Suzuki, M.; Xie, L.; Morris-Natschke, S.; Lee, K. *Med. Res. Rev.* **2003**, *23*, 322–345.

[141] Cisse, L.; Djande, A.; Capo-Chichi, M.; Delatre, F.; Saba, A.; Tine, A.; Aaron, J. *Spectrochim. Acta A* **2011**, *79*, 428–436.

[142] Bai, Y.; Zhang, F.; Ying, J.; Wu, Y. *J. Mol. Struct.* **2015**, *1089*, 53–58.

[143] Suzuki, K.; Ubukata, T.; Yokoyama, Y. *Chem. Commun.* **2012**, *48*, 765–767.

[144] Loving, G.; Imperiali, B. *J. Am. Chem. Soc.* **2008**, *130*, 13630–13638.

[145] Korhonen, H.; Pihlanto, A. *Int. Dairy J.* **2006**, *16*, 945–960.

[146] Craik, D.; Fairlie, D.; Liras, S.; Price, D. *Chem. Biol. Drug. Des.* **2013**, *81*, 136–147.

[147] Kaspar, A.; Reichert, J. *Drug Discov. Today* **2013**, *18*, 807–817.

[148] Elsadek, B.; Kratz, F. *J. Control. Release* **2012**, *157*, 4–28.

[149] Fani, M.; Maecke, H.; Okarvi, S. *Theranostics* **2012**, *2*, 481–501.

[150] Cui, H.; Webber, M.; Stupp, S. *Biopolymers* **2010**, *94*, 1–18.

[151] Gorouhi, F.; Maibach, H. *Int. J. Cosmet. Sci.* **2009**, *31*, 327–345.

[152] Udenigwe, C.; Howard, A. *Food Res. Int.* **2013**, *54*, 1021–1032.

[153] Kent, S. *Chem. Soc. Rev.* **2009**, *38*, 338–351.

[154] Mitchell, A. *Biopolymers* **2008**, *90*, 175–184.

[155] Albericio, F. *Curr. Opin. Chem. Biol.* **2004**, *8*, 211–221.

[156] Isidro-Llobet, A.; Álvarez, M.; Albericio, F. *Chem. Rev.* **2009**, *109*, 2455–2504.

[157] Cherkupally, P.; Acosta, G.; Ramesh, S.; De la Torre, B.; Govender, T.; Kruger, H.; Albericio, F. *Amino Acids* **2014**, *46*, 1827–1838.

[158] Palasek, S.; Cox, Z.; Collins, J. *J. Pept. Sci.* **2007**, *13*, 143–148.

[159] Gracia, C.; Isidro-Llobet, A.; Cruz, L.; Acosta, G.; Álvarez, M.; Cuevas, C.; Giralt, E.; Albericio, F. *J. Org. Chem.* **2006**, *71*, 7196–7204.

[160] Paradís-Bas, M.; Tulla-Puche, J.; Albericio, F. *Chem. Soc. Rev.* **2016**, *45*, 631–654.

[161] Muttenthaler, M.; Albericio, F.; Dawson, P. *Nat. Protoc.* **2015**, *10*, 1067–1083.

[162] Harris, P.; Brimble, M. *Biopolymers* **2013**, *100*, 356–365.

[163] Coin, I.; Beyermann M.; Bienert, M. *Nat. Protoc.* **2007**, *2*, 3247–3256.

[164] Hoekstra, W. *Curr. Med. Chem.* **2001**, *8*, 715–719.

[165] Bonkowski, B.; Wieczorek, J.; Patel, M.; Craig, C.; Gravelin, A.; Boncher, T. *Mod. Chem. Appl.* **2013**, *1*, 1–4.

[166] Rink, H. *Tetrahedron Lett.* **1987**, *28*, 3787–3890.

[167] Bernatowicz, M.; Daniels, S.; Köster, H. *Tetrahedron Lett.* **1989**, *30*, 4645–4648.

[168] Sieber, P. *Tetrahedron Lett.* **1987**, *28*, 2107–2110.

[169] Amblard, M.; Fehrentz, J.; Martinez, J.; Subra, G. *Mol. Biotechnol.* **2006**, *33*, 239–254.

[170] Coin, I.; Dölling, R.; Krause, E.; Bienert, M.; Beyermann, M.; Sferdean, C.; Carpino, L. *J. Org. Chem.* **2006**, *71*, 6171–6177.

[171] Subirós-Funosas, R.; Prohens, R.; Barbas, R.; El-Faham, A.; Albericio, F. *Chem. Eur. J.* **2009**, *15*, 9394–9403.

[172] Pires, D.; Bemquerer, M.; do Nascimento, C. *Int. J. Pept. Res. Ther.* **2014**, *20*, 53–69.

[173] El-Faham, A.; Subirós-Funosas, R.; Prohens, R.; Albericio, F. *Chem. Eur. J.* **2009**, *15*, 9404–9416.

[174] Hood, C.; Fuentes, G.; Patel, H.; Page, K.; Menakuru, M.; Park, J. *J. Pept. Sci.* **2008**, *14*, 97–101.

[175] El-Faham, A.; Albericio, F. *Chem. Rev.* **2011**, *111*, 6557–6602.

[176] Li, P.; Xu, J. *Tetrahedron* **2000**, *56*, 8119–81331.

[177] Katritzky, A.; Narindoshvili, T.; Angrish, P. *Synthesis* **2008**, *13*, 2013–2022.

[178] Weber, P.; Bader, J.; Folkers, G.; Beck-Sickinger, A. *Bioorg. Med. Chem. Lett.* **1998**, *8*, 597–600.

[179] Kollár, J.; Hrdlovič, P.; Chmela, Š.; Sarakha, M.; Guyot, G. *J. Photochem. Photobiol. A* **2005**, *170*, 151–159.

[180] Dessolin, M.; Guillerez, M.; Thieriet, N.; Guibé, F.; Loffet, A. *Tetrahedron Lett.* **1995**, *36*, 5741–5744.

[181] Fernández-Forner, D.; Casals, G., Navarro, E.; Ryder, H.; Albericio, F. *Tetrahedron Lett.* **2001**, *42*, 4471–4474.

[182] Genet, J.; Savignac, M. *J. Organomet. Chem.* **1999**, *576*, 305–317.

[183] Das, M.; Mishra, D.; Dhak, P.; Gupta, S.; Maiti, T.; Basak, A.; Pramanik, P. *Small* **2009**, *5*, 2883–2893.

[184] Yang, H.; Qin, C.; Yu, C.; Lu, Y.; Zhang, H.; Xue, F.; Wu, D.; Zhou, Z.; Yang, S. *Adv. Funct. Mater.* **2014**, *24*, 1738–1747.

[185] Wang, H.; Mao, D.; Wang, Y.; Wang, K.; Yi, X.; Kong, D.; Yang, Z.; Liu, Q.; Ding, D. *Sci. Rep.* **2015**, *5*, 16680/1–16680/10.

[186] Schröder, T.; Schmitz, K.; Niemeier, N.; Balaban, T.; Krug, H.; Schepers, U.; Bräse, S. *Bioconjugate Chem.* **2007**, *18*, 342–354.

[187] Malanga, M.; Jicsinszky. L.; Fenyvesi, É. *J. Drug Del. Sci. Tech.* **2012**, *22*, 260–265.

[188] Demchenko, A. *J. Fluoresc.* **2010**, *20*, 1099–1128.

[189] Quang, D.; Kim, J. *Chem. Rev.* **2010**, *110*, 6280–6301.

[190] Kroneck, P.; Vortisch, V.; Hemmerich, P. *Eur. J. Biochem.* **1980**, *109*, 603–612.

[191] Harford, C.; Sarkar, B. *Acc. Chem. Res.* **1997**, *30*, 123–130.

[192] Trapaidze, A.; Hureau, C.; Bal, W.; Winterhalter, M.; Faller, P. *J. Biol. Inorg. Chem.* **2012**, *17*, 37–47.

[193] Hureau, C.; Eury, H.; Guillot, R.; Bijani, C.; Sayen, S.; Solari, P.; Guillon, E.; Faller, P.; Dorlet, P. *Chem. Eur. J.* **2011**, *17*, 10151–10160.

[194] Taki, M.; Iyoshi, S.; Ojida, A.; Hamachi, I.; Yamamoto, Y. *J. Am. Chem. Soc.* **2010**, *132*, 5938–5939.

[195] Yuan, L.; Lin, W.; Chen, B.; Xie, Y. *Org. Lett.* **2012**, *14*, 432–435.

[196] Yin, S.; Leen, V.; Van Snick, S.; Boens, N.; Dehaen, W. *Chem. Commun.* **2010**, *46*, 6329–6331.

[197] Coskun, A.; Akkaya, E. *J. Am. Chem. Soc.* **2005**, *127*, 10464–10465.

[198] Qu, Y.; Hua, J.; Tian, H. *Org. Lett.* **2010**, *12*, 3320–3323.

[199] Jisha, V.; Thomas, A.; Ramaiah, D. *J. Org. Chem.* **2009**, *74*, 6667–6673.

[200] Min, H.; Hyun, J.; Yoon, S.; Park, N.; Jong, S. *Org. Lett.* **2008**, *10*, 213–216.

[201] Lin, W.; Yuan, L.; Tan, W.; Feng, J.; Long, L. *Chem. Eur. J.* **2009**, *15*, 1030–1035.

[202] Sapsford, K.; Berti, L.; Medintz, I. *Angew. Chem. Int. Ed.* **2006**, *45*, 4562–4588.

[203] Suresh, M.; Mishra, S.; Mishra, S.; Suresh, E.; Mandal, A.; Shrivastav, A.; Das, A. *Org. Lett.* **2009**, *11*, 2740–2743.

[204] Coskun, A.; Akkaya, E. *J. Am. Chem. Soc.* **2006**, *128*, 14474–14475.

[205] Long, L.; Lin, W.; Chen, B.; Gao, W.; Yuan, L. *Chem. Commun.* **2011**, *47*, 893–895.

[206] Zhang, X.; Xiao, Y.; Qian, X. *Angew. Chem. Int. Ed.* **2008**, *47*, 8025–8029.

[207] Jares-Erijman, E.; Jovin, T. *Nat. Biotechnol.* **2003**, *21*, 1387–1395.

[208] Rudat, B.; Birtalan, E.; Vollrath, S.; Fritz, D.; Kölmel, D.; Nieger, M.; Schepers, U.; Müllen, K.; Eisler, H.; Lemmer, U.; Bräse, S. *Eur. J. Med. Chem.* **2011**, *46*, 4457–4465.

[209] Wang, S.; Chen, Y.; Chou, S. *Biochim. Biophys. Acta-Mol. Basis Dis.* **2005**, *1741*, 307–313.

[210] Caballero, A.; Terol-Ordaz, L.; Espargaró, A.; Vázquez, G.; Nicolás, E.; Sabaté, R.; Gamez, P. *Chem. Eur. J.* **2016**, *22*, 7268–7280.

[211] Sigel, H.; Martin, R. *Chem. Rev.* **1982**, *82*, 385–426.

[212] Prenesti, E.; Daniele, P.; Berto, S.; Toso, S. *Polyhedron* **2006**, *25*, 2815–2823.

[213] Myari, A.; Malandrinos, G.; Deligiannakis, Y.; Plakatouras, J.; Hadjiliadis, N.; Nagy, Z.; Sòvágó, I. *J. Inorg. Biochem.* **2001**, *85*, 253–261.

[214] Szyrwiel, Ł.; Pap, J.; Szczukowski, Ł.; Kerner, Z.; Brasuń, J.; Setner, B.; Szewczuk, Z.; Malinka, W. *RSC Adv.* **2015**, *5*, 56922–56931.

[215] Błaszak, M.; Jankowska, E.; Kowalik-Jankowska, T. *Polyhedron* **2014**, *68*, 379–389.

[216] Fawcett, T.; Bernarducci, E.; Krogh-Jespersen, K.; Schugar, H. *J. Am. Chem. Soc.* **1980**, *102*, 2598–2604.

[217] Kowalik-Jankowska, T.; Jezierska, J.; Kuczer, M. *Dalton Trans.* **2010**, *39*, 4117–4125.

[218] Mlynarz, P.; Valensin, D.; Kozlowski, H.; Kowalik-Jankowska, T.; Otlewski, J.; Valensin, G.; Gaggelli, N. *J. Chem. Soc. Dalton Trans.* **2001**, 645–652.

[219] Jensen, M.; Hass, M.; Hansen, D.; Led, J. *Cell. Mol. Life Sci.* **2007**, *64*, 1085–1104.

[220] Gaggelli, E.; D'Amelio, N.; Valensin, D.; Valensin, G. *Magn. Reson. Chem.* **2003**, *41*, 877–883.

[221] Pap, J.; Kripli, B.; Bányai, V.; Giorgi, M.; Korecz, L.; Gajda, T.; Árus, D.; Kaizer, J.; Speier, G. *Inorg. Chim. Acta* **2011**, *376*, 158–169.

[222] Peisach, J.; Blumberg, W. *Arch. Biochem. Biophys.* **1974**, *165*, 691–708.

[223] Zink, J.; Drago, R. *J. Am. Chem. Soc.* **1972**, *94*, 4550–4554.

[224] Mital, M.; Wezynfeld, N.; Frączyk, T.; Wiloch, M.; Wawrzyniak, U.; Bonna, A.; Tumpach, C.; Barnham, K.; Haigh, C.; Bal, W.; Drew, S. *Angew. Chem. Int. Ed.* **2015**, *54*, 10460–10464.

[225] Wezynfeld, N.; Stefaniak, E.; Stachucy, K.; Drozd, A.; Płonka, D.; Drew, S.; Krężel, A.; Bal, W. *Angew. Chem. Int. Ed.* **2016**, *55*, 8235–8238.

[226] Mital, M.; Zawisza, I.; Wiloch, M.; Wawrzyniak, U.; Kenche, V.; Wróblewski, W.; Bal, W.; Drew, S. *Inorg. Chem* **2016**, *55*, 7317–7319.

[227] Geddes, C. *Meas. Sci. Technol.* **2001**, *12*, R53–R88.

[228] Tõugu, V.; Karafin, A.; Palumaa, P. *J. Neurochem.* **2008**, *104*, 1249–1259.

[229] Sokołowska, M.; Bal, W. *J. Inorg. Biochem.* **2005**, *99*, 1653–1660.

[230] Čudić, P.; Žinić, M.; Tomišić, V.; Simeon, V.; Vigneron, J.; Lehn, J. *J. Chem. Soc. Chem. Commun.* **1995**, 1073–1075.

[231] Alies, B.; Renaglia, E.; Rózga, M.; Bal, W.; Faller, P.; Hureau, C. *Anal. Chem.* **2013**, *85*, 1501–1508.

[232] De Ricco, R.; Valensin, D.; Dell'Acqua, S.; Casella, L.; Hureau, C.; Faller, P. *ChemBioChem* **2015**, *16*, 2319–2328.

[233] Abdelhamid, R.; Obara, Y.; Uchida, Y.; Kohzuma, T.; Dooley, D.; Brown, D.; Hori, H. *J. Biol. Inorg. Chem.* **2007**, *12*, 165–173.

[234] Guilloreau, L.; Combalbert, S.; Sournia-Saquet, A.; Mazarguil, H.; Faller, P. *ChemBioChem* **2007**, *8*, 1317–1325.

[235] Queval, G.; Noctor, G. *Anal. Biochem.* **2007**, *363*, 58–69.

[236] Witkowska, D.; Bielinska, S.; Kamysz, W.; Kozlowski, H. *J. Inorg. Biochem.* **2011**, *105*, 208–214.

[237] Sanna, D.; Micera, G.; Kállay, C.; Rigó, V.; Sóvágó, I. *Dalton Trans.* **2004**, 2702–2707.

[238] Bóka, B.; Myari, A.; Sóvágó, I.; Hadjiliadis, N. *J. Inorg. Biochem.* **2004**, *98*, 113–122.

[239] Liu, D.; Tangpeerachaikul, A.; Selvaraj, R.; Taylor, M.; Fox, J.; Ting, A. *J. Am. Chem. Soc.* **2012**, *134*, 792–795.

[240] Lambert, T.; Andrews, N.; Gerung, H.; Boyle, T.; Oliver, J.; Wilson, B.; Han, S. *Small* **2007**, *3*, 691–699.

[241] Mills, J.; Needham, D. *Biochim. Biophys. Acta* **2005**, *1716*, 77–96.

[242] Hollmann, A.; Delfederico, L.; Glikmann, G.; De Antoni, G.; Semorile, L.; Disalvo, E. *Biochim. Biophys. Acta* **2007**, *1768*, 393–400.

[243] Aschi, M.; D'Archivio, A.; Fontana, A.; Formiglio, A. *J. Org. Chem.* **2008**, *73*, 3411–3417.

[244] Arduini, M.; Mancin, F.; Tecilla, P.; Tonellato, U. *Langmuir* **2007**, *23*, 8632–8636.

[245] Hilderbrand, S.; Kelly, K.; Niedre, M.; Weissleder, R. *Bioconjug. Chem.* **2008**, *19*, 1635–1639.

[246] Cordes, D.; Miller, A.; Gamsey, S.; Singaram, B. *Anal. Bioanal. Chem.* **2007**, *387*, 2767–2773.

[247] Acosta, M.; Ymele-Leki, P.; Kostov, Y.; Leach, J. *Biomaterials* **2009**, *30*, 3068–3074.

[248] Opazo, C.; Luza, S.; Villemagne, V.; Volitakis, I.; Rowe, C.; Barnham, K.; Strozyk, D.; Masters, C.; Cherny, R.; Bush, A. *Aging Cell* **2006**, *5*, 69–79.

[249] Jin, Y.; Lewis, M.; Gokhale, N.; Long, E.; Cowan, J. *J. Am. Chem. Soc.* **2007**, *129*, 8353–8361.

[250] Kowalik-Jankowska, T.; Ruta, M.; Wiśniewska, K.; Łankiewicz, L.; Dyba, M. *J. Inorg. Biochem.* **2004**, *98*, 940–950.

[251] Kato, Y.; Kitamoto, N.; Kawai, Y.; Osawa, T. *Free Radic. Biol. Med.* **2001**, *31*, 624–632.

[252] Ali, F.; Barnham, K.; Barrow, C.; Separovic, F. *J. Inorg. Biochem.* **2004**, *98* , 173–184.

[253] Okeley, N.; van der Donk, W. *Chem. Biol.* **2000**, *7*, R159–R171.

[254] Michon, T.; Wang, W.; Ferrasson, E.; Guéguen, J. *Biotechnol. Bioeng.* **1999**, *63*, 449–458.

[255] Yoburn, J.; Tian, W.; Brower, J.; Nowick, J.; Glabe, C.; Van Vranken, D. *Chem. Res. Toxicol.* **2003**, *16*, 531–535.

[256] Smith, D.; Cappai, R.; Barnham, K. *Biochim. Biophys. Acta* **2007**, *1768*, 1976–1990.

[257] Leeuwenburgh, C.; Rasmussen, J.; Hsu, F.; Mueller, D.; Pennathur, S.; Heinecke, J. *J. Biol. Chem.* **1997**, *272*, 3520–3526.

[258] Souza, J.; Giasson, B.; Chen, Q.; Lee, V.; Ischiropoulos, H. *J. Biol. Chem.* **2000**, *275*, 18344–18349.

[259] Pennathur, S.; Jackson-Lewis, V.; Przedborski, S.; Heinecke, J. *J. Biol. Chem.* **1999**, *274*, 34621–34628.

[260] Krishnan, S.; Chi, E.; Wood, S.; Kendrick, B.; Li, C.; Garzon-Rodriguez, W.; Wypych, J.; Randolph, T.; Narhi, L.; Biere, A.; Citron, M.; Carpenter, J. *Biochemistry* **2003**, *42*, 829–837.

[261] Atwood, C.; Perry, G.; Zeng, H.; Kato, Y.; Jones, W.; Ling, K.; Huang, X.; Moir, R.; Wang, D.; Sayre, L.; Smith, M.; Chen, S.; Bush, A. *Biochemistry* **2004**, *43*, 560–568.

[262] Vázquez de la Torre, A.; Gay, M.; Vilaprinyó-Pascual, S.; Mazzucato, R.; Serra-Batiste, M.; Vilaseca, M.; Carulla, N. *Anal. Chem.* **2018**, *90*, 4552–4560.

[263] Lee, D.; Hwang, S.; Choi, J.; Ahn, I.; Lee, C. *Process Biochem.* **2008**, *43*, 999–1003.

[264] Skaff, O.; Jolliffe, K.; Hutton, C. *J. Org. Chem.* **2005**, *70* , 7353–7363.

[265] Oudgenoeg, G.; Hilhorst, R.; Piersma, S.; Boeriu, C.; Gruppen, H.; Hessing, M.; Voragen, A.; Laane, C. *J. Agric. Food Chem.* **2001**, *49*, 2503–2510.

[266] Dunford, H.; Marquez, L. *J. Biol. Chem.* **1995**, *270* , 30434–30440.

[267] Witting, P.; Mauk, A.; Lay, P. *Biochemistry* **2002**, *41*, 11495–11503.

[268] González-Sánchez, M.; García-Carmona, F.; Macià, H.; Valero, E. *Arch. Biochem. Biophys.* **2011**, *516*, 10–20.

[269] Giulivi, C.; Davies, K. *J. Biol. Chem.* **2001**, *276* , 24129–24136.

[270] Michon, T.; Chenu, M.; Kellershon, N.; Desmadril, M.; Guéguen, J. *Biochemistry* **1997**, *36*, 8504–8513.

[271] Wang, W.; Noël, S.; Desmadril, M.; Guéguen, J.; Michon, T. *Biochem. J.* **1999**, *340*, 329–336.

[272] Mukherjee, S.; Kapp, E.; Lothian, A.; Roberts, A.; Vasil'ev, Y.; Boughton, B.; Barnham, K.; Kok, W.; Hutton, C.; Masters, C.; Bush, A.; Beckman, J.; Dey, S.; Roberts, B. *Anal. Chem.* **2017**, *89*, 6136–6145.

[273] Proshlyakov, D. *Biochim. Biophys. Acta* **2004**, *1655*, 282–289.

[274] Kok, W.; Cottam, J.; Ciccotosto, G.; Miles, L.; Karas, J.; Scanlon, D.; Roberts, B.; Parker, M.; Cappai, R.; Barnham, K.; Hutton, C. *Chem. Sci.* **2013**, *4*, 4449–4454.

[275] Ballabh, P.; Braun, A.; Nedergaard, M. *Neurobiol. Dis.* **2004**, *16*, 1–13.

[276] Zlokovic, B. *Nat. Rev. Neurosci.* **2011**, *12*, 723–738.

[277] Cushing, B.; Kolesnichenko, V.; O'Connor, C. *Chem. Rev.* **2004**, *104*, 3893–3946.

[278] Eustis, S.; El-Sayed, M. *Chem. Soc. Rev.* **2006**, *35*, 209–217.

[279] Jain, P.; Huang, X.; El-Sayed, I.; El-Sayed, M. *Acc. Chem. Res.* **2008**, *41*, 1578–1586.

[280] Sonavane, G.; Tomoda, K.; Makino, K. *Colloids Surf. B* **2008**, *66*, 274–280.

[281] De Jong, W.; Hagens, W.; Krystek, P.; Burger, M.; Sips, A.; Geertsma, R. *Biomaterials* **2008**, *29*, 1912–1919.

[282] Arnida; Janát-Amsbury, M.; Ray, A.; Peterson, C.; Ghandehari, H. *Eur. J. Pharm. Biopharm.* **2011**, *77*, 417–423.

[283] Schleh, C.; Semmler-Behnke, M.; Lipka, J.; Wenk, A.; Hirn, S.; Schäffler, M.; Schmid, G.; Simon, U.; Kreyling, W. *Nanotoxicology* **2012**, *6*, 36–46.

[284] Daniel, M.; Astruc, D. *Chem. Rev.* **2004**, *104*, 293–346.

[285] Hauser, E. *J. Chem. Educ.* **1952**, *29*, 456–458.

[286] Dreaden, E.; Alkilany, A.; Huang, X.; Murphy, C.; El-Sayed, M. *Chem. Soc. Rev.* **2012**, *41*, 2740–2779.

[287] Burda, C.; Chen, X.; Narayanan, R.; El-Sayed, M. *Chem. Rev.* **2005**, *105*, 1025–1102.

[288] Corma, A.; Garcia, H. *Chem. Soc. Rev.* **2008**, *37*, 2096–2126.

[289] Haruta, M.; Daté, M. *Appl. Catal., A* **2001**, *222*, 427–437.

[290] Homola, J. *Chem. Rev.* **2008**, *108*, 462–493.

[291] Yin, Y.; Alivisatos, A. *Nature* **2005**, *437*, 664–670.

[292] Sperling, R.; Parak, W. *Phil. Trans. R. Soc. A* **2010**, *368*, 1333–1383.

[293] Tao, A.; Habas, S.; Yang, P. *Small* **2008**, *4*, 310–325.

[294] Murphy, C.; Sau, T.; Gole, A.; Orendorff, C.; Gao, J.; Gou, L.; Hunyadi, S.; Li, T. *J. Phys. Chem. B* **2005**, *109*, 13857–13870.

[295] Glotzer, S.; Solomon, M. *Nat. Mater.* **2007**, *6*, 557–562.

[296] Huang, X.; El-Sayed, I.; Qian, W.; El-Sayed, M. *Nano Lett.* **2007**, *7*, 1591–1597.

[297] Huang, X.; El-Sayed, I.; Qian, W.; El-Sayed, M. *J. Am. Chem. Soc.* **2006**, *128*, 2115–2120.

[298] Zhang, G.; Wang, D.; Möhwald, H. *Angew. Chem. Int. ed.* **2005**, *44*, 7767–7770.

[299] Giljohann, D.; Seferos, D.; Daniel, W.; Massich, M.; Patel, P.; Mirkin, C. *Angew. Chem. Int. Ed.* **2010**, *49*, 3280–3294.

[300] Brown, S.; Nativo, P.; Smith, J.; Stirling, D.; Edwards, P.; Venugopal, B.; Flint, D.; Plumb, J.; Graham, D.; Wheate, N. *J. Am. Chem. Soc.* **2010**, *132*, 4678–4684.

[301] Bowman, M.; Ballard, T.; Ackerson, C.; Feldheim, D.; Margolis, D.; Melander, C. *J. Am. Chem. Soc.* **2008**, *130*, 6896–6897.

[302] Ghosh, P.; Han, G.; De, M.; Kim, C.; Rotello, V. *Adv. Drug Delivery Rev.* **2008**, *60*, 1307–1315.

[303] Hong, R.; Han, G.; Fernández, J.; Kim, B.; Forbes, N.; Rotello, V. *J. Am. Chem. Soc.* **2006**, *128*, 1078–1079.

[304] Han, G.; You, C.; Kim, B.; Turingan, R.; Forbes, N.; Martin, C.; Rotello, V. *Angew. Chem. Int. Ed.* **2006**, *45*, 3165–3169.

[305] Lin, J.; Zhang, H.; Chen, Z.; Zheng, Y. *ACS Nano* **2010**, *4*, 5421–5429.

[306] Oh, E.; Delehanty, J.; Sapsford, K.; Susumu, K.; Goswami, R.; Blanco-Canosa, J.; Dawson, P.; Granek, J.; Shoff, M.; Zhang, Q.; Goering, P.; Huston, A.; Medintz, I. *ACS Nano* **2011**, *5*, 6434–6448.

[307] Baban, D.; Seymour, L. *Adv. Drug Delivery Rev.* **1998**, *34*, 109–119.

[308] Zlokovic, B. *Neuron* **2008**, *57*, 178–201.

[309] Huber, J.; Egleton, R.; Davis, T. *Trends Neurosci.* **2001**, *24*, 719–725.

[310] Tiwari, P.; Eroglu, E.; Bawage, S.; Vig, K.; Miller, M.; Pillai, S.; Dennis, V.; Singh, S. *Biomaterials* **2014**, *35*, 9484–9494.

[311] Boisselier, E.; Astruc, D. *Chem. Soc. Rev.* **2009**, *38*, 1759–1782.

[312] Laurent, S.; Forge, D.; Port, M.; Roch, A.; Robic, C.; Elst, L.; Muller, R. *Chem. Rev.* **2008**, *108*, 2064–2110.

[313] Ortega-Vinuesa, J.; Martin-Rodriguez, A.; Hidalgo-Alvarez, R. *J. Colloid Interface Sci.* **1996**, *184*, 259–267.

[314] Kobayashi, M.; Skarba, M.; Galletto, P.; Cakara, D.; Borkovec, M. *J. Colloid Interface Sci.* **2005**, *292*, 139–147.

[315] Mintzer, M.; Grinstaff, M. *Chem. Soc. Rev.* **2011**, *40*, 173–190.

[316] Ryan, S.; Mantovani, G.; Wang, X.; Haddleton, D.; Brayden, D. *Expert Opin. Drug Deliv.* **2008**, *5*, 371–383.

[317] Chen, H.; Paholak, H.; Ito, M.; Sansanaphongpricha, K.; Qian, W.; Che, Y.; Sun, D. *Nanotechnology* **2013**, *24*, 355101–355110.

[318] Qian, X.; Peng, X.; Ansari, D.; Yin-Goen, Q.; Chen, G.; Shin, D.; Yang, L.; Young, A.; Wang, M.; Nie, S. *Nat. Biotechnol.* **2008**, *26*, 83–90.

[319] Bartczak, D.; Kanaras, A. *Langmuir* **2011**, *27*, 10119–10123.

[320] Sperling, R.; Rivera, P.; Zhang, F.; Zanella, M.; Parak, W. *Chem. Soc. Rev.* **2008**, *37*, 1896–1908.

[321] Gregorczyk, K.; Knez, M. *Prog. Mater. Sci.* **2016**, *75*, 1–37.

[322] Biswas, A.; Bayer, I.; Biris, A.; Wang, T.; Dervishi, E.; Faupel, F. *Adv. Colloid Interface Sci.* **2012**, *170*, 2–27.

[323] Samuelson, L. *Materials Today* **2003**, *6*, 22–31.

[324] Agunloye, E.; Panariello, L.; Gavriilidis, A.; Mazzei, L. *Chem. Eng. Sci.* **2018**, *191*, 318–331.

[325] Turkevich, J.; Stevenson, P.; Hillier, J. *Disc. Faraday Soc.* **1951**, *11*, 55–75.

[326] Frens, G. *Nat. Phys. Sci.* **1973**, *241*, 20–22.

[327] Tran, M.; DePenning, R.; Turner, M.; Padalkar, S. *Mater. Res. Express* **2016**, *3*, 105027/1–105027/10.

[328] Martin, M.; Basham, J.; Chando, P.; Eah, S. *Langmuir* **2010**, *26*, 7410–7417.

[329] Grabar, K.; Freeman, R.; Hommer, M.; Natan, M. *Anal. Chem.* **1995**, *67*, 735–743.

[330] Wuelfing, W.; Gross, S.; Miles, D.; Murray, R. *J. Am. Chem. Soc.* **1998**, *120*, 12696–12697.

[331] Lewis, D.; Day, T.; MacPherson, J.; Pikramenou, Z. *Chem. Commun.* **2006**, 1433–1435.

[332] Chan, W.; Nie, S. *Science* **1998**, *281*, 2016–2018.

[333] Eck, W.; Craig, G.; Sigdel, A.; Ritter, G.; Old, L.; Tang, L.; Brennan, M.; Allen, P.; Mason, M. *ACS Nano* **2008**, *2*, 2263–2272.

[334] Jiang, K.; Smith, D.; Pinchuk, A. *J. Phys. Chem. C* **2013**, *117*, 27073–27080.

[335] Peterson, J.; Lu, Y.; Luais, E.; Lee, N.; Gooding, J. *Aust. J. Chem.* **2013**, *66*, 613–618.

[336] Wang, Y.; Laborda, E.; Plowman, B.; Tschulik, K.; Ward, K.; Palgrave, R.; Damm, C.; Compton, R. *Phys. Chem. Chem. Phys.* **2014**, *16*, 3200–3208.

[337] Ghosh, S.; Pal, T. *Chem Rev.* **2007**, *107*, 4797–4862.

[338] Willets, K.; Van Duyne, R. *Annu. Rev. Phys. Chem.* **2007**, *58*, 267–297.

[339] Saha, K.; Agasti, S.; Kim, C.; Li, X.; Rotello, V. *Chem. Rev.* **2012**, *112*, 2739–2779.

[340] Homola, J.; Yee, S.; Gauglitz, G. *Sens. Actuators, B* **1999**, *54*, 3–15.

[341] Anker, J.; Hall, W.; Lyandres, O.; Shah, N.; Zhao, J.; Van Duyne, R. *Nat. Mater.* **2008**, *7*, 442–453.

[342] Hu, M.; Chen, J.; Li, Z.; Au, L.; Hartland, G.; Li, X.; Marquez, M.; Xia, Y. *Chem. Soc. Rev.* **2006**, *35*, 1084–1094.

[343] Leu, C.; Chen, S.; Liu, F. *J. Am. Ceram. Soc.* **2010**, *93*, 3142–3147.

[344] Tadros, T.; Izquierdo, P.; Esquena, J.; Solans, C. *Adv. Colloid Interface Sci.* **2004**, *108–109*, 303–318.

[345] Pecora, R. *J. Nanopart. Res.* **2000**, *2*, 123–131.

[346] Bhattacharjee, S. *J. Control. Release* **2016**, *235*, 337–351.

[347] Doane, T.; Chuang, C.; Hill, R.; Burda, C. *Acc. Chem. Res.* **2012**, *45*, 317–326.

[348] Schneider, G.; Decher, G.; Nerambourg, N.; Praho, R.; Werts, M.; Blanchard-Desce, M. *Nano Lett.* **2006**, *6*, 530–536.

[349] Ma, Z.; LeBard, D.; Loverde, S.; Sharp, K.; Klein, M.; Discher, D.; Finkel, T. *PLOS One* **2014**, *9*, 1–10.

[350] Dobrovolskaia, M.; Patri, A.; Zheng, J.; Clogston, J.; Ayub, N.; Aggarwal, P.; Neun, B.; Hall, J.; McNeil, S. *Nanomedicine: NBM* **2009**, *5*, 106–117.

[351] Yen, H.; Hsu, S.; Tsai, C. *Small* **2009**, *5*, 1553–1561.

[352] Koch, F.; Möller, A.; Frenz, M.; Pieles, U.; Kuehni-Boghenbor, K.; Mevissen, M. *Toxicol. In Vitro* **2014**, *28*, 990–998.

[353] Murphy, C.; Gole, A.; Stone, J.; Sisco, P.; Alkilany, A.; Goldsmith, E.; Bazter, S. *Acc. Chem. Res.* **2008**, *41*, 1721–1730.

[354] Shenoy, D.; Fu, W.; Li, J.; Crasto, C.; Jones, G.; DiMarzio, C.; Sridhar, S.; Amiji, M. *Int. J. Nanomedicine* **2006**, *1*, 51–57.

[355] Cai, Q.; Kim, S.; Choi, K.; Kim, S.; Byun, S.; Kim, K.; Park, S.; Juhng, S.; Yoon, K. *Invest. Radiol.* **2007**, *42*, 797–806.

[356] Cho, W.; Cho, M.; Jeong, J.; Choi, M.; Cho, H.; Han, B.; Kim, S.; Kim, H.; Lim, Y.; Chung, B.; Jeong, J. *Toxicol. Appl. Pharmacol.* **2009**, *236*, 16–24.

[357] Zhang, X.; Wu, D.; Shen, X.; Liu, P.; Yang, N.; Zhao, B.; Zhang, H.; Sun, Y.; Zhang, L.; Fan, F. *Int. J. Nanomedicine* **2011**, *6*, 2071–2081.

[358] Enguita, M.; DeGregorio-Rocasolano, N.; Abad, A.; Trullas, R. *Mol. Pharmacol.* **2005**, *67*, 1237–1246.

[359] Atale, N.; Gupta, S.; Yadav, U.; Rani, V. *J. Microsc.* **2014**, *255*, 7–19.

[360] Novickij, V.; Dermol, J.; Grainys, A.; Kranjc, M.; Miklavčič, D. *PeerJ* **2017**, *5*, e3267.

[361] Zhou, J.; Sun, Y.; Zheng, Y.; Yu, C.; Lin, H.; Pang, J. *Acta Pharm.* **2017**, *67*, 557–567.

[362] Cabrera-Pérez, M.; Pham-The, H.; Fernández, M.; Hernández-Armengol, R.; Miranda-Pérez de Alejo, C.; Brito-Ferrer, Y. *Biopharm. Drug Dispos.* **2018**, *39*, 354–368.

[363] Oja, M.; Maran, U. *Eur. J. Pharm. Sci.* **2018**, *123*, 429–440.

[364] Li, X.; Mu, P.; Wen, J.; Deng, Y. *Sci. Rep.* **2017**, *7*, 1–10.

[365] Hofstetter, S.; Beck, A.; Trapp, S.; Buchholz, A. *J. Agric. Food Chem.* **2018**, *66*, 8687–8697.

[366] Malakoutikhah, M.; Teixidó, M.; Giralt, E. *J. Med. Chem.* **2008**, *51*, 4881–4889.

[367] Yoon, C.; Kim, S.; Shin, B.; Lee, K.; Yoo, S. *J. Biomol. Screen.* **2006**, *11*, 13–20.

[368] El-Sayed, I.; Huang, X.; El-Sayed, M. *Nano Lett.* **2005**, *5*, 829–834.

[369] Radde, R.; Bolmont, T.; Kaeser, S.; Coomaraswamy, J.; Lindau, D.; Stoltze, L.; Calhoun, M.; Jäggi, F.; Wolburg, H.; Gengler, S.; Haass, C.; Ghetti, B.; Czech, C.; Hölscher, C.; Mathews, P.; Jucker, M. *EMBO Rep.* **2006**, *7*, 940–946.

[370] Lee, S.; Varvel, N.; Konerth, M.; Xu, G.; Cardona, A.; Ransohoff, R.; Lamb, B. *Am. J. Pathol.* **2010**, *177*, 2549–2562.

[371] Vom Berg, J.; Prokop, S.; Miller, K.; Obst, J.; Kälin, R.; Lopategui-Cabezas, I.; Wegner, A.; Mair, F.; Schipke, C.; Peters, O.; Winter, Y.; Becher, B.; Heppner, F. *Nat. Med.* **2012**, *18*, 1812–1819.

[372] Biancalana, M.; Koide, S. *Biochim. Biophys. Acta* **2010**, *1804*, 1405–1412.

[373] Krebs, M.; Bromley, E.; Donald A. *J. Struct. Biol.* **2005**, *149*, 30–37.

[374] Wu, C.; Wang, Z.; Lei, H.; Duan, Y.; Bowers, M.; Shea, J. *J. Mol. Biol.* **2008**, *384*, 718–729.

[375] Khurana, R.; Coleman, C.; Ionescu-Zanetti, C.; Carter, S.; Krishna, V.; Grover, R.; Roy, R.; Singh, S. *J. Struct. Biol.* **2005**, *151*, 229–238.

[376] Groenning M.; Olsen, L.; van de Weert, M.; Flink, J.; Frokjaer, S.; Jørgensen, F. *J. Struct. Biol.* **2007**, *158*, 358–369.

[377] Groenning M.; Norrman, M.; Flink, J.; van de Weert, M.; Bukrinsky, J.; Schluckebier, G.; Frokjaer, S. *J. Struct. Biol.* **2007**, *159*, 483–497.

[378] Sabaté, R.; Lascu, I.; Saupe, S. *J. Struct. Biol.* **2008**, *162*, 387–396.

[379] Stsiapura, V.; Maskevich, A.; Kuzmitsky, V.; Turoverov, K.; Kruznetsova, I. *J. Phys. Chem. A* **2007**, *111*, 4829–4835.

[380] Stsiapura, V.; Maskevich, A.; Kuzmitsky, V.; Uversky, V.; Kruznetsova, I.; Turoverov, K. *J. Phys. Chem. B* **2008**, *112*, 15893–15902.

[381] Stsiapura, V.; Maskevich, A.; Tikhomirov, S.; Buganov, O. *J. Phys. Chem. A* **2010**, *114*, 8345–8350.

[382] Nilsson, K.; Åslund, A.; Berg, I.; Nyström, S.; Konradsson, P.; Herland, A.; Inganäs, O.; Stabo-Eeg, F.; Lindgren, M.; Westermark, G.; Lannfelt, L.; Nilsson, L.; Hammarström, P. *ACS Chem. Biol.* **2007**, *2*, 553–560.

[383] Hintersteiner, M.; Enz, A.; Frey, P.; Jaton, A.; Kinzy, W.; Kneuer, R.; Neumann, U.; Rudin, M.; Staufenbiel, M.; Stoeckli, M.; Wiederhold, K.; Gremlich, H. *Nat. Biotechnol.* **2005**, *23*, 577–583.

[384] Zhang, X.; Tian, Y.; Li, Z.; Tian, X.; Sun, H.; Liu, H.; Moore, A.; Ran, C. *J. Am. Chem. Soc.* **2013**, *135*, 16397–16409.

[385] White, D.; Buell, A.; Dobson, C.; Welland, M.; Knowles, T. *FEBS Lett.* **2009**, *583*, 2587–2592.

[386] Byeon, S.; Jin, Y.; Lim, S.; Lee, J.; Yoo, K.; Shin, K.; Oh, S.; Kim, D. *Bioorg. Med. Chem. Lett.* **2007**, *17*, 4022–4025.

[387] Chang, Y.; Jeong, J.; Lee, Y.; Kim, H.; Ganesha, R.; Kim, Y.; Lee, D.; Chung, J.; Lee, M. *Nucl. Med. Biol.* **2006**, *33*, 811–820.

[388] Li, G.; Xie, X. *Nature* **2011**, *475*, 308–315.

[389] Pawson, T.; Nash, P. *Science* **2003**, *300*, 445–452.

[390] Zhang, J.; Campbell, R.; Ting, A.; Tsien, R. *Nat. Rev. Mol. Cell Biol.* **2002**, *3*, 906–918.

[391] Tinnefeld, P.; Sauer, M. *Angew. Chem. Int. Ed.* **2005**, *44*, 2642–2671.

[392] Prescher, J.; Bertozzi, C. *Nat. Chem. Biol.* **2005**, *1*, 13–21.

[393] Truong, K.; Ikura, M. *Curr. Opin. Estruct. Biol.* **2001**, *11*, 573–578.

[394] Loving, G.; Sainlos, M.; Imperiali, B. *Trends Biotechnol.* **2010**, *28*, 73–83.

[395] Klymchenko, A.; Duportail, G.; Demchenko, A.; Mély, Y. *Biophys. J.* **2004**, *86*, 2929–2941.

[396] Chong, P. *Biochemistry* **1988**, *27*, 399–404.

[397] Rottenberg, H. *Biochemistry* **1992**, *31*, 9473–9481.

[398] Parisio, G.; Marini, A.; Biancardi, A.; Ferrarini, A.; Mennucci, B. *J. Phys. Chem. B* **2011**, *115*, 9980–9989.

[399] Nitz, M.; Mezo, A.; Ali, M.; Imperiali, B. *Chem. Commun.* **2002**, 1912–1913.

[400] Vazquez, M.; Rothman, D.; Imperiali, B. *Org. Biomol. Chem.* **2004**, *2*, 1965–1966.

[401] Vázquez, M.; Blanco, J.; Imperiali, B. *J. Am. Chem. Soc.* **2005**, *127*, 1300–1306.

[402] Venkatraman, P.; Nguyen, T.; Sainlos, M.; Bilsel, O.; Chitta, S.; Imperiali, B.; Stern, L. *Nat. Chem. Biol.* **2007**, *3*, 222–228.

[403] Banerjee, S.; Veale, E.; Phelan, C.; Murphy, S.; Tocci, G.; Gillespie, L.; Frimannsson, D.; Kelly, J.; Gunnlaugsson, T. *Chem. Soc. Rev.* **2013**, *42*, 1601–1618.

[404] Berque-Bestel, I.; Soulier, J.; Giner, M.; Rivail, L.; Langlois, M.; Sicsic, S. *J. Med. Chem.* **2003**, *46*, 2606–2620.

[405] Singh, S.; Singh, R. *J. Fluoresc.* **2007**, *17*, 139–148.

[406] Kolb, H.; Finn, M.; Sharpless, K. *Angew. Chem. Int. Ed.* **2001**, *40*, 2004–2021.

[407] Kolb, H.; Sharpless, K. *Drug Discov. Today* **2003**, *8*, 1128–1137.

[408] Wang, C.; Ikhlef, D.; Kahlal, S.; Saillard, J.; Astruc, D. *Coord. Chem. Rev.* **2016**, *316*, 1–20.

[409] Castro, V.; Rodríguez, H.; Albericio, F. *ACS Comb. Sci.* **2016**, *18*, 1–14.

[410] Hein, J.; Fokin, V. *Chem. Soc. Rev.* **2010**, *39*, 1302–1315.

[411] Worrell, B.; Malik, J.; Fokin, V. *Science* **2013**, *340*, 457–460.

[412] Moses, J.; Moorhouse, A. *Chem. Soc. Rev.* **2007**, *36*, 1249–1262.

[413] Iha, R.; Wooley, K.; Nyström, A.; Burke, D.; Kade, M.; Hawker, C. *Chem. Rev.* **2009**, *109*, 5620–5686.

[414] Thirumurugan, P.; Matosiuk, D.; Jozwiak, K. *Chem. Rev.* **2013**, *113*, 4905–4979.

[415] Baskin, J.; Bertozzi, C. *QSAR Comb. Sci.* **2007**, *26*, 1211–1219.

[416] Tron, G.; Pirali, T.; Billington, R.; Canonico, P.; Sorba, G.; Genazzani, A. *Med. Res. Rev.* **2008**, *28*, 278–308.

[417] Shalini, K.; Kumar, N.; Drabu, S.; Sharma P. *Belstein J. Org. Chem.* **2011**, *7*, 668–677.

[418] Aher, N.; Pore, V.; Mishra, N.; Kumar, A.; Shukla, P.; Sharma, A.; Bhat, M. *Bioorg. Med. Chem. Lett.* **2009**, *19*, 759–763.

[419] Holla, B.; Mahalinga, M.; Karthikeyan, M.; Poojary, B.; Akberali, P.; Kumari, N. *Eur. J. Med. Chem.* **2005**, *40*, 1173–1178.

[420] Gill, C.; Jadhav, G.; Shaikh, M.; Kale, R.; Ghawalkar, A.; Nagargoje, D.; Shiradkar, M. *Bioorg. Med. Chem. Lett.* **2008**, *18*, 6244–6247.

[421] Tian, L.; Sun, Y.; Li, H.; Zheng, X.; Cheng, Y.; Liu, X.; Qian, B. *J. Inorg. Biochem.* **2005**, *99*, 1646–1652.

[422] Kamal, A.; Shankaraiah, N.; Devaiah, V.; Reddy, K.; Juvekar, A.; Sen, S.; Kurian, N.; Zingde, S. *Bioorg. Med. Chem. Lett.* **2008**, *18*, 1468–1473.

[423] Singh, P.; Raj, R.; Kumar, V.; Mahajan, M.; Bedi, P.; Kaur, T.; Saxena, A. *Eur. J. Med. Chem.* **2012**, *47*, 594–600.

[424] Brik, A.; Alexandratos, J.; Lin, Y.; Elder, J.; Olson, A.; Wlodawer, A.; Goodsell, D.; Wong, C. *ChemBioChem* **2005**, *6*, 1167–1169.

[425] Giffin, M.; Heaslet, H.; Brik, A.; Lin, Y.; Cauvi, G.; Wong, C.; McRee, D.; Elder, J.; Stout, C.; Torbett, B. *J. Med. Chem.* **2008**, *51*, 6263–6270.

[426] Rida, S.; El-Hawash, S.; Fahmy, H.; Hazzaa, A.; El-Meligy, M. *Arch. Pharm. Res.* **2006**, *29*, 826–833.

[427] Da Silva, F.; De Souza, M.; Frugulhetti, I.; Castro, H.; Souza, S.; De Souza, T.; Rodrigues, D.; Souza, A.; Abreu, P.; Passamani, F.; Rodrigues, C.; Ferreira, V. *Eur. J. Med. Chem.* **2009**, *44*, 373–383.

[428] Jones, M.; Dyrager C.; Hoarau, M.; Korshavn, K.; Lim, M.; Ramamoorthy, A.; Storr, T. *J. Inorg. Biochem.* **2016**, *158*, 131–138.

[429] Jones, M.; Service, E.; Thompson, J.; Wang, M.; Kimsey, I.; DeToma, A.; Ramamoorthy, A.; Lim, M.; Storr, T. *Metallomics* **2012**, *4*, 910–920.

[430] Jiaranaikulwanitch, J.; Govitrapong, P.; Fokin, V.; Vajragupta, O. *Molecules* **2012**, *17*, 8312–8333.

[431] Farooq, S.; Shakeel-u-Rehman; Hussain, A.; Hamid, A.; Qurishi, M.; Koul, S. *Eur. J. Med. Chem.* **2014**, *84*, 545–554.

[432] Chen, X.; Jin, Q.; Wu, L.; Tung, C.; Tang, X. *Angew. Chem. Int. Ed.* **2014**, *53*, 12542–12547.

[433] Avila, B.; Roth, A.; Streets, H.; Dwyer, D.; Kurth, M. *Bioorg. Med. Chem. Lett.* **2012**, *22*, 5976–5978.

[434] Scapin, E.; Salbego, P.; Bender, C.; Meyer, A.; Pagliari, A.; Orlando, T.; Zimmer, G.; Frizzo, C.; Bonacorso, H.; Zanatta, N.; Martins, M. *Beilstein J. Org. Chem.* **2017**, *13*, 2396–2407.

[435] Kulikov, A.; Epishina, M.; Fershtat, L.; Romanova, A.; Makhova, N. *Tetrahedron Lett.* **2017**, *58*, 3998–4002.

[436] Lakshman, M.; Singh, M.; Parrish, D.; Balachandran, R.; Day, B. *J. Org. Chem.* **2010**, *75*, 2461–2473.

[437] Dabbagh, H.; Lwowski, W. *J. Org. Chem.* **2000**, *65*, 7284–7290.

[438] Cmoch, P.; Stefaniak, L.; Webb, G. *Magn. Reson. Chem.* **1997**, *35*, 237–242.

[439] Deev, S.; Shenkarev, Z.; Shestakova, T.; Chupakhin, O.; Rusinov, V.; Arseniev, A. *J. Org. Chem.* **2010**, *75*, 8487–8497.

[440] Cmoch, P.; Wiench, J.; Stefaniak, L.; Webb, G. *J. Mol. Struct.* **1999**, *510*, 165–178.

[441] Bock, V.; Hiemstra, H.; van Maarseveen, J. *Eur. J. Org. Chem.* **2006**, 51–68.

[442] Jin, L.; Romero, E.; Melaimi, M.; Bertrand, G. *J. Am. Chem. Soc.* **2015**, *137*, 15696–15698.

[443] Caselli, E.; Romagnoli, C.; Vahabi, R.; Taracila, M.; Bonomo, R.; Prati, F. *J. Med. Chem.* **2015**, *58*, 5445–5458.

[444] Hein, J.; Krasnova, L.; Iwasaki, M.; Fokin, V. *Org. Synth.* **2011**, *88*, 238–246.

[445] Amaro, M.; Birch, D.; Rolinski, O. *Phys. Chem. Chem. Phys.* **2011**, *13*, 6434–6441.

[446] Rolinski, O.; Amaro, M.; Birch, D. *Biosens. Bioelectron.* **2010**, *25*, 2249–2252.

[447] Zheng, X.; Xu, Z.; Li, H.; Fu, H. *RSC Adv.* **2018**, *8*, 15870–15875.

[448] Cao, K.; Elbel, K.; Cifelli, J.; Cirera, J.; Sigurdson, C.; Paesani, F.; Theodorakis, E.; Yang, J. *Sci. Rep.* **2018**, *8*, 6950.

[449] Yates, E.; Meisl, G.; Knowles, T.; Dobson, C. *J. Phys. Chem. B* **2016**, *120*, 2087–2094.